ASME
SETTING THE STANDARD
1880 2005

Transactions of the ASME, Journal of Turbomachinery (ISSN 0889-504X) is published quarterly (Jan., Apr., July, Oct.) by The American Society of Mechanical Engineers, Three Park Avenue, New York, NY 10016. Periodicals postage paid at New York, NY and additional mailing offices. POSTMASTER: Send address changes to Transactions of the ASME, Journal of Turbomachinery, c/o THE AMERICAN SOCIETY OF MECHANICAL ENGINEERS, 22 Law Drive, Box 2300, Fairfield, NJ 07007-2300. **CHANGES OF ADDRESS** must be received at Society headquarters seven weeks before they are to be effective. Please send old label and new address. **STATEMENT from By-Laws.** The Society shall not be responsible for statements or opinions advanced in papers or ... printed in its publications (B7.1, Par. 3).

Journal of Turbomachinery

Published Quarterly by ASME

VOLUME 127 • NUMBER 3 • JULY 2005

TECHNICAL PAPERS

(Contents continued on inside back cover)

This journal is printed on acid-free paper, which exceeds the ANSI Z39.48-1992 specification for permanence of paper and library materials. ♾™
♻ 85% recycled content, including 10% post-consumer fibers.

Journal of Turbomachinery **Volume 127, Number 3** **JULY 2005**

ERRATUM

The ASME Journal of Turbomachinery is abstracted and indexed in the following:

Aluminum Industry Abstracts, Aquatic Science and Fisheries Abstracts, Ceramics Abstracts, Chemical Abstracts, Civil Engineering Abstracts, Compendex (The electronic equivalent of Engineering Index), Corrosion Abstracts, Current Contents, Ei EncompassLit, Electronics & Communications Abstracts, Energy Information Abstracts, Engineered Materials Abstracts, Engineering Index, Environmental Science and Pollution Management, Excerpta Medica, Fluidex, Fuel and Energy Abstracts, INSPEC, Index to Scientific Reviews, Materials Science Citation Index, Mechanical & Transportation Engineering Abstracts, Mechanical Engineering Abstracts, METADEX (The electronic equivalent of Metals Abstracts and Alloys Index), Metals Abstracts, Oceanic Abstracts, Pollution Abstracts, Referativnyi Zhurnal, Shock & Vibration Digest, Steels Alert

Accelerating the Calibration of Multihole Pressure Probes by Applying Advanced Computational Methods

Arnoud R. C. Franken

Paul C. Ivey

School of Engineering,
Cranfield University,
Cranfield, Bedfordshire MK43 0AL,
United Kingdom

The miniature multihole pneumatic pressure probe is widely regarded as a cost-effective, easy-to-use, and accurate method for performing two- or three-dimensional flow field measurements in turbomachinery. The major downside to the use of these probes is that the influence of fabrication imperfections on probe characteristics necessitates an extensive and highly time-intensive and, therefore, costly calibration of each individual probe. Unless these probes can be fabricated to such standards that make individual probe calibrations superfluous, the only way to significantly reduce the time and costs associated with probe calibration is to shorten the calibration process. The latter is only possible if all essential information can be obtained from less calibration data. This paper describes an approach to the calibration of a series of multihole pressure probes in which advanced computational methods are used to make this possible. By exploiting the key features of a probe's characteristic this approach requires only a fraction of the size of a conventional calibration database for the accurate modeling of the relationships between port pressures and flow conditions. As a result, calibration time and costs can be reduced without the sacrifice of quality. [DOI: 10.1115/1.1791285]

1 Introduction

Miniature multihole pneumatic pressure probes have many advantages over other techniques for making two-dimensional (2D) or three-dimensional (3D) flow field measurements in turbomachinery. For example, pressure probes are of simple design, give pressure data, are usable at high temperatures, and do not require optical access to the machine they are used in. Of course, the use of pressure probes has disadvantages as well. From a measurement point of view, for example, pressure probes are an intrusive method, i.e., they have a disturbing effect on the flow they are placed in, resulting in contamination of the measurement results. Pressure probes, however, also have disadvantages from a user's point of view. In order to relate the port pressures to the flow field conditions the probe must be calibrated first in a known flow in a wind tunnel. When the probe is applied in an unknown flow the pressure data obtained is related to the calibration data through nondimensional pressure coefficients and the flow condition determined. This calibration process, however, is time-consuming and, therefore, costly, and must be performed for each individual probe due to the fact that these small probes are sensitive to construction imperfections. This is also a disadvantage from a business point of view. As a result of changing market dynamics, players in the gas turbine engine market are forced to continuously improve the performance of their products and/or services and to do so in ever shorter periods of time and at reduced cost. Even though pressure probes play only a miniscule role in the overall research and development (R&D) process of gas turbine engines they do not remain totally unaffected by these market pressures, resulting in depressed profit margins for their producers. If a producer of these probes wants to change the latter he must be able to offer a product that is either cheaper to produce and/or offers benefits for which customers are prepared to pay a premium [1]. This is not an easy task, especially when one keeps in mind that pressure probes used in turbomachinery testing and their general mode of operation have not changed much over the past decades. This problem can, however, be solved but it requires an innovative approach, in particular with regard to the calibration process.

Of course, taking time and costs out of miniature multihole pneumatic pressure probes will not make much of a difference to the pressure manufacturers of turbomachinery are under to improve performance while reducing time and costs. However, if it is possible to significantly lower the time and costs to get simple pressure probes ready for use in turbomachinery tests without sacrificing quality, which will be demonstrated in this paper, then it is not unthinkable that similar gains could not be achieved with other gas turbine instrumentation as well. That, in combination with more effective and efficient ways of performing turbomachinery testing, will make a difference.

2 Calibration

Background. Pneumatic pressure probes are based on the principle that the pressure recorded by an open ended tube placed in a flow will change when the angle of incidence is changed. If several of such tubes are arranged, each at a different angle, then differential pressures will be obtained that are larger than the pressure change for a single tube. By relating these differential pressures to flow conditions it becomes possible to deduce flow angles and Mach numbers from pressure measurements in unknown flow fields. There are two methods for determining these relationships and both require a calibration process in a wind tunnel. In the first method, the probe is placed in a known flow and is rotated until the direction-sensing pressures are nulled, i.e., the probe is aligned with the flow. In this way the flow direction can be directly deduced from the setting angles of the probe. Although this nulling method is very simple it is not preferable in turbomachinery testing due to factors such as space limitations, complexity, cost, safety, and system response. The second method, the nonnulling method, does not have these disadvantages. In this method, the probe remains fixed and pressure differences are recorded over a

Contributed by the International Gas Turbine Institute (IGTI) of THE AMERICAN SOCIETY OF MECHANICAL ENGINEERS for publication in the ASME JOURNAL OF TURBOMACHINERY. Paper presented at the International Gas Turbine and Aeroengine Congress and Exhibition, Vienna, Austria, June 13–17, 2004, Paper No. 2004-GT-53434. Manuscript received by IGTI, October 1, 2003; final revision, March 1, 2004. IGTI Review Chair: A. J. Strazisar.

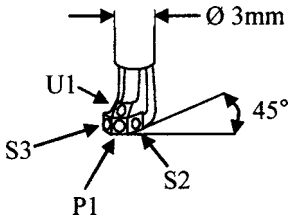

Fig. 1 Schematic of the four-hole cobra probe used in Project 1 and port numbering convention

range of yaw angle, pitch angle, and Mach number values which exceed the values expected in the unknown flow field to be measured. The step sizes used in this process, i.e., the calibration grid, are generally a result of a combination of factors:

- time and cost; if a probe is calibrated in both yaw angle and pitch angle then the number of calibration points will increased by a factor of 4 each time the angle increments are halved.
- accuracy of the data reduction technique used
- experience

The result of the above practice is a usually a large database consisting of flow parameter values and values for corresponding nondimensional pressure coefficients.

Multihole Pressure Probes. The focus in the research project described here was on the calibration of two types of four-hole cobra probes that were used in two other research projects for flow field measurements in Cranfield University's High-Speed Research Compressor (HSRC) (Bedfordshire, UK). The design of the probe used in Project 1 consists of a three-hole probe with a fourth pitch angle sensing port mounted above the yaw sensing holes (see Fig. 1) and was chosen for project-specific reasons.[2] In Project 2 six four-hole pyramid probes were used (see Fig. 2). The probes used in both these projects were calibrated using the non-nulling method, however, the probe used in Project 1 was calibrated in yaw angle, pitch angle, and Mach number while the probes used in Project 2 were only calibrated in yaw angle and Mach number (Table 1).

Calibration Coefficients. As has been mentioned before, nondimensional pressure coefficients are used to relate the flow conditions to the pressure differences measured. The formulation of these coefficients can differ slightly from probe type to probe

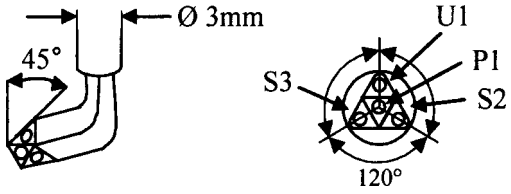

Fig. 2 Schematic of the four-hole pyramid probe used in Project 2 and port numbering convention

Table 1 Calibration points for the four-hole cobra probes used

	Cobra probe Project 1	Pyramid probes Project 2
Yaw angle [°]	−30°, −24°, −18°, −14°, −10°, −6°, −4°, −2°, 0°, 2°, 4°, 6°, 10°, 14°, 18°, 24°, 30°	−20°–+20°, 1° steps
Pitch angle [°]	−15°–+15°, 5° steps	0°
Mach number	0.2, 0.3, 0.4, 0.5, 0.6, 0.7	0.2, 0.3, 0.4, 0.5, 0.6, 0.7, 0.78
Total number of points	714	287

type and from application to application. However, in essence the dependent port pressure difference is used as the nominator, which is nondimensionalized by a dynamic pressure or probe indicated dynamic pressure as denominator. In this research project the following definitions were used for relating the pressures to the yaw and pitch angles:

$$C_{\text{yaw}} = \frac{S2 - S3}{P1 - \frac{1}{2}(S2 + S3)}, \tag{1}$$

$$C_{\text{pitch}} = \frac{P1 - U1}{P1 - \frac{1}{2}(S2 + S3)}. \tag{2}$$

An often-used coefficient for relating the measured pressures to the Mach number is the pseudo-Mach number, which can be defined as $C_{\text{Mach}} = P_{\text{avg}}/P1$ where $P_{\text{avg}} = 1/3(\text{S2} + \text{S3} + \text{U1})$[2,3]. This definition was, however, not used in this research project because it led to modeling difficulties, which will be discussed later. Due to that fact the following, more convenient definition was used:

$$C_{\text{Mach}} = \left(\frac{2}{\gamma - 1} \left[\left(\frac{P_{\text{avg}}}{P1} \right)^{-\gamma - 1/\gamma} - 1 \right] \right)^{1/2}. \tag{3}$$

with

$$P_{\text{avg}} = 1/3(S2 + S3 + U1), \qquad \gamma = 1.4 \ \text{(air)}. \tag{4}$$

Data Reduction Techniques. When a probe is used in turbomachinery testing, the pressure measurements yield C_{yaw}, C_{pitch}, and C_{Mach} values, which must be converted into the flow parameters of interest, yaw angle, pitch angle, and Mach number. Unfortunately, due to the fact, that each probe is essentially unique due to fabrication imperfections, it is unrealistic to derive the relationships between coefficients and flow conditions analytically. Therefore, these relationships are established empirically using data obtained during a calibration process. Several data reduction techniques are available to do this. However, given the range of yaw angles, pitch angles, and Mach numbers a probe is calibrated across the size of the calibration database needed to achieve a certain level of accuracy is not the same for each of these techniques as will be shown in the following sections.

Look-up Table and Interpolation Method. An often used data reduction technique is the ''look-up table and interpolation technique.'' As the name implies, a probe-specific look-up table consisting of flow parameter values and corresponding pressure coefficient values is used in combination with an interpolating technique to determine the flow conditions from the measured coefficients. This technique, however, has several drawbacks. First of all, it is a slow process because often fairly large databases have to be searched for each data point. Second, most interpolation schemes tend to take tabulated values as perfect [Ref. [4], pp. 105–128]. Unfortunately, neither the setting of yaw angle, pitch angle, nor Mach number during wind tunnel calibration is perfect nor are the pressure measurements. Although a detailed discussion of these and other imperfections and influences is beyond the scope of this paper, it is a fact that flow conditions around the probe tip, measurement uncertainties, and errors, etc., can and do lead to contamination of the measurements and thus inaccuracies. Third, commonly used interpolation techniques, for example bi- and tri-linear interpolation, have a linear nature. However, the trends through the tabulated points in a probe calibration dataset are not linear. Therefore, in order to minimize the interpolation error the database must contain many tabulated values. Furthermore, interpolation schemes are normally only used if not enough

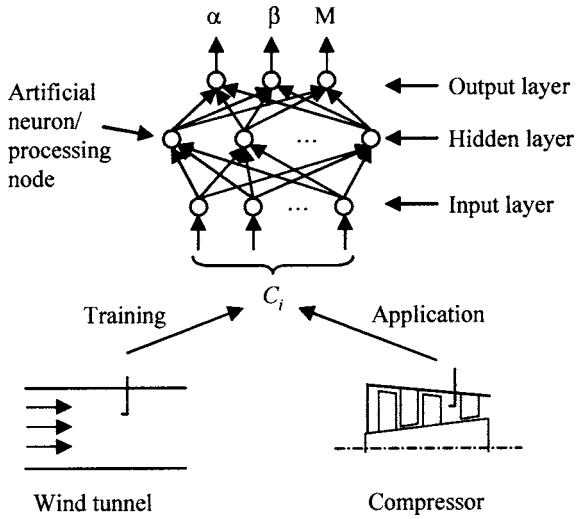

Fig. 3 Example of a neural network and its application

is known about the underlying function to compute values in an easier way. However, this is not the case with probe characteristics as will be shown later.

Rational Function Interpolation Method. Another data reduction technique, rational function interpolation, which is only closely related in name to the previous method, uses the relations between coefficients and flow parameters [see Eqs. (5) and (6), Ref. [4], pp. 105–128] to directly calculate the values of these parameters [5]. The problem with functions like Eqs. (5) and (6), however, is that the Mach number dependency of C_{yaw} and C_{pitch} is not taken into account. This means that this method will only give accurate results in situations where the fluctuations in Mach number are small.

$$\alpha = \frac{a_0 + a_1 C_{\text{yaw}} + a_2 C_{\text{pitch}} + \ldots}{1 + b_1 C_{\text{yaw}} + b_2 C_{\text{pitch}} + \ldots}, \tag{5}$$

$$\beta = \frac{c_0 + c_1 C_{\text{yaw}} + c_2 C_{\text{pitch}} + \ldots}{1 + d_1 C_{\text{yaw}} + d_2 C_{\text{pitch}} + \ldots}. \tag{6}$$

Polynomial Curve-Fit Method. As will be discussed in more detail in the next section, for a given Mach number the relation between the coefficients C_{yaw} and C_{pitch} and the yaw or pitch angle can graphically be represented by a smooth, continuous surface. This means that these relations can be modeled using a polynomial of the following general form:

$$z = a_0 + a_1 x + a_2 y + a_3 xy + a_4 x^2 + a_5 y^2 + \ldots . \tag{7}$$

An advantage of this method is not only that flow conditions can be computed directly from measured pressure coefficients it is also a smoothing process, i.e., the influence of errors, etc., in the data used to develop the polynomials is reduced.

Neural Networks. A final data reduction technique that will be mentioned here, and which is relatively recent, uses neural networks to directly compute the flow parameters from the measured pressure coefficients. Neural networks are nonlinear statistical models that are loosely based on the operation of biological neurons. Advocates of artificial neural networks believe that by emulating the basic principle of operation of biological neural networks with interlinked mathematical expressions and learning algorithms it becomes possible for a neural network to learn almost any underlying pattern in datasets, for example a probe's characteristics in a calibration dataset, [6,7] and use this information in applications (see for an example Fig. 3). A detailed discussion on how best to construct and train neural networks (i.e., storing the data pattern in the neural network) is beyond the scope of this paper. However, the following general comments will be made:

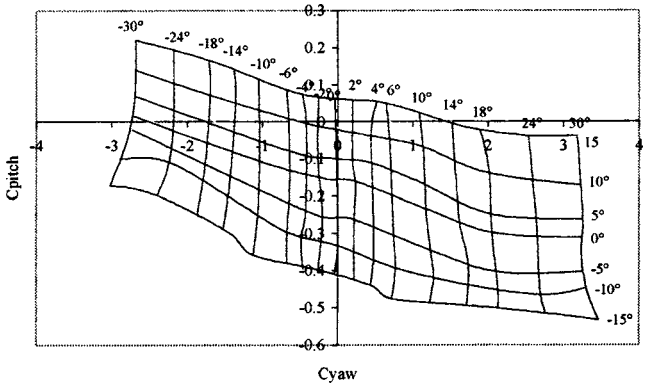

Fig. 4 Flow-direction map for the four-hole cobra probe at a Mach number of 0.4

- Neural networks should be one of many tools in a model builder's toolbox and not the only one.
- A thorough understanding of the process to be modeled is essential for effectively and efficiently constructing and training neural networks as well as appreciating the (un-) suitability of this tool.
- Finding the best neural network architecture and training the network can take a *very* long time, in particular when the previous comments are ignored.

A major drawback of many neural network models, in particular those whose architecture and operation resemble a biological neural network closest, is that they tend to be large, complex, and, therefore, difficult to understand. Furthermore, the development of those neural networks can take a very long time, which makes this method even more unattractive. However, as will be shown in later sections, neural networks are one of the few data reduction techniques that can compute the flow conditions directly from the measured pressure coefficients whilst taking into account the Mach number dependency of C_{yaw} and C_{pitch} by utilizing multiple layers of processing nodes (see Fig. 3). Furthermore, neural network types like polynomial neural networks, which emulate the operation of biological neural networks to a lesser extent, are simple in construction, quickly trained, and do not require large training datasets.

3 Analyzing Probe Calibration Graphs

Introduction. The multitude of available data reduction techniques, in particular those that allow the direct computation of flow conditions from measured pressure coefficients, demonstrates that it is possible to model the relationships in one way or another. This is an important observation because if it is possible to model the relationships, and thus understand them, it becomes possible to identify areas where the calibration procedure can be improved in order to reduce the time and costs associated with this procedure. The first step in this process is to determine the best way of modeling the relations between the pressure coefficients and flow conditions by analyzing probe calibration graphs.

Calibration Graphs. Figure 4 shows a flow-direction map for the four-hole cobra probe at a Mach number of 0.4. The nondimensional pressure coefficient C_{yaw} is plotted against C_{pitch} for all the yaw and pitch angles listed in Table 1. Several observations can be made from Fig. 4

- The grid is nonsymmetrical and nonlinear. This is due to nonuniformity in probe geometry. As a result of this, probes must always be calibrated for both negative and positive angles;
- C_{yaw} is less sensitive to pitch angle than C_{pitch} is to yaw angle.

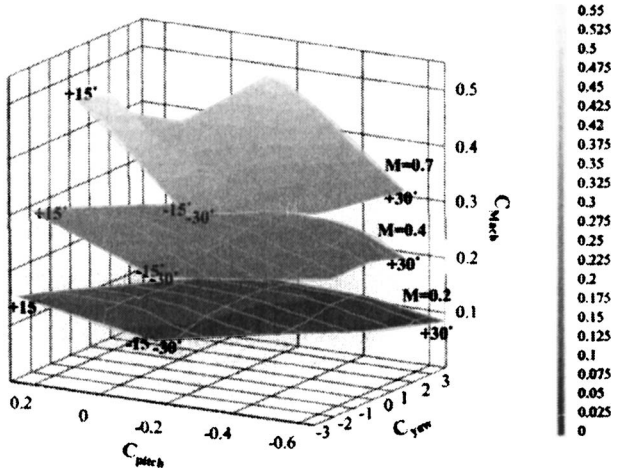

Fig. 5 The relations between C_{yaw}, C_{pitch}, and C_{Mach} for three constant Mach numbers

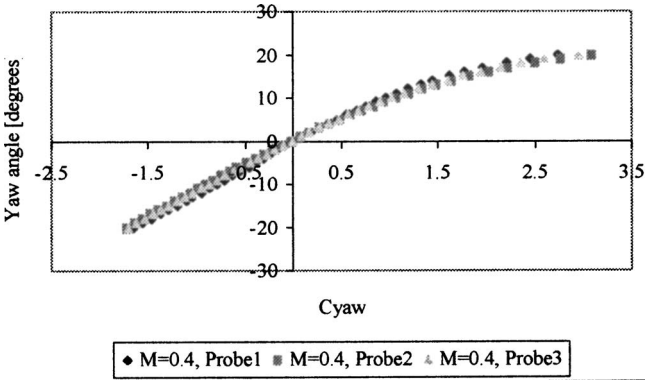

Fig. 6 Relation between C_{yaw} and yaw angle at $M=0.4$ for three of the six pyramid probes

As has been mentioned before, C_{yaw} and C_{pitch} are Mach number dependent. This dependency is clearly visible in Fig. 5 which shows the relations between C_{yaw}, C_{pitch}, and C_{Mach} for three Mach numbers and all yaw and pitch angles listed in Table 1 for the four-hole cobra probe. From this figure it is also clear that this dependency must be taken into account by any model used for direct computation of flow conditions over a large Mach number range if high approximation accuracy is required.

As is clearly visible in Fig. 5, the relations between the pressure coefficients C_{yaw} and C_{pitch} and the flow angles are smooth, continuous surfaces. This means that for constant Mach numbers the yaw and pitch angles can be approximated by polynomials of the following general form:

$$\text{yaw} = a_0 + a_1 C_{yaw} + a_2 C_{pitch} + a_3 C_{yaw} C_{pitch} + \ldots, \quad (8)$$

$$\text{pitch} = b_0 + b_1 C_{yaw} + b_2 C_{pitch} + b_3 C_{yaw} C_{pitch} + \ldots. \quad (9)$$

Analysis of the calibration data of the four-hole cobra probe revealed that these polynomials must be of the fourth degree. Of course, these models do not take into account the Mach number dependency of C_{yaw} and C_{pitch}. To do that models of the following form are required:

$$\text{yaw} = a_0 + a_1 C_{yaw}(M) + a_2 C_{pitch}(M) + \ldots, \quad (10)$$

$$\text{pitch} = b_0 + b_1 C_{yaw}(M) + b_2 C_{pitch}(M) + \ldots. \quad (11)$$

Unfortunately, after flow field measurements there is no Mach number information available only pressure information. Furthermore, Fig. 5 clearly demonstrates that this Mach number information cannot be obtained from just C_{Mach} because this pressure coefficient is highly sensitive to both yaw and pitch angle. The solution to this problem is found by analyzing the changes in C_{yaw} and C_{pitch} over the entire range of yaw angles, pitch angles, and Mach numbers. This analysis showed that these changes can be modeled too with polynomials of the fourth degree. How this is done and how these models are linked into those for approximating the yaw and pitch angles will be shown in the next section.

As was stated in the introduction, miniaturized multihole pressure probes are sensitive to fabrication imperfections which make each probe essentially unique and necessitate costly calibrations for individual probes. However, as Fig. 6 clearly shows, although each probe has a unique characteristic due to fabrication, all characteristics are similar. This key feature will be fully exploited in the next section.

4 Applying Advanced Computational Methods

Modeling Probe Characteristics. The general strategy followed for the development of the yaw angle, pitch angle, and Mach number models consists of several steps and is shown in Fig. 7. The first step is the collection and preparation of the data, i.e., analyzing data quality and converting the pressure data obtained during the calibration of a probe into nondimensional pressure coefficients, so that the end result is a table consisting of flow angle and Mach number values and corresponding C_{yaw}, C_{pitch}, and C_{Mach} values. Due to space limitations the execution of the next four stages will only be described in detail for the four-hole cobra probe yaw angle model.

As was mentioned in the previous section, in order to obtain a yaw angle model that accurately approximates the relation between the yaw angle and the nondimensional pressure coefficients C_{yaw} and C_{pitch} over the entire Mach number range it is necessary to incorporate the Mach number dependency of these coefficients in the model. The latter can be achieved by modeling the changes in C_{yaw} and C_{pitch} over the entire range of yaw angles, pitch angles, and Mach numbers. The approach taken to achieve this was to choose the C_{yaw} and C_{pitch} surfaces at $M=0.4$ as reference surfaces and to transform all C_{yaw} and C_{pitch} values in the calibration dataset to these reference surfaces. As was mentioned in the previous section, analysis of the data showed that this can be done by means of fourth degree polynomial models

$$C_{yaw,0.4} = a_0 + a_1 C_{yaw} + a_2 C_{pitch} + a_3 C_{Mach} + \ldots, \quad (12)$$

$$C_{pitch,0.4} = b_0 + b_1 C_{yaw} + b_2 C_{pitch} + b_3 C_{Mach} + \ldots. \quad (13)$$

As is shown in Fig. 7, the second step in the model-building process is determining useful subsets of input variables. For both the $C_{yaw,0.4}$ and $C_{pitch,0.4}$ models the entire set contains 35 possible input variables. Normal practice is to select subsets of input variables from this set and use these sets in steps 3 and 4 until a subset is found that leads to the development of an acceptable model. An

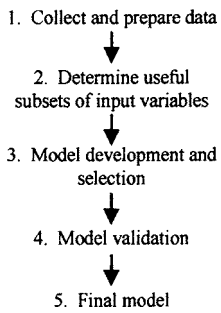

Fig. 7 Model-building strategy Ref. [9]

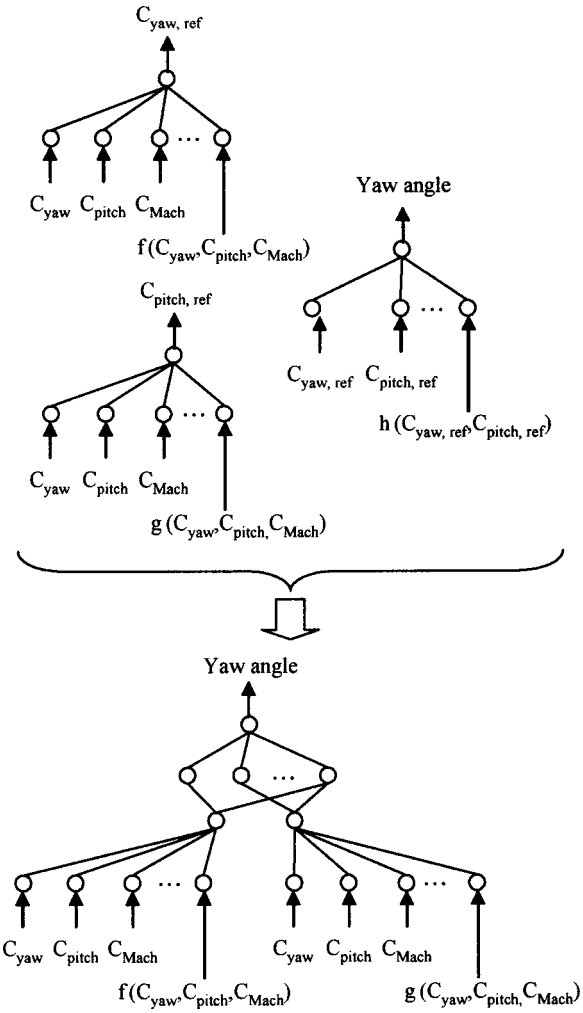

Fig. 8 Yaw angle model for the four-hole cobra probe

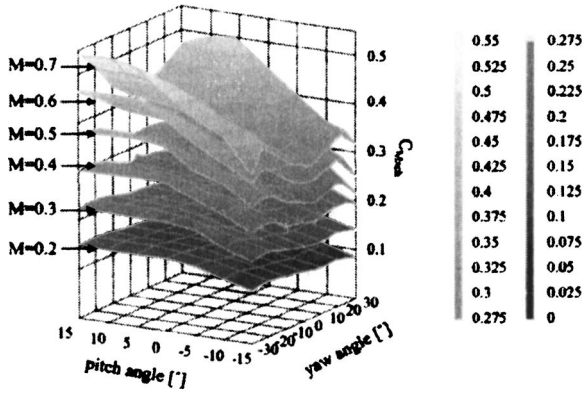

Fig. 9 C_{Mach} as function of yaw angle, pitch angle, and Mach number

algorithm that allows the automation of this process is the *Least Angle Regression* algorithm (see Refs. [8,9] for a detailed discussion of this algorithm). The yaw angle model is developed along the same lines. When these models are transformed into polynomial neural networks and combined then the end result will look like the multilayer polynomial neural network shown in Fig. 8.

The pitch angle model for the cobra probe is developed in the same way as the one for the yaw angle. The Mach number model for the cobra probe, however, must be developed in a different way. As can be clearly seen in Fig. 9, the difficulty with modeling the Mach number is that C_{Mach} values overlap each other, i.e., there are no unique combinations of C_{Mach}, yaw angle (or C_{yaw}) and pitch angle (or C_{pitch}) for each Mach number. However, for each C_{Mach} value there is a unique combination of yaw angle (or C_{yaw}), pitch angle (or C_{pitch}) and Mach number. The surfaces in Fig. 9 show these combinations graphically.

Data analysis shows that the C_{Mach} surfaces in Fig. 9 can be approximated by a fourth degree polynomial with terms consisting of C_{yaw}, C_{pitch}, and/or Mach number. This means that when the model has been developed and is applied the Mach number is found iteratively by comparing the C_{Mach} model value with the measured value.

The accuracy of this Mach number model, as well as those of the yaw and pitch angle models, will be discussed later in this paper.

Minimum Calibration Grid. The yaw angle, pitch angle, and Mach number models described above were developed using a probe calibration database designed for use with the "look-up table and linear interpolation" data reduction technique. However, as was mentioned before, when this technique is used the calibration database must contain many tabulated values in order to achieve high accuracy. Higher-order polynomials, however, are far better suited to accurately approximate curved trends. Therefore, it is reasonabe to assume that higher-order polynomials will require fewer data points to accurately approximate such trends than a linear interpolation technique, in particular when the nature of the trend is known. However, in contrast to signal processing, in this case there is no theorem like Nyquist's sampling theorem[1] available for determining the minimum number of points and their position needed for the development of an accurate multidimensional polynomial model. The solution to this problem is, however, not found in the field of sampling but in the field of numerical integration.

Many problems in engineering do not have an analytical solution but can be described by ordinary differential equations and boundary conditions (e.g., initial values). By applying numerical integration methods approximations of the solution can be obtained. In the basic form of these methods, set step sizes determine approximation accuracy. However, in more advanced methods accuracy is set and step sizes are locally adapted. A well-known method that uses adaptive step size control is the Runge–Kutta–Fehlberg (RKF) method [Ref. [4], pp. 707–752].

When the RKF method is applied to the relation between C_{yaw} and yaw angle per pitch angle and Mach number or the relation between C_{pitch} and pitch angle per yaw angle and Mach number, using the data in the calibration database, then the objective is of course not obtaining the solutions, which are already available in the form of polynomial models, but the necessary step sizes computed for a set accuracy. By applying this method to every line in the calibration grid, of which the calibration points listed in Table 1 represent the intersections, and collating the results, a picture of the minimum calibration grid for the probe type under investigation will emerge. The intersections of the trend lines through these results form the calibration points of the minimum calibration grid. This was done for the cobra probe and the six pyramid probes. The results for the former are shown in Fig. 10 while the results for the pyramid probes are listed in Table 2. If these results are compared with the grids listed in Table 1 then it is easily calculated that the minimum calibration grid for the four-hole cobra probe leads to a 64% lower calibration data requirement and in the case of the pyramid probes even 80%.

Validating the Minimum Calibration Grids. In order to validate the minimum calibration grids for the four-hole cobra

[1]The Nyquist sampling theorem states that a continuous signal can be represented by, and reconstituted from, a set of sample values providing that the number of samples per second is at least twice the highest frequency present in the signal.

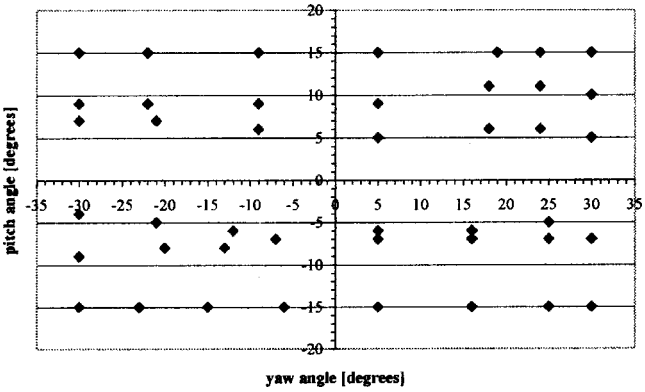

Fig. 10 The minimum calibration points for the four-hole cobra probe, consisting of 43 points per Mach number

probe and pyramid probes so called "minimum datasets" (MDS) were created from the original datasets (FDS) using the grids shown in Fig. 10 and listed in Table 2. These datasets were used to develop yaw angle, pitch angle, and Mach number models for the four-hole cobra probe, and yaw angle and Mach number models for three of the six pyramid probes. Next, the performance of these minimum dataset models was compared with those based on the full datasets. As can be seen in Table 3 the difference between the accuracy of the models based on the minimum and original calibration grids is negligible, which demonstrates that the minimum grids are valid. Furthermore, the standard deviations of the differences between model values and measured values are of the same magnitude as the measurement uncertainties, [2] which shows that the models are accurate.

5 Conclusions

Miniature multihole pneumatic pressure probes are widely regarded as an easy-to-use, cost-effective, and accurate method for performing 2D or 3D flow field measurements. However, due to these probes' sensitivity to fabrication imperfections it is necessary to calibrate each probe individually in order to achieve a high accuracy, which is time-consuming and costly. The cause for a significant part of this expense can be traced back to the calibration database and the data reduction technique used. The research project described in this paper has shown that close analysis and the application of advanced computational methods to the calibration process can significantly reduce the total expense by:

- identifying the essential number and position of calibration points.
- using knowledge gained with the first probe to effectively and efficiently calibrate other probes in the series.
- effectively and efficiently modeling the relations between flow conditions and measured pressures for fast and direct computation of flow conditions.
- by consistently fabricating miniature probes reducing the calibration need.

Table 2 Minimum calibration points for all six pyramid probes

	Pyramid probes
Yaw angle [°]	−20, −12, −3, 3, 7, 12, 18, 20
Mach number	0.2, 0.3, 0.4, 0.5, 0.6, 0.7, 0.78
Total number of points	56

Table 3 Standard deviations of the differences between model values and measured values

	Cobra probe		
	α [°]	β [°]	M
FDS	0.4	1	0.01
MDS	0.4	1	0.01

	Pyramid probes					
	#1		#2		#3	
	α	M	α	M	α	M
FDS	0.2	0.007	0.1	0.01	0.1	0.004
MDS	0.2	0.007	0.1	0.006	0.2	0.005

Acknowledgments

The authors would like to thank S. Coldrick and D. A. Lippett for providing the probe calibration datasets used in this research project.

Nomenclature

C = nondimensional pressure coefficient
FDS = full dataset
M = mach number
MDS = minimum dataset
P = pressure (Pa)
P1 = probe center port (Pa)
S2 = probe left-side port (Pa)
S3 = probe right-side port (Pa)
U1 = probe upper port (Pa)
a_i, b_i, c_i = polynomial coefficients
α = yaw angle (deg)
β = pitch angle (deg)
γ = ratio of specific heats

Subscripts

Mach = Mach number
Pitch = pitch angle
Yaw = yaw angle

References

[1] Christensen, C. M., and Raynor, M. E., 2003, *The Innovator's Solution*, Harvard Business School Press, Boston, MA.
[2] Coldrick, S., Ivey, P., and Wells, R., 2003, "Considerations for Using 3D Pneumatic Probes in High Speed Axial Compressors," ASME Paper No. GT-2002-30045.
[3] Dominy, R. G., and Hodson, H. P., 1993, "An Investigation of Factors Influencing the Calibration of Five-Hole Probes for Three-Dimensional Flow Measurements," ASME J. Turbomach., **115**, 513–519.
[4] Press, W. H., 1993, *Numerical Recipes in C: The Art of Scientific Computing* Cambridge University Press, UK, pp. 105–128; 707–752.
[5] Morrison, G. L., Schobeiri, M. T., and Pappu, K. R., 1988, "Five-Hole Pressure Probe Analysis Technique," Flow Meas. Instrum., **9**, 153–158.
[6] Fan, H.-Y., Lu, W., and Xi, G., 2003, "An Improved Neural-Network-Based Calibration Method for Aerodynamic Pressure Probes," ASME J. Fluids Eng., **125**, 113–120.
[7] Rediniotis, O. K., and Chrysanthakopoulos, G., 1998, "Application of Neural Networks and Fuzzy Logic to the Calibration of the Seven-Hole Probe," ASME J. Fluids Eng., **120**, 95–101.
[8] Neter, J., Kutner, M. H., Nachtsheim, C. J., and Wasserman, W., 1996, *Applied Linear Statistical Models*, 4th ed., McGraw-Hill, New York.
[9] Efron, B., Hastie, T., Johnstone, I., and Tibshirani, R., 2003, *Least Angle Regression*, Stanford University, Stanford, CA.

Numerical Simulation of Unsteady Wake/Blade Interactions in Low-Pressure Turbine Flows Using an Intermittency Transport Equation

Y. B. Suzen
Assistant Research Professor

P. G. Huang
Professor

Department of Mechanical Engineering,
University of Kentucky,
151 RGAN Building,
Lexington, KY 40506-0503

An extensive computational investigation of the effects of unsteady wake/blade interactions on transition and separation in low-pressure turbines has been performed by numerical simulations of two recent sets of experiments using an intermittency transport equation. The experiments considered have been performed by Kaszeta and Simon and Stieger in order to investigate the effects of periodically passing wakes on laminar-to-turbulent transition and separation in low-pressure turbines. The test sections were designed to simulate unsteady wakes in turbine engines for studying their effects on boundary layers and separated flow regions over the suction surface. The numerical simulations of the unsteady wake/blade interaction experiments have been performed using an intermittency transport model. The intermittent behavior of the transitional flows is taken into account and incorporated into computations by modifying the eddy viscosity, with the intermittency factor. Turbulent quantities are predicted by using Menter's two-equation turbulence model (SST). The intermittency factor is obtained from the transport equation model, which can produce both the experimentally observed streamwise variation of intermittency and a realistic profile in the cross-stream direction. Computational results are compared to the experiments. Overall, general trends are captured and prediction capabilities of the intermittency transport model for simulations of unsteady wake/blade interaction flowfields are demonstrated. [DOI: 10.1115/1.1860375]

1 Introduction

Experimental results from jet engine tests have indicated that the unsteady wake/blade interactions and flow separation on the suction side of the blades can significantly affect the turbine stage efficiency. Due to high temperatures and low density, these effects become more pronounced in low-pressure turbine stages. At high-altitude cruise conditions, the operating Reynolds number of a low-pressure turbine in an aircraft engine can drop below 25,000. At such low Reynolds numbers, the boundary layers on the blades are largely laminar and their development is very sensitive to unsteady disturbances. The flow is susceptible to separation over the trailing half of the blade suction surface. Due to the flow separation, nearly a 300% rise in the loss coefficient has been observed in experiments when the Reynolds number drops below 200,000 [1]. The size of the separation bubble and onset location of transition is largely impacted by the turbulence levels and other free-stream unsteadiness.

The flow field in a turbine engine is essentially unsteady. The rotor rotates relative to the stator, moving turbine blades through the turbulent wakes of upstream stators. Flow over a turbine blade row is strongly affected by periodic passing of the wakes of the upstream row. These turbulent wakes create a series of turbulent spots on the turbine blade. The turbulent spots merge and form turbulent strips, which travel along the surface of the blade. Between these turbulent wakes, flow separation can occur and laminar-to-turbulent transition can take place over the separation region. When bypass transition occurs flow separation is suppressed. At a given instant, the flow on a turbine blade surface may include laminar flow, turbulent strips due to passing wakes, flow separation, separated flow transition, bypass transition of an attached boundary layer, and reattachment of a separated flow [2]. High levels of disturbance and periodic unsteadiness of passing wakes strongly affect transition from laminar-to-turbulent flow and separation, which is the main source of loss generation.

In order to investigate the effects of unsteadiness on turbomachinery flows, several experimental studies have been performed. These studies were performed using wake simulators or using rotating rigs. Examples of studies conducted using rotating rigs are reported by Halstead et al. [3], Tiedemann and Kost [4], Kost et al. [5], and Solomon [6]. Several researchers have used wake simulators instead of rotating rigs because the measurements of boundary layer profiles in rotating turbomachines is difficult. Generally the wake simulators involve passing of solid rods in front of a flat plate or turbine passage simulator to simulate the wakes of an actual series of stator vanes. Examples of experiments conducted using wake simulators are reported by Schobeiri and Pappu [7], Schobeiri et al. [8], Stadtmuller et al. [9], Kaszeta and Simon [10], and Stieger [11].

Along with the experimental investigations, several computational efforts, including Reynolds averaged Navier-Stokes (RANS) equations, large eddy simulations (LES), and direct numerical simulations (DNS) have been undertaken. Examples of these efforts are reported by Dorney et al. [12,13], Arnone et al. [14], Fan and Lakshminarayana [15], Eulitz and Engel [16], Kim and Crawford [17], and Wu and Durbin [18].

In order to accurately model transitional flows under diverse conditions encountered in turbomachinery applications, Suzen and Huang [19] developed an intermittency transport model. The pre-

Contributed by the International Gas Turbine Institute (IGTI) of THE AMERICAN SOCIETY OF MECHANICAL ENGINEERS for publication in the ASME JOURNAL OF TURBOMACHINERY. Paper presented at the International Gas Turbine and Aeroengine Congress and Exhibition, Vienna, Austria, June 13 - 17, 2004, Paper No. 2004-GT-53630. Manuscript received by IGTI, October 1, 2003; final revision, March 1, 2004. IGTI Review Chair: A. J. Strazisar.

dicting capabilities of this model have been validated against T3-series experiments of Savill [20,21], low-pressure turbine experiments of Simon et al. [22], and separated and transitional boundary layer experiments of Volino and Hultgren [23] (Suzen and Huang [19,24] and Suzen et al. [25–27]). In addition to these experiments the model has been validated against the low-pressure turbine cascade experiments of Lake et al. [28,29] and Huang et al. [30] and blade passage experiments of Volino [31] (Suzen et al. [32]). These experiments represent a wide range of steady-state operating conditions for low-pressure turbines and include effects of pressure gradients, free-stream turbulence intensities, Reynolds numbers, and flow separation. A recent comprehensive review of the model and the test cases used in its validation are given by Suzen and Huang [33].

In this paper we concentrate on extension of the predicting capabilities of the intermittency transport model into unsteady wake/blade interaction flow fields. An extensive computational investigation of the effects of unsteady wake/blade interactions on transition and separation in low-pressure turbines has been performed by numerical simulations of two recent sets of experiments using the intermittency transport equation. The experiments considered have been conducted by Kaszeta and Simon [10] and Stieger [11]. These experiments have been performed to investigate the effects of periodically passing wakes on laminar-to-turbulent transition and separation in low-pressure turbines. The test sections were designed to simulate unsteady wakes in turbine engines for studying their effects on boundary layers and separated flow regions over the suction surface.

A summary of the experiments are given in Sec. 2. In Sec. 3, the intermittency transport model is presented, and implementation of the model and the empirical correlations employed for the onset of transition are described. In Sec. 4, details of numerical simulations are given. In Sec. 5, the predictions of the new intermittency model are compared against the experimental data. Conclusions are provided in Sec. 6.

2 Unsteady Wake/Blade Interaction Experiments

In this paper, we concentrate on simulations of two sets of recent unsteady wake/blade interaction experiments conducted by Kaszeta et al. [2,34] and Stieger [11]. These experiments have been performed to investigate the effects of unsteady wake passing on transition and separation in low-pressure turbines [10,35]. The details of the experiments are given in the following sections.

2.1 Experiments of Kaszeta et al. [2,34]. In order to investigate the effects of periodically passing wakes on laminar-to-turbulent transition and separation in a low-pressure turbine passage, Kaszeta et al. [2,34] conducted a number of experiments at the University of Minnesota. The test section was designed to simulate unsteady wakes in turbine engines for studying their effects on boundary layers and separated flow regions over the suction surface. The turbine blade passage simulator used in the experiment was a modified version of the simulator used in Qiu and Simon [36] and Simon et al. [22] consisting of a single suction surface and a single pressure surface to simulate a single PAK-B turbine blade passage. In order to produce the periodic wakes upstream of the turbine blade leading edge, a wake generator was added. The wake generator consisted of a moving sled assembly, which contained a series of 0.635 cm steel rods to simulate wakes emerging from upstream turbine stages in a LPT. A cross-sectional view of the experimental facility is shown in Fig. 1. The spacing between rods and between blade surfaces is 80% of the blade chord length. The rods are located 12 rod diameters upstream from the leading edges. Details of the blade passage geometry are shown in Fig. 2.

The wake generator is run to create a series of wakes. The sled is moved in the direction shown in Fig. 1 at a constant speed carrying the rods through the flow upstream of the blade passage. Once all the rods pass through, the sled is pulled back to its original position and the movement is repeated. Each pass of the sled generates a series of wakes (four wakes per sled passing) and each series of wakes is decomposed into individual wakes from signals provided from a photogate mounted on the wake generator that signals when each rod enters the flow upstream of the turbine passage. Each wake is then further decomposed into 45 segments, each representing 2.22% of the wake's signal. The segments from each of the wakes are then ensemble averaged to obtain the phase averaged quantities.

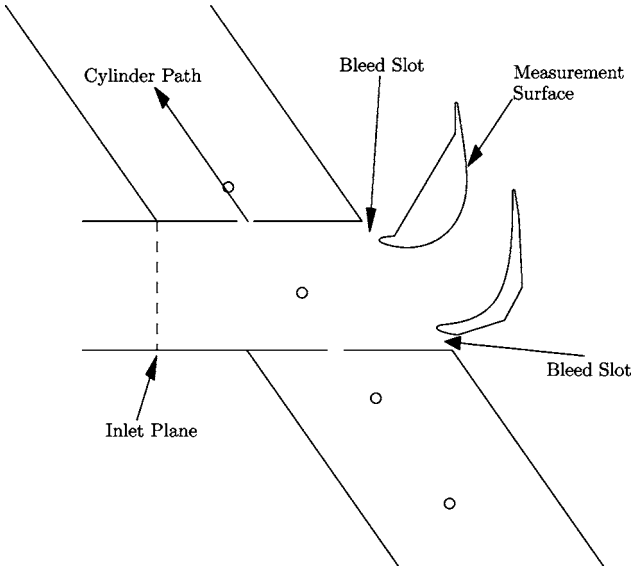

Fig. 1 Cross-sectional view of the wake generator passage [2]

Detailed time-resolved and phase-averaged wall normal profiles of velocity, turbulence intensity, and intermittency at 12 streamwise locations on the suction surface of the blade were measured using single-wire, thermal anemometry techniques. Figure 3 shows the locations of these stations on the blade surface. The corresponding s/L_{ss} values are given in Table 1.

The data collected at these stations were compared against steady-state wake-free data collected on the same geometry to identify the effects of wakes on laminar-to-turbulent transition and separation. In the experiment, the Reynolds number based on the suction surface length and exit velocity is 50,000 ($\sim$22,875 based on inlet velocity and chord length) and the free-stream turbulence intensity is 2.5%. The initial setup has the rod spacing equal to the blade pitch ($L_r/P=1$). In order to examine the effects of reduced wake frequency, additional experiments were performed increasing the rod spacing to twice the blade pitch ($L_r/P=2$), while keeping everything else the same. In addition, effects of elevated approach flow turbulence intensity are also investigated [34,37–39].

From the analysis of the collected data, it was concluded that the primary effects of wakes were an overall increase in turbulence levels due to turbulence generated by the wakes and the imposition of temporal changes in free-stream velocity. The imposition of the temporal changes in free-stream velocity affect the instantaneous velocity profiles by changing angle of attack of the approach flow. Due to these effects on the mean flow and turbulence a change of location of the separation point was observed. When the wake-passing frequency was decreased, the boundary layer had much longer period to recover from the wakes' perturbations and the boundary layer assumed a state that was more like that of the wake-free, steady flow case. In the reduced wake frequency case, the flow separated upstream of the separation location for the higher frequency case. Moreover, a significantly thicker separation bubble than the one observed in the high-

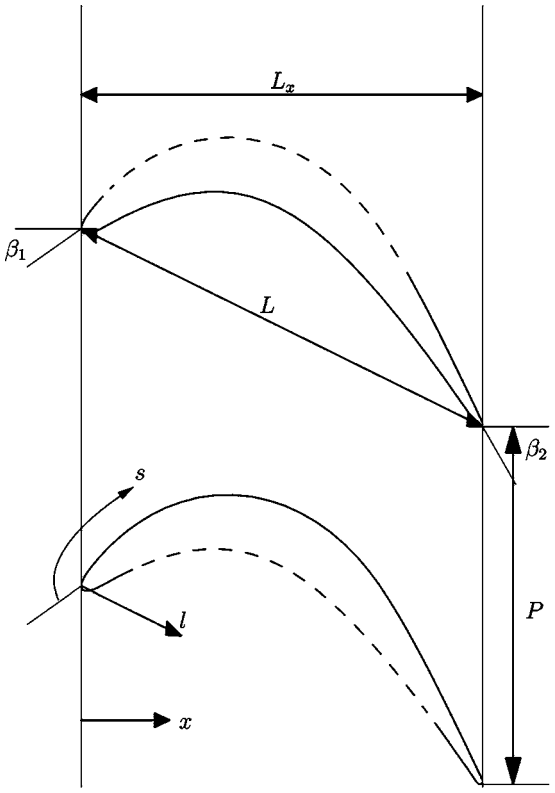

Chord length, L:	114.3 mm
Axial chord length, L_x:	103.57 mm
Suction surface length, L_{ss}:	152.76 mm
Axial chord to chord ratio, L_x/L:	0.906
Pitch to chord ratio, P/L:	0.8
Aspect ratio (span/chord), L_z/L:	6.0
Blade inlet angle, β_1:	35°
Blade outlet angle, β_2:	−60°
Rod velocity to axial velocity ratio, u_r/u_x:	~ 0.70
Rod spacing to airfoil pitch ratio, L_r/P:	1.0

Fig. 2 PAK-B airfoil geometry [2]

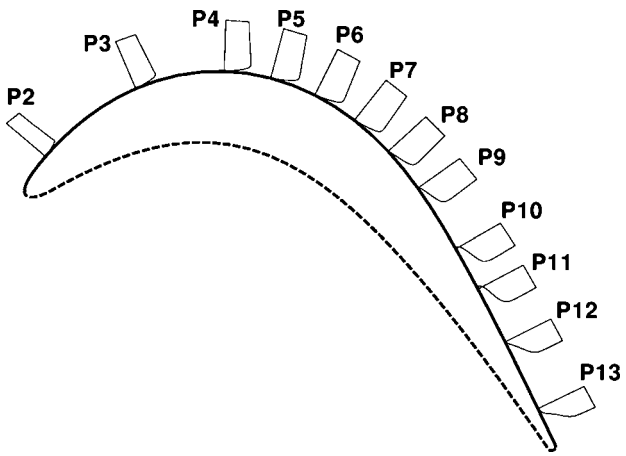

Fig. 3 Locations of experimental measurement stations on PAK-B Blade

Table 1 Measurement stations on the suction surface

Station	P02	P03	P04	P05
$s/L_{ss}(\%)$	5.19	19.78	31.36	37.35
Station	P06	P07	P08	P09
$s/L_{ss}(\%)$	43.34	49.33	55.3	61.32
Station	P10	P11	P12	P13
$s/L_{ss}(\%)$	70.31	76.11	84.00	93.49

frequency case developed. These changes were due to the increased boundary layer growth that occurred in the longer period between passing wakes.

The detailed velocity profile data and the simplified turbine passage geometry of this study allow using these data for computer simulations. These data are valuable tools for the development of turbulence and transition models for turbine flows.

2.2 Experiments of Stieger [11]. The second set of experiments performed by Stieger [11] involved T106 turbine blade cascade subjected to wake passing from a moving bar wake generator. These experiments were conducted in order to investigate the interaction of a convected wake and a separation bubble on the rear suction surface of a highly loaded low-pressure turbine blade. The test facility is shown in Fig. 4.

The wakes shed from upstream blade rows in a real turbine are simulated by an array of cylindrical bars moving across the inlet plane of the cascade. The bars are held between two nylon belts that run on two pulley sets. The configuration of the bar passing cascade required that the top and bottom walls of the cascade be slotted to permit the passage of wake generator bars. These slots provide two additional passages to the flow. The slot on the top wall does not present a problem, as it requires the flow to change direction, however, the slot on the bottom wall was more closely aligned with the flow. Moreover, the pressure gradient due to the incidence of the cascade forces flow out of the bottom slot. The result is an effective increase of incidence on the cascade and a nonuniform inlet static pressure. In order to minimize this problem and maintain inlet periodicity, an additional dummy passage was created on the suction side of the first airfoil in the cascade, which is the lowermost blade in Fig. 4. This was achieved by adding a straight flap to the bottom wall. The throat of this dummy passage was then adjusted so that the combined throat of the end-

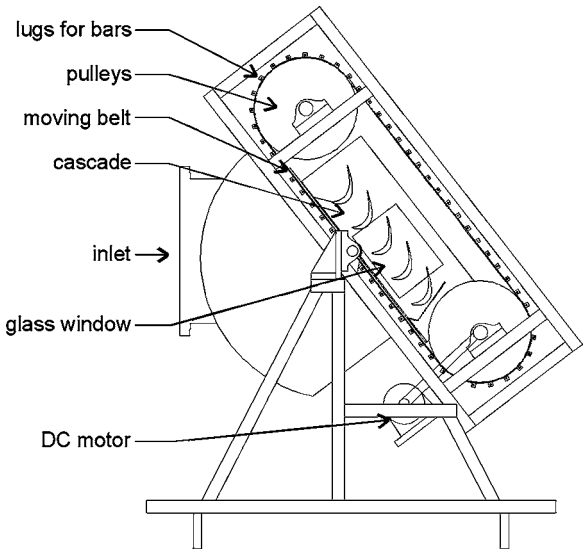

Fig. 4 Bar-passing cascade facility consisting of wake generator and cascade [11]

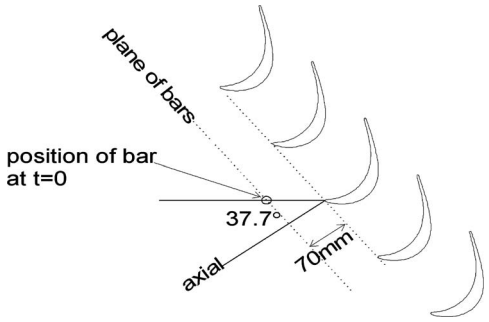

Fig. 5 Details of the bar-passing cascade [11]

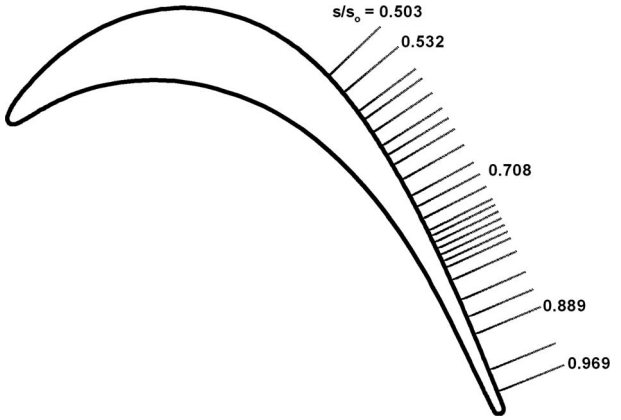

Fig. 6 Locations of the 25 measurement stations on the suction side of the blade [11]

wall gap and the dummy passage matched that of one of the cascade passages. The flap of the dummy passage was set while monitoring the inlet static pressure and thereby ensuring periodicity [11].

The unsteady wake-passing flow conditions were chosen to match those of a repeating stage of the T106 profile. The Reynolds number based on chord and inlet velocity was Re=91,077, and the free-stream turbulence intensity was FSTI=0.1%. The flow coefficient for the cascade was ϕ=0.83. The bar pitch matched the cascade pitch so that $s_b/s_c=1(f_r=0.68)$. The bar diameter of 2.05 mm was chosen to match the loss of a representative turbine blade. The cascade incidence was set to α_1=37.7 deg. The details of the T106 cascade setup are shown in Fig. 5 and summarized in Table 2.

In the experiments, a series of boundary layer traverses were performed using 2D LDA. The locations of measurements on the suction surface are shown in Fig. 6. The results obtained provided new insight into the wake-induced transition mechanisms on low-pressure turbine blades. The boundary layer state is investigated at four representative phases during the wake-passing cycle, and the rollup vortices embedded in the boundary layer are identified as the coherent structures in the boundary layer. These vortices are shown to originate from the breakdown of the separated shear layer that is triggered by the passing wake. The vortices are formed by an inviscid Kelvin-Helmholtz mechanism. Due to the inviscid nature of the rollup mechanism, there is no delay between the wake-passing and the boundary layer response. The rollup vortices are observed to breakdown into highly turbulent flow that convects along the blade surface [11].

3 Intermittency Transport Model

The transport model for intermittency has been developed to accurately predict transitional flows under diverse conditions encountered in turbomachinery applications. The model blends the transport equation models of Steelant and Dick [40] and Cho and Chung [41] in order to produce both the experimentally observed streamwise variation of intermittency and a realistic profile in the cross-stream direction. Complete details of the development and implementation of the transport model are described in Suzen and Huang [19,24], Suzen et al. [25–27] and the model in its entirety is used without any modifications to its original form in this study. A summary of the model equation and its implementation is presented in this section.

Table 2 T106 cascade details

Chord	198 mm
Blade stagger	59.3 deg
Cascade pitch	158 mm
Inlet flow angle	37.7 deg
Design exit flow angle	63.2 deg
Bar diameter	2.05 mm
Axial distance: bars to LE	70 mm
Flow coefficient ($U_{\text{axial}}/U_{\text{bar}}$)	0.83

The model equation is given by [19,24]

$$\frac{\partial \rho\gamma}{\partial t}+\frac{\partial \rho u_j\gamma}{\partial x_j}=(1-\gamma)\left\{(1-F)2C_0\rho\sqrt{u_k u_k}f(s)f'(s)+F\left[\frac{C_1\gamma}{k}\tau_{ij}\frac{\partial u_i}{\partial x_j}-C_2\gamma\rho\frac{k^{3/2}}{\varepsilon}\frac{u_i}{(u_k u_k)^{1/2}}\frac{\partial u_i}{\partial x_j}\frac{\partial \gamma}{\partial x_j}\right]\right\}+C_3\rho\frac{k^2}{\varepsilon}\frac{\partial \gamma}{\partial x_j}\frac{\partial \gamma}{\partial x_j}+\frac{\partial}{\partial x_j}\left\{(1-\gamma)\left[\gamma\sigma_{\gamma l}\mu+\sigma_{\gamma t}\mu_t\right]\frac{\partial \gamma}{\partial x_j}\right\} \tag{1}$$

The distributed breakdown function, $f(s)$ has the form

$$f(s)=\frac{as'^4+bs'^3+cs'^2+ds'+e}{gs'^3+h} \tag{2}$$

where $s'=s-s_t$, and s is the distance along the streamline coordinate, and s_t is the transition location. The coefficients are [19,24]

$$a=50\sqrt{\frac{n\sigma}{U}}$$

$$b=-0.4906$$

$$c=0.204\left(\frac{n\sigma}{U}\right)^{-0.5}$$

$$d=0.0$$

$$e=0.04444\left(\frac{n\sigma}{U}\right)^{-1.5}$$

$$h=10e \tag{3}$$

$$g=50$$

The shear stresses are defined as

$$\tau_{ij}=\mu_t\left(\frac{\partial u_i}{\partial x_j}+\frac{\partial u_j}{\partial x_i}-\frac{2}{3}\frac{\partial u_k}{\partial x_k}\delta_{ij}\right)-\frac{2}{3}\rho k\delta_{ij} \tag{4}$$

The blending function F is constructed using a nondimensional parameter $k/W\nu$, where k is the turbulent kinetic energy and W is the magnitude of the vorticity. The blending function has the form

$$F = \tanh^4\left[\frac{k/W\nu}{200(1-\gamma^{0.1})^{0.3}}\right] \tag{5}$$

The model constants used in Eq. (1) are [19,24]

$$\sigma_{\gamma l} = \sigma_{\gamma t} = 1.0 \quad C_0 = 1.0 \quad C_1 = 1.6$$

$$C_2 = 0.16 \quad C_3 = 0.15$$

Initially γ is set to zero throughout the flow field. On solid wall boundaries the value of γ is kept as zero; at the free stream, a zero gradient of γ is assumed and on outflow boundaries γ is extrapolated from inside the domain to the outer boundaries.

The intermittency is incorporated into the computations simply by multiplying the eddy viscosity obtained from a turbulence model μ_t by the intermittency factor γ. Simon and Stephens [42] showed that by combining the two sets of conditioned Navier-Stokes equations and making the assumption that the Reynolds stresses in the nonturbulent part are negligible, the intermittency can be incorporated into the computations by using the eddy viscosity μ_t^*, which is obtained by multiplying the eddy viscosity from a turbulence model μ_t, with the intermittency factor γ. That is,

$$\mu_t^* = \gamma\mu_t \tag{6}$$

is used in the mean flow equations. It must be noted that γ does not appear in the generation term of the turbulent kinetic energy equations.

In using this intermittency approach, the turbulence model selected to obtain μ_t must produce fully turbulent features before transition location in order to allow the intermittency to have full control of the transitional behavior. Menter's [43] SST model satisfies this requirement. It produces almost fully turbulent flow in the leading edge of the boundary layer and, therefore, it is used as a baseline model to compute μ_t and other turbulent quantities in the computations [27].

The value of $n\sigma$ used in evaluating the constants given by Eq. (3) is provided by the following correlation for zero pressure gradient flows [27]:

$$\hat{n}\sigma = (n\nu^2/U^3)\sigma = 1.8\times10^{-11}Tu^{7/4} \tag{7}$$

When flows are subject to pressure gradients, the following correlation is used:

$$\frac{\hat{n}\sigma}{(\hat{n}\sigma)_{\mathrm{ZPG}}} = \begin{cases} M^{E_1}, K_t < 0 \\ 10^{E_2}, K_t > 0 \end{cases} \tag{8}$$

with M, E_1, and E_2 defined as

$$M = (850Tu^{-3} - 100Tu^{-0.5} + 120)$$

$$E_1 = 1 - e^{0.75\times10^6 K_t Tu^{-0.7}}$$

$$E_2 = -3227\ K_t^{0.5985}$$

where $(\hat{n}\sigma)_{ZPG}$ is the value for flow at zero pressure gradient and can be obtained from Eq. (7) and $K_t=(\nu/U_t^2)(dU/dx)_t$ is the flow acceleration parameter. The favorable pressure gradient part of the above correlation (for $K_t>0$) is from Steelant and Dick [40]. The portion of the correlation for adverse pressure gradient flows for $K_t<0$, is formulated using the transition data of Gostelow et al. [44] and Simon et al. [22] (Suzen et al. [27]).

The current approach uses the intermittency transport model to obtain the intermittency distribution for the transitional flows, while the onset of transition is defined by correlations.

The onset of attached flow transition is determined by the following correlation in terms of turbulence intensity *Tu* and the acceleration parameter K_t,

$$\mathrm{Re}_{\theta t} = (120 + 150Tu^{-2/3})\coth[4(0.3 - K_t\times10^5)] \tag{9}$$

where K_t was chosen as the maximum absolute value of that parameter in the downstream deceleration region [27]. This correlation maintains the good features of the Abu-Ghannam and Shaw [45] correlation in the adverse pressure gradient region, and, in addition, it reflects the fact that the flow becomes less likely to have transition when subject to favorable pressure gradients by rapidly rising as K_t becomes positive.

In order to determine the onset of separated flow transition, Re_{st} is expressed in terms of the turbulence intensity *Tu* and the momentum thickness Reynolds number at the point of separation $\mathrm{Re}_{\theta s}$ in the form [26]

$$\mathrm{Re}_{st} = 874\ \mathrm{Re}_{\theta s}^{0.71} e^{-0.4Tu} \tag{10}$$

This correlation provides a better representation of the experimental data than the Davis et al. [46] correlation and is used to predict the onset of separated flow transition in the present computations.

The production term of the intermittency transport model requires calculation of streamwise distance. For simple blade geometries streamwise distance from transition onset point can be calculated based on blade geometry, however, for complex geometries this task may become difficult. In order to eliminate the difficulties associated with calculating the streamwise distance from geometric information alone we developed a transport equation for streamwise distance *s*. The derivation of the *s* equation is given below.

Streamwise distance *s* is defined as

$$s = \int \frac{udx + \nu dy}{\sqrt{u^2+\nu^2}} \tag{11}$$

Then,

$$ds = \frac{u}{\sqrt{u^2+\nu^2}}dx + \frac{\nu}{\sqrt{u^2+\nu^2}}dy \tag{12}$$

writing $dx=udt$, $dy=\nu dt$

$$ds = \frac{u^2+\nu^2}{\sqrt{u^2+\nu^2}}dt = \sqrt{u^2+\nu^2}dt \tag{13}$$

simplifying, we obtain

$$\frac{ds}{dt} = \sqrt{u^2+\nu^2} \tag{14}$$

that is,

$$\frac{ds}{dt} = \frac{\partial s}{\partial t} + u\frac{\partial s}{\partial x} + \nu\frac{\partial s}{\partial y} = \sqrt{u^2+\nu^2} \tag{15}$$

with addition of density we have

$$\rho\frac{\partial s}{\partial t} + \rho u\frac{\partial s}{\partial x} + \rho\nu\frac{\partial s}{\partial y} = \rho\sqrt{u^2+\nu^2} \tag{16}$$

In order to make the computed *s* values in free stream penetrate the boundary layer up to the solid walls and also to avoid accumulation of *s* in low-speed circulating flow regions, a diffusion term is included. With the addition of a diffusion term, making use of the continuity equation, and writing in indicial form, the equation becomes

$$\frac{\partial(\rho s)}{\partial t} + \frac{\partial(\rho u_i s)}{\partial x_i} = \rho\sqrt{u_k u_k} + \frac{\partial}{\partial x_i}\left[\frac{(\mu+\mu_t)}{\sigma_s}\frac{\partial s}{\partial x_i}\right] \tag{17}$$

where $\sigma_s=0.1$ is used. The initial condition of $s=0.0$ is used all over the flow field. The gradient of *s* is set to zero at all boundaries.

For steady-state computations once the flow field develops, *s* changes very little, and, gradually, this equation is solved simultaneously with the intermittency transport equation. For time-

dependent computations, the s equation is solved before intermittency transport equation at each time level. The changes in s are gradual from one time step to the next. The intermittency transport model uses the streamwise distance from the onset point of transition. Once the onset point of transition is calculated, the value of s at that point, s_t, is subtracted from s values of all points

$$s' = s - s_t \tag{18}$$

If s' is less than or equal to zero, then the production term of the intermittency model becomes zero, keeping flow laminar upstream of transition onset point. This method is used in computations of wake/blade interaction experiments.

4 Numerical Simulations

Computations of the experiments are performed using a recently developed multiblock Navier-Stokes solver called GHOST. The code is developed at University of Kentucky, and is a pressure-based code based on SIMPLE (Semi-Implicit Method for Pressure-Linked Equation) algorithm with second-order accuracy in both time and space. Advection terms are approximated by a QUICK (Quadratic Upstream Interpolation for Convection Kinematic) scheme, and central differencing is used for the viscous terms. The "Rhie and Chow" momentum interpolation method [47] is employed to avoid checkerboard oscillations usually associated with the nonstaggered grid arrangement. This code is capable of handling complex geometries, moving, and overset grids and includes multiprocessor computation capability using MPI (Message Passing Interface). Since multiple processors are used during the computations, it is more efficient to divide the computational domain into several smaller pieces with very fine grids and distribute the zones to processors with the consideration of load balancing. This code has been used extensively in a recent turbulence model validation effort [48] and simulations of a wide range of low-pressure turbine flows [32,33,49] conducted at University of Kentucky.

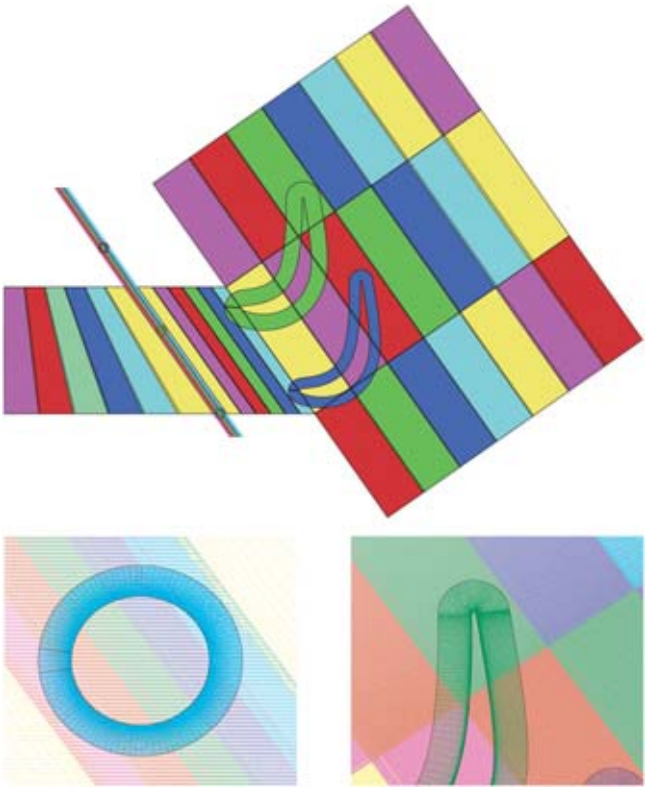

Fig. 7 Multiblock grid system used for simulating experiment of Kaszeta et al. [2,34], (*a*) (top) 43 zone multiblock grid for the computational domain, (*b*) (bottom left) close-up view of rod grid, and (*c*) (bottom right) close-up view of blade grid

5 Results and Discussion

5.1 Simulations of Experiments of Kaszeta et al. [2,34]. The first set of experiments simulated is the experiment of Kaszeta et al. [2,34]. For the simulation of these experiments a 43-zone multiblock grid with a total of nearly 0.6 million points is used for the calculation. A series of grid refinement studies has lead to this final grid shown in Fig. 7(*a*) in order to capture the details of the flow field accurately. In the experiments the flow is discharged into the surrounding atmosphere downstream of the blade passage as well as through the bleed slots shown in Fig. 1. In order to incorporate the effects of the surrounding quiescent atmosphere and the flow escaping through bleed slots, the computational domain covers the downstream region outside the passage including the bleed slots. The grid system has the first y^+ less then 0.5 near solid walls. Unlike the experiments, which make use of a sled to generate periodic wakes, the present study simulated a continuous succession of wake-generating rods. In order to achieve this, three rods are included in the computations that are overset on the zones extending outside from the bottom and top of the inflow channel as shown in Fig. 7(*a*). The close-up views of the grid for one of the rods and grid for the upper blade are shown in Figs. 7(*b*) and 7(*c*), respectively. The zones extending outside the inflow channel combined with the rod grids slide up with the experimental rod speed value of 70% of the axial flow velocity, and periodic boundary conditions at top and bottom boundaries are imposed in order to simulate a continuous succession of rods.

The grid system shown in Fig. 7(*a*) corresponds to the experimental setup, with the rod spacing equal to the blade pitch referred to as the "high wake frequency case" in the remainder of this paper. In order to simulate the reduced wake frequency case where the rod spacing is twice the blade pitch (referred to as "reduced wake frequency case" in the rest of this paper), the length of the zones extending outside the inflow channel were shortened to enable the use of only one rod grid in conjunction with the periodic boundary conditions at top and bottom boundaries.

In order to illustrate the effect of including moving rods in the simulations rather than prescribing a wake profile, the predicted isocontours of instantaneous and phase-averaged (average of 40 cycles) vorticity are shown in Figs. 8(*a*) and 8(*b*), respectively. In these figures, counterclockwise rotating vortices are identified by blue and clockwise rotating vorticities by red coloring. The Reynolds number based on rod diameter and flow speed is around 1800, and the vortex shedding behind the rod is characteristic of flow at this Reynolds number. Comparison of Figs. 8(*a*) and 8(*b*) indicate that the instantaneous vorticity contours are much stronger and much more sharply defined, whereas phase-averaged vorticity contours are smoothed out. The smoothing is due to the fact that the instantaneous shed vortices never have exactly the same structure at a given time level in a phase from one time cycle to the next. This is due to the fact that the vortex shedding frequency is not synchronized with the rod passing frequency. The instantaneous wake behind the bar is narrower when compared to the phase-averaged one. This is also evident from the wake velocity profiles shown in Fig. 9 corresponding to the reduced wake frequency case. In this figure, the predicted instantaneous and average velocity at the midpoint between the leading edges of the pressure and suction surfaces are compared to experiment. The width of the wake is narrower, and the fluctuations are apparent in the instantaneous distributions. However, since each instantaneous profile is slightly off center, these fluctuations are smoothed out and a wider wake is obtained as a large number of cycles are averaged. In Fig. 9, the experiment includes an ensemble average of 225 wakes where the computation includes only 40 cycles.

Simulations using the intermittency transport model are per-

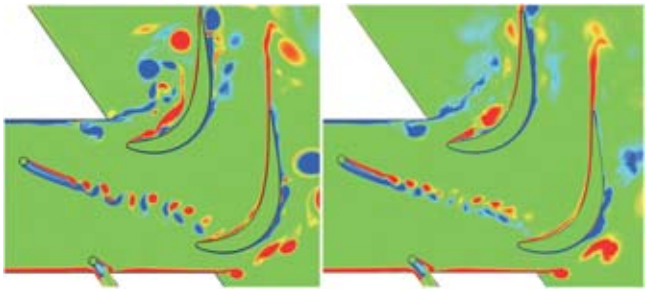

Fig. 8 Computed vorticity contours for experiment of Kaszeta et al. [2,34]. (*a*) (left) instantaneous vorticity and (*b*) (right) phase-averaged vorticity.

formed for both wake frequency cases along with a wake-free (steady) case. In addition, a fully turbulent simulation is performed for the high wake passing frequency case for comparison.

The first case considered for simulations corresponds to the experimental setup with the rod spacing equal to the blade pitch (high wake frequency case). Comparisons between the computed and experimental phase-averaged streamwise velocity variations at stations 4–13 on the suction side of the blade are shown in Figs. 10. In these figures, the horizontal axis corresponds to the phase angle in degrees and the vertical axis corresponds to the distance normal to the wall in centimeters. Although the comparisons of the experimental and numerical results are not exactly identical, they seem to exhibit a similar trend. The comparisons show a global similarity in the general shape of the velocity profiles. The predicted results showed that the maximum velocity region, corresponding to the wake interaction region, moves in a similar fashion as experiments along the suction surface. The simulations indicate a larger separation bubble at stations P9 through P12 when compared to experiment in Figs. 10(*f*) through 10(*i*) characterized by the dark blue region near the surface.

The comparison of the mean velocity profiles is presented in Fig. 11. The comparison is considered to be fair. The simulations predict a larger separation bubble evident from the velocity profiles at stations P9–P12. It should be noted that the hot wire is not adequate for velocity measurement when flow separation occurs. The fact that the experimental data do not approach zero, as at stations P9–P11, indicates that the flow may be separated. The suction surface mean pressure coefficient distribution is compared to experiment in Fig. 12 along with the distributions from a fully turbulent simulation and a transitional wake-free computation.

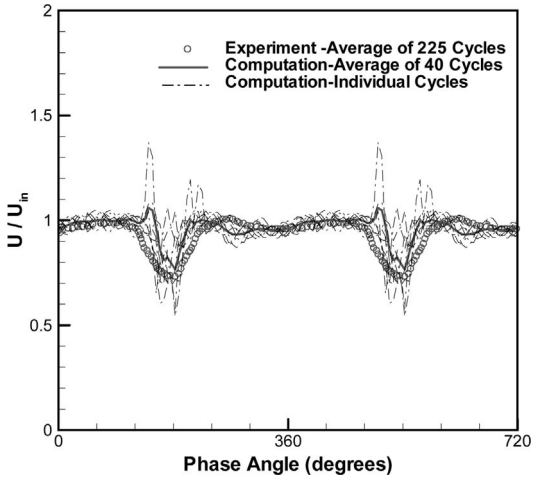

Fig. 9 Velocity at the midpoint between the leading edges of the pressure and suction surfaces for the reduced wake passing frequency case

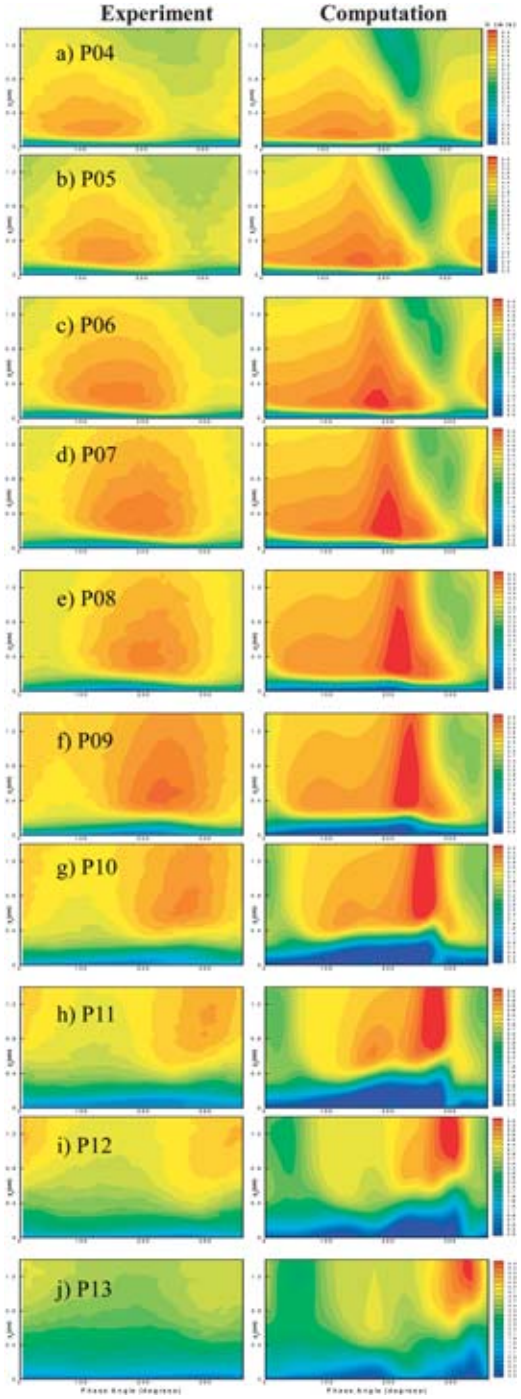

Fig. 10 Comparison of computed and experimental phase-averaged velocity distributions (m/s) at various streamwise stations on the suction surface of the blade for the high wake frequency case of Kaszeta et al. [2,34]. Horizontal axis: Phase angle (0–360 deg). Vertical axis: Wall normal distance (0–1.4 cm).

The experimental data correspond to measurements from a wake-free flow and show a plateau of the pressure distribution after $x/L_x=0.7$, indicating a flow separation, while the fully turbulent computation misses it completely. The simulation incorporating the intermittency transport model indicates separated flow in that region, however, the extent of the separation zone is shorter when compared to the wake-free computation and experiment. These results agree with the conclusion drawn from the experiments that

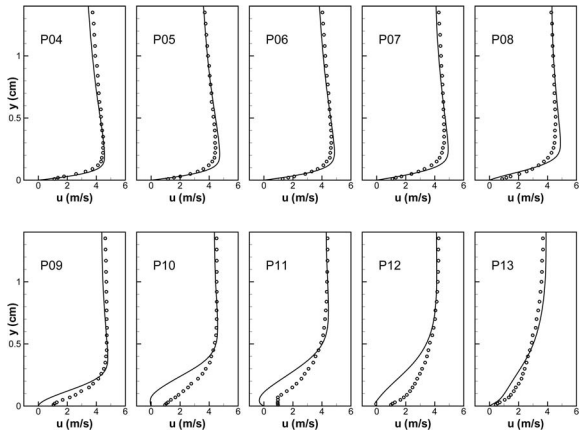

Fig. 11 Comparison of computed and experimental mean velocity profiles at various streamwise stations on the suction surface of the blade for the high wake frequency case of Kaszeta et al. [2,34]

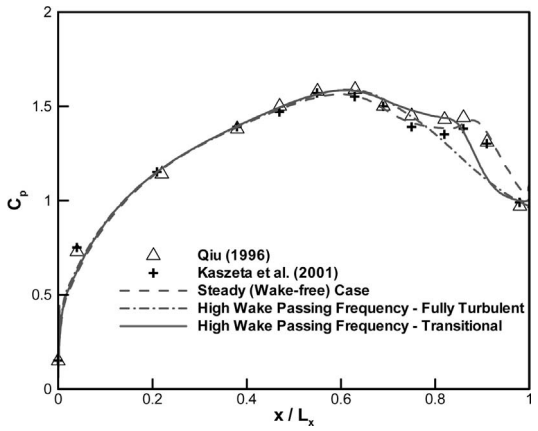

Fig. 12 Comparison of computed and experimental pressure coefficient distributions on the suction surface of the blade for the high wake frequency experiments of Kaszeta et al. [2,34]

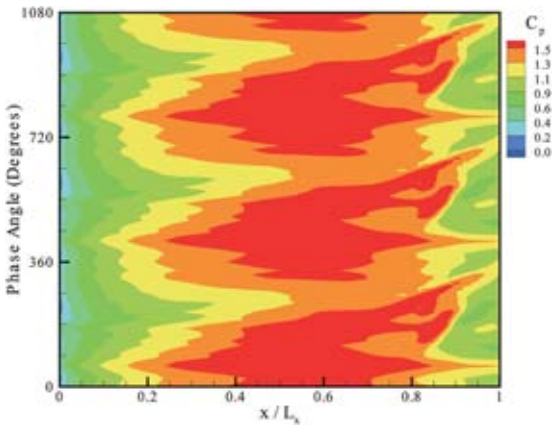

Fig. 13 Computed phase-averaged pressure coefficient distribution on the suction surface for the high wake frequency case

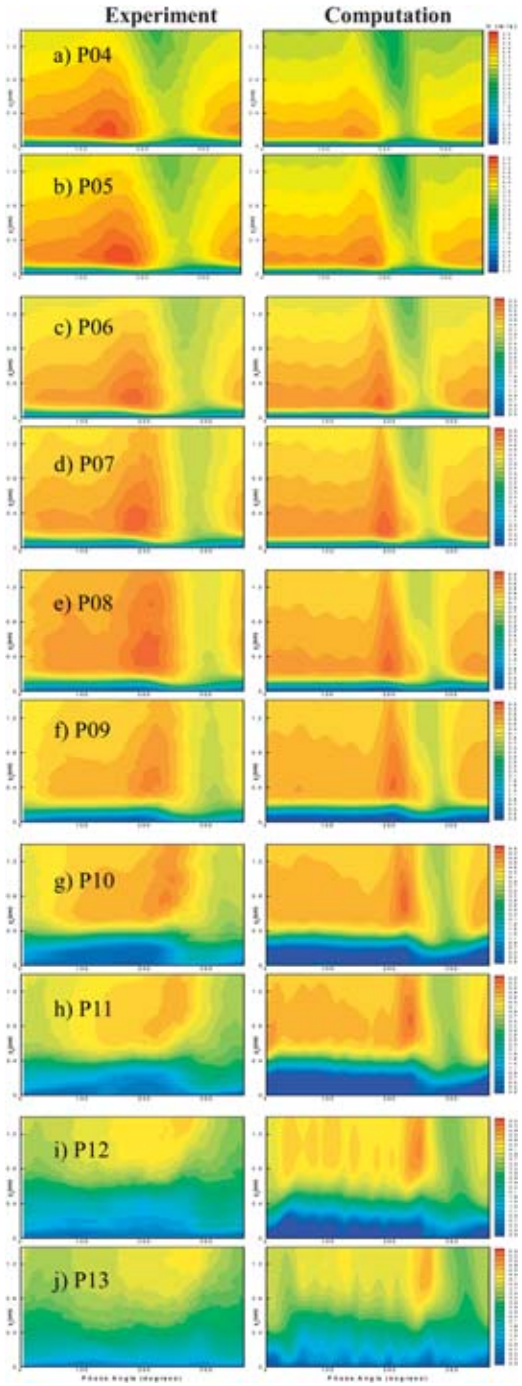

Fig. 14 Comparison of computed and experimental phase-averaged velocity distributions (m/s) at various streamwise stations on the suction surface of the blade for the reduced wake frequency experiments of Kaszeta et al. [2,34]. Horizontal axis: Phase angle (0–360 deg). Vertical axis: Wall normal distance (0–1.4 cm).

the effect of passing wakes is to reduce the size of the separation bubble due to increase in turbulence levels by wakes when compared to wake-free flow.

The variation of suction surface pressure coefficient distribution with time is shown in Fig. 13 for the transitional computation. The effects of unsteady wake boundary layer interactions on blade loading can be observed from this figure. The pressure fluctuations are due to the interaction of the wake vorticities with the suction surface boundary layer.

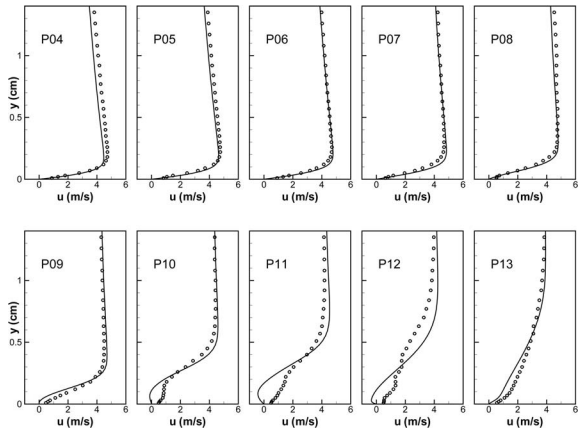

Fig. 15 Comparison of computed and experimental mean velocity profiles at various streamwise stations on the suction surface of the blade for the reduced frequency experiments of Kaszeta et al. [2,34]

Next, simulations are performed for the reduced wake frequency experiments. For this case, everything except the rod spacing is identical to the previous case, which is increased to twice the blade pitch to reduce the wake-passing frequency.

Comparisons between the computed and experimental phase-averaged streamwise velocity variations at stations 4–13 on the suction side of the blade are shown in Figs. 14(*a*)–14(*j*). The comparisons are fair. The predicted results captured the relative movement of the wake interaction region characterized by the maximum velocity regions in Figs. 14(*a*) through 14(*j*) over the suction surface well when compared to the experiment. The simulations indicate a separation bubble at stations P9 through P12 consistent with the experiment as shown in Figs. 14(*f*)–14(*i*) characterized by the dark blue colored region near the surface. The comparison of mean velocity profiles at ten streamwise stations along the suction surface shown in Fig. 15 further illustrate the good agreement between the simulations and the experiments. It must be noted that the discrepancy between the profiles in the near-wall region at stations P10–P12 in Fig. 15 is due to the inability of the hot wire to measure reversed flows. The pressure coefficient distribution is compared to experiment, transitional high wake frequency simulations, and the wake-free computation in Fig. 16. For this case, the separation bubble is slightly larger than in the high wake frequency case and the profile moves closer

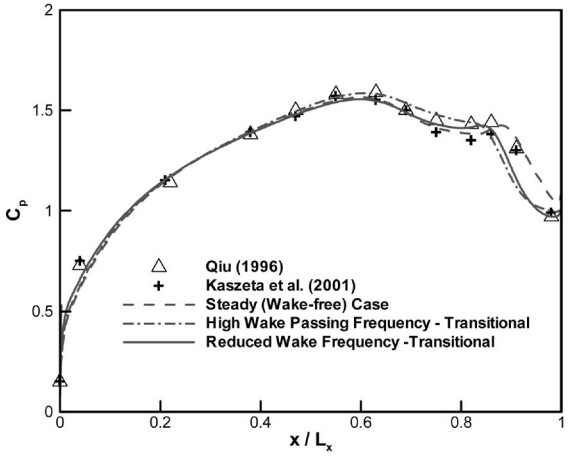

Fig. 16 Comparison of computed and experimental pressure coefficient distributions on the suction surface of the blade for the reduced frequency experiments of Kaszeta et al. [2,34]

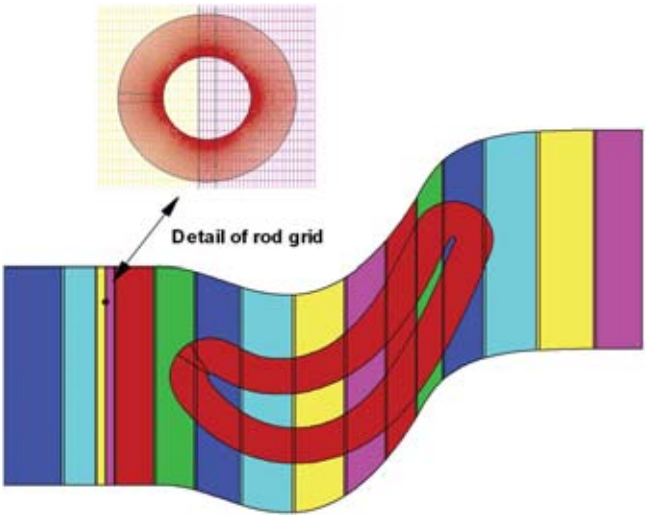

Fig. 17 Multi-block grid system used in simulations of experiments of Stieger [11]

to the wake-free computation.

Comparing the phase-averaged velocity distributions for the high and reduced wake frequency cases given in Figs. 10 and 14, respectively, along with the mean velocity profiles given in Figs. 11 and 15, it is evident that the effect of increased wake frequency is to suppress the separation zone. This is due to the fact that the increased wake frequency introduces more wake-generated perturbations and, hence, increases the turbulence level. On the other

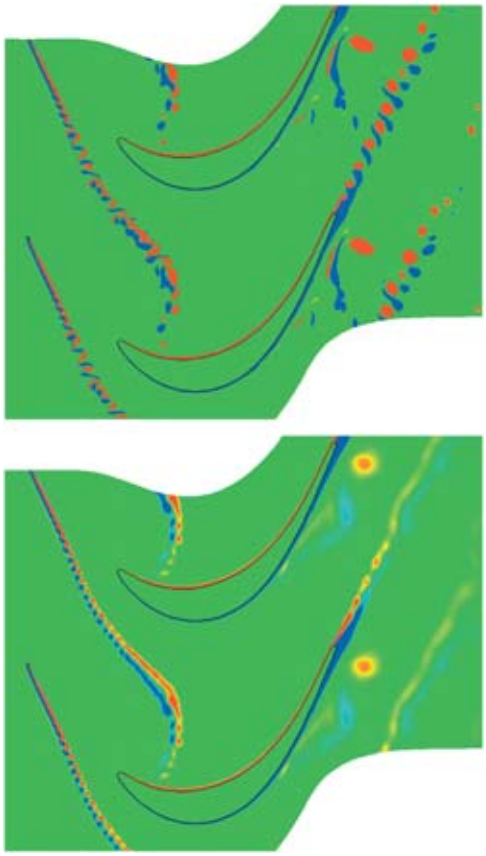

Fig. 18 Computed vorticity contours for experiment of Stieger [11]; (*a*) (top) instantaneous vorticity contours and (*b*) (bottom) phase-averaged vorticity contours

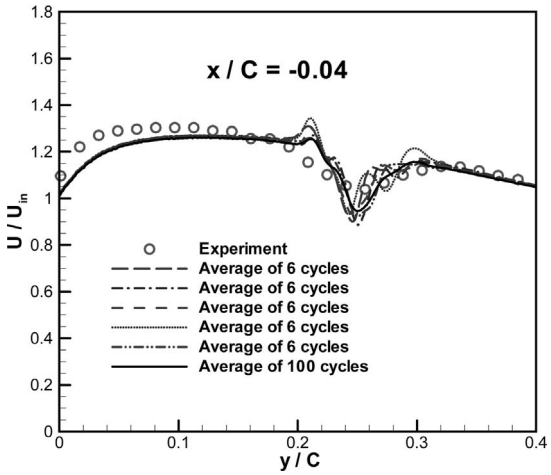

Fig. 19 Comparison of computational and experimental wake velocity profiles before the blade leading edge for the experiments of Stieger [11]

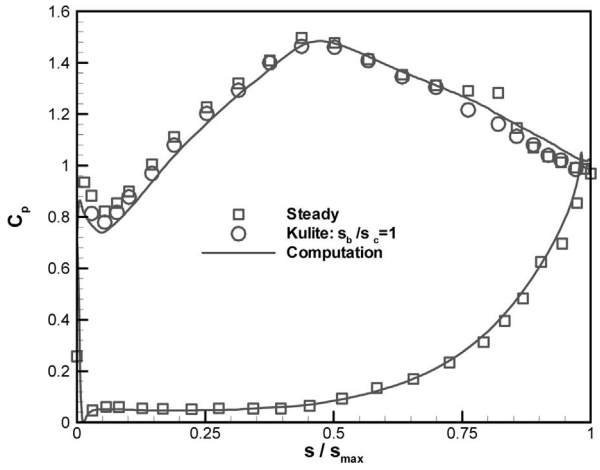

Fig. 20 Comparison of computational and experimental pressure coefficient distributions for the experiments of Stieger [11]

hand, the reduced-wake frequency, that is, increased wake temporal spacing, allows the boundary layer on the suction surface of the blade a much longer time to recover from the perturbations of the wakes and allows the boundary layer to reach a state that moves toward the steady flow case without the moving bars.

Here, we must emphasize the difference in the movement of the rods in the experiments and in the computations. In the experiments, wakes are generated by repeatedly passing of a sled carrying the rods through the flow upstream of the turbine passage. Each upward pass of the sled generates a series of wakes (four wakes per sled passing), then the sled is pulled back to its original position and the movement is repeated. In contrast, in the computations we have used a continuous (periodic) rod movement. This difference may be the cause of the discrepancy observed in the flow behavior between the experiments and the computations. Overall, simulations were able to capture the flow features well for experiments of Kaszeta et al. [2,34].

5.2 Simulations of Experiments of Stieger [11]. Simulations of experiments of Stieger [11] are performed using the multiblock grid system consisting of 18 zones and 0.8 million grid points shown in Fig. 17. The rod grid shown in the inset and the two zones it overlaps move with the specified bar speed of 1.2 times the axial flow velocity. The grid system has the first y^+ less than 0.5 near solid walls. The origin is located at the leading edge of the blade for this grid system. Periodic boundary conditions are employed at top and bottom boundaries.

Predicted instantaneous and phase-averaged (average of 100 cycles) vorticity isocontours are shown in Figs. 18(*a*) and 18(*b*), respectively. In this case the Reynolds number based on bar diameter and flow speed over the bar is 1650. The instantaneous vortex shedding behind the bar is sharper, and the wake is narrower when compared to the phase-averaged contours. The smoothing effect of phase averaging is evident from the wake velocity profile shown in Fig. 19. In this figure, the predicted wake velocity profile is compared to experiment at a location of $x/C=-0.04$ before the blade leading edge. The phase averages of five different sets of 6-cycle data are shown along with the phase average of 100 cycles. The fluctuations are apparent in each of the 6-cycle averages. However, these fluctuations are smoothed out as a larger number of cycles are included in averaging. This is evident from the average of 100 cycles.

The predicted time average pressure coefficient distribution compares well with the experiment as shown in Fig. 20. In this figure the steady-state experiment without the moving bars is also included in order to illustrate the effect of wake interaction on the suction-side pressure distribution. In the steady-state case, there is a large separation bubble on the suction side of the blade characterized by the plateau in the pressure coefficient distribution between $s/s_o=0.7$ and 0.83. On the other hand, the time-average C_p distribution obtained from the case with moving bars does not exhibit such a plateau, indicating attached mean flow over the suction surface. This is due to the effect of the wakes interacting with the boundary layer on the suction surface, causing transition to turbulence and, hence, reducing the susceptibility of the flow to separate.

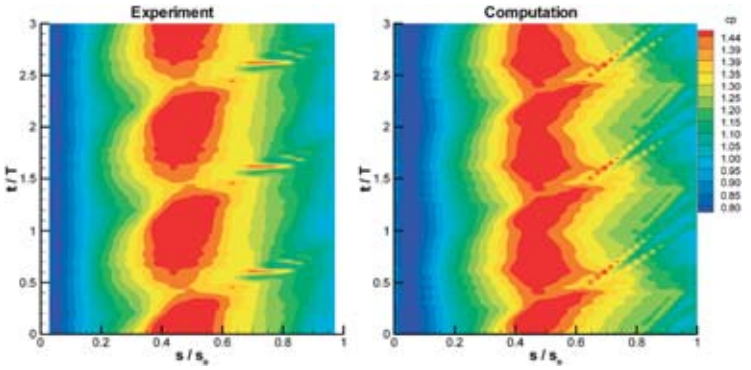

Fig. 21 Comparison of computational and experimental phase-averaged pressure coefficient distributions on the suction surface of the blade for the experiments of Stieger [11]

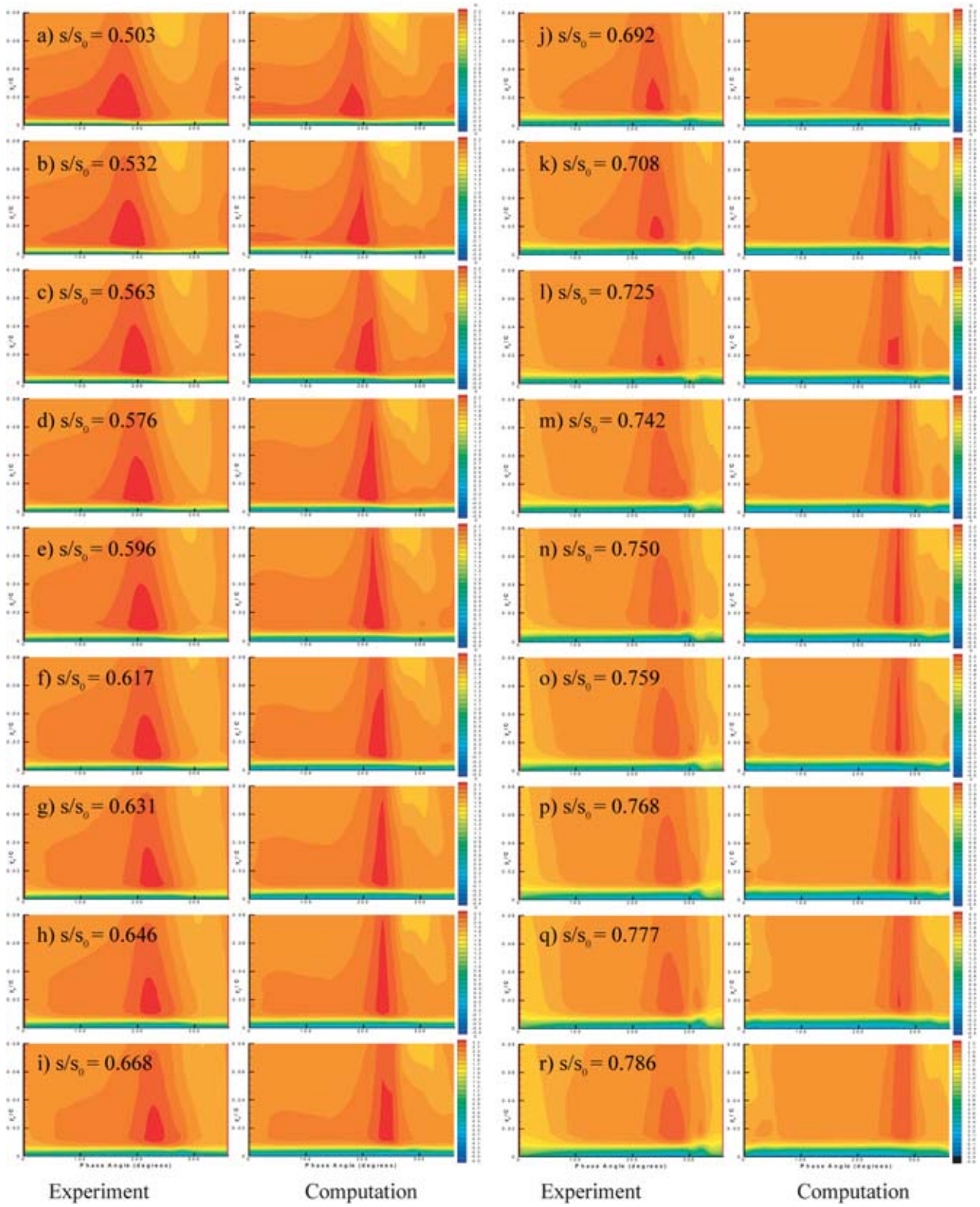

Fig. 22 Comparison of computed and experimental phase-averaged velocity distributions (U/U_{in}) at various streamwise stations on the suction surface of the blade for the experiments of Stieger [11], continued. Horizontal axis: Phase angle (0–360 deg). Vertical axis: Wall normal distance y_n/C (0–0.08).

The comparison of computed and experimental phase-averaged pressure distributions on the suction surface of the blade is fair, as shown in Fig. 21.

Comparisons between the computed and experimental phase-averaged streamwise velocity variations at 25 stations on the suction side of the blade are shown in Figs. 22. In these figures, the horizontal axis corresponds to the phase angle in degrees and the vertical axis corresponds to the distance normal to the wall non-

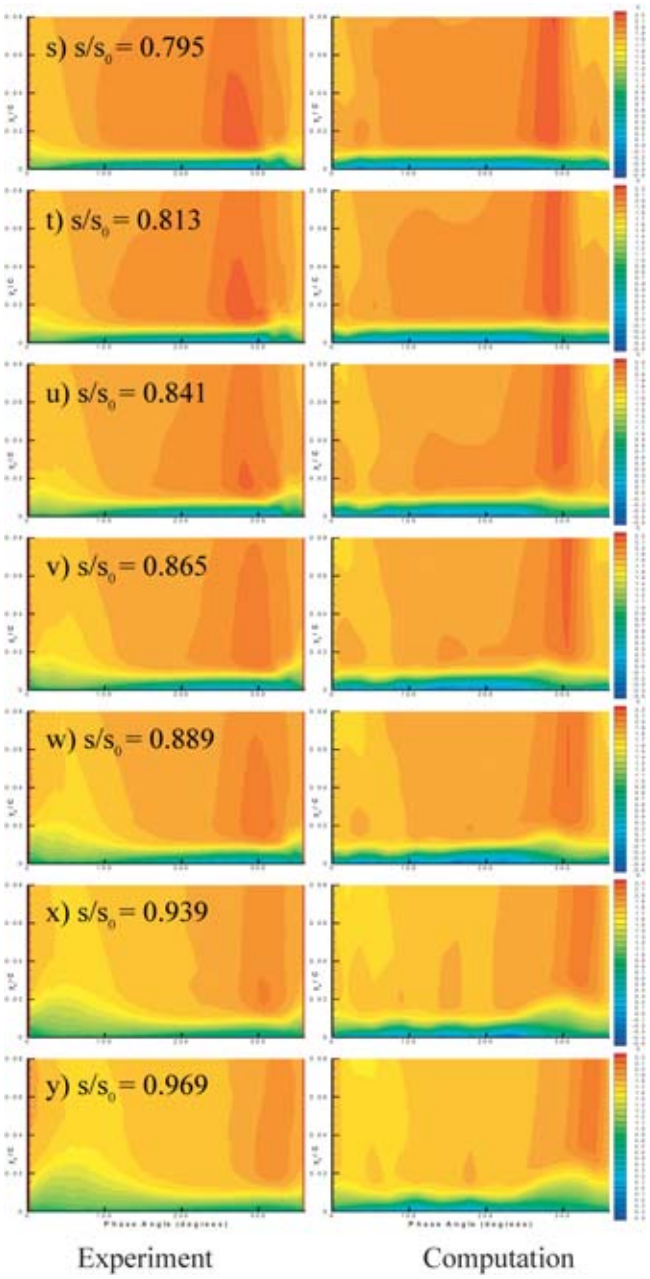

Fig. 22 (***Continued***).

dimensionalized by chord. The numerical results are in good agreement with the experiment. The movement of the wake interaction region characterized by the maximum velocity is captured well in the simulations.

The predicted mean velocity profiles at 25 stations along the suction surface are compared to experiment in Fig. 23. The simulations agree very well with the experimental data.

6 Concluding Remarks

An extensive computational investigation of the effects of unsteady wake/blade interaction on transition and separation in low-pressure turbines has been performed by numerical simulations of recent experiments of Kaszeta et al. [2,34], and Stieger [11] using an intermittency transport equation.

Computational results are compared to the experiments. Overall, general trends are captured and prediction capabilities of the intermittency transport model for simulations of unsteady wake/blade interaction flow fields are demonstrated.

Acknowledgments

This research is supported by NASA Glenn Research Center under Grant No. NCC3-590 and followed by Grant No. NCC3-1040. The project is part of the Low Pressure Turbine Flow Physics program of NASA-Glenn. The authors like to thank Dr. David Ashpis for his coordination of the LPT program. The authors also appreciate Dr. Terrence W. Simon and Dr. Richard W. Kaszeta's preparation of the experimental data and Dr. Howard Hodson's suggestion of T106 cascade experiments as a test case.

Nomenclature

C = chord
C_p = pressure coefficient, $2(P-P_\infty)/(\rho_\infty U_{in}^2)$
C_x = axial chord
FSTI = free-stream turbulence intensity(%)
f_r = reduced frequency
K_t = flow acceleration parameter, $(\nu/U^2)(\mathrm{d}U/\mathrm{d}s)$
k = turbulent kinetic energy
L = chord
L_r = rod spacing
L_{ss} = suction surface length for PAK-B blade
L_x = axial chord
L_z = blade span
N = nondimensional spot breakdown rate parameter, $n\sigma\theta_t^3/\nu$
n = spot generation rate
$\hat{n}$ = $(n\nu^2/U^3)$
P = blade pitch
P = static pressure
P_{total} = total pressure
Re = Reynolds number
Re_{st} = $(s_t-s_s)U_e/\nu$
$\mathrm{Re}_{\theta t}$ = $\theta_t U_e/\nu$
s = streamwise distance along suction surface
s_b = bar pitch
s_c = cascade pitch
s_o = suction surface length for T106 blade
Tu = turbulence intensity(%), u'/U
U = boundary layer streamwise velocity
U_e = local free-stream velocity
U_{in} = inlet free-stream velocity
u_τ = friction velocity
W = magnitude of vorticity
y_n = distance normal to the wall
y^+ = $y_n u_\tau/\nu$
α_1 = inlet flow angle for T106 blade
β_1 = inlet flow angle for PAK-B blade
β_2 = outlet flow angle for PAK-B blade
δ_{ij} = kronecker delta
ε = dissipation rate
ϕ = flow coefficient for T106 cascade
γ = intermittency factor
τ_{ij} = shear stress tensor
θ = momentum thickness
λ_θ = pressure gradient parameter, $(\theta^2/\nu)(\mathrm{d}U/\mathrm{d}s)$
μ = molecular viscosity
μ_t = eddy viscosity
ν = μ/ρ
ν_t = μ_t/ρ
ρ = density
σ = spot propagation parameter

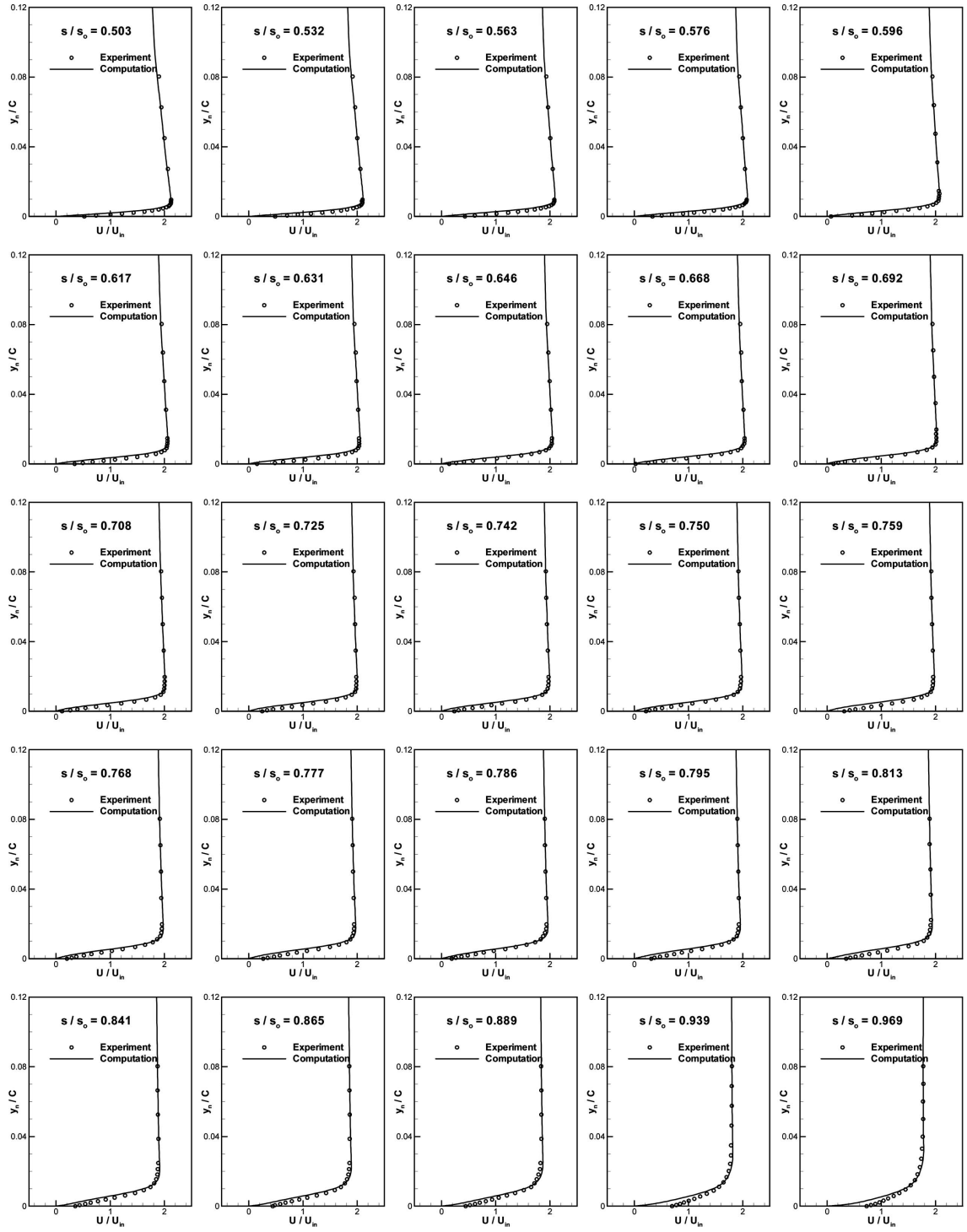

Fig. 23 Comparison of computational and experimental mean velocity profiles at various streamwise locations on the suction surface of the blade for the experiments of Stieger [11]

Subscripts

e = free-stream
s = onset of separation
t = onset of transition

References

[1] Sharma, O., 1998, "Impact of Reynolds Number of LP Turbine Performance," In NASA/CP-1998-206958, pp. 65–70.

[2] Kaszeta, R. W., Simon, T. W., and Ashpis, D. E., 2001, "Experimental Investigation of Transition to Turbulence as Affected by Passing Wakes," Proceedings of ASME Turbo Expo 2001, ASME, New York, ASME Paper No. 2001-GT-0195.

[3] Halstead, D. E, Wisler, D. C., Okiishi, T. H., Walker, G. J., Hodson, H. P., and Shin, H.-W., 1997, "Boundary Layer Development in Axial Compressors and Turbines: Part 1 of 4: Composite Picture," ASME J. Turbomach. **119**, pp. 114–127.

[4] Tiedemann, M., and Kost, F., 1999, "Unsteady Boundary Layer Transition on a High Pressure Turbine Rotor Blade," Proceedings of ASME Turbo Expo 1999, ASME, New York, ASME Paper No. 99-GT-194.

[5] Kost, F., Hummel, F., and Tiedemann, M., 2000, "Investigation of the Unsteady Rotor Flow Field in a Single HP Turbine Stage," Proceedings of ASME Turbo Expo 2000, ASME, New York, ASME Paper No. 2000-GT-432.

[6] Solomon, W. J., 2000, "Effects of Turbulence and Solidity on the Boundary Layer Development in a Low Pressure Turbine," Proceedings of ASME Turbo Expo 2000, ASME, New York, ASME Paper No. 2000-GT-273.
[7] Schobeiri, M. T. and Pappu, K., 1997, "Experimental Study on the Effect of Unsteadiness on Boundary Layer Development on a Linear Turbine Cascade," Exp. Fluids **23**, pp. 306–316.
[8] Schobeiri, M. T., Ozturk, B., and Ashpis, D. E., 2003, "On the Physics of Flow Separation Along a Low Pressure Turbine Blade Under Unsteady Flow Conditions," Proceedings of ASME Turbo Expo 2003, ASME, New York, ASME Paper No. GT2003-38917.
[9] Stadtmuller, P., Fottner, L., and Fiala, A., 2000, "Experimental and Numerical Investigation of Wake-Induced Transition on a Highly Loaded Low Pressure Turbine at Low Reynolds Numbers." Proceedings of ASME Turbo Expo 2000, ASME, New York, ASME Paper No. 2000-GT-269.
[10] Kaszeta, R. W., and Simon, T. W., 2002, "Experimental Investigation of Transition to Turbulence as Affected by Passing Wakes," NASA Contractor Report, NASA-CR-2002-212104, Cleveland.
[11] Stieger, R. D., 2002, "The Effects of Wakes on Separating Boundary Layers in Low-Pressure Turbines," Ph.D. Dissertation, Cambridge University, Eng. Dept, Cambridge, UK;
[12] Dorney, D. J., Ashpis, D. E., Halstead, D. E., and Wisler, D. C., 1999, "Study of Boundary Layer Development in a Two-Stage Low-Pressure Turbine," NASA-TM-1999-208913.
[13] Dorney, D. J., Flitan, H. C., Ashpis, D. E., and Solomon, W. J., 2000, "Effects of Blade Count on Boundary Layer Development in a Low-Pressure Turbine," AIAA Paper No. AIAA-2000-0742.
[14] Arnone, A., Marconcini, M., Pacciani, R., and Spano, E., 1999, "Numerical Prediction of Wake-Induced Transition in a Low Pressure Turbine," ISABE Paper No. 99-7058.
[15] Fan, S., and Lakshminarayana, B., 1996, "Computation and Simulation of Wake-Generated Unsteady Pressure and Boundary Layers in Cascades: Part 1-Description of the Approach and Validation," ASME J. Turbomach. **118**, pp. 96–108.
[16] Eulitz, F., and Engel, K., 1998, "Numerical Investigation of Wake Interaction in a Low Pressure Turbine," Proceedings of ASME Turbo Expo 1998, ASME, New York, ASME Paper No. 98-GT-563.
[17] Kim, K., and Crawford, M. E., 2000, "Prediction of Transitional Heat Transfer Characteristics of Wake-Affected Boundary Layers," ASME J. Turbomach. **122**, pp. 78–87.
[18] Wu, X., and Durbin, P. A., 2000, "Numerical Simulation of Heat Transfer in a Transitional Boundary Layer With Passing Wakes," ASME J. Heat Transfer **122**, pp. 248–257.
[19] Suzen, Y. B., and Huang, P. G., 1999, "Modelling of Flow Transition Using an Intermittency Transport Equation," NASA Contractor Report, NASA-CR-1999-209313, Cleveland, OH.
[20] Savill, A. M., 1993a, "Some Recent Progress in the Turbulence Modeling of By-Pass Transition," *Near-Wall Turbulent Flows*, R. M. C. So, C. G. Speziale, and B. E. Launder, eds., Elsevier Science, New York, pp. 829–848.
[21] Savill, A. M., 1993b, "Further Progress in the Turbulence Modeling of By-Pass Transition," *Engineering Turbulence Modeling and Experiments 2*, W. Rodi and F. Martelli, eds., Elsevier Science, New York, pp. 583–592.
[22] Simon, T. W., Qiu, S., and Yuan, K., 2000, "Measurements in a Transitional Boundary Layer Under Low-Pressure Turbine Airfoil Conditions," NASA Contractor Report, NASA-CR-2000-209957, Cleveland, OH.
[23] Volino, R. J. and Hultgren, L. S., 2001, "Measurements in Separated and Transitional Boundary Layers Under Low-Pressure Turbine Airfoil Conditions," ASME J. Turbomach. **123**(2), pp. 189–197.
[24] Suzen, Y. B. and Huang, P. G., 2000, "Modelling of Flow Transition Using an Intermittency Transport Equation," ASME J. Fluids Eng. **122**, pp. 273–284.
[25] Suzen, Y. B., Xiong, G., and Huang, P. G., 2000, "Predictions of Transitional Flows in Low-Pressure Turbines Using an Intermittency Transport Equation," AIAA Paper No. AIAA-2000-2654.
[26] Suzen, Y. B., Huang, P. G., Hultgren, L. S., and Ashpis, D. E., 2001, "Predictions of Separated and Transitional Boundary Layers Under Low-Pressure Turbine Airfoil Conditions Using an Intermittency Transport Equation," AIAA Paper No. AIAA-2001-0446.
[27] Suzen, Y. B., Xiong, G., and Huang, P. G., 2002, "Predictions of Transitional Flows in Low-Pressure Turbines Using an Intermittency Transport Equation," AIAA J. **40**(2), pp. 254–266.
[28] Lake, J. P., King, P. I., and Rivir, R. B., 1999, "Reduction of Separation Losses on a Turbine Blade With Low Reynolds Number," AIAA Paper No. AIAA-99-0242.
[29] Lake, J. P., King, P. I., and Rivir, R. B., 2000, "Low Reynolds Number Loss Reduction on Turbine Blades With Dimples and V-Grooves," AIAA Paper No. AIAA-00-0738.
[30] Huang, J., Corke, T. C., and Thomas, F. O., 2003, "Plasma Actuators for Separation Control of Low Pressure Turbine Blades," AIAA Paper No. AIAA-2003-1027.
[31] Volino, R. J., 2002, "Separated Flow Transition Under Simulated Low-Pressure Turbine Airfoil Conditions: Part 1- Mean Flow and Turbulence Statistics," Proceedings of ASME Turbo Expo 2002, ASME, New York, ASME Paper No. ASME-GT-30236.
[32] Suzen, Y. B., Huang, P. G., Volino, R. J., Corke, T. C., Thomas, F. O., Huang, J., Lake, J. P., and King, P. I., 2003, "A Comprehensive CFD Study of Transitional Flows in Low-Pressure Turbines Under a Wide Range of Operating Conditions," AIAA Paper No. AIAA-2003-3591.
[33] Suzen, Y. B., and Huang, P. G., 2004, "Comprehensive Validation of an Intermittency Transport Model for Transitional Low-Pressure Turbine Flows," AIAA Paper No. AIAA-2004-1121.
[34] Kaszeta, R. W., Simon, T. W., Ottaviani, F., and Jiang, N., 2003, "The Influence of Wake Passing Frequency and Elevated Free Stream Turbulence Intensity on Transition in Low-Pressure Turbines," AIAA Paper No. AIAA-2003-3633.
[35] Stieger, R. D., and Hodson, H. P., 2003, "The Transition Mechanism of Highly-Loaded LP Turbine Blades," Proceedings of ASME Turbo Expo 2003, ASME, New York, ASME Paper No. GT2003-38304.
[36] Qiu, S., and Simon, T. W., 1997, "An Experimental Investigation of Transition as Applied to Low Pressure Turbine Suction Surface Flows," Proceedings of ASME Turbo Expo 1997, ASME, New York, ASME Paper No. 97-GT-455.
[37] Jiang, N., and Simon, T. W., 2003a, "The Influence of Unsteady Acceleration and Turbulence Intensity on Transition in Low-Pressure Turbines," AIAA Paper No. AIAA-2003-3630.
[38] Jiang, N., and Simon, T. W., 2003b, "Modeling Laminar-to-Turbulent Transition in a Low-Pressure Turbine Flow Which is Unsteady Due to Passing Wakes: Part I, Transition Onset," Proceedings of ASME Turbo Expo 2003, ASME, New York, ASME Paper No. ASME-GT2003-38787.
[39] Jiang, N., and Simon, T. W., 2003c, "Modeling Laminar-to-Turbulent Transition in a Low-Pressure Turbine Flow Which is Unsteady Due to Passing Wakes: Part II, Transition Path," Proceedings of ASME Turbo Expo 2003, ASME, New York, ASME Paper No. ASME-GT2003-38963.
[40] Steelant, J. and Dick, E., 1996, "Modelling of Bypass Transition With Conditioned Navier-Stokes Equations Coupled to an Intermittency Transport Equation," Int. J. Numer. Methods Fluids **23**, pp. 193–220.
[41] Cho, J. R. and Chung, M. K., 1992, "A k-ε-γ Equation Turbulence Model," J. Fluid Mech. **237**, pp. 301–322.
[42] Simon, F. F. and Stephens, C. A., 1991, "Modeling of the Heat Transfer in Bypass Transitional Boundary-Layer Flows," NASA Technical Paper No. 3170.
[43] Menter, F. R., 1994, "Two-Equation Eddy-Viscosity Turbulence Models for Engineering Applications," AIAA J. **32**(8), pp. 1598–1605
[44] Gostelow, J. P., Blunden, A. R., and Walker, G. J., 1994, "Effects of Free-Stream Turbulence and Adverse Pressure Gradients on Boundary Layer Transition," ASME J. Turbomach. **116**, pp. 392–404.
[45] Abu-Ghannam, B. J. and Shaw, R., 1980, "Natural Transition of Boundary Layers-The Effects of Turbulence, Pressure Gradient, and Flow History," J. Mech. Eng. Sci. **22**(5), pp. 213–228.
[46] Davis, R. L., Carter, J. E., and Reshotko, E., 1987, "Analysis of Transitional Separation Bubbles on Infinite Swept Wings," ASME J. Turbomach. **25**(3), pp. 421–428.
[47] Rhie, C. M. and Chow, W. L. 1983, "Numerical Study of the Turbulent Flow Past an Airfoil With Trailing Edge Separation," AIAA J. **21**, pp. 1525–1532.
[48] Hsu, M. C., Vogiatzis, K. and Huang, P. G. 2003, "Validation and Implementation of Advanced Turbulence Models in Swirling and Separated Flows", AIAA Paper No. AIAA 2003-0766.
[49] Suzen, Y. B., and Huang, P. G., 2003, "Numerical Simulation of Wake Passing on Turbine Cascades," AIAA Paper No. AIAA-2003-1256.

Awatef A. Hamed

Widen Tabakoff

Department of Aerospace Engineering and Engineering Mechanics, University of Cincinnati, Cincinnati, OH 45220

Richard B. Rivir

Aeropropulsion and Power Directorate, Air Force Research Laboratory, Wright Laboratories Building 18, Wright Patterson AFB, OH 45433

Kaushik Das

Puneet Arora

Department of Aerospace Engineering and Engineering Mechanics, University of Cincinnati, Cincinnati, OH 45220

Turbine Blade Surface Deterioration by Erosion

This paper presents the results of a combined experimental and computational research program to investigate turbine vane and blade material surface deterioration caused by solid particle impacts. Tests are conducted in the erosion wind tunnel for coated and uncoated blade materials at various impact conditions. Surface roughness measurements obtained prior and subsequent to the erosion tests are used to characterize the change in roughness caused by erosion. Numerical simulations for the three-dimensional flow field and particle trajectories through a low-pressure gas turbine are employed to determine the particle impact conditions with stator vanes and rotor blades using experimentally based particle restitution models. Experimental results are presented for the measured blade material/coating erosion and surface roughness. The measurements indicate that both erosion and surface roughness increase with impact angle and particle size. Computational results are presented for the particle trajectories through the first stage of a low-pressure turbine of a high bypass turbofan engine. The trajectories indicate that the particles impact the vane pressure surface and the aft part of the suction surface. The impacts reduce the particle momentum through the stator but increase it through the rotor. Vane and blade surface erosion patterns are predicted based on the computed trajectories and the experimentally measured blade coating erosion characteristics. [DOI: 10.1115/1.1860376]

Introduction

Gas turbine materials have progressed rapidly beyond traditional ferrous alloys. New blade coatings and materials are continuously being developed to meet the challenging requirements of modern gas turbine engines. Because of the serious consequences of erosion on gas turbine life and performance, it is necessary to gain a better understanding of the blade surface degradation mechanisms. A complex phenomenon, such as blade surface deterioration by erosion, requires a combination of experimental and computational research efforts [1]. Experimental studies require special high-temperature erosion wind tunnels to simulate the wide range of aerodynamic and thermal conditions in modern gas turbines. Erosion test results for gas turbine super alloys and coatings demonstrated that the eroding particle characteristics are affected by temperature and impact conditions [2–4].

In compressors, erosion by particle impacts reduces the blade chord, alters the shape of the leading and trailing edges, and increases the blade surface roughness [5,6]. Surface roughness measurements on gas turbine blades indicated an order-of-magnitude increase in rms roughness [7,8]. Bons et al. [9] conducted surface roughness measurements on in-service blades and vanes of ground-based turbines. They concluded that the operating conditions and service history determine the resulting blade erosion and roughness, and documented, on average, roughness levels 4–8 times greater than the levels for production hardware. Several investigators [10–13] reported increased heat transfer on turbine blades with simulated roughness.

Particle size affects the blade impact patterns because smaller particles tend to follow the flow while larger particles impact the vane and rotor blades. However, even particles of 1–30 μm have been known to damage exposed components of coal-burning turbines [14]. Numerical simulations of the particle trajectories through gas turbine engines provide valuable information on the vane and blade impact patterns [1,15–18]. Accurate predictions require correlations based on reliable measurements of particle restitution characteristics in tunnels equipped with optical access [19,20].

In the current work, a combined experimental and numerical investigation was conducted to study the dynamics of suspended solid particles in gas turbine flows and the associated blade surface material degradation from particle surface impacts. The experimental studies characterize blade and coating material erosion and surface roughness variation with particle impact conditions. The numerical simulations of particle trajectories model the effects of aerodynamic forces on the particles through the three-dimensional (3D) turbine flow field, the change in the magnitude and direction of particle velocities due to impacts with the stationary and rotating turbine blade surfaces. The trajectory simulations provide the vane and blade surface impact patterns at the operating conditions associated with particle ingestion into the turbine. Predictions of vane and blade surface erosion patterns and the associated surface roughness are based on the computed particle impact statistics and the experimentally measured data.

Experimental Work

Tests were conducted to characterize the blade and coating material deterioration in terms of mass removal and change in surface roughness associated with particle impacts. The experiments were conducted over a range of impact angles corresponding to those encountered in the gas turbine environment. The tested samples were evaluated before and after they were tested in the tunnel with a calibrated mass of erosive particles to determine the eroded weight and to detect the change in surface roughness.

The University of Cincinnati (UC) erosion wind tunnel facility is shown schematically in Fig. 1. It consists of the following components: particle feeder (A), main air supply pipe (B), combustor (C), particle preheater (D), particle injector (E), acceleration tunnel (F), test section (G), and exhaust tank (H). Abrasive particles of a given constituency and measured weight are placed into the

Contributed by the International Gas Turbine Institute (IGTI) of THE AMERICAN SOCIETY OF MECHANICAL ENGINEERS for publication in the ASME JOURNAL OF TURBOMACHINERY. Paper presented at the International Gas Turbine and Aeroengine Congress and Exhibition, Vienna, Austria, June 13–17, 2004, Paper No. 2004-GT-54328. Manuscript received by IGTI, October 1, 2003; final revision, March 1, 2004. IGTI Review Chair: A. J. Strazisar.

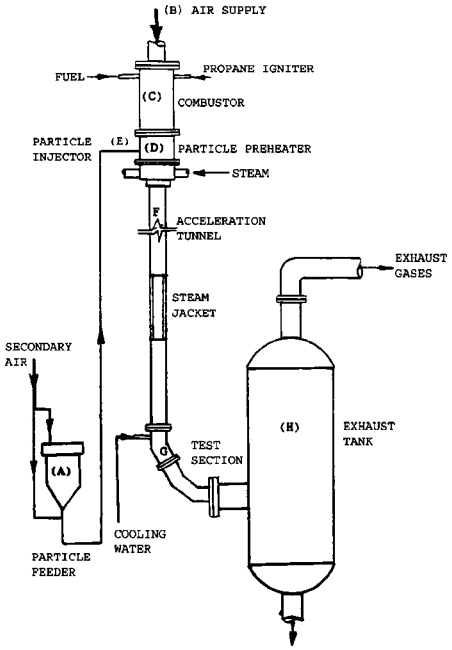

Fig. 1 Schematic of erosion test facility

particle feeder (A). The particles are fed into a secondary air source and blown into the particle preheater (D), and then to the injector (E), where they mix with the primary air supply (B), which is heated by the combustor (C). The particles are then accelerated via high velocity air in a constant-area steam-cooled duct (F) and impact the specimen in the test section (G). The particulate flow is then mixed with coolant and directed to the exhaust tank.

Varying the tunnel airflow controls particle velocity, while the particle impingement angle is controlled through the target sample rotation relative to the airflow. Heating the flow stream, which, in turn, heats the erosive media and sample(s), varies the temperature. As can be seen from Fig. 1, the tunnel geometry is uninterrupted from the acceleration tunnel throughout the test section in order to preserve the aerodynamics of the flow passing over the sample(s).

The tests were carried out for coupons of coated and uncoated power generation turbine blade materials. The coupons were mounted on a sample holder and placed in the erosion wind tunnel at the designated angles and subjected to erosion by a calibrated mass of particles. The holder protected all but one target coupon surface that was exposed to particle impacts. The samples were weighed, and their surface roughness was measured using a Taylor Hobson Talysurf before and after the erosion tests. Post erosion surface traverses were centered on the eroded portion of the sample. The two-dimensional (2D) surface roughness measurements of the coupon surface were sampled in two perpendicular directions. The arithmetic mean R_a, the root mean square deviation R_q, the maximum peak above the mean of the sample area R_p, and the maximum peak-to-valley dimension R_t of the roughness profile were determined from the unfiltered data. Three-dimensional measurements were taken in square millimeter areas at the center of selected samples to determine S_a, S_q, S_p, and S_t.

Computational Work

Numerical simulations were conducted to determine the three-dimensional flow field and the associated solid particle trajectories through a turbine stage. The compressible viscous flow and dispersed particle dynamics simulations were conducted using FLUENT 6.1 [21]. The gas phase simulations are based on the implicit solution of the Reynolds-averaged Navier-Stokes equations in conservation and the renormalization group (RNG) k-ε turbulence model with wall function [22]. The Lagrangian particle dynamics simulations were performed in the relative reference frame of each blade row and included models for the momentum exchanges with the flow field and blade passage surfaces.

Table 1 Particle size distribution

Particle size (μm)	% by weight finer than
1000	100
500	85–90
250	70–75
125	50–55
75	25–30
<75	10–15

Since the high inertia particle trajectories deviate from the flow and they impact the vane and blade surfaces. The simulations incorporate empirical particle-gas and particle-surface interaction models. Particle-gas interaction models represent the momentum exchange between the two phases through the aerodynamic forces due to the motion of particles relative to the gas flow field. Particle-surface interaction models in the trajectory simulations are based on correlations of laser Doppler velocimetry (LDV)-measured particle restitution characteristics [23,24].

Particle trajectories are determined from the stepwise integration of their equations of motion in each blade row reference frame

$$\frac{d\bar{u}_p}{dt} = F_D(\bar{u} - \bar{u}_p) + \frac{\bar{g}(\rho_p - \rho)}{\rho_p} + \bar{F}_R$$

The terms on the right-hand side represent the aerodynamic, gravitational, and forces acting on the particle due to the reference frame rotation. Neglecting interparticle collisions and particle rotation drag is the main aerodynamic force on high inertia particles

$$F_D = \frac{18\ \mu}{\rho_p D_p^2}\frac{C_D \mathrm{Re}}{24}$$

The following expression was used for the drag coefficient [25]:

$$C_D = \frac{24(1 + b_1 \mathrm{Re}^{b_2})}{\mathrm{Re}} + \frac{b_3 \mathrm{Re}}{b_4 + \mathrm{Re}}$$

The Reynolds number Re is based on the slip velocity and particle diameter, and the coefficients b_1, b_2, b_3, and b_4 are functions of the particle shape factor [21].

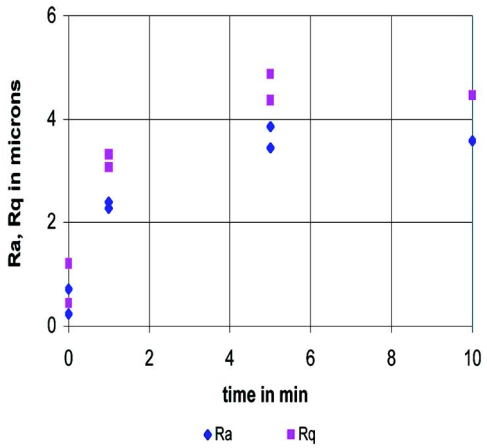

Fig. 2 Measured surface roughness for coated samples in erosion tests with 1500 μm crushed quartz at 90 deg

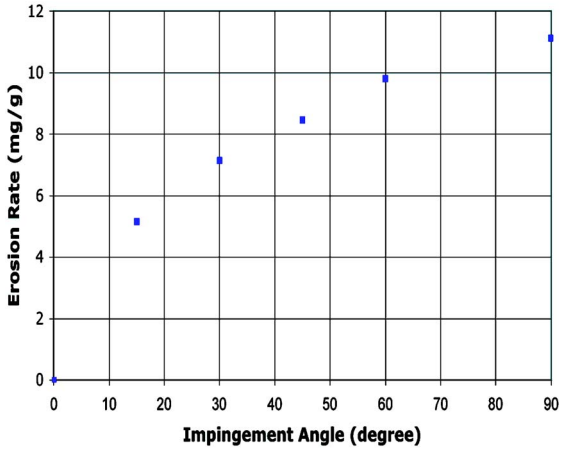

Fig. 3 Change in erosion rate with impingement angle for 1500 μm crushed quartz at 600 ft/s

The force $\bar{F}_R$ due to reference frame rotation is zero in the stator, but includes the centrifugal force and Coriolis acceleration in the rotor.

Results and Discussions

Erosion tests were conducted with runway sand and 1500 μm crushed quartz particles at 300 and 600 ft/s. The size distribution for runway sand is given in Table 1; its composition is 60% quartz, 26% gypsum, 12% calcite, and 2% soluble salts. Test coupons measuring 3×2 cm were cut from bars of coated and uncoated ground-based turbine blade materials. Before sectioning, the bar was traversed at 2.54 cm intervals along the centerline. Typical pre-erosion values of surface roughness were 1.07–2.14 μm for R_a, 1.12–4.08 μm for R_q, and 8.44–26.14 μm for R_t. Two- and three-dimensional traverses were performed on the target face after the erosion tests. The 2D traverses were 5–10 mm in length and were taken in two orthogonal directions with a minimum of 1000 points per traverse. The 3D traverses were 3×3 mm to 5×5 mm with a minimum of 1,000,000 points.

A set of erosion tests was performed initially in order to establish the erosive particle mass required to affect surface roughness in subsequent accelerated erosion tests. The results of these tests are presented in Fig. 2 for 1500 μm crushed quartz particles at 600 ft/s. The figure indicates negligible change in the surface roughness between the 5 and 10 min erosion tests. Experimental results from accelerated erosion tests of coated coupons are presented in Fig. 3 for quartz particles at 600 ft/s and Fig. 4 for runway sand at 300 ft/s. These results show that the erosion rate increases with increased velocity and impingement angle and that it is much higher in the case of 1500 μm crushed quartz. The corresponding change in measured roughness parameters with particle impact angle is shown in Fig. 5 for targets eroded by runway sand at 300 ft/s.

A photograph (magnification 2.8×) of an eroded coupon sample is shown in Fig. 6. One can see the contrast between the eroded and the uneroded portion on the right-hand side where the sample was covered by the clamp. The pictured surface measured

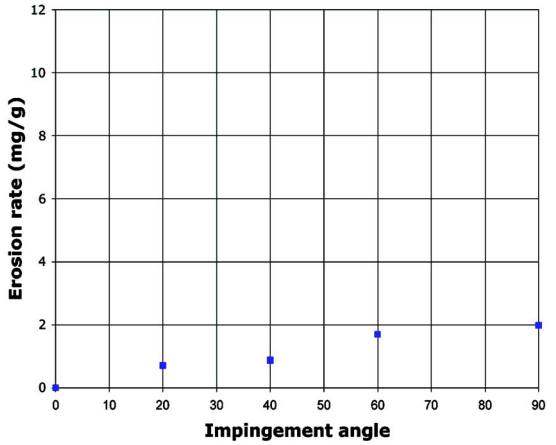

Fig. 4 Change in erosion rate with impingement angle for runway sand at 300 ft/s

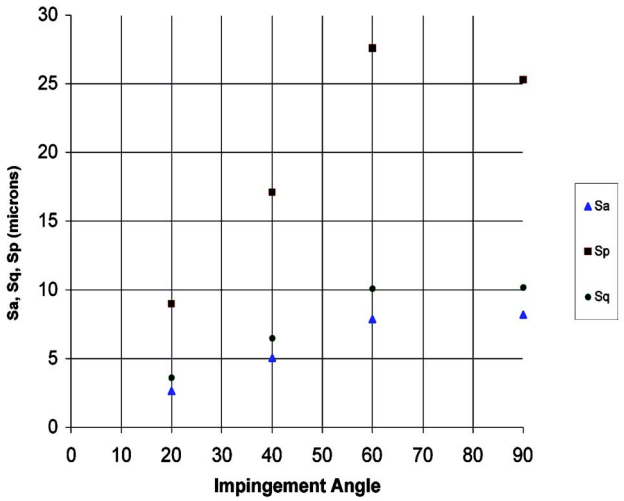

Fig. 5 Effect of impingement angle on eroded surface roughness for runway sand at 300 ft/s

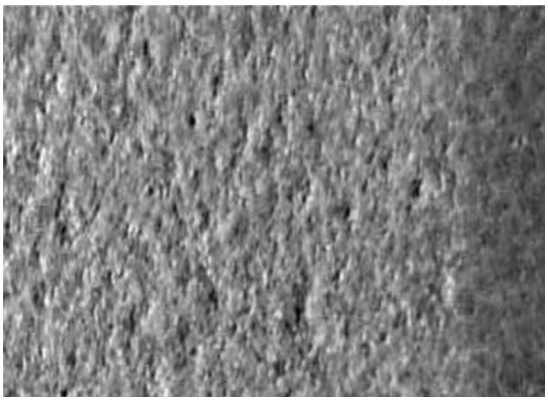

Fig. 6 Coated sample surface after testing at 300 ft/s with runway sand at 60 deg impingement angle

Table 2 Roughness parameters for pressure surface roughened blade

Location	R_a	R_q	R_p	R_t
Suction side, leading edge	5.75	7.30	13.82	44.10
Pressure side, leading edge	3.93	5.72	11.84	36.37
Pressure side, midchord	3.28	4.51	9.63	31.92
Pressure side, trailing edge	4.04	5.16	12.60	33.24

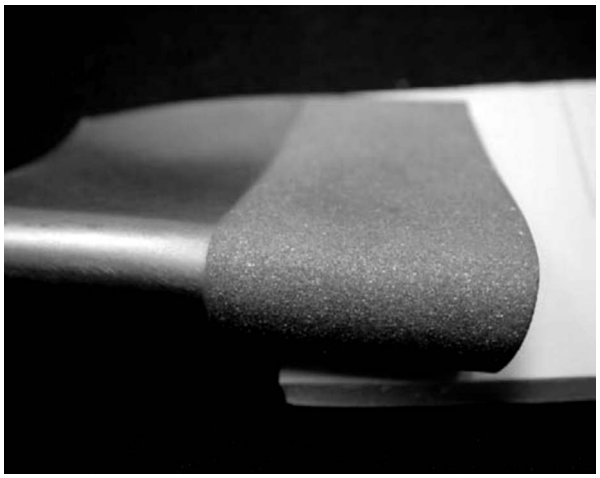

Fig. 7 Vane subjected to 1500 μm particles, 300 ft/s, 30 deg incidence. Erosion rate 5 mg/g of particles.

R_a=3.58 μm along the major axis and 3.34 μm along the minor axis compared to R_a=0.2736 μm in the clamped area.

AFRL provided a stainless steel vane with R_a surface finish of 0.34 μm for erosion testing. Table 2 summarizes the measured vane surface roughness after being subjected to impact with 20 g of 1500 μm crushed quartz particles at 300 ft/s and 30 deg angle of attack for 17 min. The measurements were obtained from four spanwise traverses. Traverse 1 was on the suction side of the leading edge and traverses 2–4 were equally spaced on the eroded pressure surface. Figure 7 presents a photograph of the eroded vane surface.

Table 3 Geometrical parameters for GE E^3 LP Turbine

	Stator (in.)	Rotor (in.)
Blade height	3.35	4.13
Midspan chord	2.10	1.16
Midspan pitch	1.10	0.68

Numerical simulations were performed for the GE E^3 first stage LP turbine at inlet stagnation temperature and pressure of 2001.6 °Rankine and 36.94 psia, respectively. Table 3 lists the geometrical parameters for the stator vanes and rotor blades. A three-dimensional H-type grid was used for the stator and rotor. The computational grid consisted of 80 grid points in the streamwise direction, 50 grid points blade to blade, and 80 grid points in the spanwise direction. A highly stretched mesh spacing was employed in the regions close to the blade passage surfaces, with y^+=25, for the first point next to the wall.

The stagnation pressure and temperature were specified at the inlet with no-slip conditions at the stationary walls and prescribed velocity conditions at the rotating walls. At the exit boundary, the static pressure was specified at the hub, and the radial pressure distribution was determined from integrating the axisymmetric radial momentum equation. The particles were introduced after the flow solution was converged, based on a four-order-of-magnitude reduction in the residuals. Because the particle loadings encountered in gas turbine applications are sufficiently low, the solid

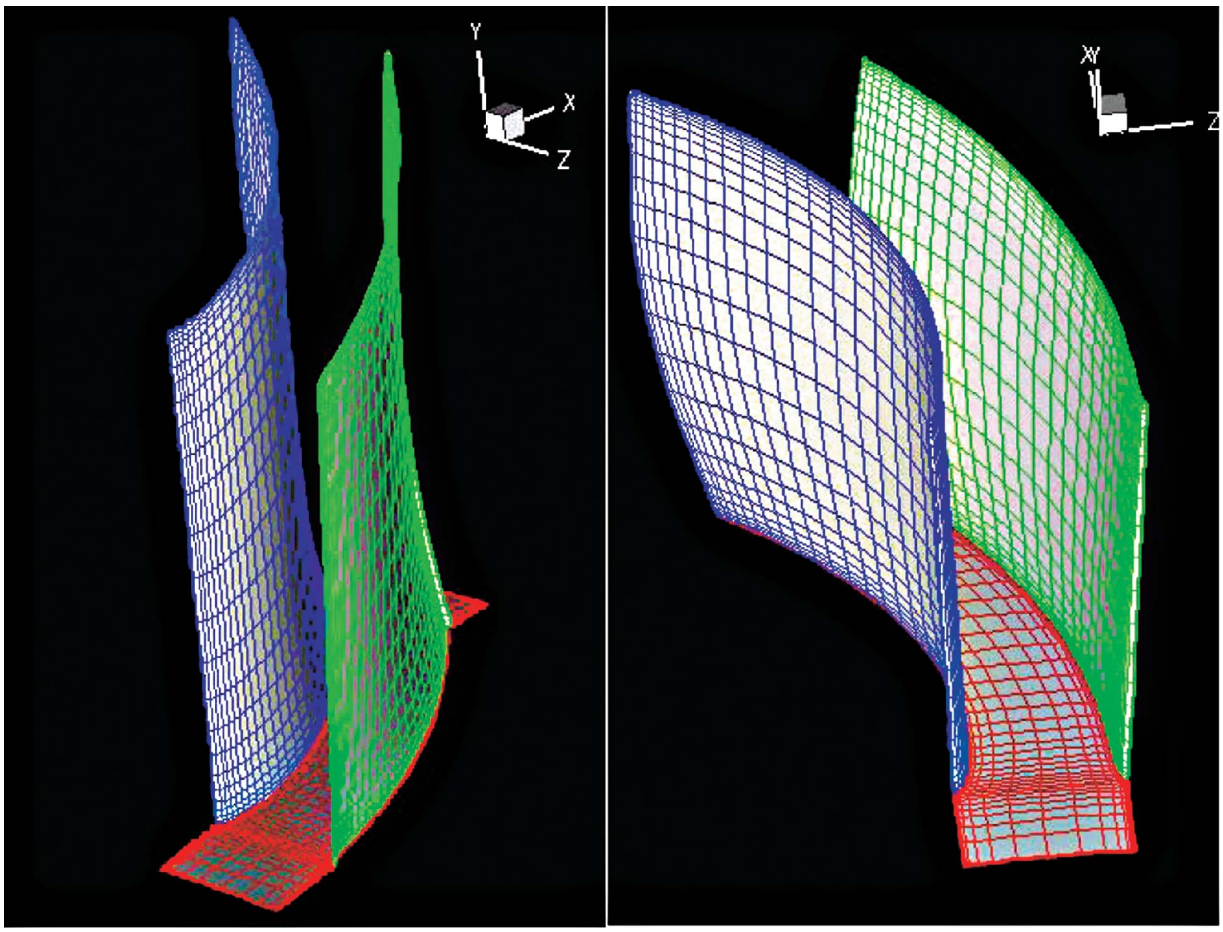

Fig. 8 Computational grid

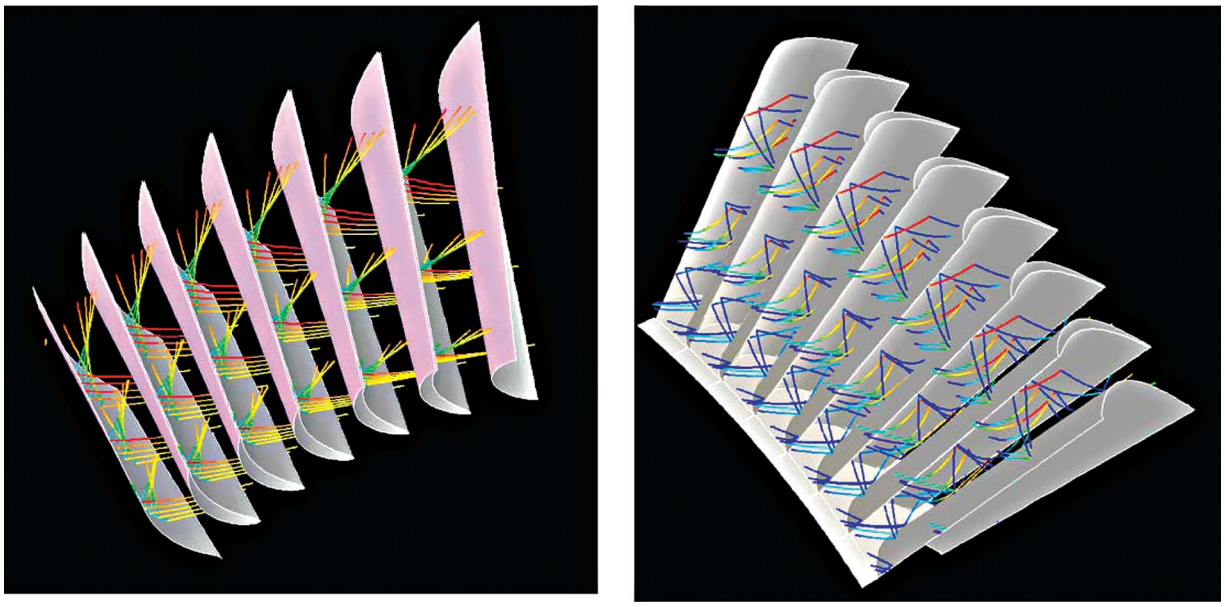

Fig. 9 30 μm particle trajectories: (a) (left) rear view of the stator and (b) (right) front view of the rotor

particle dynamics were simulated using one-way gas-particle interaction models, which do not take into consideration the effects of dispersed particles' momentum exchange on the gas flow field.

Figure 8 presents the grid used in the flow field, particle trajectories, and blade erosion rate computations. Figures 9–11 present the results of the 3D trajectory simulations for 30 and 1500 μm particles. Figure 9 shows that the 30 μm particles impact the vane pressure surface and that the vane impacts lower the particles' absolute velocities. This leads to a significant difference between the relative direction of particles as they enter the following rotor compared to the gas. The particles subsequently impact the rotor blade suction surface, as seen in Fig. 9(*b*). Figures 10 and 11 present the 30 and 1500 μm trajectories through the turbine stage mean diameter. The figures show that the inertia-dominated large particles cross the stator passage after impacting the vane pressure surface to impact the vane suction surface near the trailing edge. The smaller particles, on the other hand, also impact the vane pressure surface, but they are subsequently influenced by the gas flow and leave the flow passage without impacting the vane suction surface. The smaller particles enter the rotor blade passage and continue their trajectory after impacting the rotor blade suction surface. On the other hand, the large particles rebound from the rotor blades' leading edge and reenter the stator. In general, the particles centrifuge in the radial direction after the vane and blade surface impacts. In general, the large particles encounter more vane and blade surface impacts than the smaller particles.

The experimentally measured blade material erosion data together with the vane surface impact data from 2000 particle trajectory simulations were used to compute the vane surface erosion. Figure 12 presents the vane surface impact frequency distribution (the number of impacts per unit area per gram of ingested particles in the turbine). Figure 13 presents the corresponding impingement angles' mean values. The experimentally measured erosion rate of Fig. 4 was then used along with the vane

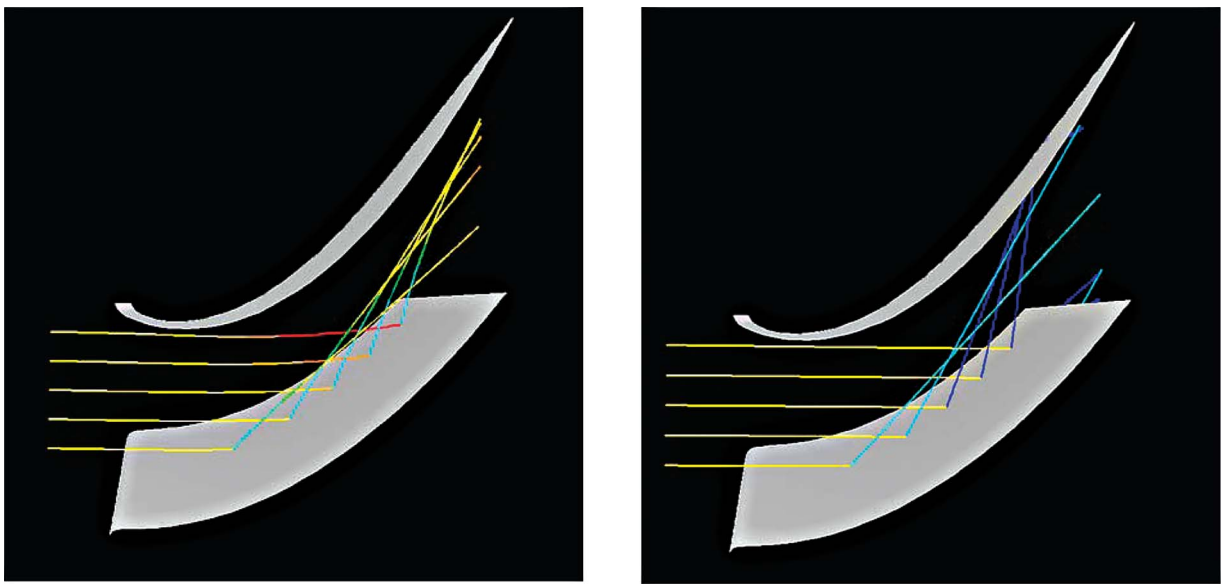

Fig. 10 Top view of particle trajectories through stator: (a) (left) 30 μm particles and (b) (right) 1500 μm particles

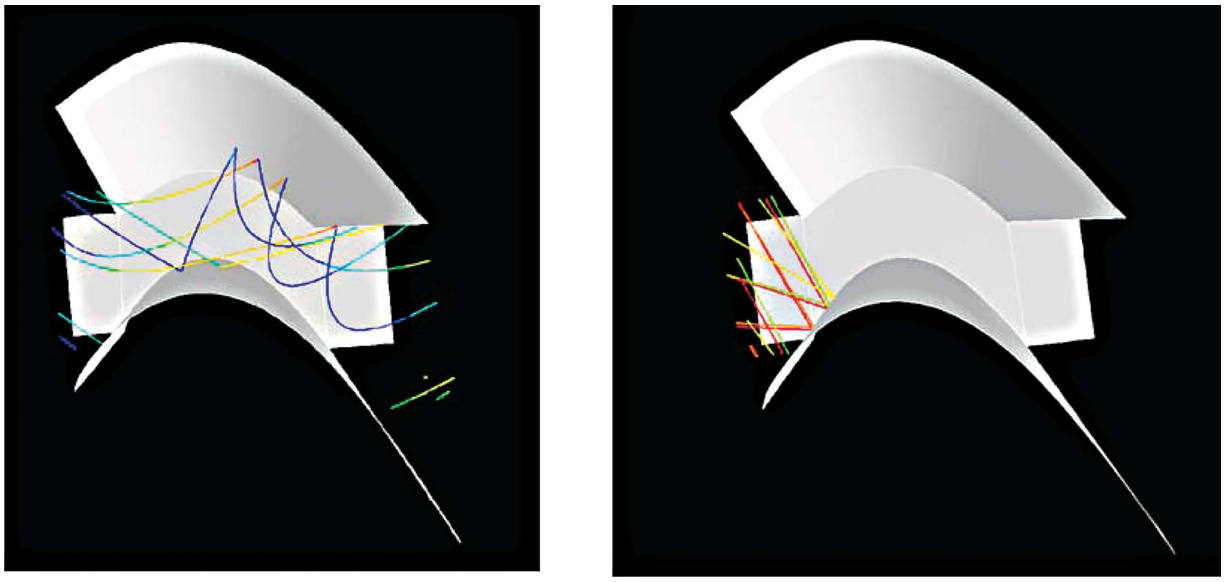

Fig. 11 Top view of particle trajectories through rotor: (a) (left) 30 μm particles and (b) (right) 1500 μm particles

surface impact data to compute the vane erosion rate per unit surface area per unit mass of ingested particles in the turbine. Figure 14 shows increasing erosion rates over the vane's pressure surface toward the trailing edge and a narrow high-erosion band at the vane's leading edge.

Summary

Turbine vane/blade surface deterioration is strongly dependent on the turbine geometry, blade surface material, and particle characteristics. Experimental results for blade and coating material erosion indicate that both erosion rate and surface roughness increase with the eroding particle impact velocities and impingement angles and that larger particles produce higher surface roughness. The computational results of particle dynamics simulations indicate that many particles impact the vane pressure surface and that the larger particles cross over and impact the vane suction surface toward the trailing edge. The vane surface impacts reduce the particles' absolute velocity and, consequently, they impact the rotor blade suction surface. Predictions based on the com-

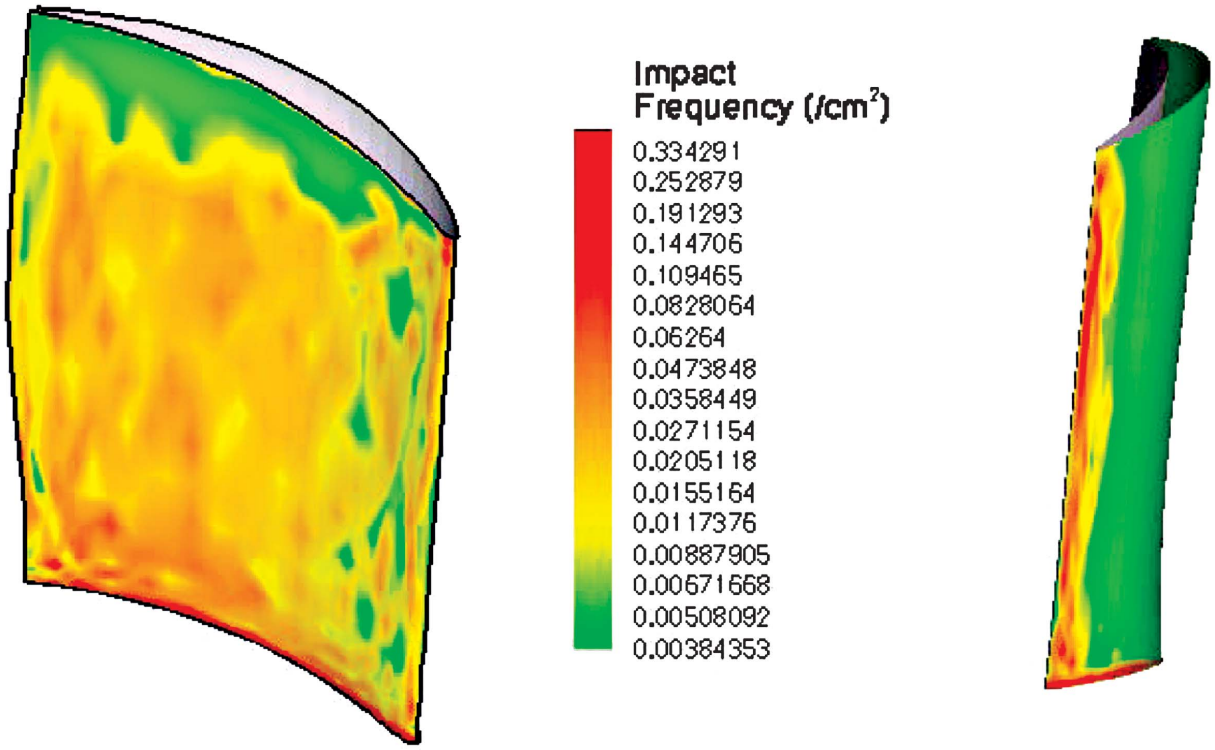

Fig. 12 Impact frequency: (a) (left) vane pressure surface and (b) (right) vane leading edge

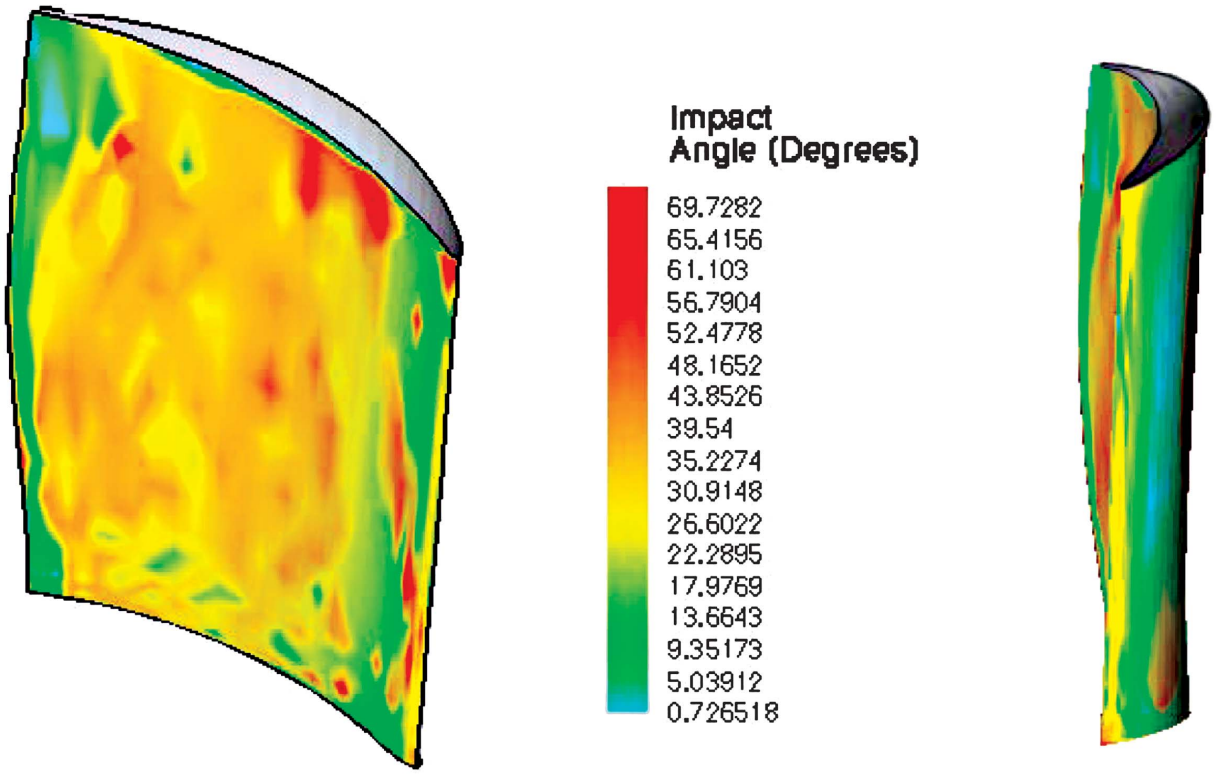

Fig. 13 Particle mean impact angle: (a) (left) vane pressure surface and (b) (right) vane leading edge

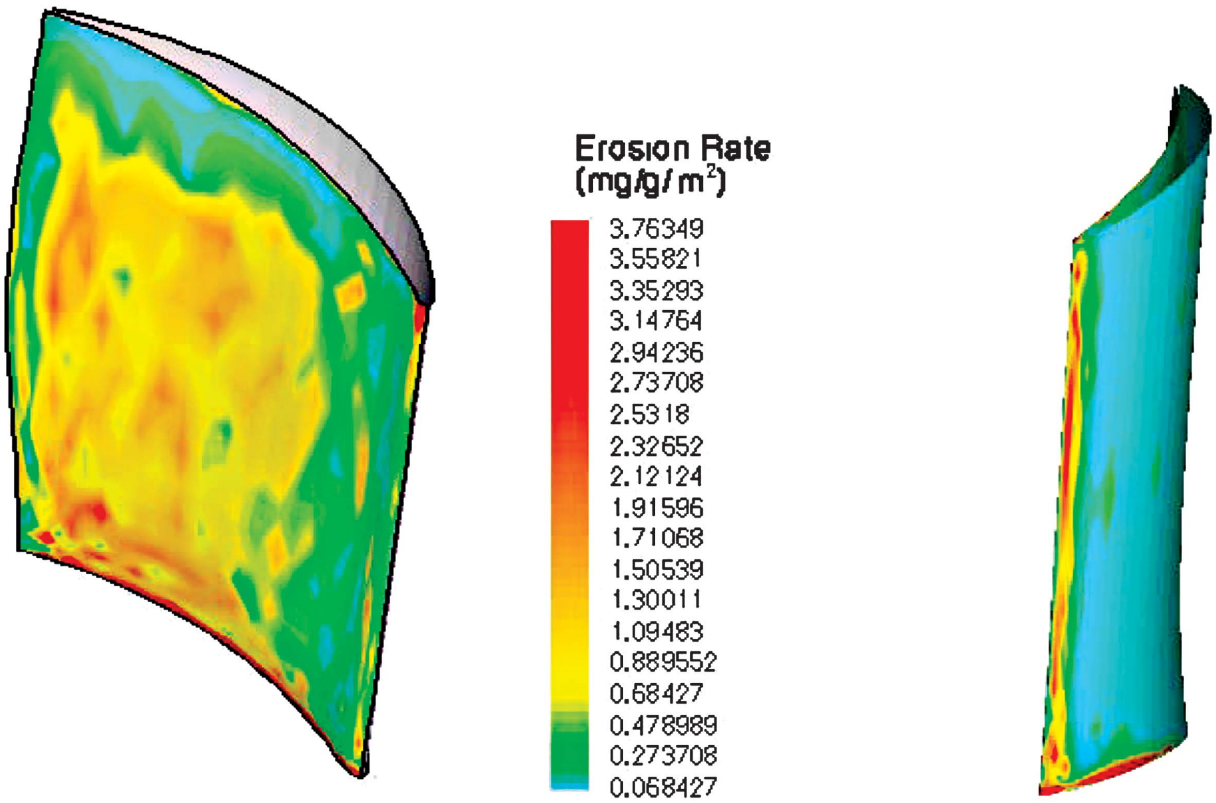

Fig. 14 Erosion Rate: (a) (left) vane pressure surface and (b) (right) vane leading edge

puted particle trajectories and the experimental characterization of coated cane material indicates a narrow band of high erosion at the vane leading edge and pressure surface erosion increasing toward the trailing edge.

Acknowledgment

This work was sponsored by the US Department of Energy through a grant in cooperation with the South Carolina Institute for Energy Studies (UTSR) at Clemson University. Project Monitor: Richard Wenglarz.

Nomenclature

D_p = particle diameter, μm
E = erosion rate (material removal per unit mass of particles)
R = roughness profile from linear 2D surface measurements, μm
S = roughness profile from linear 3D surface measurements, μm
$\bar{u}$ = gas velocity
$\bar{u}_p$ = particle velocity
Re = Reynolds number based on slip velocity $(\bar{u}-\bar{u}_p)$ and particle diameter (D_p)
ρ = density
μ = molecular viscosity
D_q = mean profile slope of the profile elements within a sampling length, deg

Subscripts

a = arithmetic mean deviation of the profile, z units
q = rms deviation of the profile, z units
v = maximum depth of the profile below the mean line of the profile, z units
p = maximum height of the profile above the mean line of the profile, z units
t = maximum peak to valley of the profile, z units
pc = mean height of the elements, z units

References

[1] Hamed, A., and Tabakoff, W., 1994, "Experimental and Numerical Simulation of Ingested Particles in Gas Turbine Engines," *AGARD (NATO) 83rd Symposium of Propulsion and Energetics Panel on Turbines, Rotterdam*, The Netherlands, April 25-28.
[2] Tabakoff, W., 1995, "High-Temperature Erosion Resistance Coatings for Use in Turbomachinery," Wear **186-187**, pp. 224–229.
[3] Tabakoff, W., 1999, "Protection of Coated Superalloys From Erosion in Turbomachinery and Other Systems Exposed to Particulate Flows," Wear **233-235**, pp. 200–208.
[4] Tabakoff, W., Hamed, A., and Wenglarz, R., 1988, "Particulate Flows, Turbomachinery Erosion and Performance Deterioration," Von Karman Lecture Series 1988–1989, May 24–27, Brussels, Belgium.
[5] Balan, C., and Tabakoff, W., 1984, "Axial Flow Compressor Performance Deterioration," AIAA 84-2108.
[6] Hamed, A., Tabakoff, W., and Singh, D., 1998, "Modeling of Compressor Performance Deterioration Due to Erosion," Int. J. Rotating Mach. **4**, pp. 243–248.
[7] Taylor, R. P., 1990, "Surface Roughness Measurements on Gas Turbine Blades," ASME J. Turbomach. **112**, pp. 175–180.
[8] Tarada, F., and Suzuki, M., 1993, "External Heat Transfer Enhancement to Turbine Blading Due to Surface Roughness," *ASME IGTI*, Cincinnati, May, ASME, New York, ASME Paper 93-GT-74.
[9] Bons, J. P., Taylor, R. P., McClain, S. T., and Rivir, R. B., 2001, "The Many Faces of Turbine Surface Roughness," *Proc. of ASME Turbo Expo*, June, New Orleans, ASME, New York, ASME Paper No. 2001-GT-0163.
[10] Blair, M. F., 1994, "An Experimental Study of Heat Transfer in a Large-Scale Turbine Rotor Passage," ASME J. Turbomach. **116**, pp. 1–13.
[11] Hoffs, A., Drost, U., and Bolcs, A., "Heat Transfer Measurements on a Turbine Airfoil at Various Reynolds Numbers and Turbulence Intensities Including Effects of Surface Roughness," *IGTI, Birmingham, UK*, June 1996, ASME, New York, ASME Paper No. 96-GT-169.
[12] Bogard, D. G., Schmidt, D. L., and Tabbita, M., 1998, "Characterization and Laboratory Simulation of Turbine Airfoil Surface Roughness and Associated Heat Transfer," ASME J. Turbomach. **120**, pp. 337–342.
[13] Abuaf, N., Bunker, R. S., and Lee, C. P., 1998, "Effects of Surface Roughness on Heat Transfer and Aerodynamic Performance of Turbine Airfoils," ASME J. Turbomach. **120**, pp. 522–529.
[14] McCay, L., 1973, "The Coal Burning Gas Turbine Project," Report of Interdepartmental Gas Turbine Steering Committee, Australian Government Publishing Service.
[15] Tabakoff, W., Hamed, A., and Metwally, M., 1991, "Effect of Particle Size Distribution on Particle Dynamics and Blade Erosion in Axial Flow Turbines," ASME J. Eng. Gas Turbines Power **113**, pp. 607–615.
[16] Metwally, M., Tabakoff, W., and Hamed, A., 1995, "Blade Erosion in Automotive Gas Turbine Engine," ASME J. Eng. Gas Turbines Power **117**, pp. 213–219.
[17] Hamed, A., and Kuhn, T. P., 1995, "Effects of Variational Particle Restitution Characteristics on Turbomachinery Erosion," ASME J. Eng. Gas Turbines Power **117**, pp. 432–440.
[18] Hamed, A., 1989, "Influence of Secondary Flow on Turbine Erosion," ASME J. Turbomach. **111**(3), pp. 310–314.
[19] Tabakoff, W., Malak, M. F., and Hamed, A., 1987, "Laser Measurements of Solid Particles Rebound Parameters Impinging 2024 Aluminum and 6Al-4V Titanium Alloys," AIAA J. **25**(5), pp. 721–726.
[20] Tabakoff, W., Murugan, D. M., and Hamed, A., 1994, "Effects of Target Materials on the Particle Restitution Characteristics for Turbomachinery Application," AIAA Paper No. 94-0143.
[21] *FLUENT 6.1 User's Guide*, 2003.
[22] Tabakoff, W., Hamed, A., Metwally, M., Yeuan, J., and Pasin, M., 1990, "Study of Particle Rebound Characteristics and Material Erosion at High Temperatures," Final Technical Report, Fossil Energy Materials Program, US Department of Energy, ORNL/Sub/84-89628/03.
[23] Tabakoff, W., Hamed, A., Metwally, M., and Yeuan, J., "Study of Particle Rebound Characteristics and Material Erosion at High Temperatures," ORNL/FMP 902, AR&TD Fossil Energy Materials Semi-Annual Progress Report for Period Ending 09-30-1990, ORNL, Part IV, pp. 381–393.
[24] Morsi, S. A., and Alexander, A. J., 1972, "An Investigation of Particle Trajectories in Two-Phase Flow Systems," J. Fluid Mech., **50**(2), pp. 193–208.
[25] Haider, A., and Levenspiel, O., 1989, "Drag Coefficient and Terminal Velocity of Spherical and Nonspherical Particles," Powder Technol. **58**, pp. 63–70.

Surface Roughness Effects on Turbine Blade Aerodynamics

Frank Hummel

Michael Lötzerich

ALSTOM Power (Switzerland),
Brown Boveri Strasse 7,
CH-5401 Baden, Switzerland

Pasquale Cardamone

Leonhard Fottner[1]

Institut für Strahlantriebe,
Universität der Bundeswehr München,
Werner-Heisenberg-Weg 39,
D- 85577 Neubiberg, Germany

The aerodynamic performance of a turbine blade was evaluated via total pressure loss measurements on a linear cascade. The Reynolds number was varied from 600 000 to 1 200 000 to capture the operating regime for heavy-duty gas turbines. Four different types of surface roughness on the same profile were tested in the High Speed Cascade Wind Tunnel of the University of the German Armed Forces Munich and evaluated against a hydraulically smooth reference blade. The ratios of surface roughness to chord length for the test blade surfaces are in the range of $Ra/c=7.6\times10^{-06}-7.9\times10^{-05}$. *The total pressure losses were evaluated from wake traverse measurements. The loss increase due to surface roughness was found to increase with increasing Reynolds number. For the maximum tested Reynolds number of* $Re=1\,200\,000$ *the increase in total pressure loss for the highest analysed surface roughness value of* $Ra=11.8$ μm *was found to be 40% compared to a hydraulically smooth surface. The results of the measurements were compared to a correlation from literature as well as to well-documented measurements in literature. Good agreement was found for high Reynolds numbers between the correlation and the test results presented in this paper and the data available from literature.* [DOI: 10.1115/1.1860377]

1 Introduction

The aerodynamic design of modern turbines for heavy duty gas turbines gives only few opportunities for further improvement in isentropic efficiency. With frozen component efficiencies the only way of major performance improvements is to improve the overall engine cycle efficiency. Therefore the trend goes continuously towards higher hot gas temperatures at the turbine inlet and higher pressure ratios. Especially intensive use of thermal barrier coatings on turbine front stages allowed a significant increase in hot gas temperature in the past decade [1]. As these coatings are sprayed on blading surfaces, changes in surface quality are observed either due to the spraying process itself, the coating material granularity or even due to erosion of the coatings under operating conditions [2]. Typically the surface roughness increases due to the coating process. Bons et al. [2] describe in detail which types of surface roughness typically occur in gas turbine applications. To maintain a constant isentropic efficiency of the coated components in comparison to uncoated parts, it is of interest to understand the impact of surface roughness on blade aerodynamic losses.

The literature on this subject is case dependent without a common understanding on how to predict the effects of surface roughness on turbine blading aerodynamics.

Abuaf et al. [3] give experimental results in terms of row efficiency loss differences of up to $\Delta\eta_{row}=0.23\%$ for a vane of $c=96$ mm chord length and surface roughness values of $Ra=0.81-2.33$ μm at Reynolds numbers from $Re=680\,000$ to $2\,300\,000$, therefore comparatively low Ra/c values of $8.46\times10^{-6}-2.4\times10^{-5}$.

Watt et al. [4] show experimental results for the total pressure loss difference due to surface roughness of a nozzle guide vane of a chord length $c=69$ mm and surface roughness values of $Ra=7-10$ μm and $Ra=2$ μm at Reynolds numbers from $Re=400\,000$ to $2\,300\,000$. The values of Ra/c for these tests are 2.9×10^{-5} and 1.23×10^{-4}.

The more recent work of Boyle and Senyitko [5] shows differences in total pressure loss for a nozzle guide vane of $c=104$ mm chord length and surface roughness values of $Ra=14.2$ μm and 1.2 μm for Reynolds numbers from $Re=150\,000$ to $1\,800\,000$. The corresponding values for Ra/c are 1.37×10^{-4} and 1.15×10^{-5}.

The mentioned literature reveals that a lot of experimental experience exists for small Ra/c values around $0.8\times10^{-5}-2.0\times10^{-5}$ and some data exists for comparatively large values around $1.1\times10^{-4}-1.4\times10^{-4}$. Therefore the main aims of this paper are to show experimental results for surface roughness to chord length ratios in between the ranges known in literature and to compare the results to a theoretical correlation available. Special emphasis was given to heavy duty gas turbine applications with Reynolds numbers $Re=600\,000-1\,200\,000$.

2 Experimental Setup and Measurement Techniques

2.1 Geometry and Test Facility. The experimental investigations were carried out at the high-speed cascade wind tunnel (HGK) of the University of the German Armed Forces in Munich (UniBwM). The HGK is a continuously running cascade wind tunnel with the capability to vary Mach and Reynolds number independently. Typical turbomachine operating conditions can be achieved. A detailed description of the facility is given by Sturm and Fottner [12]. Inlet turbulence intensity to the test cascade is varied by exchangeable grids in the inlet duct. A cross section of the test facility is shown in Fig. 1.

The blade profiles used for this test series represent a first stage blade at midspan of a heavy duty gas turbine. The main geometry parameters of the test blade profile as well as the nominal operating condition of the blade are summarized in Fig. 2. The cascade is made up of five test blades. For each test series, one of these blades in the center of the arrangement was equipped with a special surface finish.

For representing engine ready surface roughness conditions of ceramic coatings two approaches were used. For the first test series a manufactured grooved metal surface was compared to a smooth metal surface. The grooves were oriented in spanwise di-

[1]Deceased.

Contributed by the International Gas Turbine Institute (IGTI) of THE AMERICAN SOCIETY OF MECHANICAL ENGINEERS for publication in the ASME JOURNAL OF TURBOMACHINERY. Paper presented at the International Gas Turbine and Aeroengine Congress and Exhibition, Vienna, Austria, June 13–17, 2004, Paper No. 2004-GT-53314. Manuscript received by IGTI, October 1, 2003; final revision, March 1, 2004. IGTI Review Chair: A. J. Strazisar.

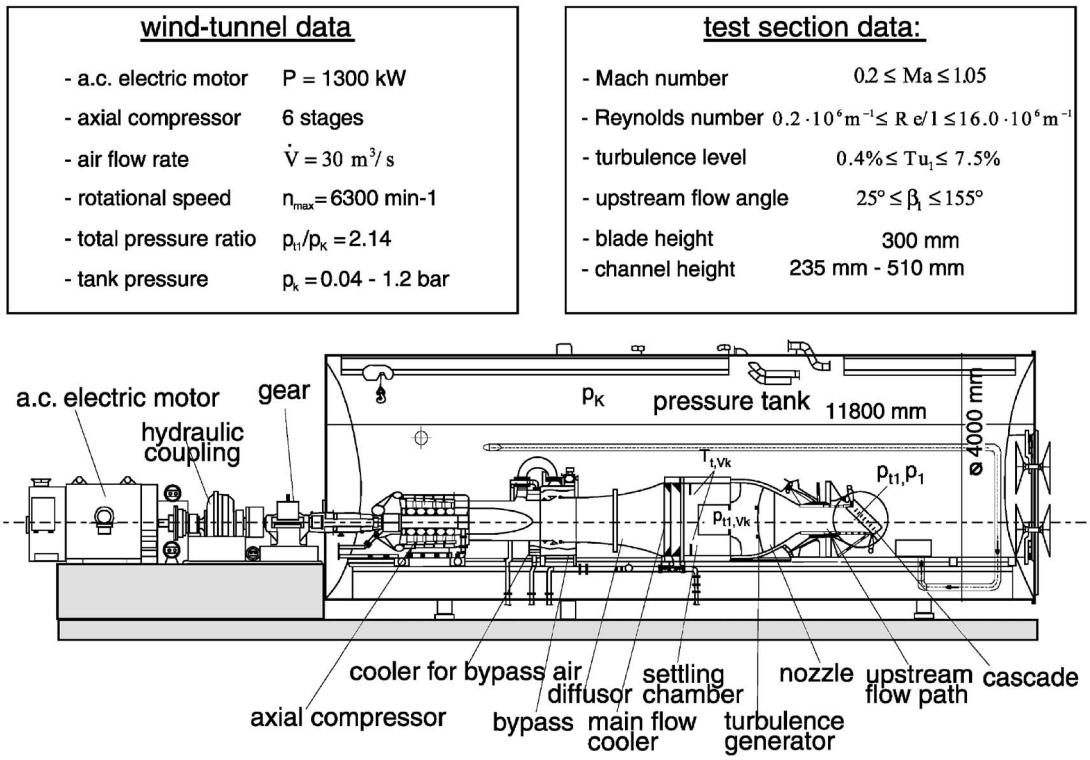

Fig. 1 The test facility (HGK) at UniBw Munich

rection therefore perpendicular to the main flow direction. For this test series one half of one test blade was equipped with the grooves, the other half had a smooth metal surface.

For the second test series a ceramic coating was sprayed on the surface of one test blade with two different surface finish qualities. Similar to the grooved blade of the first test series, one half of the ceramic layer in spanwise direction had one of the surface finish qualities. Figure 3 shows both test blades. As a reference for a hydraulically smooth surface condition, a blade with polished metal surface of R_a=0.38 μm was tested. The surface roughness values corresponding to each of the surfaces described above are given in Table 1.

The surface roughness values presented in Table 1 were obtained with a Hommel Tester T800 measuring instrument. All values are average values of several measurements at different locations on the test blade surface. For the manufactured grooves roughness measurements were taken only perpendicular to the grooves. The spread among the measurements taken was 2 μm for the rough surfaces and 1 μm for the smooth surfaces. For the manufactured grooves the distance between surface peaks is 350 μm, the absolute peak height is R_t=51.6 μm.

2.2 Measurement Techniques. The cascade operating conditions are set by varying the total temperature T_{t1} in the settling chamber, the inlet total pressure p_{t1} and the pressure in the tank p_k (downstream conditions), as indicated in Fig. 1. The total temperature is measured with a PT100 resistance thermometer in the settling chamber (see Fig. 1), the total pressure with a pitot probe 78 mm in front of the cascade. The inlet turbulence level is measured with a constant temperature anemometer (CTA) of the type "Dantec HF-55R01," positioned 500 mm upstream of the cascade inlet plane.

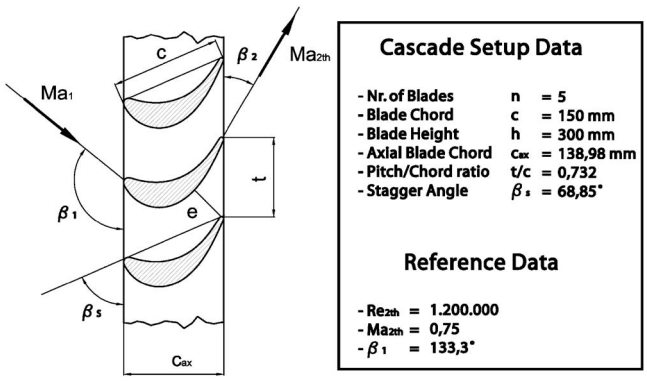

Fig. 2 Test blade geometry and design operating condition

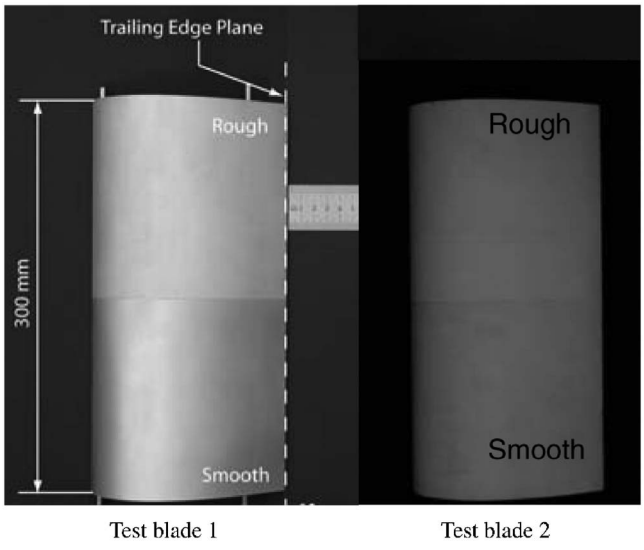

Fig. 3 Test blades with surface finish treatment

Table 1 Surface types and finishes on test blades

Surface type	Surface roughness Ra (μm)	
Reference hyd. smooth	0.38	
Smooth metal	1.14	
Manufactured grooves	11.80	Test blade 1
Ceramic sprayed rough	11.78	
Ceramic sprayed smooth	3.17	Test blade 2

Table 2 Cascade boundary condition parameter variation

Parameter	Values set for measurements
Inlet flow angle β_1	133.3 deg, 143.3 deg
Exit Mach number $Ma_{2,th}$	0.75, 0.85
Reynolds number $Re_{2,th}$	600 000, 900 000, 1 200 000
Inlet turbulence level Tu_1	3.4–3.7% for $Ma_{2,th}=0.75$
	3.4% for $Ma_{2,th}=0.85$ for $Re_{2,th}=600{,}000-1{,}200{,}000$

Besides this standard instrumentation capturing the operating condition and boundary conditions of the cascade flow, the aim of this investigation was to capture the total pressure losses of the test profiles and total pressure loss differences between profiles or profile sections of different surface finish. To capture these losses five-hole probe traverses of the profile wake flow and double pitot between profile wakes at different blade height positions were done. The double pitot probe and its geometric position behind the test blade is shown in Fig. 4 for test blade 1.

While the traverses with the five hole probe have been performed successively behind each blade half, the experimental setup of the double pitot probes allow wake traverses of two different surface qualities simultaneously. This technique allows measurements of the total pressure difference between the two parts of a test blade with highly accurate pressure transducers (25 hPa), thus isolating the roughness influence from other parameters. A detailed description of this measurement technique is given in Leipold and Fottner [13].

In addition to the wake measurements blade surface pressure distributions were taken with 45 tappings at midspan on the suction side of one test blade and 31 tappings at midspan on the pressure side of another test blade.

2.3 Test Program. As already indicated in the geometry description, two different test blades with special surface finishes were tested. For both test blades the same boundary condition parameter variation was chosen. Table 2 summarizes the test parameter variation.

The turbulence grid in front of the cascade was the same for all tests therefore the inlet turbulence intensity is a result of the flow conditions. An overall variation of the inlet turbulence intensity of 0.3% was found for the smaller exit Mach number, depending on the Reynolds number. For the higher exit Mach number no such dependence was observed.

The nominal operating condition for the test cascade is $Re_{2,th}=1\,200\,000$ and $Ma_{2,th}=0.75$, $\beta_1=133.3$ deg. The measurements taken for each parameter shown in Table 2 are given for test blades 1 and 2 in Table 3. As documented in Table 3 the emphasis of the experimental program was on the design exit Mach number $Ma_{2,th}=0.75$. Therefore mainly results for this flow condition will be shown. For the reference blade with hydraulically smooth surface only wake traverse measurements with a 5-hole probe at varying Reynolds number for both inlet flow angle and the nominal exit Mach number were taken.

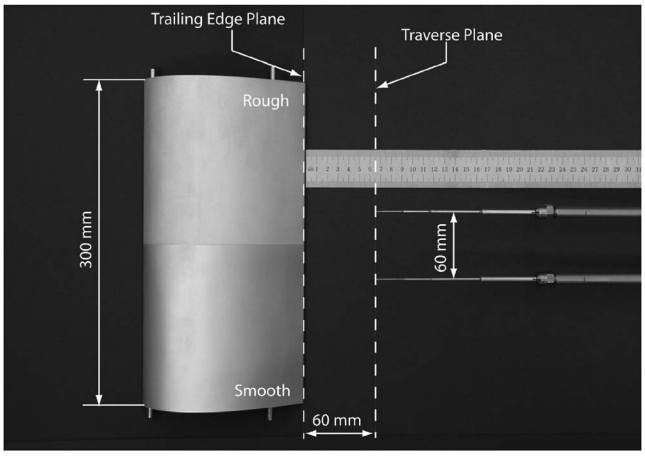

Fig. 4 Position of double pitot probe behind test blade 1

3 Experimental Results

3.1 Profile Pressure Distribution. Figures 5 and 6 show the isentropic surface Mach number distributions of the test blade at nominal inflow angle of $\beta_1=133.3$ deg for the exit Mach numbers $Ma_{2,th}=0.75$ and $Ma_{2,th}=0.85$. The isentropic Mach numbers were calculated from the surface pressure tappings described in Sec.

Table 3 Available measurements for tested operating conditions

	$\beta_1=133.3$ deg	
$Re_{2,th}$ \ $Ma_{2,th}$	0.75	0.85
600 000	PPS,[a] WT,[b] DP[c]	PPS, WT
900 000	PPS, WT, DP	PPS, WT
1 200 000	PPS, WT, DP	PPS, WT
	$\beta_1=143.3$ deg	
600 000	PPS, WT, DP	PPS, WT
900 000	PPS, WT, DP)[d]	
1 200 000	PPS, WT, DP	PPS, WT, DP

[a]PPS: Profile pressure distribution.
[b]WT: Wake Traverse (5-hole probe).
[c]DP: Double Pitot
[d]DP only available for test blade 2

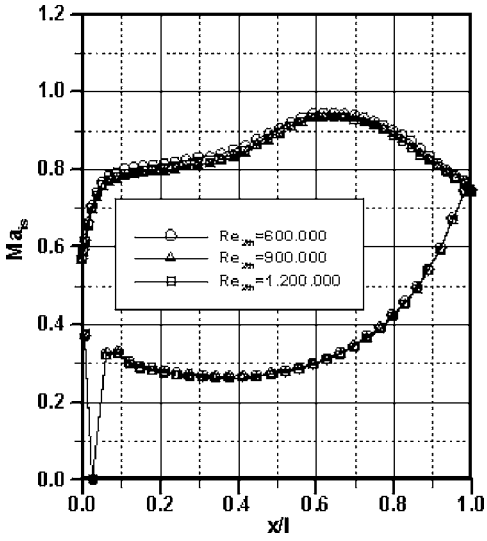

Fig. 5 Surface isentropic Mach number distribution for $\beta_1=133.3$ deg, $Ma_{2,th}=0.75$ in dependence on Reynolds number

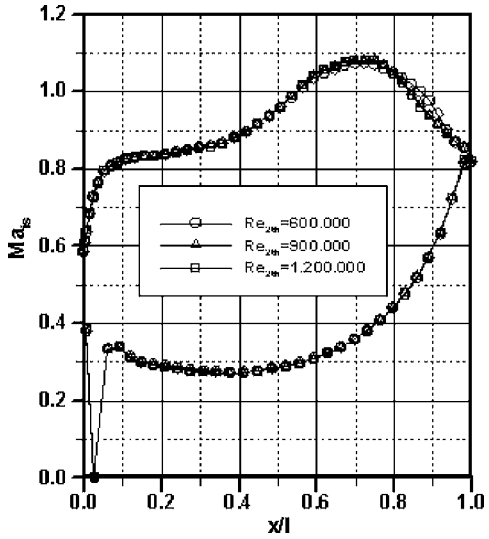

Fig. 6 Surface isentropic Mach number distribution for β_1 = 133.3 deg, $Ma_{2,th}$ = 0.85 in dependence on Reynolds number

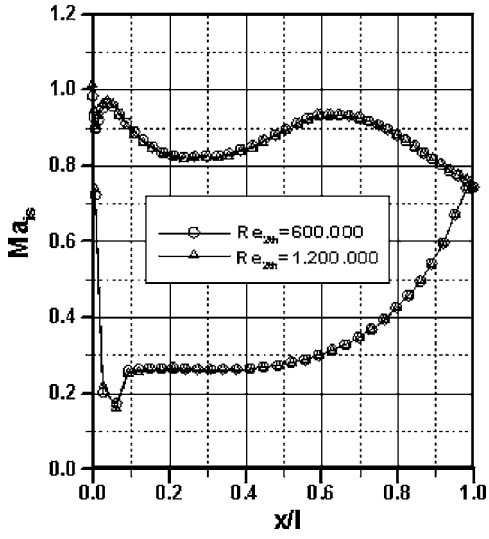

Fig. 7 Surface isentropic Mach number distribution for β_1 = 143.3 deg, $Ma_{2,th}$ = 0.75 in dependence on Reynolds number

2.2. Figures 5 and 6 document the overall comparatively small influence of the Reynolds number on the isentropic surface Mach numbers. However both figures reveal for the smallest Reynolds number tested, $Re_{2,th}$ = 600 000, in comparison to higher Reynolds number cases different shapes of the profiles on the suction side behind the peak suction part towards the trailing edge. Especially for the higher exit Mach number $Ma_{2,th}$ = 0.85 with more suction side deceleration towards the trailing edge the behaviour in Fig. 6 indicates a small laminar separation bubble in that area with turbulent reattachment. For the higher Reynolds number cases the bubble is not observed because the boundary layer is most likely already turbulent in that diffusion region and therefore can bear the deceleration without separation. Mayle [6] describes in detail the physics of this boundary layer transition phenomenon. Because of the observations described above it can be assumed that for the smallest Reynolds number of $Re_{2,th}$ = 600 000 the suction side boundary layer remains laminar all the way to the peak suction, where a separation with laminar turbulent transition occurs. For the higher Reynolds number cases it can be assumed that transition on the suction side occurs latest at peak suction.

Figures 7 and 8 depict the isentropic surface Mach number distribution for an inlet flow angle of β_1 = 143.3 deg, which corresponds to 10 deg incidence towards the pressure side. Figure 7 shows the values for an exit Mach number of $Ma_{2,th}$ = 0.75, Fig. 8 the corresponding for an exit Mach number of $Ma_{2,th}$ = 0.85.

For this inlet flow angle for both exit Mach number cases no influence of the Reynolds number was detected, therefore only two extrema 600 000 and 1 200 000 of the measurements are shown. All cases for this inflow angle show the typical overspeed area at the leading edge caused by 10 deg incidence towards the suction side. Due to the absence of any Reynolds number influence on the pressure distribution it can be assumed that laminar turbulent transition occurs in the suction side boundary layer for this inflow angle in the deceleration zone behind the local overspeed area in the leading edge region.

3.2 Wake Traverse Measurements. Figure 9 shows as a result of the wake traverse measurements for the nominal operating conditions of the cascade the total pressure loss distribution behind the rough part of test blade 2.

The local total pressure loss dp_t is normalized by the local theoretical dynamic head $q_{2,th}$. The definition for both values is given in the nomenclature. The comparison between the 5-hole probe measurements and the double pitot probes for this particular wake shows excellent agreement and served as a crosscheck for both measurement techniques. The check was carried out for several points in the test matrix and showed similar good agreement between the two measurement techniques.

Figures 10–12 show the results of the double pitot traverse measurements behind the test blade 1. The figures show for the design inflow angle of β_1 = 133.3 deg and the design exit Mach number $Ma_{2,th}$ = 0.75 for the different Reynolds numbers a comparison of the total pressure loss distribution for the wake behind the smooth and grooved part of the test blade. Like in Fig. 9 the local total pressure loss coefficient is shown versus the traverse position.

With increasing Reynolds number the wake depth for both the smooth and the rough part of the blade increases and therefore the overall profile losses which are directly linked to the wake total pressure losses are expected to increase. The second observation that can be made by comparing Figs. 10–12 is that the difference in wake total pressure loss between the smooth and the rough half of the test blade increases from $Re_{2,th}$ = 600 000 to $Re_{2,th}$ = 1 200 000. The third observation from Figs. 10–12 is a shift of the wake center towards the suction side for the rough surface

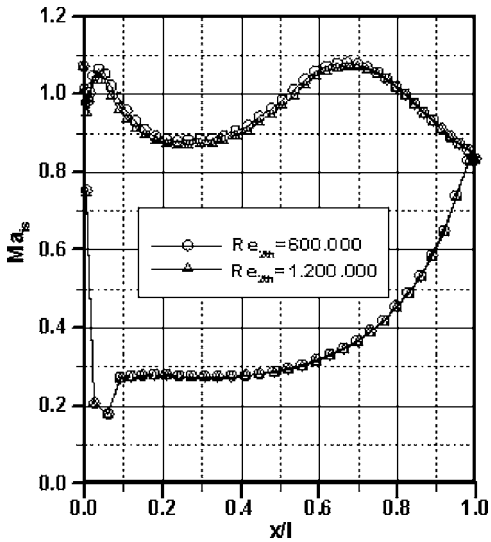

Fig. 8 Surface isentropic Mach number distribution for β_1 = 143.3 deg, $Ma_{2,th}$ = 0.85 in dependence on Reynolds number

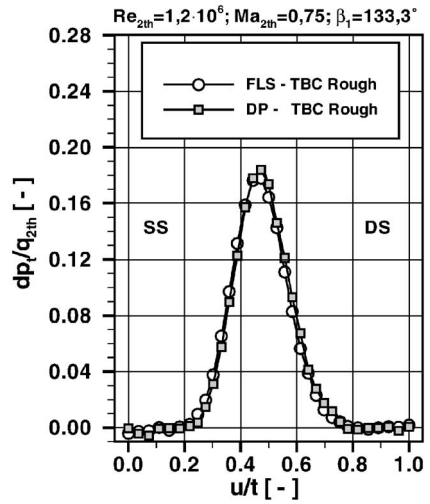

Fig. 9 Wake traverse measurements of total pressure for test blade 2, rough part under nominal boundary conditions. Comparison between five-hole probe (FLS) and double pitot (DP).

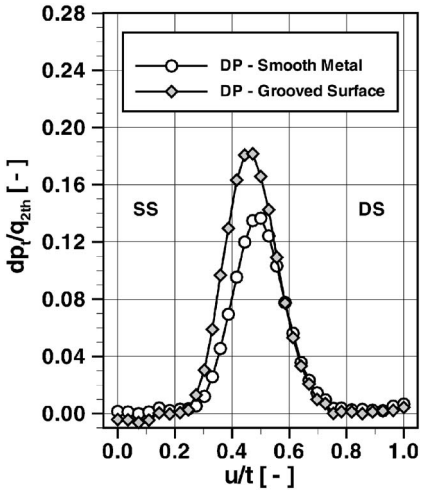

Fig. 11 Total pressure loss from wake traverse measurements of the double pitot probe for test blade 1, rough part compared to smooth part. $Ma_{2,th}=0.75$, $\beta_1=133.3$ deg, $Re_{2,th}=900\,000$.

compared to the smooth one which is present for all three Reynolds numbers analyzed. This behavior indicates a shift in exit flow angle towards less turning for the rough surface case.

Figures 13–15 show in analogy to Figs. 10–12 the total pressure loss traverse derived from the double pitot measurements behind test blade 2. The boundary conditions for the cases shown in Figs. 13–15 are the design values for exit Mach number and inlet flow angle, the Reynolds number was varied. All three observations described for the test blade 1 in Figs. 10–12 are also valid for test blade 2 in Figs. 13–15.

For comparability of the overall profile losses of the tested blade surface quality configurations the cascade exit flow condition taken from the traverse measurements was reduced to one-dimensional data by applying the conservative averaging procedure of Amecke [7,8]. As a result of this procedure, Fig. 16 shows the averaged total pressure loss coefficient $dp_t/q_{2,th}$ for test blade 1 in comparison to the assumed hydraulically smooth test blade as a function of the Reynolds number $Re_{2,th}$ for both inlet flow angles tested at the design exit Mach number $Ma_{2,th}=0.75$. The total pressure loss coefficients in Fig. 16 were calculated from the wake traverse measurements with the double pitot probe described above.

Figure 16 shows for the nominal inflow angle for the total pressure losses of the hydraulically smooth, the smooth metal and the rough, grooved part a similar trend of increasing losses with increasing Reynolds number. For the rough part of the test blade, the slope is steeper than for the smooth part and therefore the loss difference between rough and smooth part of the test blade 1 as well as between rough part and the assumed hydraulically smooth test blade is increasing with increasing Reynolds number. For the 10 deg incidence case at $\beta_1=143.3$ deg inlet flow angle both the smooth and the rough part of the test blade show less difference in loss with increasing Reynolds number. In addition the overall loss difference between smooth and rough part is larger for the 10 deg incidence tests than for the nominal inflow angle. These observations can be attributed to the state of the boundary layer affected by the surface roughness. Schlichting and Truckenbrodt [9] describe in detail the flow physics of surface roughness influences on the drag of a flat plate. According to Schlichting and Truckenbrodt a surface roughness seems hydraulically smooth as long as the surface roughness peaks stay within the laminar or viscous sublayer which makes up the lower portion of a turbulent bound-

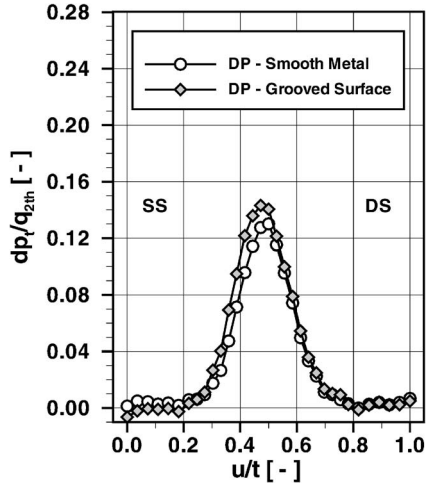

Fig. 10 Total pressure loss from wake traverse measurements of the double pitot probe for test blade 1, rough part compared to smooth part. $Ma_{2,th}=0.75$, $\beta_1=133.3$ deg, $Re_{2,th}=600\,000$.

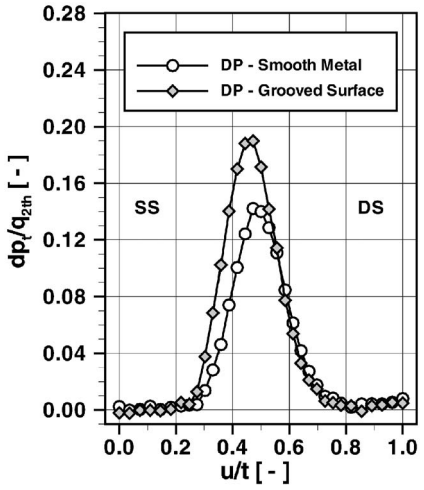

Fig. 12 Total pressure loss from wake traverse measurements of the double pitot probe for test blade 1, rough part compared to smooth part. $Ma_{2,th}=0.75$, $\beta_1=133.3$ deg, $Re_{2,th}=1\,200\,000$.

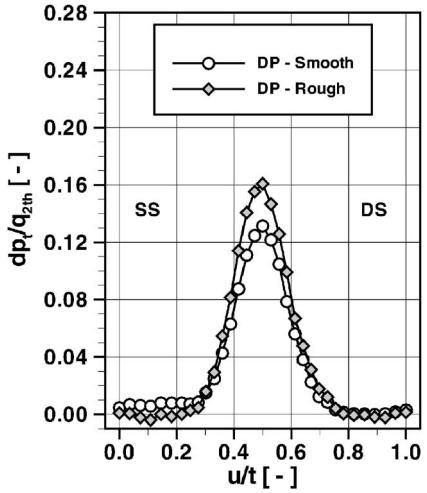

Fig. 13 Total pressure loss from wake traverse measurements of the double pitot probe for test blade 2, rough part compared to smooth part. $Ma_{2,th}=0.75$, $\beta_1=133.3$ deg, $Re_{2,th}=600\,000$.

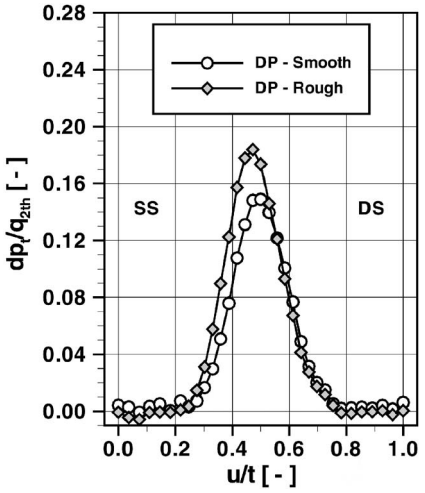

Fig. 15 Total pressure loss from wake traverse measurements of the double pitot probe for test blade 2, rough part compared to smooth part. $Ma_{2,th}=0.75$, $\beta_1=133.3$ deg, $Re_{2,th}=1\,200\,000$

ary layer. With this physical understanding the following possible explanations for the observations to Fig. 16 can be given. For the nominal inflow angle of $\beta_1=133.3$ deg the increasing Reynolds number $Re_{2,th}$ moves the laminar turbulent transition point on the blade suction side from the deceleration zone after peak suction towards the leading edge. The movement of the transition point causes on average a reduction of the laminar sublayer thickness. This results in more and more roughness peaks on the suction side that point out of the sublayer into the transition zone within the turbulent boundary layer or even into the fully turbulent part.

For the 10 deg incidence case the transition occurs as described in Sec. 3.1 most likely in the deceleration region directly after the leading edge, therefore transition is not strictly linked to the Reynolds number for the Reynolds number range analysed in this test series. The fully turbulent boundary layer regime assumed along the suction side for this case allows only a very thin laminar sublayer, resulting in a larger difference between losses on the rough and smooth part of the test blade caused by more roughness peaks summiting into the turbulent part of the boundary layer. Due to the 10 deg incidence and the corresponding Mach number distribution shown in Fig. 7 the overall profile losses for smooth and rough case are higher than for the nominal inflow angle. For the absolute loss values Fig. 16 shows that the loss increase for nominal flow conditions for the rough part of the test blade is up to 40% of the overall profile loss of the assumed hydraulically smooth reference blade for the highest Reynolds number tested.

Figure 17 shows the total pressure loss coefficient for test blade 2 as a function of the exit Reynolds number for the two inlet flow angles of $\beta_1=133.3$ deg and $\beta_1=143.3$ deg at the nominal exit Mach number of $Ma_{2,th}=0.75$. The observation concerning the loss coefficient dependency on Reynolds number and incidence angle for test blade 2 are identical to the observations described for test blade 1, shown in Fig. 16. For the Reynolds number of $Re_{2,th}=1\,200\,000$ data points derived from 5-hole probe and double pitot measurements at an exit Mach number of $Ma_{2,th}=0.85$ are added to Fig. 17. The data for this exit Mach number indicates that at high Reynolds numbers the small change in exit Mach number from $Ma_{2,th}=0.75$ to 0.85 has only a small influence on the overall total pressure loss coefficient for both smooth and rough surfaces. A comparison to the total pressure loss coefficients presented for test blade 1 in Fig. 16 shows that for the rough parts of both blades the loss coefficients display a similar magnitude, therefore the manufactured grooves on test blade 1 have sufficient

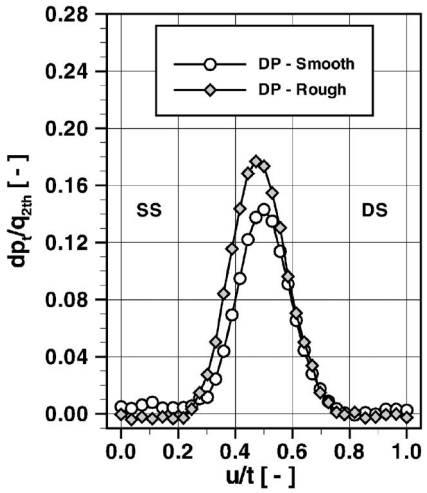

Fig. 14 Total pressure loss from wake traverse measurements of the double pitot probe for test blade 2, rough part compared to smooth part. $Ma_{2,th}=0.75$, $\beta_1=133.3$ deg, $Re_{2,th}=900\,000$.

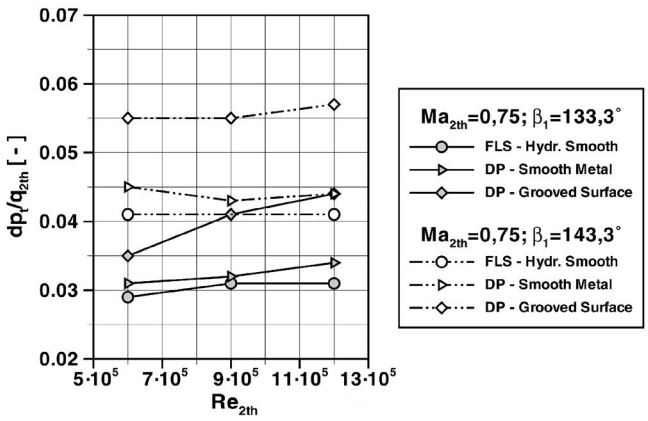

Fig. 16 Total pressure loss coefficient from wake traverse measurements of the double pitot probe for test blade 1, rough part compared to smooth part. $Ma_{2,th}=0.75$ in comparison to 5-hole probe traverse results for the assumed hydraulically smooth test blade. FLS: 5-hole probe, DP: double pitot.

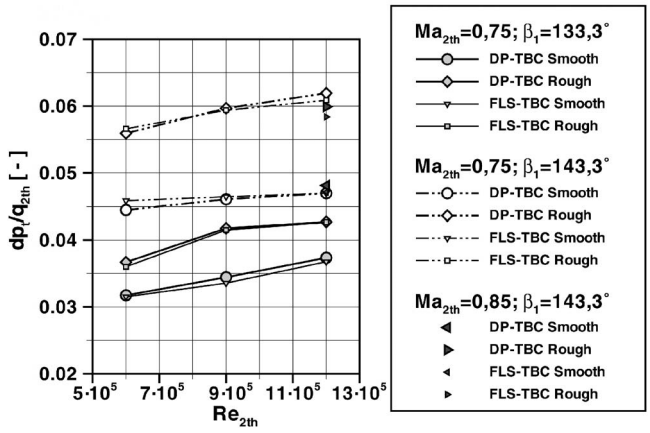

Fig. 17 Total pressure loss coefficient from wake traverse measurements of the double pitot probe (DP) and five-hole probe (FLS) for test blade 2, rough part compared to smooth part. $Ma_{2,th}=0.75$ and $Ma_{2,th}=0.85$.

capability in representing the losses of the ceramic surface on test blade 2. A comparison for the smooth part of both test blades shows that the smooth half of test blade 2 has slightly higher losses at high Reynolds numbers which is caused by its higher surface roughness compared to the smooth part of test blade 1 according to Table 1.

4 Comparison to Correlation

Traupel [10] describes an additive loss model for turbine blading, where the profile loss is defined as:

$$\zeta_P = \chi_R \chi_M \zeta_{P0} + \zeta_h + \zeta_C \tag{1}$$

ζ_{P0} describes the basic profile loss, which is a function of profile shape and the inlet and exit flow angles. ζ_h is the loss connected to the base pressure at the trailing edge. ζ_C is the loss connected to the Carnot shock the flow is experiencing when passing the blade trailing edge. The factor χ_R accounts for roughness effects, the factor χ_M for Mach number effects. Further details determining the values for these coefficients are given in Traupel's work [10]. The factor χ_R accounting for roughness effects is quantified by Traupel by transferring results of Prandtl and Schlichting [11] for a flat plate to turbine blades. To compare the results obtained from the cascade tests in Sec. 3 to the model in Eq. (1) 1D throughflow calculation for the tested blade geometry were carried out with an inhouse tool containing the Traupel loss model. For these runs only the parameter surface roughness was varied. Both Schlichting and Traupel quantify surface roughness in terms of equivalent sand grain roughness k_s, which is not a directly measurable quantity but a roughness model. This model is made up of spheres of the radius k_s resulting in the same influence on the boundary layer as the real surface. Factors to compute k_s from R_a measurements vary according to an overview by Abuaf et al. [3] from 2 to 7, depending on the surface structure. Because of this uncertainty in the R_a to k_s conversion, a parametric study was carried out.

Figure 18 shows as a result the change in row efficiency due to surface roughness according to the model in Eq. (1) as a function of R_a/c, c representing the profile chord length, for several different R_a to k_s conversion factors. The 1D inhouse tool containing the loss correlation according to Eq. (1) ran to the nominal boundary conditions of the cascade.

To compare the experimental results from Sec. 3 to this correlation, the total pressure loss values were converted to row efficiencies and related to row efficiency values of the assumed hydraulically smooth test blade results, shown in Fig. 16.

The data points for both smooth and rough part of test blades 1 and 2 in terms of $\Delta\eta_{\text{row}}$ against the assumed hydraulically smooth test blade were plotted into the Fig. 18 type of chart for the nominal flow conditions of $\beta_1=133.3$ deg and $Ma_{2th}=0.75$. Then the unknown factor for R_a to k_s conversion was adjusted to best fit for high Reynolds number data points. The result is shown in Fig. 19. Data points in Fig. 19 for test blade 1 and 2 with the higher losses at constant R_a/c represent the highest Reynolds number tested, the lower loss data point represents the lowest Reynolds number tested. For test blade 2 the two incidence cases $\beta_1=133.3$ deg and 143.3 deg are shown. The correlation in Fig. 19 was matched to represent the nominal incidence case. Therefore the data for the incidence case of $\beta_1=143.3$ deg reflects the impact of increased turbulence in the suction side boundary layer as discussed in Sec. 3.1.

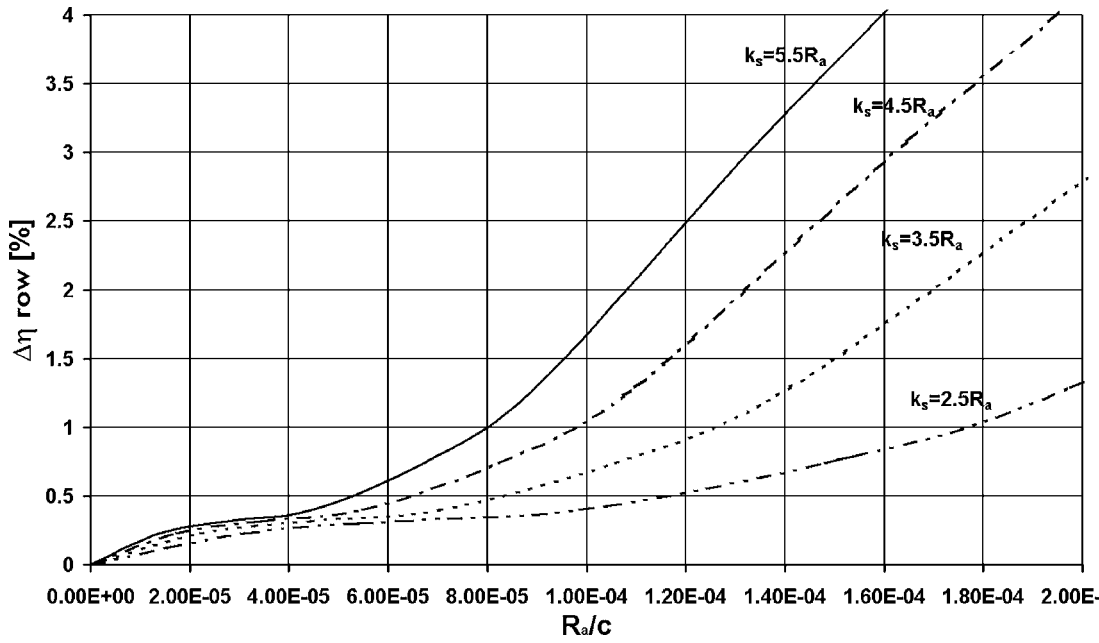

Fig. 18 Row efficiency change due to surface roughness for loss model according to Eq. (1). Parameter R_a/k_s variation.

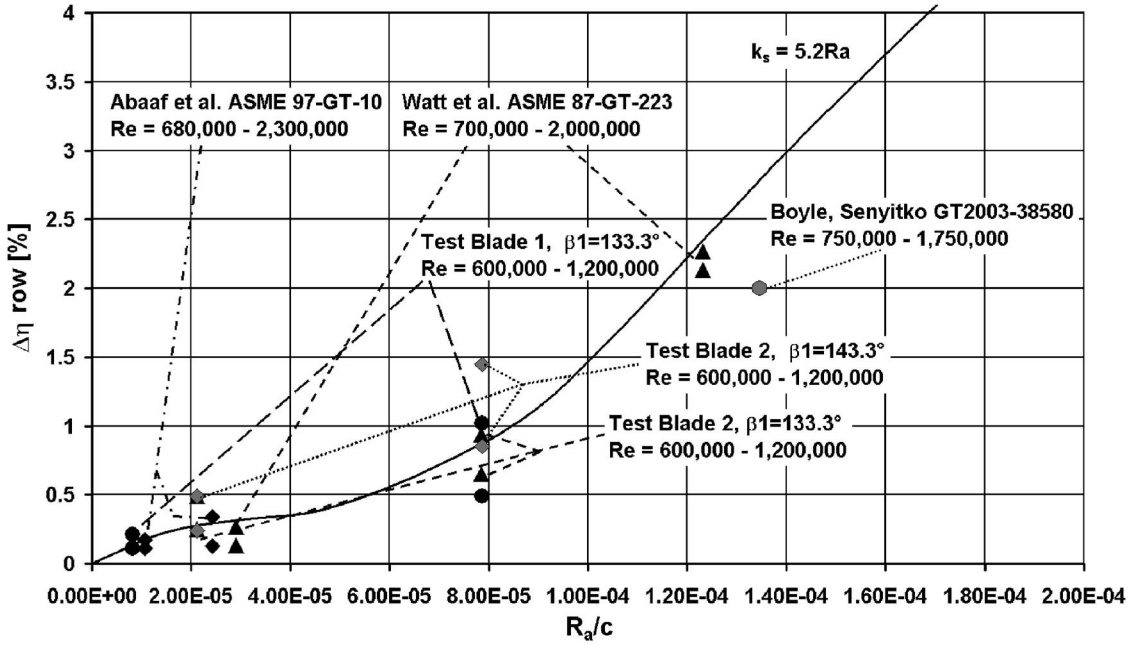

Fig. 19 Row efficiency change due to surface roughness from loss model according to Eq. (1). Parameter k_s/R_a=5.2, comparison to experimental data.

In addition to the experimental data presented in this paper, all data points available from references discussed in the introduction section are also plotted into Fig. 19. Both Watt et al. [4] and Abuaf et al. [3] measured against a polished, assumed hydraulically smooth, surface condition. Boyle and Senyitko [5] measured two roughness types with no clear reference to a hydraulically smooth condition, therefore the value of $\Delta\eta_{\text{row}}$ for the smoother surface was evaluated from the correlation in Fig. 19 and added to the row efficiency change between the two measured surface qualities to come up with a value for the rougher surface measured. Stated total pressure losses from the mentioned literature were converted to row efficiencies in the same way as for the measurements presented in Sec. 3 for test blade 1 and 2.

Figure 19 shows that the correlation in Eq. (1) with a matching of the R_a to k_s conversion factor is capable of predicting the trend due to surface roughness effects for high Reynolds number applications such as first stages in heavy duty gas turbines. Furthermore the correlation shown in Fig. 19 supports the assumption that the smooth metal test blade of R_a=0.38 μm used as a reference for the hydraulically smooth condition is with a value for Ra/c of 2.5×10^{-06} hydraulically smooth.

5 Conclusions

An experimental test series is presented which was carried out to understand the impact of surface roughness on turbine blade aerodynamics. Special emphasis was given to heavy duty gas turbine applications within the Reynolds number range of Re =600 000–1 200 000. Total pressure losses for surface roughness to chord length ratios of $Ra/c=7.6\times10^{-06}-7.9\times10^{-05}$ of 4 specially prepared surface types were evaluated from wake traverse measurements. The Reynolds number dependency was measured. It was found that maximum loss increase due to surface roughness occurs at the highest Reynolds number tested. Maximum loss increase due to the highest surface roughness analysed is 40% at nominal flow conditions compared to a hydraulically smooth reference blade. In addition to the tests a comparison to a loss model according to literature showed good agreement to both the results from this test series and further data from literature.

Acknowledgment

The authors would like to pay tribute to Professor Dr.-Ing. Leonhard Fottner, head of the Institut für Strahlantriebe from 1980 to 2002, whose support and guidance made this work possible. In addition the authors would like to thank ALSTOM Power for permission to publish this paper. Special thanks to Thomas Duda of ALSTOM Power for his effort in coating test blade 2 as well as measuring the roughness of the test blades.

Nomenclature

c = chord length
h = blade height
k_s = equivalent sand grain roughness
Ma = Mach number
n = number of blades
p = pressure
$q_{2\text{th}}$ = theor. dynamic pressure ($=p_{1,t}-p_2$)
Ra = centerline averaged surface roughness
Re = Reynolds number
T = temperature
Tu = turbulence intensity (%)
t = pitch
u = traverse direction (pitchwise)

Greek

η_{row} = row efficiency
β = flow angle
χ = loss factor
ζ = loss coefficient

Subscripts

1 = inlet condition
2 = exit condition
ax = axial
in = inlet value
k = tank condition
t = total flow condition
th = theoretical value (for Ma based on p_{tin}, p_k)

References

[1] Lakshminarayana, B., 1996, *Fluid Dynamics and Heat Transfer of Turbomachinery*, Wiley, New York.

[2] Bons, J. P., Taylor, R. P., McClain, S. T. and Rivir, R. B., 2001, "The Many Faces of Surface Roughness," ASME J. Turbomach., **123**, pp. 739–748.

[3] Abuaf, N., Bunker, R. S., and Lee, C. P., "Effects of Surface Roughness on Heat Transfer and Aerodynamic Performance of Turbine Airfoils," ASME-Paper No. 97-GT-10.

[4] Watt, R. M., Allen, J. L., Baines, N. C., Simons, J. P., and George, M., 1957, "A Study of the Effects of Thermal Barrier Coating Surface Roughness on the Boundary Layer Characteristics of Gas-Turbine Aerofoils," ASME-Paper 87-GT-223.

[5] Boyle, R. J., and Senyitko, R. G., "Measurements and Predictions of Surface Roughness Effects on Turbine Vane Aerodynamics," ASME Paper GT2003-38580.

[6] Mayle, R. E., 1991, "The Role of Laminar-Turbulent Transition in Gas Turbine Engines," ASME J. Turbomach., **113**, pp. 509–537.

[7] Amecke J., 1967, *Auswertung von Nachlaufmessungen an Ebenen Schaufelgittern*, Bericht 67 A49, AVA Göttingen.

[8] Amecke, J., and Safarik, P., 1995, "Data Reduction of Wake Flow Measurements with Injection of Other Gases," DLR Forschungsbericht 95-32, German Aerospace Center (DLR).

[9] Schlichting, H., and Truckenbrodt, E., 1967, *Aerodynamik des Flugzeuges*, Vol. 1, 2nd ed., Springer-Verlag, Berlin.

[10] Traupel, W., 1988, *Thermische Turbomaschinen*, Vol. 1, 3rd ed., Springer-Verlag, Berlin.

[11] Prandtl, L., and Schlichting, H., 1936, "Das Widerstandsgesetz rauher Platten," Werft Reed, Hafen, pp. 1–4; also in "Gesammelte Abandlungen," 1961, Springer-Verlag, Berlin, Vol. 2, pp. 649–662; English translation in Proc. Soc. Mech. Eng., U.S.A., 1936.

[12] Sturm, W., and Fottner, L., 1985, "The High-Speed Cascade Wind Tunnel of the German Armed Forces University Munich," *Proceedings of the 8th Symposium on Measuring Techniques in Transonic and Supersonic Flow in Cascades and Turbomachines*.

[13] Leipold, R., and Fottner, L., 1998, "A Measurement Technique to Investigate the Influence of Surface Roughness on the Flow Around a Highly Loaded Compressor Cascade," 14th Symposion on Measurement Techniques, Limerick.

Simulated Land-Based Turbine Deposits Generated in an Accelerated Deposition Facility

Jared W. Jensen
e-mail: jwj5@email.byu.edu

Sean W. Squire
e-mail: sws25@et.byu.edu

Jeffrey P. Bons
e-mail: jbons@byu.edu

Department of Mechanical Engineering,
Brigham Young University,
Provo, UT 84602

Thomas H. Fletcher
Department of Chemical Engineering,
Brigham Young University,
Provo, UT 84602
e-mail: tom_fletcher@byu.edu

This report presents a validation of the design and operation of an accelerated testing facility for the study of foreign deposit layers typical to the operation of land-based gas turbines. This facility was designed to produce turbine deposits in a 4-h *test that would simulate* 10 000 h *of turbine operation. This is accomplished by matching the net foreign particulate throughput of an actual gas turbine. Flow Mach number, temperature and particulate impingement angle are also matched. Validation tests were conducted to model the ingestion of foreign particulate typically found in the urban environment. The majority of this particulate is ceramic in nature and smaller than* 10 microns *in size, but varies up to* 80 microns*. Deposits were formed for flow Mach number and temperature of 0.34 and* 1150°C*, respectively, using MCrAlY coated coupons donated from industry. Investigations over a range of impingement angles yielded samples with deposit thicknesses from* 10 to 50 microns *in* 4 h*, accelerated-service simulations. Deposit thickness increased substantially with temperature and was roughly constant with impingement angle when the deposit thickness was measured in the direction of the impinging flow. Test validation was achieved using direct comparison with deposits from service hardware. Deposit characteristics affecting blade heat transfer via convection and conduction were assessed. Surface topography analysis indicated that the surface structure of the generated deposits were similar to those found on actual turbine blades. Scanning electron microscope (SEM) and x-ray spectroscopy analyses indicated that the deposit microstructures and chemical compositions were comparable to turbine blade deposit samples obtained from industry.* [DOI: 10.1115/1.1860380]

Introduction

Despite the greatest of precautions and most stringent filtering techniques, it is nearly impossible to economically provide completely clean air streams in gas turbine (GT) engines. Sand, pollutants, and moisture may all be introduced into the flow and degrade exposed surfaces in the engine. Internal sources of particulate such as dirty fuels, eroded components, and secondary chemical reactions also contribute to the flow of solid and semimolten matter passing through the GT engine. These particles may either pass through the engine with no effect or attack the surfaces of the engine through erosion, corrosion, or deposition. The adverse effects of these three degradation mechanisms are well documented in the literature. Erosion can cause significant reductions in engine performance by opening up tip clearances and altering blade contours. For example, Ghenaiet et al. [1] reported a 6%–10% loss in adiabatic efficiency for 6 h of sand ingestion in an axial fan. Deposition poses the opposite problem by clogging critical bleeds and reducing blade flow passages. Wenglarz [2] proposed a model for estimating the loss in turbine power that occurs when the choked mass flow limit is reduced due to deposit buildup at the nozzle guide vane passage throat. Kim et al. [3] documented the disastrous results of film cooling holes being plugged by massive ingestion from simulated volcanic ash. Both erosion and deposition are also known to increase levels of surface roughness which produces corresponding increases in heat transfer (up to 50%) and skin friction (up to 300%) (Bons [4]). Finally, all three degradation mechanisms (including corrosion) reduce part life and increase the risk of run-time failure.

For the case of deposition in particular, a better understanding of the characteristics of the materials deposited on turbine surfaces would allow a more accurate estimate of their impact on the efficiency and survivability of turbine blades. As GT engine technology has evolved from F-class to G-class and now to H-class, the increase in turbine inlet temperature (TIT) from 1300°C to 1500°C has increased thermal efficiency from 55% to near 60% for H-class turbines [5]. As the U.S. Department of Energy (DOE) contemplates the large-scale introduction of dirty fuels such as coal and biomass in H-type, high temperature turbine engines, the need to understand deposition mechanisms and their effects on efficiency at high temperatures will increase dramatically.

The capability of research facilities to study turbine deposition characteristics for high temperature service is presently limited by the time required to develop significant deposits in typical operating engines. Depending on the operation schedule and environment of a land-based GT, the formation of deposits may require as much as 25 000 h of operation. To reproduce this in a laboratory study would require months or years of preparation time for a single sample. Thus the obvious need to explore the possibility of accelerated testing procedures. Without this, any comprehensive investigation of new service conditions that may affect the characteristics of deposit growth would clearly be impractical.

This study investigates the suitability of such an accelerated deposition facility to specifically study the deposition of ingested particulate on the first stage turbine blades in land based GT engines. Sample turbine blade materials with coatings representative of common GT engine construction have been obtained from various gas turbine manufacturers. Deposits have been generated on these materials in a new accelerated testing facility. At the same time, actual turbine blades at various points in their service life have been obtained from the gas turbine community. These serviced components have been characterized to determine the struc-

Contributed by the International Gas Turbine Institute (IGTI) of THE AMERICAN SOCIETY OF MECHANICAL ENGINEERS for publication in the ASME JOURNAL OF TURBOMACHINERY. Paper presented at the International Gas Turbine and Aeroengine Congress and Exhibition, Vienna, Austria, June 13–17, 2004, Paper No. 2004-GT-53324. Manuscript recieved by IGTI, October 1, 2003; final revision, March 1, 2004. IGTI Review Chair: A. J. Strazisar.

ture of surface deposits including an examination of surface roughness, morphology, internal structure including porosity, and chemical composition. A comparison of these findings to the results of similar examinations of accelerated deposits is used to validate this testing procedure.

Background

Particulate flow in GT engines (either from ingestion, dirty fuel combustion, or internal erosion) results in three adverse phenomena: corrosion, erosion, and deposition. Corrosion in the HP turbine is primarily due to attack of the surface, particularly the coating, by hot gases and particles. A model has been presented by Chan et al. [6] to characterize the life of coatings when considering oxidation, fracture and spallation in the coating, inward diffusion of Al from the coating to the substrate, and the critical level of Al required at the surface to form a protective oxide layer. Critical temperature thresholds for type I and type II (hot corrosion) are 850–1000°C and 700°C, respectively [7]. While these temperature regimes are well below the inlet gas temperature for most modern turbines, they become relevant in regions of film cooling (where the metal temperature is lower than the gas temperature) and in subsequent turbine stages. Deposition rate can have an effect on the rate of hot corrosion by influencing the rate of mass flux of sulfur to the wall [7]. Thus, an understanding of depositional mechanisms and particularly their interaction with sulfur compounds would aid in the understanding of type I and II corrosion attacks in GT engines. An equally destructive deposition mechanism that has corrosive elements is evidenced during CMAS (Calcium, Magnesium, Aluminum, Silicon) attack where molten CMAS infiltrates microcracks in the TBC and creates thermal stresses leading to spallation.

Since 1979, the University of Cincinnati has operated a facility capable of accelerated erosion studies on aircraft turbine blade samples at various impingement angles and temperatures up to 1093°C [8]. Using this facility, it has been shown that impingement angle has a strong influence on the erosion rate of different surfaces [9]. Walsh et al. [10] reported that erosion rates are also a function of erodent character, temperature, and impact velocity. A study by Zaita et al. [11] of the contribution of erosion to tip clearance growth in aircraft engines indicated that erosion effects were a large contributor to efficiency loss over time and a critical parameter in determining engine efficiency degradation. It is likely that a critical threshold temperature exists between regimes where erosion is the dominant degradation mechanism and where deposition becomes critical. Once particulates exceed the temperature where they become molten, agglomeration rates increase [12] with an attendant decrease in blade erosion rates. Deposition research in aircraft engines has indicated that this threshold for the deposition mechanism in aircraft turbine engines is between 980 and 1150°C [12–14]. Kim et al. [3] looked at deposition in aircraft engines arising from ingestion of volcanic materials. Their facility consisted of engine components simulating both can-type and annular-type combustors and HP turbines. They found that deposition did not occur below 1121°C. They also reported that deposition rates increased with time as the surfaces became better captors of material and was roughly proportional to concentration given constant temperature and exposure time. However, the conditions of land-based GT engines make the investigations by Kim et al. only marginally useful, particularly since most GT inlet filters will block the majority of particles ingested by the aircraft engines examined in their volcanic ash experiments.

This temperature threshold range is still well below the TIT of H-class GT engines. It also falls below the temperature threshold (nominally 1100°C) observed by Wenglarz [2,12], where larger fractions of the particulate are molten and therefore stick to the turbine surfaces more easily. This temperature threshold dictates that a viable accelerated deposition facility must be capable of studying flow regimes at temperatures significantly above and below 1100°C.

Previous research indicates that the need for an accelerated testing facility exists, and this need will only increase as turbine inlet temperatures increase with the introduction of new materials technology. Without a good understanding of the depositional mechanisms involved at these higher temperatures, accurate estimates of turbine efficiency during extended service may prove elusive.

Accelerated Deposition Facility

In order to study the structure and thermal properties of deposits forming on first stage high pressure (HP) turbine vanes and blades, an experimental facility was constructed to duplicate conditions in the blade leading edge zone where deposition tends to be the heaviest [15]. This facility attempts to replicate the chemistry and structure of deposits occurring on turbine blades after 10 000 h service in 4-h accelerated tests. The facility is capable of matching the Mach number and flow temperature in the first stage of the turbine while also providing a means of varying the impingement angle of the flow on the sample and the particulate concentration in the flow. A photograph of the facility is shown in Fig. 1.

To properly simulate deposition mechanisms in the HPT, the gas turbine combustor exit flow conditions must be duplicated in the laboratory. The critical variables for an accurate simulation include: flow temperature, Mach number, and impingement angle, as well as particle size, chemistry, and loading. Gas (and particulate) temperature is important since it influences the state and thus susceptibility for deposition of molten particulates in the flow [12]. For particle sizes in excess of 1–2 microns, the primary means of deposition is inertial impaction, making impingement angle and particle velocity (flow Mach number) critical parameters governing the force of impact and the momentum transfer during a collision with the blade surface. Below one micron, other processes including turbulent eddy diffusion, thermophoresis, and Brownian diffusion dominate the deposition mechanism [12].

One flow parameter that is not simulated in this test facility is static pressure (the deposition occurs at pressures less than 15 kPa above atmospheric pressure). This is consistent with other deposition test facilities that operate at significantly lower pressures than those found in a GT [9,16]. The consensus from these and other studies [3,17] is that particle temperature, concentration, and residence time are the necessary parameters for proper simulation, not static pressure.

As for matching the particulate loading in the gas stream (parts per million weight or ppmw), Wenglarz [12] describes various experiments where particulate concentration and service time seemed to tradeoff between each other. Turbines exhibited large deposits or could even be driven to failure either by high particle loading at low service time or low particle loading for long periods [12]. This suggests that a throughput mass factor may be the key parameter and the time to produce a surface deposit could be reduced by increasing freestream concentration of particulate. The validation of this hypothesis is the subject of this study.

Deposition can occur from a variety of mechanisms, both internal to the GT (e.g., dirty fuels or eroded components) and from the environment (airborne sand, salts, etc.). The focus of this study is the simulation of airborne particulates ingested into a natural gas burning engine. In the laboratory, this is done by seeding a natural gas combustor with high concentrations of airborne particulates. A description of this facility follows.

The primary air stream is injected into the steel base of the natural gas combustor where it is first dispersed by passing through a volume of marbles and then straightened through a 5 cm tall honeycomb section. At this point, natural gas is injected into the flow via four stainless steel fuel injectors. The detailed chemical composition of this fuel is given by Murray [18], but it primarily consists of CH_4. The combusting flow then enters a 20° cone axisymmetric nozzle with a 370:1 inlet to exit area ratio. The elevated Mach number at the nozzle exit is maintained through a 0.9 m long pipe leading to the test coupon where entrained par-

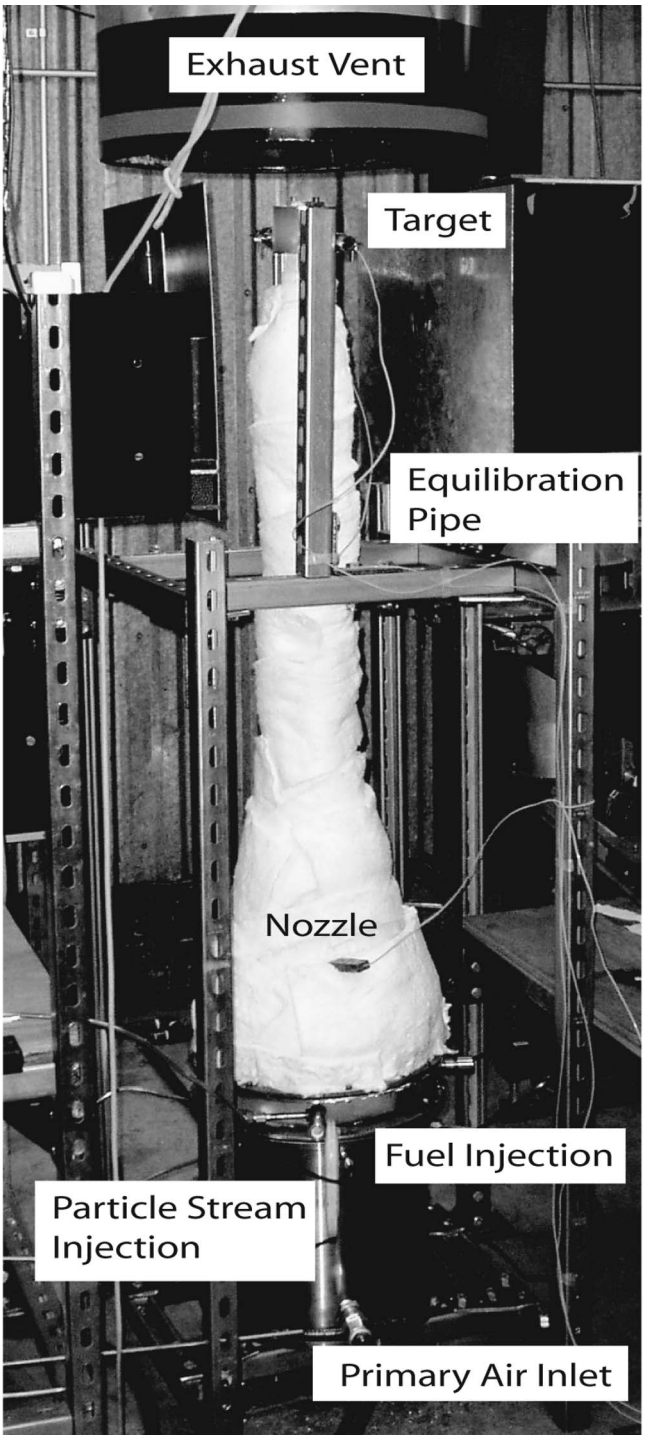

Fig. 1 Accelerated deposition test facility

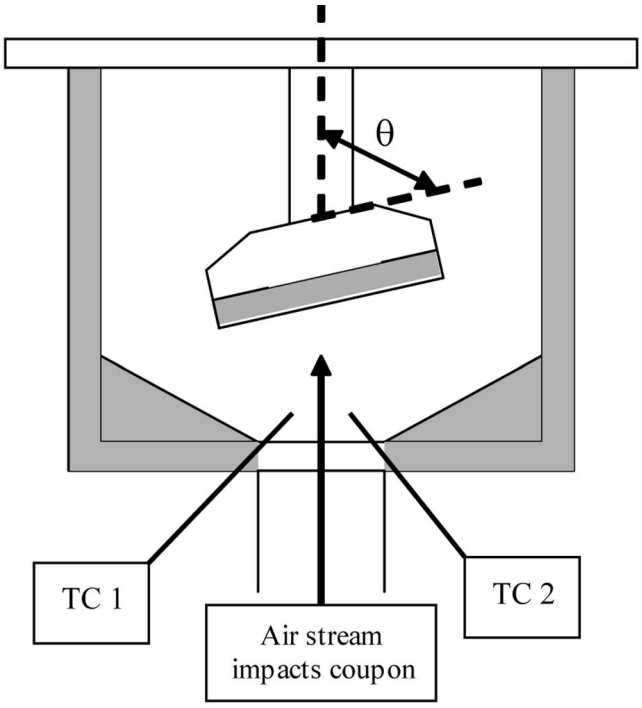

Fig. 2 Cut-away of target area (TC1 and TC2 show flow thermocouple placement)

ticles are brought up to 95% of flow velocity and temperature. The length of this pipe was dictated by the estimated residence time required for particles of up to 40 micron diameter to come to thermal and velocity equilibrium with the gas flow at the nominal test conditions. The length to diameter ratio for this equilibration pipe is 50.

The flow exits this equilibration pipe as a turbulent jet and impinges on the target coupon located 2–3 jet diameters from the pipe exit (Fig. 2). The jet exit Mach number for the experiments reported in this study has been set to match the typical inlet Mach number range (0.2–0.4) for a first-stage turbine blade row. The fixture holding the coupon can be oriented at a 30°, 45°, 60°, or 90° angle to the flow path, allowing the simulation of various impingement angles found in a turbine flowpath as the flow stagnates against the leading edge and then sweeps around the airfoil.

In order to match the high temperatures characteristic of the HP turbine, the combustion section and all other downstream components are constructed of Inconel 600 and 601 alloys for maintenance of a high temperature flow without necessitating a cooling jacket. Inconel 600 and 601 have a high lower melt temperature (1350°C) which allows experiments to operate up to a mean temperature of 1150°C with maximum temperatures of 1200°C. Temperatures are maintained using ceramic insulation around the entire combustion facility.

Simulation of a particulate-laden flow is achieved by seeding particles into the air stream by means of a secondary air flow system. Though the primary use of this facility to date has been to model the ingestion of foreign particles at the GT inlet, this facility could also be used to examine the impact of burning "dirty fuels" or excessive internal erosion in GT engines. By seeding the air flow with the proper mixture of ash, chemical impurities, GT engine material, or other elements, this facility could be used to simulate the burning of biomass, coal, heavy fuel oils, or any other of a variety of alternative fuels as well as internal erosion by ingested particles or the break-up of particles deposited upstream of the turbine.

In order to examine the case of airborne particle ingestion from the atmosphere, an understanding of the typical particulate content of the atmosphere was needed. The particulate content of a typical urban atmosphere consists of a bimodal distribution centered at 0.5 and 10 microns [19,20]. The finer of these two distributions is comprised mostly of ignition losses and the solid-state products of multiphase chemical reactions in the atmosphere (sulfates, nitrates, ammonium compounds). The coarse particle regime consists primarily of particles that have been broken down from macroscale sources by mechanical processes such as erosion, sea spray, and dust aeration by traffic. The chemical distribution of these latter particles can vary greatly from region to region depending on the dominant physical environment. In urban and

Table 1 Crustal and seed particulate composition as percent by weight. SEM analysis lists element as N/A if none was detected above measurement noise. All iron detected by SEM assumed Fe_2O_3 oxide. "Other Alkalis" detected by SEM consisted entirely of potassium. SEM assay representative of multiple assays.

	Crustal composition [21]	Manufacturer assay of seed particulate	BYU SEM assay of seed particulate
SiO_2	59.8	68.5	60.2
Al_2O3	14.9	16.0	4.5
CaO	4.8	2.9	13.7
MgO	3.7	0.8	N/A
Other Alkalies	6.2	4.6	7.3
Fe_2O_3	2.7	4.6	10.7
FeO	3.4	negligible	negligible
H_2O	2.0	0.0	N/A
Ignition losses	N/A	2.7	N/A

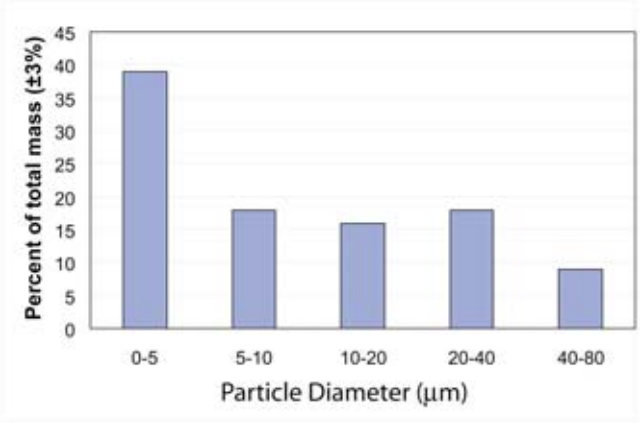

Fig. 3 Seed particle size distribution by mass

desert locations where many GT engine plants are located, these coarse particles are distributed nearly identically to standard crustal and soil elements.

Borom et al. confirmed that a "globally generic" chemical composition called CMAS (Ca–Mg–Al–Si) could be considered when studying the deposition of environmental particulate [17]. Furthermore, the distribution of materials in these deposits resembles generic weight percent distributions for the Earth's crust [21] (see Table 1). This suggests that simply injecting common dirt into a combustion facility would provide the correct ingredients and relative concentrations for the formation of deposits in a turbine so long as the particle sizes were controlled to those common to a turbine environment.

Though the majority of airborne particles are concentrated in the range of 0–20 microns, particles up to a size of 80 microns can often be found in small amounts. This forms the upper limit on what can be expected in reasonable abundance within the atmosphere. However, land-based GT engines employ inlet filters that trap out a significant portion of these particles. Many such filters are capable of blocking nearly all particulate from entering the GT engine when newly installed, but degradation over time can cause these filters to allow passage of particulate in steadily increasing amounts [22]. After significant service, most midgrade filters are capable of filtering out the majority of particles sized 20–80 microns and a significant portion of particles smaller than 20 microns [22]. But with turbine operation measured in thousands of hours, even these minute ingression rates can represent a significant quantity of net entrained particulate. It may also be argued that even if large particles are ingested through the air filter, they will be pulverized as the gas flows through the compressor to the turbine. While this is generally true, Dunn et al. reported that both bypass and ECS air in aircraft engines showed measurable amounts of particulate in excess of 20 microns in size despite having passed through the axial flow compressor [23].

Seed particles were selected to match the typical particulate size and chemistry found in the atmosphere. Contact with Air Filter Testing Laboratories, Inc. led to the selection of a particle test mixture used in the characterization of GT inlet filter performance. The dust selected conforms to the ASHRAE (American Society of Heating, Refrigeration, and Air Conditioning Engineers) test standards for size and is representative of real chemical compositions as it is collected from the atmosphere rather than artificially mixed. The chemical composition of this seed particulate is given in Table 1 while the mass-percent size distribution is shown graphically in Fig. 3. Note that an independent SEM assay of the particulate showed a different chemical composition than the manufacturer-provided assay and did not detect Mg (a prime component of CMAS) in appreciable quantities.

Approximately 9% by mass of this dust exceeds the size limit for 100% entrainment by the gas path. Though thermal equilibrium is achieved, these larger particles will not achieve velocity equilibrium (defined as 95% of gas velocity) before impingement. Because of the velocity gradients which are likewise present in the HPT, it is likely that this will not adversely affect the ability of the accelerated deposition facility to duplicate the deposit mechanisms under study.

In order to represent the flow conditions typical of ingestion of particulate in the primary air stream in a GT engine, part of the main air flow in the combustion facility (20%–40%, depending on flow conditions for the test) is branched from the main air system upstream of the combustor. This flow enters a glass bulb into which particles are steadily injected using a glass syringe. The syringe pushes particulate into the glass bulb where it is entrained into the air stream. The glass bulb is vibrated by mechanical agitation at 60 Hz in order to ensure a continuous flow of particles in the smallest agglomerates possible.

The feed rate of the syringe can be adjusted to control the overall mass concentration of particulate in the flow. This report focuses on experiments with particle concentrations from 60 to 280 parts per million weight (ppmw). Particle loading for a typical GT with adequate filtration is initially 1%–5% of ambient particulate content [22]. This value can reach as high as 25% under adverse conditions such as sandstorms, filter deterioration during regular service, or high smog. Average ambient content of 10-micron particles in an urban environment is 300 $\mu g/m^3$ [19] or about 0.244 ppmw. Filtering to 1%–25% of this ambient level yields 0.002–0.061 ppmw in the turbine intake. Thus, 50 and 230 ppmw for 4 h yields roughly the same throughput particulate mass as 0.02 and 0.092 ppmw for 10 000 hours. The particle loading is determined by weighing the particulate remaining in the syringe at the conclusion of the test and comparing it to the total weight measurement made at the start. This difference in particulate mass, divided by the testing time and normalized by the mass flow rate of air yields the required ppmw estimate. Uncertainty in the particle concentration measurement was <6 ppmw for typical flow conditions.

Test conditions are monitored real-time using mass flow and temperature sensors. Air flow is metered by a choked flow orifice plate. The gas flow rate is measured with a rotometer and line pressure measurement. The two mass flow measurements are compared to determine combustion stoichiometry. Uncertainty in mass flow was 4% at flow regimes of interest. The flow temperature is measured using two type-S thermocouples located in the jet exit, just upstream of the target coupon (Fig. 2). These 0.13 mm

bead diameter thermocouples are held in the flow with ceramic supports. The thermocouples are positioned so that they do not view any low temperature surfaces, thereby keeping the radiative temperature errors to within 3 °C. Because the convective mechanism at the Mach numbers of interest is quite high, the convective error on temperature sensing is also quite low. Overall error is less than 15 °C at 1150 °C. Metal surface temperatures are also monitored at various points along the exterior of the combustion facility as a precaution against overheating the combustor.

Samples of turbine blade materials with various coatings were provided by several GT manufacturers for testing in this facility. In order to respect proprietary concerns of the manufacturers, strict source anonymity has been maintained for all data presented in this publication. The materials were modified as necessary to fit into the 2.5 cm diameter test coupon tray. The specimens used in this study were 4 mm thick with 125 μm of MCrAlY oxidation resistant coating on a high temperature alloy substrate.

Results

The primary objective of this experimental study was to validate the use of accelerated deposition testing. This is done by comparing specific features from accelerated deposition coupons to deposit features found on in-service hardware. The criterion for determining whether the two modes of deposit formation are indeed similar rests upon thermodynamic considerations. Specifically, if an assessment of the deposits would yield comparable effects on turbine performance, then the deposits are considered to be "similar." Deposits alter the blade thermodynamics through two primary mechanisms: convection and conduction. Convection is influenced by changes in surface roughness. Bons [4] tested scaled models of actual turbine deposit roughness and found 20%–40% increases in convective heat transfer. Several roughness statistics were suggested as possible correlating parameters for the observed increase in heat transfer. Thus, if the deposits generated in this accelerated deposition facility have a statistically similar character to those found on actual in-service hardware, they would be considered "similar." Accordingly, surface topology measurements were made to allow statistical comparisons of roughness.

Deposits also form an insulating layer over the surface, thus reducing heat flow to the metal substrate. This conduction mechanism is governed by the deposit thickness, chemistry, and structure. As such, measurements were made of the deposit internal structure and chemical composition using SEM and x-ray spectroscopy. The results of these two studies are presented below. Following this, some remarks are made regarding observed variations in deposit characteristics with impingement angle, particulate concentration, and gas temperature.

Topography

Surface roughness in turbines is governed by an imposing list of parameters including: service hours, cycles, operating temperature, and environment. Bons et al. [15] reported significant variations with blade location and surface degradation mechanism (spallation, deposition, or erosion) as well. Traditionally, roughness is characterized by its statistics (e.g., Ra, Rt). These statistics can then be used with empirical correlations to estimate changes in skin friction or convective heat transfer [24,25]. With such a rich parameter space, it would be unproductive to try to match a specific surface topology from a serviced turbine to that obtained in the accelerated deposition test facility. Instead, statistical comparisons can be used to show that surface formations have similar character and thus would influence performance (e.g., convective heat transfer) in a similar way.

A Hommel Inc. T8000 surface measurement system was used to make 3D surface topology maps of a variety of surfaces. The Hommel uses a 1.5 μm radius diamond-tipped conical stylus to follow the surface features for a given part. The instrument can measure a total vertical range of 1.6 mm with a precision of 75 nm. 3D surfaces are constructed from data taken every 5–10 μm on a rectilinear grid (typically 4 mm square).

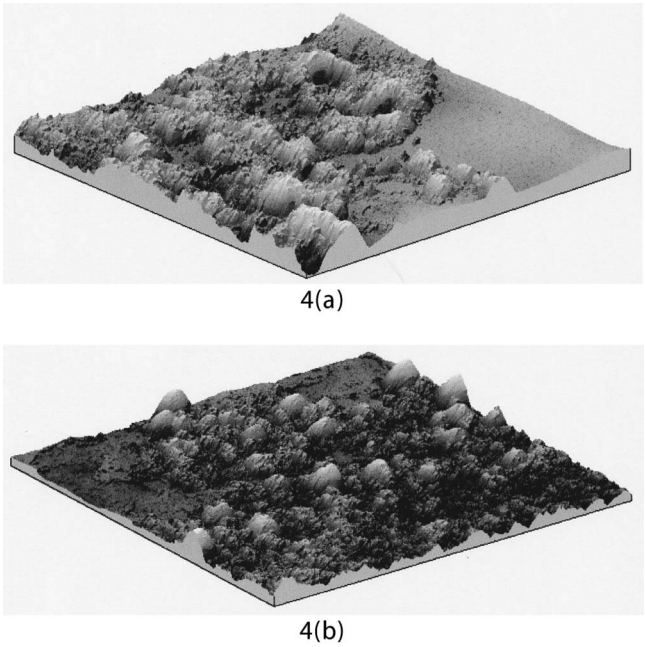

Fig. 4 Surface map of deposits from (a) first stage turbine with 25 000 h and (b) accelerated deposit surface after 4 h at 52 ppmw. Both maps are 4 mm×4 mm with approximately the same vertical scale.

Figures 4(*a*) and 4(*b*) show Hommel surface maps of two surfaces. Surface 4(*a*) is from a first stage turbine blade with 25 000 h of service. The topology map was taken at roughly 60% chord and 30% span on the blade suction surface, a region with obvious brownish deposits. Surface 4(*b*) is an accelerated deposition coupon that was tested for 4 h at 52 ppmw (T=1150 °C and M=0.33). The coupon was oriented for stagnation flow (impingement angle=90 deg), but the surface map shown was taken at the edge of the coupon where the flow was more tangential to the surface of the coupon as the impinging jet stream turned about the edges of the target. The strong similarities between the two images are reinforced by a review of their surface statistics (Table 2). Also included in Table 2 are statistics from various accelerated coupon tests and numerous serviced hardware. Though there are wide ranges of statistics for both the accelerated and serviced deposits, the ranges overlap noticeably. Thus, from a convective heat transfer standpoint, the accelerated deposits are considered "similar" to those found in actual serviced hardware.

The typical thickness of deposits in the accelerated test facility can be seen in Fig. 5 which shows the average of 800 profilometer traces across the test coupon. The ends of the trace are unexposed coating, so the average deposit thickness can be measured relative to this reference height. The deposits in this coupon appear to be roughly 45 μm thick, though the actual amount of deposit may be greater since the underlying coating experiences some degradation during testing. A weight measurement of this test coupon before and after accelerated deposition showed an increase due to deposition corresponding to 0.04 g per square mm of exposed coupon surface.

Internal Structure and Chemical Composition

When decreasing the length of exposure by three orders of magnitude, it is natural to question whether the deposition process has fundamentally changed. Though the external surface structure of accelerated deposits may bear resemblance to deposits found on turbine blades with over 10 000 h service time, in terms of

Table 2 Roughness statistics for accelerated and serviced deposits

Surface type	*Ra* (μm)	*Rt* (μm)	α_{rms}	S_W/S	Λ_s
Accelerated (4 h test)					
52 ppmw, (Fig. 4(*b*))	28	257	29	1.43	13
230 ppmw, 90 deg, impingement	32	260	16.5	1.12	82
137 ppmw, 45 deg, impingement	10	107	13.7	1.06	180
230 ppmw, at coupon edge	38	249	18	1.11	87
Serviced hardware					
25000 *h* blade (Fig 4(*a*))	32	240	27	1.36	22
22 500 *h* blade	41	296	24	1.24	36
<1000 *h* blade	19	394	18	1.11	77
24 000 *h* vane	17	220	15.8	1.09	134

internal heat conduction it is critical to determine whether the internal structure and chemical composition of the deposit is similar as well. To this end, scanning electron microscopy (SEM) was used with both the deposits formed in this accelerated facility and non-TBC coated turbine blade samples obtained from Standard Aero Inc., a third party turbine servicing corporation. To prepare the specimens for SEM analysis, each test coupon (or blade) was first potted in epoxy resin to prevent dislocation of the deposit during sectioning. Sections were then made and polished to 10 microns. Figure 6 shows side by side SEM comparisons of these microstructures. Figure 6(*a*) is from a blade with 16 000 h service while 6(*b*) is from a 4-h accelerated deposit on a coupon at $T=1150°\text{C}$, $\theta=90°$, and $M=0.33$. In both figures, the deposit is sandwiched between the epoxy (on top) and the turbine surface (on bottom). Elongated structures running parallel to the blade surface are evident in both SEM pictures. Another set of comparisons is shown in Figs. 7(*a*) (turbine blade with 25 000 h) and 7(*b*) (4-h accelerated deposit on a coupon at $T=1150°\text{C}$, $\theta=45°$, and $M=0.33$). Note that the 100-micron thick sample shown in Fig. 6(*b*) and the 50-micron thick sample shown in Fig. 7(*b*) are of the same order magnitude in size as actual turbine blade deposits shown in Figs. 6(*a*) and 7(*a*). Other microstructures including pitting and grain sintering were also observed in both turbine blade and accelerated specimen cross sections. Since the serviced hardware used in this comparison did not have TBC, a comparison was also made with the SEM analysis in Borom et al. [17]. Their study of serviced venturi and turbine shrouds with thermal barrier coating (TBC) showed significant mixing between the coating and the deposit. Figure 7(*b*) shows a region (circled and labeled) where MCrAlY coating constituents were found to penetrate into the deposit and vice versa using x-ray spectroscopy.

With the specimen cross sections in the polished state, they were also suitable for x-ray spectroscopy measurements. X-ray spectroscopy was used to determine the materials most likely to deposit on the turbine blade surface and compare this to the composition of the seed particles and to deposits on real turbine blades. Some results of the x-ray spectroscopy are shown in Table

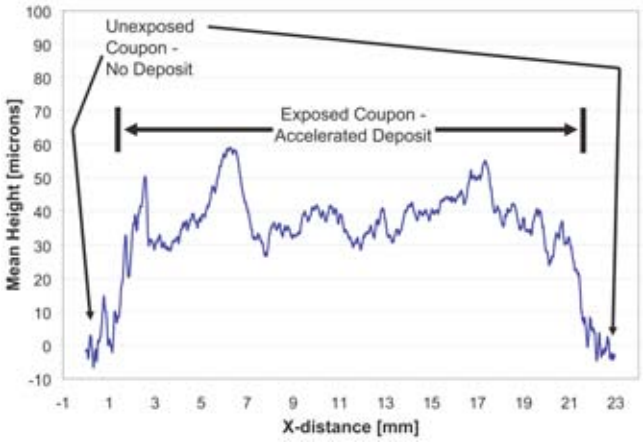

Fig. 5 23 mm long average surface trace across accelerated deposit test coupon. Vertical scale (units are microns) exaggerated for clarity. 1 mm on either end of trace is unexposed surface with no deposits.

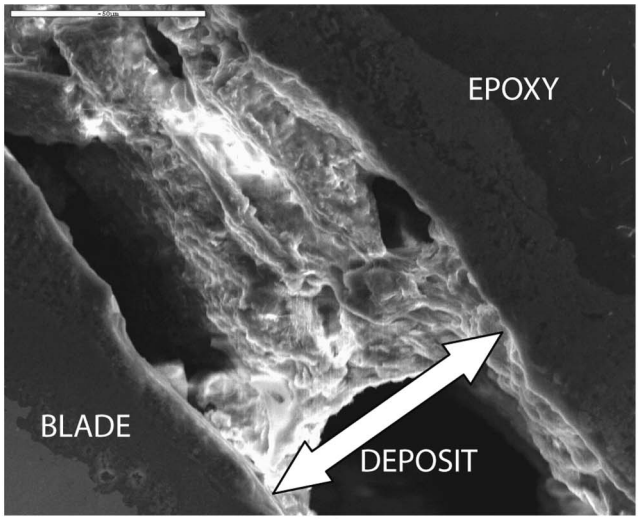

6(a)

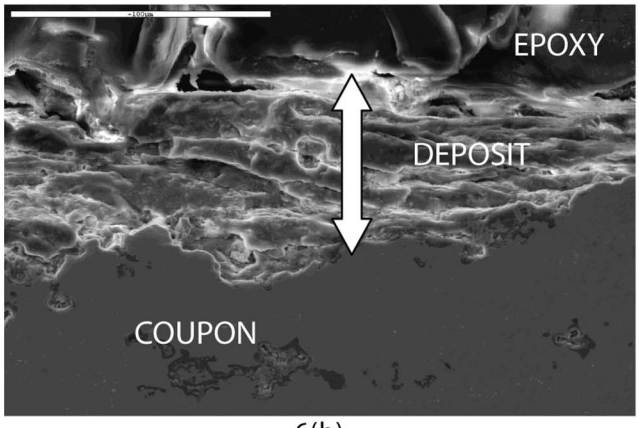

6(b)

Fig. 6 SEM cross section of (a) a 16 000 h service blade with 50-μm metering bar at top left and (b) an accelerated deposit specimen with 100-μm metering bar at top left

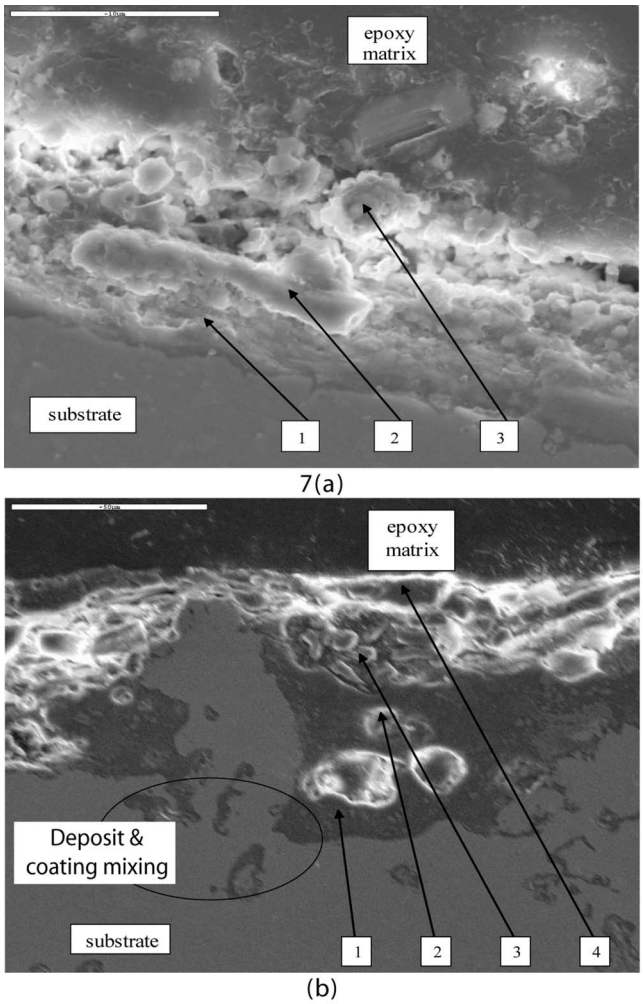

Fig. 7 SEM cross section of (a) 25 000-h service blade with 10-μm metering bar and (b) an accelerated sample with 30-μm metering bar

3 for various locations noted on Fig. 7. The deposits found on serviced turbine hardware are primarily composed of Ca–Mg–Al–Si (CMAS) as noted by Borom et al. [17]. Since these elements were nearly all (with the exception of Mg, see Table 1) present in the particulate used in this accelerated experiment, it is not unexpected that they also appear in the deposits formed.

Table 3 shows the relative abundance of the notable constituents of the deposit layer. Abundances in Table 3 are given in weight percent of the most common oxide of detected nuclei. Only those nuclei detected above the noise threshold of the SEM are considered in calculating weight percent. (Thus each row in the table sums to 100%.) Of the elements in CMAS, Mg is conspicuously absent. Mg was not detected in significant quantities in either the turbine blade deposit or the accelerated sample. As noted in the Table 1 heading, the manufacturer assays for the seed particulate indicated the presence of Mg but SEM assays at BYU failed to detect Mg above the noise of the sampling. For the turbine blade sample, the absence of Mg could be the result of specific environmental fluctuations. Note also that Ti is evident in accelerated samples though only a small amount of Ti was detected in the initial SEM assay and none was reported by the particulate manufacturer. Finally, Zn and Na are evident in the turbine deposit but were not in significant quantities in either the seed particulate or the accelerated deposit. These could again be the result of the unique chemistry of the ambient particulate mix in the turbine blade operating environment. Note that with the exception of Mg, the mass distribution of oxides in the accelerated sample approximate those reported by Borom et al. for desert deposit samples in aircraft engines (e.g., CaO=28.7%, MgO =6.4%, Al_2O_3=11.1%, SiO_2=43.7% [17]).

Figure 7(*b*) illustrates another important point regarding turbine blade deposition. Note the area circled near the bottom left corner of the SEM scan. The different colored regions represent different chemical compositions and in this case are identified as coating material and deposit-laden material. This area shows that even in these accelerated tests, solid-state diffusion occurs as the coating materials mix with the ceramic compounds in ingested particulate similar to the corrosion processes that can attack TBC during prolonged operation [7].

It is important to note that though SiO_2 is the primary component of the earth's crust and the seed particulate (roughly 60% by weight), the mass fraction of less abundant elements such as Ca and Fe are more conspicuous within the deposit. Each of these minor elements is less than 10% as abundant as Si in the earth's crust and the seed particulate, yet each is present in quantities of 30%–80% of the most abundant element (Al or Si) in the deposit for the points at which x-ray spectra were taken. This trend held true for both accelerated deposits and service turbine blades. Additionally, the turbine blade samples exhibited little constituent

Table 3 Relative abundance by percent weight at various points as noted in Fig. 7. (*a*) matches Fig. 7(*a*) and (*b*) matches Fig. 7(*b*). N/A denotes elemental counts below the noise threshold of the instrument. Percentages based only on elements detected above SEM noise threshold.

	Common elements percent weight								
(*a*) Service blade point	CaO	MgO	Al_2O_3	SiO_2	Fe_2O_3	TiO	Cr_2O_3	ZnO	Na_2O
1	0.0%	N/A	28.0%	4.1%	20.2%	N/A	25.7%	20.2%	1.8%
2	6.0%	N/A	20.8%	3.4%	26.1%	N/A	23.2%	19.2%	1.3%
3	5.1%	N/A	23.8%	3.8%	35.5%	N/A	11.7%	18.4%	1.7%
Average	3.7%	N/A	24.2%	3.8%	27.3%	N/A	20.2%	19.3%	1.6%
	Common elements percent weight								
(*b*) Accelerated sample point	CaO	MgO	Al_2O_3	SiO_2	Fe_2O_3	TiO	Cr_2O_3	ZnO	Na_2O
1	16.2%	N/A	8.4%	59.6%	9.9%	5.8%	0.0%	N/A	N/A
2	27.4%	N/A	3.7%	37.4%	16.6%	9.3%	5.6%	N/A	N/A
3	7.6%	N/A	8.4%	32.2%	20.2%	10.9%	20.7%	N/A	N/A
4	26.7%	N/A	N/A	56.3%	10.9%	6.1%	0.0%	N/A	N/A
Average	19.2%	N/A	6.8%	45.6%	14.1%	7.9%	6.5%	N/A	N/A

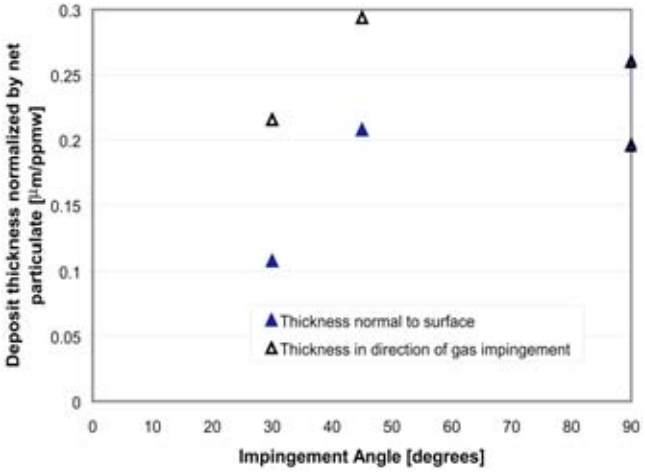

Fig. 8 Normalized deposit thickness as a function of impingement angle for 4 accelerated tests. Open symbols denote deposit thickness in flow direction.

stratification in the deposit layer. This is similar to the results given by Borom et al. [17] in which the chemical composition of the deposits seemed relatively homogeneous (i.e., roughly constant through the thickness). From the data in Table 3 it is clear that elements such as Fe, Cr, and Ca exhibit relatively constant abundance within the deposit layer. This indicates that accelerated deposition results in a homogeneous deposit layer similar to those observed in real service hardware. Thus, all indications suggest that accelerated deposition occurs by the same processes and is hence similar to deposits formed on in-service turbine hardware.

Influence of Angle

A limited number of tests (four) were conducted with the same jet Mach number and temperature, but three different flow angles to determine the influence of impingement angle on deposition. The average deposit thickness measured with the Hommel surface profilometer was normalized by the net throughflow of particulate to obtain a normalized deposit thickness. This is plotted vs impingement angles from 30 deg to 90 deg in Fig. 8 (see Fig. 2 for the definition of angle). Also shown in the figure are the deposit thicknesses measured in the direction of the impinging flow. Though the data are limited, there is no noticeable trend with angle once this adjustment is made. This corroborates similar findings by Wenglarz and Fox [16].

Another observation that may prove worthy of further study is that the statistical roughness factors (e.g., Ra, Rt, etc.) peaked at an impingement angle of 45 deg. Further investigation of this phenomenon is needed to establish the nature of this relationship with angle and determine its physical cause.

Influence of Particulate Concentration

Again, only a very limited number of tests were conducted at constant Mach number, temperature, and impingement angle but with different particulate concentration (ppmw). These results suggest a roughly constant deposit thickness to particulate concentration ratio of 0.23 μm/ppmw (see Fig. 8). Little change was observed in roughness statistics as a function of particulate concentration.

Influence of Temperature

Borom et al. reported that turbine blade deposit accumulation did not occur in aircraft turbines below a threshold temperature of 1090°C [17]. Consistent with this finding, test runs at or above 1100°C had significant deposition and topographical change to the TBC while those runs conducted at or below 900°C showed little change in topology and considerably less deposition. This temperature threshold is also dependent on other environmental and operational factors including surface condition, since some of the real turbine deposits examined during this investigation were formed at documented turbine inlet gas temperatures below 900°C.

Conclusions

This report presents a validation of the design and operation of an accelerated testing facility for the study of foreign deposit layers typical to the operation of land-based gas turbines. This facility was designed to produce turbine deposits in a 4-h test that would simulate 10 000 h of turbine operation. Based on the results presented herein, the following conclusions can be made:

(1) The surface topography of accelerated deposits closely resembles that of actual turbine blades that have seen 10 000–25 000 h of service.
(2) The microstructure and chemical composition of accelerated deposits resembles that of actual turbine blades. The deposits are relatively homogeneous in chemical composition and appear to have low porosity.
(3) A temperature threshold for accelerated deposition exists between 900°C and 1100°C for the test conditions presented herein.
(4) Deposit thickness of samples developed in the accelerated testing facility is insensitive to impingement angle (if the deposit thickness is measured in the flow direction). The deposit thickness to particulate loading ratio is roughly 0.23 μm/ppmw at the constant flow temperature and Mach number conditions studied.
(5) Since deposit structure, surface topography, and thickness all have direct influence on heat transfer, deposits generated in this accelerated facility are suitable for assessing the impact of deposition on turbine heat transfer.

Acknowledgments

Various individuals provided invaluable support to this research effort. The authors would particularly like to thank the assistance provided by Dr. Ron Bunker at General Electric Research Center, Mr. Ihor Diakunchak at Siemens-Westinghouse, Dr. Hee-Koo Moon at Solar Turbines, Mr. Alan Pauch at Standard Aero Inc., and Mr. John Fintland at Advanced Filtration Concepts, Inc who each provided invaluable insight as well as hardware. This research would not have been possible without the support of BYU students James Wammack, John Pettitt, Dave Olson, and Dan Reimann who each worked long hours monitoring experiments and assisting with the build-up of the facility. The authors also thank BYU chemical engineering doctoral candidate Shrinivas Lokare for sharing his invaluable expertise in combustion experimentation and deposit processing. Lastly, the authors thank the gifted machinists of the BYU Precision Machining Lab and Ken Forster whose skills helped produce the accelerated deposit facility. This work was partially sponsored by the U.S. Department of Energy—National Energy Technology Laboratory through a cooperative agreement with the South Carolina Institute for Energy Studies at Clemson University. The views expressed in this article are those of the authors and do not reflect the official policy or position of the Department of Energy or U.S. Government.

Nomenclature

M = flow Mach number
MCrAlY = metal–chromium–aluminum–yttrium oxidation resistant coating
Ra = centerline average roughness
Rt = maximum peak to valley roughness
S_w/S = total wetted surface area to planform area ratio

T = flow temperature
α_{rms} = rms deviation of surface slope angles
Λ_s = roughness shape/density parameter [26]
θ = impingment angle

References

[1] Ghenaiet, A., Elder, R. L., and Tan, S. C., 2001 "Particles and Trajectories Through an Axial Fan and Performance Degradation due to Sand Ingestion," ASME Paper No. 2001-GT-497.

[2] Wenglarz, R. A., 1992 "An Approach for Evaluation of Gas Turbine Deposition," ASME J. Eng. Gas Turbines Power, **114**, pp. 230–234.

[3] Kim, J., Dunn, M. G., and Baran, A. J. et al., 1993, "Deposition of Volcanic Materials in the Hot Sections of Two Gas Turbine Engines," J. Eng. Gas Turbines Power, **115**, pp. 641–651.

[4] Bons, J. P., 2002, "St and C_f Augmentation for Real Turbine Roughness With Elevated Freestream Turbulence," ASME J. Turbomach., **124**, pp. 632–644.

[5] Suao, Aoki, 2000, "Trend and Key Technologies for Gas Turbine Combined Cycle Power Generation in a Globally Competitive Market and Environmental Regulations," Proceedings of the 2000 IJPG conference.

[6] Chan, K. S., Cheruvu, N. S., and Leverant, G. R., 1999, "Coating Life Prediction for Combustion Turbine Blades," ASME J. Eng. Gas Turbines Power, **121**, pp. 484–488.

[7] Krishnan, Vaidyanathan, Kapat, J. S., Sohn, Y. H., and Desai, V. H., 2003, "Effect of Film Cooling on Low Temperature Hot Corrosion in a Coal Fired Gas Turbine," ASME Paper, GT2003-38593.

[8] Tabakoff, W., and Wakeman, T., 1979, "Test Facility for Material Erosion at High Temperature," ASTM Special Publication 664, pp. 123–135.

[9] Tabakoff, W., Metwally, M., and Hamed, A., 1995, "High-Temperature Coatings for Protection Against Turbine Deterioration," ASME J. Eng. Gas Turbines Power, **117**, pp. 146–151.

[10] Walsh, P. N., Quest, J. M., Tucker, R. C. Jr., 1995, "Coating for the Protection of Turbine Blades From Erosion," ASME J. Eng. Gas Turbines Power, **117**, pp. 152–155.

[11] Zaita, A. V., Buley, G., Karlsons, G., 1998, "Performance Deterioration Modeling in Aircraft Gas Turbine Engines," ASME J. Eng. Gas Turbines Power, **120**, pp. 344–349.

[12] Wenglarz, R. A., and Wright, I. G., 2002, "Alternate Fuels for Land-Based Turbines," *Proceedings of the Workshop on Materials and Practices to Improve Resistance to Fuel Derived Environmental Damage in Land- and Sea-Based Turbines*, October 22–24, Colorado School of Mines, Golden, Co.

[13] Toriz, F. C., Thakker, A. B., and Gupta, S. K., 1988, "Thermal Barrier Coatings for Jet Engines," ASME Paper No. 88-GT-279,.

[14] Smialek, J. L., et al., eds., 1992, The Chemistry of Saudi Arabian Sand: A Deposition Problem on Helicopter Turbine Airfoils, Advances in Synthesis and Processes, SAMPE, 3, M92-M101.

[15] Bons, J. P., Taylor, R., McClain, S., and Rivir, R. B., 2001, "The Many Faces of Turbine Surface Roughness," J. Turbomach., **123**, pp. 739–748.

[16] Wenglarz, R. A., and Fox, R. G. Jr., 1990, "Physical Aspects of Deposition From Coal-Water Fuels Under Gas Turbine Conditions," J. Eng. Gas Turbines Power, **112**, pp. 9–14.

[17] Borom, Marcus P., Johnson, Curtis A., and Peluso, Louis A., 1996, "Role of Environmental Deposits and Operating Surface Temperature in Spallation of Air Plasma Sprayed Thermal Barrier Coatings," Surf. Coat. Technol., **86–87**, pp. 116–126.

[18] Murray, Robert L., 1998, "Laser Doppler Anemometry Measurements in a Turbulent, Premixed, Natural Gas/Air Combustor," M.S. thesis, BYU, p. 17.

[19] Seinfeld, John H., and Pandis, Spyros N., 1998, *Atmospheric Chemistry and Physics*, John Wiley and Sons, New York.

[20] Finlayson-Pitts, Barbara J., and Pitts, James N., Jr., 1999 *Chemistry of the Upper and Lower Atmosphere: Theory, Experiments, and Applications*, Academic, San Diego, CA.

[21] Ford, W. E., 1954, (revision), *Dana's Textbook of Mineralogy* (after E. S. Dana) 4th ed., 16th printing, John Wiley and Sons, New York, p. 379.

[22] Fintland, John, 2003, Advanced Filtration Concepts, Inc., CA, personal correspondence with Jared Jensen.

[23] Dunn, M. G., Padova, C., and Adams, R. E., 1987, "Operation of Gas Turbine Engines in Dust-Laden Environments," AGARD-Advanced Technology Aero Engine Components, Paris, France.

[24] Blair, M. F., 1994, "An Experimental Study of Heat Transfer in a Large-Scale Turbine Rotor Passage," ASME J. Turbomach., **116**, pp 1–13.

[25] Boynton, J. L., Tabibzadeh, R., and Hudson, S. T., 1993, "Investigation of Rotor Blade Roughness Effects on Turbine Performance," ASME J. Turbomach., **115**, pp. 614–620.

[26] Sigal, A., and Danberg, J., 1990, "New Correlation of Roughness Density Effect on the Turbulent Boundary Layer," AIAA J., **28**, pp. 554–556.

Latticework (Vortex) Cooling Effectiveness: Rotating Channel Experiments

S. Acharya

F. Zhou

J. Lagrone

G. Mahmood

Turbine Innovation and Energy Research (TIER) Center, Louisiana State University, Baton Rouge, LA 70803

R. S. Bunker

General Electric Global Research Center, Niskayuna, NY 12309

The heat transfer and pressure drop characteristics of latticework coolant blade passages have been investigated experimentally under conditions of rotation. Stationary studies with the latticework configuration have shown potential advantages including spatially-uniform streamwise distributions of the heat transfer coefficient, greater blade strength, and enhancement levels comparable to conventional rib turbulators. In the present study, a latticework coolant passage, with orthogonal-ribs, is studied in a rotating heat transfer test-rig for a range of Reynolds numbers (Re_s)*, Rotation numbers* (Ro_s)*, and density ratios. Measurements indicate that for* $Re_s \geq 20{,}000$*, the latticework coolant passage provides very uniform streamwise distributions of the Nusselt number* (Nu_s) *with enhancement levels (relative to smooth-channel values) in the range of 2.0–2.5. No significant dependence of* Nu_s *on* Ro_s *and density ratio is observed except at lower* Re_s *values* ($\leq 10{,}000$)*. Nusselt numbers are highest immediately downstream of a turn indicating that bend-effects play a major role in enhancing heat transfer. Friction factors are relatively insensitive to* Ro_s*, and thermal performance factors at higher* Re_s *values appear to be comparable to those obtained with conventional rib-turbulators. The present study indicates that latticework cooling geometry can provide comparable heat transfer enhancements and thermal performance factors as conventional rib-turbulators, with potential benefits of streamwise uniformity in the heat transfer coefficients and added blade strength.* [DOI: 10.1115/1.1860381]

1 Introduction

The demand for higher turbine inlet temperatures in advanced gas turbines require more effective internal cooling strategies for turbine blades. Current designs for internal cooling primarily involve rib-turbulators or pin fins, which typically enhance heat transfer by factor of 2–3 over the smooth channel values [1–3]. In recent years, improved internal-cooling strategies involving profiled-ribs [4,5], screw-cooling [6,7], dimples, [8,9] and vortex-generators [10,11] have been explored. While higher enhancement levels have been achieved with some of these approaches, they have generally been at the expense of additional pressure drop and/or manufacturing complexities. Thus, there is a continued need to explore internal cooling strategies that can potentially provide higher enhancement levels while preserving ease of manufacturing and low pressure drop penalty. This paper deals with the latticework cooling geometry (described in detail by Bunker [12]), and reports heat transfer and pressure drop measurements in coolant passages with rotation.

Internal cooling with rib-turbulators has been studied extensively. Wagner et al. [13,14] report the effects of rotation and density ratio on heat transfer in smooth channels with square cross sections. Their results show that rotation significantly affects heat transfer characteristics, with an increase in heat transfer by a factor of 3.5 on the pressure-side (at a Rotation number of 0.35), and a corresponding decrease of nearly 40% on the suction side of the blade as compared to the stationary case. Wagner et al. [15] report measurements of heat transfer and pressure drop in ribbed coolant channels with ribs normal to the flow. At a Rotation number of 0.35, the heat transfer on the pressure side increased to 4 times the stationary value, while the suction side heat transfer is reduced by 50%. For a model with skewed ribs, Johnson et al. [16] conclude that skewed ribs result in higher heat transfer coefficients and lower sensitivity to buoyancy (density ratio) effects. Thus, rotation clearly has a significant influence on the internal cooling heat transfer characteristics of the blade, and therefore, in order to optimize and accurately predict blade performance and life, rotational effects on the heat transfer must be considered during the design process.

Researchers in the former Soviet Union have extensively utilized the concept of latticework cooling or vortex cooling (Nagoga [17]). The study of Bunker [12] describes this concept in detail. The passage geometry consists of coplanar crossing channels on the pressure and suction sides that dead-end on the sidewalls, and turn the flow around from the pressure/suction side channel to the suction/pressure side channel. The crossing channels from either side extend to the mid-plane, and the crossing angle is typically in the range of 35–60 deg. As noted by Bunker [12], latticework cooling potentially has some intrinsic advantages including higher blade strength and more uniform distribution of heat transfer coefficients. This configuration has however received rather limited attention in the published English literature.

Goreloff et al. [18] report the overall cooling effectiveness of a stationary turbine blade with latticework passages using the zinc melt technique. Gillespie et al. [19] use the transient liquid crystal method to measure the detailed local heat transfer coefficient distributions in a stationary vortex channel with flow ejection through film-cooling holes on the trailing edge. Bunker [12] presents the detailed distributions of local heat transfer coefficients and pressure drop along individual subchannels in stationary radial latticework passages and document the effects of the turns of the subchannels and the fin effects of the lattice ribs.

There have been no studies reported in the literature on the effect of rotation on lattice-cooling passages. The objectives of the present study are to document the rotation effects on the heat

Contributed by the International Gas Turbine Institute (IGTI) of THE AMERICAN SOCIETY OF MECHANICAL ENGINEERS for publication in the ASME JOURNAL OF TURBOMACHINERY. Paper presented at the International Gas Turbine and Aeroengine Congress and Exhibition, Vienna, Austria, June 13–17, 2004, Paper No. 2004-GT-53983. Manuscript recieved by IGTI, October 1, 2003; final revision, March 1, 2004. IGTI Review Chair: A. J. Strazisar.

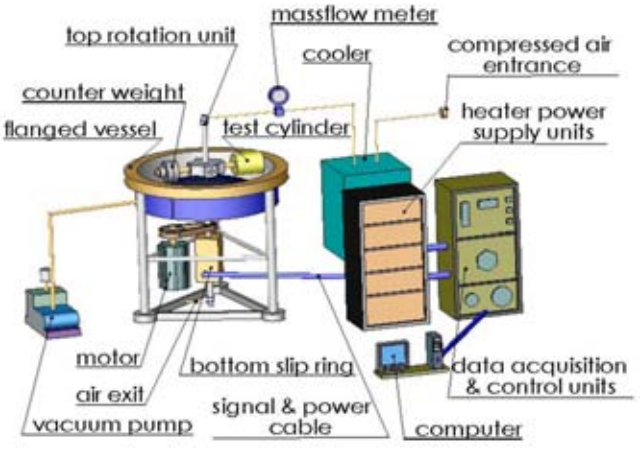

Fig. 1 Experimental setup

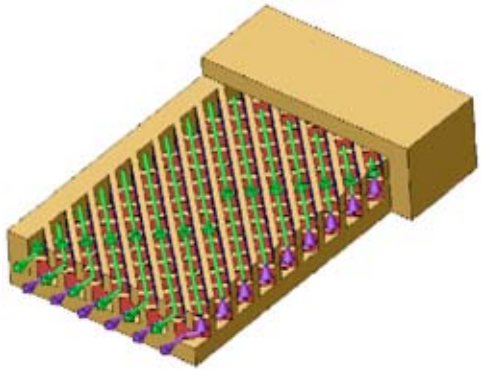

Fig. 2 Lattice geometry and flow paths

transfer in a radial latticework channel. Heat transfer and pressure drop measurements have been performed for a range of Reynolds numbers, density ratios, and rotation numbers.

2 Experimental Setup

2.1 Rotating Heat Transfer Facility. The rotating rig shown in Fig. 1, originally used by Wagner et al. [13,14], has been utilized in the present study. The facility has two major components: the containment vessel and the rotating arm assembly. The containment vessel is 1.83 m (6 ft.) in diameter and consists of two symmetrical flanged sections. The upper section (not shown in Fig. 1) of the vessel is removable to allow access to the rotating arm, and the lower section is anchored and supported by a steel support frame shown in Fig. 1. The vessel was designed for operation at 5 mm Hg absolute pressure to reduce the viscous heating and the power requirement of the rotating arm.

The arm assembly consists of the vertical shaft and the horizontal arm. A 15 HP dc motor drives the entire rotating assembly. The rotational speed of the shaft can be varied from 0 to a maximum of 1500 rpm by a feedback electronic controller. The vertical shaft consists of the main outer shaft and an inner concentric shaft. Together the shafts provide dual fluid paths for the rotary unions mounted on each end of the main shaft. In the present experiments, only the inner shaft is used as the air path. The rotary unions and the paths in the shafts were designed to sustain 1034 kPa (about 10 atm).

On the exterior surface of the main shaft, recessed grooves allow signal and power leads to run from the rotating arm assembly to two slip rings, one located on the upper end of the main shaft (not shown in the figure) and the other on the lower end. The two slip rings provide a total of 240 channels for power and instrumentation wires between the stationary and rotating frames. A cylindrical pressure vessel containing the test section is mounted on one end to the horizontal arm. On the other end, a counter weight, with variable mass and positioning capabilities, is mounted to allow for static and dynamic balancing of different test sections. Stainless steel tubing along the arm provides an air passage from the test section to the shaft. A Kulite and a Scanivalve pressure transducers are mounted on the arm to measure the absolute pressure and differential pressure inside the test section, respectively.

Air entering the test section is circulated through a refrigerant cooling loop to alter and maintain the temperature of the inlet airflow in order to achieve the desired density ratio. The air is provided by a compressor-dryer-reservoir system, with a maximum mass flow rate and pressure of 0.5 kg/s and 300 psia (about 20 atm), respectively. The power supply unit has 72 independent channels for providing the 0–45 V of dc power for the heaters inside the test section. An HP 3497A and HP 3498A Extender serve as the primary data acquisition system. They are connected to a Dell computer through a GPIB port and controlled by a custom-written C program. The pressure signals, shaft speed, thermocouple voltages, and heater power are all recorded by this system. The mass flow rate of the airflow is read separately through a Rosemount Mass Flow Unit.

2.2 Latticework Model. Figure 2 shows a schematic of the latticework test section. The crossing-rib configuration on the leading (suction side) and trailing (pressure side) surfaces result in a coolant passage with inclined-serpentine subchannels. In the present study, the ribs are inclined at 45 deg to the radial direction. The alignment of the crossing ribs are such that, along the sidewalls, the subchannel along one surface turns smoothly into the subchannel on the opposite surface, thus forcing the fluid to change directions by 90 deg (Fig. 2).

Figure 3 shows a top-section view of the latticework model. The portion of the model shown (leading/suction side) consist of: a 1.27 cm (0.5 in.) thick G-10 Garolite (continuous-woven laminated glass fabric, with a thermal conductivity of 0.1 W/(m K)) for the bottom plate, 0.079 cm (0.031 in.) thick silicon rubber sheet between the bottom plate and the supporting frames (the outer frame and the central frame), and a 1.27 cm (0.5 in.) thick G-10 Garolite for the central and outer frames that define the shape of the U-bend. The leading and trailing edges of the test section are each formed by 17-copper elements, with the adjacent elements separated from each other by insulation spacers of G-10

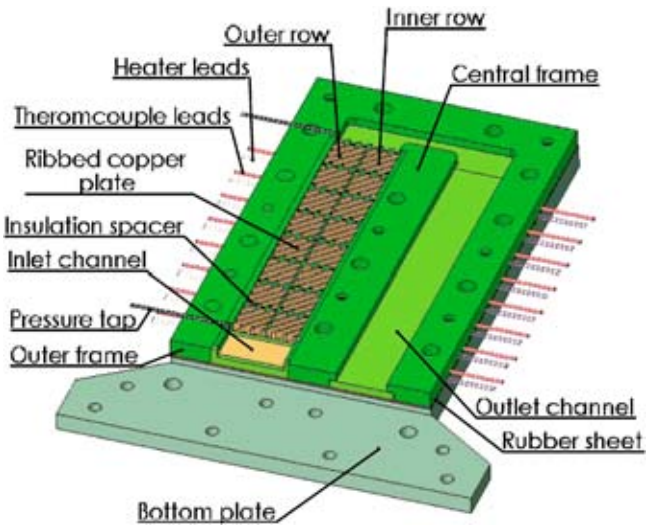

Fig. 3 Test Model (leading side)

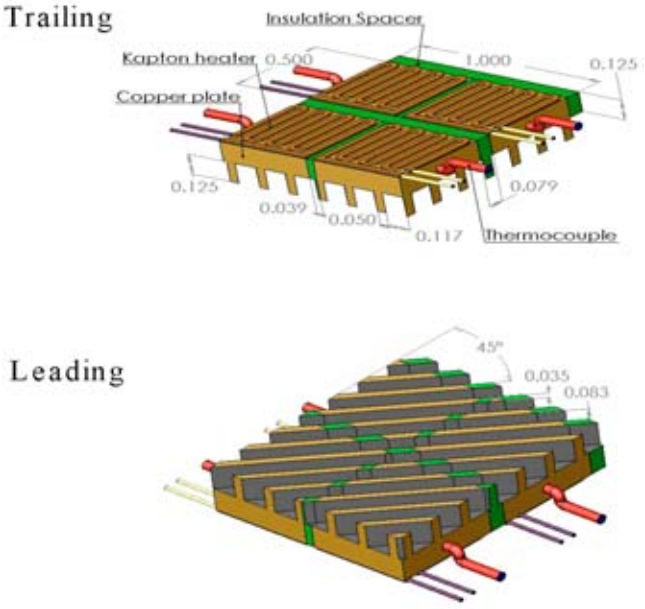

Fig. 4 Lattice element details (all dimensions in cm)

Garolite. The crossing ribs are integrally machined on the copper plates and the sandwiched Garolite spacers. The bend and the outlet leg, which are not heated, are formed by 0.317 cm (0.125 in.) thick G-10 Garolite sheets supported by the outer and central frames. The passage cross section has an aspect ratio of 4:1 with dimensions of 2.54 cm × 0.635 cm (1 in. by 0.25 in.). The trailing half of the latticework model is a mirror image of the leading side except that the latticework ribs on the copper elements are orthogonal to the ones on the leading side. Screws through the top (not shown) and bottom plates run through and tightened to hold the test section together.

A steel two-channel transition section is inserted between the top and bottom G-10 plates and aligned with the inlet and exit planes of the test section. This section provides for a smooth transition between the rectangular test channel and the circular airfeeds on the rotation rig. The transition section is also equipped with screens to stabilize the flow, and two *K*-type thermocouples to measure the inlet and outlet flow temperatures.

The whole unit is bolted between two steel support plates, and the assembly is mounted inside a cylindrical pressure vessel. The thermocouple leads, power wires, and the pressure transducer tubes are routed out of the vessel through sealed plugs on one of the cylinder's planar faces.

The active portion of the test channel is 11.71 cm (4.61 in.) long and consists of 32–0.635 cm (0.25 in.) thick copper plates. Machined in these copper plates are the ribs on the trailing and leading surfaces. The ribs on the trailing surface extend up to the orthogonal ribs on the leading surface to form the series of ribbed serpentine sub-channels shown in Fig. 2. The dimensions of the subchannel cross section are 0.317 cm (0.125 in.) × 0.211 cm (0.083 in.) giving it a hydraulic diameter of 0.253 cm (0.1 in.). The ribs are 0.089 cm (0.035 in.) thick and 0.317 cm (0.125 in.) high as shown in Fig. 4. The passages formed by the ribs on the leading side are oriented at an angle of 45û clockwise to the streamwise direction, while the passages on the trailing side are at a 45 deg angle counterclockwise to the streamwise direction. The individual copper plates are isolated by a 0.2 cm (0.079 in.) G-10 Garolite strip in the streamwise direction and a 0.1 cm (0.039 in.) G-10 Garolite strip in the spanwise direction. The overall channel, whose cross section has dimensions of 2.54 cm × 0.635 cm (1 in. × 0.25 in.), has a hydraulic diameter of 1.02 cm (0.4 in.). Each copper plate is equipped with a Minco Kapton etched foil heater, and a *K*-type thermocouple, allowing the heat flux of each copper plate to be individually regulated to give an isothermal wall condition as measured by the thermocouple. The first copper element (see Fig. 3), one on each side, serve the role of guard heaters, and are smooth 0.317 cm (0.125 in.) thick copper plates which span the width of the channel. These elements are also heated with Minco Kapton etched foil heaters.

3 Data Reduction

The isothermal wall condition was achieved by varying the power input to each heater attached to the individual copper plates. For the experiments, the temperatures of each copper plate was maintained within ±0.5°C of the average wall temperature, T_w. By varying T_w and inlet flow temperature, T_{in}, different density ratios are obtained. The local heat transfer coefficient, h_i, at the ith copper plate is calculated from the net heat flux, $q''_{\text{net},i}$ from the heated plate to the cooling air, the surface temperature of the plate, T_w, and the local bulk mean air temperature, $T_{b,i}$, as follows:

$$h_i = q''_{\text{net},i} / (T_w - T_{b,i}), \quad \text{where } q''_{\text{net},i} = (q_i - q_{\text{loss},i}) / A_i \text{ and } q_i = I_i^2 \cdot R_i \tag{1}$$

where I_i and R_i are the current and the resistance of the ith copper plate heater, respectively, $q_{\text{loss},i}$ is the heat loss from the ith plate, and A_i is the total area (including the area of the rib-surfaces) of the copper plate exposed to the flow. The maximum temperature reached by the plates over the range of test conditions is 376 K, and the resistance of the heaters (in Eq. (1)) are constant for temperatures less than 383 K as per data sheets provided by Minco Inc. The heat loss $q_{\text{loss},i}$ is determined by a series of stationary tests, without flow, where for steady state conditions, the power input is balanced by the heat loss. Thus a calibration of the heat loss with respect to the wall temperature is initially obtained and used in the data analysis.

The local bulk mean air temperature, $T_{b,i}$, is calculated at the midpoint of each copper-strip, and is given by an energy balance equation as

$$T_{b,i} = T_{in} + \left(\sum_{j=1}^{i-1} (q_j - q_{\text{loss},j})_{\text{leading}} + \frac{1}{2}(q_i - q_{\text{loss},i})_{\text{leading}} \right) \Big/ (\dot{m} \cdot C_p) + \left(\sum_{j=1}^{i-1} (q_j - q_{\text{loss},j})_{\text{trailing}} + \frac{1}{2}(q_i - q_{\text{loss},i})_{\text{trailing}} \right) \Big/ (\dot{m} \cdot C_p). \tag{2}$$

where $\dot{m}$ is the mass flow rate and C_p is the specific heat. The Nusselt number, Nu_i, is then obtained from

$$\text{Nu}_i = h_i \cdot D_h / k \tag{3}$$

where D_h is the hydraulic diameter, and k the air conductivity. Then Nu_i is normalized by the Dittus–Boelter correction: $\text{Nu}_0 = 0.023 \cdot \text{Re}^{0.8} \cdot \text{Pr}^{0.4}$ [20] yielding

$$\text{Nu}_i / \text{Nu}_0 = h_i \cdot D_h / (k \cdot 0.023 \cdot \text{Re}^{0.8} \cdot \text{Pr}^{0.4}) \tag{4}$$

The average friction factor, f, is calculated by

$$f = (\Delta P \cdot D_h) / (4L \cdot 1/2 \cdot \rho \cdot V^2) \tag{5}$$

where L is the distance between the two pressure taps, ΔP is the pressure drop, ρ is the flow density, and V is the mean velocity of the flow. The friction factor is normalized by the Karman–Nikuradse equation [21], $f_0 = 0.046 \cdot \text{Re}^{-0.2}$, resulting in

$$f / f_0 = (\Delta P \cdot D_h) / (4L \cdot 1/2 \cdot \rho \cdot V^2 \cdot 0.046\, \text{Re}^{-0.2}) \tag{6}$$

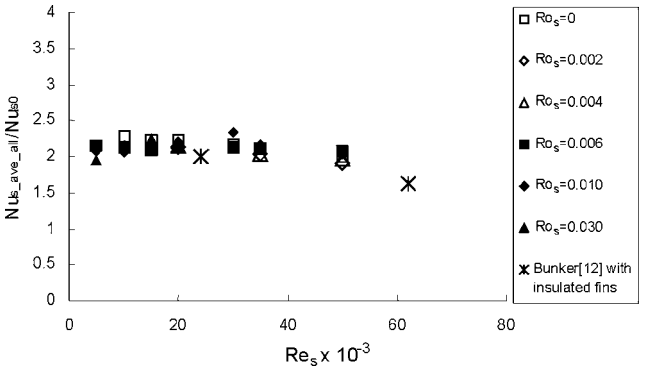

Fig. 5 Channel-averaged Nusselt numbers as a function of Re_s

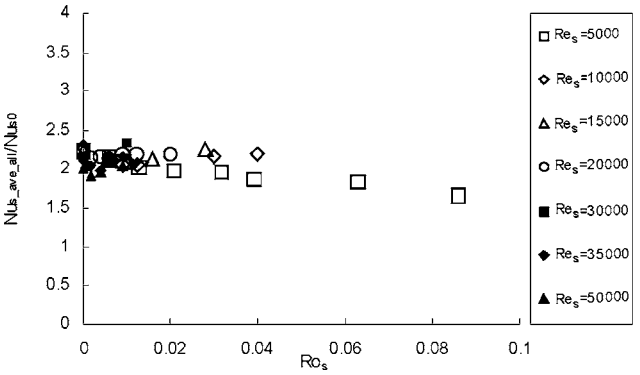

Fig. 6 Channel-averaged Nusselt numbers as a function of Ro_s

The maximum relative uncertainty in the calculated heat transfer ratio is estimated to be approximately 10%, which occurs at the channel exit where the difference between the wall temperature and bulk temperature is the smallest. The average error from inlet to exit was approximately 7% for the current test conditions. The largest contribution to this uncertainty comes from the measurement of temperature. The maximum relative uncertainty in the friction factor is estimated to be nearly 13%. These uncertainties were estimated using the method for single sample experiments described by Kline and McClintock [22]. Estimates were also made to determine the effects of pumping on the enthalpy rise. At 1000 rpm this contributed to about 1% increase in temperature at the exit of the channel, and therefore these effects were not significant.

4 Results and Discussions

During the experiments, the pressure in the test section was maintained at 150 psia. The inlet air temperature varied from 25°C for stationary tests to 35°C for tests at high rotational speeds. The Reynolds number based on the hydraulic diameter of the subchannel (D_{hs}), Re_s, was varied from 5000 to 50,000, the rotation number based on the subchannel hydraulic diameter, Ro_s, was varied from 0 to 0.086, and inlet density ratio, DR, was varied from 0.075 to 0.18. Note that the maximum Reynolds number and Rotation number based on the hydraulic diameter of the entire channel ($D_h=4D_{hs}$) are 200,000 (corresponding to Re_s of 50,000) and 0.34 (corresponding to a Ro_s of 0.086), respectively. Uniform wall temperature was maintained during each test run with a maximum temperature variation between the copper elements of ±0.5°C. The highest wall temperature was set at 103°C at T_{in} =35°C for DR=0.18, and the lowest wall temperature was set at 49.5°C at T_{in}=25°C for DR=0.075. In the following discussions, the density ratio DR is 0.075 unless otherwise stated.

4.1 Channel-Averaged Nusselt Numbers. Figure 5 presents the Nusselt number averaged along both leading and trailing surfaces as a function of Re_s. Also shown is the stationary data of Bunker [12] with 45 deg insulating ribs and 6-subchannels. Of the cases considered in [12], this case most closely represents the configuration considered in the present study (45 deg copper ribs and 6-subchannels). The all-metal configuration considered by Bunker [12] uses 40 deg steel ribs with either 4 or 8 subchannels. As seen in Fig. 5, the present data with metal ribs agrees well with the data with insulating-ribs reported by Bunker [12]. The present data is only about 20% higher than the data of Bunker [12] due to fin-effects; it should be noted that the current results match more closely with the insulated rib result than the metal ribs results of Bunker [12]. This could be the result of several different factors including the difference in boundary conditions (constant wall temperature in the present experiments versus constant heat flux in [12]), differences in the transient technique [12] versus the present steady state technique, variations in rib angle (45 deg in the present case to 40 deg in [12]), and differences in subchannels (6 in the present study to either 4 or 8 in [12]). The insulated rib configuration in [12] matches the present configuration with metal ribs exactly, and was therefore used for the comparison.

Figure 5 suggests that the overall normalized Nusselt number is relatively independent of the Reynolds number, showing only a small decrease at higher Re_s. The streamwise Nusselt number distributions (shown later) however do indicate a Reynolds number effect that appear to average out over the length of the coolant passage.

Rotation does not produce a significant effect on the channel-averaged Nusselt number (Fig. 6), with a noticeable decrease (nearly 25% at $Ro_s=0.086$) only at the lowest Re_s studied. The effect of rotation on the local Nusselt numbers are presented later. Note that the Ro_s values shown are based on the subchannel hydraulic diameter, and will be four times greater if based on the full passage hydraulic diameter. From this perspective, the Ro_s considered in the present study are representative of realistic operating conditions.

4.2 Turn Effects. As stated in the section of "Latticework Model," the air in each subchannel on the leading (suction) wall flows from the outer sidewall to the inner sidewall (Fig. 2). When the flow reaches the inner sidewall it turns 90 deg and is oriented into the crossing subchannel on the trailing (pressure) wall, completing one vortex turn. When the airstream reaches the inner sidewall it undergoes a second vortex turn. The airflow undergoes four vortex turns from the entrance to the exit.

Since at each streamwise location, two spanwise copper elements are used, Nusselt number information is obtained at two spanwise locations (identified as inner and outer and indicative of the sidewall closest to the measurement location). Figure 7 shows the streamwise Nu_s/Nu_{s0} distributions along the inner and outer locations at $Re_s=20{,}000$ for stationary conditions. As observed by Bunker [12], the Nusselt numbers, from the inlet to the exit, are quite uniform along the flow direction with enhancement levels in the range of 2–2.5. The spatial uniformity of the heat transfer coefficients in the streamwise direction is considered to be an advantage of the latticework cooling scheme. The heat transfer along the outer row of the leading (suction-side) wall is higher (by about 20%) than that along the inner row, while on the trailing (pressure-side) wall the heat transfer along the inner row is comparably higher than that along the outer row. The average Nu_s/Nu_{s0} along the leading inner row and the trailing outer row is 2.0, while the average Nu_s/Nu_{s0} along the leading outer row and the trailing inner row is about 2.4 for $Re_s=20{,}000$. The higher values along the leading-outer and trailing-inner are associated with the flow turning into the subchannels from the opposite walls at these locations. The same behavior was observed in the stationary experiments of Bunker [12]. Wagner et al. [13,14] and Zhou et

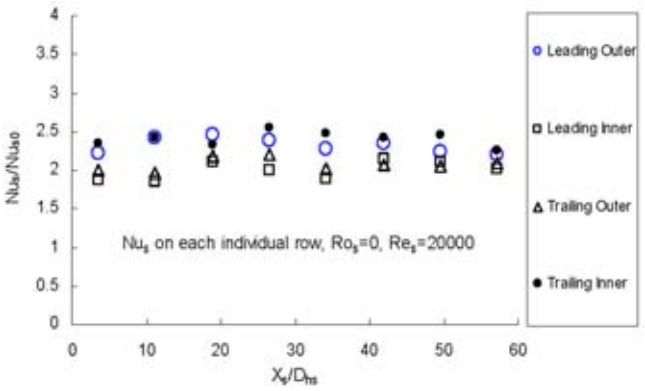

Fig. 7 Nusselt number distributions on individual rows for stationary channel

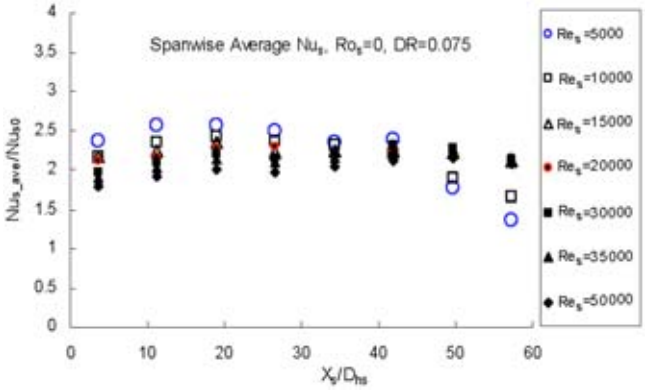

Fig. 9 Spanwise average Nusselt numbers for stationary channel

al. [23], in their studies of flow past bends in serpentine cooling passages, have noted that the heat transfer at the exit of a 180 deg turn is much stronger than at the entrance of the turn. In the present study, the exits of the vortex turns are located on the leading-outer row and trailing-inner row, and these regions are therefore associated with higher heat transfer coefficients. Furthermore, each time the flow turns around, the boundary-layer development is interrupted along the subchannel, leading to enhanced heat transfer coefficients.

Figure 8 shows the streamwise-averaged Nusselt numbers $Nu_{s\text{-row}}/Nu_{s0}$ plotted as a function of Re_s under stationary conditions. No significant Reynolds number effect is observed, and the trends observed in Fig. 7 at Re=20,000 are consistently noted at all Reynolds numbers. The results shown in Fig. 8 also seem to support the observation of Bunker [12], in that, even though there is no barrier between the subchannels on the leading and trailing edges, the two channels seem to have no apparent interaction.

While Figs. 7 and 8 are presented for stationary conditions, the turn effects (higher Nu_s along the leading-outer and trailing-inner) are also observed for the rotating cases, and are not presented in Figs. 7 and 8 for preserving the clarity in the figures. Additional discussion on rotation effects is provided later.

4.3 Reynolds Number Effects. The spanwise-averaged (both leading and trailing walls) Nusselt number, Nu_{s_ave}/Nu_{s0}, is presented as a function of the Reynolds number in Figs. 9 and 10 for $Ro_s=0$ and $Ro_s=0.012$, respectively. At the higher Re_s values ($\geq$20,000), there is essentially no change in Nu_{s_ave}/Nu_{s0} with streamwise distance. However, at the lower Re_s values ($\leq$10,000) there is a decrease in the Nusselt number in the streamwise direction (35%–45% over $50D_h$ at $Re_s=5{,}000$), and this decrease primarily occurs in the downstream regions of the coolant passage ($X_s/D_{hs}\geq 40$). Therefore, in the upstream half passage ($X_s/D_{hs}<30$), Nu_{s_ave}/Nu_{s0} decreases with increasing Reynolds number, but this trend reverses for $X_s/D_{hs}\geq 40$ due to the sharp decrease in the Nusselt number in this region at low Re_s. This effect is clearly greater under rotational conditions due to the greater dependence of the Nusselt number on Ro_s at the lower Reynolds number values.

4.4 Rotation Effects. In view of the differences in the Nusselt numbers along the inner and outer sides of the leading and trailing surfaces (Figs. 7 and 8), the rotation effects are first examined for the inner and outer rows along the leading and trailing surfaces. To enable this comparison, Nu_s/Nu_{s_st} is plotted, where Nu_{s_st} is the corresponding Nusselt number for the stationary condition. Figure 11 shows the Nu_s/Nu_{s_st} streamwise distributions along each of the four rows at $Re_s=20{,}000$ for different values of the Rotation number. Until X/D_{hs} of 40 (the initial 2/3rds of the coolant passage), Nu_s/Nu_{s_st} is essentially unity for Ro_s between 0 and 0.02, indicating no rotational effects. For $X/D_{hs}>40$, differences can be observed between the various Rotation numbers. These rotation-induced differences are generally small (less than 20%), and do not conform to the rotation effects observed in smooth or normal/angled-ribbed coolant passages. It is well known that in the smooth and ribbed passages with radial outflow, rotation-induced secondary flow enhances the heat transfer on the pressure-side or trailing wall, but reduces the heat transfer on the suction-side or leading wall. In the present study, two factors contribute to a decrease in the rotation effects. First, due to the significantly added surface area, viscous or frictional effects play a

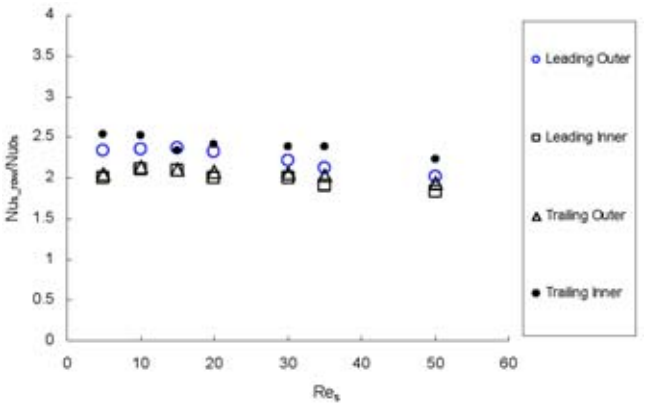

Fig. 8 Streamwise-averaged Nusselt numbers for stationary channel

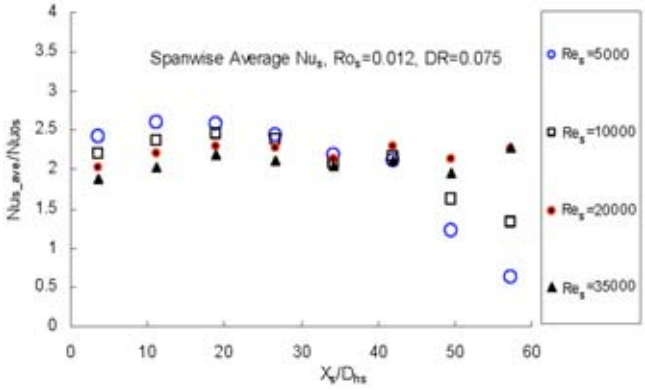

Fig. 10 Spanwise average Nusselt numbers at $Ro_s=0.012$

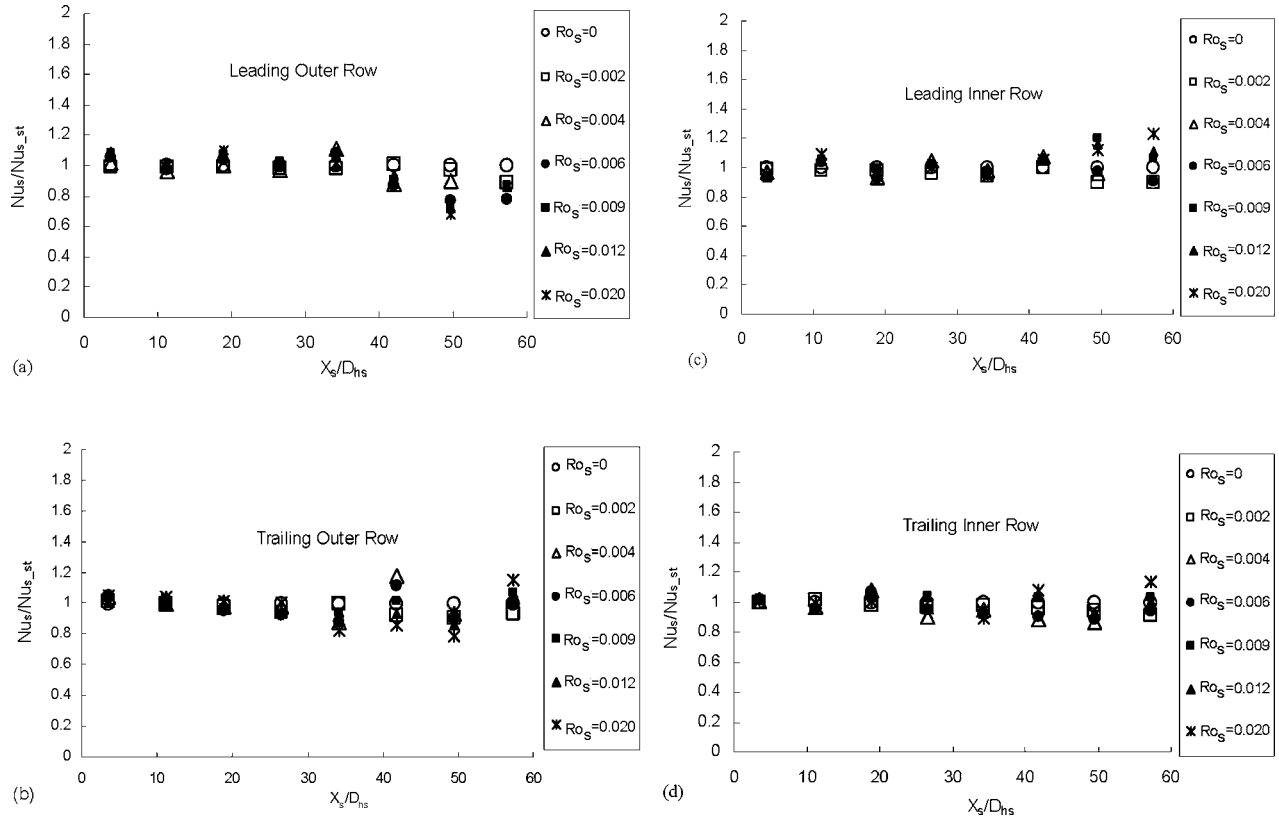

Fig. 11 Rotation effects on the individual rows at Re_s=20 k

more important role, and are likely to damp secondary flows. Second, the repeated turning of the flow through the 90° bends makes it much more difficult to maintain sustained secondary patterns, compared to the flow in straight smooth and ribbed passages. Flow measurements and computations past bends in conventional turbulated channels indicate that the bend alters the rotation-induced secondary flow pattern [1–3,13–16], and that a certain development length is needed beyond the bend for the rotation-induced flows to be re-established. This observed insensitivity to rotational effects, for moderate and high values of Re_s, can be viewed as a benefit of the latticework cooling concept since no heat transfer degradation on the stabilized surface is observed with rotation. At a lower Re_s, however, the rotation effects are slightly more evident, as noted earlier in Fig. 6, and is discussed below.

Figures 12 and 13 show the spanwise-averaged (both leading and trailing walls) Nusselt number ratio Nu_{s_ave}/Nu_{s0} plotted as a function of the streamwise distance at Re_s=35,000, and 5000, respectively. The data in Fig. 12 is representative of the behavior at the higher Re_s($\geq$20,000), and shown earlier along the inner and outer rows in Fig. 11. No effect of rotation is observed until X/D_{hs} of about 40, and the effects of rotation are established only after a substantial development region of nearly 40 D_{hs}. The rotation effects appear to indicate an initial decrease in Nu_{s_ave} with Ro (till Ro_s of 0.004) followed by an increase.

At the lowest Re_s considered (Re_s=5,000), a substantial rotation effect can be observed in the second half of the coolant passage ($X/D_{hs} \geq 30$), with a decrease in Nu_{s_ave} with Ro. At the lower Re_s, in Figs. 9 and 10, the Nusselt numbers are seen to decrease significantly in the later-half of the coolant passage. Thus, for ($X/D_{hs} \geq 50$), the Nu_{s_ave}/Nu_{s0}, at the higher Rotation

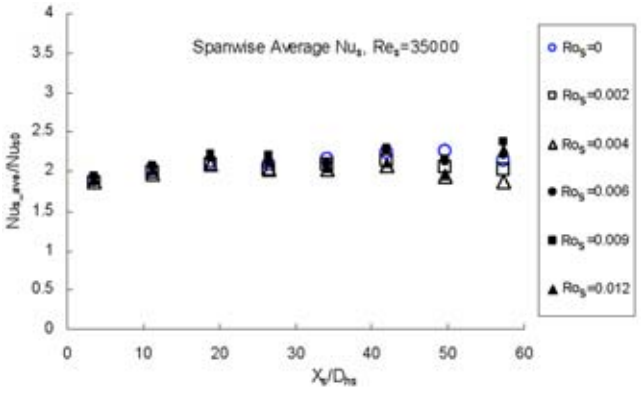

Fig. 12 Rotation effects at Re_s=35 k

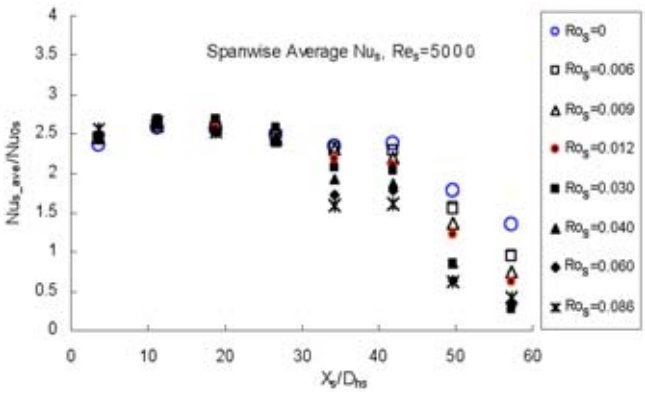

Fig. 13 Rotation effects at Re_s=5 k

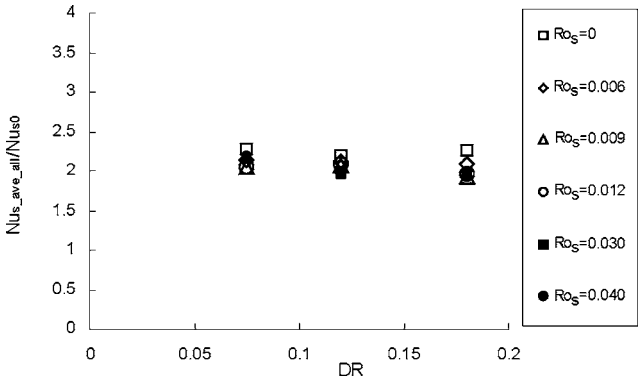

Fig. 14 Nusselt number averaged over the whole channel versus DR (Re_s=10 k)

numbers decreases substantially toward the end of the trailing passage, achieving Nu_{s_ave}/Nu_{s0} values even lower than 1. Thus the performance of the latticework geometry appears to degrade in the trailing-half of the blade passage. However, even at the lower Re_s, the first-half of the coolant passage is relatively unaffected by rotation, and when averaged across the entire channel, the influence of rotation number on the channel-averaged Nu is about 20% at Re_s=5,000, as seen in Fig. 6.

4.5 Density Ratio Effects. Channel-averaged Nu_s ratios are presented as a function of the inlet density ratio for different Ro_s values in Fig. 14 for Re_s=10,000. No significant density ratio is observed in the channel-averaged values. Figure 15 presents the streamwise distributions of the spanwise-averaged Nusselt number ratio, Nu_{s_ave}/Nu_{s0}, for Re_s=10,000, and Ro_s=0.04, for three different density ratios. As in Fig. 14, the density ratio effects are seen to be small. These results are in distinct contrast with the smooth channel results of Zhou et al. [23] with the same overall aspect ratio (4:1) as in the present study. For the smooth channel, density ratio was observed to enhance the spanwise-averaged heat transfer [23]. Clearly centrifugal-buoyancy effects are inhibited with the latticework ribs. This may be due, in part, to the flow being channeled at 45 deg to the vertical direction, which, in turn, reduces the component of centrifugal buoyancy in the flow direction.

4.6 Friction Factors. The friction factor ratio (f_s/f_0) is shown as a function of the Ro_s and Re_s in Fig. 16. No effect of rotation is seen on the friction factor (Fig. 16(*a*)), while there is a linear decrease in f_s/f_0 with Re_s (Fig. 16(*b*)). The thermal performance factor values (Fig. 17) are generally in the range of 1.2–1.3 over the range of Re_s and Ro_s studied. In the Re_s range of 30,000–50,000, these numbers are comparable to the values reported by

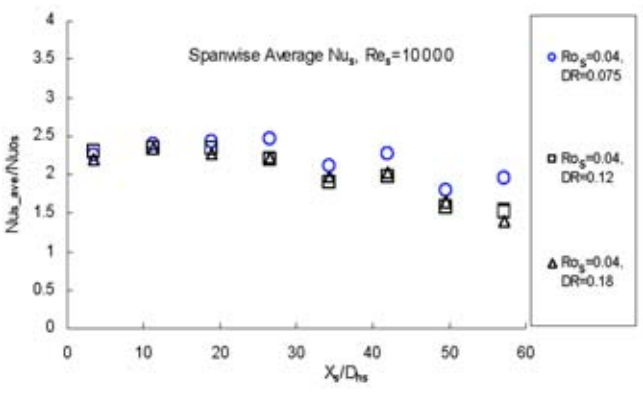

Fig. 15 Density ratio effects at Ro_s=0.04 and Re_s=10 k

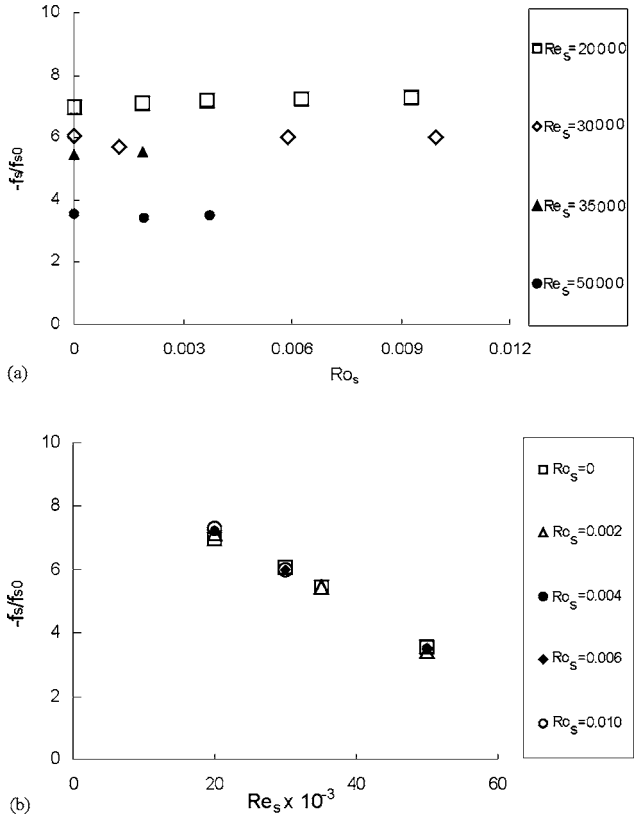

Fig. 16 Friction factors at different (a) Ro_s and (b) Re_s

Lau [24] for 90 deg-ribbed square channel. Since at the higher Re_s values, f_s/f_{s0} decrease with Re_s (Fig. 16(*b*)), while Nu_s/Nu_{0s} remains relatively constant (Fig. 5), the thermal performance of the latticework becomes increasingly more attractive at higher Re_s. This is particularly so given the insensitivity of Nu_s to rotation, and the streamwise uniformity of Nu_s at representative Re_s.

5 Concluding Remarks

An experimental study is conducted to investigate the effects of rotation on the heat transfer and pressure drop in a latticework coolant passage. Measurements have been performed for orthogonal-lattice ribs in a rotating heat transfer rig for a range of parameter values, with a maximum Re_s and Ro_s, based on the subchannel hydraulic diameter, of 50,000 and 0.086, respectively. The corresponding maximum parameter values based on the full

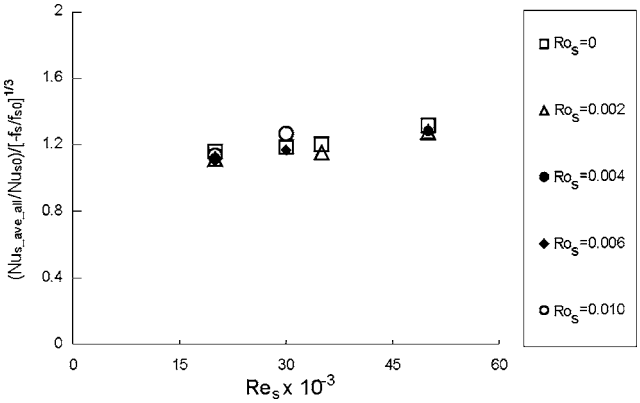

Fig. 17 Thermal performance factor

channel hydraulic diameter are $Re_D=200{,}000$, and $Ro_D=0.34$. The following are the main conclusions of the present study:

(1) For $Re_s \geq 20{,}000$, the latticework coolant passage provides very uniform streamwise distributions of the spanwise-averaged Nusselt numbers, with enhancement levels (relative to smooth-channel values) in the range of 2.0–2.5. These enhancement levels agree well with the stationary latticework passage results of Bunker [12].
(2) For $Re_s \leq 10{,}000$, the streamwise distribution of Nu_s exhibits a drop-off beyond X/D_h of about 40. Thus, for operation at lower Re_s, a shorter length for the latticework coolant passage is recommended.
(3) Both in the stationary and rotating cases, the turn effects lead to higher Nusselt numbers immediately downstream of the vortex turns. Thus the leading-outer and trailing-inner regions see the highest heat transfer coefficients with values that are about 20% higher than the corresponding values along the leading-inner and trailing-outer regions.
(4) At the higher Re_s values ($\geq 20{,}000$), no significant rotation effects and density ratio effects are observed on the heat transfer coefficients. However, at lower Re_s values ($\leq 10{,}000$), rotation effects are observed in the trailing half of the coolant passage where the Nusselt number ratios decrease with increasing Ro_s. The channel-averaged Nu-ratio, however, appears to be relatively insensitive to rotation, exhibiting only a small decrease with Ro_s at the lowest Re_s value considered.
(5) Friction factors are relatively insensitive to Ro_s, but exhibit a near-linear decay with Re_s over the parameter ranges studied. The thermal performance factor appears to be in the range of 1.2–1.3, and is comparable to 90 deg-ribbed channel values.

Acknowledgment

This work was supported by a grant from General Electric Global Research with Dr. Ronald S. Bunker as the program monitor. Their support is gratefully acknowledged.

Nomenclature

A = area
C_p = specific heat
D = diameter
DR = coolant to wall density ratio at the inlet, $(\rho_w-\rho_b)/\rho_w = (T_w-T_b)/T_w$
f = average friction factor
h = heat transfer coefficient
I = current applied to heater
k = heat conductivity of air, or thousands in representing Re values
L = channel length
$\dot{m}$ = mass flow rate
Nu = Nusselt number
P = pressure
Pr = Prandtl number
ΔP = pressure drop
q = heat transferred through copper element
q'' = heat flux per unit area
R = resistance of heater
Re = Reynolds number, $\rho VD/\mu$
Ro = Rotation number, $\Omega D_h/V$
T = temperature
V = average velocity
X = distance along streamwise direction
Ω = rotational speed
ρ = density of air

Subscripts

0 = smooth conditions
b = bulk value
D = based on the hydraulic diameter of the main channel
H = hydraulic
i = the ith copper plate
s = subchannel
w = wall

References

[1] Han, J. C., and Dutta, S., 2001, "Recent Developments in Turbine Blade Internal Cooling," *Heat Transfer in Gas Turbine Systems*, Ann. N.Y. Acad. Sci. **934**, pp. 162–178.
[2] Webb, R. L., Eckert, E. R. G., and Goldstein, R. J., 1971, "Heat Transfer and Friction in Tubes With Repeated-Rib Roughness," Int. J. Heat Mass Transfer **14**, pp. 601–617.
[3] Abuaf, N., and Kercher, D. M., 1994, "Heat Transfer and Turbulence in a Turbulated Blade Cooling Circuit," J. Turbomach. **116**, pp. 169–177.
[4] Acharya, S., Eliades, E., and Nikitopoulos, D., 2001, "Heat Transfer Enhancements in Rotating Two-Pass Coolant Channels With Profiled Ribs—Part I: Average Results," J. Turbomach. **123**, pp. 97–106.
[5] Nikitopoulos, D., Eliades, V., and Acharya, S., 2001, "Heat Transfer Enhancements in Rotating Two-Pass Coolant Channels With Profiled Ribs—Part II: Detailed Results for Two Profile Configurations," J. Turbomach. **123**, pp. 107–114.
[6] Glezer, B., Moon, H. K., Kerrebrock, J., Bons, J., and Guenette, G., 1998, "Heat Transfer in a Rotating Radial Channel With Swirling Internal Flow," ASME Paper No. 98-GT-214.
[7] Hedlund, C. R., Ligrani, P. M., Moon, H. K., and Glezer, B., 1998, "Heat Transfer and Flow Phenomena in a Swirl Chamber Simulating Turbine Blade Internal Cooling," ASME Paper No. 98-GT-466.
[8] Mahmood, G. I., Hill, M. L., Nelson, D. L., Ligrani, P. M., Moon, H. K., and Glezer, B., 2000, "Local Heat Transfer and Flow Structure on and Above a Dimpled Surface in a Channel," ASME Turbo Expo, 2000, Munich.
[9] Zhou, F., and Acharya, S., 2001, "Flow and Heat Transfer in Dimpled Two-Pass Channel," *Heat Transfer in Gas Turbine Systems*, Ann. N.Y. Acad. Sci. **934**, pp. 424–431.
[10] Hibbs, R., Acharya, S., Chen, Y., Nikitopoulos, D., and Myrum, T., 1998, "Heat Transfer in a Two-Pass Internally Ribbed Turbine Blade Coolant Channel With Cylindrical Vortex Generators," J. Turbomach. **120**, pp. 724–734.
[11] Hibbs, R., Acharya, S., Chen, Y., and Nikitopoulos, D. E., 2000, "Mass/Heat Transfer in a Ribbed Coolant Passage With Cylindrical Vortex Generators: The Effect of Generator-Rib Spacing," J. Heat Transfer **122**, pp. 641–652.
[12] Bunker, R. S., 2004, "Latticework (Vortex) Cooling Effectiveness—Part I: Stationary Channel Experiments," ASME Paper No. GT-2004-54157.
[13] Wagner, J. H., Johnson, B. V., and Hajek, T. J., 1991, "Heat Transfer in Rotating Passages With Smooth Walls and Radial Outward Flow," J. Turbomach. **113**, pp. 42–51.
[14] Wagner, J. H., Johnson, B. V., and Kopper, F. C., 1991, "Heat Transfer in Rotating Serpentine Passages With Smooth Walls," J. Turbomach. **113**, pp. 321–330.
[15] Wagner, J. H., Johnson, B. V., Graziani, R. A., and Yeh, F. C., 1992, "Heat Transfer in Rotating Serpentine Passages With Trips Normal to the Flow," J. Turbomach. **114**, pp. 847–857.
[16] Johnson, B. V., Wagner, J. H., Steuber, G. D., and Yeh, F. C., 1994, "Heat Transfer in Rotating Serpentine Passages With Trips Skewed to the Flow," J. Turbomach. **116**, pp. 113–123.
[17] Nagoga, G. P., 1996, "Effective Methods of Cooling of Blades of High Temperature Gas Turbines," (Moscow Aerospace Institute, Moscow, Russian), p. 100.
[18] Goreloff, V., Goychengerg, M., and Malkoff, V., 1990, "The Investigation of Heat Transfer in Cooled Blades of Gas Turbines," AIAA Paper No. 90-2144.
[19] Gillespie, D., Ireland, P. T., and Dailey, G. M., 2000, "Detailed Flow and Heat Transfer Coefficient Measurements in a Model of an Internal Cooling Geometry Employing Orthogonal Intersecting Channels," ASME Paper No. 2000-GT-653.
[20] Dittus, F. W., and Boelter, L. M. K., 1930, *Publications on Engineering*, 2, University of California at Berkeley, Berkeley, CA, p. 443.
[21] Kays, W. M., and Crawford, M. E., 1993, *Convective Heat and Mass Transfer*, 3rd Ed., McGraw–Hill, New York.
[22] Kline, S. J., and McClintock, F. A., 1953, "Describing Uncertainties in Single-Sample Experiments," Mech. Eng. (Am. Soc. Mech. Eng.) **75**, pp. 3–8.
[23] Zhou, F., Lagrone, J., and Acharya, S., 2004, "Internal Cooling in 4:1 AR Passages at High Rotation Numbers," ASME Paper No. GT2004-53501.
[24] Lau, S. C., 2001, *Cooling of Gas Turbine Airfoils, in Heat Transfer in Gas Turbines*, B. Sunden, and M. Faghri, eds., WIT Press, Southampton, U. K., pp. 109–173.

Combined Effects of Surface Trips and Unsteady Wakes on the Boundary Layer Development of an Ultra-High-Lift LP Turbine Blade

Xue Feng Zhang

Howard Hodson

Whittle Laboratory,
Cambridge University,
Madingley Road,
Cambridge CB3 0DY, UK

An experimental investigation of the combined effects of upstream unsteady wakes and surface trips on the boundary layer development on an ultra-high-lift low-pressure turbine blade, known as T106C, is described. Due to the large adverse pressure gradient, the incoming wakes are not strong enough to periodically suppress the large separation bubble on the smooth suction surface of the T106C blade. Therefore, the profile loss is not reduced as much as might be possible. The first part of this paper concerns the parametric study of the effect of surface trips on the profile losses to optimize the surface trip parameters. The parametric study included the effects of size, type, and location of the surface trips under unsteady flow conditions. The surface trips were straight cylindrical wires, straight rectangular steps, wavy rectangular steps, or wavy cylindrical wires. The second part studies the boundary layer development on the suction surface of the T106C linear cascade blade with and without the recommended surface trips to investigate the loss reduction mechanism. It is found that the selected surface trip does not induce transition immediately, but hastens the transition process in the separated shear layer underneath the wakes and between them. In this way, the combined effects of the surface trip and unsteady wakes further reduce the profile losses. This passive flow control method can be used over a relatively wide range of Reynolds numbers. [DOI: 10.1115/1.1860571]

Introduction

The recent studies of wake-separated boundary layer interaction have made the development of the high-lift low pressure (LP) turbine blades possible. The wakes from the previous blade row impinge on the blade surface and induce transition around the separation onset location on the suction surface. The wake-induced turbulent region as well as the calmed region that follows it will suppress the separation bubble. The calmed region, which is laminar-like in nature and attached, will reduce the production of profile loss [1]. The understanding of the unsteady flow behavior has been successfully incorporated into the design of new high-lift LP turbine profiles [2].

Further increases in the blade loading, in the expectation of reducing cost, weight, and fuel burn, will result in an even higher adverse pressure gradient and a larger separation bubble on the blade suction surface. Howell et al. [2] showed that the wake unsteadiness was still effective in the case of ultra-high-lift blades at Reynolds numbers around 200,000. However, in the case of lower Reynolds numbers, the incoming wakes may not be strong enough to suppress the large separation bubble. Furthermore, the separation bubble will have more time to reestablish between the wake-passing events due to the lower wake-passing frequency. Therefore, there will be a larger separation bubble between the wakes, resulting in a larger profile loss. Another loss reduction mechanism is thus required.

Contributed by the International Gas Turbine Institute (IGTI) of THE AMERICAN SOCIETY OF MECHANICAL ENGINEERS for publication in the ASME JOURNAL OF TURBOMACHINERY. Paper presented at the International Gas Turbine and Aeroengine Congress and Exhibition, Vienna, Austria, June 13–17, 2004, Paper No. 2004-GT-53081. Manuscript received by IGTI, October 1, 2003; final revision, March 1, 2004. IGTI Review Chair: A. J. Strazisar.

Several studies of separation control for use in LP turbines have been reported recently. Generally, they can be classified as either active control or passive control. Active flow control typically refers to the use of time-dependent disturbances that are introduced into the flow field by actuators, such as suction, blowing, or vortex generator jets (VGJ). In steady flow conditions, Bons et al. [3,4] and Volino [5] used steady and pulsed VGJs to control the separation on the suction surface of a high-lift LP turbine blade. They found that the pulsed jet is more effective than the steady jet because of the high disturbances associated with the start and end of the pulse rather than the jet itself. The pulsed VGJs generate a turbulent strip followed by a calmed region, which is similar to that created by a passing wake.

Active flow control techniques have the advantage that they can be shut off whenever they are not required; but, they are complex and expensive. Passive control methods are usually simpler. However, they may cause a deterioration in the performance in conditions where flow control is not required.

In a series of steady flow experiments, Lake et al. [6] studied the reduction in losses at low Reynolds number caused by recessed surface dimples, recessed V-grooves, or a trip wire on the suction side of a high-lift LP turbine blade. Although the surface treatments were tested at different streamwise locations, the depth or height of the disturbance was not optimized and each configuration only worked in certain conditions. Also in steady flow, Volino [7] successfully employed two-dimensional (2D) rectangular trip wires with different heights to control the boundary layer separation and transition on a LP turbine blade over a wide range of Reynolds numbers. They concluded that the height and the location of the trailing edge of the trip wires were the most important parameters and the most effective location was close to the

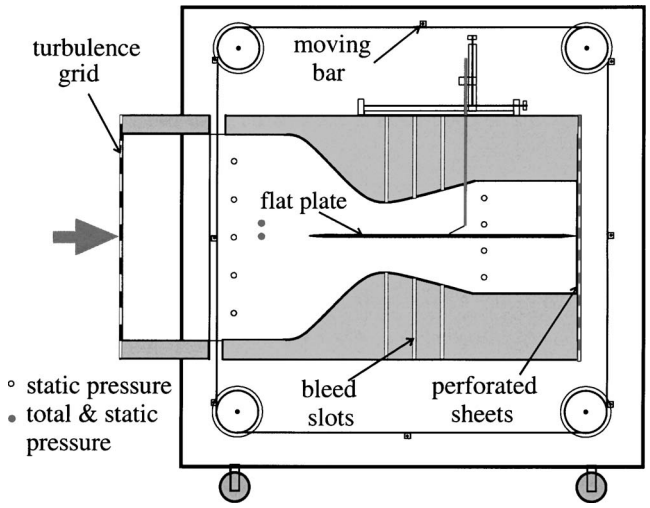

Fig. 1 Flat plate test section with moving bars

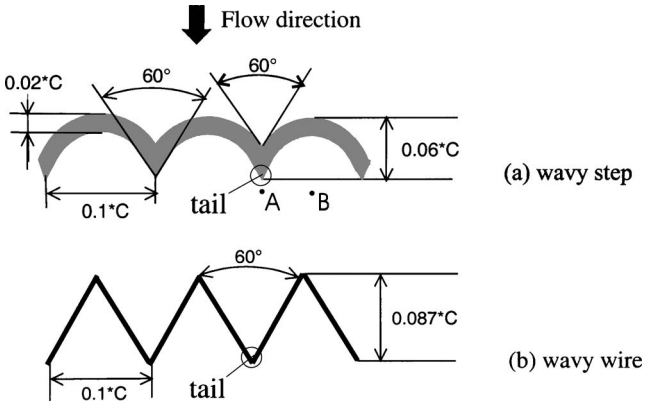

Fig. 2 Geometry of wavy surface trips

suction peak. The optimum trip was not large enough to prevent separation, but rather to promote an earlier, but not immediate, transition in the separated shear layer.

Surface roughness can be an effective method of boundary layer control. However, there are few studies of the effects of surface roughness under unsteady flow conditions. Ramesh et al. [8] and Roman [9] tested the effect of sand-grain roughness on the boundary layer development on an ultra-high-lift LP turbine profile in unsteady flow conditions. Ramesh et al. [8] concluded that the combined effects of a strip of surface roughness and wake unsteadiness permitted a 12% increase in blade loading without a significant increase in the profile loss. The loss reduction caused by the selective surface roughness strip came from the larger extent of the calmed region, which followed the earlier wake-induced transition to turbulent flow as well as the smaller separation bubble between wakes, which resulted from an earlier transition of the separated shear layer.

The current study, funded by the European Commission, is concerned with the combined effects of unsteady wakes and surface trips on the boundary layer development on an ultra-high-lift LP turbine blade, T106C. The object is to determine if these disturbances and their effects can further reduce the profile losses and, if so, to further understand the physical mechanisms involved. The parametric study conducted on a flat plate is aimed at optimizing the trip parameters (i.e., their size, type, and location in unsteady flow condition). The linear cascade study investigates the boundary layer development on the suction surface under the effects of wakes and/or surface trips to further understand the flow physics and to demonstrate the successful use of the surface trip.

Experimental Facilities and Techniques

The parametric study of the surface trips was conducted on a flat plate test rig, which is fitted with a moving bar system. A schematic of the test section is shown in Fig. 1. The test rig consists of an aluminium plate that is 738 mm long by 458 mm wide and 12.8 mm thick. In the present study, only the front 500 mm of the plate was used. This was to enable low Reynolds numbers to be tested with reasonable measurement accuracy. The Reynolds numbers based on the plate surface length (S_0 =500 mm) and the isentropic exit velocity V_{2is} covered a range between 134,000 and 285,000. A pair of contoured walls, designed by Industria de Turbo Propulsores of Spain (ITP), was used to impose the same pressure distribution on the flat plate as that on the suction surface of the T106C LP turbine blade. To create more realistic LP turbine conditions, the free-stream turbulence intensity can be increased to 3.5% by a biplanar cylindrical rod-type turbulence grid placed at the inlet to the test section.

The upstream unsteady wakes were generated by the moving bars across the inlet to the test section. The flow coefficient ϕ was defined as the ratio of the isentropic exit velocity V_{2is} to the bar speed U_{bar} (i.e., $\phi=V_{2is}/U_{bar}$) [10] and $\phi=0.83$ was chosen. The reduced frequency, defined as $f_r=f_{bar}S_0/V_{2is}$, was set at 0.84. More details of this test rig can be found in Zhang and Hodson [11].

The surface trips used in the parametric study include straight cylindrical wires, straight rectangular steps, wavy steps with a rectangular cross section, and wavy cylindrical wires. They were fixed to the plate surface using double-sided tape. The wavy trips were proposed by MTU Aero Engines, a partner in the present program. The geometry of the wavy trips is shown in Fig. 2. Table 1 summarizes the parameters of the selected surface trips used in the parametric study on the flat plate. The relative height k/δ^* is calculated from the measured local boundary layer displacement thickness δ^* at $50\%S_0$ with Re=174,000 and $Tu=0.5\%$ on the smooth surface in steady flow condition. The local trip Reynolds number Re_k is based on the height of the surface trip and the local free-stream velocity at Re=174,000.

A schematic of the T106C linear cascade is shown in Fig. 3. The T106C cascade has a pitch-to-chord ratio that is 20% larger than that of the more familiar T106A cascade (see, for example, [12,13]). The blade profile is unchanged. In order to reduce the large leading-edge overspeed that would occur because of the change of circulation, an incident angle of −5 deg was used. A T106C blade does not represent the ideal profile by today's standard, nevertheless, it has the important feature of a large separation bubble on the suction surface, which is a consequence of the large suction-side diffusion factor that is associated with the high blade loading. The parameters of the bar-passing cascade facility are presented in Table 2. The Reynolds numbers based on the blade suction surface length S_0 and the isentropic exit velocity V_{2is} covered the same range as that of the flat plate test. Moving bars

Table 1 Surface trip parameters on the flat plate

Trip type	Height k (mm)	k/S_0 (%)	k/δ^*	Re_k	Code
Straight wire	1.20	0.24	1.01	442	SW120
Straight wire	0.81	0.16	0.68	285	SW81
Straight wire	0.74	0.15	0.62	257	SW74
Straight wire	0.68	0.14	0.57	233	SW68
Straight wire	0.61	0.12	0.51	205	SW61
Straight wire	0.56	0.11	0.47	185	SW56
Straight step	0.68	0.14	0.57	233	SS68
Wavy step	0.68	0.14	0.57	233	WS68
Wavy wire	0.68	0.14	0.57	233	WW68

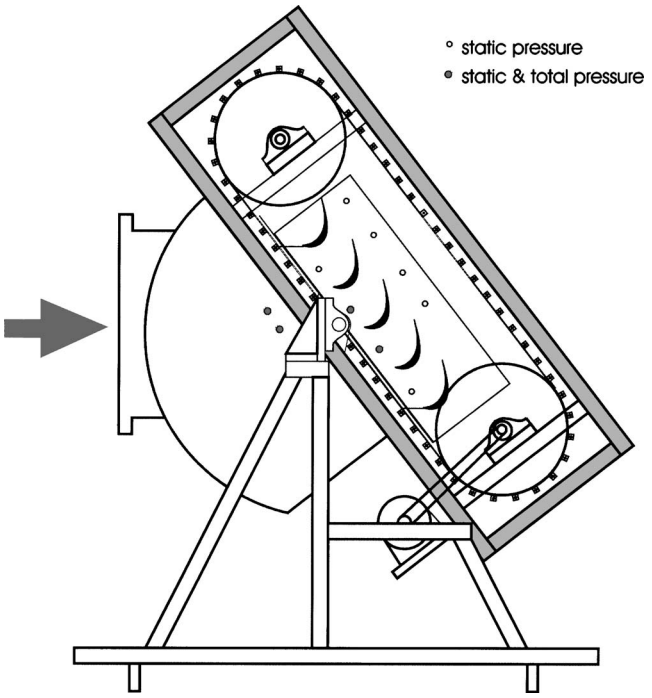

Fig. 3 Schematic of T106C cascade with moving bars

with a diameter of 2.05 mm were used to generate the upstream wakes. A flow coefficient ($\phi = V_{1x}/U_{\text{bar}}$) of 0.83 was chosen to be consistent with the work on the T106A cascade. The bar pitch can be changed to achieve different reduced frequencies (here $f_r = U_{\text{bar}}/s_{\text{bar}} * C/V_{2\text{is}}$). In the current study, the bar pitch was set equal to the blade pitch resulting in $f_r = 0.57$, which is slightly different from the value in the flat plate test because of the different definitions of ϕ and f_r.

The time mean surface static pressure distributions on the flat plate and on the linear cascade were measured by using a Scanivalve system. The surface static pressure coefficient C_p is defined as the ratio of the local dynamic head to the isentropic exit dynamic head, i.e.,

$$C_p = \frac{P_{01} - P_s}{P_{01} - P_{s2}} \tag{1}$$

where P_{01} is the inlet total pressure, P_{s2} is the exit static pressure, and P_s is the measured surface static pressure.

In the T106C linear cascade study, Kulite SCX-062 fast-response pressure transducers were used to measure the unsteady surface static pressure. Further details concerning the use of the Kulite sensors can be found in Stieger et al. [12].

Table 2 T106C bar-passing linear cascade details

Chord (C)	198.0 mm
Axial chord (C_x)	170.0 mm
Pitch (s)	189.6 mm
Suction surface length (S_0)	264.7 mm
Design inlet flow angle (α_1)	32.7 deg
Design exit flow angle (α_2)	63.2 deg
Incident angle (i)	−5.0 deg
Zweifel coefficient (Z_w)	1.19
Bar diameter (d_{bar})	2.05 mm
Axial distance: bars to LE (d)	70.0 mm
Flow coefficient ($\phi = V_{x1}/U_{\text{bar}}$)	0.83
Reduced frequency ($f_r = f_{\text{bar}} * C/V_{2\text{is}}$)	0.57

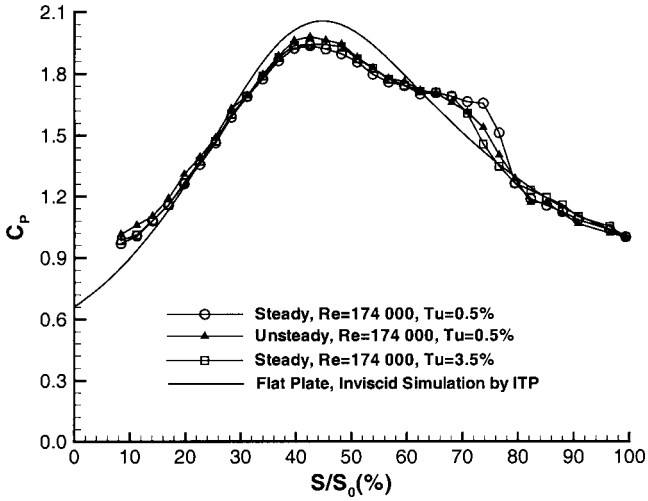

Fig. 4 Flat plate surface pressure C_p distributions on smooth surface at Re=174,000

A constant temperature anemometry system was used for hot-wire measurements. The boundary layer was surveyed by a Dantec single-wire 55P15 boundary layer probe. The hot wire was calibrated in accordance with King's Law. The effects of the ambient temperature drift were taken into account using the correction of Bearman [14]. Hot-wire traverses were performed normal to the blade surface. The distance between positions increased exponentially with the minimum distance of 0.1 mm as the probe left the surface. In order to account for the influence of the surface proximity on the cooling of the heated wire, the Cox correction [15] was applied to the measured data.

The profile loss coefficients in the linear cascade tests are determined from a series of Pitots placed upstream of the bars and the Neptune probe traverses conducted $0.5C_x$ downstream of the blade trailing edge. The profile loss values given here include the measured loss and mixing loss. In the case of unsteady flow conditions, the change in stagnation pressure across the moving bars is subtracted from the total loss to give the profile losses [1].

Results and Discussions

Flat Plate Parametric Study. The measured flat plate surface static pressure distributions C_p under different flow conditions as well as the inviscid numerical simulation result from ITP at Re =174,000 are presented in Fig. 4. Apart from the effect of the separation bubble, the measurement results agree well with the inviscid predictions. Under steady flow conditions at $Tu=0.5\%$, the velocity peak occurs around $43\%S_0$. The boundary layer separates at $55\%S_0$ and reattaches at $80\%S_0$. At $Tu=3.5\%$, the higher level of disturbances in the inlet free stream helps the separated flow to reattach earlier and results in a smaller separation bubble. The time-mean C_p under unsteady flow conditions with $\phi=0.83$ and $f_r=0.84$ at Re=174,000, $Tu=0.5\%$ is also presented in Fig. 4. The incoming wakes periodically reduce the size of the separation bubble. This results in a lower level of the time-mean C_p in the separation region.

Effect of surface trip height. The height of the surface trip directly affects the boundary layer development and, thus, the profile loss. To study the effect of the trip height on the profile loss, straight cylindrical wires with different diameters were tested in both steady and unsteady flow conditions. The straight wires were placed at $50\%S_0$ (i.e., midway between velocity peak and the separation onset location).

The suction surface profile loss coefficient is defined by Curtis et al. [16] as

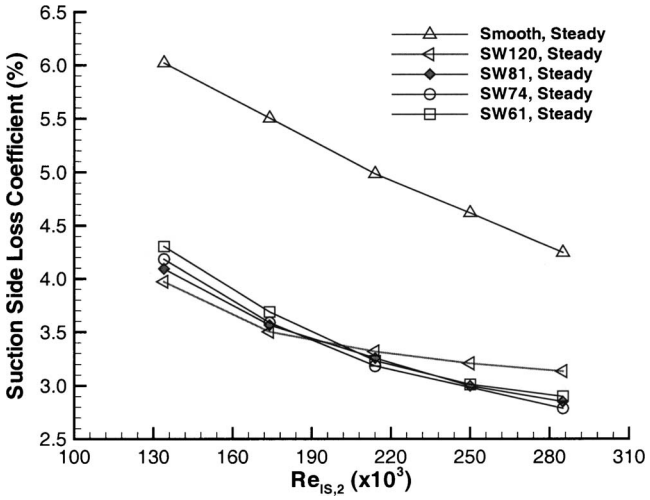

Fig. 5 Effects of trip height on losses under steady flow conditions at *Tu*=0.5%

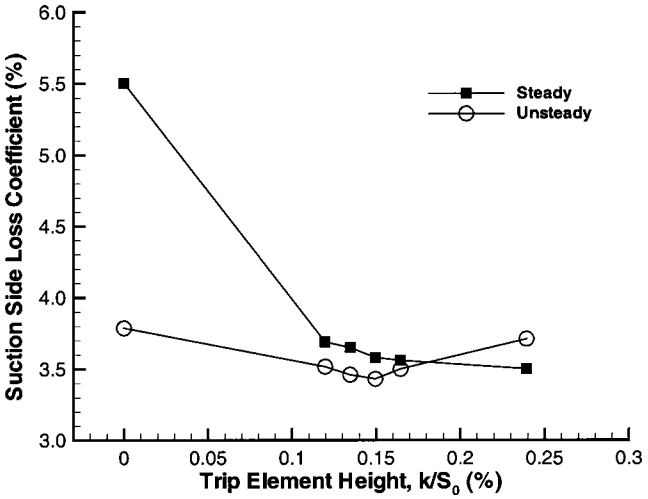

Fig. 7 Effects of trip height on losses at Re=174,000 and *Tu*=0.5%

$$\xi = \frac{2\theta}{s\cos(\alpha_2)} \tag{2}$$

where θ is the trailing-edge momentum thickness measured from hot-wire traverses, s is the equivalent pitch of the pressure distribution under investigated, and α_2 is the exit flow angle of the linear cascade.

The effect of the surface trip height on the profile losses under steady flow conditions at Tu=0.5% is shown in Fig. 5. On the smooth surface, the measured loss coefficients are high because of the large separation bubble as shown in Fig. 4. The surface trips reduce the loss coefficient significantly at all tested Reynolds numbers. At low Reynolds numbers, the loss coefficients decrease as the surface trip height increases. As the Reynolds number increases, the larger trip wires result in higher loss coefficients than the smaller trip wires because the transition onset was induced too early.

Figure 6 shows the loss coefficient varying with the diameter of the straight wires under unsteady flow conditions with ϕ=0.83 and f_r=0.84 at Tu=0.5%. Initially, as the wire diameter is reduced, the loss coefficient decreases. However, as the wire diameter further reduces, the loss increases again at low Reynolds numbers. This is because the smaller diameter wire cannot induce transition effectively at low Reynolds numbers and, therefore, a large separation bubble exists. In contrast the larger diameter wire induces transition too early. This results in a large amount of turbulent flow. Thus, there is an optimum diameter for each flow condition.

In the current study, the main interest is focused on the blade performance at low Reynolds numbers under unsteady flow conditions. Figure 7 shows the loss coefficients varying with the diameter of the straight trip wires (normalized by the surface length) at Re=174,000 and Tu=0.5% in steady and unsteady flow conditions. In the steady flow conditions, the loss coefficient with surface trip was reduced significantly compared to that on the smooth surface (i.e., k/S_0=0.0). The loss continues to decrease as trip height increases, even for the largest tested wire. However, under the unsteady flow conditions, there exists an optimum height. At Re=174,000 and Tu=0.5%, SW74, which has a relative height of k/S_0=0.15% or k/δ^*=0.62, produces the lowest loss under unsteady flow conditions. It should be noted that the loss coefficient under unsteady conditions is lower than that in the steady condition provided the trip is not too high. In this case, the benefit can come from both the surface trip and the unsteady wakes.

The measured loss coefficients at Tu=3.5% are presented in Fig. 8. On the smooth surface, the loss coefficients at Tu=3.5%

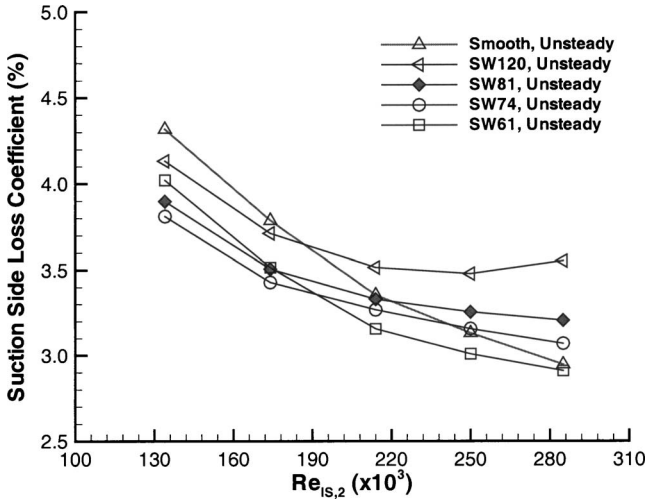

Fig. 6 Effects of trip height on losses under unsteady flow conditions with *f*=0.83 and *fr*=0.57 at *Tu*=0.5%

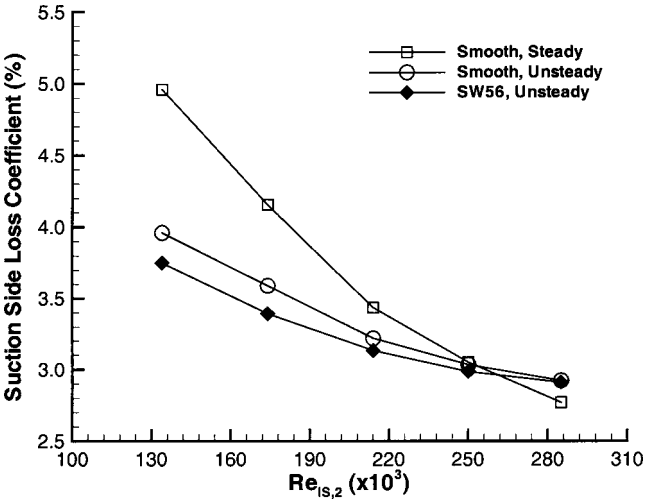

Fig. 8 Effects of surface trip on losses at *Tu*=3.5%

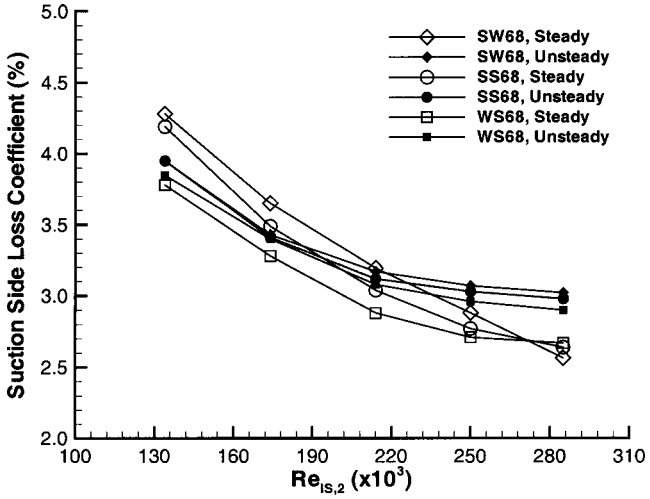

Fig. 9 Effects of trip shape on losses at $Tu=0.5\%$

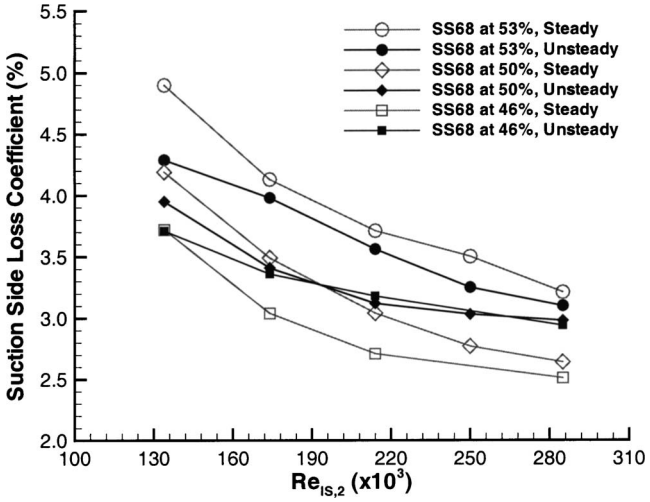

Fig. 10 Effects of trip location on losses at $Tu=0.5\%$

are lower than those at $Tu=0.5\%$ in both steady and unsteady flow conditions, respectively, because of the higher turbulence in the free stream, which induces earlier boundary layer transition. At low Reynolds numbers, the unsteady wakes help to reduce the profile losses. However, at the highest tested Reynolds number, the unsteady profile loss is higher than the steady one because the separation bubble is already small in the steady flow condition. Consequently, there is little benefit from suppressing the separation bubble, and the wakes create a larger turbulent-wetted area, which increases the loss. With surface trip SW56 ($k/S_0=0.15\%$), which is the optimum one at Re=174,000 with $Tu=3.5\%$, the profile loss can be further reduced in unsteady flow conditions at low Reynolds numbers. At high Reynolds numbers, the benefit is small.

Effect of surface trip shape. The shape of the surface trip has an effect on the transition process of the boundary layer. To investigate the influence of the trip shape on the loss reduction, different types of trips were tested. The tested trips include straight cylindrical wire, straight rectangular steps, wavy rectangular steps, and wavy cylindrical wires.

The measured loss coefficients for the straight rectangular step SS68 ($k/S_0=0.14\%$ or $k/\delta^*=0.57$) placed at $50\%S_0$ are presented in Fig. 9. The location of step-type trips was determined by the trailing edge of the step. The loss coefficient for a straight cylindrical wire SW68, which has the same diameter as the height of SS68, is also plotted in Fig. 9. Under steady conditions, the step is more effective at reducing the loss than the wire with the same heights. Pinson and Wang [17,18] made the same observation. This is because the disturbance generated by the sharp trailing edge of the step is stronger than that after the wire, which hastens the transition process in the separated shear layer [11]. However, under unsteady flow conditions, the difference in the loss coefficients for these two trips is small. This is again because of the compromise between the separation bubble reduction and larger turbulent wetted area.

The width and the leading-edge shape of the rectangular trips were changed. The measurement results showed that these changes have less effect on the profile losses as long as the rear step edge was placed at the same location. This is not the case when using strips of distributed roughness [9]. In that case, the disturbances were generated over the length of the roughness strip. For the rectangular trips, the disturbance is mainly generated by the sharp trailing edge.

Another two types of surface trips—wavy rectangular steps and wavy cylindrical wires—were also tested. The measured loss coefficients with the wavy rectangular step WS68 are presented in Fig. 9 as well. Under steady flow conditions, the wavy step is more effective than the straight step SS68 in loss reduction although they have the same height. To find the reason for this difference, the disturbance levels in the boundary layer after WS68 were measured at two different spanwise locations: downstream of the tail (A) and between the tails (B) (refer to Fig. 2). Between the tails the rms velocity fluctuations were similar to those after SS68. However, there was a very high level of rms after the tail because of the streamwise vortices generated in this region. These help to trigger early transition and further reduce the losses in steady conditions [11]. Under unsteady conditions, the streamwise vortices introduce more turbulent mixing, resulting in higher losses. The wavy cylindrical wire WW68 produced results that were similar to that of the wavy rectangular step WS68, suggesting that for the wavy-type trips the effect of the wavy tails dominates.

Effect of surface trip location. To study the effect of the location of the trips on the loss reduction, the straight rectangular step SS68 was placed at three different streamwise locations between the velocity peak and the separation onset location (i.e., at $46\%S_0$, $50\%S_0$, and $53\%S_0$). The measured loss coefficients under steady and unsteady flow conditions are presented in Fig. 10.

When the trip SS68 was moved downstream to $53\%S_0$, the loss coefficients increased significantly under steady and unsteady conditions. This is not only because the surface trip induces transition a little later, but also because the separation after the trip merges with the separation bubble induced by the pressure gradient. The combined effect is that the bubble is larger, especially in height. Once the trip is placed inside the separation bubble, there will be little effect of the trip on the boundary layer transition.

As the trip was moved upstream to $46\%S_0$, just after the velocity peak, it induced transition earlier because of the higher local velocity. This results in smaller separation bubbles. In the case of the steady flow conditions, the loss is reduced at all the Reynolds numbers. In the case of the unsteady flow conditions, the loss is further reduced at the lowest Reynolds number. However, at the higher Reynolds numbers, the earlier induced transition does not produce any more benefit because of the larger turbulent wetted area. Furthermore, the surface trip at the suction peak may cause unwanted effects at high Mach numbers. Therefore, the optimum location of the surface trip is midway between the velocity peak and the separation onset location.

Summary of parametric study. Based on the flat plate parametric study results discussed above, the combined effects of surface trips and unsteady wakes can further reduce the profile loss of the ultra-high-lift LP turbine blade. Due to its simplicity, for practical

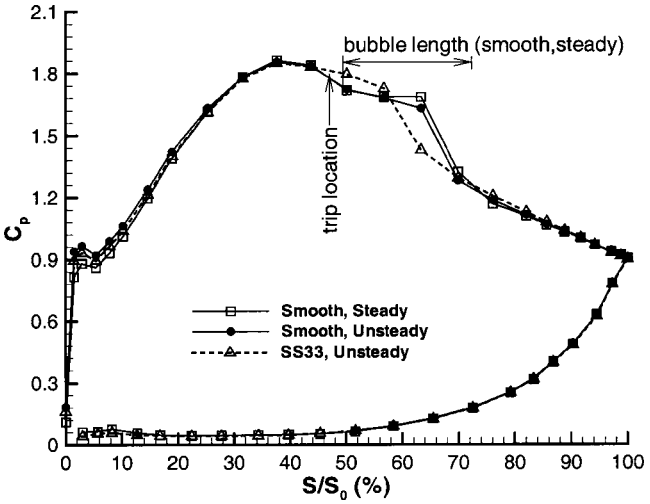

Fig. 11 T106C linear cascade blade surface pressure C_p distributions at Re=174,000 and Tu=0.5%

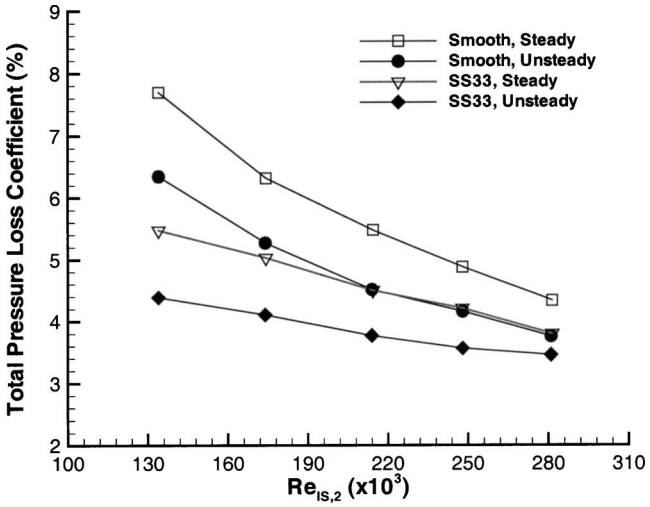

Fig. 12 Total pressure loss coefficients of T106C linear cascade at Tu=0.5%

applications, the straight rectangular step located midway between the velocity peak and the separation onset location is recommended. The optimum height of the straight rectangular step at Re=174,000 and Tu=0.5% is 0.14%S_0 or 57%δ^*. This corresponds to SS68 in the case of the current flat plate study.

T106C Linear Cascade Study. The boundary layer development on the T106C cascade was studied to demonstrate that the combined effects of the unsteady wakes and surface trips work on the ultra-high-lift LP turbine blade and to further understand the loss reduction mechanism. The discussion of the physical processes will mainly focus on the interaction of the wakes with a separation bubble that was modified by the trips. The question of how the wake modifies the tripping mechanism by interacting with the flow structures generated by the trips will not be addressed in the present study.

The geometry and the location of the surface trips were chosen based on the results of the parametric study on the flat plate. The straight rectangular step SS33 reported here has a height of 0.33 mm (k/δ^*=0.51). This is slightly smaller than the optimum height determined from the flat plate study due to the availability of the rectangular step.

Surface static pressure distributions. The measured time-mean surface static pressure distributions C_p at Re=174,000 and Tu=0.5% are presented in Fig. 11. In steady flow, the velocity peak on the suction surface occurs around 42%S_0 and the laminar boundary layer separates at 50%S_0. The separation on the T106C linear cascade occurs a little earlier in comparison to that on the flat plate. The separation bubble covers about 23% of the suction surface length. The length of the separation bubble, which is determined from the hot-wire boundary layer traverses, is indicated in Fig. 11.

Under unsteady flow conditions with ϕ=0.83 and f_r=0.57, the incidence of the incoming flow was changed slightly due to the passing bars turning the inlet flow. However, there is no significant difference in the time-mean C_p after 20%S_0 except around the separation bubble. The incoming wakes interact with the separation bubble and periodically change the bubble size, which can be identified from the difference between the time-mean C_p in the separation zone. However, the difference in C_p is not big on this ultra-high-lift blade because of the larger separation bubble due to the stronger adverse pressure gradient and the lower wake-passing frequency, which allows the separation more time to reestablish between the passing wakes.

The time-mean pressure distribution under unsteady flow conditions with the straight rectangular step SS33 is also plotted in Fig. 11. The trip was fixed at 47%S_0 on the suction surface. The trip changes the pressure distribution locally. The size of the separation bubble is reduced due to the disturbances created by the trip and the periodic wake passing.

Profile losses. The total pressure loss coefficients measured at different Reynolds numbers with or without SS33 in steady and unsteady flow are presented in Fig. 12. On the smooth surface, the large separation bubble, because of the large diffusion on the suction surface, results in a high level of profile loss in the steady flow. Although the periodic interaction between the passing wakes and the separated boundary layer can lower the profile loss, the profile loss is still large on this ultra-high-lift LP turbine blade, especially at low Reynolds numbers. This is partly because the wakes are not strong enough to periodically suppress the large separation and, on average, the separation bubble on the smooth surface is still large, as shown in the plot of C_p in Fig. 11.

The combined effects of unsteady wakes and surface trips can further reduce the profile losses. The benefit comes from both the surface trip and the unsteady wake. The loss reduction occurs over the entire range of test Reynolds numbers (i.e., from 134,000 to 285,000). This is very important for LP turbine blades due to their wide range of working conditions. The current observation is different to that of Volino [7]. He found that the loss with surface roughness increased at high Reynolds number. The optimum height of the surface trip in the current unsteady study is smaller than that used in Volino's steady flow study. Furthermore, the calmed region caused by the unsteady wakes creates a benefit with respect to the profile loss.

Although the combined effects of the surface trips and the wakes can further reduce the profile losses of ultra-high-lift LP turbine blades, the loss level of T106C is still higher than that of conventional profiles. It is partly because a large part of the suction surface (more than 30%) is covered by turbulent flow after reattachment. It is recommended that the ultra-high-lift LP turbine blade should be aft loaded to minimize the profile losses.

Unsteady surface pressures. To investigate the flow mechanisms involved in the profile loss reduction, the boundary layer development on the suction surface of the T106C blade, with and without the selected surface trip, was studied. The unsteady pressure fluctuations on the suction surface were measured by Kulite pressure transducers. The ensemble-averaged pressure traces, normalized as C_p, on the smooth surface and with the trip SS33 at Re=174,000 and Tu=0.5% are plotted in Fig. 13. The horizontal

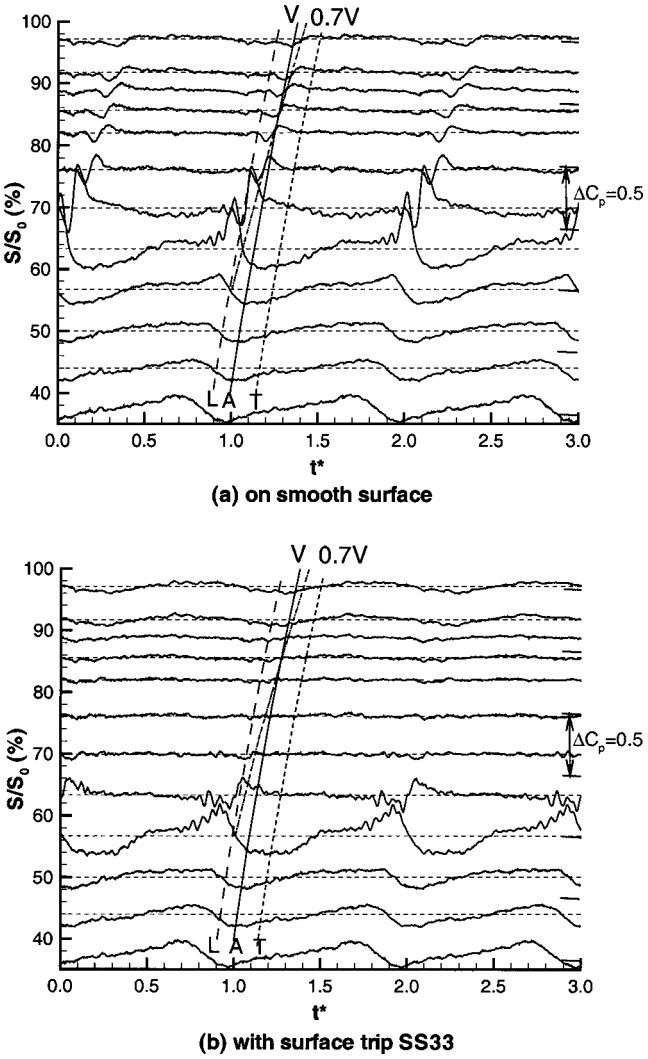

Fig. 13 Ensemble-averaged unsteady pressure traces at Re =174,000 and *Tu*=0.5% with *f*=0.83 and *fr*=0.57; (*a*) on smooth surface (*b*) with surface trip 5533

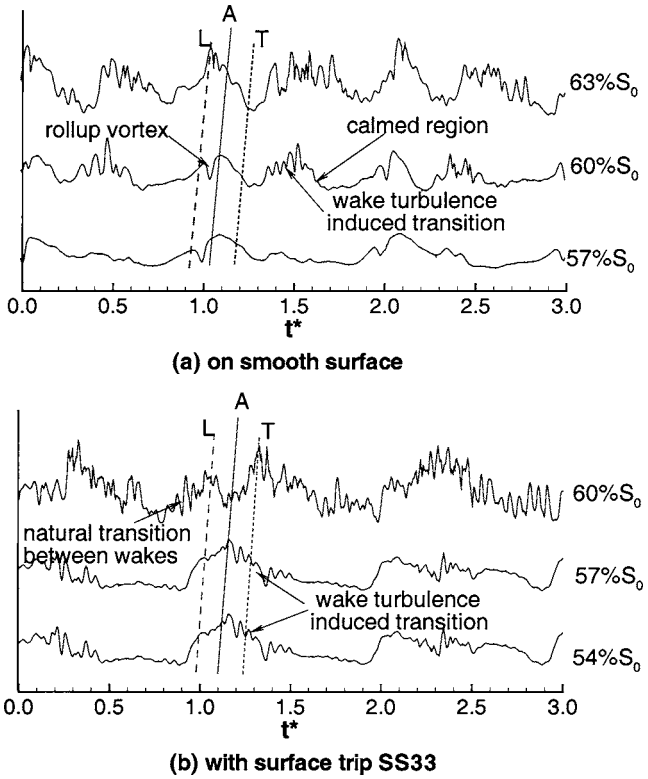

Fig. 14 Raw velocity traces at Re=174,000 and *Tu*=0.5% with *f*=0.83 and *fr*=0.57 at Y_n=0.2 mm

dashed lines indicate the location of the Kulite sensors, whereas the solid lines are the ensemble-averaged traces of the measured fluctuation of C_p. The scale of C_p fluctuation is the same for all the traces, as is indicated in the figures. Two velocity trajectories corresponding to 100% and 70% of the local free-stream velocity are also plotted in the figures. The wake convects over the blade surface at the local free-stream velocity. The leading edge and trailing edge of each wake are defined as the peak and valley caused by the negative jet behavior of the wake in the free-stream velocity traces obtained from hot-wire measurements. These are indicated as dashed lines L and T in the figures, respectively.

On the smooth surface, as shown in Fig. 13(*a*), the variations in the unsteady pressure upstream of the separation onset location (i.e., before $50\%S_0$) can be explained with reference to the negative jet behavior of the wake. The negative jet increases the surface pressure locally as it convects over the suction surface. Within the separation region, there are large pressure oscillations associated with the wake passing. They are due to the so-called rollup vortices created by the interaction between the wake's negative jet and the inflectional shear layer through a forced Kelvin-Helmholtz mechanism [12]. The rollup vortex first occurs around $63\%S_0$, just after the leading edge of the wake has arrived at that location, and convects downstream along the blade surface at about 70% of the local free-stream velocity. The signature of the rollup vortex does not appear immediately downstream of the separation onset location, which suggests that the vortex can only form when the separation bubble is at a certain height.

The maximum peak-to-peak variation in the unsteady pressure is as high as 50% of the exit dynamic head. Stieger et al. [12] reported three rollup vortices following each other on the T106A cascade with a maximum peak-to-peak magnitude of 30% of the exit dynamic head. The reason for this difference probably lies in the fact that the separation bubble on this ultra-high-lift T106C blade is larger, especially in height. Thus, the first formed rollup vortex is much bigger, which prevents the formation of other vortices. This single larger rollup vortex has a stronger effect on the shear layer than that on the T106A profile. The signature of the vortices in the pressure traces becomes smaller after the reattachment point. However, it is still visible close to the trailing edge.

With the straight trip SS33, as shown in Fig. 13(*b*), the variation in the unsteady pressure upstream of separation is similar to that on the smooth surface. However, in the separation region, there is no clear evidence of the existence of rollup vortex. The rollup mechanism related to the interaction between the wake's negative jet and the separated boundary layer seems to be absent. Examining the raw data shows that the rollup vortex may occur in some wake-passing periods but not very often. Stieger and Hodson [13] show that high levels of turbulent kinetic energy production are associated with the formation and decay of the rollup vortices. This must eventually turn into profile loss. Thus, the absence of the rollup vortex is likely to lead to a loss reduction under the combined effects of surface trip and unsteady wakes.

Suction-side boundary layer traverses. The suction-side boundary layers on the T106C blade were surveyed by a single boundary layer hot-wire traversing in the surface normal direction at different streamwise locations. Figure 14 presents selected raw velocity traces at Y_n=0.2 mm with Re=174,000 and *Tu*=0.5% under the unsteady flow conditions of ϕ=0.83 and f_r=0.57. The leading edge and trailing edge of the wake are indicated as line L

and line T in the figure.

Figure 14(*a*) presents the raw velocity traces on the smooth surface at $57\%S_0$, $60\%S_0$, and $63\%S_0$, respectively. At $60\%S_0$, the raw trace clearly shows two separate events. Underneath the passing wakes between lines L and T, there is an oscillation in the signal. This is caused by the rollup vortex, which is the same as that identified from the unsteady surface pressure traces. The turbulence in the wake also induces boundary layer transition, lagging behind the wake center. However, it does not appear to occur at $57\%S_0$. The wake turbulence-induced transition happens around $10\%S_0$ downstream of the separation onset location. This is the condition that is necessary to allow the wake negative jet to induce the rollup vortex. The characteristic relaxing signal after the turbulence-induced transitional or turbulent region shows the existence of the calmed region. At $63\%S_0$, the rollup vortex starts to develop into turbulent flow. The wake turbulence-induced transitional or turbulent region further develops downstream. The calmed region breaks down at this streamwise location. On this ultra-high-lift blade, the calmed region only lasts for a short distance because of the strong adverse pressure gradient.

The velocity traces shown in Fig. 14(*b*) were obtained at $54\%S_0$, $57\%S_0$, and $60\%S_0$, respectively, with surface trip SS33. There is no clear oscillation underneath the wake to show the existence of any rollup vortex, which agrees well with the observation from the unsteady surface pressure measurements. Due to the disturbance caused by the surface trip, the wake turbulence induces transition shortly after the separation onset location, as shown in the velocity trace at $54\%S_0$. This early wake turbulence-induced transition prevents the wake's negative jet from inducing the rollup vortex. Because of the smaller separation bubble, the time delay between the wake turbulence-induced transition and the wake center is smaller. The higher turbulence after the surface trip causes the separated boundary layer between passing wakes to transition earlier, indicated by the spikes before line L at $60\%S_0$. There is no clear evidence of the strengthened calmed region reported by Ramesh et al. [8].

The distance-time (*s-t*) diagrams of the shape factor H_{12} and momentum thickness θ on the smooth suction surface in unsteady flow condition are presented in Fig. 15. The dots on the top of the pictures indicate the traverse locations—the smallest interval between them being $1.5\%S_0$. Three velocity trajectories are also plotted in the figures. Lines A, B, and C correspond to 100%, 50%, and 30% of the free-stream velocity, respectively. The leading edge and trailing edge of the wake are indicated as dashed lines L and T.

The shape factor clearly shows the periodic change of the separation bubble in both length and height associated with the wake passing. Values around 3.5 usually indicate the presence of laminar separated flow. The periodic variation before $50\%S_0$ shows the wake's negative jet effect on the attached laminar boundary layer, which agrees with the observation from unsteady pressure measurements. In the time-mean separation region (i.e., between $50\%S_0$ and $73\%S_0$), there is a sudden decrease that is immediately followed by an increase in the shape factor within the separation bubble between lines L and T. This is consistent with the patterns of the unsteady pressure variation and results from the rollup vortex. The rollup vortex convects downstream at about 70% of the free-stream velocity, shown by the dash-dotted line in the figure. The effect of the vortex can be clearly detected even in the reattached turbulent flow through to the trailing edge.

The high level of turbulence in the wake induces transition downstream of the separation onset location and lags behind the wake center. The trailing edges of the wake turbulence-induced turbulent region and the calmed region travel along lines B and C, respectively. On this ultra-high-lift blade, the separation bubble is never completely suppressed because of the strong adverse pressure gradient. After the trailing edge of the calmed region (line C), the separation bubble starts to regrow. The reattachment line, marked as E-F in Fig. 15 shows that the separation bubble grows

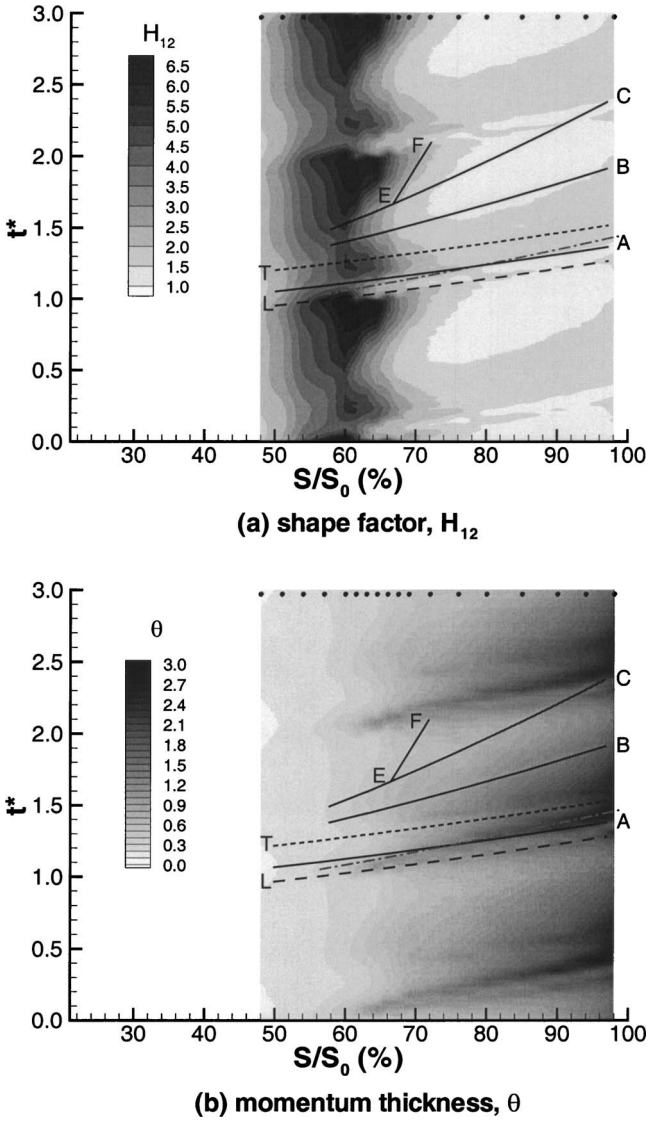

Fig. 15 Unsteady boundary layer integral parameters on smooth surface at Re=174,000 and *Tu*=0.5%

continuously until the next wake arrives.

The effects of the unsteady wake on the boundary layer development can also be detected from the *s-t* diagram of the momentum thickness θ in Fig. 15(*b*). Two ridges in θ develop along two different paths to form two wedges. One is developing underneath the wake between lines L and T along the dashed-dotted line, which results from the rollup vortex. This agrees well with the comments of Stieger and Hodson [13] that the rollup vortices are associated with high levels of losses. The other ridge in θ occurs in the wake turbulence-induced turbulent region between lines A and B. Although the calmed region only lasts for a short distance on this blade, the beneficial effect is still visible. There is a lower momentum thickness between lines B and C. The variation of the momentum thickness at the trailing edge in one wake-passing period shows the effects of the rollup vortex, the wake turbulence-induced transition, calmed region, and the natural transition of the separated boundary layer between wakes sequentially. On the smooth surface, the loss reduction under the unsteady flow condition results from the effect of the calmed region and the smaller separation bubble between wakes.

Figure 16 presents the *s-t* diagrams of the unsteady shape factor H_{12} and the momentum thickness θ with the straight rectangular step SS33 placed at $47\%S_0$. The shape factor does not signifi-

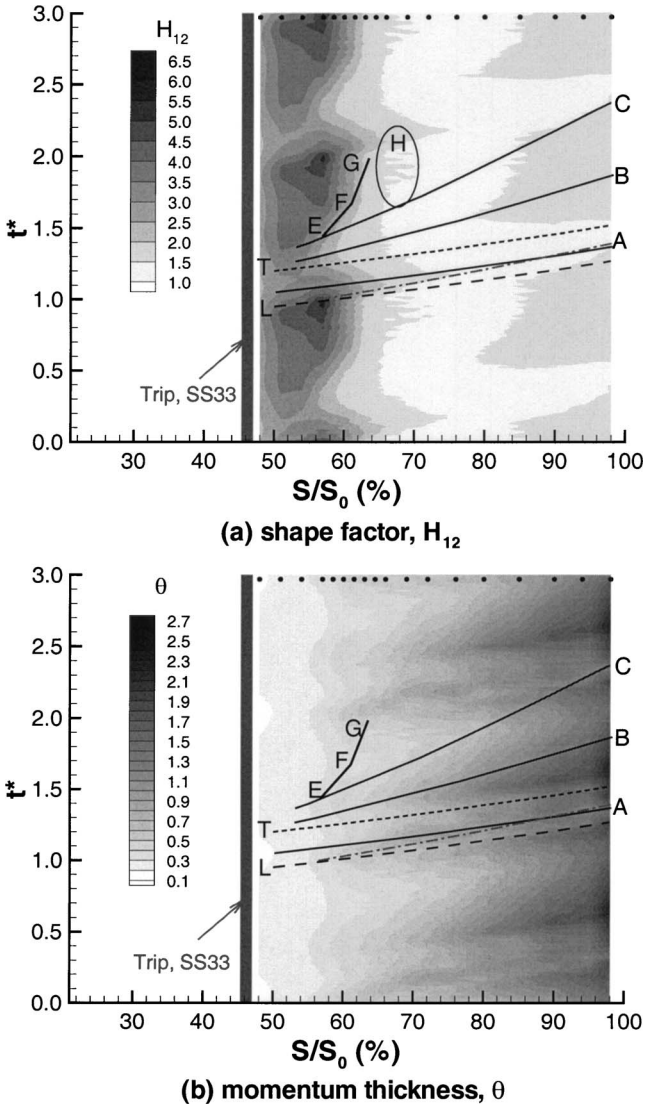

Fig. 16 Unsteady boundary layer integral parameters with straight step SS33 at Re=174,000 and *Tu*=0.5%

cantly change between lines L and T, indicating that the interaction between the negative jet and the separation bubble is very weak. Rollup vortices do not appear to be generated. The transition induced by the wake turbulence occurs earlier in both space and time due to the higher level of turbulence after the trip and the smaller separation bubble. After the wake passing, it takes a short time for the bubble to reestablish, indicated by the reattachment line E-F. Then the bubble size remains almost constant, which is shown by the reattachment line F-G, until the next wake arrives. The bubble size between the wakes is smaller than that on the smooth surface. Moreover, the lower maximum level of H_{12} indicates that the maximum height of the separation bubble is much smaller than that on the smooth surface. Downstream of the reattachment line F-G, there are wiggles with a coherent frequency in the region indicated as H in the figure. They result from the natural transition of the separated boundary layer between the passing wakes [10].

Figure 16(*b*) shows that the momentum thickness over the entire wake-passing period is smaller than that on the smooth surface, indicating the reduction in profile losses. Underneath the passing wake, between lines L and T, there is no region of significantly high momentum thickness. This again indicates the absence of the rollup vortices. The momentum thickness associated with the wake turbulence-induced turbulent region between lines A and B is also lower than that on the smooth surface because of the smaller separation with the surface trip. Between the wakes, the momentum thickness after the reattachment point is lower than that on the smooth surface, which results from the early transition induced by the surface trip. Thus, the loss reduction under the combined effects of surface trip and unsteady wakes results from the absence of the strong rollup vortices and the smaller separation bubble between wake-passing events, as well as the weak viscous interactions between the wakes and the inflected boundary layer due to the smaller separation after the surface trip.

Conclusions

The combined effects of surface trips and unsteady wakes can further reduce the profile losses of the ultra-high-lift LP turbine blades, for which the separation bubble is large because of the high adverse pressure gradient and the low wake-passing frequency. The profile loss at Re=174,000 was reduced by 20% compared to that on the smooth surface. It is believed that the surface trip hastens the transition process in the separated shear layer underneath the wakes and between them. This therefore results in a weaker interaction between the wake's negative jet and the separated boundary layer, which reduces the turbulent kinetic energy production and dissipation and, consequently, the profile losses. The loss reduction is also a compromise between the positive effects from the separation bubble reduction and the calmed region and the negative effects from having a larger turbulent wetted area.

There is an optimum height of the surface trip for each flow condition. The optimum trip height in the unsteady flow conditions is about 60% of the local boundary layer displacement thickness. The trip does not induce transition immediately after itself, but only hastens the transition process in the separated shear layer. By properly choosing the parameters of the surface trip, this passive flow control method will not reduce the performance at the highest Reynolds number tested, which is important for LP turbine blades because of their wide range of working conditions.

The step-type trips are more effective at inducing boundary layer transition than the wire-type trips because of the higher disturbance level generated after the sharp trailing edges. The location and the shape of the leading edge of the step are not important compared to the height and the trailing-edge location. The optimum location of the surface trip is midway between the velocity peak and the separation onset location. The wavy trips further reduce the profile losses under steady flow conditions, but not under unsteady flow conditions because of the production of streamwise vortices.

Acknowledgments

The work reported in this paper was conduced as a part of the research project UTAT, "Unsteady Transitional Flows in Axial Turbomachineries," funded by the European Commission under Contract No. GRD1-2001-40192. The authors wish to thank ITP for the work performed to design the shape of the flat plate endwalls and for supplying the corresponding CFD results.

Nomenclature

C = blade chord
C_p = isentropic pressure coefficient
C_x = blade axial chord
f_r = reduced frequency
H_{12} = shape factor
k = height of surface trip
Re = Reynolds number
rms = root mean square
S = distance along suction surface
S_0 = suction surface length
s = blade pitch

s_{bar} = moving bar pitch
t^* = time normalized by wake-passing period
Tu = turbulence intensity
U_{bar} = bar moving velocity
V_{1x} = axial inlet velocity
V_{2is} = isentropic exit velocity
Y_n = surface normal coordinate
$\alpha_{1,2}$ = inlet and outlet flow angle, respectively
$\beta_{1,2}$ = inlet and outlet metal angle, respectively
δ^* = displacement thickness
θ = momentum thickness
ξ = loss coefficient based on θ
ϕ = flow coefficient

References

[1] Schulte, V., and Hodson, H. P., 1996, "Unsteady Wake-Induced Boundary Layer Transition in High Lift LP Turbines," ASME Paper No. 96-GT-486.
[2] Howell, R. J., Hodson, H. P., Schulte, V., Schiffer, H. P., Haselbach, F., and Harvey, N. W., 2001, "Boundary Layer Development in the BR710 and BR715 LP Turbines: The Implementation of High Lift and Ultra High Lift Concepts," ASME Paper No. 2001-GT-0441.
[3] Bons, J. P., Sondergaard, R., and Rivir, R. B., 2001, "Turbine Separation Control Using Pulsed Vortex Generator Jets," ASME J. Turbomach., **123**(2), pp. 198–206.
[4] Bons, J. P., Sondergaard, R., and Rivir, R. B., 2001, "The Fluid Dynamics of LPT Blade Separation Control Using Pulsed Jets," ASME Paper No. 2001-GT-0190.
[5] Volino, R. J., 2003, "Separation Control on Low-Pressure Turbine Airfoils Using Synthetic Vortex Generator Jets," ASME Paper No. GT-2003-38729.
[6] Lake, J. P., King, P. I., and Rivir, R. B., 2000, "Low Reynolds Number Loss Reduction on Turbine Blades With Dimples and V-Grooves," 38th AIAA Aerospace Sciences Meeting and Exhibit, AIAA-00-0738.
[7] Volino, R. J., 2003, "Passive Flow Control on Low-Pressure Turbine Airfoils," ASME Paper No. GT-2003-38728.
[8] Ramesh, O. N., Hodson, H. P., and Harvey, N. W., 2001, "Separation Control in Ultra-High Lift Aerofoils by Unsteadiness and Surface Roughness," ISABE.
[9] Roman, K. M., 2003, "The Effect of Roughness and Wake Unsteadiness on Low-Pressure Turbine Performance," MPhil thesis, Cambridge University, UK.
[10] Stieger, R. D., and Hodson, H. P., 2003, "Unsteady Dissipation Measurements on a Flat Plate Subject to Wake Passing," 5th European Turbomachinery Conference.
[11] Zhang, X. F., and Hodson, H. P., 2003, "Parametric Study of Surface Roughness and Wake Unsteadiness on a Flat Plate with Large Pressure Gradient," *Proc. of 10th ISUAAAT*, Duke University.
[12] Stieger, R. D., Hollis, D., and Hodson, H. P., 2003, "Unsteady Surface Pressures Due to Wake Induced Transition in a Laminar Separation Bubble on a LP Turbine Cascade," ASME J. Turbomach., **126**(4), pp. 544–550.
[13] Stieger, R. D., and Hodson, H. P., 2003, "The Transition Mechanism of Highly-Loaded LP Turbine Blades,"ASME J. Turbomach., **126**(4), pp. 536–543.
[14] Bearman, P. W., 1971, "Correction for the Effect of Ambient Temperature Drift on Hotwire Measurements in Incompressible Flow," DISA Information, No. 11, pp. 25–30.
[15] Cox, R. N., 1957, "Wall Neighborhood Measurements in Turbulent Boundary Layers Using Hot-wire Anemometer," A. R. C. Report 19101, Feb.
[16] Curtis, E. M., Hodson, H. P., Banieghbal, M. R., Denton, J. D., Howell, R. J., and Harvey, N. W., 1997, "Development of Blade Profiles for Low-Pressure Turbine Applications," ASME J. Turbomach., **119**, pp. 531–538.
[17] Pinson, M. W., and Wang, T., 2000, "Effect of Two-Scale Roughness on Boundary Layer Transition Over a Heated Flat Plate: Part 1—Surface Heat Transfer," ASME J. Turbomach., **122**, pp. 301–307.
[18] Pinson, M. W., and Wang, T., 2000, "Effect of Two-Scale Roughness on Boundary Layer Transition Over a Heated Flat Plate: Part 2—Boundary Layer Structure," ASME J. Turbomach., **122**, pp. 308–316.

Investigation on a Type of Flow Control to Weaken Unsteady Separated Flows by Unsteady Excitation in Axial Flow Compressors

Xin-qian Zheng

Xiao-bo Zhou

Sheng Zhou

Chinese National Key Laboratory of Aerodynamics and Thermodynamics of Aeroengine,
Beijing University of Aeronautics and Astronautics,
Beijing, 100083, P. R. China

By solving unsteady Reynolds-averaged Navier-Stokes equations discretized by a high-order scheme, the results showed that the disordered unsteady separated flow could be effectively controlled by periodic suction and blowing in a wide range of incidences, resulting in enhancement of time-averaged aerodynamic performances of an axial compressor cascade. The effects of unsteady excitation frequency, amplitude, and excitation location were investigated in detail. The effective excitation frequency spans a wide spectrum, and there is an optimal excitation frequency that is nearly equal to the characteristic frequency of vortex shedding. Excitation amplitude exhibits a threshold value (nearly 10% in terms of the ratio of maximum velocity of periodic suction and blowing to the velocity of free flow) and an optimal value (nearly 35%). The optimal excitation location is just upstream of the separation point. We also explored feasible unsteady actuators by utilizing the upstream wake for constraining unsteady separation in axial flow compressors. [DOI: 10.1115/1.1860572]

1 Introduction

Prandtl introduced the concept of the boundary layer, discussed separation phenomenon, and presented an experimental technique for eliminating it. Long before the theory was put forward, people already confronted the problems brought about by flow separation. Separation drastically reduces lift and increases drag of airfoils, and reduces the efficiency of nozzles and turbomachinery. Preventing separation and improving the behavior of unsteady separated flows are long-standing key problems in fluid dynamics research.

Since then, there has been a large amount of research and development in the area of boundary layer control. It is well known that strong adverse pressure gradient (or local surface curvature [1]) and decreased momentum inside the boundary layer are two critical factors underlying boundary layer separation. Early work in separation control was concentrated on passive control, choosing optimal airfoil and nozzle geometries to delay separation. While extensive research has been conducted for passive flow control, over the past several years, aerospace research has led to the development of several active flow control (AFC) methods [2–6], particularly the application of integrated MEMS systems to construction structure. AFC improved aerodynamic efficiency and reduced noise levels that are generally caused by unsteady flow phenomen.

An explosion of interest in the control of separation using unsteady excitation has been seen in the recent several years. In this approach, low amplitude periodic disturbances are introduced, generally just upstream of the separation point. Either surface-based actuators (e.g., leading-edge slats, slotted flaps, vortex generators, moving wall, etc.), where some appendage of the aerodynamic body interacts with the free stream and/or the boundary layer, are applied to directly energize the low-momentum region; or fluidic-based actuators (e.g., dynamic excitation [7–9]) are adopted to energize the low-momentum regions by unsteady excitation, where the flow is controlled by the removal or the addition of momentum to the free stream. The targets of all of these separation control methods focus on how to enhance the low momentum of fluids under adverse pressure gradient. For instance, vortex generators, tangential suction and blowing, and acoustic excitation are dissimilar; however, they all generate or induce arrays of spanwise vortices that are convected downstream and continue to mix across the boundary layer. It has been speculated that the mechanism is to move the boundary layer reattachment forward via large-scale convection of free-stream momentum toward the surface.

There are a number of experimental and numerical studies showing the general effectiveness of flow control for a single airfoil. In some investigations, leading-edge suction is applied to delay the transition [10], and people find that using steady suction is much more effective than steady blowing; particularly, oscillatory suction and blowing is about ten times more effective than steady blowing in increasing lift. In this category, unsteady controls are much more effective than steady ones and can be realized at a very low level of power input. Hence, periodic blowing and suction can be applied to a wide variety of cases where steady blowing would be either ineffective or require too high of a mass transfer rate. To study flow control by periodic excitation, various blowing coefficients are investigated at a given excitation frequency. By changing the excitation frequency at a constant intensity, an optimum frequency can be identified [4]. Furthermore, in experimental work at the Illinois Institute of Technology and NASA Langley Research Center, the effectiveness of periodic disturbances to control separation at higher Mach numbers is currently being tested. For purely oscillatory disturbances, i.e., with no net mass flux, preliminary results seem to indicate that separation control by periodic disturbances remains effective even at high subsonic Mach numbers [11].

Unfortunately, as we know, the adverse pressure gradient in

Contributed by the International Gas Turbine Institute (IGTI) of THE AMERICAN SOCIETY OF MECHANICAL ENGINEERS for publication in the ASME JOURNAL OF TURBOMACHINERY. Paper presented at the International Gas Turbine and Aeroengine Congress and Exhibition, Vienna, Austria, June 13–17, 2004, Paper No. 2004-GT-53167. Manuscript received by IGTI October 1, 2003; final revision, March 1, 2004 IGTI Review Chair: A. J. Strazisar.

axial flow compressors is generally stronger than that in any other fluid machines. Axial flow compressors rely fundamentally on aerodynamic diffusion to achieve pressure rise. Since the adverse pressure gradient associated with the diffusion becomes stronger at the high loading levels in modern designs, unsteady separation is inevitable. This has a negative impact on the stall margin, efficiency, and pressure rise capability. To the authors' knowledge, little research has been performed on separation control by using unsteady excitations in axial flow compressors. Is it appropriate for separation control in inner flows to use unsteady excitations that have been relatively well rounded in outer flows? The present paper aims at finding a new way to achieve separation control in axial flow compressors.

In this paper, we used periodic suction and blowing as an unsteady excitation to weaken the separation inside an axial compressor cascade. In view of complex flows in axial compressors, we only considered a two-dimensional (2D) case in the present paper. Specifically, we ran cases at Ma=0.5, where compressibility effects were taken into consideration, but not yet supersonic. The first step of the present work is to simulate the unexcited separated flows by solving the unsteady Navier-Stokes equations at predetermined incidences. Based on this, we successfully control the separation on the suction side of the blade by using periodic suction and blowing at a specific location and obtain a general picture of excited flows inside a compressor cascade. Finally, we studied the effects of key excitation parameters on excited flows. Considering the inherent unsteady effects in a compressor, we regard the wakes of the upstream rows as unsteady actuators to control the unsteady separated flow over the downstream blades and obtain primary positive results.

2 Numerical Methods

The code used in this simulation is based on a 2D unsteady compressible finite difference scheme to solve the Reynolds-averaged Navier-Stokes equations in conservative formulation. A third-order TVD Runge-Kutta time-marching scheme was used for time integration, because time accuracy was critical for this simulation. It is generally recognized that high-order spatial schemes are recommended, especially for time-dependent simulations. In this code, a fifth-order accurate generalized compact scheme [12] is used for spatial difference of inviscid fluxes and a sixth-order compact finite difference scheme [13] for viscous fluxes. For the turbulence model, the standard algebraic model of Baldwin and Lomax [14] is adopted, which is theoretically appropriate for unsteady separated flows of small or medium scale, but is not so satisfactory for large-scale separated flows. However, in Reynolds-averaged computations of unsteady separated turbulent flow, to find a proper yet simple turbulence model is an extremely delicate and difficult issue.

The 2D airfoil is a blade root element of the first stage rotor blade in a high-pressure compressor of generator CFM56. The computational domain is from one chord length upstream up to four chord lengths downstream, as shown in Fig. 1. H-type computational mesh is adopted and created by solving an elliptic differential equation. Different grid solutions had been compared. With CPU time and precision taken into consideration, mesh dimensions were 220×41 (streamwise$\times$pitchwise) for all cases, with locally denser mesh points near walls, leading edges, and trailing edges, to enhance computation precision.

This imposed normal periodic suction and blowing was assumed to be completely 2D and have no net mass flux. The width of the excitation slot is about 7% of the chord length. Steady boundary conditions were given at both the inlet and outlet boundaries. The total pressure, total temperature, and inlet flow angle were specified uniformly at the inlet boundary, whereas the static pressure was fixed at the outlet.

To reduce the computational cost, we adopted a simplified model to model the effects of unsteady excitation. Normal periodic suction and blowing was modeled by using simplified boundary conditions imposed at the excitation location. The perturbation to the flow field was introduced through the wall-normal component of velocity at the excitation location

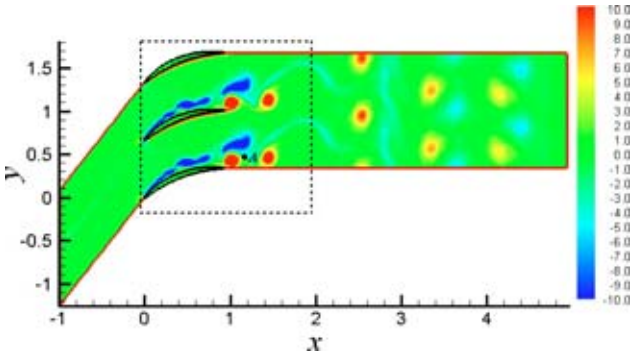

Fig. 1 Computational domain and instantaneous vorticity field without excitation at i=10 deg

$$\begin{cases} u_{\text{wall}} = 0 \\ v_{\text{wall}} = |v|_{\max} \cdot \sin(2\pi f_e t) \end{cases} \tag{1}$$

where u_{wall} is the velocity in the wall-tangent direction, v_{wall} is the velocity in the wall-normal direction, $|v|_{\max}$ is the maximum velocity of the periodic suction and blowing, and f_e is the excitation frequency. A modified boundary condition on the pressure at the excitation location was introduced through a consideration of the normal momentum equation.

No-slip and impermeability conditions were imposed on the blade surface, except at a few grid points at the suction and blowing location, and adiabatic temperature condition were imposed all over the blade.

Period conditions were imposed on the extend region. A uniform flow was simply taken as the initial condition. After starting, the transient state evolves to a quasi-periodic state. Data were recorded after the quasi-periodic state was reached.

3 Unexcited Unsteady Separated Flows

To prepare for further study, the first step of the present work is to investigate the characteristic frequency of vortex shedding f_{shed} and the separation point in an unexcited unsteady separated flow at a series of incidences. The characteristic frequency of vortex shedding will be the reference frequency for the unsteady excitation, and the excitation location is chosen to be located within a small region (about 7% of the chord length) just upstream of the separation point.

3.1 Obtaining the Characteristic Frequency of Vortex Shedding. Because of flow viscosity and strong adverse pressure gradient, unsteady separation is inevitable. The instantaneous vorticity (nondimension, as follows) field at i=10 deg is shown in Fig. 1, which reveals that the separation point on the suction side is about 25% of the chord length from the leading edge, and vortices are produced in a separated region and then convected downstream. We name them as separated vortices on the suction side. Meanwhile, these vortices induce some reversed vortices at the trailing edge. The vortices shed from the trailing edge with some natural shedding frequency and convected downstream, alternately.

The total pressure at point A (Fig. 1) is analyzed to obtain the characteristic frequency of vortex shedding f_{shed}. Figure 2 presents the time domain graph of total pressure at point A. The corresponding spectrum of total pressure at point A is obtained by fast Fourier transform (FFT) and shown in Fig. 3. Obviously, there is a frequency whose amplitude is maximal in Fig. 3, but is it the characteristic frequency of vortex shedding? Sufficient condition for this criterion is proposed as follows. Analyze the trend

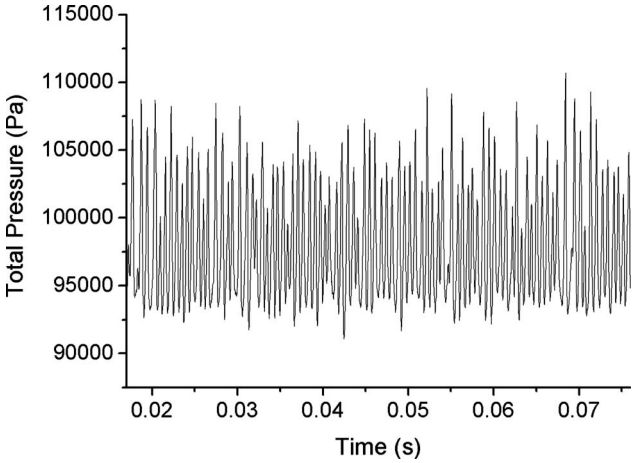

Fig. 2 Time domain graph of total pressure at *i*=10 deg

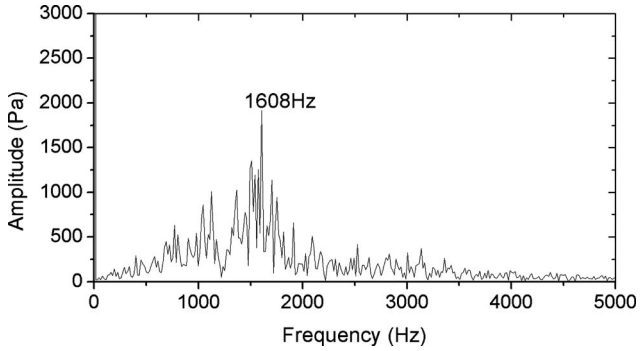

Fig. 3 Spectrum of total pressure at *i*=10 deg

of frequency and its amplitude of some points that are out of separation region and wakes. If the amplitude damp quickly in the spectrum of total pressure and the closer the point is to the vortex core the higher the amplitude becomes, then the frequency should be the characteristic frequency of vortex shedding. The evolvement of vortex shedding can be demonstrated clearly by flow animation.

The present study simulated the unsteady separated flow at a wide range of incidence ($0\ \text{deg} \leqslant i \leqslant 25\ \text{deg}$). The characteristic frequencies of vortex shedding in unsteady separated flow f_{shed} determined by the above criterion at various incidences are listed in Table 1. As shown in Table 1, f_{shed} decreases while i increases. The larger i is, the larger the separation scale is, and the larger the scale of shedding vortices becomes. The shedding frequencies of large-scale vortices are lower than those of small scale ones.

After obtaining the characteristic frequency of vortex shedding at a series of incidences, let us define two important excitation parameters:

Relative excitation frequency

$$\bar{f}_e = f_e / f_{\text{shed}} \tag{2}$$

Relative excitation amplitude

$$\bar{A} = |v|_{\max} / c_\infty \tag{3}$$

where c_∞ is free-stream velocity.

3.2 Obtaining the Separation Point. The condition of 2D steady separation is

$$\begin{cases} \left(\dfrac{\partial u}{\partial y}\right)_O = 0 \\ \left[\dfrac{\partial}{\partial x}\left(\dfrac{\partial u}{\partial y}\right)\right]_O = 0 \end{cases} \tag{4}$$

where subscript o denotes the separation point. The condition of 2D unsteady separation has not been established; although this paper eventually discusses the unsteady separation problem. Therefore, the condition of 2D steady separation is lent to unsteady separation. Equation (4) is adapt to time-averaged unsteady flows. There are two methods to determine the separation point. Because of the existence of a recirculation zone after the separation point, there must be two lines on which $u=0$. One of the two lines overlaps the blade surface (impermeability conditions). The intersection point of the other line $u=0$ and the blade wall is the separation point. According to 2D separated flow characteristics, the separation point is the intersection point of the line (the vorticity of which is zero) and the blade surface. This is the other approach to obtain separation point. In order to make the determination reliable, the present paper uses both the methods to determine the separation point. The distance (nondimensioned by chord length) between the leading edge and the separation point at various incidences are also listed in Table 1. The larger the incidence, the closer to the leading edge the separation point is.

4 Effect of Unsteady Excitation on Unsteady Separated Flows

4.1 Improvement of Aerodynamic Performances. For unexcited unsteady separated flow, the characteristic frequency of vortex shedding, separation point, and time-averaged aerodynamic performance have been studied at various incidences. The effects of unsteady excitation on unsteady separated flow will be studied in this section. The essential unsteady excitation parameters are frequency, amplitude, and excitation location. For comparison, the excitation parameters are kept unchanged and given below. The relative excitation frequency $\bar{f}_e=1$, the relative excitation amplitude $\bar{A}=30\%$, and the excitation location is just upstream of the separation point at corresponding incidences (Table 1). The effects of excitation parameters on unsteady separated flow will be discussed in Sec. 5.

As shown in Figs. 4 and 5, the unsteady excitation substantially reduced loss coefficient and increased the static pressure ratio. The $\bar{\omega}$ was reduced at all computational incidences, particularly at $i=12$ deg where the $\bar{\omega}$ was reduced by 32.65%. Moreover, the static pressure ratio was also increased greatly, particularly at $i=10$ deg and $i=12$ deg. The ratio of static pressure was increased by 61.02% when an unsteady excitation was imposed on the unsteady separated flow. The time-averaged aerodynamic performances were improved in all computation cases. The effectiveness is particularly prominent around $i=10$ deg. There would be some decrease of effectiveness if the incidence exceeded 20 deg.

Table 1 Characteristic frequency (Hz) of vortex shedding in unsteady separated flow and separation point at different incidences (Ma=0.5)

i	0°	3°	5°	8°	10°	12°	15°	18°	20°	22°	25°
f_{shed}	2561	2312	2287	1712	1608	1374	1238	1060	1040	878	856
$\bar{l}_{sep}$	60%	51%	45%	30%	25%	20%	16%	14%	10%	8%	3%

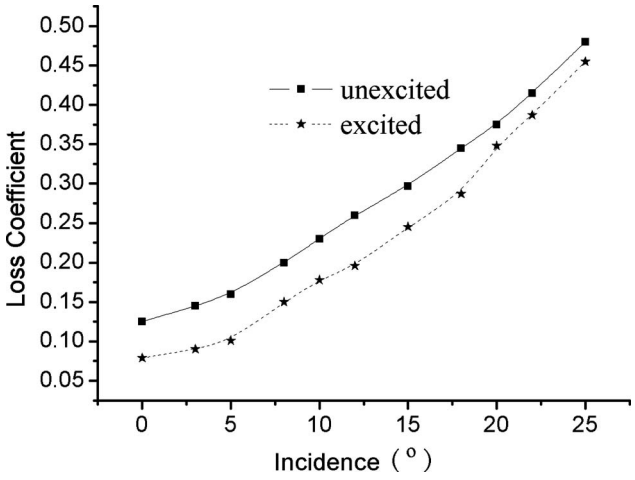

Fig. 4 Loss coefficient at different incidences, excited versus unexcited

4.2 Changes of the Time-Space Structure. The improvement of time-averaged performances is associated with the change of the time-space structure of the flow field, which will be interpreted by means of an instantaneous and time-averaged vorticity field at $i=10$ deg. Figures 6 and 7 are instantaneous vorticity fields unexcited and excited by periodic suction and blowing, respectively. Figures 8 and 9 are time-averaged vorticity fields unexcited and excited by periodic suction and blowing, respectively. The domain shown in Figs. 6–9 is the area marked with a broken line in Fig. 1. Figure 10 is the phase diagram at some fixed point on the exit section of the cascade.

The unsteady excitation caused several small discrete vortices to quickly merge into a large vortex. It was observed that the large vortex had a rolling-up structure, when it was strong enough it would have the ability to entrain most disordered fluid into its core. The fresh free stream brought larger momentum into the large vortex and made it tend to turn downward. This would bring about a very favorable effect that the trailing-edge vortices, due to the induction of the large vortex, were greatly suppressed. At the same time, by comparing Figs. 8 and 9 (or comparing Figs. 6 and 7), it was obvious that the thickness of the boundary layer on the blade suction side was greatly reduced, and the separation on suction side was thus effectively controlled. The separation point moved downstream from 25% chord length to 60% chord length at $i=12$ deg.

Also, the originally chaotic and disorganized flow becomes a well-organized flow (as shown in Fig. 10). The physical mechanisms underlying the phenomena might be that unsteady excitation with appropriate frequency, amplitude, and location causes the response frequencies of shedding vortices to lock up into the harmonics of the excitation frequency, while other random modes are suppressed.

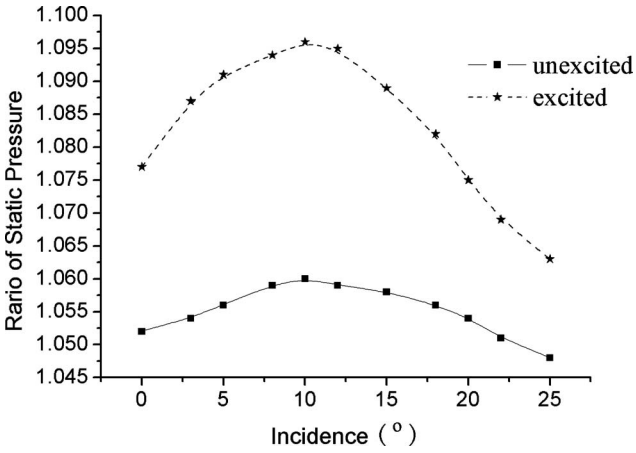

Fig. 5 Ratio of static pressure at different incidences, excited versus unexcited

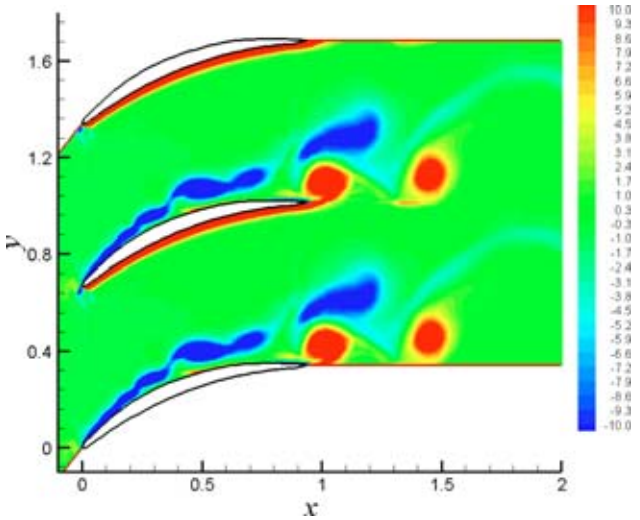

Fig. 6 Instantaneous vorticity field by computation at $i=10$ deg, unexcited

4.3 Comparison With the Experimental Results. In order to investigate the effects of unsteady excitation on the weakening and control of unsteady separated flow, corresponding experiments have been carried out in a stationary annual cascade wind tunnel, and positive results have been obtained. Acoustic excitation is used to simulate the effect of unsteady excitation. Of course, the acoustic excitation is merely a simplified simulation of unsteady excitation; it cannot reflect the full effects of periodic suction and blowing. However, acoustic excitation is convenient and easy to implement. Moreover, no matter what kind of specific actuator was used to produce it, as long as the excitation disturbance has the proper frequency, amplitude, and excitation location, qualitatively, the same end result could be anticipated. Thus we believe that qualitative analyses of the experimental results are reliable. Since emphasis is not placed on experiments, the details

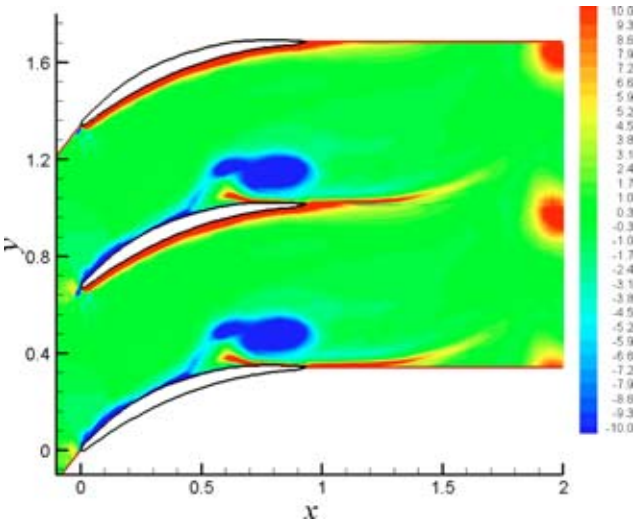

Fig. 7 Instantaneous vorticity field by computation at $i=10$ deg, excited

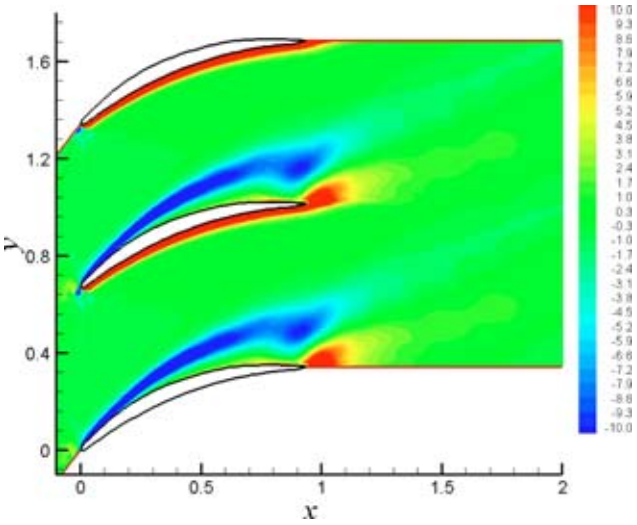

Fig. 8 Time-averaged vorticity field by computation at i =10 deg, unexcited

will not be given in the present paper, only part of the experimental results were presented to validate the reliability of CFD simulation. The detail procedure and results of the experiments will be presented in another paper.

Figures 11 and 12 show the instantaneous vorticity field in an unexcited flow and a flow excited by acoustic excitation, respectively. They were obtained by the PIV (Particle Image Velocimetry) technique. The scale and intensity of wake vorticity induced by the separated vortex as well as the separated vortex on the suction side were greatly weakened by the acoustic excitation. The separated boundary layer was moving toward the suction side of the blade and might reattach to the blade surface somewhere. Comparing the CFD results (Figs. 6 and 7) to the PIV results (Figs. 11 and 12), we obtain the same trends of changes in time-space structure. Both of them show that unsteady excitations can weaken unsteady separation and reduce vorticity, and the experimental results lend support to the reliability of the present simulation.

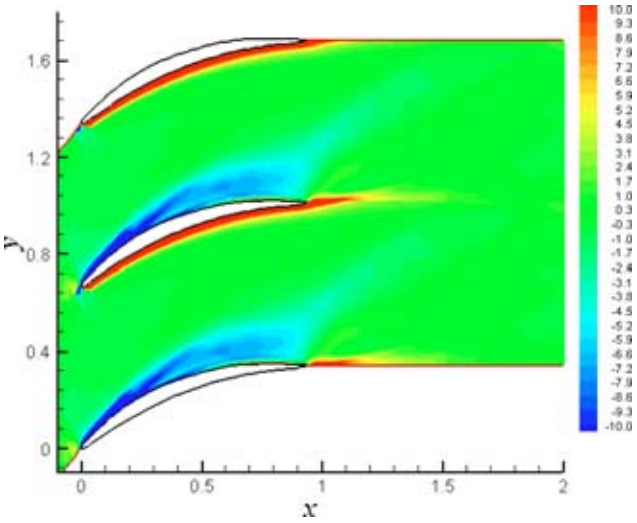

Fig. 9 Time-averaged vorticity field by computation at i =10 deg, excited

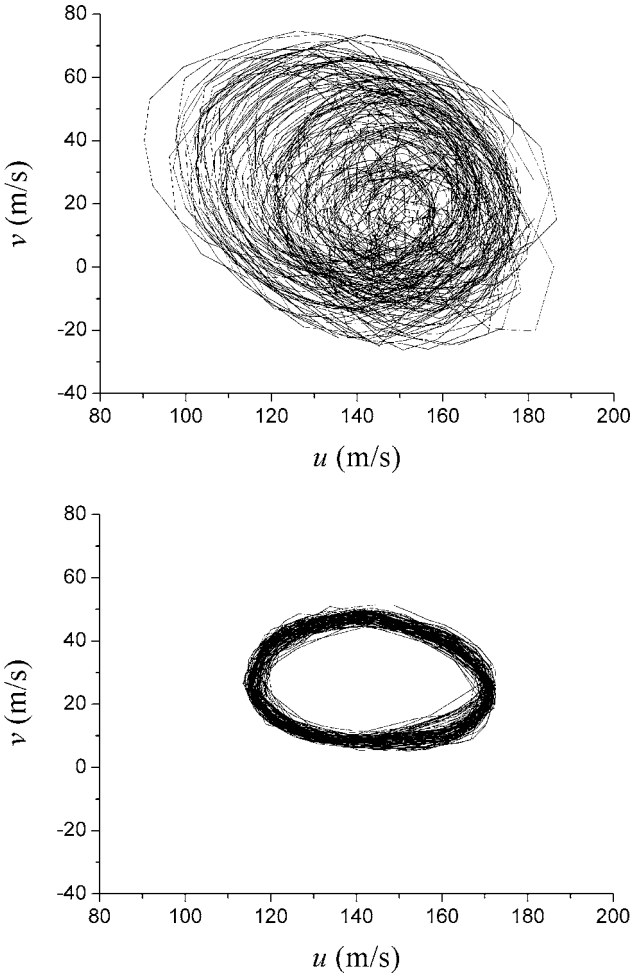

Fig. 10 Phase diagram at some fixed point on the exit section of cascade at i=10 deg: (a) unexcited and (b) excited

5 Trends of Excitation Parameters

Positive results of unsteady separation control by means of periodic suction and blowing were obtained at a series of incidence (0 deg $\leqslant i \leqslant$ 25 deg). The influence of excitation frequency, excitation amplitude, and excitation location in the simulation are discussed for different incidence (as shown in Table 1). In this section, the trends of parameter variation are discussed at i=10 deg because the effect of excitation was found to be prominent at that incidence.

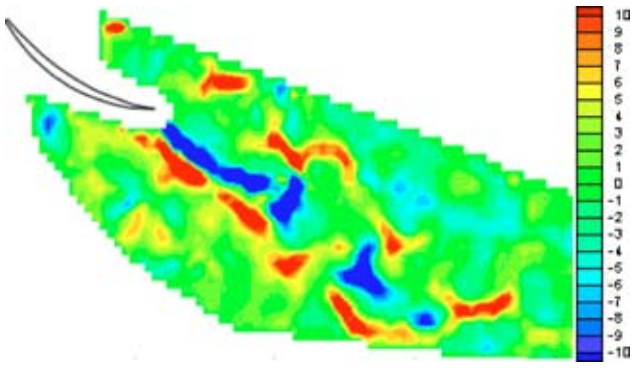

Fig. 11 Instantaneous Vorticity Field by PIV, unexcited

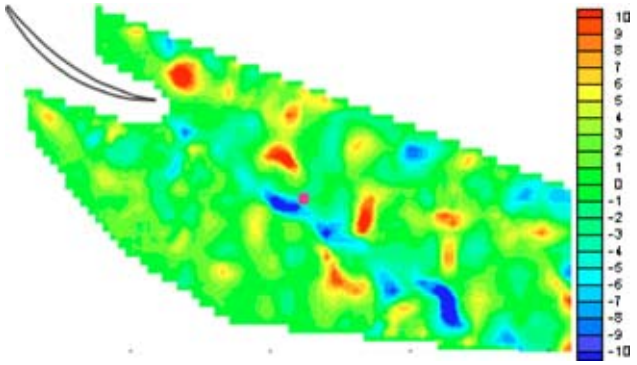

Fig. 12 Instantaneous Vorticity Field by PIV, excited

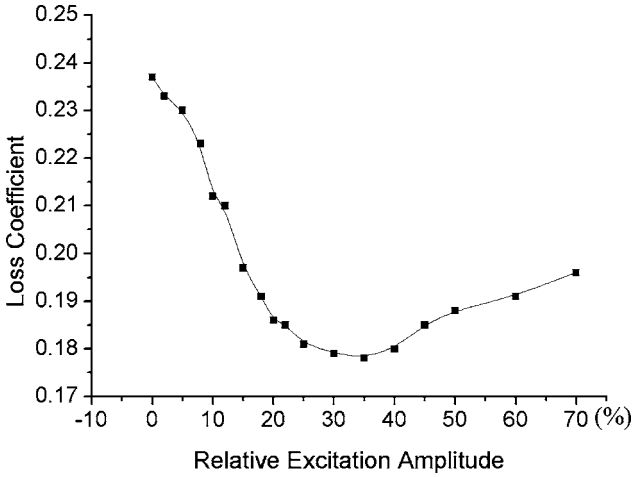

Fig. 14 Loss coefficient for different relative excitation amplitude ($\bar{f}_e$=1 and i=10 deg)

5.1 Effect of Excitation Frequency. In order to illustrate the effect of excitation frequency, we fix the relative excitation amplitude and incidence as $\bar{A}=30\%$ and $i=10$ deg. The excitation location is located just upstream of the separation point at $i=10$ deg, which is given in Table 1. Figure 13 presents the effect of relative excitation frequency on loss coefficient. The first data point on the left of Fig. 13 is the performance without excitation, which is taken as the baseline.

It is obvious that the time-averaged performance of the flow field is remarkably improved (compared to the unexcited case) in a wide range of excitation frequency (approx $0.4<\bar{f}_e<1.5$). When the excitation frequency is equal to the characteristic frequency of vortex shedding (i.e., $\bar{f}_e=1$), the maximum reduction of loss coefficient is obtained almost by 25%. However, there will be a significant decrease in effectiveness once the excitation frequency is far away from the characteristic frequency of vortex shedding. It is suggest that optimal relative frequency $\bar{f}_e$ should be from about 0.4 to 1.5.

5.2 Effect of Excitation Amplitude. Similarly, to illustrate the effect of excitation amplitude, relative excitation frequency, and the incidence are fixed as $\bar{f}_e=1$ and $i=10$ deg. The excitation location is again located just upstream of the separation point at $i=10$ deg, which is given in Table 1. Figure 14 shows the effect of excitation amplitude on the loss coefficient. Similarly, the first data point on the left of Fig. 14 is the performance without excitation. It is demonstrated that the periodic excitation has a negligible effect on the flow dynamics when the excitation amplitude is relative small. Therefore, positive results obtained must satisfy the condition that the relative excitation amplitude is above a threshold value ($\bar{A}\approx 10\%$). Basically, the aerodynamic performance increases monotonically with excitation amplitude up to about $\bar{A}=35\%$. If the excitation amplitude goes beyond the limit ($\bar{A}=35\%$), then the periodic excitation effect is weakened with the excitation amplitude. Hence, it is not the case that the greater the unsteady excitation, the better the results are. On the one hand, to control and attenuate unsteady separation to have a positive effect, the field structure must also be simultaneously transferred to have the destructive effect. Therefore, there must exist optimal excitation amplitude in controlling unsteady separated flow by periodic excitation.

5.3 Effect of Excitation Location. Up to now, the excitation location has been located just upstream of the separation point on the suction side of blade in all cases. To study the effect of varying excitation locations, we fix $\bar{f}_e=1$, $\bar{A}=30\%$, and $i=10$ deg. Figure 15 shows the loss coefficient for different excitation locations. The best results were obtained when unsteady excitations were excited within a small upstream region (about 7% chord length) covering the separation point. If the excitation location moves backward or forward further from the separation point, then the

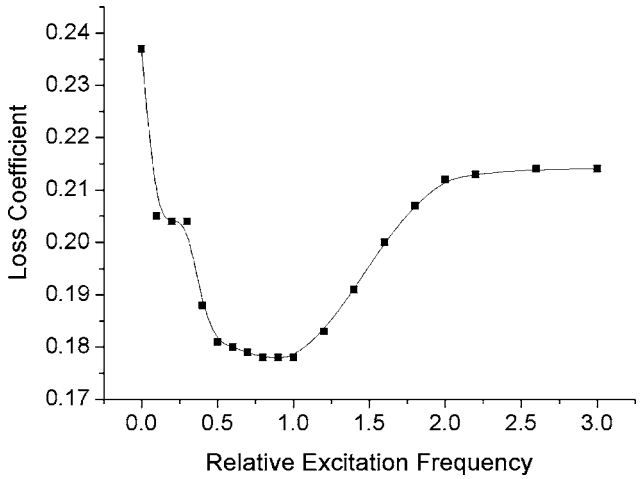

Fig. 13 Loss coefficient for different relative excitation frequency ($\bar{A}$=30% and i=10 deg)

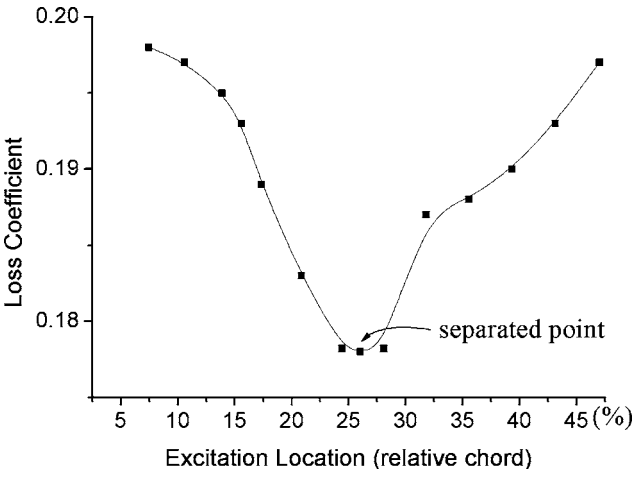

Fig. 15 Loss coefficient for different excitation location ($\bar{f}_e$=1, $\bar{A}$=30%, i=10 deg)

effectiveness of periodic excitation becomes weakened sharply.

It is speculated that the boundary layer close to the separation point is sensitive to disturbance. Just around this specific local region, the boundary layer is receptive to unsteady excitation. The basic steady flow has a high velocity component upward at the local region near the separation point, which will amplify the effect of any nonlinear streaming and thus make local oscillations an effective actuator in delaying separation on the blade. This amplification mechanism, which cannot be found in attached flows, will enhance the primary entrainment and rolling-up coalescence inherent in boundary layer, resulting in a reduced separation region. Hence, it is not surprising that periodic suction and blowing would have a strong resonance and nonlinear streaming effects when excited on unsteady separated flow inside the compressor cascade.

6 Engineering Application

There is strong hope to find a separation control technique that is not only effective in reducing or eliminating separation, but also simple in realization. In this paper, we applied numerical methods to simulate periodic suction and blowing for controlling unsteady separation inside the compressor cascade. The approaches are extremely effective in controlling, or essentially eliminating, the existent separation. Considering the complicated configuration, periodic suction and blowing have never been applied heretofore, although the integrated MEMS systems are promising. A question to ask is: what is the feasible unsteady actuator in axial flow compressors?

Current design practice of aeroengines generally ignores unsteady effects and adopts steady flow theory to design compressor and turbine blade elements. It is important for designers to appreciate the influences of unsteady conditions under which axial flow compressor blade elements have to operate [15]. It is reasonable to make use of the unsteady effects inherent in the compressor, e.g., the blade wakes from the upstream stators, as an unsteady actuator to control the unsteady separated flow over the downstream rotor blade.

The flow inside an axial compressor is a typical flow around multibodies and involves a transformation between two coordinate systems. The wake of the upstream stator blade can be considered as an unsteady actuator, which has a definite frequency and amplitude once it is transformed from the absolute to the relative coordinate. If the upstream wake-passing frequency is properly arranged to couple with the characteristic frequency of vortex shedding, then the time-space structure of flow over the downstream rotor blade might be improved and the separation would be weakened. In this way, we might make use of the unsteady flow in axial flow compressors. In addition, it gives us a new viewpoint to think about the interaction between various rows of blades within each stage. We are now conducting the numerical simulations and experiments using wakes of upstream blades as unsteady actuators, rather than the periodic suction and blowing as used in this paper, and preliminary results are positive and encouraging [16].

7 Concluding Remarks

Our numerical results indicated that the unsteady separation would be weakened or delayed effectively by unsteady excitation. This unsteady excitation might modulate the evolution of the boundary layer and promote the coalescence of small vortices. Thus, most of the disordered separated flow becomes organized, resulting in enhanced time-averaged performances.

The effective excitation frequency spanned a wide, smooth spectrum. If the excitation frequency was approximately equal to the characteristic frequency of vortex shedding, then the optimal effects of unsteady excitation on separation flows could be obtained. The threshold value for excitation amplitude was about 10% (relative to free-stream velocity). Only if the excitation amplitude exceeds this value, will the improvement be prominent. However, it was not the case that the greater the unsteady excitation, the better the results were. When increasing too much, it could destroy the configuration of the flow field somewhat. The optimal excitation location was located just upstream of the separation point. Once the excitation location was far away from the separation point, the effectiveness of excitation decreased sharply.

The inherent unsteadiness in axial flow compressors should be the best actuator in engineering applications. Future direction was given and the preliminary results were inspiring.

Acknowledgments

This work was supported by grants from the National Natural Science Foundation of China (No. 10072008 and No. 50176001) and from the Ph.D. Programs Foundation of Ministry of Education of China (No. 2000000615).

Nomenclature

$\bar{A}$ = relative excitation amplitude
b = blade length
c_∞ = free-stream velocity
f_{shed} = characteristic frequency of vortex shedding
f_e = excitation frequency
$\bar{f}_e$ = relative excitation frequency
i = incidence
l_{sep} = distance between leading edge and separation point
$\bar{l}_{\text{sep}}$ = nondimensional distance between leading edge and separation point ($\bar{l}_{\text{sep}}=l_{\text{sep}}/b$)
Ma = Mach number
u = velocity in axial direction
u_{wall} = velocity in wall-tangent direction
v = velocity in circumferential direction
$|v|_{\max}$ = maximum velocity of periodic suction and blowing
v_{wall} = velocity in wall-normal direction
x = Cartesian coordinate in axial direction
y = Cartesian coordinate in circumferential direction
$\bar{\omega}$ = loss coefficient

References

[1] Pack, L. G., and Seifert, A., 2000, "Dynamics of Active Separation Control at High Reynolds Numbers," AIAA Paper No. 2000-0409.
[2] Volino, R. J., 2003, "Separation Control on Low-Pressure Turbine Airfoils Using Synthetic Vortex Generator Jets," ASME J. Turbomach. **125**, pp. 765–777.
[3] Greenblatt, D., and Wygnanski, I. J., 2000, "The Control of Flow Separation by Periodic Excitation," Prog. Aerosp. Sci. **36**(7), pp. 487–545.
[4] Schatz, M., and Thiele, F., 2001, "Numerical Study of High-Lift Flow With Separation Control by Periodic Excitation," AIAA Paper No. 2001-0296.
[5] Schaeffler, N. W., Hepner, T. E., Jones, G. S., and Kegerise, M. A., 2002, "Overview of Active Flow Control Actuator Development at NASA Langley Research Center," AIAA Paper No. 2002-3159.
[6] Tung, S., Maines, B., Jiang, F. K., and Tsao, T., 2001, "Transonic Flow Separation Control by MEMS Sensors and Actuators," AIAA Paper No. 2001-0123.
[7] Ahuja, K. K., and Burrin, R. H., 1984, "Control of Flow Separation by Sound," AIAA Paper No. 84-2298.
[8] Bons, J. P., Sondergaard, R., and Rivir, R. B., 2002, "The Fluid Dynamics of LPT Blade Separation Control Using Pulsed Jets," ASME J. Turbomach. **124**, pp. 77–85.
[9] McCormick, D. C., 2000, "Boundary Layer Separation Control with Directed Synthetic Jets," AIAA Paper No. 2000-0519.
[10] Maddalon, D. C., Collier, F. S., Montoya, L. C., and Land, C. K., 1989, "Transition Flight Experiment on a Swept Wing With Suction," AIAA Paper No. 89-1893.
[11] Israel, D. M., and Fasel, H. F., 1999, "Investigation of Separation Control in Compressible Boundary Layers Using Periodic Disturbances," AIAA Paper No. 99-3657.
[12] Shen, M. Y., Niu, X. L., and Zhang, Z. B., 2001, "The Three-Point Fifth-Order Accurate Generalized Compact Scheme and Its Applications," Acta Mech. Sin. **17**(2), pp. 142–150.
[13] Lele, S. K., 1992, "Compact Finite Difference Schemes with Spectral-Like Resolution," J. Comput. Phys. **103**, pp. 16–42.

[14] Baldwin, B. S., and Lomax, H., 1978, "Thin Layer Approximation and Algebraic Model for Separated Turbulent Flows," AIAA Paper No. 78-257.
[15] Walker, G. J., Hughes, J. D., and Solomon, W. J., 1998, "Periodic Transition on an Axial Compressor Stator-incidence and Clocking Effects—Part I: Experimental Data," ASME Paper No. 98-GT-363.
[16] Zheng, X. Q., and Zhou, S., 2004, "Numerical Investigation of Wake Impact Effect in Low-Speed Axial Compressor," J. Propul. Technol. **25**(5), pp. 421–425 (in Chinese).

Predicting Transitional Separation Bubbles

John A. Redford

Mark W. Johnson

Department of Engineering,
University of Liverpool,
Brownlow Hill, Liverpool,
Merseyside L69 3GH, UK

This paper describes the modifications made to a successful attached flow transition model to produce a model capable of predicting both attached and separated flow transition. This transition model is used in combination with the Fluent CFD software, which is used to compute the flow around the blade assuming that it remains entirely laminar. The transition model then determines the start of transition location and the development of the intermittency. These intermittency values weight the laminar and turbulent boundary layer profiles to obtain the resulting transitional boundary layer parameters. The ERCOFTAC T3L test cases are used to validate the predictions. The T3L blade is a flat plate with a semi-circular leading edge, which results in the formation of a separation bubble the length of which is strongly dependent on the transition process. Predictions were performed for five T3L test cases for differing free-stream turbulence levels and Reynolds numbers. For the majority of these test cases the measurements were accurately predicted. [DOI: 10.1115/1.1860573]

Introduction

Recent developments in the understanding of wake-induced transition [1] have led to the design of gas turbines with a reduced number of more heavily loaded blades. Separation bubbles are therefore more likely to form on these blades for at least some part of the engine operating range. Engine designers must, therefore, be able to predict both the position and size of these bubbles if they are to be able to calculate the engine performance reliably. The length of the separation bubble is highly dependent on transition, and although separated flow transition models exist [e.g., [2–4]], their reliability tends to be rather variable. The objective of the work described in this paper was to extend an existing physical model for attached flow transition [5] to separated flow. This model has previously been shown to be accurate in predicting both transition onset and length for attached flows for a wide range of pressure gradient and free-stream turbulence situations. The physics governing separated flow transition is not fully understood. Experimental observations suggest that although the location of the separation point is invariant with time, the reattachment point can move periodically in the streamwise direction by distances of 20–30% of the bubble length. This movement is associated with the shedding of fluid from the separation bubble. It is not clear though whether this process is at a fixed frequency, suggesting that a Kelvin-Helmholtz instability is responsible, or whether this is more random in nature and hence is linked to the turbulent intermittency. It should also be noted that if a Tollmien-Schlichting instability is responsible for the transition process, then the resultant intermittency would also exhibit a fixed periodic behavior. The approach adopted in the current work is to assume that the transition mechanism for separated flows is basically the same as that for attached flows and, therefore, that the unsteadiness observed where a transitional separation bubble reattaches is a result of the intermittency.

Theory

Transition Model. The transition model used in the current work is an adaptation of the model developed by Johnson and Ercan [5] for attached flow. This method modelled the physics of the transition process rather than relying on experimental correlations such as that due to Abu-Ghannam and Shaw [6]. Johnson and Ercan divided the transition process into three stages. In the first stage, velocity fluctuations developed in the near wall region of the pretransitional laminar boundary layer. This process is governed by the receptivity of the boundary layer to the free-stream turbulence. Once these fluctuations reach a critical amplitude the second stage commences where individual turbulent spots are generated, and in the final third stage, the turbulent spots grow in size and merge until the entire flow field becomes turbulent. Johnson and Ercan modeled the receptivity of the pretransitional boundary layer to free-stream turbulence using the gain parameter, which was obtained from hot-wire experimental data. Recently though, Johnson [7,8] developed a technique for determining the gain numerically, and it is this approach that has been used in the current work.

Figure 1 shows the gain computed for a zero pressure gradient boundary layer for three Reynolds numbers. These curves indicate that the boundary layer is most receptive to low streamwise frequencies and that this receptivity increases with the boundary layer Reynolds number. Gain calculations were performed for a full range of adverse pressure gradients from $\lambda=-30$ to 0 at increments of 3 and Re_θ values of 25, 50, and 100. The Reynolds number based on the grid to the leading-edge distance was assumed to be 200,000. Figure 2 shows how the gain increases by about an order of magnitude for adverse pressure gradients typical of separated flow conditions. Johnson and Ercan [5] fitted their gain curves with Eq. (1)

$$G=\frac{a}{C_f^c+(2\pi bf/u_{yo})^2} \tag{1}$$

where a, b, and c were empirical constants.

This equation is unsuitable for separated flows however as C_f is negative. For this reason this equation was replaced in the current work by

$$G=\frac{a(H)}{\mathrm{Re}_\theta^{-b}+c(H)\Omega_X^2} \tag{2}$$

where $a(H)=(7.07H^2-0.647H+18.0)\times10^{-5}$, $b=2.3$, and $c(H)=0.0625H-0.116$ were found to provide good fits to the predicted gain data, as shown in Fig. 1 and 2. A Pohlhausen velocity profile

Contributed by the International Gas Turbine Institute (IGTI) of THE AMERICAN SOCIETY OF MECHANICAL ENGINEERS for publication in the ASME JOURNAL OF TURBOMACHINERY. Paper presented at the International Gas Turbine and Aeroengine Congress and Exhibition, Vienna, Austria, June 13–17, 2004, Paper No. 2004-GT-53353. Manuscript received by IGTI, October 1, 2003; final revision, March 1, 2004. IGTI Review Chair: A. J. Strazisar.

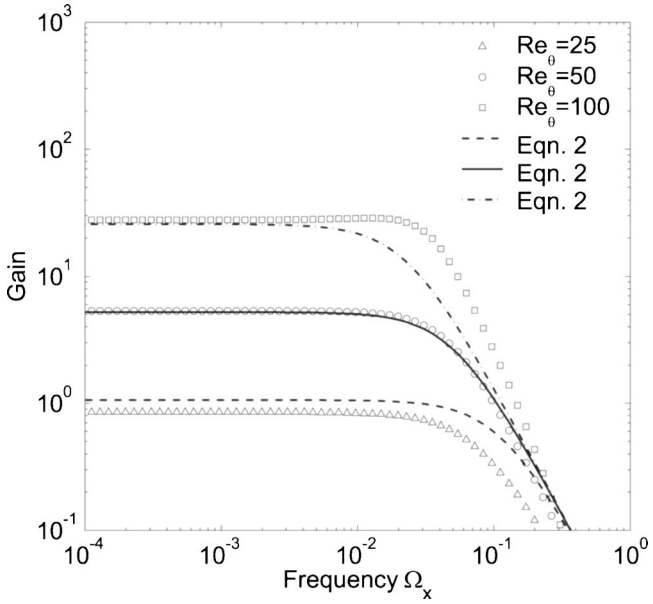

Fig. 1 Predicted near-wall gains for a boundary layer with no streamwise pressure gradient

$$\frac{u}{U} = 2\left(\frac{y}{\delta}\right) - 5\left(\frac{y}{\delta}\right)^4 + 6\left(\frac{y}{\delta}\right)^5 - 2\left(\frac{y}{\delta}\right)^6 + \frac{\lambda}{6}\left(\frac{y}{\delta}\right)\left(1 - \frac{y}{\delta}\right)^3 \quad (3)$$

was assumed in the gain calculations and, hence, the shape factor H is given by

$$H = \frac{\frac{2}{7} - \frac{\lambda}{120}}{\frac{985}{9009} - \frac{2\lambda}{1485} - \frac{\lambda^2}{9072}} \quad (4)$$

The overall turbulence level in the near-wall region is now evaluated using the Johnson and Ercan [5] procedure to obtain

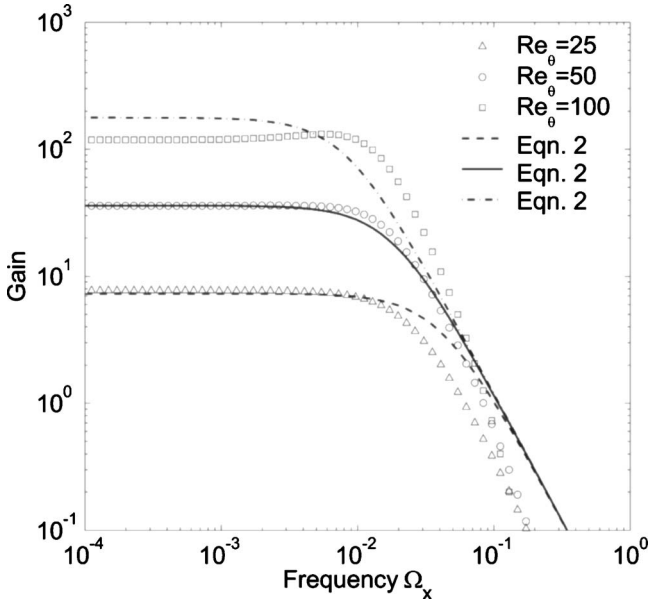

Fig. 2 Predicted near-wall gains for a boundary layer with a strong streamwise pressure gradient (H=7.7)

$$\frac{\mathrm{Tu}_{NW}}{\mathrm{Tu}} = \frac{a(H)\mathrm{Re}_\theta^b}{B+1}\left(\frac{B}{2}+1\right)^{0.5} \quad (5)$$

where $B=[c(H)\mathrm{Re}_\theta^b]^{0.5}(\delta/L)$ and L is the free-stream turbulence length scale. The near-wall length scale is evaluated following Johnson and Ercan from Eq. (2)

$$\frac{2}{\pi}\frac{B}{B^2-1}\left[\frac{1}{4}\sin(2\phi)+\frac{\phi}{2}\right] + \frac{2}{\pi(B^2-1)^2}\left[\tan^{-1}\left(\frac{L}{\ell}\right) - B\phi\right] = \frac{B+2}{4(B+1)^2} \quad (6)$$

where $\phi=\tan^{-1}(BL/\ell)$. The near-wall length scale determines the minimum distance between turbulent spot initiation sites, as described by Johnson and Ercan [5]. Fasihfar and Johnson's [9] criterion for turbulent spot initiation is used in the original transition model. This criterion states that a turbulent spot is generated each time the near-wall velocity drops below 50% of the local time mean velocity. This criterion cannot be used, however, for flows close to the separation point where the time mean velocity close to the wall will be very close to zero. The criterion was therefore modified following Johnson [8] by defining the near-wall location as the point below which the flow rate is equal to that in the laminar sublayer, which is assumed to extend to $y^+=10$. This definition is effectively identical to that used by Johnson and Ercan [5] for attached flows, but for separated flows the near-wall position moves to a location just outside the separation bubble and, hence, the local time mean velocity remains positive throughout the flow. Justification for this approach is provided by the experiments of D'Olivio et al. [10], which showed that turbulent spots generated upstream of a separation bubble do not enter the bubble, but are convected over the top of it. The position of the base of the spots is therefore consistent with the near-wall location defined here. The procedure used to compute the intermittency is identical with the distributed breakdown model for turbulent spot generation used by Johnson and Ercan [5]. The spot generation rate is given by

$$\frac{dN}{dx} = \frac{(1-\gamma)\sigma}{U\tan\alpha}\int_0^x PU\left(\frac{z}{\ell}\right)^3 dx - \frac{2N^2\tan\alpha}{1-\gamma} \quad (7)$$

where P is the probability that a trough in the near wall velocity signal will initiate a spot. The signal level is normally distributed and hence the probability is given by

$$P = \frac{1}{4}\left(\frac{1}{2\pi}\right)^{0.5}\int_\infty^{u/\overline{u'}}\left(\frac{u}{\overline{u'}}\right)^2\exp\left[-\frac{1}{8}\left(\frac{u}{\overline{u'}}\right)^2\right]d\left(\frac{u}{\overline{u'}}\right) \quad (8)$$

is the number of troughs per integral wavelength given by the z correlation

$$z = 3.2 - 2.5\exp\left(-0.043\frac{\ell}{L}\right) \quad (9)$$

The first term on the right-hand side of Eq. (7) represents the generation of new spots and the second term, the merging of existing spots. The intermittency increases due to the spreading of the spots and is therefore given by Eq. (10)

$$\frac{d\gamma}{dx} = 2N\tan\alpha \quad (10)$$

Johnson and Ercan [5] demonstrated that the distributed breakdown model described by these equations is consistent with the concentrated breakdown model where the probability integral in Eq. (7) would change from zero to a constant at the start of transition location. In the current work, the spot-spreading half-angle α and propagation parameter σ are given by Gostelow's correlations [11]

$$\alpha = 4 + \left(\frac{22.14}{0.79 + 2.72\, e^{47.63\lambda_\theta}} \right) \tag{11}$$

$$\sigma = 0.03 + \left(\frac{0.37}{0.48 + 3.0\, e^{52.9\lambda_\theta}} \right) \tag{12}$$

The original Johnson and Ercan transition model for attached flows has therefore been modified in four ways:

1. Numerically derived values for the gain are used to model the receptivity process in place of the original empirical values.
2. The equations used to fit these gain values are functions of both Re_θ and H rather than just Cf.
3. The criterion for spot initiation is modified to allow for flow reversal within the separation bubble.
4. The Gostelow spot propagation correlations are used.

It should be noted that these changes have been made in such a way that the model will give virtually identical results to the original for attached flows. The numerical procedure in boundary layer integral techniques, such as the one used for attached flows by Johnson and Ercan [5], it is assumed that the boundary layer has a negligible effect on the free-stream flow. When boundary layer separation occurs, the large increase in boundary layer displacement thickness has the effect of reducing the adverse pressure gradient in the free stream. As this strong interaction between the boundary layer and inviscid free-stream flow field is not computed with a simple boundary layer integral technique, a different approach was adopted in the current work. The first step was to compute the laminar flow field using the Fluent CFD software. The predicted laminar boundary layer parameters were then used to predict the receptivity of the boundary layer and the development of the intermittency from the transition model equations presented in the previous section. The transitional boundary layer parameters were finally computed using an intermittency weighted average of the laminar and turbulent values in a manner similar to that used by Johnson and Ercan [5]. The turbulent boundary layer integral properties are determined from the equations of Ludwieg and Tillmann [12]

$$C_f = 0.246 \times 10^{-0.678H}\, \mathrm{Re}_\theta^{-0.268} \tag{13}$$

and Göksel [13]

$$\ln\left(\frac{H}{H-1} \right) = 0.1016 \ln \mathrm{Re}_\theta + 0.4822 \tag{14}$$

Results

In the current work, the transition model has been validated using the ERCOFTAC T3L test cases [14]. The T3L blade consists of a flat plate of thickness 10 mm, which has a semi-circular leading edge. A separation bubble forms close to the leading edge, the length of which depends both on the free-stream velocity and turbulence level. Figure 3 shows how an increase in the free-stream turbulence level leads to a reduction in the separation bubble length due to a more rapid transition process. Figure 4 shows the Fluent predictions for laminar flow at free-stream velocities of 2.5 and 5 m/s. For laminar flow, the flow is reluctant to reattach resulting in a long bubble. This length also increases with the velocity U and, hence, with the Reynolds number.

Figure 5 shows the results when the Fluent laminar prediction is combined with the transition model for the highest free-stream turbulence level of 5.7%. Separation occurs at $x=7.4$ mm and is virtually unaltered by transition, which commences ($\gamma=1\%$) at $x=6.9$ mm. Laminar reattachment does not occur until $x=84$ mm, whereas the transitional bubble reattaches at $x=24$ mm, when transition is nearing completion. Two predicted shape factor curves are shown in Fig. 5. The "true H" values are computed using the full profile results, including those within the reversed flow zone, whereas the H values for the second curve are computed omitting all the data points in the reversed flow zone excepting the zero velocity point on the wall. This is the method used to calculate H for the hot-wire experiments, where it is impossible to determine the flow direction. This correction has a negligible effect for shape factors less than 5, but above this value H can be significantly reduced. This correction brings the predicted shape factors much closer to the measured values. A similar observation was made by Vicedo et al. [15] in their predictions of these test cases. For the remaining predictions, only the corrected shape factors are plotted.

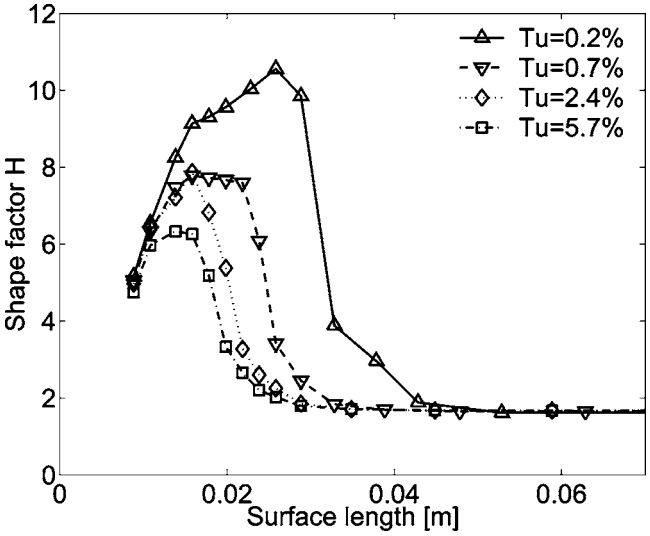

Fig. 3 ERCOFTAC T3L transitional separation bubbles for a free-stream velocity of 5 m/s

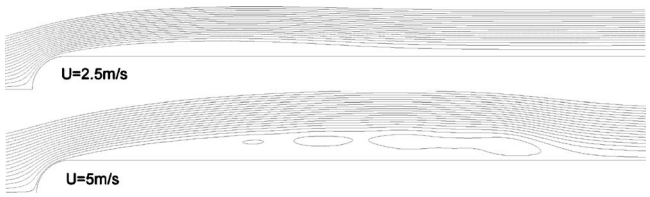

Fig. 4 Predicted streamlines for laminar flow using Fluent

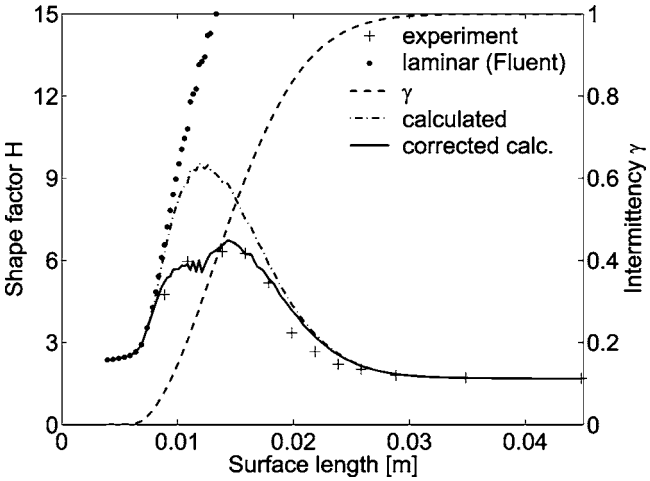

Fig. 5 Transitional separation bubble results for a free-stream velocity of 5 m/s and a turbulence level of 5.7%

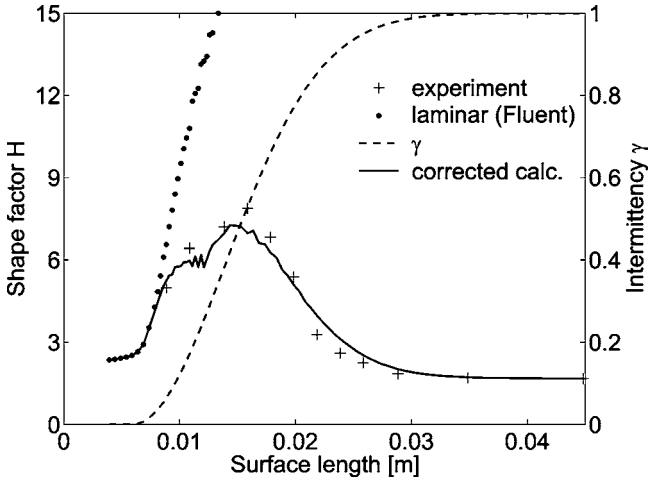

Fig. 6 Transitional separation bubble results for a free-stream velocity of 5 m/s and a turbulence level of 2.4%

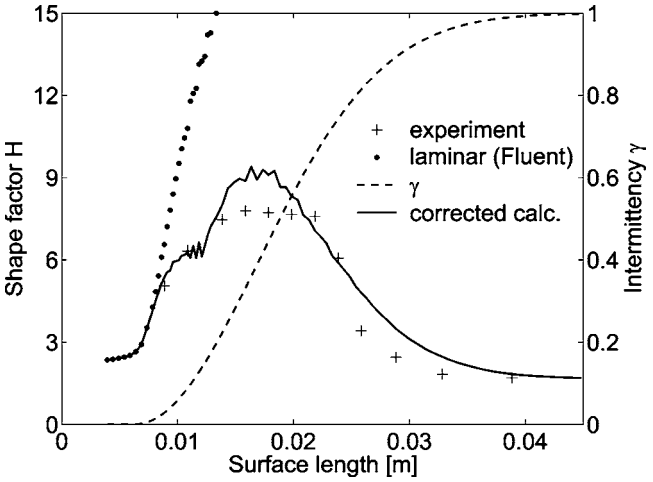

Fig. 8 Transitional separation bubble results for a free-stream velocity of 5 m/s and a turbulence level of 0.7%

When the free-stream turbulence level is reduced to 2.4%, the shape factors within the transition bubble increase with an associated increase in the bubble length. These changes are predicted accurately by the transition model as shown in Fig. 6. The end of transition location (γ=99%) only moves downstream from x =28.4 mm to 30.7 mm, despite the more than twofold reduction in turbulence level. This is because the near-wall gain levels rise very rapidly in the separation region to a level where the spot production rate is close to its theoretical maximum at both of these free-stream turbulence levels. Figure 7 illustrates this, as there is little difference between the number of turbulent spots in these two cases.

A further threefold decrease in free-stream turbulence level to 0.7% again increases the shape factor values within the bubble and increases the bubble length as shown in Fig. 8. Separation now occurs just prior to the start of transition, and the transition zone continues for a significant distance downstream of reattachment. The number of turbulent spots during the transition process is also reduced in Fig. 7 compared to the higher free-stream turbulence levels. In this case the predicted bubble is longer than the measured one, and the predicted shape factors are also too high. The difference between the predicted and measured bubble length is, however, only about 3 mm, or about 10% of the overall bubble length. The reason for this discrepancy is more apparent in the results for the lowest free-stream turbulence level of 0.2%, shown in Fig. 9. In this case the predicted bubble length is much longer than the measured one. The reason for this is that the free-stream turbulence level is now well below the threshold of 1%, where natural transition rather than bypass transition is regarded as dominant. The current transition model does not account for the Tollmien Schlichting waves generated in natural transition, and these will dominate the transition in this case and are also likely to influence the case shown in Fig. 8 for a free-stream turbulence level of 0.7%. Nevertheless, the predicted transition bubble length in Fig. 8 is significantly shorter than that for the laminar bubble.

The final case considered is for the lower free stream velocity of 2.5 m/s for the intermediate turbulence level of 2.4%. For this case gain curves for a Reynolds number based on grid to leading edge distance of 100,000 was used for consistency. The corresponding coefficients in Eq. (2) were $a(H)=(17.5H^2+120H-61.9)\times10^{-5}$, $b=2.0$, and $c(H)=0.0838H-0.111$. A comparison of the results in Fig. 10 for 2.5 m/s with those in Fig. 6 for 5 m/s shows that when the free-stream velocity doubles, an approximately similar increase in bubble length occurs. The current transition model predicts this trend well, although the predicted shape factors in the separation bubble are slightly lower than measured.

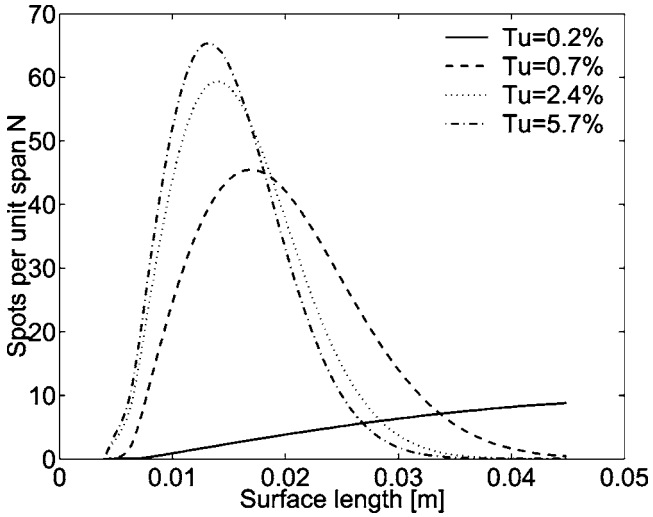

Fig. 7 Variation in the number of turbulent spots through transition for a free-stream velocity of 5 m/s

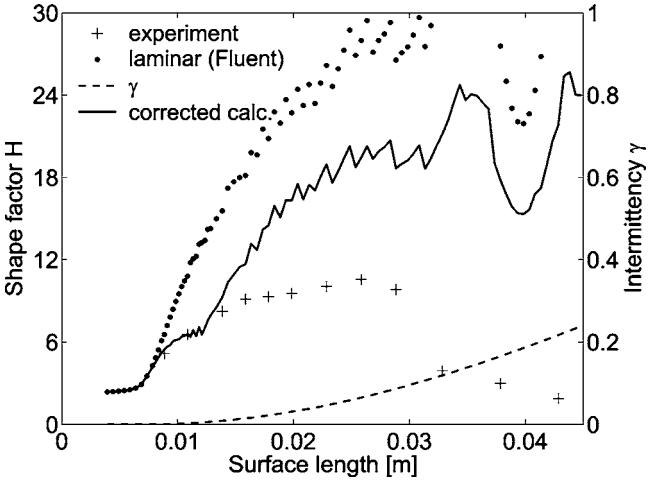

Fig. 9 Transitional separation bubble results for a free-stream velocity of 5 m/s and a turbulence level of 0.2%

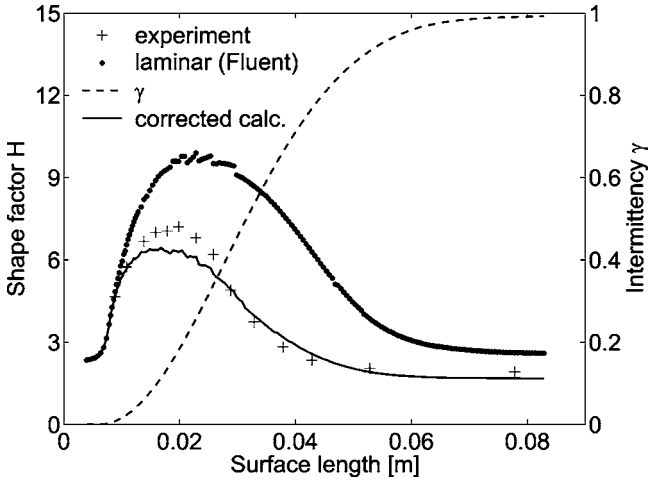

Fig. 10 Transitional separation bubble results for a free stream velocity of 2.5 m/s and a turbulence level of 2.4%

Conclusions

1. The methodology from the Johnson and Ercan [5] attached flow transition model has been developed to produce a separated flow transition model. The new model can be used to predict the transition of both attached and separated flows.
2. If the velocities within the reversed flow region are assumed to be negligible, as is frequently the practice for hot-wire results, then the computed shape factors will be reduced by up to 50% for cases where the shape factor exceeds 5.
3. For free-stream turbulence levels within the bypass transition regime (above 1%), the model accurately predicts the separation bubble length and shape factor evolution through transition.
4. As the free-stream turbulence level decreases below 1%, the length of the separation bubble becomes increasingly over predicted.

Further Work

1. Experimental work is in progress to obtain gain values for separated flows. These results will be used to validate the numerically derived values used in the current work.
2. The coefficients in Eq. (2) are dependent on the Reynolds number based on grid to leading-edge distance. Work is in progress to establish this dependence over the full range of shape factors such that the transition model can be used to accurately predict transition in both attached and separated flow regimes.

Nomenclature

a, b, c = empirical constants
$a(H), c(H)$ = empirical functions in Eq. (2)
C_f = skin friction coefficient
f = streamwise fluctuation frequency
$G(=uy0\prime\delta/[2(U\prime 2+V\prime 2)0.5])$ = gain
H = boundary layer shape factor
ℓ = near wall turbulence length scale
L = free stream turbulence length scale
N = number of spots per unit blade span
P = probability that a signal trough will induce a spot
Re_θ = momentum thickness Reynolds number
Tu_{NW} = free-stream turbulence level
Tu_{NW} = near-wall turbulence level
u = local time mean velocity
$\underline{u'}$ = local instantaneous velocity
$\overline{u'}$ = local rms velocity
u_{y0} = velocity gradient at the wall
U = free stream velocity
U' = free stream fluctuation velocity
V' = normal fluctuation velocity
x = distance measured along the blade surface
y = wall normal co-ordinate
γ = intermittency
δ = boundary layer displacement thickness
γ = pohlhausen pressure gradient parameter
Ωx $(=2\pi f\delta/U)$ = dimensionless streamwise frequency

References

[1] Schulte, V. and Hodson, H. P., 1998, "Unsteady Wake-Induced Boundary Layer Transition in High Lift LP Turbines," ASME J. Turbomach., **120**, pp. 28–35.
[2] Roberts, B., 1975, "The Effect of Reynolds Number and Laminar Separation on Axial Cascade Performance," ASME J. Eng. Power **97**, pp. 261–274.
[3] Mayle, R. E., 1991, "The Role of Laminar-Turbulent Transition in Gas Turbine Engines," ASME J. Turbomach. **113**, pp. 509–537.
[4] Hatman, A., and Wang, T., 1999, "A Prediction Model for Separated Flow Transition," ASME J. Turbomach. **121**, pp. 594–602.
[5] Johnson, M. W., and Ercan, A. H., 1999, "A Physical Model for Bypass Transition," Int. J. Heat Fluid Flow **20**, pp. 95–104.
[6] Abu-Ghannam, B. J., and Shaw, R., 1980, "Natural Transition of Boundary Layers - The Effects of Turbulence, Pressure Gradient and Flow History," J. Mech. Eng. Sci. **22**, pp. 213–228.
[7] Johnson, M. W., 2002, "Predicting Transition Without Empiricism or DNS," ASME J. Turbomach. **124**, pp. 665–669.
[8] Johnson, M. W., 2003, "A Receptivity Based Transition Model," ASME Paper No. 2003-GT-30873.
[9] Fasihfar, A., and Johnson, M. W., 1992, "An Improved Boundary Layer Transition Correlation," ASME Paper No. 92-GT-245.
[10] D'Olivio, A., Harkins, J. A., and Gostelow, J. P., 2001, "Turbulent Spots in Strong Adverse Pressure Gradients, Part 1 - Spot Behaviour," ASME Paper No. 2001-GT-0194.
[11] Gostelow, J. P., Melwani, N., and Walker, G. J., 1996. "Effects of Streamwise Pressure Gradient on Turbulent Spot Development," ASME J. Turbomach. **118**, pp. 737–743.
[12] Ludwieg, H., and Tillmann, W., 1950, "Investigation of the Wall Shear stress in Turbulent Boundary Layers," NACA TN1284.
[13] Göksel, O. T., 1968, "Some Effects of Spherical Roughness Upon the Incompressible Flow of a Boundary Layer With Zero Pressure Gradient," Ph.D. thesis, University of Liverpool.
[14] Coupland, J., 1995, "Transition Modelling for Turbomachinery Flows," ERCOFTAC Bulletin No. 24, pp 5–8.
[15] Vicedo, J., Vilmin, S., Dawes, W. N., and Savill, A. M., 2003, "Intermittency Transport Modelling of Separated Flow Transition," ASME Paper No. GT-2003-38719.

Simultaneous Heat Flux and Velocity Measurements in a Transonic Turbine Cascade

D. G. Holmberg
Building Environment Division,
BFRL, NIST,
Gaithersburg, MD 208 99-8631

T. E. Diller
Mechanical Engineering Department,
Virginia Tech,
Blacksburg, VA 24061-0238

The gas turbine engine combustor generates turbulence that increases heat transfer on downstream turbine blades, but the mechanisms of that heat transfer are not fully understood. In this work, simultaneous time-resolved surface heat flux and velocity measurements have been made at three locations on the pressure surface of a high-turning transonic airfoil. Grids were used upstream of the linear turbine cascade to produce free-stream turbulence with two different inlet length scales, but the same turbulence intensity. High-frequency response instrumentation was used to obtain both steady and unsteady measurements. Results show that the time-averaged heat transfer is larger for the flow with the smaller integral length scale. Frequency-domain analysis demonstrates coherence between the fluctuations of heat flux and velocity over a broad range of frequencies. This is a direct indication that free-stream turbulent eddies penetrate completely through the boundary layer to the surface. [DOI: 10.1115/1.1860576]

Introduction

Gas turbine engine performance is a function of the turbine thermal characteristics and control of turbine heat transfer. The role of free-stream turbulence has been shown to be important in understanding the heat transfer from the hot gas flowing over the turbine blades. The combustor imparts high turbulence levels to the flow, and the upstream blades add shocks and flow unsteadiness. For research a stationary cascade without upstream blades and rotation eliminates the usual shocks and wakes, which allows a clearer view of the interaction of free-stream turbulence with surface heat flux. Use of a transonic, high-turning blade gives a more realistic look at turbulence effects than is possible with a flat plate.

Previous studies of the effects of free-stream turbulence on boundary layer heat transfer have included experimental studies with geometries ranging from flat plates to cylinders and turbine blades with a variety of flow conditions. A number of empirical correlations have been developed predicting the increase in heat transfer as a function of the turbulence intensity and sometimes turbulent length scale. Some of the better known include those by Ames [1], Dullenkopf and Mayle [2], and Van Fossen et al. [3] for predicting the time-averaged heat transfer.

Presently, there are limited time-resolved heat transfer data on turbine blades, and of the work done with time-resolved heat flux, very few measurements include simultaneous velocity information. Two such experiments have been reported on flat plates. Moss and Oldfield [4] used a single-wire probe traversed above thin-film gages on a flat plate in a short duration flow to produce heat flux and velocity correlations. They show that heat flux is apparently controlled by the u' fluctuating velocity field, and primarily by large free-stream eddies reaching deep into the boundary layer. This agrees with correlations based on mean heat transfer showing heat flux scaling on u' for high free-stream turbulence [5]. Work by Holmberg and Pestian [6] in a flat plate wall-jet facility measured simultaneous u', v', q', and T' and also showed time-resolved heat flux fluctuations matching the u' fluctuating velocity field. The present work presents simultaneous u' and q' measurements on a high turning turbine blade at realistic transonic flow conditions. High-frequency instrumentation is used to investigate the details of the flow and surface phenomena.

Facilities and Instrumentation

The Virginia Tech Cascade Tunnel is a long-duration blowdown wind tunnel with inlet air heated via a regenerator-type heater [7]. The cascade used in this work uses small-chord (4.5 cm), high-turning blades that operate at an engine-similar Reynolds number. At the inlet, the chord Reynolds number is 6.6×10^5 and the Mach number is 0.36. The Mach number at the blade exit is 1.25. The extent of the end-wall boundary layer was observed by flow visualization to have little effect on the mainstream flow. Work in this facility is focused on understanding the unsteady interactions of passing shocks and turbulence on blade heat transfer and pressure.

In addition to the baseline case ($Tu_u=0.3\%$), two turbulence conditions were generated using round-wire, square-mesh screens (G2 is 0.9 mm diam and 4.2 mm spacing, G4 is 3.1 mm diam and 19.0 mm spacing) set at the same angle as the blade inlet row angle, 59 deg from vertical. These two screens were set at different upstream locations in order to produce an equivalent blade inlet turbulence intensity of $Tu_u=5\%$ with differing integral length scales ($\Lambda_x=0.9$ mm for G2 set at 3 cm upstream of the blade and $\Lambda_x=2.7$ mm for G4 set at 12 cm upstream.). This inlet free-stream turbulence (FST) was found to be nearly isotropic.

For the present work the blades were instrumented with surface heat flux gages located near the midspan of the blade. Single-wire velocity measurements were made in the flow above these gages. Three blade axial measurement locations were used as shown in Fig. 1. Sensors PS1, PS2, and PS3 are located at 0.43, 1.47, and 2.46 cm from the leading-edge stagnation point on the pressure side (9, 30, and 50% chord), respectively. The heat flux gages are Vatell model HFM-6 inserted into the blade. The HFM actually consists of two thin-film sensors sputtered on an aluminum-nitride substrate. The substrate properties have been measured as $k=165$ W/m K, $C=713$ J/kg K, and $\rho=3290$ kg/m^3, which are close to those of the aluminum blades. Because the value of k and $\sqrt{k\rho C}$ are within approximately 5% of the values for the aluminum blade, the thermal disruption of the steady and transient conduction resulting from the presence of the gage is minimal. Because of this careful matching of properties, the "heat island" effect has been eliminated. The sensor is flat, however, which causes a small surface discontinuity at the edges that was

Contributed by the Turbomachinery Division of THE AMERICAN SOCIETY OF MECHANICAL ENGINEERS for publication in the ASME JOURNAL OF TURBOMACHINERY. Manuscript received July 8, 2004, final revision, August 17, 2004. Editor: D. Wisler.

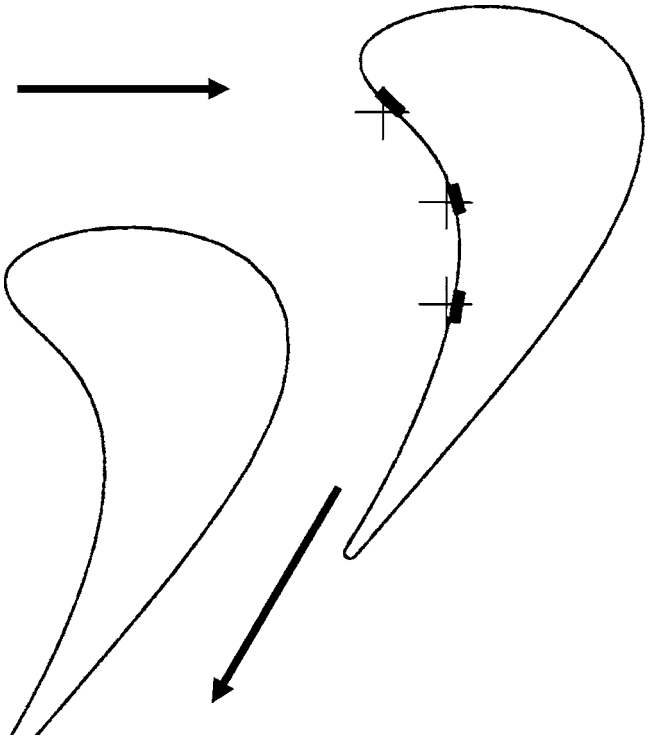

Fig. 1 Heat flux sensor and hot-wire measurement locations on the blade. Arrows indicate flow direction at inlet and exit of blade row.

smoothed with filler. The main sensor is a thermopile (HFS) consisting of 180 pairs of thermocouples sputtered above and below a thin thermal resistance layer (less than 2 μm thick), giving a voltage directly proportional to the heat flux [8]. Surrounding this is an outer ring, which is a thin-film resistance temperature sensor (RTS) to measure surface temperature.

The HFS calibration was performed by two methods. A radiation calibration was done by the manufacturer prior to and again following the experiments. This was checked during testing by means of an in situ calibration procedure that utilizes the tunnel transient start data and the simultaneous surface temperature measurement. This method was used for each individual test and is documented by Holmberg and Diller [8]. These calibrations showed excellent consistency, with only 5% variation in both the HFS heat flux sensitivity and temperature sensitivity over the entire course of testing. The estimated precision uncertainty of the heat flux measurements was 3.0% with an additional uncertainty in the calibration of 5%.

The hot wire used was a single-wire probe with the wire aligned spanwise above the blade surface. The probe strut is a flattened 1 mm diam tube, with 3 mm prongs that extend over the HFM gage, and a wire length of approximately 1 mm. Calibration of these probes was performed in situ, with an uncertainty on absolute velocity for the passage measurement of approximately 10% [9]. The estimated precision uncertainty of the velocity measurements was 2.3%.

The frequency response of the HFM-6 (both the HFS and RTS) has been demonstrated to be above 100 kHz [8]. The probes (hot wire and HFS) have spatial resolution limitations due to their size relative to the flow and cannot see scales less than the separation distance between the surface and the wire (in the case of coherence measurements). Turbulent eddies smaller than the probe size (1 mm for the hot wire, 3 mm diam HFS) are significantly attenuated. The spatial resolution issue was carefully examined and reported by Holmberg [9]. For the physically larger HFS, estimates of attenuation showed one-third of the spectral energy would be lost at 10 kHz and 75% at 20 k Hz. Attenuation due to spatial resolution results in undervalued intensities based on fluctuating quantities q' and u', but comparisons between data sets can still be made fairly. Coherence magnitude is limited to lower frequencies and distorted proportional to the energy spectrum attenuation. However, measured coherence magnitude still reveals turbulent activity as a function of frequency, even if attenuated at higher frequencies, and coherence phase (time shift) is unaffected.

Mean and Integral Results

The time-resolved velocity and heat flux can be decomposed into mean and fluctuating components. The rms of the signals is normally calculated from the time series

$$u(t) = \bar{u} + u', \quad q(t) = \bar{q} + q' \tag{1}$$

with

$$u'_{\text{rms}} = \sqrt{\overline{u'^2}}, \quad q'_{\text{rms}} = \sqrt{\overline{q'^2}} \tag{2}$$

and

$$Tu_u = \frac{u'_{\text{rms}}}{\bar{u}}, \quad Tu_q = \frac{q'_{\text{rms}}}{\bar{q}} \tag{3}$$

The rms of the fluctuating components u'_{rms} and q'_{rms} can also be calculated from the integral of the power spectral density

$$u'^2_{\text{rms}} = \int_0^\infty E_u(f)df, \quad q'^2_{\text{rms}} = \int_0^\infty E_q(f)df \tag{4}$$

The integral length scale (Λ_x) is a measure of where the energy is in this spectrum and has been calculated directly from the average energy spectrum

$$\Lambda_x = u_\infty T_x, \quad \text{and} \quad T_x = \sum_{\tau=0}^{\tau|_{R(\tau=0)}} R_{xx}(\tau)\Delta t \tag{5}$$

where the autocorrelation is a cosine transform of the spectrum [10]

$$R_{xx}(t) = \frac{1}{u_\infty{}^2}\int_0^\infty E(f)\cos(2\pi ft)df \tag{6}$$

Mean flow velocity and integral parameters ($u'_{\text{rms}}, Tu_u, \Lambda_x$) based on the energy spectrum are presented in Table 1 for the hot-wire measurements at different distances above the blade surface. Mean heat flux and integral parameters (Tu_q) are given in Table 2 where the heat transfer coefficient is calculated from the directly measured $\bar{q}$ and the surface to adiabatic wall temperature difference, $T_{aw} - T_s$. The data in Table 2 show that at all sensor locations the heat transfer is higher for Grid 2. This is true despite a significantly higher local turbulence intensity measured for Grid 4. This is attributed to the smaller integral length scale Λ_x (corresponding to higher frequency turbulence) for Grid 2 than for Grid 4.

In Table 1 the turbulent velocity u'_{rms} is seen to decay continuously through the passage (PS1-PS2-PS3). G4 intensity is seen to decay more rapidly than G2 from PS1 to PS2 because of the constriction of larger scale G4 turbulence. A large decrease in scale is seen from PS2 to PS3, attributed to passage constriction and flow acceleration. This corresponds to a general decrease in coherence magnitude.

The progression of heat flux fluctuations along the pressure side (Table 2) contrasts sharply to that of u'_{rms} in Table 1. Although u'_{rms} is seen to decrease continuously, q'_{rms} instead increases continuously. This increase is very large for G0 and G4 from PS2 to PS3, but the energy causing this increase does not correlate with the flow energy.

Table 1 Summary of simultaneous velocity and heat flux data

	y_{wire} (mm)	$\bar{u}$ (m/s)	u'_{rms} (m/s)	Tu_u (%)	Λ_x (mm)	Coherence mag. peak	Freq. of peak (kHz)
PS1 G0	0.2	93	2.1	2.3	4.5	0.29	4.9
	0.4	93	2.6	2.8	3.7	0.56	5.9
	1.0	101	2.2	2.2	3.7	0.36	5.9
G2	0.2	91	5.3	5.8	2.1	0.45	3.9
	0.4	93	4.5	4.9	2.0	0.45	6.4
	1.0	104	4.7	4.6	1.5	0.31	4.4
G4	0.2	91	7.2	7.9	3.4	0.48	2.0
	0.4	92	6.2	6.7	3.9	0.57	2.0
	1.0	97	6.9	7.2	3.9	0.49	1.0
PS2 G0	0.2	85	2.6	3.1	3.2	0.31	0.0
	0.4	88	2.2	2.5	2.9	0.43	0.0
	1.0	90	2.3	2.5	3.5	0.36	0.0
G2	0.2	87	4.7	5.4	2.0	0.46	2.9
	0.4	92	5.0	5.4	2.6	0.33	5.4
	1.0	92	4.3	4.7	2.6	0.14	3.4
G4	0.2	86	5.5	6.5	3.4	0.52	2.0
	0.4	89	5.8	6.5	3.8	0.48	2.9
	1.0	91	5.1	5.6	3.7	0.38	2.0
PS3 G0	0.2	127	1.6	1.2	7.5	-	-
	1.0	126	1.4	1.1	7.2	-	-
G2	0.2	125	4.1	3.3	1.3	0.26	5.9
	1.0	126	3.0	2.4	1.6	0.04	6.8
G4	0.2	113	6.0	5.3	4.0	0.02	2.4
	1.0	127	3.9	3.1	2.5	0.02	4.9

Frequency Domain Results

The power spectral density (PSD) of the hot-wire velocities at 1.0 mm above the blade surface at PS1 for all grid cases is shown in Fig. 2. Comparing the energy of the different grids, G4 has much more energy at low frequencies and higher energy overall as shown by u'_{rms} in Table 2, while G2 has more energy at higher frequencies. The corresponding heat flux spectra at PS1 are shown in Fig. 3. The difference in energy levels at low frequencies is actually very large, in agreement with the large variation in fluctuating energy in the free stream seen in Fig. 2.

Table 2 Summary of heat flux data (without hot-wire present)

	h (W/m^2 K)	Tu_q (%)	$\Delta h/h$ (%)
PS1 G0	800	5.0	-
G2	1085	6.0	35.6
G4	970	8.5	21.3
PS2 G0	820	9.5	-
G2	930	8.9	13.4
G4	875	11.0	6.7
PS3 G0	845	19.9	-
G2	1005	10.8	18.3
G4	925	33.5	9.5

There are some differences in the spectral distributions between Figs. 2 and 3. At 10 kHz in the PS1 velocity spectra, no difference is seen between G2 and G4. However, in the heat flux spectra at 10 kHz, there is both a higher mean energy level and a significant peak for G4 above G2. The frequencies of maximum energy for all of the spectra at all locations are generally near 1 kHz.

The coherence magnitudes for PS1-PS2 are shown in Figs. 4 and 5. Coherence is a frequency domain representation of the correlation between two simultaneously sampled signals, defined as the square of the averaged cross-spectrum divided by the product of each averaged power spectrum

$$\text{Coherence} = \frac{\overline{S_{xy}(f)^2}}{\overline{|S_{xx}||S_{yy}|}} \tag{7}$$

A significant coherence magnitude indicates two independent signals have energy that correlates in time at some frequency with a phase that varies independently of the magnitude. If no coherence is measured, this indicates that no turbulent flow structures of a scale larger than the wire distance above the surface are influencing heat flux fluctuations. Comparison of coherence levels at different distances of the wire above the surface allows identifying the scales of structures at specific frequencies. For isotropic turbulence the estimated frequency where the spectrum tails off

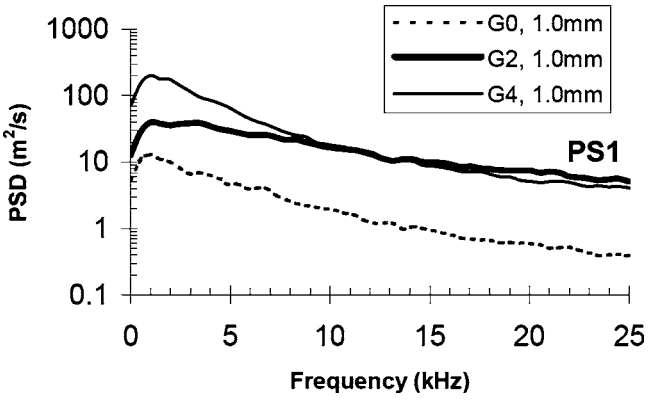

Fig. 2 Velocity energy spectra of flow above PS1 comparing grid turbulence

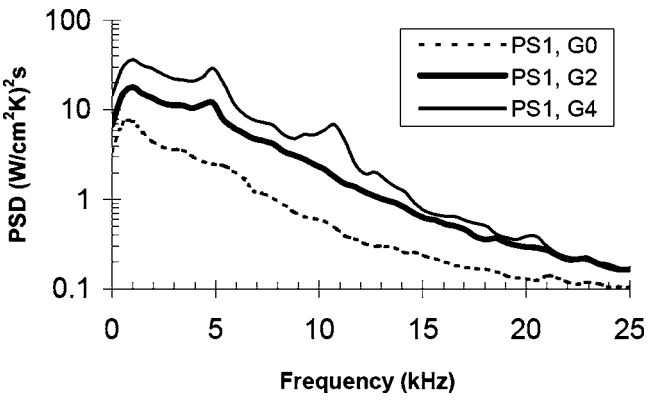

Fig. 3 Surface heat flux spectra (normalized by $T_{aw} - T_s$) at PS1 for three grid conditions (no hot-wire present)

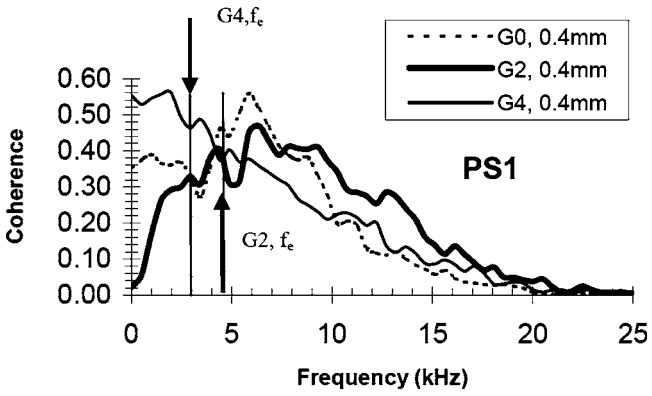

Fig. 4 Coherence magnitude for velocity and heat flux spectra at PS1

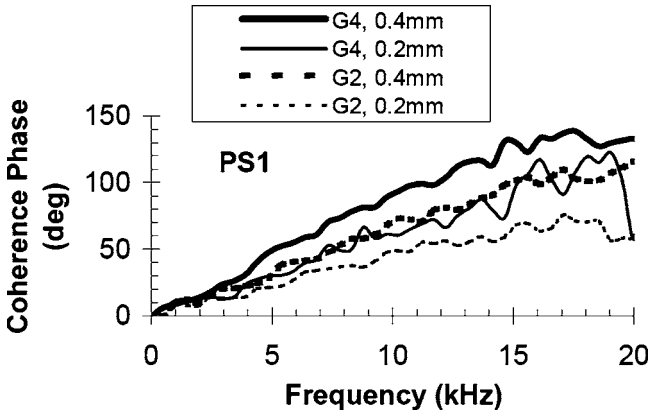

Fig. 6 Phase shift of heat flux response lagging velocity turbulence at PS1

(most energetic frequency) can be related to the integral length scale [10] by $f_e = 3u_\infty/8\pi\Lambda_x$. These frequencies are shown on the coherence plots by arrows with the larger value for the G2 grid and the smaller value for the G4 grid.

The coherence at PS1 for the wire spacing at 0.4 mm is shown in Fig. 4. The coherence magnitudes for the 0.2 and 1.0 mm positions are similar in distribution but slightly lower magnitude. Large values of coherence are demonstrated over a broad range of frequencies. This indicates that the turbulent eddies are reaching all the way through the boundary layer to the surface. In addition, the scale of much of the turbulence is larger than the hot-wire spacing above the heat flux gage, even for the 1 mm spacing. The peak coherence values for both grids are close to the frequencies corresponding to the integral length scales of the turbulence. The peaks are closer together for the PS2 location in Fig. 5, but the coherence for G4 is still at much lower frequencies than for G2. In addition, the coherence is generally not as large or over as large a range of frequencies.

In contrast, the coherence at location PS3 is nearly zero for all situations except for the G2 grid with the hot wire at 0.3 mm above the surface. The large values of Tu_q in Table 2 and the lack of coherence suggest a highly transitional boundary layer at this location.

The coherence phase at PS1 is given in Fig. 6. Phase can be converted to time shift (lag of surface heat flux fluctuations behind passing flow structure at the wire) by dividing phase (deg) by $360f$, where f is the frequency (Hz). As expected, a larger time shift is seen at higher frequencies. The phase shift at the 1.0 mm positions is nearly the same as for the 0.4 mm positions. At PS2 and PS3, the four traces of Fig. 6 track on top of one another with the same trend as seen at PS1. The phase lag is greater, however, reaching 200 deg at 20 kHz at PS2 and 180 deg at 20 kHz at PS3.

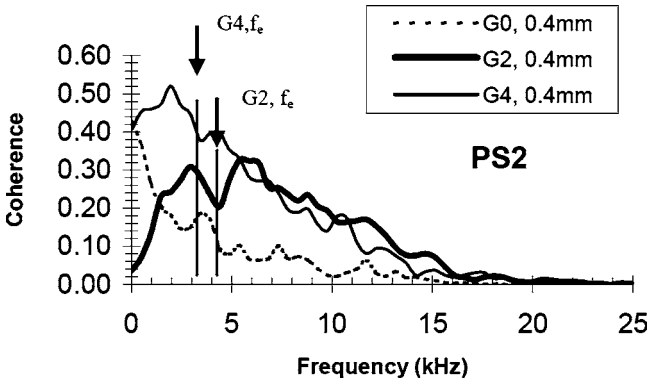

Fig. 5 Coherence magnitude for velocity and heat flux spectra at PS2

Conclusions

At the same turbulence intensity the mean heat transfer at all three locations on the pressure side of the turbine blade was higher for the smaller length scale free-stream turbulence. The high coherence between the velocity outside the boundary layer and the surface heat flux at the first two locations was indicative that the free-stream eddies penetrated through the boundary layer all the way to the surface. An increase of the surface heat flux fluctuations at the last location with little coherence to the velocity signal was an indication of boundary layer transition. Finally, the data provide more evidence of the complex flow situation at different locations on the turbine blade.

Acknowledgment

The support of the US Air Force via the Laboratory Graduate Fellowship program administered through the Southeast Center for Electrical Engineering Education is gratefully acknowledged. The support of the AFOSR, under Grant No. F49620-93-1-0047 and monitored by Dr. Jim McMichael, is also acknowledged.

Nomenclature

$E_u(f)$ = velocity power spectral density, m^2/s
$E_q(f)$ = heat flux power spectral density, $(W/m^2)^2$ s
C = substrate specific heat, J/Kg K
f_e = most energetic frequency = $3u_\infty/8\pi\Lambda_x$, Hz
h = heat transfer coefficient, W/m^2 K
k = substrate thermal conductivity, W/m K
$\bar{q}$ = time-average surface heat flux, W/m^2
q' = fluctuating component of surface heat flux, W/m^2
Tu_u = turbulence intensity based on the local velocity, $u'_{\rm rms}/\bar{u}$
Tu_q = heat flux turbulence intensity, $q'_{\rm rms}/\bar{q}$
$u(t)$ = streamwise velocity component, m/s
u' = fluctuating velocity component, m/s
$\bar{u}$ = time-averaged freestream velocity, m/s
T_{aw} = adiabatic wall temperature, K
T_s = surface temperature, K
Λ_x = integral length scale, m
ρ = density, kg/m^3
τ = integral time scale, s

References

[1] Ames, F. E., 1997, "The Influence of Large-Scale High-Intensity Turbulence

on Vane Heat Transfer," ASME J. Turbomach. **119**, pp. 23–30.
[2] Dullenkopf, K. and Mayle, R. E., 1995, "An Account of Free-Stream-Turbulence Length Scale on Laminar Heat Transfer," Darryl E. Metzger Memorial Session Paper, ASME J. Turbomach. **117**, pp. 401–406.
[3] Van Fossen, G. J., Simoneau, R. J. and Ching, C. Y., 1995, "Influence of Turbulence Parameters, Reynolds Number, and Body Shape on Stagnation Region Heat Transfer," ASME J. Heat Transfer **117**, pp. 597–603.
[4] Moss, R. W., and Oldfield, M. L. G., 1996, "Effect of Free-Stream Turbulence on Flat-Plate Heat Flux Signals: Spectra and Eddy Transport Velocities," ASME J. Turbomach. **118**, pp. 461–467.
[5] Maciejewski, P. K. and Moffat, R. J., 1992, "Heat Transfer with Very High Free Stream Turbulence: Part II—Analysis of Results," ASME J. Heat Transfer **114**, pp. 834–839.
[6] Holmberg, D. G. and Pestian D. J., 1996, "Wall-Jet Turbulent Boundary Layer Heat Flux, Velocity, and Temperature Spectra and Time Scales," ASME, ASME Paper No. 96-GT-529.
[7] Holmberg, D. G., Reid, T., Kiss, T., Moses, H. L., Ng, W. F., and Diller, T. E., 1994, "Effects of Shock Wave Passing in a Transonic Turbine Cascade," ASME, ASME Paper No. 94-GT-179.
[8] Holmberg, D. G., and Diller, T. E., 1995, "High Frequency Heat Flux Sensor Calibration and Modeling," ASME J. Fluids Eng. **117**, pp. 659–664.
[9] Holmberg, D. G., 1996, "A Frequency Domain Analysis of Surface Heat Transfer/Freestream Turbulence Interactions in a Transonic Turbine Cascade," Ph.D. dissertation, Virginia Tech.
[10] Hinze, J., 1975, *Turbulence*, 2nd Edition, McGraw-Hill, New York.

Transition on Concave Surfaces

Antonis Dris

Mark W. Johnson

Department of Engineering,
University of Liverpool,
Liverpool L69 3GH, UK

Boundary layer measurements have been made on the concave surfaces of two constant curvature blades using hot wire anemometry. All the current experiments were performed with negligible streamwise pressure gradient. Grids were used to produce a range of freestream turbulence levels between 1% and 4%. The freestream velocity increases with distance from a concave wall according to the free vortex condition making the determination of the boundary layer edge difficult. A flat plate equivalent boundary layer procedure was adopted, therefore, to overcome this problem. The Taylor–Goertler (TG) vortices resulting from the concave curvature were found to make the laminar and turbulent boundary layer profiles fuller and to increase the skin friction coeffiicent by up to 40% compared with flat plate values. This leads to a more rapid growth in boundary layer thickness. The evolution in the intermittency through transition is very similar to that for a flat plate, however, the shape factors are depressed slightly throughout the flow due to the fuller velocity profiles. For all the current experiments, curvature promoted transition. This was very marked at low freestream turbulence level but remained significant even at the highest levels. It appears that the velocity fluctuations associated with the TG vortices enhance the freestream turbulence resulting in a higher effective turbulence level. A new empirical correlation for start of transition based on this premise is presented. The ratio of end to start of transition momentum thickness Reynolds numbers was found to be approximately constant. [DOI: 10.1115/1.1861914]

Introduction

The majority of boundary layer research has concentrated on flows on flat plates. Reasonably accurate predictive techniques now exist for attached flows [1–3] and much progress has been made over the last few years in understanding and predicting separated flow transition [4,5]. Concave curvature is known [6–8] to modify boundary layer development in the laminar, transitional and turbulent regimes because of the presence of Taylor–Goertler (TG) vortices, which result from the instability induced by the streamline curvature. Generally the spanwise locations of the TG vortices are only fixed for low Goertler numbers (low curvatures). At higher Goertler numbers (above about 20) the vortices meander across the span. TG vortices lead to spanwise variations due to the upwash and downwash regions, such that the boundary layer thickness at the upwash location may be as much as double that at the downwash location [9]. The skin fricton coefficient is also lowered at the upwash and raised at the downwash location, although overall the skin friction is increased because of the increased momentum transport resulting from the vortices. The boundary layer profile is also fuller particularly at the downwash location. This has important implications for the boundary layer profile stability. The upwash boundary layer profile has a less stable shape and is also thicker and hence undergoes transition earlier. Transition at the downwash locations follows quickly though through spreading of turbulence from neighbouring upwash positions.

The objective of the current work was to determine the effect of curvature on boundary layer growth rates and transition. Blades with a constant radius of curvature were chosen for the work for simplicity.

Experimental Arrangements

The measurements were performed on the concave surfaces of two blades with constant radii of 0.5 and 1.02 m and chords of 0.78 and 1.01 m, respectively. Each blade had an elliptical leading edge and a span of 0.6 m and was placed in the purpose built exit section of a wind tunnel as shown in Fig. 1. The section wall opposite the concave surface was shaped such that the streamwise pressure gradient on the concave surface was negligible. A baffle plate behind the blade was adjusted such that the incidence angle at the blade leading edge was negligibly small. The freestream turbulence level was varied between 1% and 4% using turbulence generating grids placed upstream of the blade.

Measurements were taken with a miniature hot wire boundary layer probe which was traversed through the boundary layer using a computer controlled traverse system. Boundary layer traverses consisted of a minimum of 50 spatial data points which were distributed logarithmically to ensure high resolution near the wall. At each measurement point, data samples, typically of 150,000 measurements, were taken from the hot wire signal at a frequency of 10 kHz using an Amplicon A-D card. This voltage data was then linearised to obtain the instantaneous velocities using the hot wire calibration data. The turbulent intermittency was computed in real time using Fasihfar and Johnson's [10] algorithm. The experimental uncertainties in the mean and rms velocities were estimated as 1% and 2%, respectively. The uncertainty in the intermittency is more difficult to establish, but is probably around 2%. Further details of the experimental arrangement can be found in Hachem [11] or Dris [12].

Data Processing. On a concave surface with a constant radius of curvature r, the freestream velocity U varies with the distance y from the wall according to the free vortex condition $U(r-y)$ =constant. The fact that the velocity continues to increase beyond the boundary layer edge means that this point can not be identified as simply as for a flat plate boundary layer. To overcome this problem the flat plate equivalent boundary layer (FPEBL) was determined from the experimental velocities for each boundary layer using the technique due to Riley et al. [9]. The FPEBL is the boundary layer which would be formed if the boundary layer on the concave surface were to flow on to a flat plate with no further viscous dissipation such that the normal pressure gradient is relieved. The Bernoulli and continuity equations together with the free vortex condition lead to

Contributed by the International Gas Turbine Institute (IGTI) of THE AMERICAN SOCIETY OF MECHANICAL ENGINEERS for publication in the ASME JOURNAL OF TURBOMACHINERY. Paper presented at the International Gas Turbine and Aeroengine Congress and Exhibition, Vienna, Austria, June 13–17, 2004, Paper No. 2004-GT-53352. Manuscript received by IGTI, October 1, 2003; final revision, March 1, 2004. IGTI Review Chair: A. J. Strazisar.

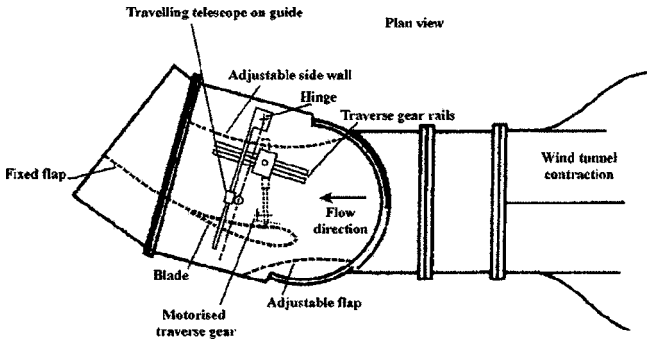

Fig. 1 Schematic of concave blade working section

$$u_e^2 = u_m^2 + 2\int_0^{y_m} \frac{u_m^2}{r - y_m} dy_m \tag{1}$$

and

$$\int_0^{y_e} u_e dy_e = \int_0^{y_m} u_m dy_m \tag{2}$$

where the m and e subscripts refer to the measured and FPEBL values, respectively. These equations are integrated numerically to obtain the FPEBL. An example of a measured and FPEBL profile are shown in Fig. 2. The boundary layer integral parameters were evaluated from the FPEBL profile.

The turbulent intermittency was determined from the digitized hot wire signal following the procedure devised by Fasihfar and Johnson [10]. The start and end of transition locations were identified using the method defined by Narasimha [13] and more recently described by Gostelow [14].

Results

Mean Velocity Profiles. Figure 3 shows typical boundary layer profiles through transition on a concave surface. Both the fully laminar (γ=0) and fully turbulent (γ=1) profiles are fuller than the laminar Pohlhausen and turbulent one seventh power law profiles also shown in this figure. Although this type of distortion occurs on flat plates due to high levels of freestream turbulence, the effect measured here is much greater. This is a result which has been observed in other studies (e.g., Volino and Simon [15]) and is due to the TG vortices which enhance the momentum transport within the boundary layer. The action of the TG vortices

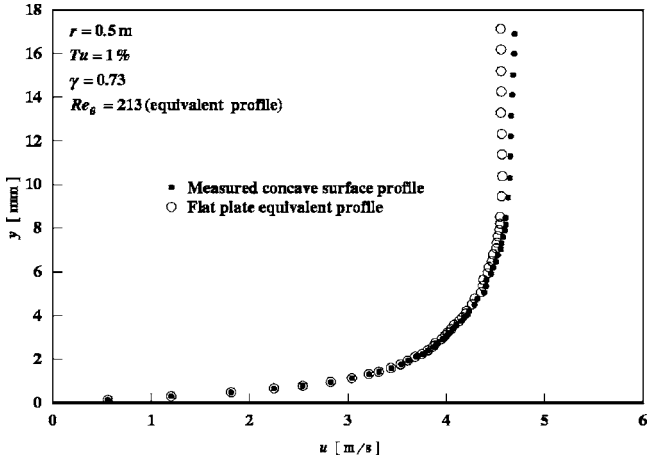

Fig. 2 Measured and flat plate equivalent boundary layer profiles

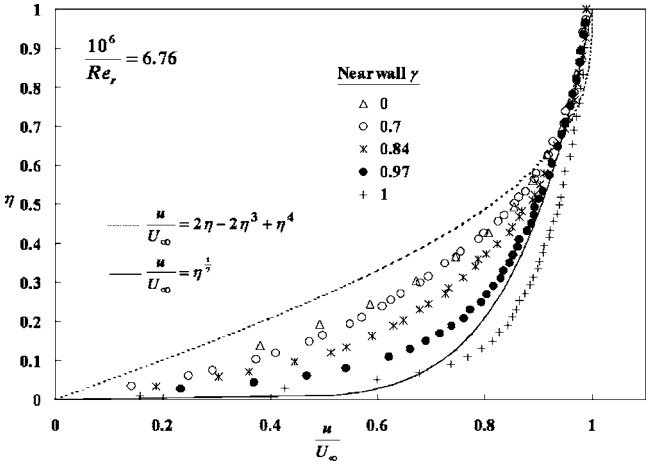

Fig. 3 Boundary layer profiles through transition

continues downstream of the transition region. These vortices have fixed spanwise locations at low (less than about 20) Goertler numbers $=(U\theta/\nu)(\theta/r)^{0.5}$ [16], however, in the present study the vortices meandered in the spanwise direction such that separate up and downwash profiles could not be measured.

Boundary Layer Development. Hachem and Johnson [16] identified the blade radius Reynolds number $Re_r = Ur/\nu$ as a suitable parameter for determining the effect of curvature. Figure 4 shows how the growth rate of the pre-transitional boundary layer increases with increased blade curvature. The empirical correlation

$$Re_\theta = 0.664\, Re_x^{0.5}\left(1 + 0.036\left(\frac{10^6}{Re_r}\right)\right) \tag{3}$$

was found to be a reasonable fit to the data as shown in the figure. This formula reduces to the Blasius formula for a flat plate where Re_r is infinite.

Figure 5 shows the skin friction coefficient variation through transition. Curvature increases skin friction which is indicative of the fuller profiles. Figures 6 and 7 compare C_f with the flat plate value for the laminar and turbulent profiles, respectively. C_f is enhanced by up to 40% for both laminar and turbulent flow, however, for laminar flow the enhancement does not alter with Re_θ, whereas the enhancement decreases with Re_θ in turbulent flow. This suggests that in a laminar flow the TG vortices have a fixed strength which is only dependent on the amount of curvature,

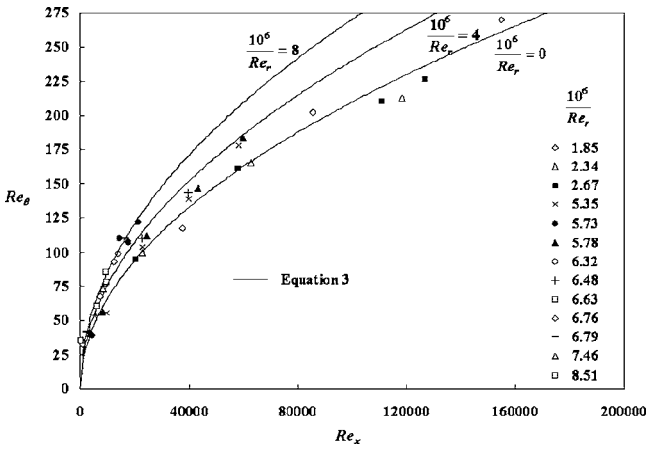

Fig. 4 Laminar boundary layer development

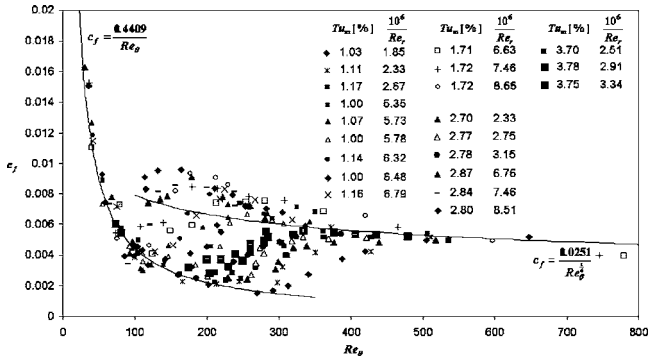

Fig. 5 Skin friction coefficient development through transition

whereas in turbulent flow the vortex structure is increasingly disrupted by the turbulence. The empirical relationships derived from these results were, for the laminar layer

$$\frac{C_f}{C_{fFP}} = \left(1 + 0.036\left(\frac{10^6}{Re_r}\right)\right)^2 \tag{4}$$

and for the turbulent layer

$$\frac{C_f}{C_{fFP}} = 1 + 0.09\left(\frac{10^6}{Re_r}\right)\exp(-0.004Re_\theta) \tag{5}$$

Equation (4) leads to Eq. (3) when substituted into the boundary layer momentum integral equation for a zero pressure gradient boundary layer. These expressions can only be considered as approximate because of the degree of scatter in the data.

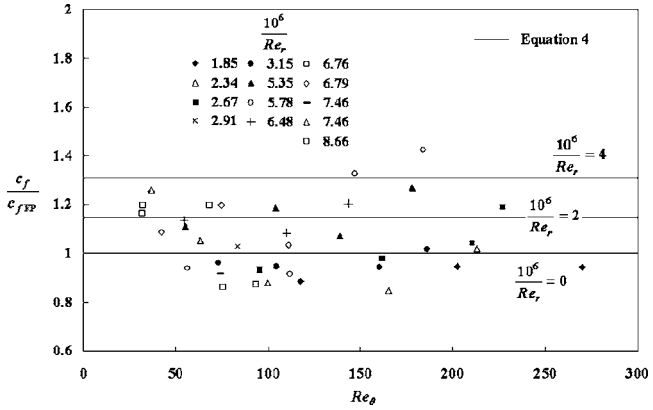

Fig. 6 Comparison of skin friction coeffiecient with the flat plate value for laminar flow

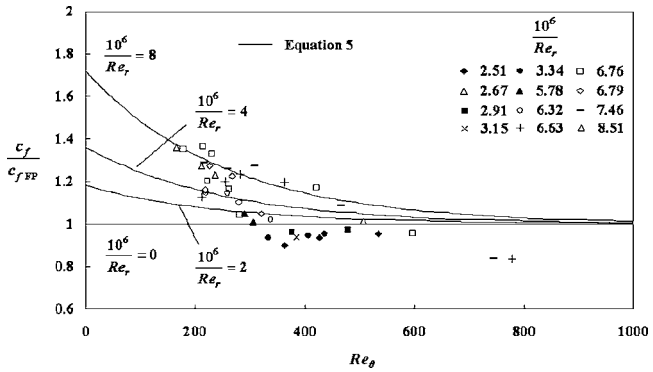

Fig. 7 Comparison of skin friction coefficient with flat plate value for turbulent flow

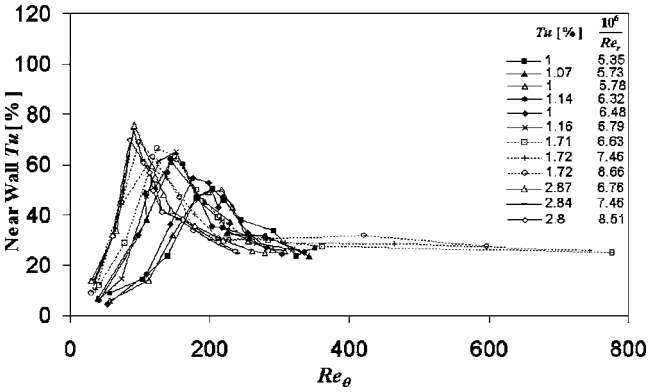

Fig. 8 Variation in the near wall turbulence level through transition

Transition. Figure 8 shows the evolution of the near wall turbulence level through transition, which is very similar to that on a flat plate. The near wall location is defined here as being at a height of 10% of the boundary layer thickness. One significant difference is that the turbulence in the turbulent layer is slightly higher than the value of 26% found on flat plates (Klebanoff [17]). This is due to the extra fluctuation level resulting from the meandering TG vortices. The changes in shape factor H through transition are depicted in Fig. 9. There is only moderate deviation from the flat plate values. The variation in the laminar region can be most likely attributed to minor deviations from a zero streamwise pressure gradient. It is apparent that the H values decrease slightly with increasing curvature due to the fuller velocity profiles. Some of the measured intermittencies are compared with the Narasimha concentrated breakdown distribution in Fig. 10. This distribution matches the data except in the low intermittency range where the measured values are higher. This result is also typical of flat plate results (Johnson and Ercan [18]).

The start of transition Re_θ values are plotted in Figure 11. The data of Liepmann [19] and Tani and Aihara [20] show how even modest curvature strongly promotes transition at low freestream turbulence levels. The current data indicate that although curvature promotes transition the effect at higher freestream turbulence levels is less dramatic. This suggests that the velocity fluctuations associated with the TG vortices may combine with the freestream turbulence to enhance the effective turbulence level. The empirical formula

$$Re_{\theta\,\mathrm{Start}} = 400(\mathrm{Tu} + 9.9 \times 10^4\, Re_r^{-0.84}\,\mathrm{Tu}^{0.26})^{-0.625} \tag{6}$$

is found to be a reasonable fit to the data. This equation is an adaption of the Mayle [21] equation where the turbulence term

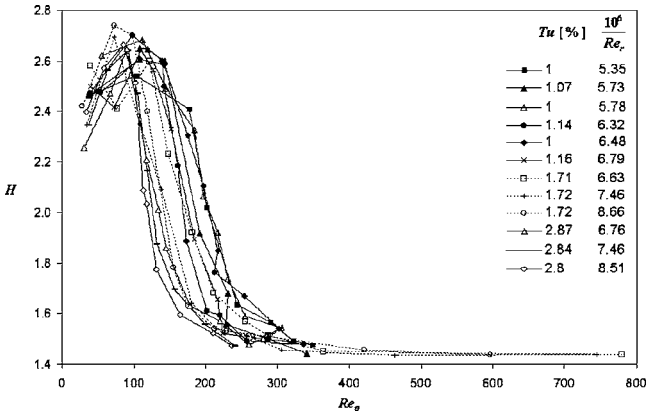

Fig. 9 Shape factor variation through transition

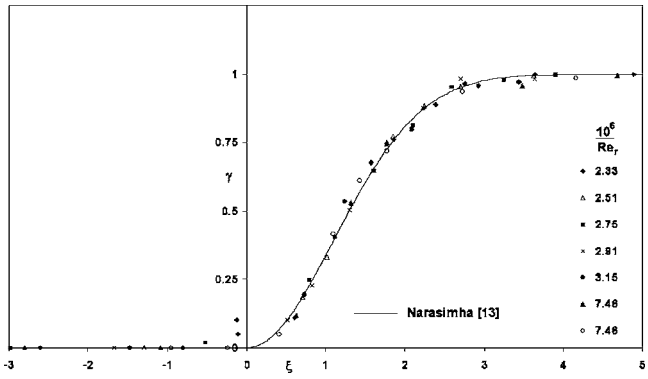

Fig. 10 Intermittency evolution

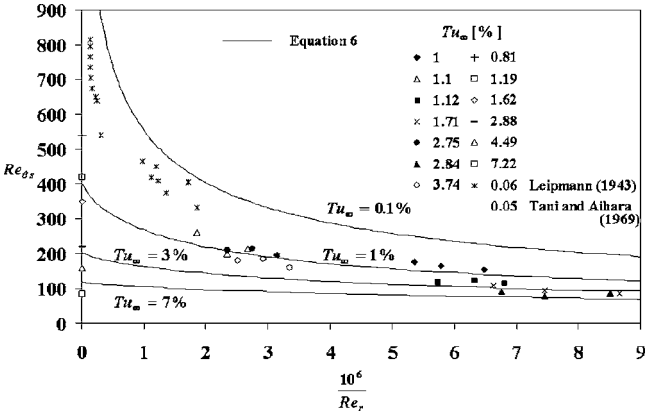

Fig. 11 Start of transition

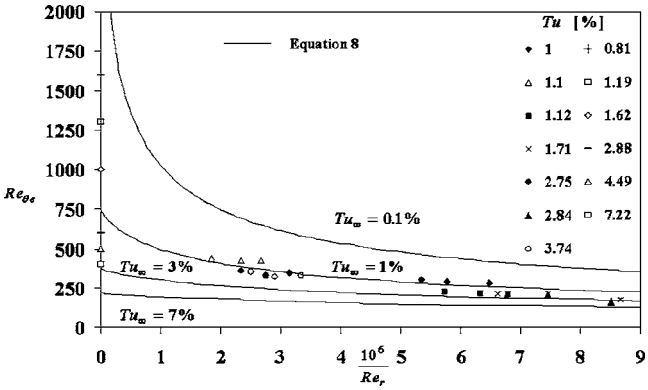

Fig. 12 End of transition

has been enhanced by the curvature.

The end of transition momentum thickness Reynolds number is plotted in Fig. 12. The Abu–Ghannam and Shaw correlation

$$Re_{\theta\,\mathrm{End}} = 2.667 Re_{\theta\,\mathrm{Start}} \tag{7}$$

over estimates the value for $Re_{\theta \mathrm{End}}$. A better fit was obtained with

$$Re_{\theta\,\mathrm{End}} = 1.85 Re_{\theta\,\mathrm{Start}} \tag{8}$$

Conclusions

(1) A flat plate equivalent boundary layer profile has been used in evaluating integral parameters to overcome the difficulty that the freestream velocity increases with distance from a concave wall;
(2) velocity profiles on concave surfaces are fuller then on flat plates both in the laminar and turbulent flow regions due to the additional momentum transport generated by the TG vortices;
(3) the skin friction coefficient is increased by the TG vortices. This leads to boundary layer growth rates up to 40% higher than on a flat plate;
(4) the shape factor is decreased slightly in all flow regions by curvature;
(5) the fluctuation velocity and intermittency variations through transition are very similar to those on a flat plate;
(6) concave curvature promotes transition. This effect is extremely strong at low freestream turbulence levels but more modest at higher levels.

Future Work

Hot wire signals obtained in the current work have been used to determine the receptivity of the pre-transitional boundary layer to freestream turbulence using the near wall gain defined by Johnson and Ercan. These results will be used to extend the transition model originated by Johnson and Ercan for flat plates to concave surfaces.

Nomenclature

C_f = skin friction coefficient
H = shape factor
r = blade radius
Re_r = blade radius Reynolds number
Re_x = surface length Reynolds number
Re_θ = momentum thickness Reynolds number
u = local velocity
U = freestream velocity
y = wall normal coordinate
γ = intermittency
θ = boundary layer momentum thickness
ν = kinematic viscosity
ξ = distance from start of transition nondimensionalized with the distance between the 25% and 75% intermittency points

Subscripts

e = flat plate equivalent
FP = flat plate value
m = measured

References

[1] Abu-Ghannam, B. J., and Shaw, R., 1980, "Natural Transition of Boundary Layers—The effects of Turbulence, Pressure Gradient and Flow History," J. Mech. Eng. Sci., **22**, p. 213.
[2] Johnson, M. W., and Ercan, A. H., 1999, "A Physical model for Bypass Transition," Int. J. Heat Fluid Flow, **20**, p. 95.
[3] Solomon, W. J., Walker, G. J., and Gostelow, J. P., 1995, "Transition length prediction for flows with rapidly changing pressure gradients," ASME J. Turbomach., **118**, p. 185.
[4] Vicedo, J., Vilmin, S., Dawes, W. N., and Savill, A. M., 2003, "Intermittency Transport Modeling of Separated Flow Transition," ASME paper GT-2003-38719.
[5] Redford, J. A., and Johnson, M. W., "Predicting transitional separation bubbles," ASME paper GT-2004-53353.
[6] Kim, J., and Simon, T. W., 2004, "Free-stream turbulence and concave curvature effects on heated transitional boundary layers," 1, final report, NASA CR 187150.
[7] Kim, J., Simon, T. W., and Russ, S. G., 1992, "Free-stream turbulence and concave curvature effects on heated transitional boundary layers," ASME J. Heat Transfer, **114**, p. 338.
[8] Schultz, M. P., and Volino, R. J., 2001, "Effects of concave curvature on boundary layer transition under high free-stream turbulence conditions," ASME paper GT-2001-0191.
[9] Riley, S., Johnson, M. W., and Gibbings, J. C., 1989, "Boundary layer transi-

tion on strongly concave surfaces," ASME paper 89-GT-321.
[10] Fasihfar, A., and Johnson, M. W., 1992, "An improved boundary layer transition correlation," ASME paper 92-GT-245.
[11] Hachem, F., 2003, "Boundary layer transition on concave surfaces," PhD thesis, Dept. of Engineering, University of Liverpool.
[12] Dris, A., 1957, "Boundary layer transition on a flat plate and concave surfaces," PhD thesis, Dept. of Engineering, University of Liverpool.
[13] Narasimha, R., 2003, "On the distribution of intermittency in the transition region of a boundary layer," J. Aeronaut. Sci., **24**, p. 711.
[14] Gostelow, J. P., and Walker, G. J., 1991, "Similarity behaviour in transitional boundary layers over a range of adverse pressure gradients and turbulence levels," ASME J. Turbomach., **113**, p. 617.
[15] Volino, R. J., and Simon, T. W., 1997, "Measurements in a transitional boundary layer with Görtler vortices," ASME J. Turbomach., **119**, p. 562.
[16] Hachem, F., and Johnson, M. W., 1990, "A boundary layer transition correlation for concave surfaces," ASME paper 90-GT-222.
[17] Klebanoff, P. S., 1954, "Characteristics of turbulence in boundary layers with zero pressure gradient," National Bureau of Standards, NACA TN No. 3178.
[18] Johnson, M. W., and Ercan, A. H., "Predicting Bypass Transition: A Physical Model versus Empirical Correlations," Proc. ASME paper 97-GT-475.
[19] Liepmann, H. W., 1943, "Investigations on laminar boundary-layer stability and transition on curved boundaries," NACA Wartime Report W-107.
[20] Tani, I., and Aihara, Y., 1969, "Görtler vortices and boundary layer transition," Z. Angew. Math. Phys., **20**, p. 609.
[21] Mayle, R. E., "The role of laminar–turbulent transition in gas turbine engines," ASME J. Turbomach., **113**, p. 509.

Experimental Investigation of Vane Clocking in a One and One-Half Stage High Pressure Turbine

Charles W. Haldeman

Michael Dunn

Gas Turbine Laboratory,
Ohio State University,
2300 West Case Road,
Columbus, OH 43235

John W. Barter

Brian R. Green

Robert F. Bergholz

General Electric Aircraft Engines,
Cincinnati, OH 45215

Aerodynamic measurements were acquired on a modern single-stage, transonic, high-pressure turbine with the adjacent low-pressure turbine vane row (a typical civilian one and one-half stage turbine rig) to observe the effects of low-pressure turbine vane clocking on overall turbine performance. The turbine rig (loosely referred to in this paper as the stage) was operated at design corrected conditions using the Ohio State University Gas Turbine Laboratory Turbine Test Facility. The research program utilized uncooled hardware in which all three airfoils were heavily instrumented at multiple spans to develop a full clocking dataset. The low-pressure turbine vane row (LPTV) was clocked relative to the high-pressure turbine vane row (HPTV). Various methods were used to evaluate the influence of clocking on the aeroperformance (efficiency) and the aerodynamics (pressure loading) of the LPTV, including time-resolved and time-averaged measurements. A change in overall efficiency of approximately 2–3% due to clocking effects is demonstrated and could be observed using a variety of independent methods. Maximum efficiency is obtained when the time-average surface pressures are highest on the LPTV and the time-resolved surface pressure (both in the time domain and frequency domain) show the least amount of variation. The overall effect is obtained by integrating over the entire airfoil, as the three-dimensional (3D) effects on the LPTV surface are significant. This experimental data set validates several computational research efforts that suggested wake migration is the primary reason for the perceived effectiveness of vane clocking. The suggestion that wake migration is the dominate mechanism in generating the clocking effect is also consistent with anecdotal evidence that fully cooled engine rigs do not see a great deal of clocking effect. This is consistent since the additional disturbances induced by the cooling flows and/or the combustor make it extremely difficult to find an alignment for the LPTV given the strong 3D nature of modern high-pressure turbine flows. [DOI: 10.1115/1.1861915]

1 Introduction

This paper focuses on the effect of vane clocking in a one and one-half stage turbine rig. The concept of "clocking" has evolved over the years, but the basic idea behind clocking is to improve overall turbine operation by changing the position of one vane (or blade) row relative to another vane (or blade) row. From a pure "efficiency" perspective, one could imagine that the overall viscous losses through the stage would be reduced if the second row were bathed by the low-momentum wakes of the first row.

Denton [1] presented some of the earliest theoretical clocking work. Denton lays the conceptual groundwork for why clocking should work through his description of the mechanisms involved in "blade boundary layer loss." Clocking has often been done in high pressure turbines by changing the position of the second vane relative to the first [2], but it can also be done with rotor blades as was done in the Westinghouse ATS turbine where the blade rows of the first two stages of a high pressure turbine were clocked relative to each other [3]. The potential benefits of clocking can be applied to many areas of turbine design, but the first efforts were generally contrived to improve overall turbine efficiency. Later efforts have focused on clocking for its ability to reduce (or perhaps increase) vibratory stresses. A necessary condition for clocking to be effective is for the upstream vane wakes to remain coherent as they pass through the rotor. Dunn [4] demonstrated that this was true for a transonic turbine in 1989.

This paper is a continuation of the work presented in Haldeman [5]. Although similar in design, the turbine rig configuration in this work is from a completely different machine and manufacturer. The limitations of the previous work (discussed later), lead to some of the main analytical work reported in Ref. [6] of which this paper is a partial summary. More detailed discussion of other aspects of the experiment including heat-transfer measurements can also be found in companion papers to this study [7–9].

Clocking research has been widespread and has taken several forms with both experimental and numerical studies. Dunn [10] has provided a good review of the clocking studies involving heat transfer and aeroperformance. As noted earlier one of the major works in this area was reported in a two part paper authored by Huber et al. [2,11]. In this study the effect of clocking was investigated on a relatively low-pressure ratio turbopump (approximately 1.5 over the full two stages of turbine) using only inlet and exit flow-field measurements (total temperature and total pressure), and the measured torque generated by the machine. These measurements separate into the two commonly referred to measurements of efficiency: thermodynamic and mechanical. This study showed that both the mechanical and thermodynamic measurements had the same sinusoidal shape with approximately an 0.8% variation in efficiency over the range of clocking positions at the midspan location (although there was on offset between

Contributed by the International Gas Turbine Institute (IGTI) of THE AMERICAN SOCIETY OF MECHANICAL ENGINEERS for publication in the ASME JOURNAL OF TURBOMACHINERY. Paper presented at the International Gas Turbine and Aeroengine Congress and Exhibition, Vienna, Austria, June 13–17, 2004, Paper No. 2004-GT-53477. Manuscript received by IGTI, October 1, 2003; final revision, March 1, 2004. IGTI Review Chair: A. J. Strazisar.

these two methods). However, what was also observed in this work was a distinct variation in which position provided the highest efficiency based on spanwise location of the measurements. Averaging the spanwise measurements of Fig. 8 (Huber et al. [2]) yielded an overall variation of 0.1% (a factor of 8 less) with a stated accuracy of the measurements of 0.07%. Huber et al. [2] also examined the amplitudes of the fast-Fourie-transform (FFT) at the fundamental blade passing frequency of the exit rake data. Huber showed (at least at midspan), that the amplitude also changed with clocking position with their position 5 having the lowest magnitude and their position 3 having the highest. This location was not at the measured maximum efficiency at midspan, but was the next point over which may indicate that it was hard to distinguish between the two positions.

At about the same time as the Huber paper, two papers by Dorney et al. [12,13] were published. These were both numerical studies and point to some interesting aspects of clocking that one might be able to observe experimentally, even if the experiment was not quite the same as the numerical investigation. In Ref. [12], Dorney et al. examined the affect of combustor hot streaks on a one and one-half stage turbine. In this case, the clocking was of the first vane relative to the hot spots generated by the combustor. The main result of this study was that the positioning of the first vane changed which surface of the rotor and second vane had the higher temperatures. In Ref. [13], Dorney's work focuses on modeling the United Technologies large scale rotating rig, which is a relatively low pressure ratio turbine. The conclusions from this work were that a 2% change in efficiency could be seen due to clocking and that the relative unsteadiness levels increase on the second vane at the clocking positions that correspond to maximum efficiency. Determining if this result would apply to higher work turbines at design corrected conditions was one of the goals of the present study.

There have been other papers dealing with different aspects of clocking in turbines. Eulitz et al. [14] used unsteady two-dimensional Reynolds average equations with a one equation turbulence model to examine the effects of clocking. Their results show about a 0.4% change in time average efficiency with clocking, but this was one of the first papers to look at how the time average and the fundamental and first and second harmonics of blade passing change amplitude with clocking position. Another important point, although not well developed is that clocking seems only to influence the second vane and not any other parts of the turbine (to be addressed later). Johnston and Fleeter [15] examined the effect of clocking on heat transfer measurements, although their work included pressure measurements as well. Their major findings reflect both the strong three-dimensional components of clocking (i.e., the effect varies with span location), and the fact that the time resolved data for both pressure and heat-flux data changes as the flow progresses along the wetted distance of the airfoil and across the span of the airfoil. The effect on multistage low turbines was numerically investigated using a three-dimensional (3D) time accurate code by Arnone et al. [16]. While the main goal of this study was to investigate the effects of turbulence modeling on the low turbine, they found that the efficiency range estimate was about 0.7% and that there were no major changes due to Reynolds number effects in the results. Reinmoller et al. [17] studied the influence of clocking on the flow field downstream of the second vane of a one and one-half stage axial turbine. In their experimental configuration, the vane-blade-vane rows are close together and an S-duct does not appear between the blade row and the second vane row as is used in this experimental configuration. In addition, measurements are not performed on the airfoils, but rather in the flow field. The authors made measurements at ten different locations in the flow field downstream of the second vane using pneumatic probes for the time averaged pressure field and hot-wire probes for the unsteady pressure field. The unsteady pressure measurements were compared with the predictions of a three-dimensional unsteady viscous flow computation. The relative efficiency is shown to vary by about 1% with clocking position and the numerical and analytical results are demonstrated to be in relatively good agreement.

At the Ohio State University Gas Turbine laboratory (OSU GTL), clocking experiments were done in three major experimental programs. In order of performance, these were the Westinghouse ATS program 1994–1996 [3] the Pratt and Whitney MTFE (Mid Thrust Family of Engines) program, 1994–1997 [18,5] and then most recently this work, 1999–2001. There was a distinct effort made to improve the measurements and the experiments throughout these programs, building upon the knowledge gained in the previous programs. Tracing the uncertainty estimates through these programs shows that as the measurement and data reduction accuracy improved, the overall ability to detect clocking changes also improved.

Summarizing the current state of clocking research; several studies existed outside the data generated by the OSU GTL which showed clocking effects, but experimental work was tied either to very low pressure ratio machines, or to rigs that were not operating at proper operating points. In addition, the rig geometry was relatively benign, without the "S" ducts that connect the modern high-pressure turbine with the low-pressure vane. In addition, while experimental work had shown clocking effects, these were very small, and the uncertainty analysis was not sufficiently developed to interpret if the observed characteristics were within the repeatability of the measurements. The fact that integrating over the entire airfoil in the case of Huber et al. [2] reduced the calculated effect, and the location of maximum efficiency changed (although not much) indicated that the effect was probably real, but it seemed as though the whole picture was not being observed properly. At the OSU GTL, several different rigs had been used in clocking experiments which were of more modern turbine design (higher pressure ratio) and were much more three dimensional. Clocking effects had been observed in all cases by examining the pressure distribution on the airfoils, but correlating these measurements to an overall measurement of the machine efficiency was elusive.

The work in this paper builds on the results in Haldeman [5]. That data set showed that clocking was clearly observable from the airfoil measurements, and the effect was strongly three dimensional. Although the uncertainty analysis presented with the data showed that the effect was present, no measure of the effect from a "macro" perspective (specifically overall stage efficiency) could be made.

Thus, one of the goals for this experiment was to improve the measurement accuracy to the point where aeroperformance measurements of clocking (both from a mechanical and thermodynamic perspective) could be made and to compare these with time-resolved and time-averaged measurements of clocking affect on the airfoils. In addition, it was important to determine if one measurement technique might show clocking effects more substantially than another. Both of these goals were attempted to see if some of the seemingly different perspective on clocking in the literature could be reconciled. The desire was to improve both the measurements and the data reduction to the point where the uncertainty analysis could properly bound the measurements to a resolution that would allow accurate comparisons between clocking positions. We wanted to see if the results from the MTFE turbine stage (particularly the influence of the spanwise position on clocking results) would be replicated on a different machine. Finally, we wanted to see if modern industrial research codes (i.e., the codes used at large engine companies) could help in verifying the wake migration trajectory and in understanding of the interactions between the low-pressure turbine vane (LPTV) and high-pressure turbine vane (HPTV) in clocking.

2 Experimental Setup

The facility used for these experiments is the OSU Gas Turbine Laboratory Turbine Test Facility (TTF). The TTF is a short-

duration shock tunnel facility capable of achieving variable inlet pressures and temperatures up to engine conditions. The actual construction and operation of the facility was documented by Dunn [19] but more accessible descriptions of the operation of the facility have been reported in Dunn [20–22] as examples. Shock tunnel facilities such as the TTF have a wide variety of uses, but they have not been used extensively outside of Calspan or the OSU GTL for turbine work. This is almost entirely due to the complexities involved in running shock tunnel facilities, a technique pioneered at the Cornell Aeronautical Laboratory. As a result, newer facilities have generally been blowdown facilities, although the light isentropic piston at Oxford, Pyestock, and VKI form a third type.

The TTF operates, and was used in these experiments, in two modes. One mode is the traditional shock-tube mode as described by Ref. [19]. A second mode, which has become more widely used for aerodynamic work (as opposed to heat-transfer work) is the blowdown mode. For the clocking part of the experiments, the facility was operated in blowdown mode and is described more fully in Ref. [6] along with comparisons between the modes of operation. Briefly, the blowdown mode (used in this work) eliminates the use of the copper diaphragms in the tunnel. Using an external pressure source, the entire shock tube is pressurized to the same pressure (around 1000 psia) that would have been created from the shock wave in a traditional shock mode. The difference is that in a shock mode, one also gets higher operating temperatures (about 600 K), whereas in blowdown mode the temperatures are much closer to room temperature (300 K). Hence, the reason the blowdown mode is not used for heat-transfer studies. Once the tube is pressurized, operation is very similar in both modes. A fast-acting valve is opened to start the flow over the rig. The rotating system is already spinning in a vacuum at about 1% below design speed. The flow establishment time is a little longer in the blowdown mode since the speed of sound is lower (about 20 ms vs 10 ms for the shock-mode operation). However, since there are no diaphragms involved, the fast-acting valve can remain open longer and not run the risk of copper debris going through the rig, and overall flow times in the blowdown mode are on the order of 50–100 ms instead of the more normal 25–35 ms for a shock-mode experiment. Usable data exist over several rotor revolutions. Generally, time windows are chosen over one rotor revolution and the variation in the design properties are within fractions of a percent. Enough data exist within any one run to look at conditions in the ±2% of the test design property. Since this facility has been reported in great detail over many years, readers unfamiliar with it are referred to the many other papers using this facility and no further discussion of the facility will be given here

2.1 Turbine Rig. The turbine used in this study is a large stage and one half [HPTV, High-Pressure Turbine Blade (HPTB) and LPTV] machine, configured in a manner that replicates current placement of the airfoil rows in a modern engine. Since it is a modern machine, the airfoils are of strong three-dimensional design and the total pressure ratio across the stage is in excess of 5.

A sketch of the rig is shown in Fig. 1, with some of the main components highlighted. The different colors represent the major subassemblies used during the buildup. To provide an overall scale, the area shown in Fig. 1 represents a portion approximately 2 m in length and 1.3 m in diameter. The overall rig is actually about 4.1 m long. A more detailed sketch of the main turbine stage is shown in Fig. 2.

Here one can see the relative location of the airfoil rows. The region of the flow path under investigation is defined by the location of the inlet and exit rakes. At each of these locations, there are two total temperature rakes and two total pressure rakes (5 sensors each placed at the center of equal areas). For this turbine configuration there are 38 vanes (both HP and LP) and 72 blades. The exit choke is movable, so that a variety of pressure ratios are

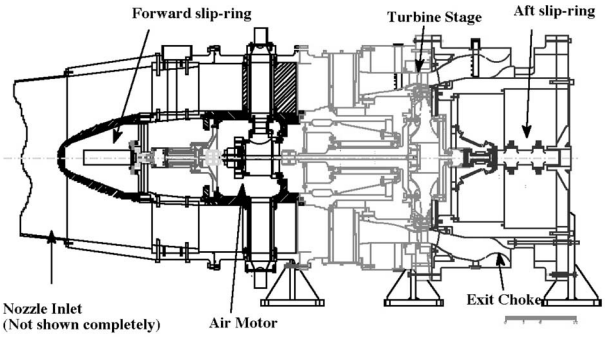

Fig. 1 Sketch of overall rig

available.

The experimental procedure for performing the clocking experiments is relatively simple. As shown in Fig. 2, there is a dividing line in the rig between the LPTV assembly (shown in purple) and the forward part of the model ending with the rotor shroud (shown in blue). To clock the LPTV, the model was separated as this point and the rear part of the model was moved back to allow access to the LPTV ring. Removing a few screws and rotating the assembly moved the LPTV ring. The entire procedure took less than an hour. For the data reported in this paper, there were five positions of interest that change the location of the leading edge of the LPTV by 1/4 of a vane passage. Since there were five positions, the first and last ones were repeat positions (although one vane passage apart). It is important to note, that it was unclear where the wakes were migrating to in this rig, so the position 0 does not necessarily line up with a wake impinging on one part of the LPTV. The validity of the assumption that beginning and ending positions replicate each other is discussed in Appendix D of Ref. [6]. The actual clocking procedure was quite straight forward, and it illuminates the great match between short-duration facilities and this type of experiment.

As mentioned earlier, the clocking experiments were part of an overall research effort using this rig and were composed of two separate entries. The first entry was intended to investigate the aerodynamics of the turbine stage and contained mostly pressure data and utilized only one slip ring. The second entry added rotor, rotor shroud, low vane heat-flux sensors, rotor tip pressures, heat-flux sensors, and a second slip ring. At the end of the second entry there were 485 instruments allocated throughout the rig. Each blade row had sensors distributed at three span locations (15%, 50%, and 90% spans, with the exception of the LPTV which was at 10%, 50%, and 90% spans), and there were heat-flux and pressure sensors mounted on the HPTV inner and outer end walls, and pressure sensors mounted in the area between the rotor and the LPTV on the inner and outer end walls. The rotor was instrumented with heat-flux sensors and pressure sensors on the platform, and on various blade-tip configurations in addition to the

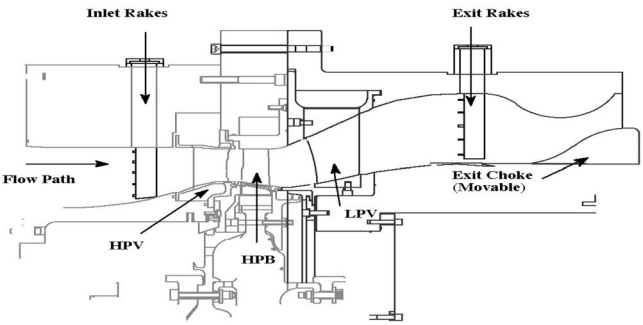

Fig. 2 Main flowpath

Table 1 Experiment descriptions

Run No.	Low vane clock setting	Speed at fire (rpm)
9	D-75% vane passage	6982
10	C-50% vane passage	6979
11	B- 25% vane passage	6983
12	A- 0% vane passage	6982
15	E- 100% vane passage	7000

three spanwise locations noted earlier.

The pressure sensors where variants of the Kulite XCQ-062-100A sensors mounted either as total pressures (for the rakes) static pressures (at the rake locations), or as chip sensors on the airfoils themselves. The heat-flux gauges were all built at OSU and are of similar type to the Calspan heat-flux gauges (a thin platinum film on a Pyrex substrate).

The data acquisition system and basic calibration procedures have been described previously and have been summarized in Ref. [6]. As there is not much new information it will not be discussed in detail here other than saying that the data was all acquired at 100 kHz using a set of anti-aliasing filters set at 45 kHz. This facilitated obtaining the proper resolution of the time-resolved data.

2.2 Clocking Experiments. The overall clocking experiments were split into several subsections that examined the effects of Reynolds number on clocking, overall repeatability, and intermediate spacing. In this paper, only a subset of those data will be reported. The data runs of interest are shown later.

Runs 13 and 14 were repeats of position E and are not used in this part of the analysis to avoid biasing the overall clocking data to one position (E in this case). There are additional runs, from other parts of the experiment that provide the repeatability of the results, which will be discussed later in the data analysis section.

An overall comparison between the experimental conditions is shown later, which provides both an idea of the individual variations within a group as well as the variation in properties that occurs when different conditions are being set.

Here we can see a great deal about the overall repeatability of the experimental test conditions. The data that will be discussed in this paper are shown in bold, and correspond to the runs shown in Table 1. For this group the overall variation in corrected speed is about 0.52%. However, one can see that the variation between the overall groups is also quite low; showing that even thought the inlet pressure had changed between groups (to change the Reynolds number) the ability to reproduce the main corrected conditions remains within about 1.5% (worst case).

3 Data Reduction/Uncertainty Analysis

The main data for these runs have been processed relatively simply. No filters have been applied to the data, and the only real choice left to the engineer is the time window over which to examine the data. For the data presented here, all the data were examined over one rotor revolution [as all the speeds were nominally the same, this reduced to the same size window for all runs (about 8.4 ms)]. Averaging the raw time-resolved data over that one revolution created the time-average data. To examine the effects of clocking from different perspectives several different experimental measures of clocking were investigated.

(1) time-averaged measurements

(a) airfoil static pressure measurements
(b) stage efficiency measurements based on inlet total pressure and temperature and rotor acceleration (mechanical measurement of efficiency), and based on change in total properties across the stage (aerodynamic measurement of efficiency)

(2) time-resolved measurements

(a) in the frequency domain, power spectrums of airfoil static pressures (FFTs)
(b) in the time domain, pressure envelopes

The goal, as mentioned earlier, was to observe similar clocking effects from each of these measures, and to discern if some measures are better than others (due to instrument resolution) for observing clocking effects.

The challenge is to figure out the proper time window over which to examine the data. Due to the nature of the facility and the rig (primarily, but not exclusively due to the lack of a brake on the rig), there is a small change in physical speed that occurs during the experiment. This change is enough that over the course of an entire experiment the speed changes by about ±1% around the nominal value. During one or two revolutions of data the variation is much less, however, there is some leeway in how the exact time window is chosen for each run. Traditionally, the windows are chosen to match the design pressure ratio and the corrected speed conditions. Usually, variations in the valve opening times, initial variations in speed and temperature may vary the starting times for each run by 1 or 2 ms (or less) and these variations are not accounted for, since the time windows were chosen to match the design operating conditions.

When this traditional approach was used with this data, the results were the same as the MTFE data [5], essentially observed clocking effect on the airfoil data but no connection to the overall stage performance. However, changes in the experimental matrix, and the wide variety of conditions performed gave even tighter uncertainty estimates than were available on the MTFE data, so it was clear that something was not being accounted for properly.

The key to understanding the problem came when it was realized that very small changes in the where the time window starts would effect the overall machine efficiency measures, but not the airfoil pressure distributions (in fact not much affects these as has been shown in Ref. [6]). What was happening was that by finding a window that equated the design pressure ratio across the machine for each run, one was inadvertently canceling the clocking effect as measured by the stage efficiency. If a certain clocking position were less efficient than another, then the pressure drop across the machine would seem a little lower. One could force a slightly different pressure ratio (more like the average) by choosing a time window that occurs a little later in the experiment, but still the same length (one revolution). However, in doing this one had just over compensated for clocking position. The key to this is that even large clocking effects are very small (1–2% max) and washing out a fraction of this can lead to confusion.

Thus a method of choosing the time windows for the analysis was created that accounted for delays in the starting process and then matched runs in a submatrix (such as the group that is being presented) so that all the time windows started at the same relative location in the experiment relative to the flow starting time. For the nominal run, the window start times were chosen to match the design pressure ratio and corrected speeds. For the other clocking runs in the submatrix, the starting times for the windows were chosen to match the same amount of time that flow had been going through the rig as the nominal run, and no attempt was made to match the design pressure ratios. As shown by Ref. [6], there were some other ways of choosing windows which accounted for the secondary effects of changes in the choke position, but it turns out that the actual method of choosing the windows is not that critical once one has stepped away from the logic of trying to match design pressure ratios for clocking runs.

The overall variation shown in Table 2 is the variation in properties observed when this method is used. Thus the percent range for each group seems large (1.7% for the corrected speed for instance, since this is a measure of the clocking effects), but the

Table 2 Average experimental conditions

	Corrected speed (rpm/$K^{.5}$)	PTR (%)	PTUA (K pa)	Re	Speed (rpm)	TUA (K)
Avg. (high Reynolds)	364.56	98.09	434.36	6.37*E6*	7154.40	385.31
%range	1.63	1.68	0.61	5.8	0.01	3.27
Avg. (intermediate clocking)	361.59	101.06	333.78	4.78*E6*	7131.38	389.17
%range	1.71	1.72	0.38	5.0	0.02	3.39
Avg. (main clocking runs) (5 runs)	**357.71**	**100.85**	**340.23**	**4.64E6**	**7117.60**	**395.94**
%range	**0.52**	**1.54**	**0.57**	**3.0**	**0.25**	**1.05**
Avg of groups	**361.29**	**100**	**NA**	**NA**	**7134.46**	**390.14**
%range	**0.95**	**1.50**	**NA**	**NA**	**0.26**	**1.36**

overall variation between the averages of the groups is smaller (since there should not be any clocking effect for the average of each group, if the data are all taken from the same number of different clock positions).

Armed with this system, the focus shifted to creating better estimates of the uncertainty of the data by examining repeatability issues as well as propagation issues. As noted in Ref. [6], the sensitivity of the answers to the time-window selection was analyzed and found to be smaller than the run-to-run repeatability which occurred when experimental conditions were changed. The data in Table 2 consist of three different submatrices that were done at different points in the overall experiment after the choke had been moved. The repeatability of the measurements was taken by comparing the measurements for clock position D (the nominal position) across all these runs. This gave the largest uncertainty (since it incorporated overall condition setting and was used throughout [6]). In addition, another large change from the MTFE data was the incorporation of uncertainty bands for every individual sensor. This made substantially more sense than trying to group sensors by airfoil location (e.g., treating every sensor on the LPTV as having the same uncertainty) since there are locations where the flow physics force variations among the runs to a much greater degree than other locations.

With the addition of these two items, the change in setting the time windows and the individual sensor uncertainty based on repeat runs at clock position D, the data were capable of being analyzed in a manner similar to that done in Ref. [5]. All the pressures were normalized by the total inlet pressure as measured by the upstream rakes (creating the normalized pressure which is the basic scientific variable used in this paper). However, expanding on that work which essentially only examined the time-averaged values, and the time-resolved values in terms of FFT amplitudes, other measures were also employed.

(1) Overall stage isentropic efficiency. These were based on the upstream and downstream total temperature and total pressure rakes and essentially all sensors at the upstream location were averaged together to create one measurement and all sensors downstream were averaged together to get one measurement which was then used in the calculation of the isentropic efficiency. The only change to this was that the flow time through the model was accounted for, so that the change in energy was measured on a flow particle basis. This is different from what Huber [2] did where the rakes were traversed and the overall effect was created by integrating over all the data. Thus in this system there was no accounting for span variation.
(2) Time-resolved data-frequency domain. As was done previously, the time-resolved data were examined by looking at the data in the frequency spectrum by converting standard FFT plots into power-spectrum plots that provided the amplitude at a given frequency. For the main analysis, three frequencies were tracked: the fundamental blade passing frequency, and the first two harmonics. However, in this paper, only the fundamental will be presented.
(3) Time-resolved data-time domain. An additional variable, the envelope size, was examined. In this case the data were ensemble averaged over all the blade passages in a rotor revolution and the average minimum and maximum were found for this passage shape (the actual shapes will be shown later). This range is called the envelope and it has the benefit of capturing the overall periodic shape without worrying about whether or not the energy is being transferred from one frequency to another (discussed in more detail later).

Essentially, for each property (time average, time resolved, airfoil pressures, or stage efficiencies), the group average (for all the clocking runs) was determined, and the effect due to clocking was calculated by looking at the percentage variation for the individual run from the average. Thus the clocking effect for clock position C (50% vane passage) for the time average airfoil pressure would be

$$\text{Clocking effect}(C) = \frac{\text{avg . pressure}(C) - \text{avg . pressure group}}{\text{avg . pressure group}}$$

And the uncertainty band (unless otherwise noted) would be the variation in results as measured for LPTV position D for several different cases, instead of propagating the uncertainty for the average pressure of the individual run and the overall group average. This essentially uses a measure of the run-run variation as our measure of the repeatability of the data for each sensor. Since there are only a few runs, a typical confidence level cannot be estimated. However, if the errors were distributed in a Gaussian fashion, then this range would correspond to a 6σ range, which would be over a 99.99% confidence limit.

4 Data, Predictions, and Results

In this section, several different combinations of data, predictions, and overall results will be presented. They will be split into different topics, which discuss the overall clocking comparisons, the time-resolved measurements and the predictions. More detail on any of these comparisons and conclusions can be found in Ref. [6].

4.1 Global Clocking Comparisions. With the advent of the methods described in Sec. 3, a comparison plot of all the different measurements of clocking can be shown.

This plot is not one of change in absolute efficiency; rather it is a relative improvement over the current value. Also, it is important to note that due to the nature of the facility (being isothermal) a correction would have to be done involving estimating the heat transfer to the rig to obtain an adiabatic efficiency. Since we are interested in relative changes this is not a problem but it is critical to remember that the values of ±4% shown in this figure will translate into smaller numbers such as ±2–±3% if these were absolute efficiencies. In addition, while theoretically positions A and E should be the same, differences could be attributed to individual vane variations. In fact the limited tests done on a vane 2 passages away from A replicates the results of A better than E. There are lots of reasons this may be the case. Specifically the

vanes are each installed separately and small variations in one vane will be accounted for in changes in the next vane spacing. Unfortunately, not enough data were taken at these multiple vane spacings to check this assumption but it will be part of future work. In this plot the errors bars have not been shown, since the plot is essentially a comparison between methods of measuring clocking effects. This plot shows the cumulative effect of clocking as a percentage change from the average condition for a stage efficiency measurement (isentropic efficiency, red circles), the same effect based on the airfoil static pressures on the low vane based on different techniques: time-average measurements—blue, time-resolved measurements in the time domain, envelopes—black, and time-resolved measurements in the frequency domain, FFTs—green. Remember that these last three measures all come from the same sensors. Further, the differences in span locations are also shown in this plot with the open symbols representing the measures taken only at the 10% span, while the solid symbols represent the data integrated over all three spans on the LPTV. This plot requires that the individual sensors measurements be integrated together to form an overall effect. Some interesting conclusions can be drawn from this plot.

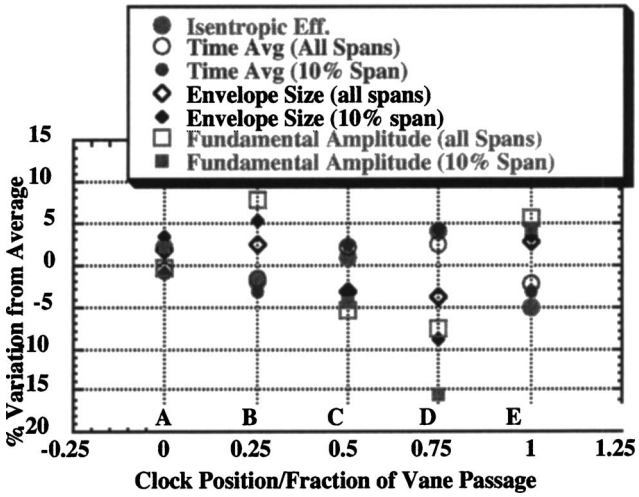

Fig. 3 Comparison of clocking effects based on measurement type

(1) For all the measurements of clocking based on the airfoil static pressure measurements (time-averaged, time-resolved, frequency, or time-domain based), there is a spanwise variation that is significant. The clocking effects at 10% are much great than that observed when looking at all three span locations. At some clocking locations where the clocking effect is not great, the differences between the 10% and overall average are small (such as at positions, A, C, and E). But where the clocking effect seems to be greatest (B and D) the difference in span is dramatic.
(2) The time-average values of the pressures on the airfoils show similar effects (shapes and magnitudes) as the isentropic efficiency measurements, indicating that measures of the changes due to clocking are observable even from different fundamental measurements. Further, as will be shown in the next section, the procedure for integrating the results over the three spans comes close to reproducing the overall effect as isentropic efficiency measured by the rakes which also provides verification of the integration method.
(3) The time-resolved measurements, which are split into two groups the time domain measurements as defined by the envelope sizes, and the frequency domain measurements as defined by the power spectrum amplitudes, show effects opposite in direction from the time-averaged measurements. However, the power spectrum measurements as indicated by the amplitude at the fundamental frequency, tend to over predict the effect, while the envelope size much more closely replicates the effect as measured by the time-average or isentropic efficiency, but the direction is opposite. So for clock position D, which shows about at ±4% change from the average for the isentropic and time-average measurements, the envelope size shows about −4% measurement, although the FFT would indicate about a −7% overall measurement.

Thus it would appear from this plot that the area of maximum efficiency occurs when the overall time-average pressure on the LPTV is the highest, and the overall envelope size (and frequency amplitudes) are the smallest.

As discussed previously, the results shown in Fig. 3 come from integrating the results of each sensor over the airfoil surface. The underlying data for this method come from the variation of the properties of interest with respect to clocking. The variation due to clocking for the time average data is shown in Fig. 4.

From these data, one can see that on the pressure surface, toward the leading edge at the 10% span location, clock position D results in higher pressures. But on the suction surface, or at other span locations the effect is not as well established. Thus, one needs a way of integrating the data over the entire airfoil surface. There are many ways to do this and the scheme used here helps to reduce interpolation error by accounting for points that are not evenly distributed. As pointed out in Ref. [6] different techniques do not produce the exact same answer, but they all produce similar trends, with position D being slightly better than the others, and that a majority of that effect arises from the contribution at 10% span. This problem points to the need for having specific sensor patterns, which are repeated at all spans. The variation between just the straight average and the integral over equal areas does not change the trend (as shown in Ref. [6]), and thus once again one can be confident that the main physics of the flow are being captured.

4.2 Time-Resolved Measurements. Turning towards the time-resolved measurements, there is an inconsistency in Fig. 3 between the magnitudes of the changes as measured by the fundamental amplitude and the envelopes that needs to be resolved.

4.2.1 Frequency Domain. The frequency data for each run were processed and all the amplitudes at the main frequencies (fundamental, first, and second harmonics) were averaged to form an average magnitude for each frequency (fundamental, first, and second harmonics) to get the data shown below for the 10% and 50% spans (90% span not shown since it is not as important).

In this case, the range bars represent the standard deviation of this averaging technique. While the range bars do not explicitly show the effect of clocking, one can relate larger variations to larger effects from clocking. Using these plots one can see how the overall magnitudes change for location along the airfoil and span, and the relative importance of these different frequencies. The data at 90% span show all three of theses frequencies to be at about the same level (about 0.008). While these may seem to be unimportant, a plot of the relative change of these amplitudes as a function of clocking can show that there often is an energy transfer from one frequency to another, which may often over predict the clocking effect.

Examining the pressure side, the fundamental amplitude for clock B seems to be a little below the average, whereas for the first and second harmonics are above the average. Returning to Fig. 5, one can see that at certain locations in this area, the fundamentals are not so large as compared to the other frequencies to completely ignore them. Thus in general terms, it appears as though examining just one frequency is not enough to gain the

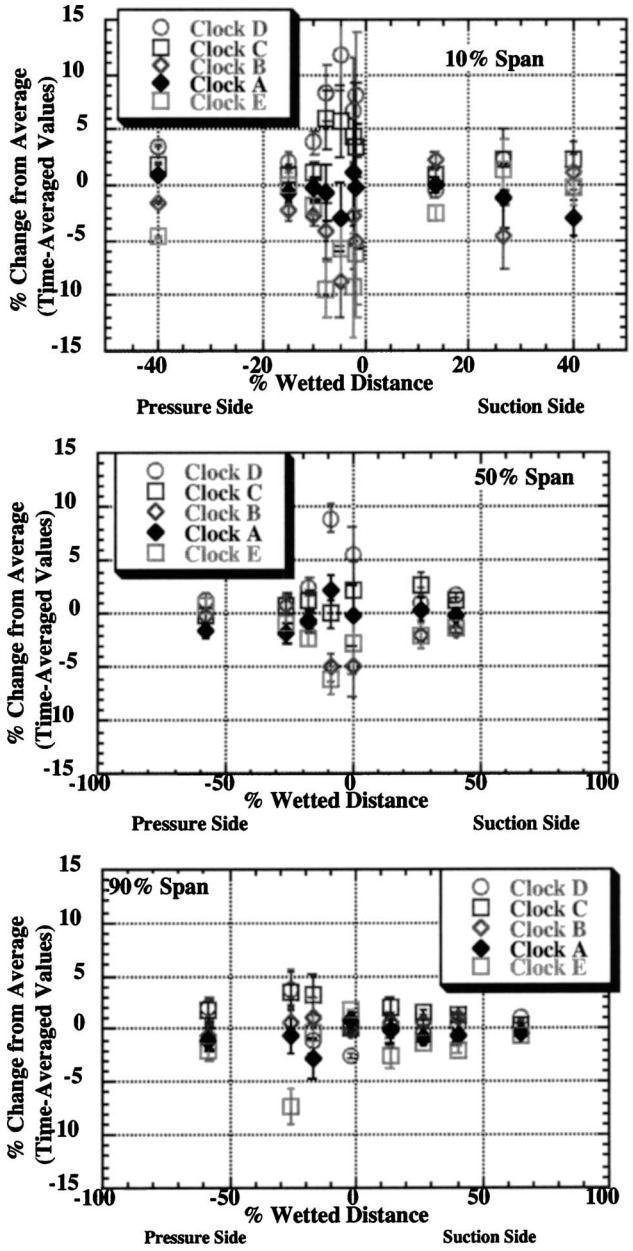

Fig. 4 Variations due to clocking, LPTV time-average values

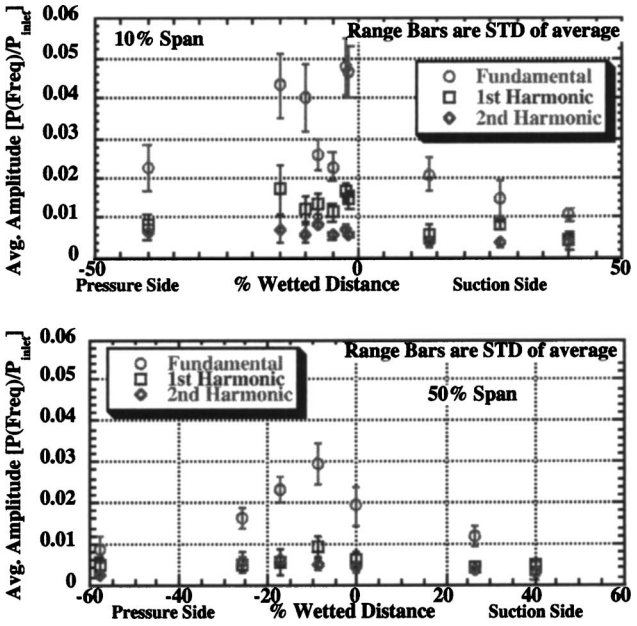

Fig. 5 Variations in FFT amplitudes for LPTV

entire picture of the time-resolved domain.

4.2.2 Time Domain. The relative sizes of the envelopes are shown later, and are similar in structure to Fig. 5, where the average for all the runs are plotted, and the variation shown by the range bars is proportional to the clocking effect (similar to Fig. 5).

One can see from the range bars that most of the main action is again at the 10% span on the pressure surface towards the leading edge (as shown also in the FFT plots). Due to space constraints, the envelope shapes will not be presented, but one can see distinct variations in the envelope shapes at the 10% span which diminish in variation as one extends outward on the airfoil.

What is probably the most important piece of information from this section is that examination of a single frequency in a FFT (such as the fundamental frequency) can lead to overestimates of the clocking effect because of energy leakage to other harmonic frequencies. In other words it is possible for the fundamental frequency to either increase or decrease due to clocking at one wetted distance location, but the first and second harmonics may go in the opposite direction. And while the higher frequencies may not mask the total effect of the fundamental, it can change the absolute level enough. This effect may be real, or it may be an artifact of the FFT algorithm. From the envelope perspective, this is not a problem since the overall size (which nominally incorporates all the frequencies) keeps track of this.

4.3 Predictions. Before the experiments were started, the code MSU TURBO described in detail in Barter et al. [23] and in Chen and Barter [24] was used to provide estimates of the effect of clocking, and to see if the code could resolve clocking effects.

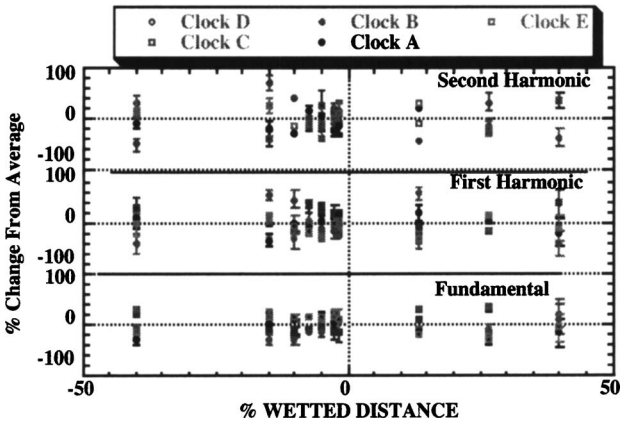

Fig. 6 Amplitude change for LPTV at 10% span

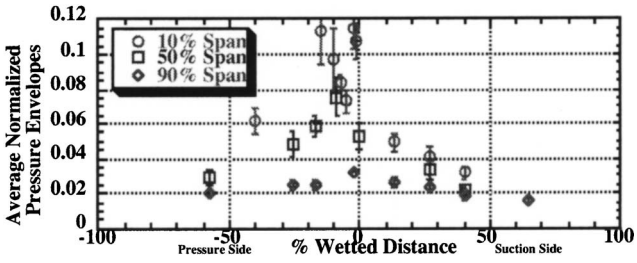

Fig. 7 Normalized pressure envelopes, LPTV all spans

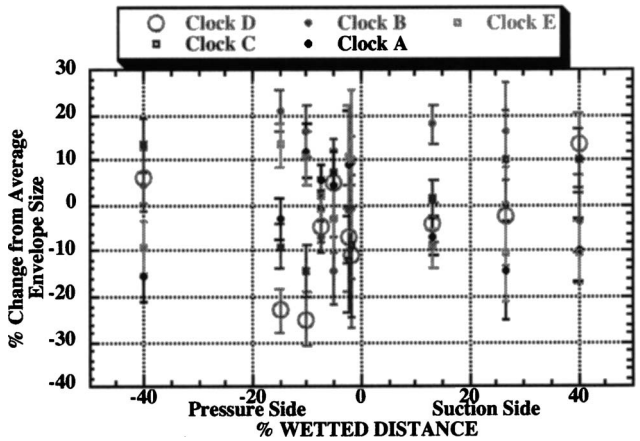

Fig. 8 Variations in envelope size 10% span, LPTV

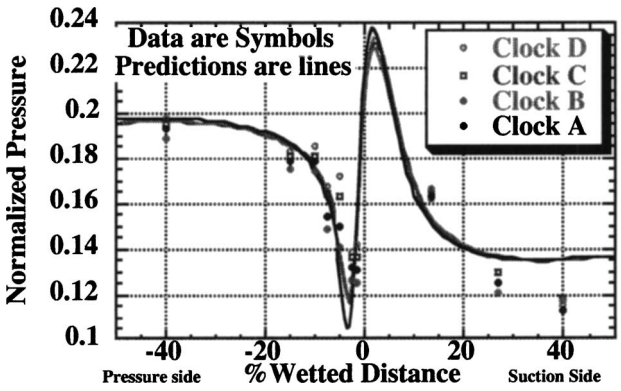

Fig. 11 LPTV average pressures at 10% span

This code is a 3D, viscous, time-accurate code that solves the Reynolds-averaged Navier-Stokes equations in Cartesian coordinates. The present paper will not attempt to show the current state of the art in the prediction capability, and as such, it will not go into grid refinement studies, insensitivities to geometry, or griding issues. These issues are all handled in Refs. [23,24]. Rather the results of the calculation will be used as a comparative diagnostic when examining the data. The three main uses for the predictions are in the average pressure on the blades, the envelope sizes, and finally for helping to trace the wakes from the HPTV onto the LPTV leading edge. To begin, the quality of the prediction for both the average and the envelopes are shown at clocking position D for the 10% and 50% span locations below. For the 10% span data because so much of the interesting behavior is close to the leading edge only the ±50% wetted distance range will be plotted.

With these two plots, one can see that the predictions capture both the trends in the average value and the variations in the envelope as a function of wetted distance. More impressively, it captures the basic differences that occur with span as shown below for the two extreme span locations, 10% and 90%.

The plots show more variation in the average data with clocking position than the predictions tend to suggest. This is not true of the actual envelope sizes (as shown later) where the code tends to predict the variation in envelope size in a manner similar to the data.

While sometimes the absolute magnitude is off a little, the code does a very good job at both spans of picking up the areas along the airfoil where the maximum and minimum variation occurs. Also, the code does tend to get the clock position with the largest

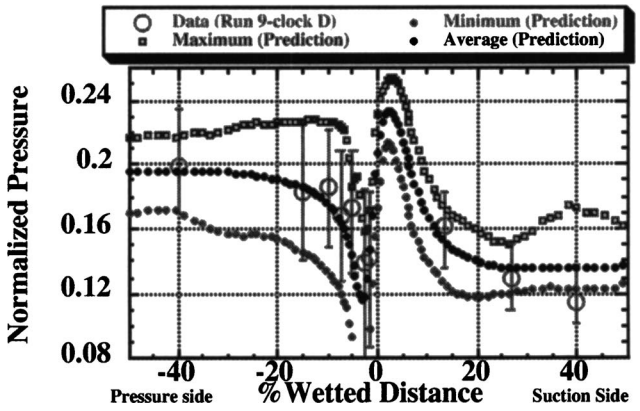

Fig. 9 LPTV 10% span normalized data

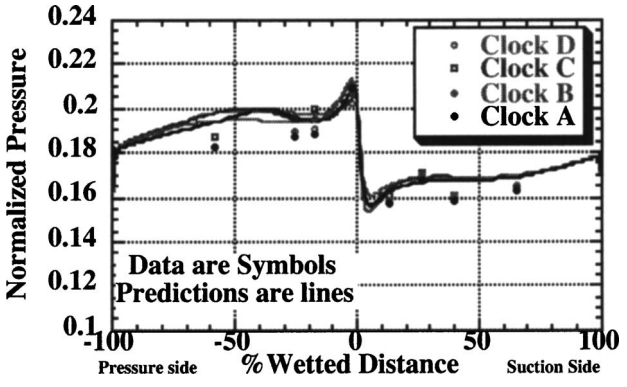

Fig. 12 LPTV average pressures at 90% span

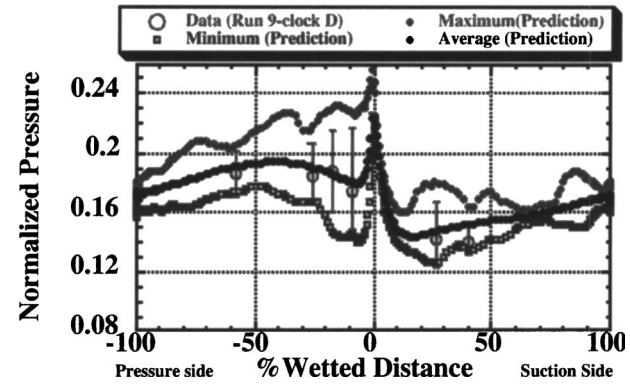

Fig. 10 LPTV 50% span normalized pressure

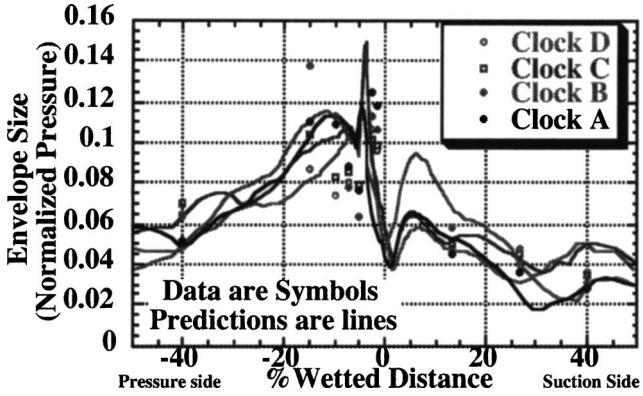

Fig. 13 LPTV 10% span envelope sizes

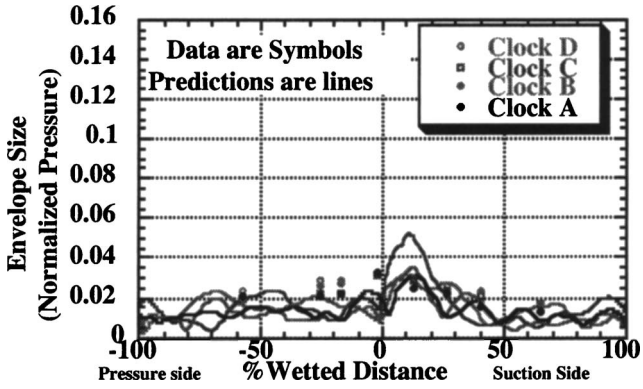

Fig. 14 LPTV 90% span envelope sizes

variations (clock B at 10%) and the smallest variation (clock D). The code, while capturing the trends well, does seem to over predict the pressure value that occurs at about −5% wetted distance. It is important to realize that the particular behavior at that location is extremely dependent on the physical geometry of the LPTV, and hardware variations (design drawings versus actual construction) may be dominating in this area.

The last area that the computations can help us with is in the predictions of the HPTV wakes and where they impinge on the LPTV. To do this two plots will be shown that show the total pressure (at 10% span) as it propagates from the beginning of the computational space for the LPTV (about half way between the HPTB and LPTV) to the LPTV leading edge plane.

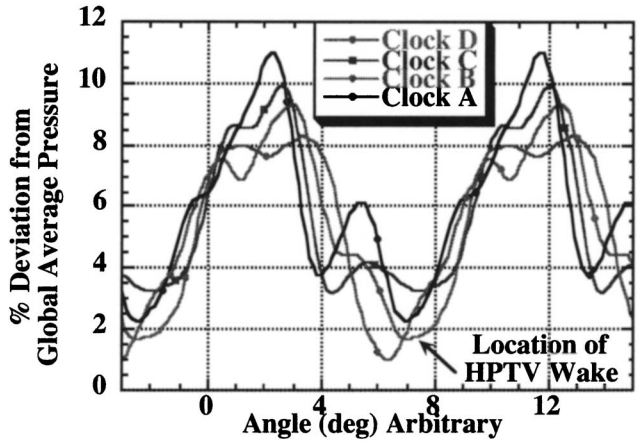

Fig. 15 Total pressure variation at 10% span, LPTV inlet

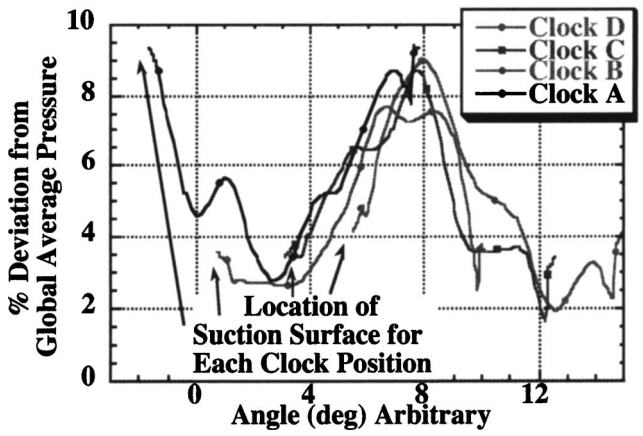

Fig. 16 Total pressure at leading edge of LPTV

In these plots, the total pressure deviation from the average over all spans is plotted as a percentage so that the wakes can be more easily seen. If one were to look at the 50% and 90% spans, one would see different shapes, which align at slightly different angles because of the skewed nature of the wake. In Fig. 15, the location of the wake is about 6–7 deg. However, what is most interesting in this plot is the implication that the LPTV position has an effect on the HPTV wakes, or in other words, has an interaction with the HPTV. This was shown slightly in the MTFE data [5] where on the trailing edge of the HPTV a small effect from clocking was observed. However, as one expects, at this axial location all clocking positions produce wakes (although slightly different in shape) that occur at the same location.

Moving on to the data at the leading edge plane, we can again plot the global average.

In this plot the location of the suction surface for each clocking position is marked and moves (in the positive direction) from position A at about −1.5 deg to position D at about 5 deg. In this viewpoint, one is looking at the passage with the suction side of one vane on the left and the pressure side of a second vane on the right. While the shapes have changed a little from Fig. 15, the point to note is how much the wake has moved as the flow has progressed downstream. Clearly from this plot, it appears as though position A has close to the maximum total pressure impinging on the leading edge, while clock positions C, B, and D are all closer to the wake. However, position D is the most offset which makes one think that the region of lowest total pressure (and thus lowest velocity) is aligning with the pressure surface.

5 Conclusions

A major goal of this work was to create a data set that attempted to address some of the inconsistencies in the literature having to do with clocking data, and to compare the features of this data set with predictions. The first task was to try to match clocking data that had been obtained on airfoils with aeroperformance measurements obtained for the overall turbine stage. This was accomplished by changing the time windows slightly over which the data were analyzed so that the clocking effects were not washed out by a misadjustment of the time windows to match the total pressure ratio for this stage. With this done, the variations in clocking effects due to span that had been seen previously on a different machine, although similar in configuration, were replicated. Further, the different magnitudes that are attributed to clocking which come from different time-resolved measurements have been reconciled. Because of energy leakage issues, typical frequency analysis (while extremely useful for issues involving high-cycle fatigue) may overestimate the clocking effects dramatically due to energy leakage to the other frequencies. A better measure of overall clocking effect in the time-resolved domain is obtained from examining the pressure envelopes. Further, by using a variety of methods, each of which has many built in assumptions in the derivations of the results, one can see similar trends. This shows that the clocking effects, while small, are observable. By comparing techniques we obtain a better estimate of the overall effect, even if individual techniques of measuring clocking are more error prone. From a flow physics perspective, the CFD code msu turbo has provided the ability to trace the HPTV wake, and show that the wake is impinging on the LPTV leading edge, and thus the mechanism for the clocking effect is in fact the velocity changes that occur. The results suggest that to improve overall efficiency one wants the highest static pressure on the LPTV surface and the lowest envelope size. The procedure for integration of the data is important to quantify the actual effect, although the effect is large enough that trends are readily apparent, and consistent for different integration schemes. The comparison between the airfoil pressures and the overall effect as measured across this stage, suggests that measurements at three span locations are enough to quantify the effect.

As a final note, it is important to realize that clocking the LPTV may only have a marginal impact on the overall machine performance; it may have a large effect on other issues. From the predictions and the measurements we see that the LPTV does have an effect on the HPTV, albeit small. The interaction between the LPTV and the HPTV does change the inlet conditions to the LPTV substantially and this changes both the unsteady pressure envelope shape and the frequency content of the time-resolved pressures. Both of which have implications for cooling and high-cycle fatigue issues that may be more important to the designer than the marginal benefit in performance. As a last note, since the clocking effect depends so much on aligning the LPTV with the HPTV wake, as one progresses from uncooled turbine rigs to fully cooled turbine rigs, one would expect the ability to match the LPTV with all the wakes that are generated (momentum, temperature, etc.) to become harder and for the overall effect of clocking to diminish.

Acknowledgment

The authors would like to thank the many individuals who have contributed to this work. Specifically the research group at the OSU Gas Turbine Lab, Jeff Barton, Ken Copley, Michael Jones, and Packy Underwood for their work in assembling and operating the rig. In addition, they would like to thank the numerous students who have played an important role in this work, specifically Matt Krumanaker, who was responsible for most of the instrumentation calibrations. Finally, the OSU Gas Turbine Lab wishes to thank GEAE for their funding of the project, and also for the in depth collaboration that their GE-USA research program has provided them. This has resulted in a much more detailed collaboration between the university and industrial environments than was previously possible.

Nomenlature

LPTV = low-pressure turbine vane
HPTV = high-pressure turbine vane
HPTB = high-pressure turbine blade
PTR = total pressure ratio across the stage (measured) normalized by the design total pressure ratio—given as a percent
PTUA = total pressure as measured by the upstream rakes
Re = Reynolds number of the flow based on HPTV inlet area
Speed = rotor Speed (rpm)
Corrected = speed=physical rotor speed/[inlet total temperature(TUA)]^.5
TUA = Total temperature at upstream rake locations
Avg = average of all measurements
%range = (maximum measurement -minimum measurement)/(2*average), Given as a percentage

References

[1] Denton, J. D., 1993, "Loss Mechanisms in Turbomachines," ASME J. Turbomach., **115**, pp. 621–658.
[2] Huber, F. W., Johnson, P. D., Sharma, O. P., Staubach, J. B., and Gaddis, S. W., 1994, "Performance Improvement Through Indexing of Turbine Airfoils: Part 1—Experimental Investigation," ASME J. Turbomach., **118**, pp. 630–635.
[3] Jouini, D. B.M., Little, D., Dunn, B. E. M., Haldeman, C., and Johnson, P. D., 2003, "Experimental Investigation of the Aerodynamic Effects of Clocking Vanes and Blade Rows in a 1/3 Scale Model Turbine," ASME Paper No. GT2003-38872.
[4] Dunn, M. G., Seymour, P. J., Woodward, S. H., George, W. K., and Chupp, R. E., 1989, "Phase Resolved Heat-Flux Measurements on a Blade of a Full-Scale Rotating Turbine," ASME J. Turbomach., **111**, pp. 8–19.
[5] Haldeman, C. W., Krumanaker, M., and Dunn, M. G., 2003, "Influence of Clocking and Vane/Blade Spacing on the Unsteady Surface Pressure Loading for a Modern Stage and One-Half Transonic Turbine," ASME Paper No. GT2003-38724.
[6] Haldeman, C. W., 2003, "An Experimental Investigation of Clocking Effects on Turbine Aerodynamics Using a Modern 3-D One and One-half Stage High Pressure Turbine for Code Verification and Flow Model Development," *Aeronautical and Astronautical Engineering*, Ohio State University, Columbus, OH, p. 345.
[7] Haldeman, C. W., Dunn, M. G., Barter, J. W., Green, B. R., and Bergholz, R. F., 2004, "Aerodynamic and Heat-Flux Measurements with Predictions on a Modern One and 1/2 Stage High Pressure Turbine," ASME Paper No. GT2004-53478.
[8] Green, B. R., Barter, J. W., Haldeman, C. W., and Dunn, M. G., 2004, "Time-Averaged and Time-Accurate Aero-Dynamics for the Recessed Tip Cavity of a High-Pressure Turbine Blade and the Outer Stationary Shroud: Comparison of Computational and Experimental Results," ASME Paper No. GT2004-53443.
[9] Tallman, J. A., 2004, "CFD Heat-Transfer Predictions for a High-Pressure Turbine Stage," ASME Paper No. GT2004-53654.
[10] Dunn, M. G., 2001, "Convective Heat Transfer and Aerodynamics in Axial Flow Turbines," ASME J. Turbomach., **113**, pp. 637–686.
[11] Huber, F. W., Johnson, P. D., Sharma, O. P., Staubach, J. B., and Gaddis, S. W., 1996, "Performance Improvement Through Indexing of Turbine Airfoils: Part 2—Numerical Simulation," ASME J. Turbomach., **118**, pp. 636–642.
[12] Dorney, D. J., and Gundy-Burlet, K., 1995, "Hot-Streak Clocking Effects in a 1–1/2 Stage Turbine," ASME Paper No. 95-GT-202.
[13] Dorney, D. J., and Sharma, O. P., 1994, "A Study of Turbine Performance Increases Through Airfoil Clocking," AIAA Paper No. 96-2816.
[14] Eulitz, F., Engel, K., and Gebing, H., 1994, "Numerical Investigation of the Clocking Effects in a Multistage Turbine," ASME Paper No. 96-GT-26.
[15] Johnston, D. A., and Fleeter, S., 1999, "Turbine Blade Unsteady Heat Transfer Change Due To Stator Indexing, International Gas Turbine and Aeroengie Congress and Exhibition in Indianapolis, Indiana," ASME Paper No. 99-GT-376.
[16] Arnone, A., Marconcini, M., Pacciani, R., Schipani, C., and Spano, E., 2001, "Numerical Investigation of Airfoil Clocking in a Three-Stage Low Pressure Turbine," ASME Paper No. 2001-GT-0303.
[17] Reinmoller, U., Stephan, B., Schmidt, S., and Niehuis, R., 2001, "Clocking Effects in a 1.5 Stage Axial Turbine- Steady and Unsteady Experimental Investigations Supported by Numerical Simulations," ASME Paper No. 2001-GT-0304.
[18] Clark, J. P., Stetson, G. M., Magge, S. S., Haldeman, C. W., and Dunn, M. G., 2000, "The Effect of Airfoil Scaling on the Predicted Unsteady Pressure Field in a 1+1/2 Stage Transonic Turbine and Comparison with Experimental Results," ASME Paper No. 2000-GT-0446.
[19] Dunn, M. G., Moller, J. C., and Steel, R. C., 1989, "Operating Point Verification for a Large Shock Tunnel Test Facility," Paper No. WRDC-TR-2027.
[20] Dunn, M. G., 1984, "Heat-Flux Measurements for the Rotor of a Full-Stage Turbine: Part 1—Time-Averaged Results," ASME J. Turbomach., **108**, pp. 90–97.
[21] Dunn, M. G., Bennett, W. A., Delaney, R. A., and Rao, K. V., 1992, "Investigation of Unsteady Flow Through a Transonic Turbine Stage: Data/Prediction Comparison for Time-Averaged and Phase-Resolved Pressure Data," ASME J. Turbomach., **114**, pp. 91–99.
[22] Dunn, M. G., and Haldeman, C. W., 1995, "Phase-Resolved Surface Pressure and Heat-Transfer Measurements on the Blade of a Two-Stage Turbine.," ASME J. Turbomach. **117**, pp. 653–658.
[23] Barter, J. W., Vitt, P. H., and Chen, J. P. 2000, "Interaction Effects in a Turbine Stage," ASME Paper No. 2000-GT-0376.
[24] Chen, J. P., and Barter, J. W., 1998, "Comparison of Time-Accurate Calculations for the Unsteady Interaction in a Turbine Stage," AIAA 98-3292.

Aerodynamic and Heat-flux Measurements with Predictions on a Modern One and One-Half State High Pressure transonic Turbine

Charles W. Haldeman

Michael G. Dunn

Gas Turbine Laboratory,
Ohio State University,
2300 West Case Road,
Columbus, OH 43235

John W. Barter

Brain R. Green

Robert F. Bergholz

General Electric Aircraft Engines,
Cincinnati, OH 45215

Aerodynamic and heat-transfer measurements were acquired using a modern stage and 1/2 *high-pressure turbine operating at design corrected conditions and pressure ratio. These measurements were performed using the Ohio State University Gas Turbine Laboratory Turbine Test Facility. The research program utilized an uncooled turbine stage for which all three airfoils are heavily instrumented at multiple spans to develop a full database at different Reynolds numbers for code validation and flow-physics modeling. The pressure data, once normalized by the inlet conditions, was insensitive to the Reynolds number. The heat-flux data for the high-pressure stage suggests turbulent flow over most of the operating conditions and is Reynolds number sensitive. However, the heat-flux data do not scale according to flat plat theory for most of the airfoil surfaces. Several different predictions have been done using a variety of design and research codes. In this work, comparisons are made between industrial codes and an older code called UNSFLO-2D initially published in the late 1980's. The comparisons show that the UNSFLO-2D results at midspan are comparable to the modern codes for the time-resolved and time-averaged pressure data, which is remarkable given the vast differences in the processing required. UNSFLO-2D models the entropy generated around the airfoil surfaces using the full Navier-Stokes equations, but propagates the entropy invisicidly downstream to the next blade row, dramatically reducing the computational power required. The accuracy of UNSFLO-2D suggests that this type of approach may be far more useful in creating time-accurate design tools, than trying to utilize full time-accurate Navier-Stokes codes which are often currently used as research codes in the engine community, but have yet to be fully integrated into the design system due to their complexity and significant processor requirements.* [DOI: 10.1115/1.1861916]

1 Introduction

This work presents the results of an experimental study utilizing a modern uncooled high-pressure turbine stage with the adjacent low-pressure turbine vane row (a typical civilian one and one-half stage rig) operating transonically (loosely referred to in this paper as a "stage"). The overall experiment consisted of two different entries, approximately a year apart. The first set of entries focused primarily on aerodynamic measurements, including clocking effects. The second entry focused more on heat-flux measurements; although a great deal of work was also done on turbine tip pressure and heat transfer during this entry. Companion papers discuss different aspects of these experiments. The low-vane clocking aerodynamic and aeroperformance results are discussed in Ref. [1], turbine blade recessed tip-region time-averaged and time-accurate pressures are discussed in Ref. [2], and predictions comparing the present heat transfer data with another design code are presented in Ref. [3]. The experimental matrix performed for these two entries was designed for code verification and to acquire a baseline data set for the cooled rig, which will be operated in 2004.

Contributed by the International Gas Turbine Institute (IGTI) of THE AMERICAN SOCIETY OF MECAHNICAL ENGINEERS for publication in the ASME JOURNAL OF TURBOMACHINERY. Paper presented at the International Gas Turbine and Aeroengine Congress and Exhibition, Vienna, Austria, June 13–17, 2004, Paper No. 2004-GT-53478. Manuscript received by IGTI, October 1, 2003 final revision; March 1, 2004. IGTI Review Chair: A. J. Strazisar.

While the data are primarily used for code verification by the sponsor of this work (since the airfoil geometry is not public information), a great deal of interesting behavior can be observed from this data which are applicable to many different aspects of turbine design. The focus will be on turbine aerodynamics and heat transfer behavior at the midspan location only. There exist (as shown in previous work [4]), a great deal of spanwise variation due to the highly loaded nature of this rig (total pressure ratio in excess of 5). However, due to space limitations, the dependence of the data on span location will be described at a later date.

2 Literature Review/Background

Heat-flux and aerodynamic measurements in full rotating rigs, operating at corrected engine conditions are still relatively limited. The number of facilities that can produce these measurements is still relatively small, and the number of groups that can support these large projects has not expanded greatly over the years. However, it is important to note that these type of measurements are still only a part of the overall research that goes on in turbine heat transfer and often smaller rigs are more adept at measuring more localized issues. An overview of both the current state of heat-transfer measurements and the path by which the scientific community has attained to this point is given in Ref. [5].

The focus of this paper is twofold. The first is to show the pressures and heat-flux measurements over a stage and one-half turbine at midspan. This is currently one of a very few data sets

that present both the aerodynamic and heat-flux data. The second is to show the results of a simplified flow model originally conceived in the 1980's as a predictive tool.

The Ohio State University (OSU) Gas Turbine Laboratory (GTL) has historically focused on the experimental aspects of aeropropulsion research, but has wanted some type of capability for modeling the unsteady vane/blade interaction that occurs in the turbine stage. Our attention was drawn to a simpler model originally conceived at the Massachusetts Institute of Technology (MIT) by Giles [6] called UNSFLO and since then renamed UNSFLO-2D. The OSU GTL has permission from Rolls Royce England to use this code for research studies performed at the GTL.

UNSFLO-2D is both an analytic model and a numeric implementation of this model. The analytic part can be easily described, and most of the key insights of Giles and co-workers have been incorporated into later codes. Analytically, Giles hypothesized that the core problem in vane/blade interaction was obtaining the unsteady, periodic solution, and that could be done by separating the region into the area immediately around the blade where the full viscous equations are solved, and an area over most of the passage where the entropy generated in the immediate blade area is convected invisicidly. This simplification required two different grids to be created and two different solutions run, but this became manageable on computers of the 1980's. Giles' work built upon four main pieces of work in the early 1980's [7–10]. Giles intentionally used his computing resources on the unsteady part of the problem instead of proceeding with trying to calculate a full three-dimensional (3D) passage.

It is beyond the scope of this work to go into the details of the code. The main components can be summarized in the following fashion: the code operates over two regimes. In the viscous region, the equations are unsteady Reynolds averaged Navier-Stokes equations, using an implicit scheme. One has a choice of turbulence model and can several different types such as algebraic or *K*-epsilon. In the inviscid region, an unstructured grid is used, solving the unsteady Euler equations along a stream tube using an explicit solution.

The code has the ability to handle unsteady boundary conditions and arbitrary pitch ratios (number of blades in each row). The three main numerical innovations were the hybrid grid used for the solution, the ability to use arbitrary pitch ratios (which led to the development of the time-tilting algorithm used widely today), and the variety of boundary conditions.

Several papers were published during the development of UNSFLO-2D, which cover the time from 1988 to 1991 [11,12]. Over the period of 1989–1992, the code was validated using data from the MIT blowdown turbine. Two papers dealt specifically with rotor heat transfer and compared the data to the numerical predictions and to cascade data [13,14]. This work was also supported by the work of Korakianitis [15,16]. A literature review turned up two other reports where UNSFLO was listed (other than the work done at the OSU GTL), both 1998 reports done by Singh from Pyestock in England [17,18].

Actually, while the open literature has not included a large number of verification papers written with UNSFLO-2D, in the 1990's a great deal of work has been done with similar types of codes. UNSFLO-2D was part of a family of codes that were developed in the late 1980's {Allison's VBI code [19], Pratt's Ni code [20], and Mississippi State Universities TURBO code (created in conjunction with NASA) [21] are all similar in concept}. All these codes were used extensively by their respective companies in the design process in the 1990's. Currently, some of the most promising research codes that may actually make the transition to design codes are 3D codes that have a model similar to UNSFLO-2D in the generation of entropy and inviscid propagation.

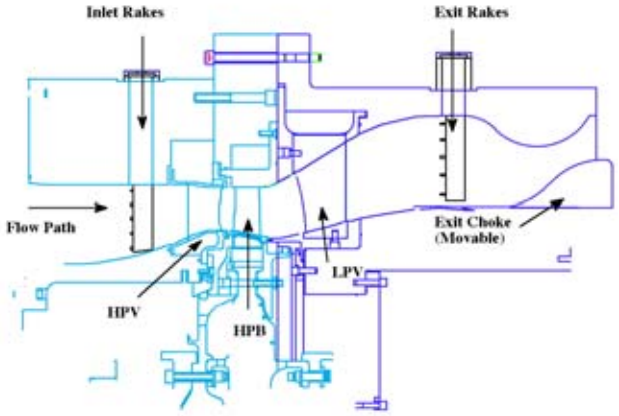

Fig. 1 Main flowpath

3 Experimental Procedure

3.1 Experimental Facility/Rig. The main facility used in these experiments is the OSU Gas Turbine Laboratory Turbine Test Facility (TTF). The TTF is a short-duration shock tunnel facility capable of achieving variable inlet pressures and temperatures up to engine conditions. The actual construction and operation of the facility was first documented by Dunn [22] but more accessible descriptions of the operation of the facility have been reported in Dunn [23–25] as examples.

The TTF was operated in two modes for these experiments. One mode is the traditional shock-tube mode as described by Ref. [22]. A second mode, which has become more widely used for aerodynamic work (as opposed to heat-transfer work) is the blowdown mode. The two modes of operation provide different types of data and in this paper both modes of operation will be discussed.

The key to any short-duration full-scaled rotating rig is the ability to match the nondimensional parameters of interest. Briefly, these generally are the ratio of the metal to gas temperatures (for heat-transfer studies), the Reynolds number, the pressure ratio, the corrected speed, and the Rosby number (for rotating effects). The Rosby number is usually matched if the same physical equipment is used with the proper corrected speed and thus it is not usually explicitly defined. For the heat-transfer studies, the metal temperature is scaled to room temperature, which usually dictates the inlet gas temperature of about 600 K. If one is interested in aerodynamic studies as opposed to heat-transfer studies, this requirement is not present and one can match the Reynolds number, pressure ratio, and corrected speed with warm gas from a blowdown experiment. Since this facility has been reported in great detail over many years, readers unfamiliar with it are referred to the many other papers using this facility and no further discussion of the facility will be given here

3.2 Turbine Rig. The turbine rig used in this study is a large stage and one half [high-pressure turbine vane (HPTV), high-pressure turbine blade (HPTB), and low-pressure turbine vane (LPTV)] machine, configured in a manner that replicates current placement of the airfoil rows in a modern engine. Since it is a modern machine, the airfoils are of very strong three-dimensional design and the total pressure ratio across the rig is in excess of 5.

A sketch of the main turbine stage is shown in Fig. 1.

Here one can see the relative location of the airfoil rows. Scientifically, the region of the flow path under investigation is defined by the location of the inlet and exit rakes. At each of these locations, there are two total temperature rakes and two total pressure rakes (five sensors each placed at the center of equal areas). In this rig, there are 38 vanes (both HP and LP) and 72 blades.

Table 1 Experimental conditions used for heat-flux and pressure data

Main runs	Entry	Date	Type	Approx. press.	Approx Rey. #	Exp. group
25	1	April 3, 2001	Blowdown	45	4.61E6	1*a*
31	1	April 10, 2001	Blowdown	60	6.16*E*6	1
32	1	April 10, 2001	Blowdown	60	6.06*E*6	1
2	2	Feb. 26, 2002	Shock	46–48	2.51*E*6	2
3	2	Feb. 27, 2002	Shock	46–48	2.88*E*6	2
4	2	Feb. 28, 2002	Shock	46–48	2.89*E*6	2
5	2	Feb. 28, 2002	Shock	58–60	3.08*E*6	3
6	2	March 1, 2002	Shock	58–60	3.14*E*6	3
7	2	March 1, 2002	Shock	58–60	3.29*E*6	3
9	2	March 5, 2002	Shock	58–60	3.06*E*6	3
10	2	March 5, 2002	Shock	58–60	3.03*E*6	3
11	2	March 5, 2002	Shock	58–60	3.17*E*6	3
12	2	March 12, 2002	Shock	78–80	4.14*E*6	4
13	2	March 12, 2002	Shock	78–80	4.17*E*6	4
14	2	March 13, 2002	Shock	78–80	4.12*E*6	4
16	2	March 18, 2002	Shock	85–90	4.56*E*6	5
17	2	March 18, 2002	Shock	85–90	4.50*E*6	5
18	2	March 19, 2002	Shock	85–90	4.59*E*6	5
19	2	March 19, 2002	Shock	85–90	4.69*E*6	5
20	2	March 19, 2002	Shock	85–90	4.56*E*6	5
26	2	April 22, 2002	Blowdown	60	5.92*E*6	6
27	2	April 22, 2002	Blowdown	60	5.74*E*6	6

The exit choke is movable, so that a variety of pressure ratios are available. By controlling the pressure ratio across the stage, the inlet pressure and the corrected speed, a wide variety of engine operating conditions can be replicated.

As mentioned earlier, the overall research effort using this rig was comprised of two separate entries. The first entry was intended to investigate the aerodynamics of the turbine stage and contained mostly pressure data and utilized only one slip ring. The second entry added rotor, rotor shroud, and low vane heat-flux sensors, rotor tip pressures and heat-flux sensors, and the second slip ring and concentrated (but not exclusively) on heat-flux measurements at different Reynolds number conditions. At the end of the second entry there were 485 instruments allocated throughout the rig. Each airfoil had sensors distributed at three span locations (15%, 50%, and 90% spans, with the exception of the LPTV which was at 10%, 50%, and 90% spans), and there were heat-flux and pressure sensors mounted on the HPTV inner and outer end walls, and pressure sensors mounted in the area between the rotor and the LPTV on the inner and outer end walls. The rotor was instrumented with heat-flux sensors and pressure sensors on the platform, and on various blade-tip configurations in addition to the three spanwise locations noted earlier. This number of instruments surpassed even the relatively large analog-to-digital (A/D) system (300 channels) at the OSU GTL, and thus the second entry was split into different "patches" where part of the sensors would be connected for the first runs, and others connected for different runs.

The pressure sensors where variants of the Kulite XCQ-062-100A sensors mounted either as total pressures (for the rakes) static pressures (at the rake locations), or as chip sensors on the airfoils themselves. The heat-flux gauges were all built at OSU and are of similar type to the Calspan heat-flux gauges (effectively a thin platinum film on a Pyrex substrate).

The data acquisition system and basic calibrations have been described previously and have been summarized in Ref. [26]. As there is not much new information it will not be discussed in detail here other than saying that the data was all acquired at 100 kHz using a set of anti-aliasing filters set at 45 kHz. This insured that proper resolution of the time-resolved data was obtained.

3.3 Experiments. The data in this paper come from a subset of runs from both entries that were designed to look at Reynolds number effects and to compare data from blowdown runs and shock runs. As discussed previously, the blowdown runs are exceptionally well suited to aerodynamic measurements, where the shock runs are better suited for heat-flux sensors. However, most boundary layer codes used for heat-transfer predictions need as an input the surface pressure distribution. For sensor numbers that did not exceed the total number of A/D channels this was not a problem. Both pressure and heat-flux sensors were recorded simultaneously. However, for this entry there was so many of the heat-flux sensors that vary few pressure sensors could be recorded at the same time, and the detailed pressure distribution had to come from other experimental runs. As will be shown, combining the data in this manner works well.

In the data subset shown below in Table 1, the first six columns are relatively self-explanatory. The last column is the experimental group, which combines the different runs that should form a repeat condition. For entry 1 data runs 25 and 26 were supposed to be at the same condition as runs 31 and 32, but the change in the position of the exit choke modified these runs a little thus they are listed as condition 1 and 1*a*. Experimental groups 2 and 4 were derived from setting the main conditions for experimental groups 3 and 5, and were a little lower than anticipated, but these conditions provide data at slightly different Reynolds numbers.

The derivation of the main experimental set points and the variation within each group, as well as the variation between the groups is shown in Ref. [26]. The overall variation for all experimental groups is on the order of ±1.7% (this is a range, not a standard deviation) over all runs. The Reynolds number range for the experimental points is shown in Fig. 2. One can see that the Reynolds number comes close to doubling, while the pressure ratio variation between the experimental points is well within the variation at each experimental point.

The slight downward trend in the pressure ratio in Fig. 2 is related to the corrected speed. As shown in Ref. [26], the connection between the pressure ratio and the corrected speed is not surprising. The key point is that as the corrected speed changes, the incident angle on the rotor is changing. This has the effect of changing the blockage area for the flow, which changes the pressure ratio. These effects are small (as seen earlier) since turbines are more forgiving than compressors, but are noticeable. An over-

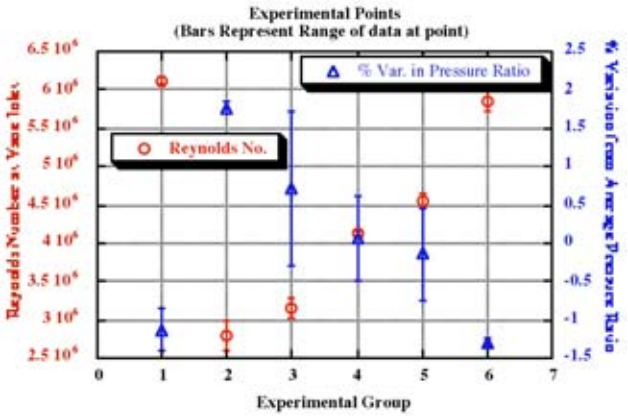

Fig. 2 Reynolds number and pressure ratio variation

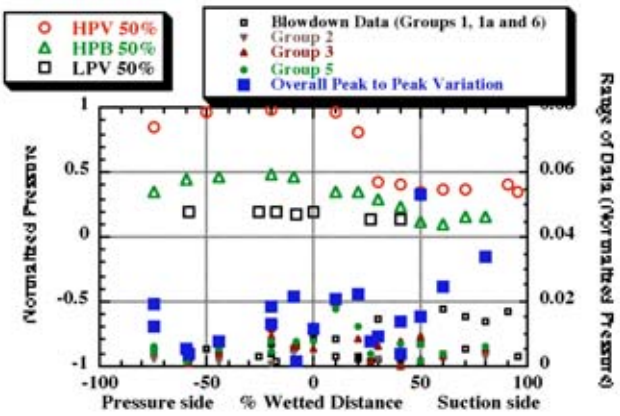

Fig. 3 Time-averaged pressures for all experimental cases

all comparison for all the runs listed in Table 1 (this includes both shock runs and blowdown runs and runs from two different entries a year apart) for the properties that should be constant is shown in Table 2. For all runs, the range in corrected speed is ±1.3% and the range in pressure ratio is ±1.7, which is comparable to the variation seen in the conditions for just one group of heat-flux runs. This is another example that there is no difference between the shock and blowdown data sets in terms of ability to set the experimental conditions.

3.4 Data Reduction/uncertainty analysis. The data reduction procedure is relatively straightforward. All the raw pressures are normalized by the average total inlet pressure for the given experiment and time window, creating the normalized pressure, which forms the basic pressure data used in this paper. The normalized pressure data then varies from 0 to 1 and is dimensionless. Usually one revolution of data was examined and the time average was taken over that same revolution. Ensemble data were created in time space by equally splitting a revolution of data into the proper number of passages and then bin averaging these together to get individual ensemble plots. This avoids interpolation errors for the peak pressures but does require some interpolation on the blade passage axis. The power spectrums are created by applying a Hamming window to the data and using an interpolation scheme to get the proper peak amplitudes and frequencies. The heat-flux data are created using a semi-infinite solid approximation and a Cook-Felderman algorithm (standard procedure). The heat flux was then normalized to a Stanton number based on the total inlet temperature, inlet mass flow, and gauge temperature.

When combining different runs together to form a group, two different techniques were used depending on what information one was interested in obtaining. When looking at repeatability of the experimental condition, a relative average technique was used. This allowed the inclusion of information about the quality of the sensor, but kept the periodicity of the sensor out of the uncertainty estimates. The range for this average technique was taken from the maximum and minimum experimental variations that form the overall group average. When one was looking for the effects of the blade passage variation, the maximum and minimum variation was taken from the envelopes. More detailed descriptions of all these operations can be found in Ref. [26].

4 Experimental Results

4.1 Combination of Shock and Blowdown Runs. The later figures show the time-average pressure (relative average) of each individual experimental group at the 50% span location for all three airfoils. The range bars will show the maximum and minimum variation from the average and is used to determine repeatability. The relative average is used (as described earlier) because it can account for relative accuracies of each individual sensor, without actually incorporating the data variation that arises from the natural periodic pressure envelope of the sensor. Figure 3 shows the average of all the different experimental groups (both shock runs and blowdown runs) on the left axis for the three blade rows. The x axis in this case (and throughout similar figures in the paper) represents the wetted distance along the airfoil where −100% represents the training edge on the pressure side, +100% is the trailing edge on the suction side, and 0 is the nominal stagnation point. The relative uncertainties for each experimental group as well as an overall peak to peak range taken across all the groups is given on the right axis. The data are shown in this manner since the range bars are not viewable on the left axis scale. One can see that the blowdown pressure data (even though it is acquired later in an experiment) fits in very well with the shock runs. Outside of two points, all the uncertainties are below 2% of the total inlet pressure, which is very close to the calibration accuracy of the pressure sensors, and there is no viewable difference between the different experimental groups in terms of overall accuracy. This implies that the run-to-run variation that occurs is not dependent on the type of facility operation.

These results are critical for several reasons. Primarily this analysis validates a split in the data acquisition that was forced on us by necessity and will probably become a more standard approach for us in the future. The ability to split off the pressure transducers and run them completely separately from the heat-flux

Table 2 Overall variation in "constant" conditions for all experimental groups

Overall variation for values that should be constant for all experimental groups	Corrected rotor speed	Total pressure ratio	Total inlet pressure/exit static pressure
	RPM/K^.5	% of avg	
Avg	359.676	100%	5.658
%range/avg	1.286	1.683	2.202
%STD/avg	0.709	1.073	1.289

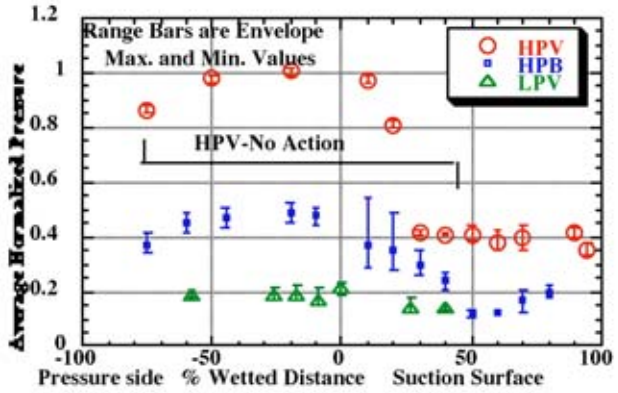

Fig. 4 Time-average pressures with envelope range, 50% span, all airfoils

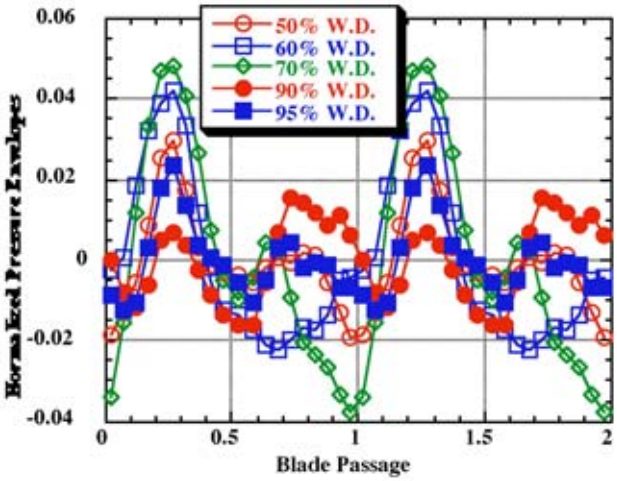

Fig. 5 HPTV envelope shapes, 50% span

sensors and then recombine the data afterwards allows each individual type of measurement program to be tailored to its particular needs: the shock-tube mode for the heat-flux sensors and the blowdown mode for the pressure sensors. In addition to creating higher quality data, this system also allows for more instruments to be utilized.

Another result of this work, which is more critical to the clocking analysis [1], is that even over these large Reynolds numbers variations, no significant Reynolds number effect on the pressure has been noticed (and one would not expect to see one). This is critical, because in the past, there has been some concern that experimental results have seen slight Reynolds number effects on clocking data. These have usually been very hard to resolve due to the very low levels of the clocking effects. Having a decent measure of the normalized pressure as a function of Reynolds numbers, helps to bound the resolution of the Reynolds number effects that may be observed in the clocking experiments.

4.2 Time-Resolved Pressure Data. Since there is no Reynolds number dependence, and the shock runs and blowdown runs produce the same normalized pressure distributions, in this section the data from the blowdown runs will be presented. The time-resolved pressure data are important in visualizing how the envelope sizes, and fast-Fourier transforms (FFTs) amplitudes change throughout the stage. They will be presented in two modes: a time domain mode, which will be envelopes, and a frequency based mode that will be power spectrums (FFTs).

As a comparison to Fig. 3, Fig. 4 shows the time average pressure for the blowdown cases, but the range bars represent the range of the data over one revolution (the envelope extremes). This shows the advantage of using the relative average technique when trying to show repeatability, since it eliminates the periodicity that occurs.

On this plot, one can see the relative importance of the unsteadiness in the data for the different airfoils. For the HPTV there is no action on the pressure side all the way to the 40% location on the suction surface. Only the last five sensors show any significant variation. However, at these locations, the time average of the HPTV locations are comparable to the variations seen on the HPTB at the leading edge on the suction side. In addition, the envelope sizes at the trailing edge of the HPTV are comparable to the envelope sizes over most of the HPTB and LPTV. To complete the picture the envelopes ranges in Fig. 4 can be expanded to examine the shape in the time domain.

For the HPTV, the trailing edge envelope data on the suction side are shown in Fig. 5. This plot shows the normalized pressure fluctuations (time-average subtracted out) versus the HPTB blade passage. This scale (and throughout this paper) represents the variation that a sensor sees in time as the adjacent blade row moves by the sensors location. Locations 0 and 1 are not necessarily fixed to any given location on the HPTB (for instance the leading edge), but they do represent the exact same location one blade apart. One can see from this figure that there is more than just changing amplitudes happening. At 50% span the waves are essential dual peaked, but at 60% the second peak has diminished, and then after 60% the second peak grows again. This of course has an implication for the cooling patterns on the HPTV. The same data can be seen in the frequency domain, which helps for the mechanical designer who is interested in the frequency content of the loading pressures for high-cycle fatigue issues.

The change in the envelope shape is shown more dramatically in Fig. 6. The left axis is the normalized pressure, thus at 70% wetted distance (WD), there is about 2.7% of the total inlet pressure at the fundamental blade frequency. However, if this same data were normalized by the local averages it would be closer to 8%. What is important to realize is that the fluctuations can represent a significant fraction of the average local pressure. As opposed to the absolute level, probably more interesting is the change in the energy content as one moves further toward the trailing edge. At 70% wetted distance the first harmonic is far more important than at 60%, whereas the second harmonic does not change substantially based on wetted distance.

For the HPTB, the data will be split up into plots of the pressure surface and suction surface as shown in Figs. 7 and 8. For the HPTB on the pressure side there is not much variation with the exception of the displacement between the local max and minimum of the envelope, which steadily decreases as the location

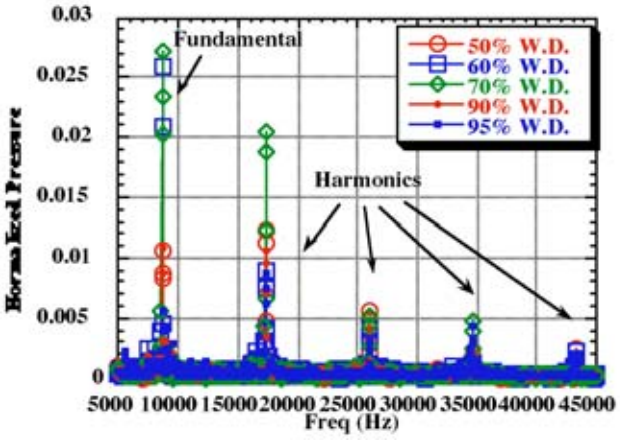

Fig. 6 HPTV frequency content, 50% span

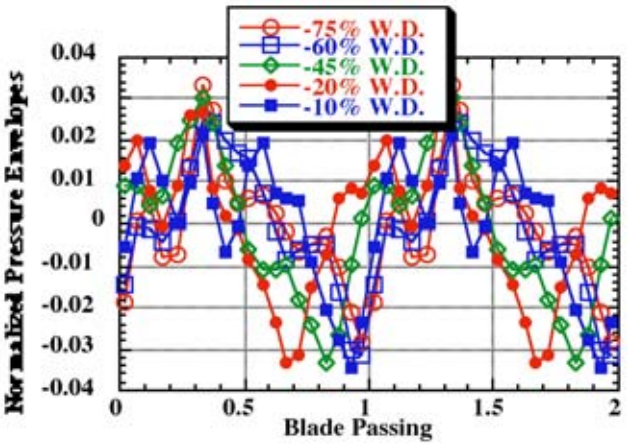

Fig. 7 HPTB normalized pressure envelopes, pressure surface, 50% span

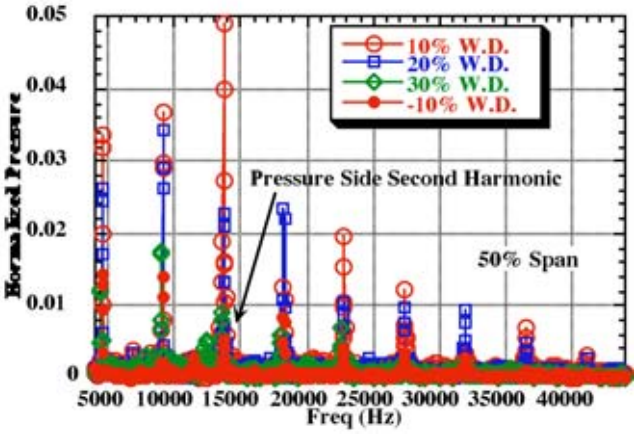

Fig. 9 HPTB normalized pressure leading edge, 50% span

moves forward to the leading edge. On the suction surface the 10% and 20% locations dominate, and the envelopes die down in the 50–60% range, only to start to build again as one approaches the trailing edge.

Due to space limitations, only the FFT data for the area around the leading edge will be presented (shown in Fig. 9), although there is a great deal of information available at all locations. On the suction surface the second harmonic dominates, although both the fundamental and first harmonic is close in size, whereas on the pressure side, the second harmonic is virtually nonexistent. While the fundamental and first harmonic are of similar size between the two positions, the effect of not having that second harmonic makes the ensemble shape very different and generates a range of the envelope of about three times less on the pressure side. While not shown on this plot, moving towards the trailing edge on the pressure side an energy transfer between the higher harmonics and the main frequencies occurs with the second harmonic growing again in importance at −45%, and then dying off, leaving the fundamental. While the shape of the envelope changes a little in this area, the range stays fairly constant at about ±0.04.

On the suction surface, the story is much different. Here there is a great deal of harmonic energy that dies of by about the 30% location. The frequencies and the envelopes become hard to discern from about 40% to about 70%. After that the main frequencies increase a little and the envelope becomes more defined. This seems to indicate that the influence of the HPTV is prevalent over the early part of the blade, and the LPTV over a latter part, but that there is an area where there is not much influence from either airfoil row (on this machine at the 50% span location!)

The LPTV envelope data is shown in Fig. 10. There is a steady decay in the amplitude of the envelope as one moves away from the leading edge. The maximum amplitude occurs at −8.7% WD, suggesting that the LPTV may be running a little off incidence in this case. This may be due to slight imperfections in the hardware. In addition, the leading edge on the vane is exceptionally sharp. Another interesting point is the development of the second peak at −17.3%, which then decays again.

The main frequencies are also apparent on the LPTV (Fig. 11). Here only the data from ±26% wetted distance are plotted. One can see the development of the second peak at −17.3% wetted distance, as the relative increase in the importance of the second harmonic. One can also see the steady decrease in the harmonic amplitude as one moves away from the leading edge. Probably the most interesting observation is that the unsteadiness on the pressure side toward the leading edge can be about the same magnitude as on the HPTB (Figs. 8 and 9). Thus, the relative fraction of the average pressure for each frequency can be relatively high on the LPTV.

4.3 Pressure Data with UNSFLO-2D Predictions. The focus of this part of the paper is to show a comparison between the data and a simplified model of the flow that shows promise in performing unsteady predictions. In using the UNSFLO-2D model it is important to realize that certain assumptions about the flow

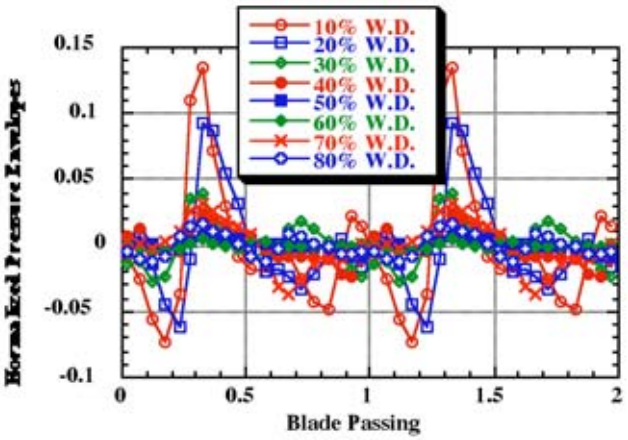

Fig. 8 HPTB normalized pressure envelopes, suction surface, 50% span

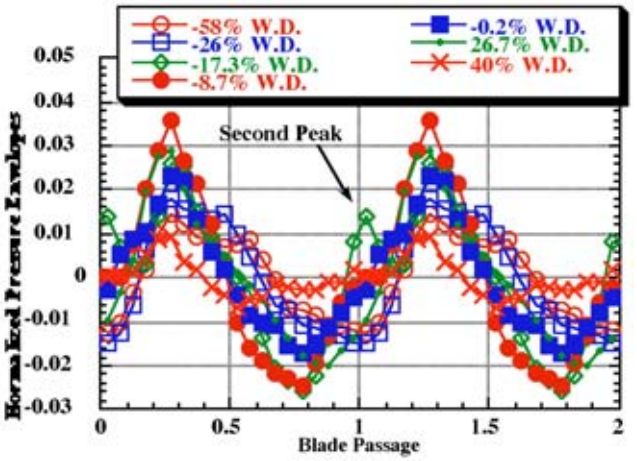

Fig. 10 LPTV normalized pressure envelopes, 50% span

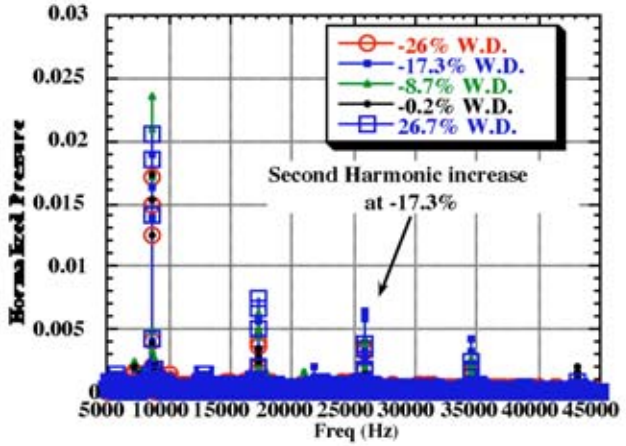

Fig. 11 LPTV normalized pressure FFT amplitudes, 50% span, ±26% wetted distance

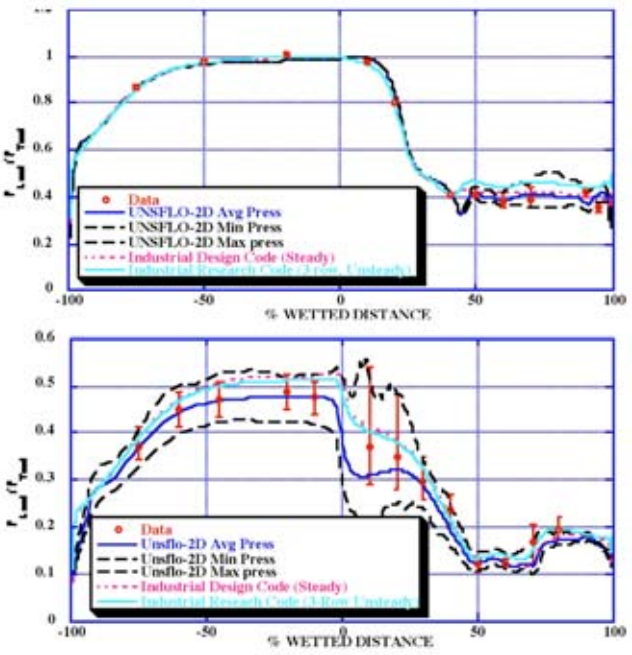

Fig. 12 UNSFLO predictions HPTV and HPTB 50%

are already being made (specifically the importance of local 3D effects). As a result, full 3D unsteady Navier-Stokes codes were needed as a bench mark comparison to see how important some of these issues are in real flows. This has been done in the past with a model which is more two dimensional (2D) in nature [27] with good results. With this data set, most of the pieces to revisit the applicability of the UNSFLO-2D model are in place. We have a full 3D data set of both pressure and heat flux over three blade rows, and industrial design codes and research codes to compare against.

Detailed specifics of the code and how it was run will not be discussed, since it is not that relevant to the work. No attempt was made at grid refinement. The goal was to see if the code could be used as a prediction tool, once it was compiled and the proper input geometry was applied. A converged solution was obtained, without a lot of modification of the input conditions. Probably the only relevant material is that the solution shown below was done with a *K*-epsilon turbulence model using a freestream turbulence level between 5% and 10%, (which did not alter the aerodynamic solution). For these solutions only the first two blade rows were modeled, and the streamtube thickness variation for 2% span location (49–51% span) was provided from an inviscid streamtube code used by industry.

As seen in the figures, all three codes do a very good job predicting the time-average values at the midspan location. At the vane trailing edge on the suction surface and on the blade leading edge area of the pressure surface the data aligns a little better with UNSFLO-2D than with the industrial design codes. The reason for this is due to the fact that the UNSFLO-2D solution is first done on the vane and then the rotor, and then combined, and thus the pressure ratio across the vane was matched to the data, and then the pressure ratio across the entire stage. For the industrial codes, only the pressure ratio across the entire stage was matched. Another interesting point is that the unsteady bands predicted by UNSFLO-2D match the data passage envelopes quite well. This information was not immediately available from the industrial codes. It is also interesting that the influence of the low-pressure vane is not great on the time-averaged pressure for the blade as shown at the trailing edge of the blade, since all three codes predict similar values. No attempt was made to optimize either code, and an attempt to numerically quantify the differences between the codes and the data would be misleading.

To reiterate, the main goal in using UNSFLO-2D for predictions was to see if that code specifically could be used to generate reasonably accurate predictions of the time-resolved pressure as an engineering design tool. It is not surprising that both the industrial design code would reproduce the time-average values, or that the research code would also function to get similar answers. What is different is the scale of effort that goes into running each code. The industrial design code will not generate the periodic information that UNSFLO-2D or the research code generates. However, UNSFLO-2D will run on a Macintosh or PC, and the research code takes several large machines running in parallel to reproduce similar answers. To be fair, the research codes will handle the strong 3D effects and provides information over the entire blade surface, including the tip and platform regions of the airfoil. However, in the present state the code does not provide an estimate of the heat flux. UNSFLO-2D has that possibility, although for this work it was not examined.

Returning to the main principles of UNSFLO-2D, we see that at least at the 50% span location, the basic idea of convecting the entropy generating wakes downstream invisicidly works well in terms of reproducing the pressure fields (Fig. 12). The influence of the low-pressure vane row on the upstream rows (potential effect) is not critical to the upstream envelopes and that is probably due more to the design of this particular machine than any other issue. The time has probably passed for this version of UNSFLO-2D to become important to the industry. Computer power has increased, and the problems have changed to the point where the 3D unsteady Navier-Stokes codes that can handle the entire airfoil surface are receiving much more attention. However, UNSFLO-2D remains a very powerful tool for use in generating unsteady predictions.

4.4 Heat Flux Data. The heat-flux data were reduced using the techniques described earlier. There is a great deal of information available from the four Reynolds numbers cases that were examined as well as the off-design corrected speed data. The goal of this section is to show some typical variations in Stanton number that occur with Reynolds number as shown in Fig. 13. The ranges for each group are shown via the bars. One can see that while the patterns are fairly tight, there are some variations that occur with Reynolds number. Locations where one expects the least amount of periodic behavior (HPTV pressure side), the groupings of the data are extremely tight, while areas where there is more periodic behavior (LPTV) the range bars are larger. It is important to note the dramatic decrease in the Stanton number as

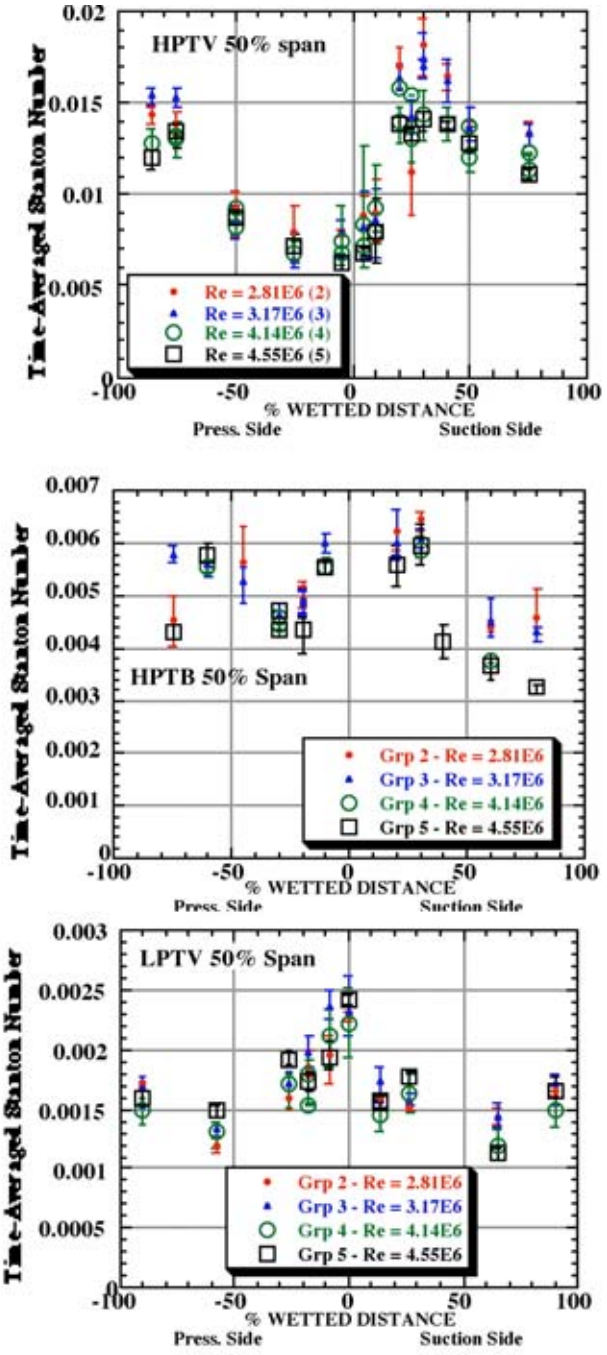

Fig. 13 Locations on the three airfoil rows as a function of Reynolds number

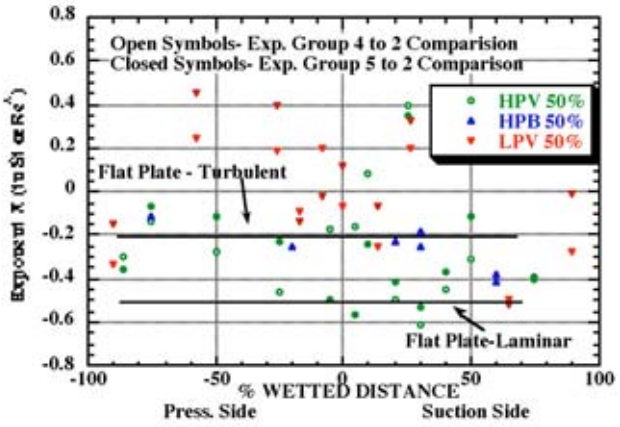

Fig. 14 Exponent in stanton number/Reynolds number relationship

one progresses steadily through the machine, so much so that the ranges on the LPTV are not the same magnitude as the ranges at the HPTV.

One simple relationship that can be tested is the idea of the flat plat correlation between the Stanton number and the Reynolds number (Fig. 14). Most empirical correlations show that for turbulent boundary layer flow, the Stanton number should scale with the Reynolds number to the −0.2 power and to the −0.5 power for laminar flow. In the following plots the actual exponent could be found from the following derivation. If

$$\mathrm{St} \propto \mathrm{Re}^{x}$$

then,

$$\frac{\mathrm{St}_1}{\mathrm{St}_2} = \left(\frac{\mathrm{Re}_1}{\mathrm{Re}_2}\right)^{x} \Rightarrow X = \frac{\ln\left(\frac{\mathrm{St}_1}{\mathrm{St}_2}\right)}{\ln\left(\frac{\mathrm{Re}_1}{\mathrm{Re}_2}\right)}$$

The exponent X can be found from performing this ratio. In the plots that follow this exponent was calculated for groups 4 and 5 relative to group 2 (to give the largest change in Stanton number in an effort not to get lost in the variation within each group).

One can see that the patterns tend to be repeatable across all the airfoils, with groups four and five having similar values. For the HPTV on the pressure side, the average exponent value is indeed about −0.2. However, on the suction side it varies quite a bit.

While there are not enough sensors on the HPTB for all the different runs at this span location to show a great deal about the trend, one can see that on the suction side also there is substantial variation from the idealized flat plate. One very interesting item is that the high exponent values seen on the HPTV at about 25% on the suction side are duplicated on the LPTV at the same location, which is a point of maximum curvature on both airfoils. This trend emphasizes the strong effect that the pressure gradient has on the heat flux, and shows why the flat-plate correlations are not very useful for regions where strong pressure gradients exist on turbine airfoils. However, the strong repeatability of the patterns from group to group and from airfoil to airfoil suggests that the data are not random.

As a final example of the information available in this data set, the time-resolved heat flux will be examined. Due to space limitations only the FFT data will be shown since that may be of the most interest to designers worried about crack initiation. The philosophical reasons for studying unsteady heat flux have been discussed briefly in Ref. [26]. Theoretically, as shown by Boley and Weiner [28], the idea of thermal induced vibrations in thin plates has shown that thin plate configurations similar to the skin on a cooled blade might produce thermal deflections up to twice the static deflections in certain cases. Only the blade designers at the engine companies know the practical necessity for this type of work. Examples of the information that can be obtained from a more detailed examination of the unsteady heat-flux envelopes are shown below. Figure 15 shows two gauges close together about half way back on the suction side of the HPTV. These were chosen because it shows how the energy dissipates as one moves forward.

These data are shown over one revolution using the interpolation techniques describe earlier (actual FFT resolution is 149 Hz). For the gauge at 50% location (HV16), one can see that the main peak occurs at 10.6 kHz, which is very close to the calculated blade passing frequency. There are other characteristic frequencies

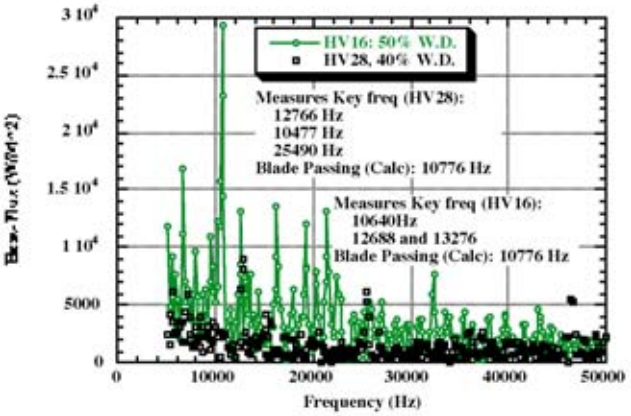

Fig. 15 HPTV 50% span FFT, selected gauges

that show up at 12,688 and 13,276. The 13,276 Hz number is interesting because it represents a combined frequency of the rotor blade count and 1/2 of the vanes. However, clearly it is a very low signal. Just a little forward of this location at 40% span (HV28), the main blade passing frequency is almost completely gone.

There is more action on the LPTV as is shown in Fig. 16, which shows three different locations on the LPTV suction surface. One can see the main frequency decays as one moves downstream. What is interesting is that there is some action at 15 kHz for the 27% location, and a slightly lower frequency (that 13 kHz number) for the 40% location. In addition, the 40% location clearly has multiple harmonics while the first harmonic seems to die away by the 90% location. Another interesting point is that the frequency content remains viewable even as one processes the temperature data into heat flux suggesting that relative sizes of the unsteady envelopes should be obtained from the raw temperature data instead of the heat-flux sensors if one wanted to try to reduce noise.

As a note, comparisons between frequency data obtained from the Stanton number of Nusselt number do not yield any substantial differences in the frequencies (similar to the comparison between the temperature and the heat flux). This implies that in fact we are capturing all the main frequencies and that no extraneous frequencies are being incorporated into our data. Similarly, comparisons between runs for the same gauge yield similar results, indicating no significant run-run variation in sensor performance.

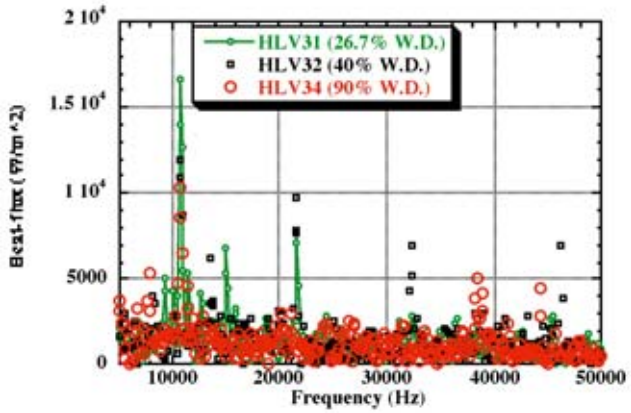

Fig. 16 LPTV 50% span FFT, selected gauges

5 Conclusions

This paper has shown examples of the heat-flux data and pressure data for a one and one-half stage rig. The normalized pressure data was shown to be insensitive to the operation modes of the facility and to be Reynolds number insensitive (as expected). Only the 50% span data have been shown, but there is a variety of data (both heat flux and pressure) available at other span locations and on the end walls and blade tips. The data show that we can combine data from shock-tube mode runs and blowdown runs to create fuller data sets, and that doing this does not affect the stability setting the experimental design point.

In addition, this paper shows that for the flow physics involved in this rig, the simplifying assumptions (reduced griding resolution, inviscid propagation of entropy, etc.) required of a 2D unsteady code are not great and do not affect the accuracy of the predictions, with this code performing equally as well as a more modern 3D unsteady code. This has a significant implication for those involved in the research community that need unsteady predictions, but that do not have an in-house CFD group that worries about proper griding for the full 3D solutions.

Finally, the heat-flux data have shown (yet again) that the assumptions of flat plate scaling of Stanton number with Reynolds number is not a very good assumption. Surprisingly it seems better on the HPTB than the HPTV, but it is not great on any surface.

Acknowledgments

The authors would like to thank the many individuals who have contributed to this work; specifically, the research group at the OSU Gas Turbine Lab, comprising of Jeff Barton, Ken Copley, Michael Jones, and Packy Underwood for their work in assembling and operating the rig. In addition, they would like to thank the numerous students who have played an important role in this work. In addition they would like to acknowledge the contributions of Colin Scrivener of Rolls-Royce and Professor Mike Giles of Oxford University for their help with UNSFLO-2D. Dr. Scrivener was instrumental in obtaining formal permission for the OSU GTL to use UNSFLO-2D and Professor Giles was extremely helpful in the resurrection of the code on the authors machines. Finally, the OSU Gas Turbine Lab wishes to thank GEAE for their funding of the project, and also for the in depth collaboration that their GE-USA research program has provided them. This has resulted in a much more detailed collaboration between the university and industrial environments than was previously possible.

Nomenclature

St = Stanton number
St = $\dot{q}(T_g)/(\dot{m}/A_{\text{ref}})(Cp_{T_{\text{inlet}}}T_{\text{inlet}} - Cp_{T_g}T_g)$
Re = Reynolds No. based on ref. length
Re_x = Reynolds No. based on length along airfoil
Re_x = $\text{Re}(X/L)$
$\dot{q}$ = heat flux (at gauge temperature), measured
m = fluid viscosity
T_g = gauge temperature, measured
T_{inlet} = total temperature at inlet rakes, measured
Cp = specific heat (evaluated at a specific temperature)
$\dot{m}$ = mass flow through stage (calculated based on measured properties)
A_{ref} = reference area (vane inlet)
L = reference length (1 m)

References

[1] Haldeman, C. W., Dunn, M. G., Barter, J. W., Green, B. R., and Bergholz, R. F., 2004, "Experimental Investigation of Vane Clocking in a One and 1/2 Stage High Pressure Turbine," ASME Paper No. GT2004-53477.
[2] Green, B. R., Barter, J. W., Haldeman, C. W., and Dunn, M. G., 2004, "Time-Averaged and Time-Accurate Aero-Dynamics for the Recessed Tip Cavity of a High-Pressure Turbine Blade and the Outer Stationary Shroud: Comparison of Computational and Experimental Results," ASME Paper No. GT2004-53443.

[3] Tallman, J. A., 2004, "CFD Heat-Transfer Predictions for a High-Pressure Turbine Stage," ASME Paper No. GT2004-53654.
[4] Haldeman, C. W., Krumanaker, M., and Dunn, M. G., 2003, "Influence of Clocking and Vane/Blade Spacing on the Unsteady Surface Pressure Loading for a Modern Stage and One-Half Transonic Turbine," ASME Paper No. GT2003-38724.
[5] Dunn, M. G., 2001, "Convective Heat Transfer and Aerodynamics in Axial Flow Turbines," ASME J. Turbomach., **113**, pp. 637–686.
[6] Giles, M. B., 1988, "Calculation of Unsteady Wake/Rotor Interaction," J. Propul. Power, **4**(4), pp. 356–362.
[7] Arts, T., 1985, "Calculation of the Three-Dimensional, Steady Inviscid Flow in a Transonic Axial Turbine Stage," ASME J. Eng. Gas Turbines Power, **107**(2), pp. 286–292.
[8] Homes, D. G., and Tong, S. S., 1985, "A Tree-Dimensional Euler Solver for Turbomachinery Blade Rows," ASME J. Eng. Gas Turbines Power, **107**(2), pp. 258–264.
[9] Koya, M., and Kotaka, S., 1985, "Numerical Analysis of Fully Three-Dimensional Periodic Flows Through a Turbine Stage," ASME J. Eng. Gas Turbines Power, **107**, pp. 945–952.
[10] Rai, M. M., 1985, "Navier-Stokes Simulations of Rotor/Stator Interaction Using Patched and Overlaid Grids," ASME Paper No. AIAA 85-1519.
[11] Giles, M. B., 1990, "Stator/Rotor Interactions in a Transonic Turbine," J. Propul. Power, **6**(5), pp. 621–627.
[12] Giles, M. B., and Haimes, R., 1993, "Validation of a Numerical Model for Unsteady Flow Calculations," ASME J. Turbomach., **115**, pp. 110–117.
[13] Guenette, G. R., 1989, "Fully Scaled Transonic Turbine Rotor Heat Transfer," ASME J. Turbomach., **111**, pp. 1–7.
[14] Abhari, R., 1992, "Comparison of Time-Resolved Turbine Blade Heat Transfer Measurements and Numerical Calculations," ASME J. Turbomach., **114**, pp. 818–827.
[15] Korakianitis, T., 1992, "On the Prediction of Unsteady Forces on Gas Turbine Blades: Part 1 Description of Approach," ASME J. Turbomach., **114**, pp. 114–122.
[16] Korakianitis, T., 1992, "On the Prediction of Unsteady Forces on Gas Turbine Blades: Part 2 Analysis of Results," ASME J. Turbomach., **114**, pp. 123–131.
[17] Singh, 1998, "A Comparison of Measurement and Predicted Unsteadiness in a Transonic Fan," ASME Paper No. 98-GT-274.
[18] Singh, 1998, "Unsteady Flow in a Single Stage Turbine," ASME Paper No. 98-GT-531.
[19] Rai, M. M., 1987, "Navier-Stokes Simulations of Rotor-Stator Interaction Using Patched and Overlaid Grids," J. Propul. Power, **3**(5), pp. 387–396.
[20] Ni, R. H., and Bogoian, J. C., 1989, "Prediction of Three-Dimensional Multistage Turbine Flow Field Using a Multiple-Grid Euler Solver," ASME Paper No. AIAA 89-0203.
[21] Whitfield, D. L., Janus, J. M., and Simpson, L. B., 1988, *Implicit Finite Volume High Resolution Wave- Split Scheme for Solving the Unsteady Three-Dimensional Euler and Navier-Stokes Equations on Stationary or Dynamic grids*, Mississippi State University.
[22] Dunn, M. G., Moller, J. C., and Steel, R. C., 1989, "Operating Point Verification for a Large Shock Tunnel Test Facility," ASME Paper No. WRDC-TR-2027.
[23] Dunn, M. G., 1986, "Heat-Flux Measurements for the Rotor of a Full-Stage Turbine: Part 1—Time-Averaged Results," ASME J. Turbomach., **108**, pp. 90–97.
[24] Dunn, M. G., Bennett, W. A., Delaney, R. A., and Rao, K. V., 1992, "Investigation of Unsteady Flow Through a Transonic Turbine Stage: Data/Prediction Comparison for Time-Averaged and Phase-Resolved Pressure Data," ASME J. Turbomach., **114**, pp. 91–99.
[25] Dunn, M. G., and Haldeman, C. W., 1995, "Phase-Resolved Surface Pressure and Heat-Transfer Measurements on the Blade of a Two-Stage Turbine," ASME J. Fluids Eng., **117**, pp. 653–658.
[26] Haldeman, C. W., 2003, "An Experimental Investigation of Clocking Effects on Turbine Aerodynamics Using a Modern 3-D One and One-Half Stage High Pressure Turbine for Code Verification and Flow Model Development," *Aeronautical and Astronautical Engineering*, Ohio State University, Columbus, p. 345.
[27] Venable, B. L., Delaney, R. A., Busby, J. A., Davis, R. L., Dorney, D. J., Dunn, M. G., Haldeman, C. W., and Abhari, R. S., 1998, "Influence of Vane-Blade Spacing on Transonic Turbine Stage Aerodynamics, Part I: Time-Averaged Data and Analysis," ASME Paper No. 98-GT-481.
[28] Boley, B. A., and Weiner, J. H., 1960, *Theory of Thermal Stresses*, Dover, Mineola, NY, p. 586.

Experimental Investigation of Local Heat Transfer Distribution on Smooth and Roughened Surfaces Under an Array of Angled Impinging Jets[1]

Lamyaa A. El-Gabry
General Electric Company,
Global Research Center,
Niskayuna, NY 12309
e-mail: elgabry@research.ge.com

Deborah A. Kaminski
ASME Fellow
Department of Mechanical, Aerospace, and
Nuclear Engineering,
Rensselaer Polytechnic Institute,
Troy, NY 12180-3590
e-mail: kamind@rpi.edu

Measurements of the local heat transfer distribution on smooth and roughened surfaces under an array of angled impinging jets are presented. The test rig is designed to simulate impingement with crossflow in one direction. Jet angle is varied between 30, 60, and 90 deg *as measured from the target surface, which is either smooth or randomly roughened. Liquid crystal video thermography is used to capture surface temperature data at five different jet Reynolds numbers ranging between 15,000 and 35,000. The effect of jet angle, Reynolds number, gap, and surface roughness on heat transfer and pressure loss is determined along with the various interactions among these parameters.*
[DOI: 10.1115/1.1861918]

Introduction

Impingement is a common means of convectively cooling surfaces in numerous industrial applications. One such application is the cooling of gas turbine hot gas path components such as the combustion liner, transition piece, and turbine buckets and nozzles (airfoil, end wall, and shroud). Other applications for impingement include cooling of electronic components.

A two- or three-dimensional array of jets can be used for convectively cooling turbine parts. The air jets impinge at the surface to be cooled and are directed along a channel formed by the cool surface and the jet plate. In such arrangements, the downstream jets are subjected to a crossflow from the upstream jets.

There have been several experimental studies on the heat transfer characteristics of impinging jets. Researchers including Florschuetz [1–4] and Andrews [5] have studied the effect of various parameters on impingement heat transfer. Jet spacing, distance between the jet plate and target surface, and initial crossflow are among the factors studied. Tests have been conducted on staggered and inline arrays of circular jets with cossflow in single and multiple directions. Gillespie [6], Son [7], and Huang [8] used a transient liquid crystal technique for obtaining heat transfer coefficients. Gillespie [6] tested a configuration consisting of a double row of seven impingement holes exhausting through a single row of five inclined film-cooling holes. Son [7] studied the heat transfer characteristics of an impingement cooling system with uniform and nonuniform staggered array. Huang [8] conducted a detailed analysis of the heat transfer distribution under an inline array of orthogonal impinging jets. Results have shown that increasing jet Reynolds number increases the local heat transfer coefficients. Exit cross-flow direction affects flow and heat transfer distribution on the surface; the highest heat transfer coefficients were obtained for a cross-flow orientation in which the air exits from both ends of the channel that is formed by the jet plate and the target surface.

In the previously mentioned studies, jets were directed orthogonal to a smooth surface. Perry [9] studied the effect of jet angle for a single jet of hot air impinging on a surface using a water-cooled jet plate and a calorimeter to measure the impingement plate heat transfer characteristics.

Trabold [10] studied the impingement and the effect of crossflow in the presence of surface roughness elements. The surfaces were roughened with square ribs of constant rib height and varying pitch to height. Results show that roughness elements can be used to compensate for the decay in heat transfer in the cross-flow direction that is often observed with impingement on smooth surfaces.

Haiping [11] conducted an experimental investigation on the effects of certain geometric parameters including jet hole spacing, jet to surface spacing, rib pitch to height ratios, and rib height to hole diameter ratios on heat transfer. Rib roughened surfaces were also tested by Failia et al. [12]. Results show there is an optimum ratio of fin width to channel width (about one) that yields the best overall heat transfer for the lowest possible pressure requirements.

The objective of this investigation is to determine the detailed heat transfer distribution for various jet impingement configurations. The effect of randomly roughened surfaces on heat transfer is quantified and the effect of jet angle on local heat transfer distribution is determined. The use of randomly roughened surfaces provides significant heat transfer enhancement with lower pressure drops than ribbed surfaces. The method and apparatus used in these experiments are capable of reaching jet Reynolds numbers of over 35,000; this is typical of many industrial applications using jet impingement. The use of liquid crystal provides information on local heat transfer distributions.

Being able to quantify the *local* heat transfer distribution is important for two reasons. First, practical industrial experience has shown that designs that are based on average heat transfer coefficients may fail in operation due to thermal cycling and fatigue resulting from extreme temperature gradients. Another reason for measuring local distribution of heat transfer is to validate computational fluid dynamics (CFD) models used to predict heat transfer coefficients. In order to validate numerical models, it is imperative to have highly detailed experimental results.

[1]First presented at the 2001 International Mechanical Engineering Congress and Exposition of the ASME. Paper No. 2-14-1-1.

Contributed by the Turbomachinery Division of THE AMERICAN SOCIETY OF MECHANICAL ENGINEERING for publication in the JOURNAL OF TURBOMACHINERY. Manuscript received by the Turbomachinery Division December 12, 2003; revised manuscript received August 31, 2004. Associate Editor: R. S. Bunker.

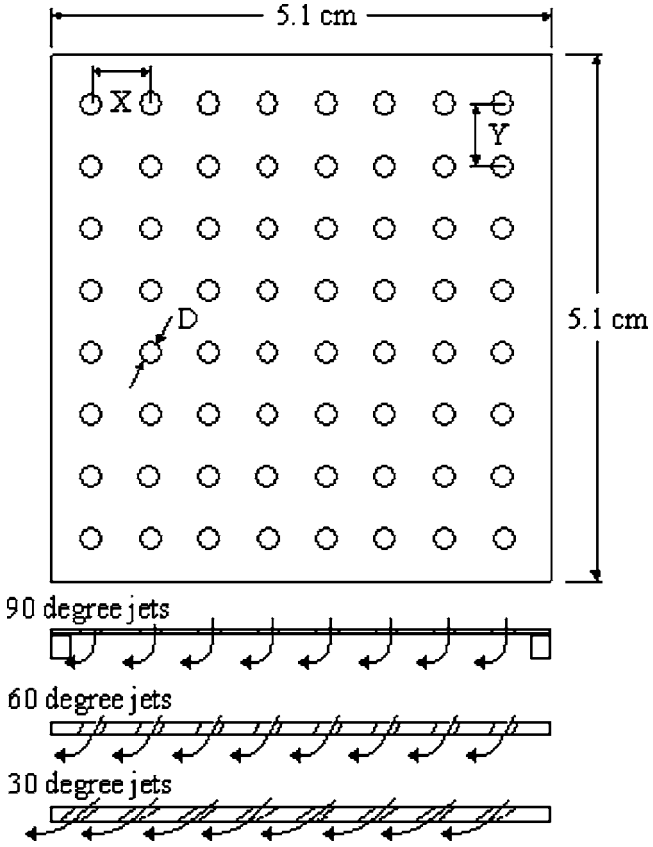

Fig. 1 Jet configuration and plate geometry

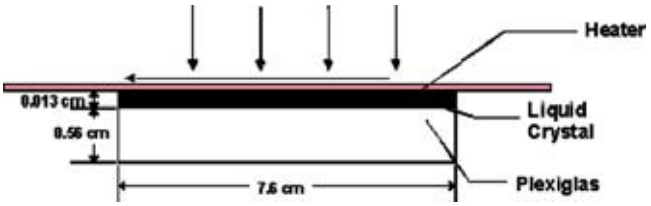

Fig. 2 Test coupon for smooth surface impingement test

Experimental Facility

Three jet plates of size 5.1 cm by 5.1 cm (2×2 in.) were tested at different Reynolds numbers ranging from 10,000 to 35,000 impinging at two channel heights. The test rig simulates impingement heat transfer with crossflow in one direction. Air is supplied to a pressure chamber (plenum). At one end of the plenum, a jet plate is mounted. Air passes from the plenum through the jet plate and impinges on either a smooth or rough surface. A passage is formed between the jet plate and the target surface by using a three-sided spacer to guide the flow to exit in one direction. There is no initial crossflow of air; the crossflow is generated from upstream rows of jets. A turbine nozzle uses this type of cooling configuration.

The holes of the jet plate were laid out in a square array as shown in Fig. 1.

The hole spacing in the x and y directions are equal (i.e., $X = Y$). The centerline distance between two adjacent holes (X) and the jet diameter (D) form a single nondimensional parameter, X/D. The gap height was also nondimensionalized with respect to jet hole diameter (Z/D). The jet diameter was 1.27 mm (0.05 in.), the spacing between jets was 6.35 mm (0.25 in.), and the height of the channel or gap was 1.27 mm (0.05 in.) and 2.54 mm (0.1 in.). The jet plates, shown in Fig. 1, are characterized by a ratio (X/D) of 5. The nondimensional parameter Z/D was set to 1 and 2 for the configurations tested.

Figure 2 is an illustration of the test coupon that consists of a target surface, heater, liquid crystal, and Plexiglas insulation. The surface is heated using a thin Inconel foil heater 0.0254 mm (0.001 in.) in thickness. This provides a constant heat flux boundary condition. Since the heater is very thin and highly conductive, the temperature across the thickness of the heater is considered negligible. In testing rough surfaces, a roughened test plate is mounted to the heater surface using an industrial grade adhesive material. The test plate is thicker than the foil heater and a thermal gradient across its thickness is accounted for using one-dimensional conduction. A calibrated liquid crystal sheet is mounted on the other side of the heater using the adhesive. A Plexiglas cover is placed on the liquid crystal face to allow visual observation of the temperature (color) fields of the target surface. The heat loss through the Plexiglas was estimated using a one-dimensional conduction model and was found to be less than 0.8% of the heat generated by the heater.

The rough surface test coupons were created using a brazing process developed by the GE Global Research Center [13]. The surface roughness was measured using a profilometer at several locations; the average roughness value was R_a of 33 μm and R_z of 179 μm. The roughness was uniform sandpaper like roughness. A photograph of the rough surface details is shown in Fig. 3.

The entire rig including plenum, jet plate, test plate, heater, liquid crystal, and Plexiglas is placed in a pressure vessel or enclosure as shown in Fig. 4. This allows control of the pressure ratio across the jet plate and, hence, allows the tests to be run at higher jet Reynolds numbers than would be possible if the air discharged to the atmosphere directly. The pressure chamber is equipped with a transparent pressure window for viewing the liquid crystal image. An RGB camera is used to grab images through the pressure window using a Data Translation DT-2871™ frame grabber. Fiber optic lighting is adjusted to provide an image of adequate quality for processing. The lighting is maintained constant throughout the experiments.

The air flow rate is measured using a venturi calibrated to ±0.5% reading located in the air supply system as described by El-Gabry [14]. The tests were run at a pressure ratio of about 1.17 that is close to the operating conditions in gas turbine applications. The chamber pressures and temperatures were measured and the flow function for each jet plate configuration was calculated.

Fig. 3 Test coupon for smooth surface impingement test (13.28×; average bump diameter ~0.25 mm)

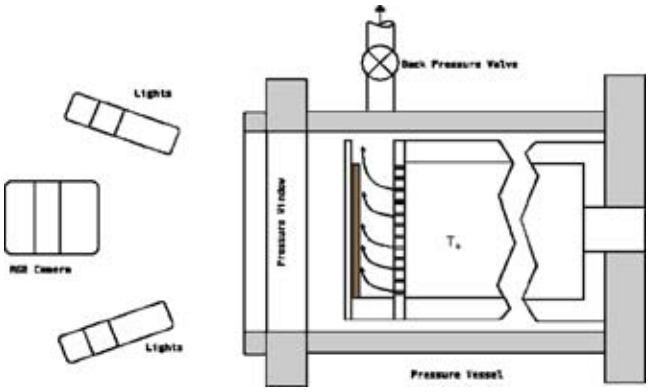

Fig. 4 Test rig in pressurized enclosure

Table 1 Average flow function for test case

	Jet angle	Z/D	Surface	Flow function[a]
1	90	2	Smooth	0.0412
2		2	Rough	0.0412
3		1	Smooth	0.0294
4	60	2	Smooth	0.0473
5		2	Rough	0.0476
6		1	Smooth	0.0393
7	30	2	Smooth	0.0460
8		2	Rough	0.0469
9		1	Smooth	0.0390

[a]Flow function is a mass flow parameter with units of $\sqrt{kg/N}$. An alternative would be to compute an effective area, which would be dimensionless. The area ratio equation can be found in Ref. [16], p. 86.

Liquid Crystal Calibration. In order to apply the "multicolor" liquid crystal technique used in this investigation, it is necessary to calibrate the liquid crystal. The calibration apparatus consists of an insulated metal bar which is heated at one end and cooled at the other thereby applying a temperature gradient to the liquid crystal sample. Thermocouples are embedded at equal distance along the calibration apparatus where the liquid crystal strip is located. As the liquid crystal temperature drops, the colors of the liquid crystal progress in this order: clear-red-yellow-green-blue-violet-clear. The clear color occurs when the temperature is outside the range of the liquid crystal. In this experiment, Hallcrest Liquid Crystal™ R40C5W is used which has a "red start" temperature of 40°C with a temperature band of 5°C. The colors of the liquid crystal are correlated to the temperatures measured by the embedded thermocouples.

Data Collection and Reduction. To collect data, the airflow rate and pressure ratio are set to the desired point to yield a given Reynolds number. Once the Reynolds number is set, a constant heat flux is applied to the target surface and once steady state has been reached, the image is captured and saved. The system has reached steady state when the liquid crystal temperature does not change more than 0.1°C over a 15–20 min interval.

In general, surface temperature variations are greater than the bandwidth of the liquid crystal (5°C) and, hence, several images need to be taken at various heat flux levels in order to get a color change in each element of the liquid crystal. These images are then superimposed and averaged to yield the heat transfer distribution on the entire surface. This process assumes that the heat transfer coefficient is not a function of heat flux making it possible to obtain an overall heat transfer coefficient distribution by averaging the partial distributions of the individual images. Details on the data reduction method using broadband steady state liquid crystal are in El-Gabry [14].

Results and Discussion

A study of the repeatability of the results was performed using one of the jet plate configurations. This study involved repeating heat transfer measurements three times at different times of day on two different days using the same jet plate. Measurements were taken using this jet plate at a jet Reynolds number of approximately 19,000. Several factors can potentially influence the experimental results. These include variation in compressor setting, ambient conditions, the lighting on the liquid crystal, the camera setting with respect to the image, and the performance of the pressure transducer. In this study, these aspects of the experimental setup were varied in order to determine the sensitivity of the results to these experimental noise parameters. The study showed that Nusselt number results for this typical plate are repeatable to within a standard deviation of 0.37 (the mean Nu for the jet plate was 79). Using the mean and standard deviation as well as some statistical relationships found in Johnson [15], one can assert with 95% confidence that at least 99% of all data obtained by repeating the test procedure described earlier will fall within 1.50 Nusselt number. This is equivalent to an error of +/−1.92% in Nusselt number using the statistical approach described in Johnson [15, p. 531] where "error" is defined in terms of deviation from the mean.

Flow Results. The flow function for each jet plate configuration was calculated to determine the effect of angle, gap height, and surface roughness on flow. This parameter is similar to the mass flow parameter defined in Shapiro [16]:

$$\text{Flow function} = \frac{\dot{m}}{A} * \frac{\sqrt{T_0}}{P_0} * \sqrt{\frac{(k-1)R}{2gk}}$$

The flow function characterizes the resistance of a flow circuit. It is commonly used in the gas turbine industry when working with impingement and orifice systems or in studying turbine blade cooling circuits from a flow effectiveness perspective. The flow function indicates the pressure needed to drive a given flow rate of air through the impingement jet plate and the cross flow channel. The higher the flow function, the lower the force needed to drive air through the system. Table 1 is a summary of the average flow functions for each configuration tested.

Flow results show that orthogonal jets have a lower flow function than angled jets regardless of surface roughness or impingement gap height. This means that the driving forces needed to flow air through the orthogonal jet plate are higher. Decreasing the gap between the jet plate and the target surface decreases the flow function (i.e., increases the driving forces needed to push air through the system). The addition of surface roughness did not measurably increase pressure drop. One explanation for this observation is that in impinging flows, the pressure drop across the jet plate (essentially an array of orifices) is greater than that through the channel. Hence, the contribution of surface roughness to overall pressure loss is small when compared to the contribution of the jet plate.

Heat Transfer Results. The local surface heat transfer coefficient is nondimensionalized using the thermal conductivity of coolant air and the jet diameter as the characteristic length. The dimensionless Nusselt number is defined as

$$\text{Nu} = hD/k_{\text{air}}$$

The conductivity of air is a function of the measured bulk fluid temperature in the plenum. The local heat transfer coefficient is defined in terms of the net heat input to the target surface and the temperature difference between the gas temperature in the plenum and the target surface temperature (derived from liquid crystal). The net heat input is equal to the heat generated by the heater less the heat lost through the Plexiglas insulator. The heat transfer coefficient is

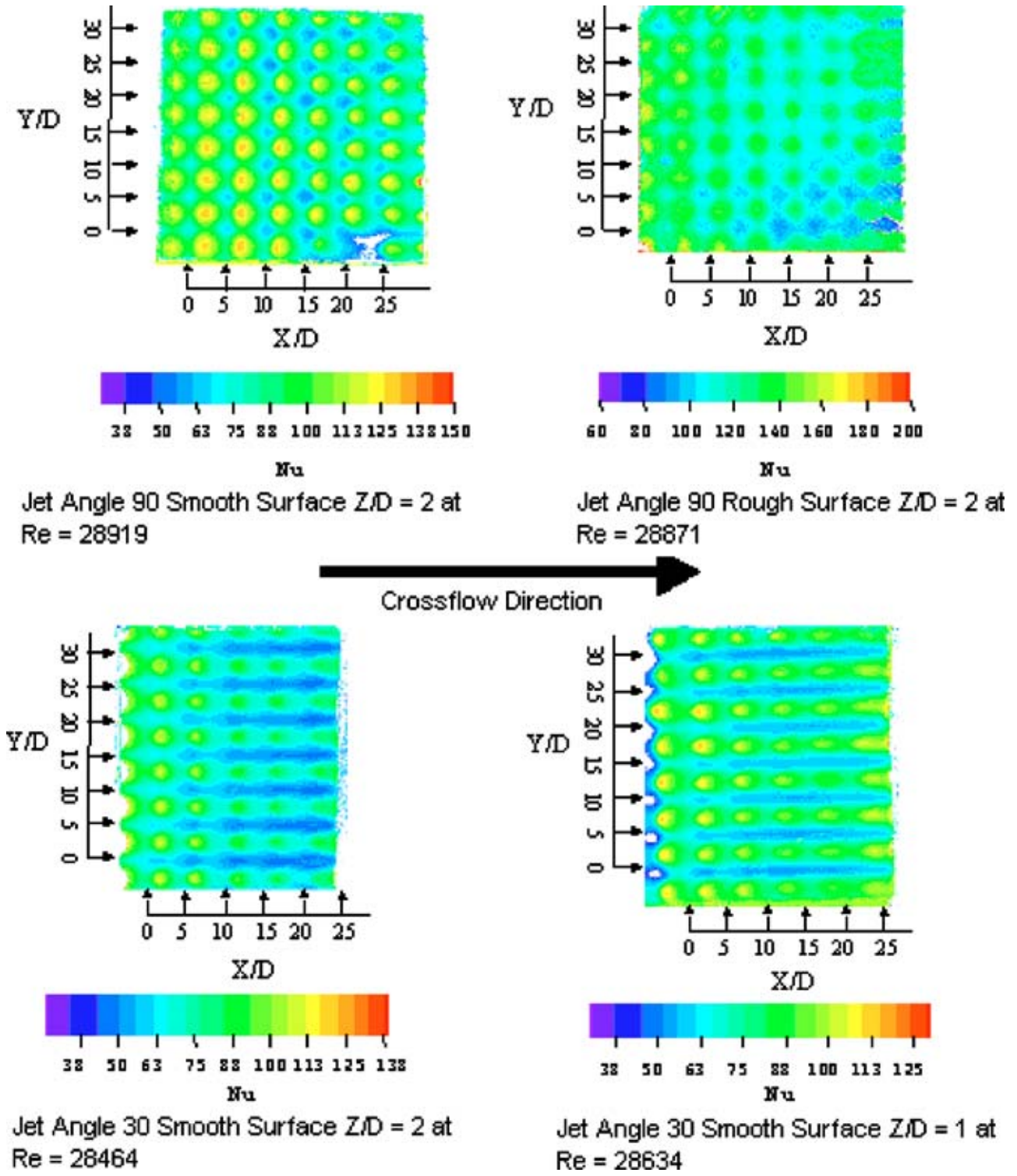

Fig. 5 Contour plots of Nusselt number distribution for various jet plate configurations

$$h = (Q_{\text{net}}/A_{\text{heater}})/(T_w - T_0)$$

The uncertainty in Nusselt number is approximately 5–10% using the method of Kline and McClintock [17].

Results show that the local Nusselt number decreases in the cross-flow direction. Figure 5 shows the Nusselt number contour plots for various configurations. Note: the Nusselt number scale is not identical for each of the contour plots in Fig. 5. A single scale cannot capture the variations in results.

In general, the highest local heat transfer is farthest from the outlet and decreases in the discharge direction. The images also show that the regions between rows of jets have lower Nusselt numbers (represented by blue on the color scale) suggesting that inline array of jets may have limited capability of uniformly cooling a surface. The angled jets yield Nusselt number distributions that appear streaked; beneath the row of jets is a strip of high heat transfer and between the rows is a strip with low heat transfer. For the orthogonal jets, there are no distinct strips with low and high heat transfer; rather there are circular regions of high heat transfer beneath the jets that extend radially outward forming smaller regions of low heat transfer between jets.

The rough surfaces exhibit a more uniform heat transfer distribution than smooth surfaces independent of jet angle.

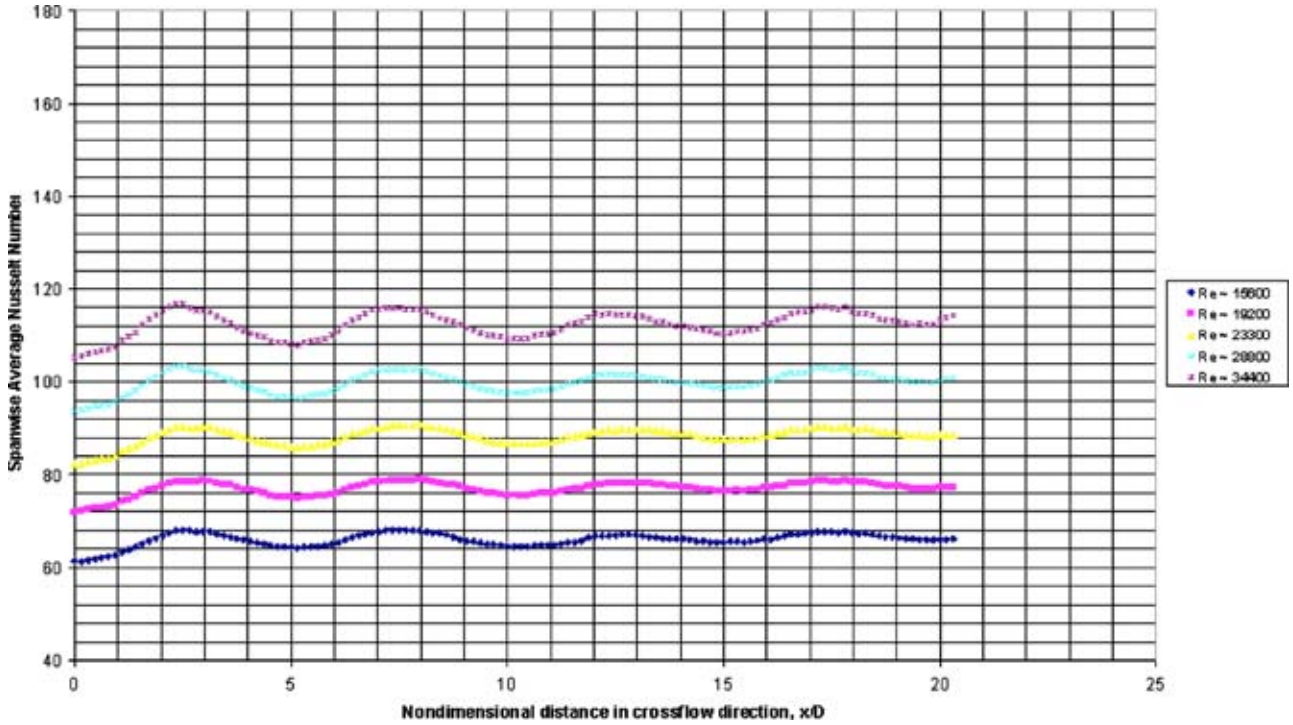

Fig. 6 Nusselt number results for 30 deg jets impinging on rough surface at gap height *Z*/*D* of 2

The spanwise averaged Nusselt number as a function of nondimensional distance in the crossflow direction (X/D) for the various test configurations are shown in Figs. 6–14. Each point in the figures represents an average of Nusselt numbers derived for all pixels at a particular X/D location. Generally peaks are near the x-location where there is a row of jets discharging fresh air into the flow stream and minima are near the x-location midway between two adjacent rows of jets.

Figures 6–8 show the Nusselt number results for configurations using the 30 deg angled jet plate. A comparison of Figs. 6 and 7 shows the effect of surface roughness on Nu number for the 30 deg jet plate. Roughness increases the average Nu and yields a more uniform heat transfer distribution; there is less decay of Nu in the cross-flow direction (increasing x/D).

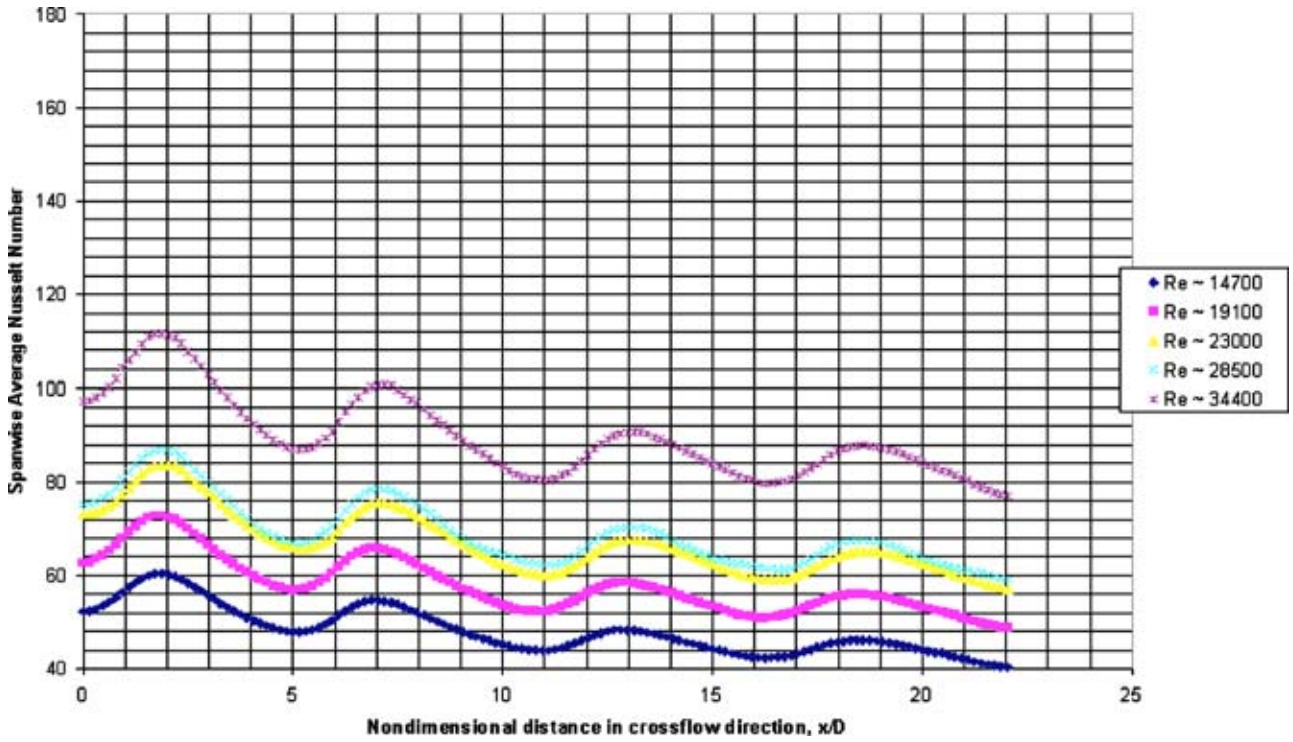

Fig. 7 Nusselt number results for 30 deg jets impinging on smooth surface at gap height *Z*/*D* of 2

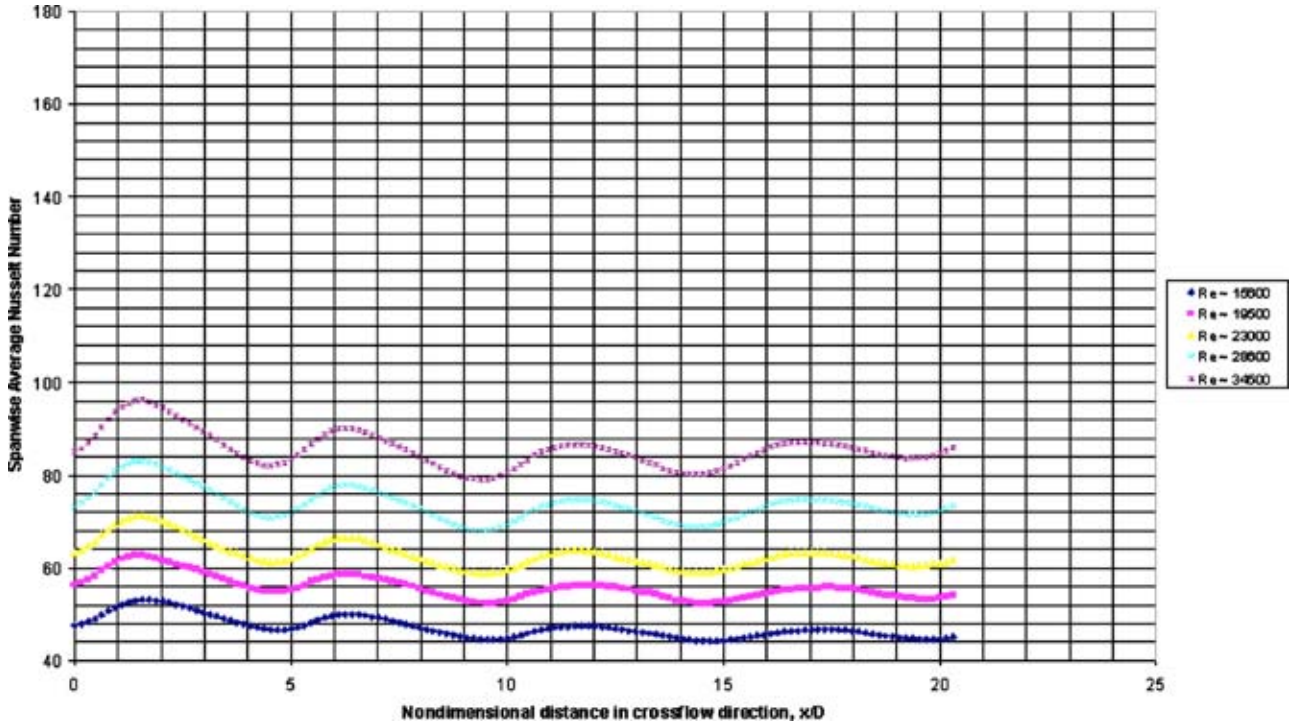

Fig. 8 Nusselt number results for 30 deg jets impinging on smooth surface at gap height *Z*/*D* of 1

At the smaller gap height (Fig. 8), the difference between neighboring maxima and minima in Nu appears lower than that for the larger gap height (Fig. 7). This is particularly evident at lower Reynolds number. In general, data, which have primarily been taken for orthogonal jets, show that the heat transfer coefficients increase with decreasing gap height. The results presented here for the 30 deg jets show an opposite trend where the heat transfer coefficient is higher at the higher gap height. One reason for this observation is that at the small gap height, the flow is predominantly channel-type flow while at the large gap, the flow is more typical of a jet impinging on a surface. The impinging jet type flow yields higher heat transfer coefficients than channel flow. However, since only two levels of gap height were tested, it is not possible to draw conclusions on a general trend between

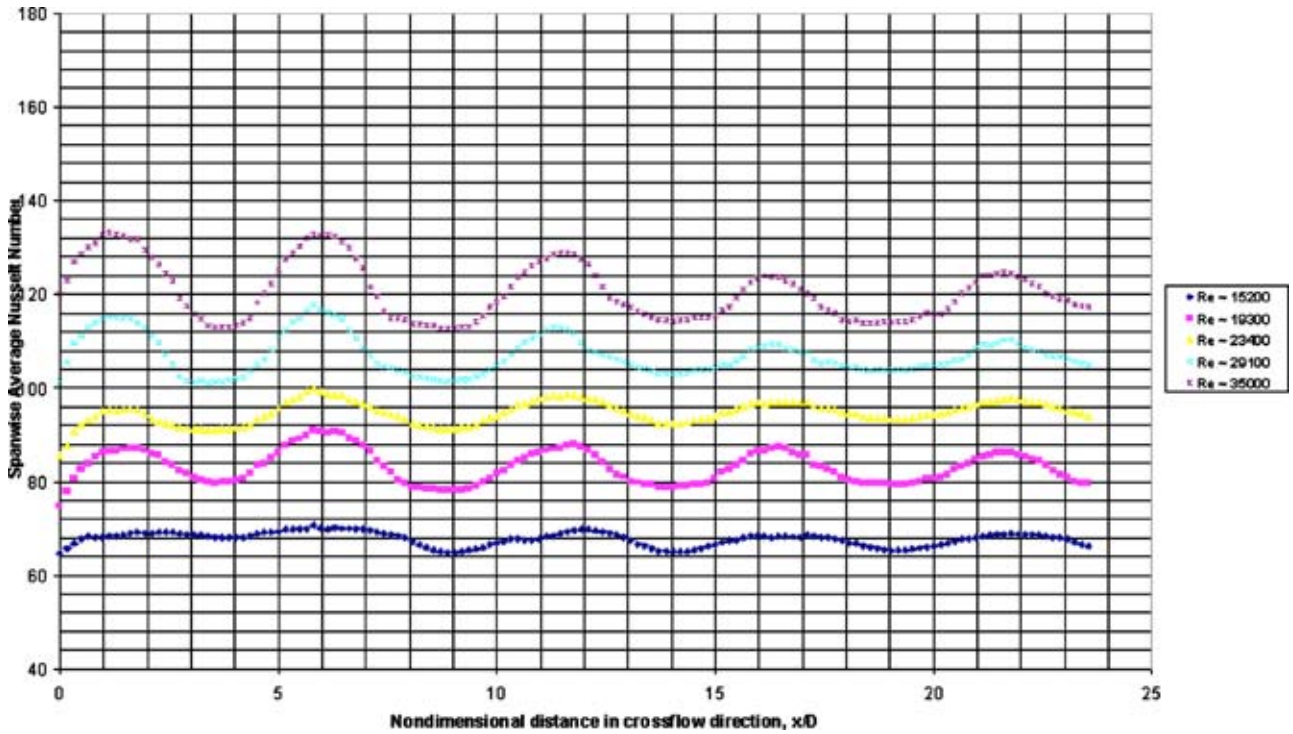

Fig. 9 Nusselt number results for 60 deg jets impinging on rough surface at gap height *Z*/*D* of 2

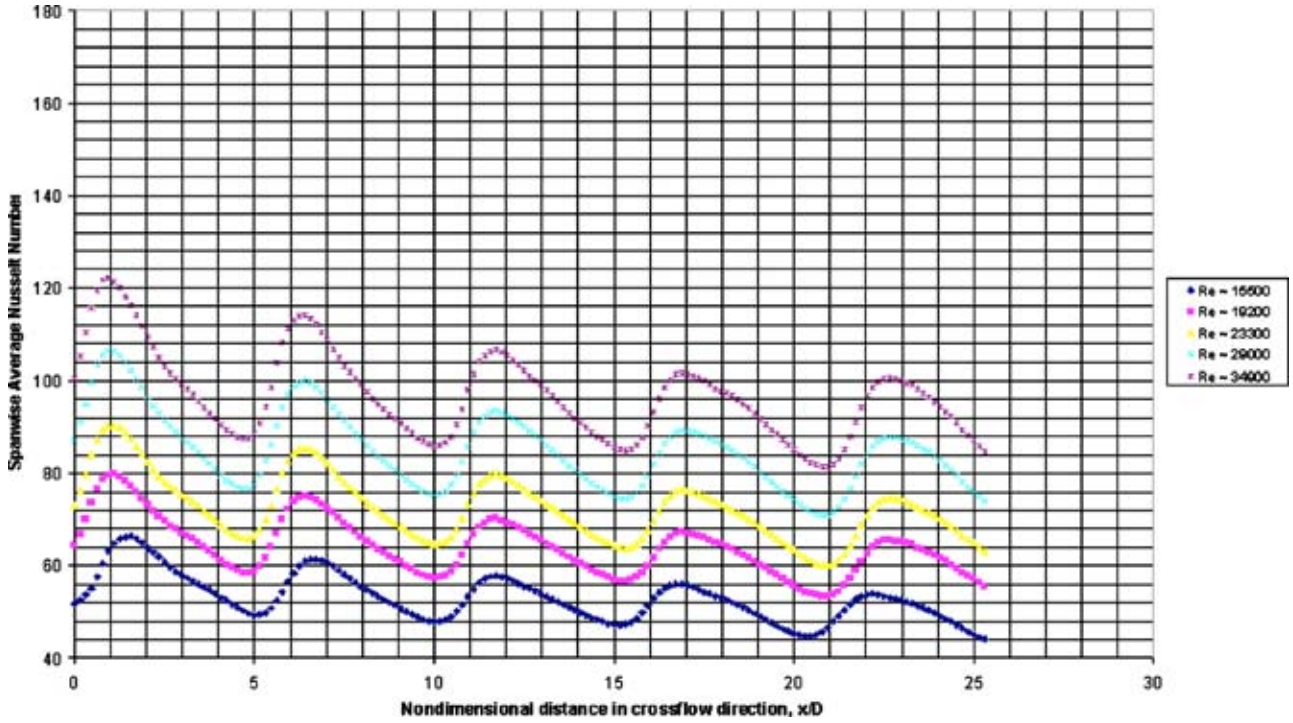

Fig. 10 Nusselt number results for 60 deg jets impinging on smooth surface at gap height *Z*/*D* of 2

gap height and thermal performance.

Figures 9–11 show the heat transfer results for the 60 deg jet plate configurations. Similar to the 30 deg jets, results from the 60 deg jets show that surface roughness increases heat transfer and yields a more uniform distribution. However, the effect of gap height is not significant to differentiate between the average heat transfer coefficients at the small and large gap heights.

Results for the 90 deg jet plate configurations are presented in Figs. 12–14. Although roughness increases uniformity of Nu on the surface, the nonuniformity is greater for the orthogonal jets than the angled jets impinging on the same roughened surface. Also worth noting is the shape of the Nusselt number distribution at the peak values (near the stagnation region). The drop in Nu on the downstream side of the stagnation region is less steep than the drop in the upstream region similar to observations reported by other researchers [3].

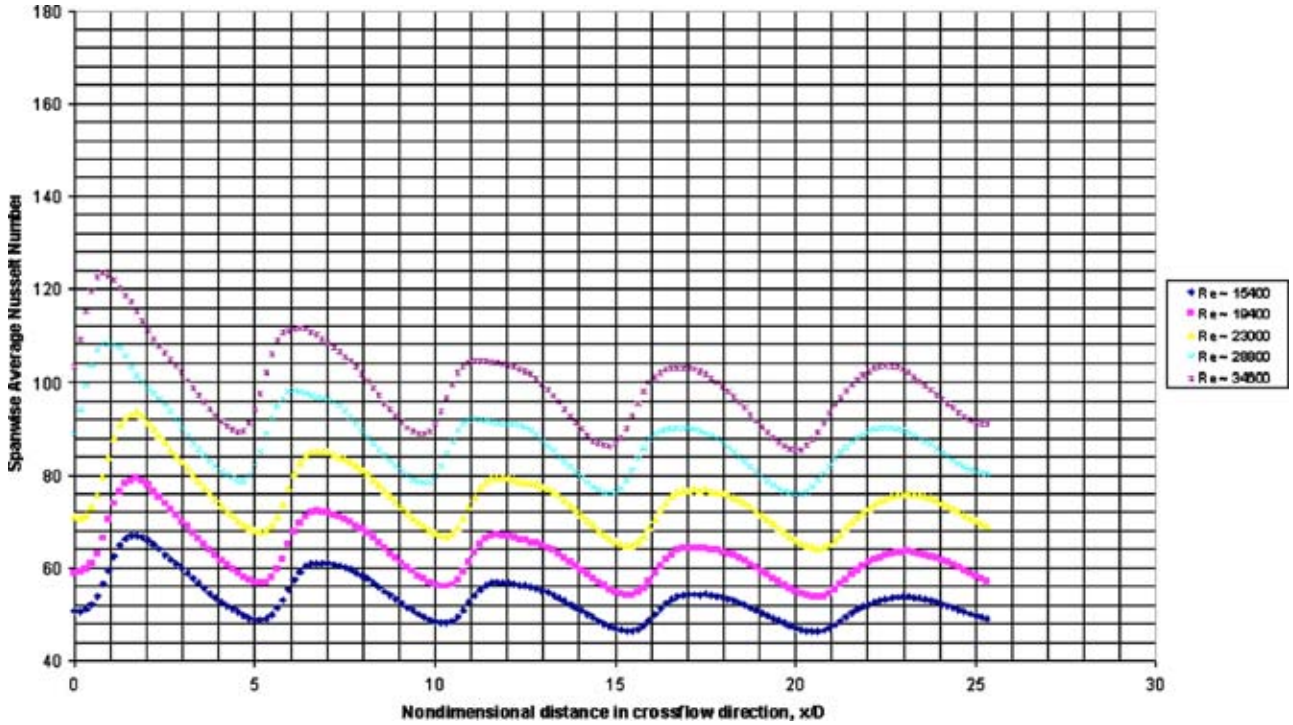

Fig. 11 Nusselt number results for 60 deg jets impinging on smooth surface at gap height *Z*/*D* of 1

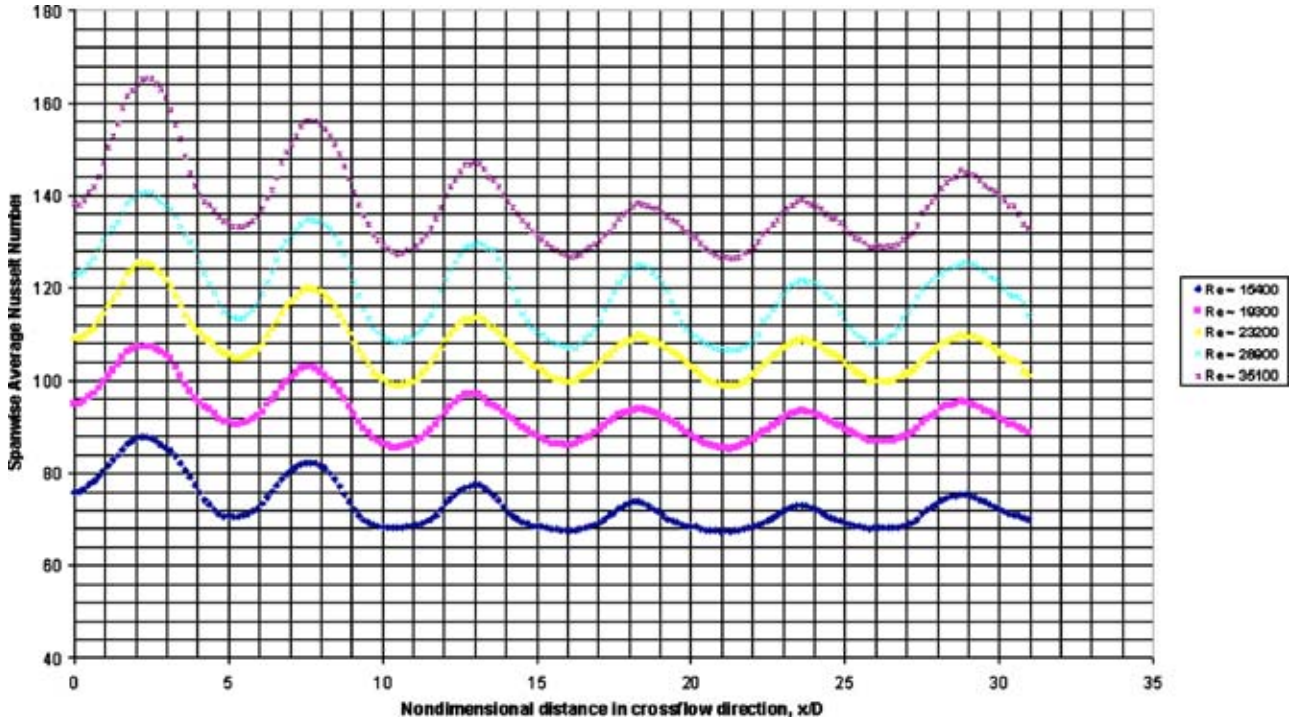

Fig. 12 Nusselt number results for 90 deg jets impinging on rough surface at gap height *Z/D* of 2

The results for the 90 deg jets impinging on a smooth surface at a gap height Z/D of 1 shown in Fig. 14 do not follow the same trend as other configurations; the spanwise averaged Nusselt number does not decrease in the crossflow direction. One possible explanation for this observation is that the smaller gap may be causing a large pressure drop in the channel in the crossflow direction. This pressure drop leads to nonuniform pressure drop across the jet plate in the cross-flow direction. This forces more air to flow through the jet plate holes closer to the discharge section because the channel pressure is lower in that region than it is below the upstream jet holes in the entrance region. Florschuetz et al. [2] report streamwise distribution of jet velocities for various jet plate configurations which support the results obtained for the 90 deg jet plate at $Z/D \sim 1$. For large Z/D, the jet velocities are relatively constant in the streamwise direction; however, for small Z/D, the jet velocity increases in the direction of crossflow.

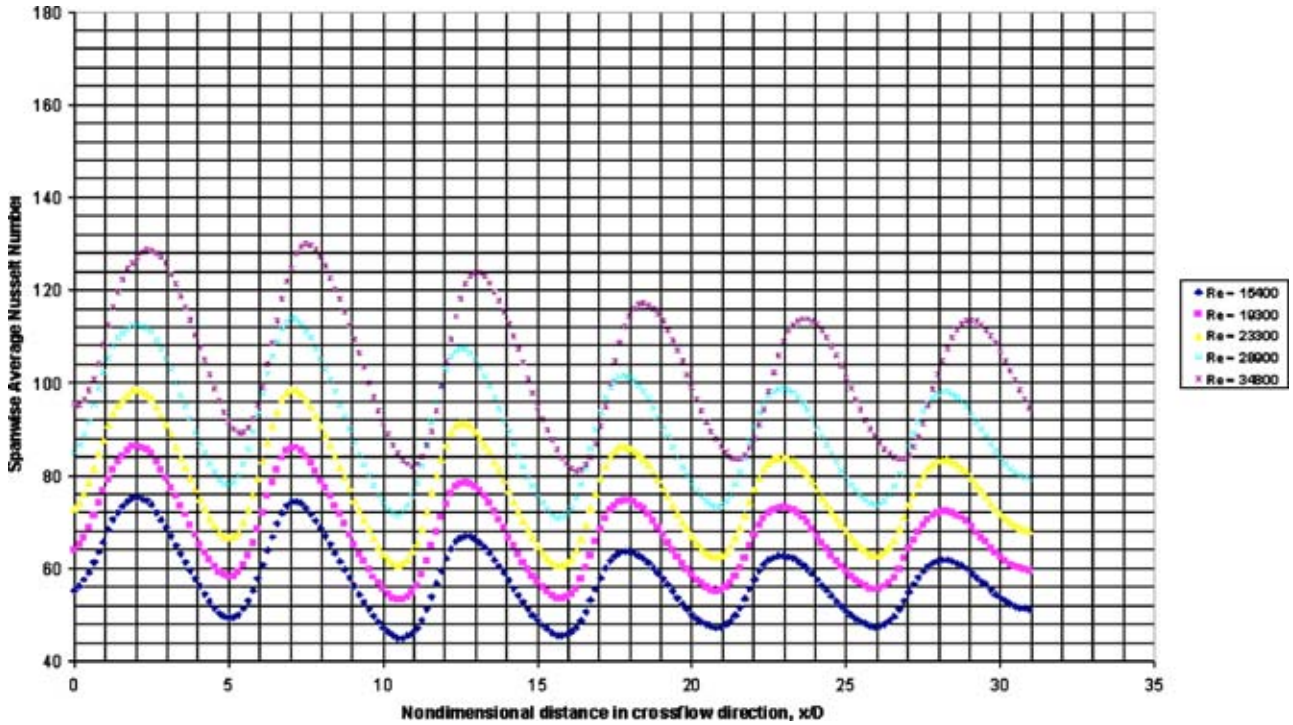

Fig. 13 Nusselt number results for 90 deg jets impinging on smooth surface at gap height *Z/D* of 2

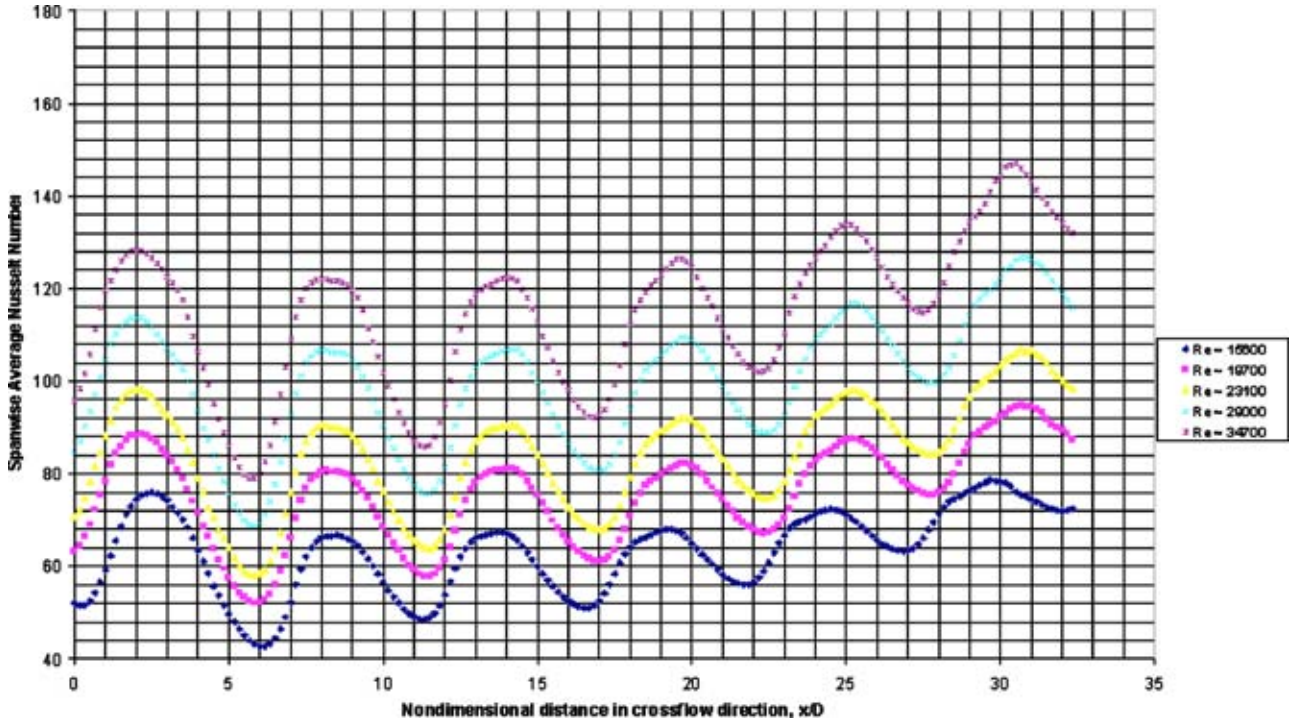

Fig. 14 Nusselt number results for 90 deg jets impinging on smooth surface at gap height *Z/D* of 1

Therefore, observing an increase in local Nusselt number in the cross-flow direction for the 90 deg configuration with a $Z/D \sim 1$ could be due to the increasing jet velocities.

Tables 2 shows the peak Nusselt number, average Nu, the ratio of peak to surface average Nu, and the decay rate for all test cases. Decay rate is defined as the difference between the first peak Nu (at small x/D) and the last peak Nu (at large x/D; close to discharge) divided by the first peak Nu. This definition of decay rate is used to quantify the decrease in Nusselt number in the crossflow direction as a result of the spent air heating. The results for the decay rate for the 90 deg jets impinging on a smooth surface at a gap Z/D of 1 are not shown in Table 2 because this configuration yielded results in which heat transfer was not decreasing in the crossflow direction and it is not possible to draw conclusions about decay rates.

Effect of Reynolds Number. Increasing the Reynolds number increases peak Nusselt number and average Nusselt number for all jet plate configurations. Generally, as Reynolds number increases, the peaks and troughs in the Nusselt number line plots become more defined. This means that at low Reynolds numbers, the Nusselt number distribution is more uniform.

Reynolds number appears to have no impact on decay rate; however, the amount of decay in terms of difference between first and last peak increases with increasing Re for various cases. For instance, Fig. 7 indicates that at the lowest Reynolds number the decay rate is about 23.8% while at the highest Reynolds number it is 21.1% and the trend is that decay rate decreases with increasing Reynolds number. However, the actual decay in terms of the difference between the first and last peak Nu values is 14.4 for the lowest Re and 23.6 for the highest Re; therefore, the amount of decay in Nusselt number increases with increasing Reynolds number.

The effect of crossflow is to decrease Nu in the direction of spent airflow; increasing Reynolds number increases the heat transfer coefficients at the stagnation region and also increases the amount by which Nu decays as measured from neighboring peak to valley.

Effect of Jet Angle. The surface average Nusselt number increases with increasing jet angle, as does the peak Nusselt number, independent of gap height, surface roughness, and Reynolds number. This is to be expected because when the jet is directed orthogonal to the surface, it can pickup the most heat upon striking the surface. Increasing the angle increases the stagnation point heat transfer.

Effect of Gap Height. Figure 15 shows the effect of gap height on surface average Nu. Increasing gap height decreases both peak and average Nusselt numbers for the 90 deg array of jets. The effect is not as significant for the 60 deg jets and for the 30 deg jets, the average Nusselt number increases with increasing gap height.

Effect of Roughness. For any given jet Reynolds number, roughness increases the average Nu for all jet plates tested regardless of jet angle as shown in Fig. 16. Note the highest surface average Nu obtained with a smooth surface is lower than the lowest average Nu obtained with a roughened surface for any given jet Reynolds number. A comparison of the top two contour plots in Fig. 5 for the 90 deg smooth and rough surfaces demonstrates the effect of roughness; the rough surface shows higher and more uniform heat transfer. A comparison of Figs. 6 and 7 for the 30 deg jets, Figs. 9 and 10 for the 60 deg jets, and Figs. 12 and 13 shows that roughness has the same effect of yielding increased, uniform heat transfer independent of jet angle.

Comparison with Existing Data. In the literature, there are heat transfer results for arrays of jets impinging orthogonal to a flat smooth surface. The surface average Nusselt number for the orthogonal jets was compared with data tabulated in the NASA CR 3217 [18] and with the predicted values using an empirical relation posed by Kercher and Tabakoff [19] for a square array of circular jets impinging orthogonal to a flat smooth surface.

The average Nusselt number as a function of Reynolds number is plotted for Z/D of 1 and 2. The results, shown in Fig. 17, are close to published values. Note, however, that the effect of Z/D is

Table 2 Nusselt number results of interest

Jet angle	Gap height Z/D	Surface	Jet Re	Peak Nu	Aug Nu	Peak/avg	Decay rate (%)
30	2	Rough	15600	68	66.04	1.030	2.9
			19200	79	77.02	1.026	2.5
			23300	91	88.39	1.030	2.9
			28800	104	99.95	1.041	2.9
			34400	117	112.42	1.041	2.6
30	2	Smooth	14700	60.4	48.2	1.253	23.8
			19100	72.8	57.9	1.257	23.1
			23000	83.8	67.1	1.249	22.4
			28500	86.9	69.2	1.256	21.7
			34400	111.6	89.8	1.243	21.1
30	1	Smooth	15600	53.1	47.2	1.125	13.4
			19500	62.7	55.9	1.122	10.7
			23000	71.3	63.1	1.130	10.2
			28600	83.2	73.8	1.127	8.7
			34500	96.3	85.7	1.124	8.6
60	2	Rough	15200	70.7	67.8	1.043	3.8
			19300	91	83.1	1.095	5.5
			23400	99.8	94.8	1.053	2.8
			29100	118	107	1.103	6.8
			35000	133	120.6	1.103	6.8
60	2	Smooth	15500	66.3	53.1	1.249	18.6
			19200	79.8	64	1.247	17.3
			23300	90.3	72.5	1.246	16.9
			29000	106.4	85	1.252	17.3
			34900	112.1	96.9	1.157	9.0
60	1	Smooth	15400	67.1	53.5	1.254	19.5
			19400	79.3	62.7	1.265	19.3
			23000	93.6	74.9	1.250	18.8
			28800	108.1	87.5	1.235	16.7
			34600	123.4	99.4	1.241	15.7
90	2	Rough	15400	88	73.2	1.202	15.9
			19300	107.3	92.8	1.156	12.4
			23200	125.5	107.9	1.163	12.4
			28900	140.5	119.7	1.174	13.2
			35100	165.5	138.4	1.196	15.4
90	2	Smooth	15400	76	57.6	1.319	18.4
			19300	86	67.2	1.280	16.3
			23300	99	77.2	1.282	15.2
			28900	112	90.3	1.240	11.6
			34800	129	103.8	1.243	11.6
90	1	Smooth	15600	78.7	63.2	1.246	
			19700	94.8	75.5	1.256	
			23100	106.9	84.4	1.267	N/A
			29000	126.7	99.9	1.268	
			34700	147.1	114.8	1.281	

not as pronounced in the Florschuetz data as it is in the experimental results obtained in this study. Also note that this study used square arrays of jets, however, the data reported by Florschuetz et al. [16] used rectangular arrays where the Y/D was 4; the X/D spacing is the same for both sets of data. Another difference between the two data sets was in how the heat transfer coefficient was obtained; Florschuetz used a series of embedded thermocouples to measure the surface temperature, this study used liquid crystals to get a more detailed description of the temperature. The results obtained from the correlation proposed by Kercher et al. [19] suggest that the average Nu is higher for the larger gap than the smaller gap. The difference, however, between the average values predicted by Kercher at $Z/D=1$ and $Z/D=2$ is small (about 6.5%) and may be statistically insignificant considering experimental uncertainty and the variance between Kercher's data and the curve fit used in developing the correlation.

In addition to the comparison of overall average Nu, an attempt was made to compare spanwise average Nu results obtained in this experiment with predicted spanwise values using the correlation proposed by Florschuetz et al. [2]. Results were compared at the highest and lowest jet Reynolds numbers for both Z/D heights; in all, four comparisons were made. The results of the comparison at the low Re are shown in Fig. 18.

The agreement in Nu is fair. In cases where the predicted Nu does not match the measured Nu, the trend in streamwise direction is the same. For the smaller Z/D, both the test data and Florschuetz correlation show that Nu does not decay in the streamwise direction for the entire length of the passage. The differences between the measurement techniques used by the authors may contribute to the differences in results. The correlation yields a spanwise average Nu as a function of row number; hence, one has a single discrete Nu value for each row. The liquid crystal technique results in a more continuous detailed stream of data results. Therefore in order to compare test results with the correlation, it was necessary to subdivide the test results (such as those shown in Fig. 6) into subsections and average over the entire subsection to obtain a value comparable to the "row" value that the correlation would yield. This process in itself may cause some differences.

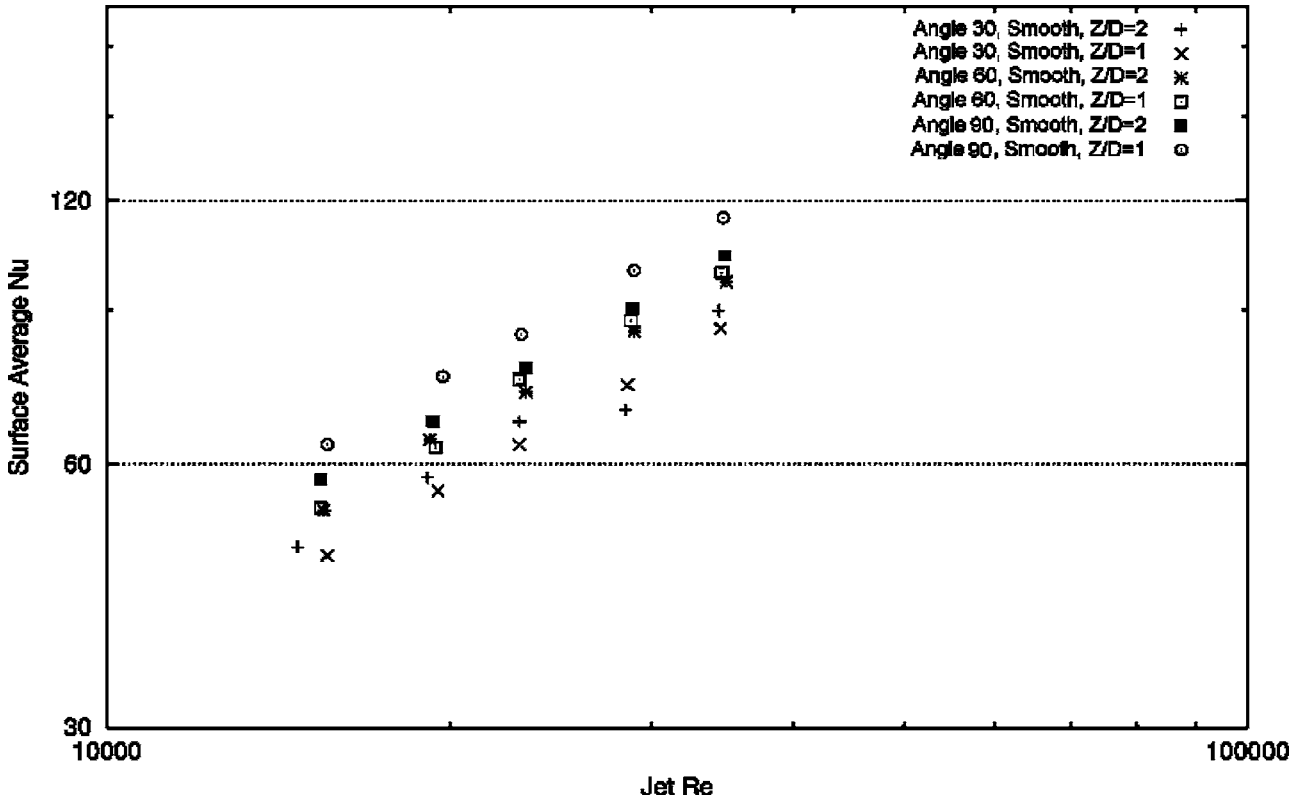

Fig. 15 Effect of gap height Z/D on average Nusselt number

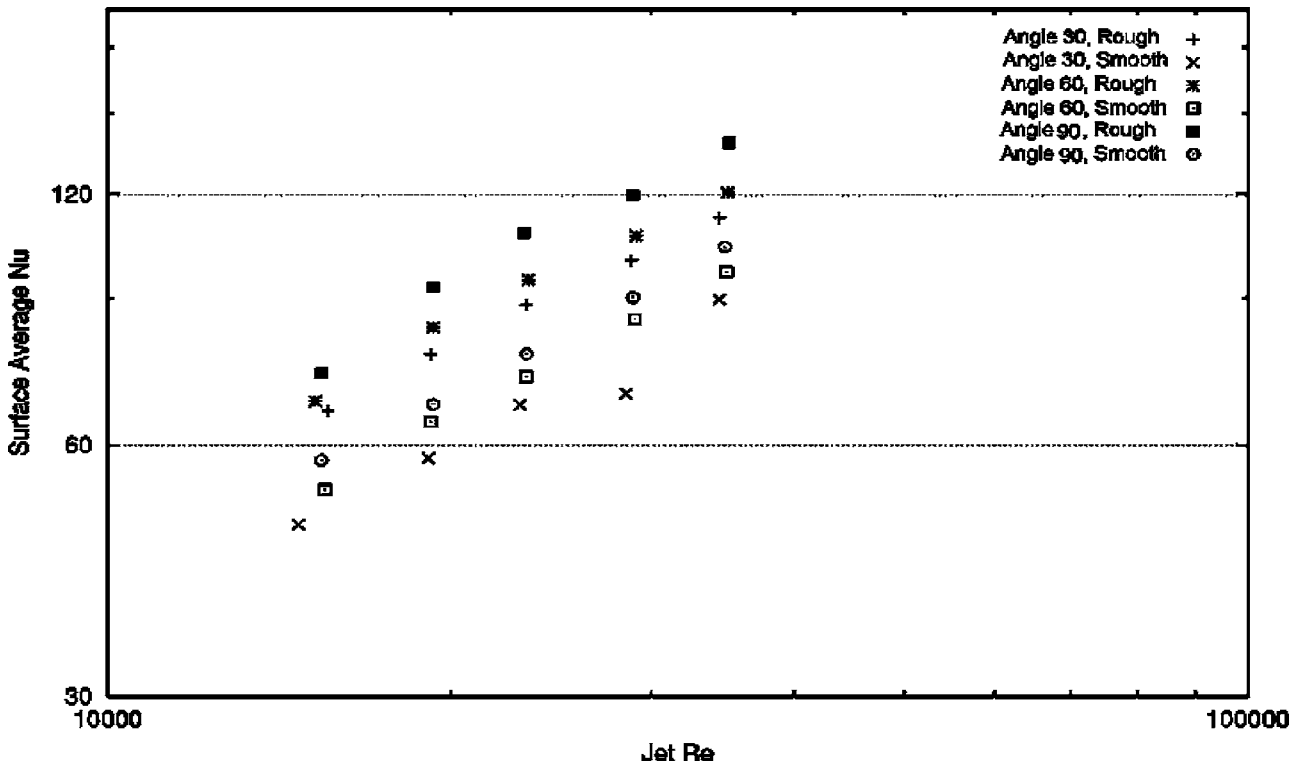

Fig. 16 Effect of roughness on average Nusselt number at $Z/D=2$

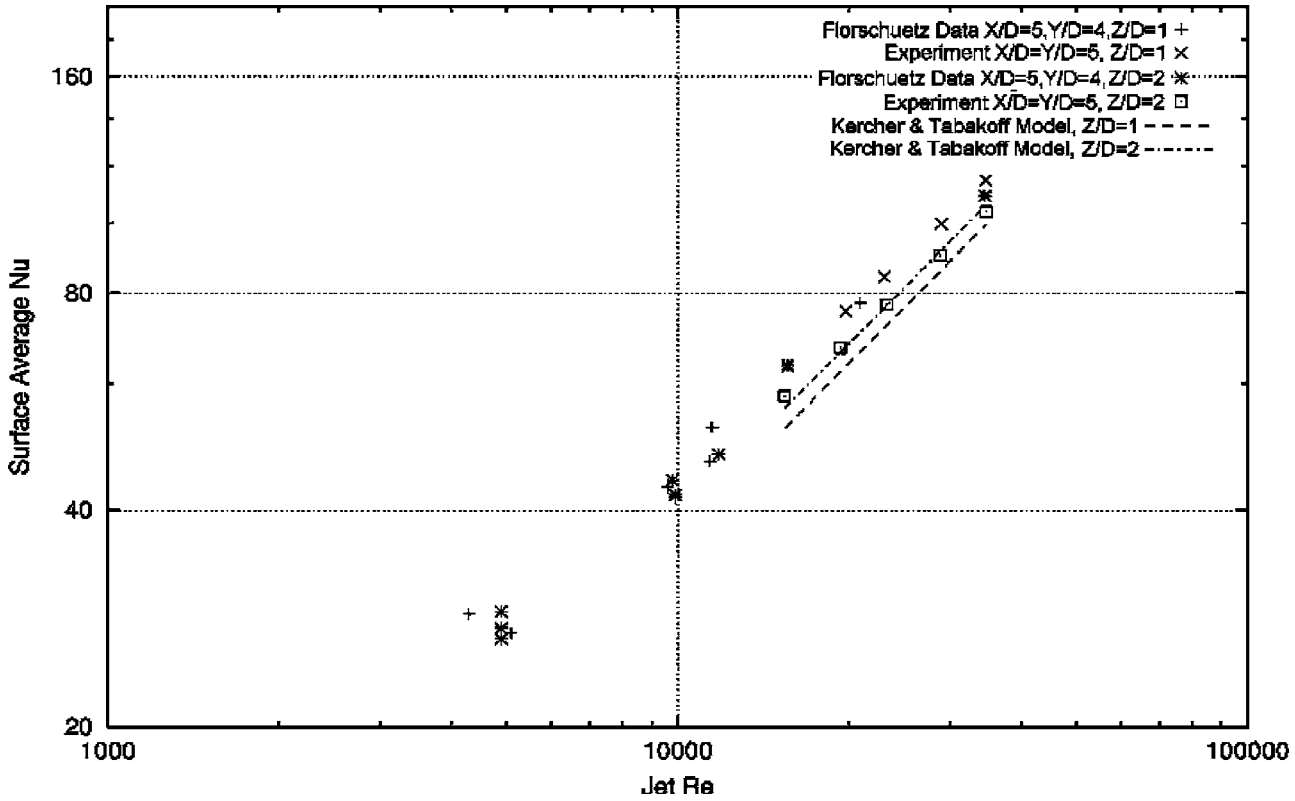

Fig. 17 Comparison of average Nusselt number for 90 deg jets with published results

Conclusions

In summary, the optimum design would utilize roughened surfaces since they enhance heat transfer significantly. Furthermore, rough surfaces reduce nonuniformity of surface temperature. Reducing nonuniformity can increase part life by reducing thermal gradients and thermal-induced stresses. The additional pressure drop due to the surface roughness is negligible when compared to the pressure drop through the jet plate. The small gap height presents a higher system pressure drop without significantly increasing heat transfer; hence, small gap heights should be avoided. Nonorthogonal jets reduce heat transfer but tend to generate more uniform heat transfer distributions. Hence, jet angle is yet another parameter that can be varied in a design to reduce thermal gradients especially when maximizing overall heat transfer coefficients is not the only important objective.

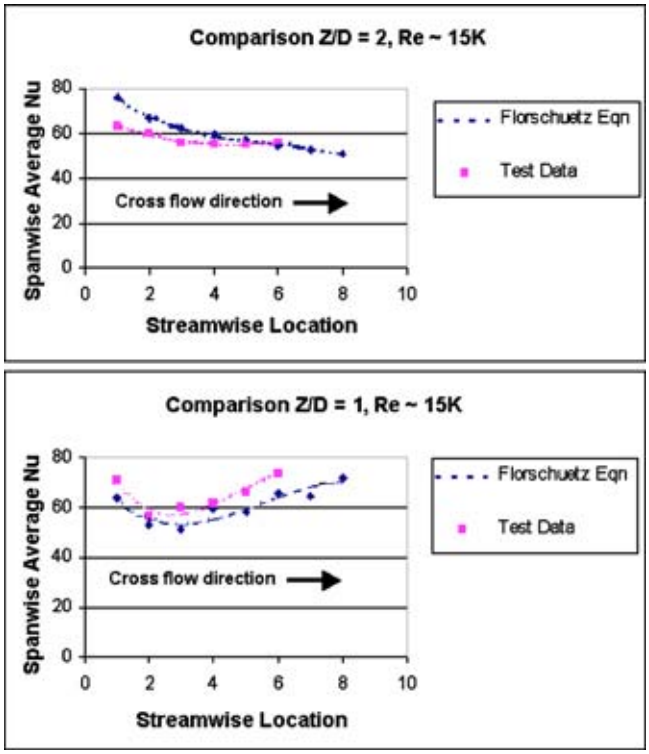

Fig. 18 Comparison of spanwise average Nusselt number for 90 deg jets

Acknowledgments

The authors would like to acknowledge N. Nirmalan, J. Bailey, R. Bunker, and S. Brzozowski at the General Electric Global Research Center for their support and insight

Nomenclature

A = flow area of array of jets
D = impingement jet hole diameter
g = acceleration due to gravity
k_{air} = thermal conductivity of air
k = specific heat ratio, Cp/Cv
$\dot{m}$ = measured mass flow rate of air
N = number of circular holes in jet plate
Nu = Nusselt number$=hD/k_{air}$
P_0 = pressure in the pressure chamber
P_{ex} = discharge pressure at exit of impingement channel
Q_{heater} = heat generated by foil heater
Q_{loss} = estimated heat loss through Plexiglas insulation
R = gas constant of air

R_a = centerline average roughness—arithmetical average value of all distances of the roughness profile from its centerline over a length of 15 mm[2]

R_z = average peak to peak roughness—average value of the greatest single peak to peak reading from five sequential lengths of 2.5 mm on the surface trace

Re = average jet Reynolds number=$4\dot{m}/\mu\pi DN$

T_0 = temperature in the plenum chamber

T_w = temperature of target surface (cold gas side)

X = stream-wise spacing of jet holes of impingement plate

Y = span-wise spacing of jet holes of impingement plate

Z = distance between the jet plate and the target surface

μ = dynamic viscosity of air

θ = jet angle (90 deg is orthogonal to the target surface)

References

[1] Florschuetz, L. W., Berry, R. A., and Metzger, D. E., 1980, "Periodic Streamwise Variations of Heat Transfer Coefficients for Inline and Staggered Arrays of Circular Jets with Crossflow of Spent Air," ASME J. Heat Transfer, **102**, pp. 132–137.

[2] Florschuetz, L. W., Truman, C. R., and Metzger, D. E., 1981, "Streamwise Flow and Heat Transfer Distributions for Jet Array Impingement with Crossflow," ASME J. Heat Transfer, **103**, pp. 337–342.

[3] Florschuetz, L. W., Metzger, D. E., and Su, C. C., 1984, "Heat Transfer Characteristics for Jet Array Impingement with Initial Crossflow," ASME J. Heat Transfer, **106**, pp. 34–41.

[4] Florschuetz, L. W., and Isoda, Y., 1983, "Flow Distributions and Discharge Coefficient Effects for Jet Array Impingement with Initial Crossflow," ASME J. Eng. Power, **105**, pp. 296–304.

[5] Andrews, G. E., and Hussain, C. I., 1986, "Full Coverage Impingement Heat Transfer: The Influent of Channel Height," *Proceedings of the 8th International Heat Transfer Conference*, Vol. 3, pp. 1205–1211.

[6] Gillespie, D. R. H, Wang, Z. Ireland, P. T., and Kohler, S. T., 1998, "Full Surface Local Heat Transfer Coefficient Measurements in a Model of an Integrally Cast Impingement Cooling Geometry," ASME J. Turbomach., **120**, pp. 92–99.

[7] Son, C., Gillespie, D., Ireland, P., and Dailey, G., 2001, "Heat Transfer and Flow Characteristics of an Engine Representative Impingement Cooling System," ASME J. Turbomach., **123**, pp. 154–160.

[8] Huang, Y., Ekkad, S. V., and Han, J., 1998, "Detailed Heat Transfer Distribution under an Array of Orthogonal Impinging Jets," J. Thermophys. Heat Transfer, **12**(1), pp. 73–79.

[9] Perry, K. P., 1954, "Heat Transfer by Convection from a Hot Gas Jet to a Plane Surface," Proc. Inst. Mech. Eng., Vol. **168**, pp 775–784.

[10] Trabold, T. A., and Obot, N. T., 1987, "Impingement Heat Transfer Within Array of Circular Jets: Part II—Effects of Crossflow in the Presence of Roughness Elements," ASME J. Turbomach., **109**, pp. 594–601.

[11] Haiping, C., Jingyu, Z., and Taiping, H., 1998, "Experimental Investigation on Impingement Heat Transfer From Rib Roughened Surface within Array of Circular Jet: Effect of Geometric Parameters," ASME Paper No. 98-GT-208.

[12] Failla, G., Bishop, E. H., and Liburdy, J. A., 1996, "Enhanced Jet Impingement Heat Transfer with Crossflow at Low Reynolds Numbers," ASME National Heat Transfer Conference, HTD-Vol. 324, pp. 107–113.

[13] Johnson, R. A., Loprinzo, A. J., Lee, C., Abuaf, N., Hasz, W. C., and Morton, L. M., 2003, "Method & Apparatus for Enhancing Heat Transfer in a Combustor Liner for a Gas Turbine." U. S. Patent No. 6,526,756 B2 (Mar. 4, 2003).

[14] El-Gabry, L. A., 2003, "Local Heat Transfer Distribution on Smooth and Roughened Surfaces under an Array of Angled Impinging Jets," Ph.D. thesis, Rensselaer Polytechnic Institute.

[15] Johnson, R. A., 1994, *Miller and Freund's Probability and Statistics for Engineers*, Prentice–Hall, Englewood Cliffs, NJ.

[16] Shapiro, A. H., 1953, *The Dynamics and Thermodynamics of Compressible Fluid Flow*, Vol. 1, Wiley, New York.

[17] Kline, S. J., and McClintock, F. A., 1953, "Describing Uncertainties in Single-Sample Experiments," Mech. Eng. (Am. Soc. Mech. Eng.), **75**, pp. 3–8.

[18] Florschuetz, L. W., Metzger, D. E., Takeuchi, D. I., and Berry, R. A., 1980, "Multiple Jet Impingement Heat Transfer Characteristic—Experimental Investigation of In-Line and Staggered Arrays With Crossflow," NASA-CR-3217, Arizona State University, Tempe, AZ.

[19] Kercher, D. M., and Tabakoff, W., 1970, "Heat Transfer by a Square Array of Round Air Jets Impinging Perpendicular to a Flat Surface Including the Effect of Spent Air," ASME J. Eng. Power, **92**, pp. 73–82.

[2]The lengths of 15 and 2.5 mm in the R_a and R_z definitions are specific to the profilometer settings.

On the Three-Dimensional Structure of Turbulent Spots

T. P. Chong

S. Zhong

School of Engineering,
University of Manchester,
Manchester M13 9PL, UK

A detailed measurement of turbulent spots propagating in a laminar boundary layer over a flat plate was made at a zero pressure gradient and three favorable pressure gradients. Data were recorded across the span of turbulent spots at a number of streamwise locations along the plate using a hot-wire probe and surface-mounted hot films. In this work we aim at extending the existing studies that are largely based upon measurements made in the plane of symmetry of the spots and away from the wall and investigating the three-dimensional structure of turbulent spots and its dependence on streamwise pressure gradients. The results from the present experiment reveal some interesting aspects of the overall structure of the spots and the role that regions with negative velocity perturbations play in the spanwise growth of turbulent spots. The presence of a spanwise overhang is also confirmed that is believed to be responsible for the smaller spreading angle of spots measured at the wall. This finding is expected to have important implications to the development of improved transition models that are used to predict heat transfer and skin friction for turbine blades. [DOI: 10.1115/1.1928286]

Background

It has been well known that boundary layer transition from laminar to turbulent flows starts by the random formation of localized turbulent regions known as "turbulent spots." These turbulent spots grow in both streamwise and spanwise directions and eventually emerge with each other to form a fully turbulent boundary layer [1,2]. Being the active features in the transition process, turbulent spots have been studied for decades since they were first discovered by Emmons in the 1950s [3]. A substantial amount of understanding has been achieved about the characteristics of the spots and quantitative measurements of their streamwise and spanwise growth [4,5] have been accumulated that form the basis of the most promising transition models [1].

Most of the aforementioned investigations were carried out on artificially created spots since their known origin of formation greatly simplifies the experimental arrangements. A majority of these measurements were carried out on the plane of symmetry of the spots from which a portrait of the turbulent spot on its central streamwise plane emerges. It is shown that in the wall normal direction the spot protrudes the height of the laminar boundary layer. In the streamwise direction, the front of the spot stretches forward above the wall in the form of a leading edge overhang, whereas the rear of the spot is trailed by a becalmed region in which the turbulent boundary layer relaxes to reassume its laminar state (see Fig. 1(*a*)). However, up to date experimental data on off-centered streamwise planes and spanwise cross sections of the spots are still very scarce. Furthermore, the knowledge about the spot in its plane view is still limited to its commonly known arrowheaded shape and spanwise spreading angles measured at some chosen distances from the wall. As a result, in the spot-based transition models, it commonly assumes that the spreading angle is the same across the boundary layer without further examination.

The authors have been using temperature-sensitive liquid crystals to visualize the footprints of turbulent spots and their spanwise growth in a number of experiments [6,7]. In all these experiments, a smaller spreading angle was obtained from the liquid crystal coating than that reported in the literature, which largely consists of investigations using hot wires. Results from supplementary measurements with surface-mounted film gauges and a hot-wire probe prompt the authors to propose that an overhang must be present in the spanwise cross section of the spot (see Fig. 1(*b*)). They believe that the spanwise overhang results in a smaller spanwise width of the spot that is in contact with the wall, thus a smaller spreading angle at the wall.

In the present experiments, a series of detailed measurements on artificially created spots was made to investigate their three-dimensional structure and to confirm the above hypothesis. The measurements were carried out across the entire half-span of the spots using surface-mounted hot film gauges and a hot-wire probe located at various distances from the wall. The data were used to construct the three-dimensional ensemble-averaged structure of the spots. The tests were conducted in laminar boundary layers at a zero pressure gradient and three favorable pressure gradients in order to examine the influence of streamwise pressure gradients. This study is expected to yield detailed information about the spanwise structure of turbulent spots that can be used to develop improved transition models for predicting heat transfer and skin friction on the surface of turbine blades.

Experimental Setup

The experiment was conducted in a low-turbulence closed return wind tunnel at the Goldstein Aeronautical Research Laboratory, the Manchester School of Engineering. The wind tunnel has a test section measuring $0.5\ \text{m} \times 0.5\ \text{m} \times 3\ \text{m}$ and is equipped with a three-dimensional automated traverse system. The measurement accuracy of this traverse system in the wall normal direction is ±0.01 mm. A test plate 1.6 m in length was mounted horizontally across the entire width of the test section. A trailing edge flap was used in the zero pressure gradient case to ensure that a fully attached laminar boundary layer was obtained at the leading edge of the plate.

The streamwise favorable pressure gradients were generated by attaching wedges of different angles to the ceiling of the test section, as shown in Fig. 2. This configuration produced an accelerating flow with a constant pressure gradient parameter, K, where

$$K = \frac{\nu}{u_\infty^2}\frac{du_\infty}{dx}. \tag{1}$$

To investigate the effect of variable strengths of favorable pressure gradients on the growth of turbulent spots, experiments were conducted at mild (K1), medium (K2), and strong (K3) favorable pressure gradients, respectively, with a zero pressure gradient as

Contributed by the International Gas Turbine Institute and presented at the International Gas Turbine and Aeroengine Congress and Exhibition, Atlanta, GA, June 16–19, 2003. Manuscript received by the IGTI December 1, 2002; final revision March 1, 2003. Paper No. GT2003-38435. Review Chair: H. R. Simmons.

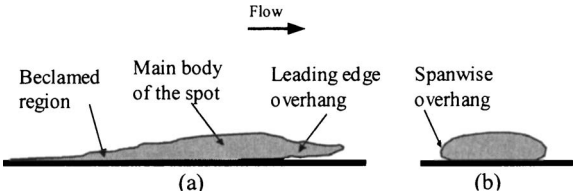

Fig. 1 A schematic sketch of a turbulent spot on (*a*) its plane of symmetry and (*b*) its spanwise cross-section

the baseline case. The distributions of laminar boundary layer thickness and momentum thickness for all the test cases are shown in Fig. 3. Table 1 summarizes the corresponding flow conditions in detail.

Turbulent spots were created artificially by injecting puffs of air through a 0.5 mm diameter orifice in the test plate at 275 mm downstream of the leading edge. The small air jet was generated by driving a miniature loudspeaker that was attached to the back of the test plate with square wave pulses.

A DANTEC 55P15 boundary-layer type hot wire probe was used to measure the velocity fluctuations produced by the spots at different distances from the wall. The nearest measuring point of the hot wire was about 0.2 mm above the wall. An adjustment of the wire position relative to the wall was aided by the reflective surface of the flat plate. The measurement was extended to the wall using an array of surface-mounted hot film sensors fixed along the centerline of the plate. In order to avoid thermal interference between the hot wire and hot films, a 5 mm spanwise offset was introduced between the two sensors. In the experiments, the spanwise location of the hot wire and hot films were

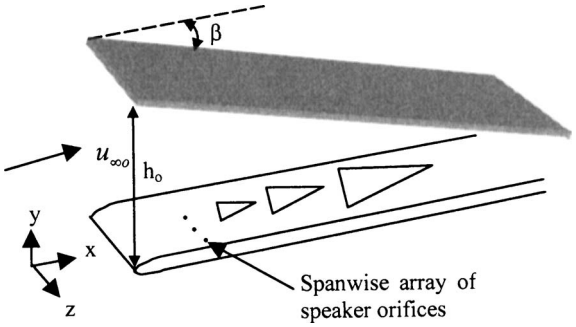

Fig. 2 Schematic diagram of the test configuration

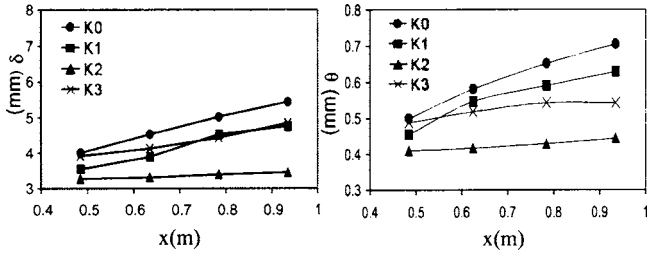

Fig. 3 Distributions of laminar boundary layer thickness (δ) and momentum thickness (θ)

Table 1 Summary of flow conditions

Pressure gradient	Notation	$u_{\infty o}$ (m/s)	β (°)	K
Zero	K0	11	0	0
Mild favorable	K1	11	2.7	0.24×10^{-6}
Medium favorable	K2	11	5.5	0.56×10^{-6}
Strong favorable	K3	7.5	5.5	0.85×10^{-6}

fixed. To facilitate the three-dimensional mapping of turbulent spots, the measurements were carried out with the loudspeaker being attached in turn to one of 28 different orifices that are spaced 5 mm apart across the half-span of the test plate (see Fig. 2). The measurements were repeated at four streamwise locations x_s=210, 360, 510, and 660 mm from the spot generator to capture the streamwise growth of the spots.

Data Processing Methods

During the experiment, 32 768 samples were captured at each measurement point at a sampling frequency of 5 kHz. The signals were filtered at a low-pass frequency of 2 kHz before they were digitized using a 12-bit A/D converter. In order to maximize the number of spots captured in the fixed sample size at each streamwise station, the spot production rates were adjusted accordingly. Each data set typically contains 75 spots.

The time variations of ensemble-averaged velocity $\langle u(x,y,t_j)\rangle$ produced by the spots at each measurement point can be obtained by averaging the velocity signals with reference to the rising edge of the pulses that were used to generate the spots. The velocity perturbation caused by an ensemble-averaged turbulent spot is given by

$$\tilde{u}(x,y,t_j) = \frac{\langle u(x,y,t_j)\rangle - u_L(x,y)}{u_\infty(x)} \tag{2}$$

where $u_L(x,y)$ is the local velocity in the undisturbed laminar boundary layer. The rms values of velocity fluctuations at corresponding instant were also obtained,

$$\mathrm{rms}\langle u\rangle = \sqrt{\frac{\sum_N [u(x,y,t_j) - \langle u(x,y,t_j)\rangle]^2}{N}} \tag{3}$$

where N is the total number of spots. They are normalized by the local free-stream velocity when presented in the graphs.

In this study, the propagation rates of the leading edge and trailing edge of turbulent spots in the plane of symmetry were also obtained to provide information about the growth of spots in the streamwise direction. In order to obtain the propagation rates, an effective algorithm is required to identify the location of the leading edge and trailing edge of each turbulent spot. The method used by Clark et al. [8] was employed in the present study to locate the interface between the turbulent flow inside the spots and the laminar flow outside. This method can be applied directly to raw signals from both the hot wire and surface-mounted film gauges.

In this method, a detector function was used to highlight high frequency fluctuations that are associated with turbulence. It is defined as

$$D(x,y,t) = m(x,y,t)\left(\frac{\partial E(x,y,t)}{\partial t}\right)^2 \tag{4}$$

where $E(x,y,t)$ is the raw signal and $m(x,y,t)$ is the normalized signal magnitude, which is given by

$$m(x,y,t) = \frac{E(x,y,t) - E_{\min}}{E_{\max} - E_{\min}} \tag{5}$$

The rate of change in the raw signal is obtained using the central difference scheme.

A smoothing function is then obtained from the detection function

$$C(x,y,t = i\,\Delta t) = \frac{(\Delta t)^2}{1 + (\tau_s/\Delta t)}\left[\sum_{j=i-(\tau_s/2\,\Delta t)}^{j=i+(\tau_s/2\,\Delta t)} w_j D(x,y,j\,\Delta t)\right] \tag{6}$$

so as to eliminate zero crossings in the detection function within a turbulent spot. Here Δt is the sampling period and τ_s is the smoothing period. The weighting factor w_j is defined as

$$w_j = \exp\left[-\left(\frac{0.625}{\tau_s/\Delta t}\right)|j-i|\right]. \quad (7)$$

Finally the turbulent portion of the signal produced by each spot is identified by employing a threshold to the smoothing function. In this study, this threshold value was chosen through a trial and error procedure until the interface between the turbulent and laminar region identified using this algorithm was consistent with that from visual inspection of the raw signal.

Once the locations of the leading and trailing edge of each spot were identified and ensemble averaged, the spot propagation rates were calculated by linear best-fitting the data obtained at a series of streamwise locations. This was done by plotting the integral arrival time against the time of flight of the characteristic parts of spots from a reference point to some known locations. In the present experiments, measurements were conducted at four streamwise stations. The time of flight is taken as the actual time it takes for either the leading edge or the trailing edge of the spots to convect from the most upstream measurement point to one of the remaining three streamwise locations. The integral arrival time is the time required for the spot to travel across the same distance at the local free-stream velocity, i.e.

$$t_{\text{integral}} = \int_{x_{\text{ref}}}^{x} \frac{dx}{u_\infty(x)} \quad (8)$$

The slope of the best-fit line gives the propagation rate as a constant proportion of the local free-stream velocity.

In order to find the spot spanwise spreading angle, the time-averaged location of the spanwise extreme of spots (wing tips) at a given streamwise station has to be identified. However, in this region the flow is not always turbulent since statistically some spots may exhibit a smaller spanwise width than the others and thus will not be detected. An intermittency method is hence used in which the intermittency factor is defined as the ratio between the number of spots identified at that location and the total number of spots actually produced upstream. In this study, an intermittency of 0.5 was chosen as the criterion in locating the averaged location of the spot wing tips. A similar method has been used by other researchers to identify the boundary of ensemble-averaged spots [9,10]. The spreading angle of the spot is finally taken as the angle between the best-fit line that depicts the locus of spot wing tips at four streamwise locations and the central line of the test plate.

Results and Discussion

Characteristics of Turbulent Spots on the Plane of Symmetry. Before the spanwise structure of turbulent spots is studied, the characteristics of spots on their plane of symmetry are examined. This allows the spots to be assessed in a more conventional sense and thus also forms a basis for comparison with existing data presented in the literature.

Figure 4 shows the variations of normalized spot leading and trailing edge propagation rates across the boundary layer at different levels of pressure gradients. Note that the distance from the wall is normalized using the local turbulent boundary layer thickness δ_{tur} instead of that of the laminar boundary layer, in view of the fact that the maximum height of spots grows at the rate of turbulent boundary layers. The results indicate that the spot leading and trailing propagation rates at the zero-pressure gradient are the highest among all the test cases. Furthermore, as the level of favorable pressure gradient increases, C_L decreases more dramatically than C_T, leading to a reduction in the streamwise growth of spots. The observation of a reduction in the streamwise growth of spots with increasing favorable pressure gradients is consistent with that reported in the literature. However, some researchers (Gostelow et al. [5]) found that this reduction was the result of a much larger increase in C_T than C_L. The authors of this paper would like to argue in favor of their own observation in view of

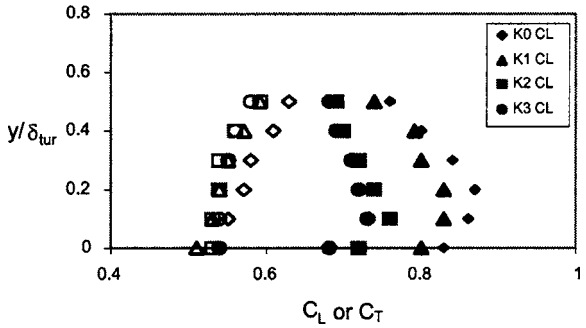

Fig. 4 Variations of the leading edge and trailing edge propagation rate across the boundary layer

that since the spot leading edge represents the locus of breakdown of laminar flow into turbulent, a favorable pressure gradient that is expected to inhibit this breakdown would result in a slower leading edge propagation rate of the spot.

The spot propagation rates, especially at the leading edge, are also found to vary across the boundary layer. The rate appears to be the lowest at the wall and the highest at the leading overhang around $y/\delta_{\text{tur}}=0.2$. Table 2 summarizes the spot leading and trailing edge propagation rates at $y=0$ and $y=0.2\delta_{\text{tur}}$ for all the test cases. In the zero pressure gradient case, the spots propagate at $C_L=0.83$, $C_T=0.54$ at the wall and $C_L=0.87$, $C_T=0.57$ at $y=0.2\delta_{\text{tur}}$. These values closely resemble the finding of other researchers in zero pressure gradient flows using various methods [5,6,8,11]. The difference in C_L at the wall and at $y=0.2\delta_{\text{tur}}$, which is near the tip of the leading edge overhang of the spot, implies that the length of the leading edge overhang should increase as the spot propagates downstream.

Phase-averaged contour maps of velocity perturbations and rms velocity fluctuations on the plane of symmetry of the turbulent spots are presented in Figs. 5 and 6, respectively, for the K0 case. The leading edge of the turbulent spots can be clearly identified in both figures, whereas the trailing edge can only be located in the rms contours. It is also seen that the most forward protruding turbulent region at the leading edge (streamwise overhang) stands out more clearly in the rms velocity fluctuation contours. And interestingly, a close examination of the rms contours reveals a concentrated region of a high level of turbulence near the leading edge of the spot, and this region is always beneath the overhang. This region must be where the turbulence is produced. This observation is consistent with those made by Glezer et al. [9] and Gad-El-Hak et al. [12], in which a strong destabilized regime was found under the overhang of the leading edge of the spot.

Characteristics of Spots in Spanwise Planes. Figures 7(*a*)–7(*h*) show a sequence of spanwise slices of velocity perturbation contours as the ensemble-averaged turbulent spot passes through the measurement plane at $x_s=510$ mm at the zero pressure gradient. Each slice is denoted by the time of flight t_s that takes the corresponding section of the spot to travel from where the spot was born to the measurement plane. Only half of the spot off its plane of symmetry is shown here. The corresponding loca-

Table 2 Summary of spot propagation rates

	C_L		C_T	
	$y=0$	$y=0.2\delta_{\text{tur}}$	$y=0$	$y=0.2\delta_{\text{tur}}$
K0	0.83	0.87	0.54	0.57
K1	0.80	0.83	0.51	0.54
K2	0.72	0.74	0.53	0.54
K3	0.68	0.72	0.54	0.54

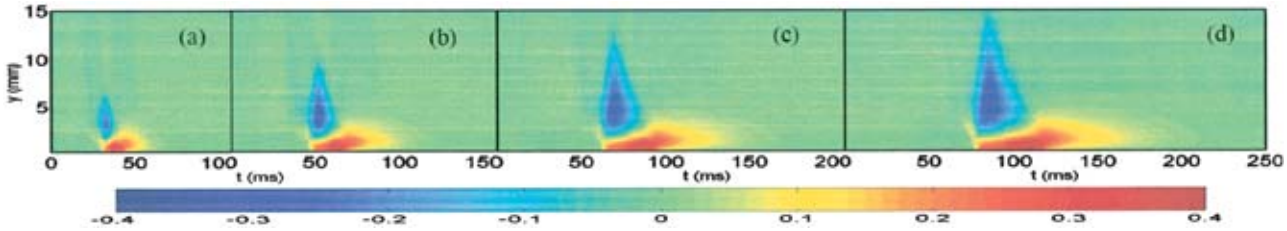

Fig. 5 Contours of velocity perturbation at K0, x_s=(*a*)210 mm, (*b*) 360 mm, (*c*) 510 mm, (*d*) 660 mm

tion of each spanwise cut across the spot can be referred to as the enlarged velocity perturbation contour on the plane of symmetry shown in Fig. 7(*aa*).

As it can be seen in Fig. 7(*a*), the arrival of the spot is indicated by the appearance of a region with negative velocity perturbations inside the overhang of the spot at about the height of the thickness of the undisturbed laminar boundary. A region with positive velocity perturbations in the near wall region begins to develop underneath the region with negative velocity perturbation as the main body of the spot arrives (see Figs. 7(*b*)–7(*d*)). This region initially appears to have a narrower width than the region with negative velocity perturbations.

Figure 7 shows clearly that in the forward part of the spot the outer part of the spot is dominant by a region with negative velocity perturbations whereas the near wall region is dictated by the presence of a region with positive velocity perturbations. The region with negative velocity perturbations grows both in width and height until the spot fills the height of the local turbulent boundary

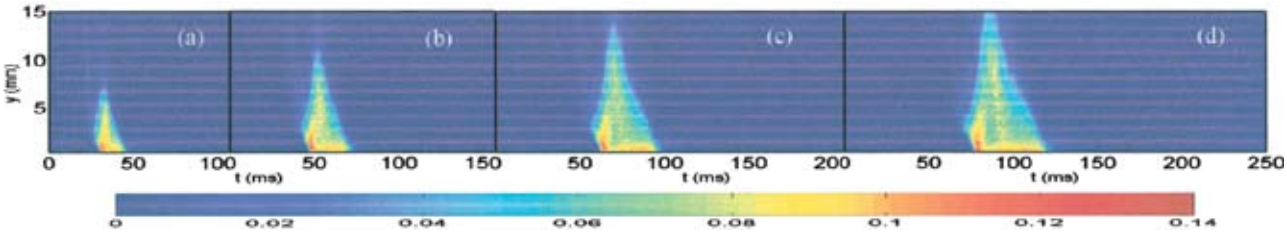

Fig. 6 Contours of rms velocity fluctuation at K0, x_s=(*a*) 210 mm, (*b*) 360 mm, (*c*) 510 mm, (*d*) 660 mm

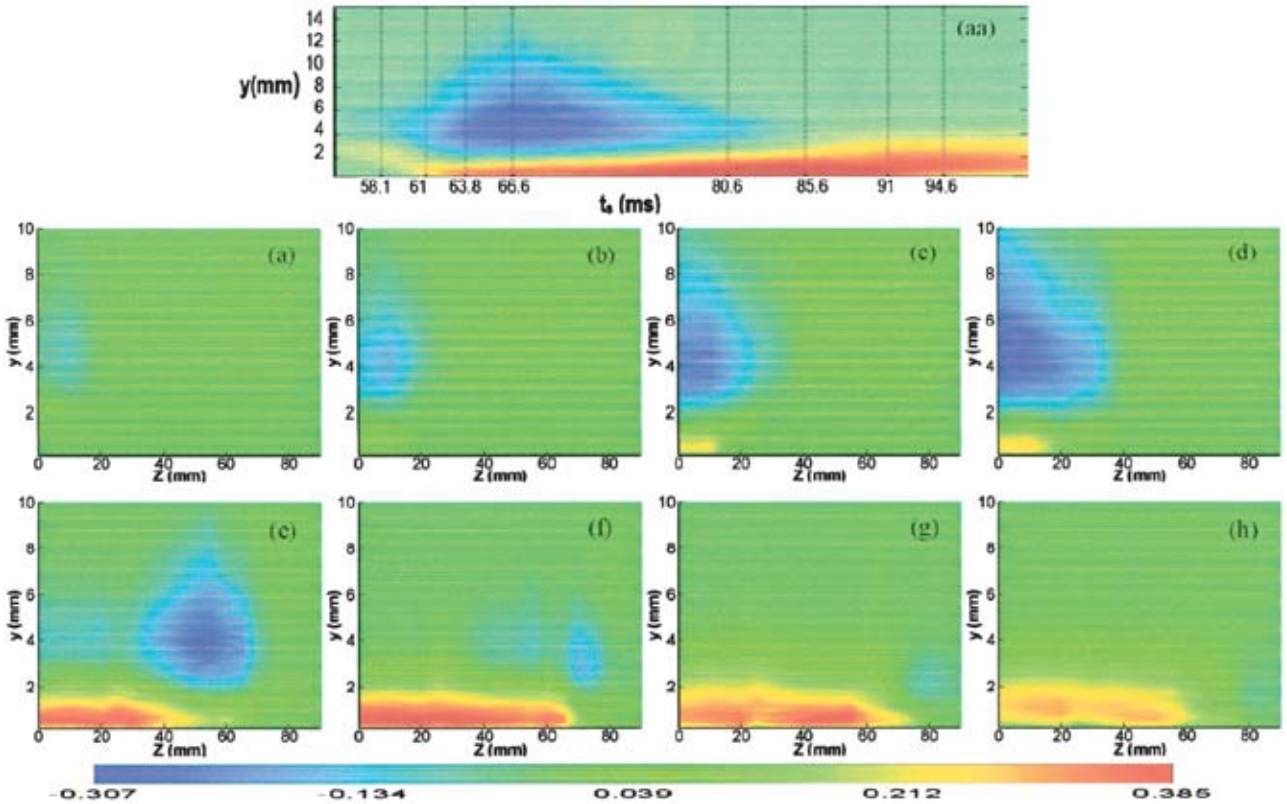

Fig. 7 (*aa*) Streamwise velocity perturbation contour at the plane of symmetry; Spanwise velocity perturbation contours at time t_s=(*a*) 58.1 ms, (*b*) 61 ms, (*c*) 63.6 ms, (*d*) 66.6 ms, (*e*) 80.6 ms, (*f*) 85.6 ms, (*g*) 91 ms, and (*h*) 94.6 ms.

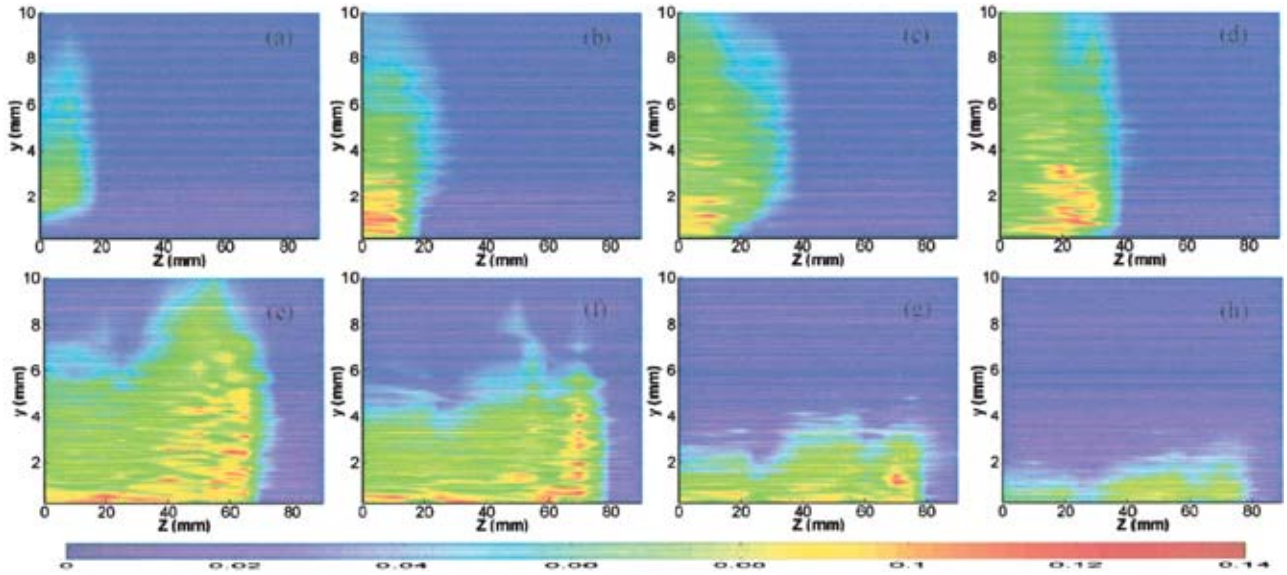

Fig. 8 Spanwise rms velocity fluctuation contours at time t_s=(*a*) 58.1 ms, (*b*) 61 ms, (*c*) 63.6 ms, (*d*) 66.6 ms, (*e*) 80.6 ms, (*f*) 85.6 ms, (*g*) 91 ms, and (*h*) 94.6 ms

layer (Figs. 7(*b*)–7(*d*)). Right after the spot has developed to its maximal height, the region with negative perturbations begins to break down and drift away from the spot central plane toward the wing tip (Figs. 7(*e*)–7(*h*)). Its strength reduces rapidly and becomes diffused almost completely as it drifts beyond the wing tip. At the same time, the region with positive perturbations continues to gain strength and width until the spot grows to its maximum width near the trailing edge of the spot (Fig. 7(*f*)). After that the strength of the positive perturbation begins to decrease as the becalmed region in the form of a highly stable laminar boundary layer sets in. The region of positive perturbation eventually dies down as the laminar boundary layer relaxes to reassume its original state (Fig. 7(*g*) and 7(*h*)).

The behavior of the region with negative velocity perturbations is worth noticing. It is seen to undergo steady changes in the spanwise direction and eventually drift beyond the spanwise extreme of the region with positive velocity perturbations. Throughout the main body of the spot, the region with negative velocity perturbations always extends farther away from the spot centerline than the region with positive velocity perturbations underneath. This gives an impression that a spanwise overhang as shown in Fig. 1(*b*) is present.

Similar observations were also observed in the remaining three favorable pressure gradient cases. Due to limited space, the velocity perturbation contours for the pressure gradient cases are not presented here. The key observations of these data are that the perturbation level decreases as favorable pressure gradient increases and the extent of the spanwise overhang also reduces.

The corresponding rms velocity fluctuation contours of the spots are shown in Fig. 8. In correspondence to Fig. 7(*a*), Fig. 8(*a*) shows that the arrival of a spot leading edge overhang is marked by an increased level of turbulent intensity than its surroundings. As the main body of the spot arrives, a region with high turbulence intensity is seen to develop in the inner part of the boundary layer under the region with negative velocity perturbations (Figs. 8(*b*) and 8(*c*). After that the location of peak turbulence intensity is seen to drift outward to the spanwise extreme of the spot as the trailing edge of the spot arrives (Figs. 8(*d*)–8(*f*)). The peak turbulence intensity tends to be confined near the wall and around the spanwise periphery of the spot. Comparing Fig. 7(*f*) with 8(*f*), one sees that the location of peak turbulence roughly coincides with that of the maximum negative velocity perturbation near the wing tip.

The region occupied by the spot that is marked by a relatively higher turbulence level than the surrounding grows both in height and width until the trailing edge of the spot. The residue of turbulence is still present in the becalmed region, as shown in Fig. 8(*f*), and it dies down with time. The presence of spanwise overhang is obvious in the forward part of the spot (see Figs. 8(*c*) and 8(*d*)). In Figs. 8(*e*) and 8(*f*) the boundary between the spot and the laminar surrounding appears to be straight, showing no obvious sign of a spanwise overhang at first sight. But a careful examination of the contour in the vicinity of the wall (Figs. 8(*e*) and 8(*f*)) reveals a narrow spanwise band immediately next to the wall with a lower turbulence intensity than the region right above, suggesting that a spanwise overhang is also present in the context of rms velocity contours.

In order to assist the interpretation of the three-dimensional structure of turbulent spots, "isometric surfaces" of the ensemble-averaged velocity perturbations are shown in Fig. 9. The interface between the turbulent and laminar regions is identified by employing a threshold of ±2% velocity perturbation. This criterion had been used by a number of researchers [10,13,14] to identify the boundary of turbulent spots. In Fig. 9, the surface with +2% positive velocity perturbations (shown in light grey) appears thin and flat, whereas that with −2% negative velocity perturbations (shown in dark grey) appears upright and sweep backward at its side.

The height of the spot, which is represented by the −2% isometric surface, is at its maximum on the plane of symmetry and it decreases across the span. The height initially decreases slowly, but at some point it declines dramatically toward the wall and the spanwise extreme of this region extends beyond the location of the outmost +2% velocity perturbation shown in light grey. It is found that the location of this sudden declination in spot height varies with pressure gradients. Let z_1 denote the spanwise location of the sudden decrease in height and z_2 the spanwise width of the −2% isometric surface. It is found that in the K0 case, $(z_2 - z_1)/z_2 = 49\%$) and this ratio decreases steadily with increasing favorable pressure gradients to 47% at K1, 38% at K2, and 22% at K3, resulting in a shorter wing over which the height of spot decreases rapidly. It is commonly accepted that the spot grows in the direction normal to the wall by the entrainment of irrotational fluids from outside the boundary layer and in the spanwise direction by the destabilization effect [12]. The sudden change in the

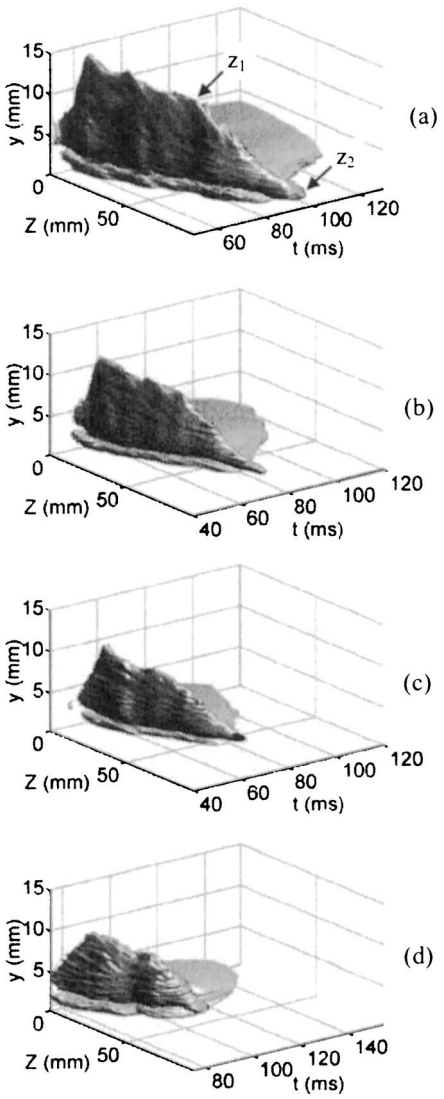

Fig. 9 Isometric surfaces of a half turbulent spot at x_s =510 mm at (*a*) K0, (*b*) K1, (*c*) K2, and (*d*) K3. Light grey represents –2% velocity perturbation and dark grey +2% velocity perturbation.

slope is likely to be associated with a switching between these two different mechanisms involved in the growth of spots in the two perpendicular directions.

Table 3 summarizes the spreading angle of turbulent spots at the wall and at $y=0.2\delta_{tur}$. As expected, the spreading angle decreases as the favorable pressure gradient increases. At the zero pressure gradient the turbulent spots spreads at 10.6° at a distance of $0.2\delta_{tur}$ from the wall, which is in agreement with the finding by other researchers [4,12]. However, the spreading angle at the wall is smaller (8.6°). A smaller angle was also found by the authors

Table 3 Summary of turbulent spot spreading angles

	Spreading angle, α (°)	
	$y=0$	$y=0.2\delta_{tur}$
K0	8.6	10.6
K1	7.6	8.3
K2	6.3	6.6
K3	4.4	4.6

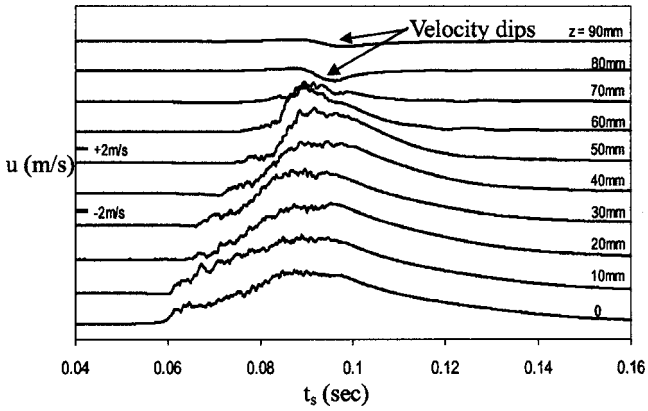

Fig. 10 Ensemble-averaged velocity produced by the spots at different spanwise locations (K0, x_s=510 mm, $y=0.2\delta_{tur}$)

using liquid crystal coatings [6,7]. The difference in the spreading angles at the two different heights decreases as the favorable pressure gradient increases.

Since both the hot wire data and hot film data were obtained in the same experiment, the discrepancy observed at $y=0$ and $0.2\delta_{tur}$ is not due to differences in flow conditions. The smaller spreading angle at the wall is likely to be caused by the damping of turbulence by the wall, as indicated by the rms contours (Fig. 8(*f*)). The results from the present study imply that the spot spreading angle measured away from the wall is not representative of that measured at the wall. Thus, in order to predict the heat transfer rate and skin friction coefficient more accurately, the characteristics of spots measured at the wall should be used. This finding would have an important implication to the development of spot-based transition models for turbine blades.

Discussion. By far, the 3D structure of ensemble-averaged turbulent spots have been examined in the context of a sequence of spanwise velocity perturbation contours and rms velocity contours through the entire length of the spot. From the velocity perturbation contours, it is found that the regions with negative velocity perturbations always extend farther outward in the spanwise direction than the region with positive velocity perturbations. Together with the observation that low rms fluctuations exist in the vicinity of the wall beneath the wing tip, the presence of a spanwise overhang similar to that at the leading edge of the spot is confirmed. The presence of spanwise overhang is also believed to be responsible for the smaller spots spreading measured at the wall.

Figure 10 shows the ensemble-averaged velocity variations across the span of the spot at a distance of $y=0.2\delta_{tur}$ at x_s =510 mm at the zero pressure gradient. The velocity traces between $z=0$ and 70 mm exhibit a distinct rise in velocity typically associated with the passage of a spot whereas beyond $z=70$ mm a velocity dip is clearly visible. This dip is located near the wing tip of the spot and is produced by the spanwise overhang. From the ensemble-averaged velocity variations at different distances from the wall, it is clearly seen that the velocity away from the wall is characterized by a dip at the arrival of the spot (see Fig. 11(*a*)). This results in a velocity profile that overlaps with that of the undisturbed laminar boundary layer in the near wall region and exhibits a considerable velocity deficit in the outer part of the layer (see Fig. 11(*b*)). It is likely that this velocity deficit could be more profound in an instantaneous velocity profile so that an inflection point results, making the flow more susceptible to disturbances.

The spanwise rms velocity contours show that peak turbulence intensity tends to be confined near the spanwise periphery of the spot. It is believed that the combination of the high turbulence intensity in the spanwise periphery of the spot and the spanwise

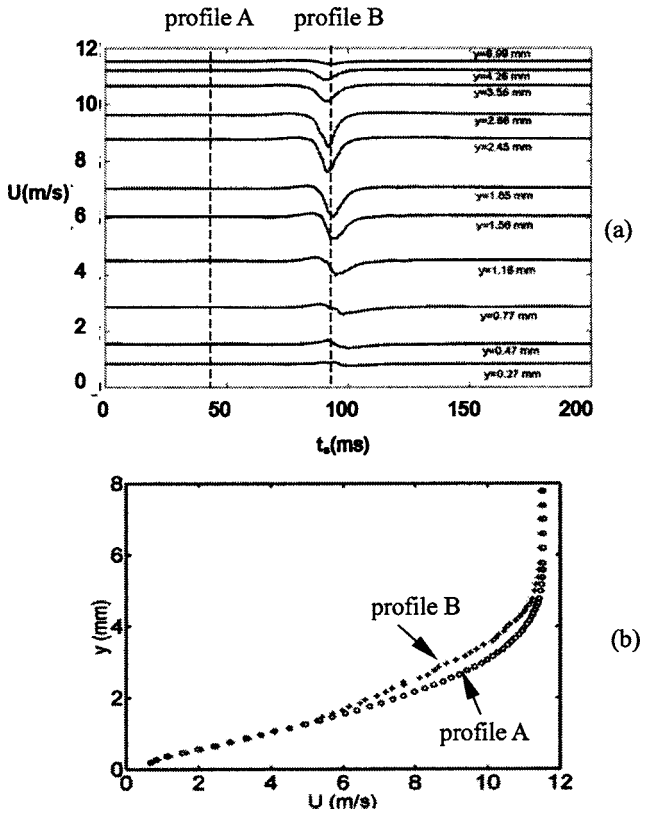

Fig. 11 (*a*) **Ensemble-averaged velocity variations at different distances from the wall;** (*b*) **a comparison between the velocity profile across the wing tip and that in an undisturbed boundary layer (K0,** x_s**=510 mm,** z**=80 mm).**

overhang provides the necessary condition for the breakdown of a laminar boundary layer into turbulent flow and hence the spanwise growth of the spot. (This is also likely to be the mechanism behind the streamwise growth of the spots since this condition is also fulfilled at the front of the spots.) Since both the negative perturbation level and the rms velocity fluctuations decrease with increasing favorable pressure gradients, the likelihood of a laminar flow breakdown should decrease accordingly, leading to a reduced spreading angle of spots. This is also manifested by a shorter spanwise length of the spot wing shown in isometric surface plots (Fig. 10) as the favorable pressure gradient increases.

Conclusion

A detailed measurement of turbulent spots propagating in a laminar boundary layer over a flat plate was made at a zero pressure gradient and three favorable pressure gradients. Data were recorded across the span of turbulent spots at a number of streamwise locations along the plate using a hot-wire probe and surface-mounted hot films. In this work we aim at extending the existing studies that are largely based upon measurements made in the plane of symmetry of the spots and away from the wall and investigating the three-dimensional structure of turbulent spots and its dependence on streamwise pressure gradients.

The results from the present experiment reveal some interesting aspects of the overall structure of the spots and the role that regions with negative velocity perturbations play in spanwise growth of turbulent spots. The presence of a spanwise overhang is also confirmed, which is believed to be responsible for the smaller spreading angle of spots measured at the wall. This finding is expected to have important implications to the development of improved transition models that are used to predict heat transfer and skin friction for turbine blades.

Acknowledgments

The work reported in this paper is sponsored by the Engineering and Physics Science Research Council in the UK. The valuable comments from Professor Howard Hodson at the Whittle Laboratory, Cambridge University and the contribution of Mr. Mark Watson at the Manchester School of Engineering at the preparation stage of the experiments are appreciated.

Nomenclature

C_L = turbulent spot leading edge propagation rate normalized by local free-stream velocity
C_T = turbulent spot trailing edge propagation rate normalized by local free-stream velocity
K = pressure gradient parameter, $K=(\nu/u_\infty^2)(du_\infty/dx)$
u_∞ = free-stream velocity, ms^{-1}
$u_{\infty o}$ = free-stream velocity at the leading edge of the test plate, ms^{-1}
x = streamwise distance from leading edge of plate, mm
x_s = streamwise distance from spot generator, mm
y = distance normal to the wall, mm
z = spanwise distance from centerline of spot, mm
α = spreading angle of turbulent spots, degrees
β = wedge angle of the wind tunnel ceiling, degrees
ν = kinematic viscosity, $m^2\ s^{-1}$

References

[1] Mayle, R. E., 1991, "The Role of Laminar–Turbulent Transition in Gas Turbine Engines," ASME Paper No. 91-GT-261.
[2] Wygnanski, I., 1978, "On the Possible Relationship Between the Transition Process and the Large Coherent Structures in Turbulent Boundary Layers," AFOSR/Lehigh University Workshop on Coherent Structure of Turbulent Boundary Layers, edited by C. R. Smith and D. E. Abbott, p. 168.
[3] Emmons, H. W., 1951, "The Laminar–Turbulent Transition in a Boundary Layer—Part I," J. Aerosp. Sci., **18**, pp. 490–498.
[4] Schubauer, G. B., and Klebanoff, P. S., 1955, "Contribution on the Mechanism of Boundary Layer Transition," NACA TN-3489.
[5] Gostelow, J. P., Melwani, N., and Walker, G. J., 1996, "Effects of Streamwise Pressure Gradient on Turbulent Spot Development," ASME J. Turbomach., **118**, pp. 737–743.
[6] Zhong, S., Kittichaikarn, C., Hodson, H. P., and Ireland, P. T., 2000, "Visualisation of Turbulent Spots Under the Influence of Adverse Pressure Gradients," Exp. Fluids, **28**, pp. 385–393.
[7] Zhong, S., Chong, T. P., and Hodson, H. P., "On the Spreading of Turbulent Spots in Non-Isothermal Laminar Boundary Layers Under the Influence of Favorable Pressure Gradients," ASME Paper No. GT-2002-30222.
[8] Clark J. P., Jones, T. V., and LaGraff, J. E., 1994, "On the Propagation of Naturally-Occurring Turbulent Spots," J. Eng. Math., **28**, pp. 1–19.
[9] Glezer, A., Katz, Y., and Wygnanski I., 1989, "On the Breakdown of a Wave Packet Trailing the Turbulent Spot in a Laminar Boundary Layer," J. Fluid Mech., **198**, pp. 1–26.
[10] Katz, Y., Seifert, A., and Wygnanski, I., 1990, "On the Evolution of the Turbulent Spot in a Laminar Boundary Layer With a Favorable Pressure Gradient," J. Fluid Mech., **221**, pp. 1–22.
[11] Wygnanski, I., Sokolov, M., and Friedman, D., 1976, "On a Turbulent Spot in a Laminar Boundary Layer," J. Fluid Mech., **78**, pp. 785–819.
[12] Gad-el-Hak, M. Blackwelder, R. F., and Riley, J. J., 1981, "On the Growth of Turbulent Regions in a Laminar Boundary Layer," J. Fluid Mech., **110**, pp. 73–99.
[13] Coles, D, and Barker, S. J., 1975, "Some Remarks on Synthetic Turbulent Boundary Layers," *Turbulent Mixing of Reactive and Nonreactive Flows*, S. N. B. Murthy, ed., Plenum, New York.
[14] Wygnanski, I., Zilberman, M., and Haritonidis, J., 1982, "On the Spreading of a Turbulent Spot in the Absence of a Pressure Gradient," J. Fluid Mech., **123**, pp. 69–90.

Capturing Sudden Increase in Heat Transfer on the Suction Side of a Turbine Blade Using a Navier–Stokes Solver

Faisal Rahman

Jan A. Visser

Reuben M. Morris

Department of Mechanical and Aeronautical Engineering,
University of Pretoria,
Lynwood 0002,
Pretoria, South Africa

The numerical modeling of heat transfer on the suction side of a cooled gas turbine blade is one of the more difficult problems in engineering. The main reason is believed to be the transition from laminar to turbulent flow and the inability of standard Navier–Stokes solvers to predict the transition. This paper proves that sudden changes in heat transfer on the suction side of a turbine blade can indeed also be caused by localized shocks disrupting the boundary layer. In contrast to transition, the position of these shocks and the effect of the shocks on the pressure distribution and heat transfer rate can be predicted to within an acceptable degree of accuracy using standard Navier–Stokes solvers. Two well-documented case studies from the literature are used to prove that the pressure distribution around the profile can be predicted accurately when compared to experimental data. At the same time this method can be used to capture sudden changes in heat transfer rate caused by localized shocks. The conclusion from this study is that localized shock waves close to the suction side surface of a turbine blade can have the same effect on the heat transfer rate to the blade as transition. [DOI: 10.1115/1.1928287]

Introduction

The gas turbine engine has wide ranging applications in various industries today. The aerospace and power generation sectors are probably the best known. The efficiency of the gas turbine engine is one of its biggest advantages, but the high capital and maintenance costs when exposed to cyclic operating conditions have been a limiting factor. Therefore, the gas turbine designer needs to carefully balance efficiency, capital and maintenance costs when designing a new engine. An increase in combustor exit temperatures is one method of improving the overall efficiency of the gas turbine engine whilst keeping operational costs low. However, raising the operating temperature increases the thermal load on several hot end components.

For this reason, nozzle guide vanes and first stage rotor blades are cooled in modern engines. This results in complex flow phenomena and heat transfer that induces large thermal gradients. This is of particular importance during start-up and shut-down procedures, since the thermal gradient will induce *thermal stresses* in the blade. However, thermal stresses also occur during normal operation.

Determining the temperature distribution accurately over a cooled nozzle guide vane is one of the most challenging problems facing gas turbine designers. Therefore, much research and effort has been applied to determine the heat transfer both experimentally and using numerical modeling techniques [1]. The rate of heat transfer; along with the effect of Mach number, Reynolds number, inlet flow angle, and free stream turbulence all have a major influence on thermal distributions in blades [2]. The temperature distributions are then used to calculate thermal stresses, which are used to predict the expected usable life of the component. For instance, a study on impingement cooled turbine blades showed that a rise in turbulence level from four to twelve percent decreased the blade life by ten percent [3]. The problem in determining temperature distributions on gas turbine blades is directly linked to calculating the heat transfer coefficients. Several studies have been conducted on turbine nozzle guide vanes and rotor blades to obtain the heat transfer coefficients numerically. In general, numerically predicted results are within 10% of the experimental data.

Capturing the sudden increases of heat transfer on the suction side of a turbine blade remains a challenge. These changes are of particular importance in cooled blades where the increase in heat transfer can have a severe effect on the thermal stresses in the blade. In most of the experimental research studies these sudden changes in heat transfer coefficient are assumed to be the result of transition from laminar to turbulent flow. Since the turbulence models used in Navier–Stokes solvers cannot accurately predict the transition from laminar to turbulent flow, the solvers are in many cases not used to solve the heat transfer distribution over a turbine blade.

The aim with this paper is to prove that sudden changes in the heat transfer coefficient on the suction side of a turbine blade can, in many cases, also be caused by localized shocks that disturb the boundary layer. The presence of these shocks can be predicted accurately with commercial CFD solvers. Two cases will be presented to show this effect.

Case 1: Nozzle Guide Vane Mounted in a Linear Cascade Arrangement. The first application involves the prediction of the heat transfer rate for a well-known experiment conducted by the von Karman Institute for Fluid Dynamics (VKI) on a turbine nozzle guide vane mounted in a linear cascade arrangement [4]. The physical cascade geometry has been obtained from the literature and the same test conditions are used as boundary conditions for the current simulations. The simulations are carried out using the commercial CFD code, FLUENT. For the first application, the Spalart–Allmaras one-equation turbulence model is used in order to evaluate its accuracy to such applications.

Boundary Conditions. The boundary conditions used are shown in Fig. 1. At the inlet a pressure boundary condition was used. The total inlet pressure was 339.5 kPa and the static inlet pressure was 334.2 kPa. A free-stream turbulence intensity of 1% was used at the inlet boundary to match the measured turbulence level in the

Contributed by the Computational Fluid Dynamics Committee of THE AMERICAN SOCIETY OF MECHANICAL ENGINEERS for publication in the ASME JOURNAL OF TURBOMACHINERY. Manuscript received by the CFD Committee, March 14, 2004, final revision, January 4, 2005. Associate Editor: R. L. Davis.

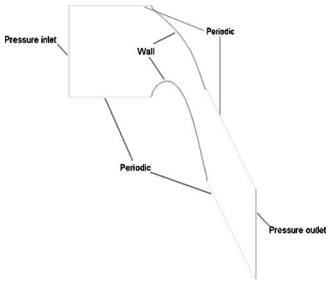

Fig. 1 Boundary conditions

experiment. At the outlet a static pressure boundary condition of 196 kPa was used. An inlet air temperature of 320 K was specified. These values were given in the experimental report. Standard air was the medium.

All other nonsolid boundaries are modelled as periodic boundaries. Flow periodicity had been ensured during the experiments conducted at VKI by means of wall static pressure measurements and Schlieren flow visualizations [4]. Due to the high velocities, the fluid is modelled as compressible with the fluid properties as obtained from the experimental data. The blade shape was generated through use of the manufacturing coordinates [4] and along the solid walls, a wall temperature of 302.15 K was specified.

Computational Grid. The grid was generated using FLUENT's pre-processor **GAMBIT**. The grid consisted of 10,000 unstructured quadrilateral cells. A boundary layer consisting of 3 cell rows was also created to have better cell resolution at the wall. Figure 2 shows the computational grid for the problem considered. The y^+ range was between 30 and 120.

Results. The simulated heat transfer coefficients are compared to the available experimental data. The heat transfer measurements in the experiments were conducted by means of 45 platinum thin films. These were located on both the suction and pressure surfaces of the blade and positioned relative to the measured stagnation point on the blade. As part of the numerical procedure, the heat fluxes are calculated at the same locations. With the heat flux known, the heat transfer coefficient at that location can be calculated using Eq. (1):

$$h = \frac{q_w}{T_{01} - T_w} \tag{1}$$

where T_{01} and T_w are the total inlet temperature, and wall temperature, respectively. The same equation was used to calculate the experimental heat transfer coefficients. The heat transfer coefficients obtained from the simulations are compared to the experimental data in Fig. 3.

The heat transfer results shown in Fig. 3 shows good agreement with the experiment on the pressure side of the blade. However, on the suction side of the blade the heat transfer coefficients are over-predicted over the first section of the blade. At about 60 mm downstream of the stagnation point, the sudden increase in the

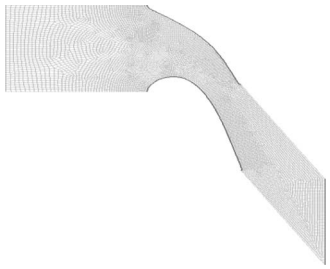

Fig. 2 Computational grid

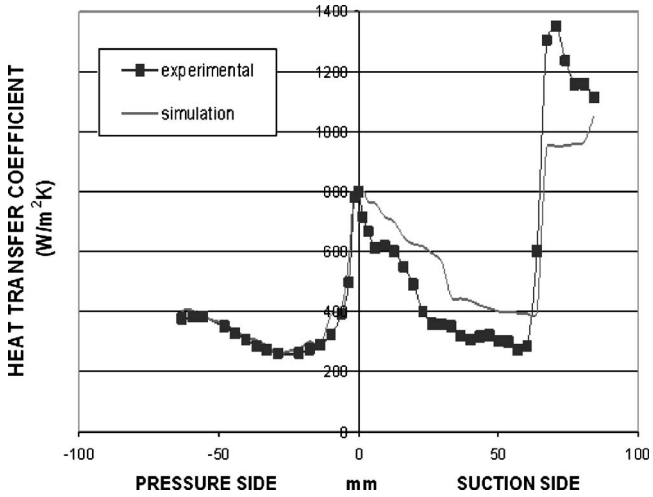

Fig. 3 Heat transfer coefficient on the blade surface

heat transfer coefficient is predicted as measured. The sudden increase in heat transfer can best be explained using the Mach number contours shown in Fig. 4.

The Mach number contours indicate that as the flow passes through the throat section, it accelerates to supersonic conditions in a localized area on the suction side of the blade. As the pressure recovers towards the trailing edge of the blade, a shock develops that radically changes the boundary layer at that point. This is consistent with the Schlieren visualizations conducted in the experiment [4] where a shock wave was seen to form on the suction surface. Thus, it can be concluded that the shock disrupted the boundary layer, resulting in a sudden increase in heat transfer coefficient.

Summary. The heat transfer was predicted with fair accuracy on the pressure side of the blade. On the initial part of the suction side the heat transfer rate was over predicted by approximately 10%. The location of a normal shock and the resulting sudden increase in heat transfer coefficient is predicted accurately in the numerical model, although the heat transfer rate after the shock is under predicted.

Case 2: 2-D Cooled Turbine Blade. The second well-documented case study is a cooled turbine blade and known as the MARKII blade [5]. The physical cascade geometry has been obtained from the literature and the same test conditions have been used as boundary conditions for the current simulations. The simulations were again carried out using the commercial CFD code, FLUENT. For this case study, the realizable k-ε turbulence model [6] is used to evaluate its accuracy on such an application. The geometry is shown in Fig. 5.

Boundary Conditions. The operating conditions were specified as supplied by the experimental study. The blade is internally cooled by means of ten round cooling holes through which cold air was passed. The boundary types are shown in Fig. 5. The MarkII blade is a transonic analysis. This implies that inlet and

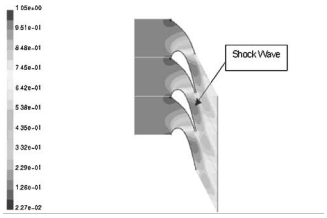

Fig. 4 Mach number contours

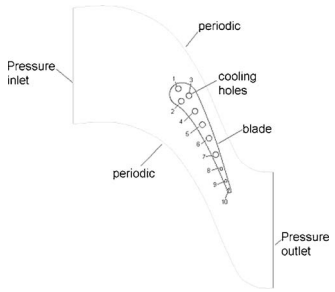

Fig. 5 General outline of MarkII blade

outlet pressures must be specified. At the inlet a total pressure of 334 kPa is used with an inlet Mach number of 0.19 and a total inlet temperature of 788 K. The static pressure at the inlet can, therefore, be calculated as 325.695 kPa [7]. At the outlet a static pressure boundary of 167 kPa was used and the Mach number is 1.04. Periodic boundaries are used to include the effect of other blades on the flow and heat transfer without having to actually model the other blades and the fluid was modeled as compressible. The convective heat transfer coefficients for the cooling holes were supplied and are shown in Table 1. In order to calculate the steady-state temperature distribution within the blade, it is necessary to specify the thermal conductivity of the solid. In this case the blade is fabricated from 310 stainless steel [8] and its thermal conductivity was specified as temperature dependent.

Computational Grid. The computational domain was divided into several smaller sections to enable a better quality grid to be applied on the blade. The exterior fluid zone consisted of structured quadrilateral cells. The blade interior has an unstructured grid due to the layout of the cooling holes that make building a structured grid a difficult task that leads to poor quality cells. A mesh with excess of 130,000 cells was generated. The computational grid is shown in Fig. 6.

In generating the computational grid, it is important to balance the cell densities in the fluid and solid regions. This is important to obtain the correct conjugate heat transfer from the blade surfaces. Therefore, the transition in cell size from the fluid zone into the solid zone must match and all changes in cell size must be gradual. Equally important is the number of grid cells in the boundary layer to ensure that the grid resolution is adequate to capture both the flow and thermal boundary layers. Therefore, a fine grid was necessary for the correct y^+ criteria to be met for the accurate determination of the surface heat transfer [9]. Y^+ was typically in the region of one. Figure 7 shows that the mesh densities in the fluid and solid regions have been balanced in terms of change of grid cells.

Pressure Distribution. For this application the pressure distribution data is available and the simulated pressure distribution could be compared to the experimental data. For the simulation a coupled implicit solver was used that implies that the continuity and momentum equations are solved simultaneously. As a turbulence model, the *realizable* k-ε model using enhanced wall treatment is used. Figure 8 shows the pressure distribution over the blade. The average error on the pressure side is 3%. The error margin on the suction side is slightly higher at 5%.

Table 1 Convective heat transfer coefficients for cooling holes [5]

Hole	Heat transfer coefficient [W/m^{2}K]	Coolant temperature [K]
1	1943.67	336.39
2	1881.45	326.27
3	1893.49	332.68
4	1960.62	338.86
5	1850.77	318.95
6	1813.36	315.58
7	1871.88	326.26
8	2643.07	359.83
9	1809.89	360.89
10	3056.69	414.85

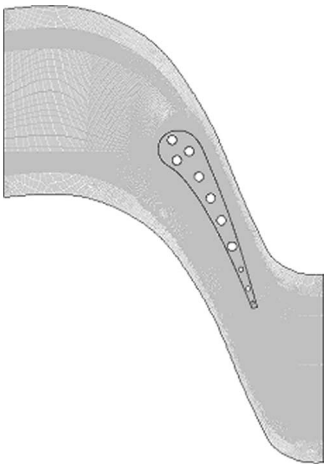

Fig. 6 Computational grid

The model also captured the shocks accurately. The mach contours presented in Fig. 9 show the presence of a strong shock just past the leading edge on the suction side. The high-pressure ratio and large reduction of the flow area cause the flow to accelerate up to a maximum of Mach 1.39. This shock is evident in the pressure plots shown previously. There is also a second milder shock occurring just before the trailing edge on the suction side where the flow reaches approximately Mach 1.2.

Thermal Results. The simulated temperature distribution over the suction side of the blade is presented in Fig. 10. The general trend is well predicted with the average error on the suction side at 7%. When analysing the difference, one has to consider the fact that discrepancies of up to 10% are generally accepted between experimental data and simulations using basic k-ε turbulence formulations. Again, the surface temperature of the blade is over predicted, but the sharp increase in heat transfer as a result of the shock on the suction side of the blade is captured accurately. The predicted cross-sectional temperature distribution through the blade is shown in Fig. 11 and can be compared to the calculated results shown in Fig. 12 [5].

The hottest section of the blade occurs on the trailing edge as the result of a recirculation zone at this point. The abrupt ending of the blade causes the recirculation zone and the breaking up of the boundary layer in that section. The highest temperature is 645 K and is close to the analysis of Bohn et al. [5], in which the value was 663 K, thus giving a difference of less than 3%. The minimum temperature was slightly higher in this analysis at 434 K

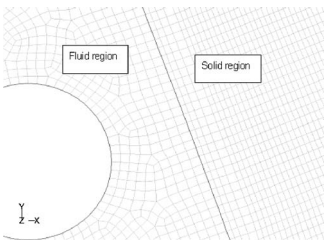

Fig. 7 Computational grid in the vicinity of cooling hole 7

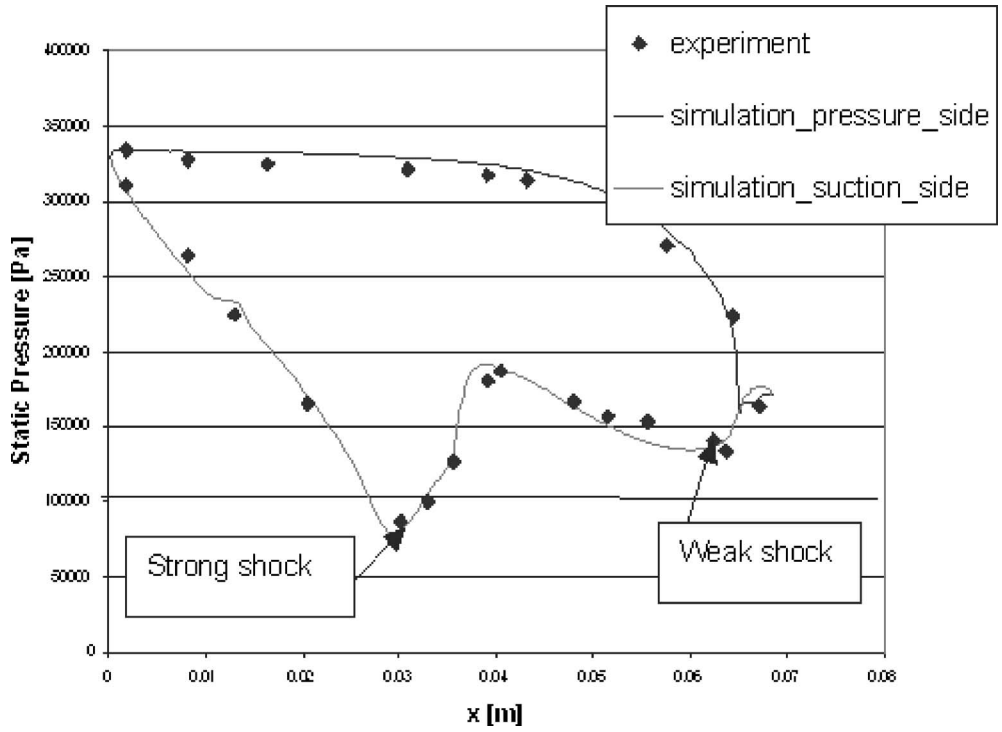

Fig. 8 Pressure distribution: *Realizable k-ε* model, enhanced wall treatment

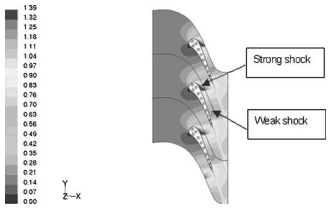

Fig. 9 Contours of Mach number

whereas Bohn recorded 400 K, an error of 8.5%. The location of the lowest temperature occurred in the same geometric area between cooling holes two and three in both simulations. This is due to the fact that both these holes have very high convective heat transfer coefficients and the material in between them is furthest from the hot air.

Summary. From the second case study it can be concluded that the pressure distribution over the blade was predicted accu-

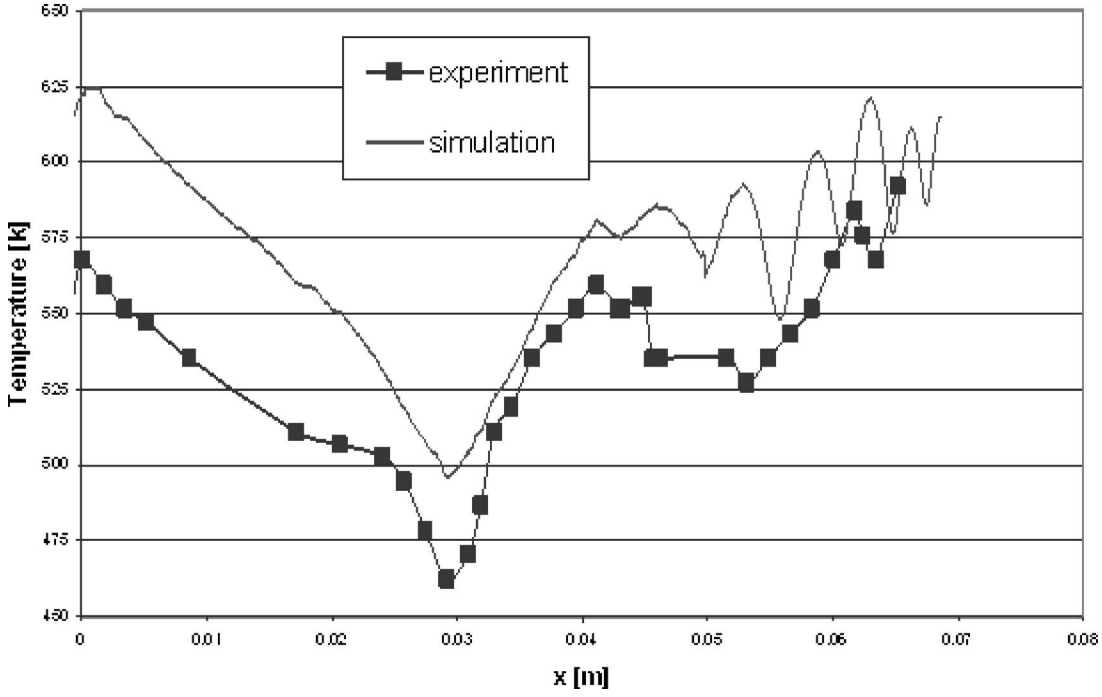

Fig. 10 Temperature distribution: *Realizable k-ε* model, enhanced wall treatment

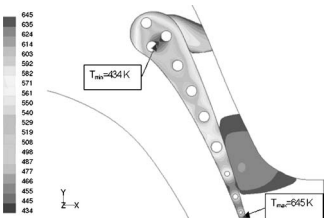

Fig. 11 Simulated temperature distribution through the blade

rately and that the heat transfer on the suction side of the blade was predicted within 7% of the experimental data. Importantly, the location of the sudden increase in heat transfer of the suction side of the blade was captured in the correct location. The sudden increase in heat transfer was once again found to be the result of the shocks disrupting the boundary layer.

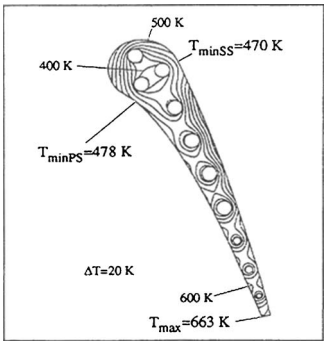

Fig. 12 Temperature distribution as calculated by Bohn et al. [5]

Conclusions

After carefully evaluating the results obtained from the two case studies it can be concluded that the transonic behavior of flow along the suction side of a turbine blade has a distinct influence on the heat transfer profile along that surface. Sudden changes in surface temperature values were predicted in the correct location and found to be caused by localized shocks that disrupt the boundary layer in that section of the blade.

Nomenclature

English Symbols

C_p = specific heat (J/kgK)
x = distance from stagnation point (m)

Greek Symbols

ρ = density (kg/m^3)

References

[1] Nealy, D. A., Mihelc, M. S., Hylton, L. D., and Gladden, H. J., 1984, "Measurements of Heat Transfer Distribution Over the Surfaces of Highly Loaded Turbine Nozzle Guide Vanes," ASME J. Eng. Gas Turbines Power, **106**, pp. 149–158.
[2] Consigny, H., and Richards, B. E., 1982, "Short Duration Measurements of Heat-Transfer Rate to a Gas Turbine Rotor Blade," ASME J. Eng. Power, **104**, pp. 542–551.
[3] Kirsten, T. J., Greenblatt, D., and Dedekind, M. O., 1993, "Thermal Fatigue Life Assessment of a convection-cooled gas turbine blade," AIAA and International Symposium on Air Breathing Engines.
[4] Arts, T., and Lambert de Rouvroit, M., 1992, "Aero-Thermal Performance of a Two-Dimensional Highly Loaded Transonic Turbine Nozzle Guide Vane: A Test Case for Inviscid and Viscous Flow Computations," ASME J. Turbomach., **141**, pp. 147–154.
[5] Bohn, D., Lang, G., Schonenborn, H., and Bonhoff, B., 1995, "Determination of Thermal Stress and Strain Based on a Combined Aerodynamic and Thermal Analysis for a Turbine Nozzle Guide Vane," ASME Cogen-Turbo Power Conference, Vienna.
[6] FLUENT, 1998, *Fluent 5 User's Guide* Volume 2, Fluent Incorporated, Lebanon, pp. 21–26, Chap. 9.
[7] White, F. M., 1994, *Fluid Mechanics*, 3rd ed., McGraw-Hill, NY.
[8] Rothman, M. F., 1998, *High-Temperature Property Data: Ferrous Alloys*, ASM International.
[9] White, F. M., 1991, *Viscous Fluid Flow*, 2nd ed., McGraw-Hill, NY.

R. M. Mathison
M. G. Dunn
Gas Turbine Laboratory,
Ohio State University,
Columbus, OH 43235

M. M. Weaver
General Electric Aircraft Engines,
Cincinnati, OH 45215

A. Dushko
GE-ETEC Moscow,
Moscow, Russia

Measurement of Air Film Damping Effectiveness

Air film damping systems have attracted considerable interest within the gas turbine industry because of their effectiveness at controlling modes of vibration without environmental limitations. Though still in the early stages of development, air film dampers have promise for improving the high cycle fatigue characteristics of solid gas turbine airfoils. This study used experimental methods to compare the vibrational response of a solid flat plate with the response of an identically sized plate that incorporated an air film damper. It also investigated the influence of elevated pressures on air film damping effectiveness, the impact of the damper on the various vibration modes, and the relative strain levels of the air film cover plate to the solid backing. The results show that the air film damper is very effective in controlling the two-stripe mode for which it was designed. Increasing the surrounding air pressure makes the damper more effective and shifts the resonant frequencies lower. [DOI: 10.1115/1.1928288]

Introduction

The primary goal of an air film damping system is to limit the vibration of a given structure by dissipating the energy to the air within the film. For the purpose of this investigation, this was accomplished by affixing a cover plate over the structure while leaving a thin air gap between the two pieces. A properly sized cover plate will oscillate relative to the main structure at certain frequencies, and this transverse motion pumps the air within the thin gap, creating a strong shear layer along the two surfaces of the gap. The development of this pumping motion is clearly visible in Fig. 1, which shows a finite element model of an air film damped plate in a pumping mode.

At these resonances, viscous flow near the walls along the length of the film is responsible for the majority of the losses [1]. Although the air film dampers used in this study are vented to the surrounding atmosphere, Jones et al. have shown that a fully enclosed gap can also create these flows and be effective as a damping device [2]. At lower frequencies, the mass of the air can affect the damping of the device, with inertial effects potentially lowering the frequency and decreasing the response of the plate [3].

Much of the original work in this area was driven by investigations of compressible film bearings. These studies, performed in the early 1960s, deviated from the mainstream tendency to focus on the behavior of the film when the two bearing surfaces were moving in parallel directions by concentrating on the damping produced by the film when the bearing surfaces moved in a normal direction to each other [4,5]. It did not take long for other studies to begin investigating the role of these behaviors in independent damping mechanisms such as thin plates mounted to vibrating beams supporting industrial machinery [6,7]. However, it was not until the late 1990s when the paper by Jones et al. [2] was published that air film dampers reemerged as a potential technique for controlling vibrations in a wide range of situations. Of course, it did not take long for this technology to be investigated for potential applications in the gas turbine industry.

This study is intended to be an extension of work already performed on a flat-plate geometry, but it will focus specifically on issues to be resolved for incorporation into a gas turbine engine by using a cantilevered plate with an aspect ratio similar to a gas turbine airfoil. Our goals in this study are to verify the effectiveness of an air film damping system, determine the influence of elevated pressures, and search for areas of increased strain that may occur on the cover plate of the damper. In addition, a parallel computational program was undertaken, but those results will be discussed in a later paper.

Experimental Method

In this experiment, the plates were excited by piezoelectric crystals and the response was measured by strain gauges located around the outside edges of each plate. The base of the plate being tested was clamped in the jaws of a large vice, as shown in Fig. 2.

The piezoelectric crystals were excited using a computer controlled signal generator, and the computer simultaneously recorded the response of the strain gauges. The frequency of the signal driving the piezoelectric crystals was swept over a wide range, and measurements of the plate response were made at each driving frequency so that the response of the plate could be studied at frequencies ranging from 65 Hz to 6500 Hz. The entire experimental assembly was located inside a large vessel that could be either evacuated or pressurized; measurements were performed at vacuum, one atmosphere, two atmospheres, and four atmospheres. From these measurements, the resonant frequencies, amplitudes, and damping ratios were determined using a curve-fitting technique described below in the Data Analysis section.

Plate Geometry. Both the air film damped and solid plates were made of 6061 aluminum and had identical outside dimensions of 241.3 mm (9.5 in.) long, 101.6 mm (4 in.) wide, and 4.83 mm (0.19 in.) thick. The bottom 38.1 mm (1.5 in.) of each plate was used as a clamping region, as indicated in Fig. 3 by the hatching. One plate was left as a solid piece of aluminum, and the other was modified to include an air film damping system.

The vertical line at the right end of the plate indicates the beginning of the air film damper, which was created by cutting a step into the tip of the plate and affixing a thin aluminum cover plate in its place. Figure 4 provides a more detailed view of the profile of the air film damper.

Epoxy is used to hold the cover plate in place and to create a 0.127 mm to 0.152 mm (0.0055–0.006 in.) thick air gap between the cover plate and the solid backing. It is shown as the checkerboard area in Fig. 4. Trochidis [8] indicated that the thickness of the air gap should have a very significant influence on the effectiveness of the air film damper. For this reason, the cover plate

Contributed by the International Gas Turbine Institute (IGTI) of THE AMERICAN SOCIETY OF MECHANICAL ENGINEERS for publication in the ASME JOURNAL OF TURBOMACHINERY. Paper presented at the International Gas Turbine and Aeroengine Congress and Exhibition, Vienna, Austria, June 13–17, 2004, Paper No. 2004-GT-53057. Manuscript received by the IGTI, October 1, 2003; final revision, March 1, 2004. IGTI Review Chair: A. J. Strazisar.

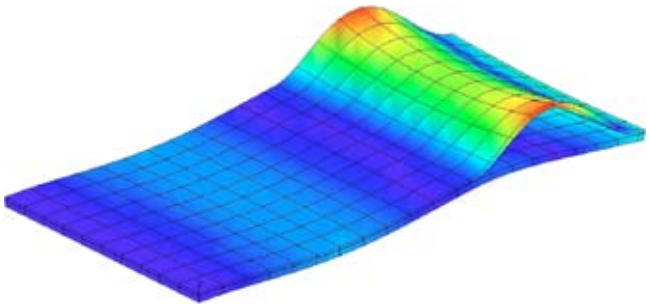

Fig. 1 Pumping mode of air film damper plate

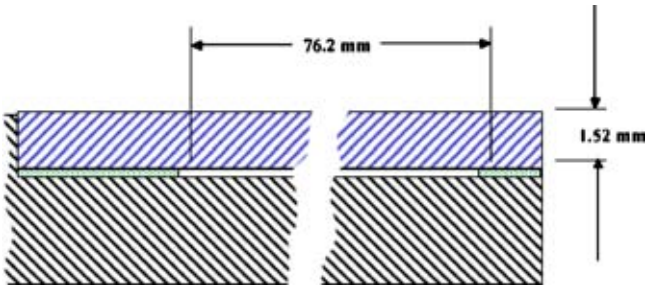

Fig. 4 An illustration of air film damper cover plate with exaggerated thickness

was carefully located using removable shims to achieve the correct gap thickness. However, warping in both the cover plate and solid backing made it nearly impossible to achieve a uniform gap thickness. This distortion led to very noticeable changes in the gap thickness of the first plate constructed. Figure 5 shows the thickness of this gap for the first plate as it was measured using feeler gauges. Although the variation in the air gap was decided to be too significant for comparison to computational models, some experimental work was performed on this plate to verify the procedure to be used. At the same time, a second air film plate was constructed using refined building techniques. It began as a thicker plate than necessary and was machined down to the proper thickness in the same machine process that cut the step for the cover plate. The supporting epoxy was then built up to a greater thickness than needed and machined down to just under the proper thickness. A thin film of epoxy was then used to affix the cover plate. This more time-consuming process produced a plate with much more uniform gap thickness than the original plate. The air gap thickness of this second plate is shown in Fig. 6.

This gap thickness is still not completely uniform, but it was determined that further attempts to improve the gap thickness would require large amounts of time and probably yield only marginally different results. All of the data shown in this paper is from this second air film plate.

Instrumentation. Figure 7 shows the location of the five upper surface strain gauges that were used to measure the response on both the solid plate and air film plate. The air film plate had an additional three gauges on its base plate backside so that the cover plate motion could be studied relative to the solid backing. These three gauges were placed opposite locations 2, 3, and 4.

A static strain gauge calibration was performed. In this procedure, the solid plate was bent to a known tip displacement and the

Fig. 2 The air film damped plate clamped into position with strain gauges around the edges and the piezoelectric crystal in the middle

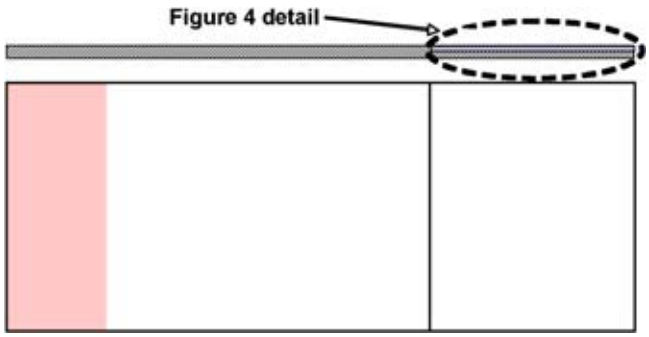

Fig. 3 Overall layout of experimental plates

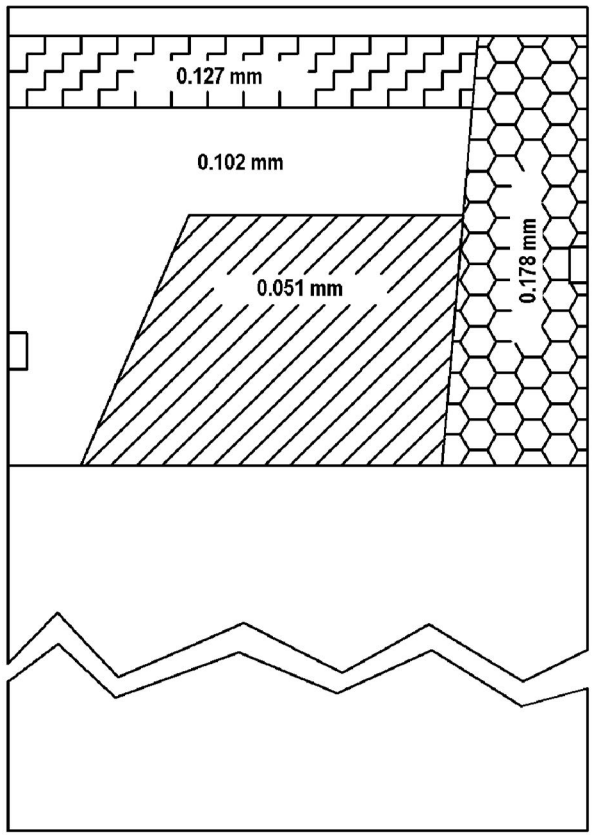

Fig. 5 Gap thickness for first air film plate

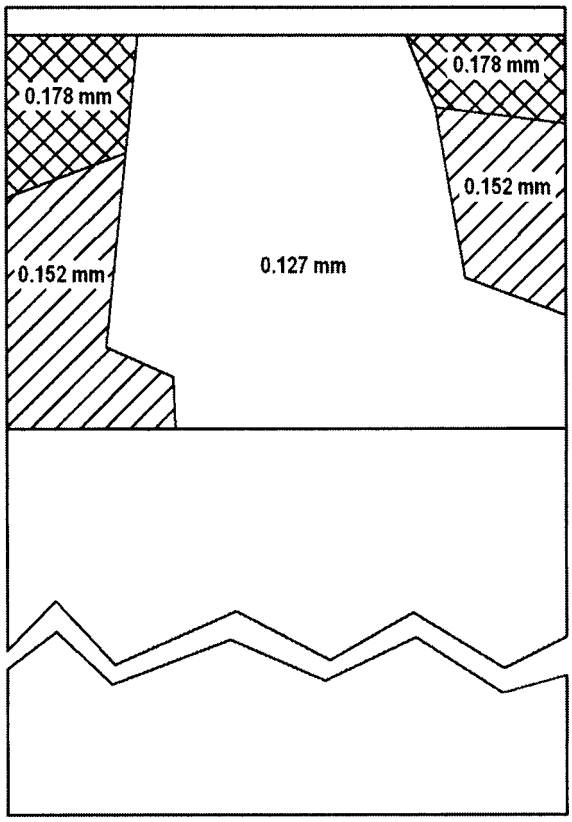

Fig. 6 Gap thickness for second air film plate

strains measured by the gauges were compared to those calculated for a simple cantilevered beam using Eq. (1) [9].

$$\varepsilon = \frac{-3y_{\max}d_t c}{L^3} \tag{1}$$

The gauge location was specified in this equation by choosing the proper distance from the unsupported tip of the plate, d_t.

It was noted in early calibration runs that the strain gauges always measured slightly lower values than the equation predicted, indicating that a small amount of flexibility was present in the clamping mechanism. By switching to a larger vice and increasing the clamping force, this divergence was nearly eliminated for all but the highest strain positions. It is unlikely that the low strains created during the vibration experiments were significant enough to deform this larger vice. With the addition of 10 kHz low-pass filters, it was possible to resolve the deformation of the plate to within two microstrain of the predicted value.

The strain gauge measurements were valuable in the vibrational study because they provided synchronized measurements of exactly what was occurring at a number of key locations. Less intrusive measurement techniques could have avoided the effects of the added mass of wiring and the gauges, but they could not have

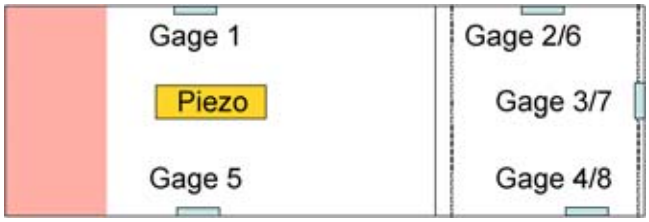

Fig. 7 Location of strain gauges and piezoelectric crystals

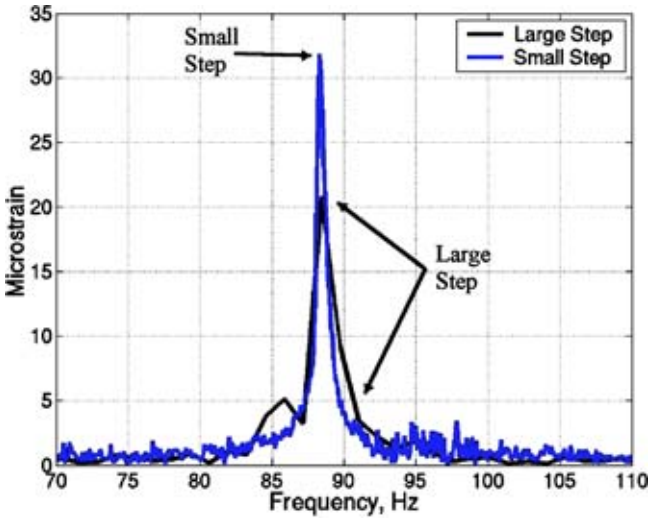

Fig. 8 Effect of data acquisition frequency step size on measured mode shape

determined the strain at discrete locations. This capability made it possible to compare the strains experienced by the cover plate to the strains experienced in the solid backing plate.

The piezoelectric crystal used to excite the system was located in the center of the plate and is shown in Fig. 7.[1] The crystal used could accept excitation voltages up to 500 V peak to peak. The solid plate featured an additional piezoelectric crystal mounted perpendicularly to the left side of the one shown in Fig. 7. This was intended to provide an alternative force to help investigate modes that were not excited by the primary crystal. However, preliminary experiments revealed that it was not capable of producing vibrations of sufficient amplitude for measurement.

Data Acquisition. The piezoelectric crystals were driven by the computer controlled output of a set of DSPT Siglab 20-42 dynamic signal analyzers. These devices used a control loop to maintain a constant amplitude output signal over a frequency range from 65 to 6500 Hz. The output signal was fed back into an input port to close the control loop and ensure accurate control. This measured signal was used as the basis for all transfer functions later computed using the Siglab programs. Since each device was capable of handling only four input channels and one input was used for controlling the piezoelectric output, three of these devices were chained together to obtain sufficient channels to take simultaneous data from all eight strain gauges.

The output signal from the Siglab was then amplified to nearly 500 V peak to peak before being supplied to the piezoelectric crystals. The procedure was to start with a driving frequency of 6500 Hz and then step down by small increments to a final frequency of 65 Hz. The sizes of these frequency steps were 2 Hz from 6500 to 1500 Hz, 1 Hz from 1500 to 200 Hz, and 0.2 Hz from 200 to 65 Hz.

It became clear in preliminary runs that the frequency step size at a given location could greatly affect the shape of the peak observed in the data. At lower driving frequencies, the resonant peaks were quite narrow, and a large step size might only register four data points on that peak. This not only provided a poor indication of the width of the peak, but in most cases, it also failed to capture the location of the maximum response. Figure 8 shows the difference in the measured response between identical peaks measured with a wide frequency step and a smaller step. To speed data acquisition, larger step sizes were used at higher frequencies,

[1]These crystals were provided to OSU by Dr. Keats Wilkie of the Army Vehicle Technology Directorate, Langley Field, VA.

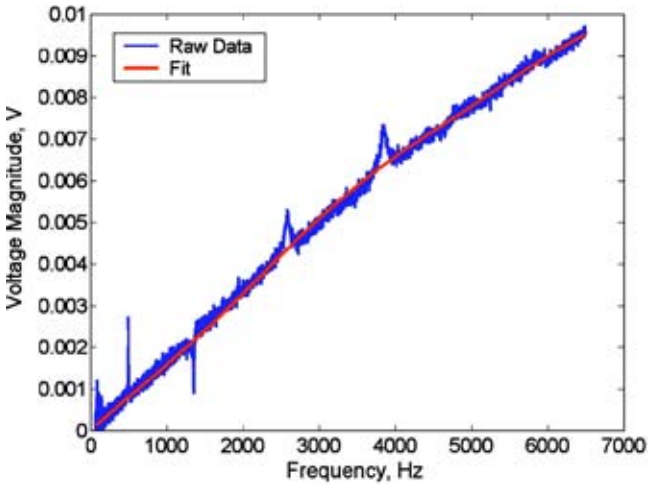

Fig. 9 The raw data shows the influence of capacitive cross-talk

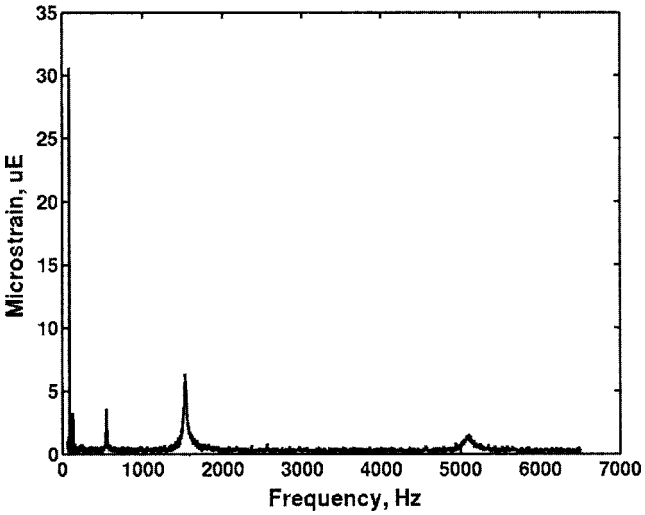

Fig. 10 Cleaned data after cross-talk has been removed

where the peaks were wider and could be adequately resolved with larger steps, while smaller steps were used where greater resolution was needed.

At each step, the Siglab allowed the vibration to stabilize at the new frequency and then sampled all of the strain gauges simultaneously. The data was automatically converted to a series of averaged transfer functions relating the strain gauge output to the driving signal for each frequency step. This process was repeated at every frequency within the experimental range so that at the end of the experiment, a dataset contained the amplitude of vibration measured by each strain gauge at each frequency step.

Data Analysis

Unfortunately, the raw amplitudes contained in the dataset required further processing before they could be considered useful indicators of the plate's response. In addition, determining other important characteristics of the plate's vibration such as the damping ratio and resonant frequency required a more complicated curve fitting procedure.

The first step was to remove cross-talk interference on the strain gauge output from the piezoelectric input signal. This is not surprising since the plate featured the high voltage piezoelectric input signal running very close to the low voltage strain gauge output signals. Figure 9 shows a typical raw dataset; the resonant peaks of vibration are plainly visible, but they are built on top of the linearly increasing cross-talk signal.

This linear increase was due to the capacitive nature of the piezoelectric crystal. Equation (2) shows that, for such a system, a decrease in impedance is expected as the frequency of oscillation increases.

$$Z = \frac{1}{j\omega C} \tag{2}$$

The decrease in impedance of the piezoelectric crystal allowed more current to flow through the input wires. Of course, the increased current through the line increased the strength of the surrounding electric field and therefore induced more interference on the strain gauge output lines.

Jeffers proposed a reasonably simple process for removing this cross-talk in [10]. In his process, a polynomial is fit to the data, averaging out the resonant peaks and approximating the true baseline. The red line in Fig. 9 shows this fit. Next, the fit is subtracted from the data, and the magnitude of the strain remains in a usable form, as shown in Fig. 10.

Once the cross-talk has been removed from the data, the largest resonant peaks are plainly visible. From this, only a short search function is required to identify the approximate maximum strain and resonant frequency of each mode. However, determining the damping ratio from this information requires a procedure that fits the single degree of freedom vibration equation (Eq. (3)) to a given peak.

$$y = \frac{A}{\sqrt{\left(1 - \left(\frac{\omega_{\text{res}}}{\omega}\right)^2\right)^2 + \left(2\zeta\frac{\omega_{\text{res}}}{\omega}\right)^2}}. \tag{3}$$

The parameters of this equation are optimized using the Marquardt method of nonlinear curve fitting [11]. By changing the resonant frequency, damping ratio, and amplitude, the curve is adjusted to closely match the data, as shown in Fig. 11.

The optimized parameters from the curve fit provide the damping ratio of the peak. In addition, the resonant frequency and amplitude found in the curve fit procedure are more useful than the values found by searching for the maximum data point because they represent a smoothed average of the curve properties predicted by an entire series of points rather than just the value of a single point.

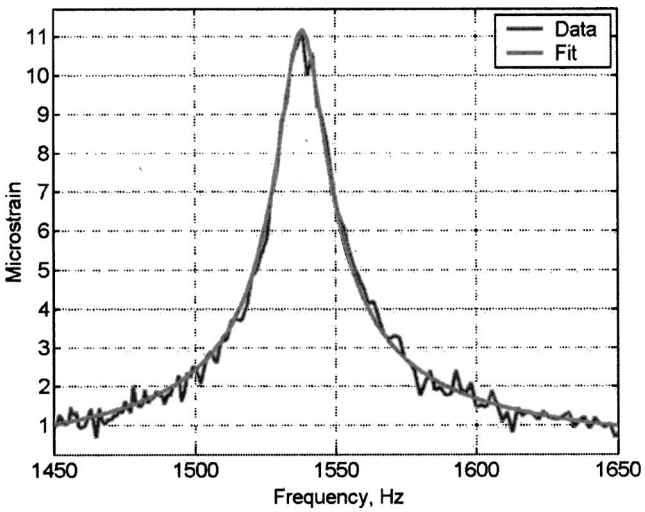

Fig. 11 The single degree of freedom vibration equation is fit to the data to determine the damping ratio, resonant frequency, and amplitude of each mode

Perhaps the most challenging aspect of this analysis was identifying smaller modes for curve fitting. While the large-amplitude resonances were quite clear, the smaller peaks could be nearly obscured by the normal vibration of the plate. In addition, a single erroneous data point could appear to be a small resonance. For this reason, curve fits were applied to every peak that had even the slightest potential of being a true mode. Then, curve fit data from three identical runs was averaged together. Peaks that appeared in all three runs were assumed to be true modes, and peaks that were only present in single runs were discarded as noise.

Further help in identifying true modes came when combining the readings from all of the strain gauges. The larger modes were detected by all of the gauges on the plates, but even the smaller modes were generally detected by two or three gauges. These results were then compared to a finite element model of the solid plate so that each mode could be identified. These combination techniques made it possible to confidently identify a number of the predicted plate modes.

Simple Finite Element Model

A small finite element model of the solid aluminum plate was created to provide guidance in identifying the measured modes. It used 11808 nodes with 10 node tetrahedral elements. The bottom 38.1 mm (1.5 in.) of the plate was constrained in the normal direction to simulate the clamping conditions. These constraints were applied to the two surfaces that were touched by the vice in the experiment.

A modal analysis was used to find the resonant frequencies of the modes along with the predicted strains at the locations of the strain gauges. The relative strain of each gauge was then computed by dividing each predicted strain by the maximum strain for each mode. This permitted a comparison of the mode shape predicted by the finite element model with the relative strain mode shape measured experimentally. An overall goodness of fit criteria [12], shown in Eq. (4), was used to quantify the degree to which experimental modes correlated to the computational results. This equation uses a weighted combination of both frequency and mode shape matching to verify that the best match was obtained. The frequency component was weighted by 25% and the mode fit dot product component was weighted by 75%. Frequency was included in this criteria because it is an important indicator of mode matching in addition to the mode shape factor used in more traditional modal assurance criteria.

$$\mathrm{OGF} = w_{\mathrm{freq}}\left[1 - \frac{|f_A - f_T|}{f_T}\right] + w_{\mathrm{MFDP}}\left(\frac{\vec{\varepsilon}_T^{\,T} \cdot \vec{\varepsilon}_A}{\|\vec{\varepsilon}_T\|\|\vec{\varepsilon}_A\|}\right) \tag{4}$$

An OGF value close to one indicates that the two modes compare very well. The strain vectors in this equation contain the strains from every gauge location from either the measured or the predicted results.

The technique described above made it possible to relate the various experimental modes to graphical representations of each mode shape. From these images of the modes, it was possible to identify the named modes of interest such as the two-stripe mode (first cordwise bending). Once these modes were identified for the solid plate; another correlation was performed to locate their counterparts on the air film plate.

Results

The effectiveness of this measurement system can be observed by comparing the response of the solid plate to that predicted by the finite element model. Table 1 shows the two resonant frequencies along with the overall goodness of fit criteria, which factors in the strain mode shape.

As mentioned earlier, the closer the OGF is to one, the better the correlation. For the purpose of this study, values greater than 0.85 were considered validated. This means that modes 3, 5, 7, 8, 11, and 12 were experimentally identified. The repeatability and high amplitude of the first mode also indicate that it was most likely picked up in the experiment, even though its OGF value is 0.83. It is also important to note that good correlation was observed for the two-stripe mode (Mode 7) around which this study was designed. An OGF value of 0.99 indicates that the piezoelectric crystal was properly located to excite this mode and that the strain gauges were well placed to detect it. On the other hand, the piezoelectric and strain gauges were not well located to excite or identify modes 2, 4, 6, 9, and 10. The low amplitude of these vibrations at the gauge locations could not produce an adequate signal-to-noise ratio for accurate measurement. A different experimental setup would be needed to examine these modes.

Table 1 Overall goodness of fit comparison of solid plate measurements with ANSYS predictions

	Experimental freq.	FEM freq.	OGF
1	92.5	94.1	0.83
2	321.6	399.7	0.70
3	548.5	587.6	0.98
4	1134.3	1298.0	0.72
5	1536.8	1642.8	0.97
6	2362.2	2485.8	0.73
7	2565.2	2561.1	0.99
8	2978.8	3211.2	0.95
9	3319.1	3401.9	0.53
10	3992.9	4093.3	0.73
11	4551.4	4750.1	0.89
12	5097.5	5312.0	0.91

The damping ratios calculated with the curve-fitting technique have a great value for comparing the actual damping effectiveness of the air film system to the effectiveness predicted by computational models, but the most obvious demonstration of the damper's effectiveness is a direct visual comparison of the response of the solid plate and the air film plate. For example, Fig. 12 compares the amplitude of vibrations measured at gauge location five (base of the plate) for the solid and air film plates at one atmosphere surrounding pressure.

A number of characteristics of the air film plate are immediately visible from this graph. The most obvious difference is also the most expected; the vibration amplitude of the air film plate is significantly reduced from the response of the solid plate at several modes. Even though none of the peaks on this graph represent the mode the damper was designed to control, it demonstrates its ability to suppress a range of modes simultaneously. The mode occurring at 5000 Hz appears to be completely eliminated, and the

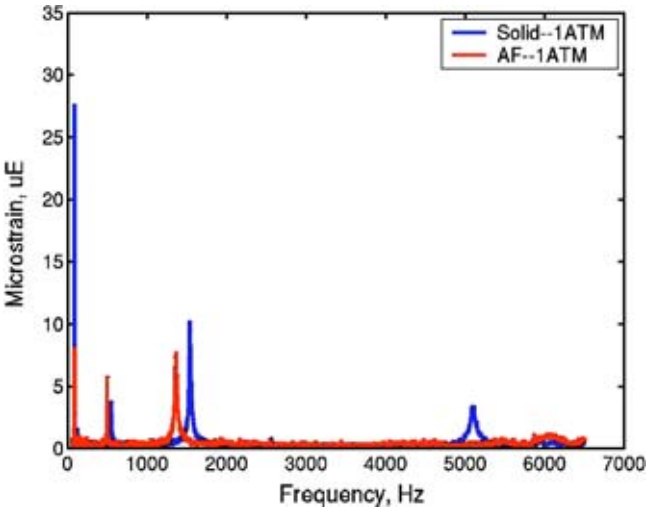

Fig. 12 A comparison of a solid plate with air film plate response measured by gauge 5 at one atmosphere

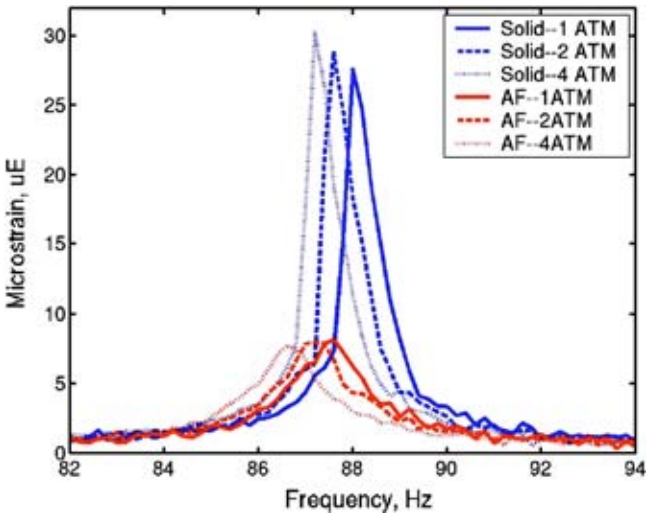

Fig. 13 Effect of air film damper on first bending mode at gauge location five

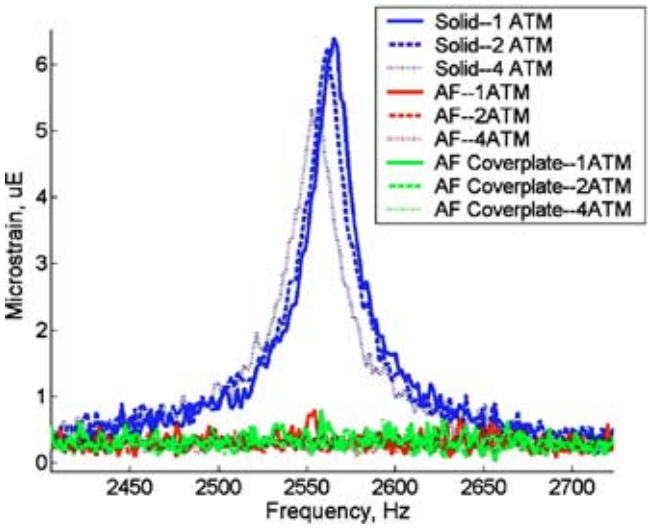

Fig. 14 Reduction of amplitude achieved by air film damper on the two-stripe mode

bending mode at 88 Hz shows a significant reduction. In fact, the only problem seems to occur near 500 Hz, where the reduced structure of the air film damper creates too much of a change for the air film damping to overcome, and the air film plate actually shows a slightly greater response than the solid plate.

Figure 12 shows another interesting characteristic of the air film damper: its ability to shift the resonant frequency of a mode lower. Since the magnitude of this shift increases with the resonant frequency, this phenomenon is most evident on the peak occurring near 1500 Hz, where the resonant frequencies of the two plates are separated by nearly 200 Hz. This suggests that for modes that cannot be completely controlled by an air film damper it may be possible to shift the mode away from an operating point. Unfortunately, the converse could also be true, so care will have to be exercised in implementing an air film system since the damper could bring higher-frequency modes that were previously outside of the operating range closer to an operating point.

For further observations of the effectiveness of the air film damper, it is helpful to zoom in on individual modes. Figure 13 shows only the first bending mode as measured at gauge location five. In this figure, the effectiveness of the air film damper is very impressive, even though this is not the mode it was designed to control. The amplitude of the strain measured on the air film plate was less than one-third the strain observed on the solid plate. Although there is very little separation between the resonant frequencies of the two plates at this low frequency, the effect of the changing pressure on the resonant frequency of each plate is evident. Increasing pressure consistently shifts the resonant frequency of each plate slightly lower.

To this point, all the data presented has focused on modes that were not targeted by the damper design. The damper made significant reductions in many modes, but its true effectiveness is most visible when examining the two-stripe mode for which it was designed. Not every gauge measured a significant response for this mode, but it was clearly indicated at gauge location three on the solid plate. Figure 14 shows the effect of the damper on the strain measured at this location as well as at gauges 3 and 7 on the air film plate.

The response of the air film plate at the two-stripe mode is indistinguishable from the normal vibratory noise floor. Even at just one atmosphere, the mode is completely eliminated; it was not detected on the solid backing or on the cover plate.

It is also important to identify the true source of these reductions since it is possible that the change in structure of the plate alone could have significant changes on its mechanical damping. Figure 15 shows the response of the air film plate at vacuum, one atmosphere, two atmospheres, and four atmospheres. Several peaks of interest are indicated by pointers for clarity. In this graph, it is plainly evident that the majority of the damping in the system comes from air film effects. The less rigid structure of the air film plate allows much larger amplitude vibrations when the plate is excited in a vacuum than when even a small amount of air is present. At one atmosphere, most of the modes present in vacuum are almost completely wiped out, and one of the remaining modes of significance was greatly reduced. Only the mode near 500 Hz showed a resistance to the effects of the air film damper. While it is still reduced by almost 25% in moving from vacuum to one atmosphere, the change in this mode is much less than that observed in all other modes. This was consistent across a number of different gauges, indicating that a different damper shape would be needed to control this mode.

It is also interesting to note that increasing the pressure above one atmosphere does not have nearly as large an effect. In many modes, the response measured at one, two, and four atmospheres nearly overlap, showing little change in amplitude and only a slight shift in resonant frequency with increased pressure. This is consistent with the response observed by Fox and Whitton [1] for increasing pressure on very large air film damped plates. There are

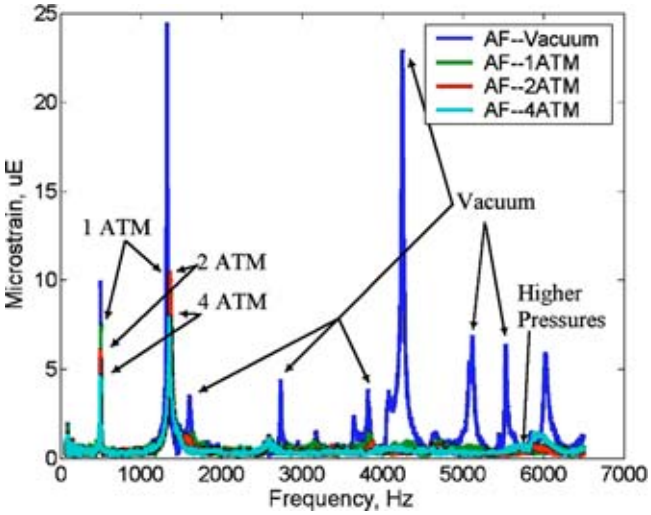

Fig. 15 The change of air film cover plate response with a change in surrounding pressure

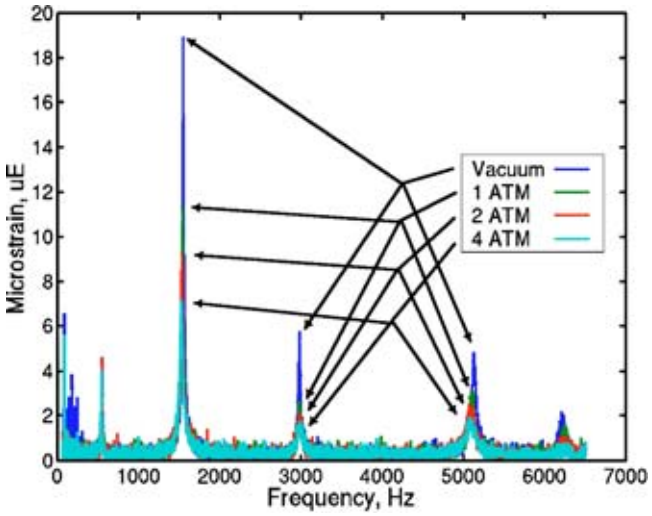

Fig. 16 The change of solid plate response with a change in the surrounding pressure

a few modes, such as the mode at 500 Hz discussed above, that do show notable reductions in amplitudes with higher pressures, but there are not many. This indicates that for the air film thickness chosen, one atmosphere of pressure provided more than enough density to damp most of the modes for the available excitation.

Another area of concern in implementing air film damping systems has been that the new device would be effective in controlling some modes but would introduce new modes of its own because of the presence of the cover plate. For this reason, it was important to compare the strain measured on the cover plate with the strain measured on the solid backing. At vacuum, there were a number of high-frequency modes that existed only on the cover plate of the air film damper or seemed to originate there and excite new modes on the solid backing. However, in moving to one atmosphere, all of the modes disappeared, and the strain measured on the cover plate was always very close to that measured on the solid backing. In addition, the strains at these locations remained below or very comparable to those for the solid plate.

The easiest way to observe both the appearance and elimination of these cover plate modes is to compare the cover plate response shown in Fig. 15 with the response of the solid plate shown in Fig. 16. The most notable difference between the two graphs is that many of the higher-order modes observed at vacuum for the cover plate are not present on the solid plate at vacuum. This indicates that these modes are indeed excited by the structure of the cover plate but that they are also quickly damped by the introduction of even one atmosphere of the surrounding air pressure. It is interesting to note that while fewer modes appear on the solid plate, they are more resistant to increasing pressure than the large number of modes that appear on the air film damped plate. This indicates that most of the damping in the air film system comes from the action of the damper.

Conclusions

The results presented herein demonstrate the potential of air film damping systems for controlling blade vibrations. Dampers can be designed to almost completely eliminate certain modes, and can achieve broadband reductions in other vibrations. At the same time, the designer should be aware that air film damping systems can significantly change the resonant frequencies of the modes, which may change the modes in the operating range. Elevated pressure beyond one atmosphere had relatively little influence on the performance of the damping system for the air film thickness tested. However, increased pressures did provide some small changes, which in every case slightly improved the damper's effectiveness. Cover plate only modes are not a problem, since they are well damped with the cover plate strains being very similar to those on the solid backing.

Air film dampers are very effective when incorporated into a flat-plate geometry but further work is needed to verify their functionality in an airfoil. Lewis, et al. have performed a significant amount of work in this area and have had success in building an air film damper into a fan blade [13]. The manufacturing technology and cost effectiveness challenges for such a system are significant, but so are the benefits.

Acknowledgments

The work described in this paper was performed as part of the General Electric University Strategic Alliance program at The Ohio State University. The assistance of GE personnel in all stages of the project is greatly appreciated. The authors would also like to thank Mr. Jeffrey Barton and Mr. Michael Jones of the Ohio State Gas Turbine Laboratory for their work in setting up an amplification system capable of driving the piezoelectric crystals. Mr. Jones's work in instrumenting the second air film plate is also greatly appreciated. In addition, the authors would like to thank Mr. Ken Copley for his role in constructing the second air film plate with a more precisely fixed air gap.

Nomenclature

A = amplitude of vibration, in microstrain
C = capacitance
L = unsupported length of plate
OGF = overall goodness of fit
Z = impedance
c = distance to neutral axis from plate surface
d_t = distance from unsupported tip of plate
f_A = experimentally measured frequency
f_T = predicted frequency
j = imaginary constant, $\sqrt{-1}$
w_{freq} = weighting factor of importance of frequency term
w_{MFDP} = weighting factor of mode shape importance
$y_{\max}$ = tip displacement of statically bent plate
ε = strain
ε_A = vector of strains measured experimentally
ε_T = vector of strains predicted at gage locations
ω = frequency
ω_{res} = resonant frequency
ζ = damping ratio

References

[1] Fox, M. J. H., and Whitton, P. N., 1980, "The Damping of Structural Vibration by Thin Gas Films," J. Sound Vib., **73**, pp. 279–295.
[2] Jones, D. I. G., Lewis, T., and Michael, C., 1997, "Partial Coverage Air Film Damping of Cantilever Plates," J. Sound Vib., **208**, pp. 869–875.
[3] Chow, L. C., and Pinnington, R. J., 1987, "Practical Industrial Method of Increasing Structural Damping in Machinery, I: Squeeze-Film Damping with Air," J. Sound Vib., **118**, pp. 123–139.
[4] Langlois, W. E., 1961, "Isothermal Squeeze Films," Q. Appl. Math., **20**, pp. 131 150.
[5] Salbu, E. O. J., 1964, "Compressible Squeeze Films and Squeeze Bearings," ASME J. Basic Eng., **86**, pp. 355 366.
[6] Maidanik, G., 1966, "Energy Dissipation Associated with Gas-Pumping in Structural Joints," J. Acoust. Soc. Am., **40**, pp. 1064–1072.
[7] Ungar, E. E., and Carbonell, J. R., 1966, "On Panel Vibration Due to Structural Joints," AIAA J., **4**, pp. 1385 1390.
[8] Trochidis, A., 1982, "Vibration Damping Due to Air or Liquid Layers," Acustica, **51**, pp. 201–212.
[9] Riley, W. F., Sturges, L. D., and Morris, D. H., 1999, *Mechanics of Materials*, Wiley, New York.
[10] Jeffers, T. R., Kielb, J. J., and Abhari, R. S., 2000, "A Novel Technique for Measurement of Rotating Blade Damping," ASME Paper No. 2000-GT-0359.
[11] Bevington, P. R., and Robinson, D. K., 1969, *Data Reduction and Error Analysis for the Physical Sciences*, McGraw-Hill, New York.
[12] Nichol, K., 2003, "Holistic T&E and the Role of Model Validation," *Proceedings of the 8th High Cycle Fatigue Conference*.
[13] Lewis, T., Notestine, K., Walls, J., Jones, D., McCormick, M., and Vetters, D., 2003, "Recent Advances in Air Film Damping for Gas Turbine Engine Applications," *Proceedings of the 8th High Cycle Fatigue Conference*.

Calculation of the Mixed-Out State in Turbomachine Flows

Anil Prasad
Aerodynamics Division,
Pratt & Whitney Aircraft Engines,
East Hartford, CT 06108

A systematic and rational methodology for the calculation of an equilibrium state from an initial nonuniform flow field, is presented with particular emphasis on the underlying assumptions and their attendant justifications. The imposed conservation criteria that are used to define a final state from the initial one depend on the coordinate system and flow configuration being analyzed. The imposition of these criteria for flow in parallel-walled annular ducts defines a state of complete (mechanical and thermal) equilibrium, for which radial profiles of the velocity components, static pressure and temperature assume a specific form for a perfect gas. A robust method for solving the system of equations that define the state of complete equilibrium (or mixed-out state) is presented using an efficient algorithm. The procedure is applied to the swirling flow exiting an isolated transonic compressor, and comparisons are made with other available methods of averaging flow fields. [DOI: 10.1115/1.1928289]

Introduction

The steady three-dimensional simulation of the flow through turbomachinery is now an integral part of the design process. Such a simulation results in the definition of flow field variables on a grid that extends upstream and downstream of the airfoil passage. In practical applications, the one-dimensional performance figures are desired of the airfoil row or series of airfoil rows in a multistage simulation, so as to be able to make comparison either with experimental data or a meanline analysis. This involves characterizing the upstream and downstream total pressure and temperature by values averaged in some manner over prescribed inlet and exit planes. The calculation of these averaged quantities from a spatially nonuniform initial state requires careful definition. For the most part, suitably weighted integral averages are used to construct these one-dimensional values; these include the conventional mass-averaged, density-averaged, and area-averaged values, defined by Dring and Oates [1]. However, these weighted averages suffer from the drawback that they are strongly dependent on the location at which the averaging operation is performed. The natural mixing that occurs downstream of a blade row generates additional loss that manifests itself as a decrease in total pressure with increasing distance from the trailing edge. This implies that calculated values of the pressure ratio across an airfoil row can assume different values as one moves downstream of the trailing edge. Furthermore, comparison between airfoil designs becomes problematic if based on the total pressure downstream of the airfoil, with no consideration given to degree of mixing undergone.

In order to overcome such a situation and to arrive at a value of total pressure that is independent of location one seeks a state of complete equilibrium, which includes all accumulated losses that can be incurred from the initial state. The stipulation that the viscous fluid be in mechanical and thermal equilibrium is used in the present work to define the state of complete equilibrium for flows emanating from an annular turbomachine airfoil row. The choice of conserved quantities between the final and initial states depends, to some extent, on the particular flow field being investigated. For example, it is common to use the stream-thrust weighted average in an analysis of nozzle flow fields. A comprehensive discussion of the various possibilities for defining the final state is available in Greitzer, Tan, and Graf [2].

Although the concept of the state of complete equilibrium, commonly referred to as the mixed-out state is not new, there exists some ambiguity in its calculation. In the past, direct experimental measurements, in conjunction with some deduced quantities, have been employed to specify the initial state. Pianko and Wazelt [3] present various methods for estimating deduced quantities from ones that are measured; it is apparent that such estimations do not result in the unique definition of the initial state. Furthermore, experimental definition of the initial state is usually not performed to the degree of spatial resolution required to include all possible sources of loss that could be incurred due to mixing.

The introduction of computational methods in the design of turbomachines has provided the means to define flow fields to a significantly higher level of detail than can be provided by experimental measurement. The initial state extracted from a computational simulation is thus a solution to the conservation equations and, therefore, completely defined.

It is the set of conservation conditions of mass, momentum and energy that forges the link between the initial state and the mixed-out one. The calculation procedure that permits this link depends on the particular case of swirling flow through an annular turbomachine geometry or the flow through a planar cascade, as will be shown presently. The former requires a formulation in the cylindrical coordinate system whereas the latter is more conveniently developed in the Cartesian system.

As clarified by Dzung (see Pianko and Wazelt [3]), the irreversible mixing process involved in attaining the mixed-out state is imagined to occur in a plane of discontinuity akin to a shock. Thus the planar areas occupied by the initial state and the mixed-out one are required to be identical, which precludes application to blade passages of radial turbomachines. Equivalently, the mixing process can be presumed to occur in an infinitely long settling duct or channel possessing inviscid walls. The latter condition ensures that wall boundary layers do not continue to evolve in this infinite duct, while simultaneously not limiting the necessary mixing action of viscosity in the region away from the walls. Consequently, this abstract mixed-out state, attained in the asymptotic limit, cannot be achieved through the construction of physical processes. In what follows, the necessary assumptions required to calculate the mixed-out state are rigorously derived from the equations of motion and justified accordingly; Pianko and Wazelt [3] merely present the final form of the radial profiles derived below. Furthermore, a method for solving the system of equations

Contributed by the International Gas Turbine Institute (IGTI) of THE AMERICAN SOCIETY OF MECHANICAL ENGINEERS for publication in the ASME JOURNAL OF TURBOMACHINERY. Paper presented at the International Gas Turbine and Aeroengine Congress and Exhibition, Vienna, Austria, June 13–17, 2004, Paper No. 2004-GT-54021. Manuscript received by IGTI, October 1, 2003; final revision, March 1, 2004. IGTI Review Chair: A. J. Strazisar.

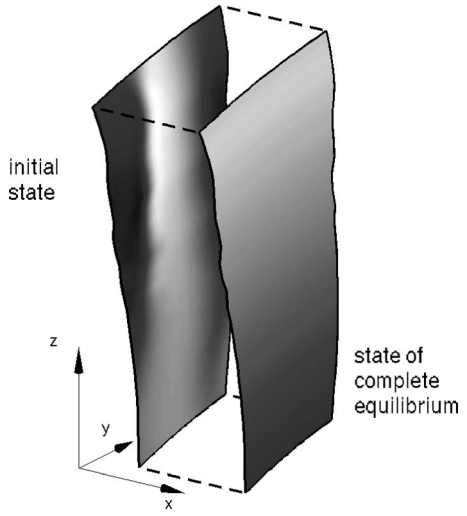

Fig. 1 Conceptual schematic of the procedure to extract the equivalent state of complete equilibrium from an initial nonuniform state

to determine the mixed-out state is described here that is far more robust than that indicated in [3]. Finally, application of the method to a computational solution of the flow exiting a transonic compressor is used to illustrate features of the mixed-out state.

Swirling Flow in Annular Geometries

The mixed-out state for flows generated by annular turbomachine airfoil rows is defined in the present context to be one of complete (mechanical and thermal) equilibrium and to conform to the following specific criteria:

1. **Axial invariance**. This implies that the state of complete equilibrium can be evolved in a constant area annular duct with inviscid walls for arbitrary distances, without alteration in its properties.
2. **Circumferential uniformity**. This implies that the state of complete equilibrium possesses no variation in the circumferential coordinate, as depicted in Fig. 1.
3. **Radial variation**. In general, all quantities are allowed to vary in the radial direction, as shown schematically in Fig. 1.
4. **Thermal equilibrium**. This implies that the state of complete equilibrium cannot support any gradients of temperature, thereby precluding both heat conduction as well as radiation.
5. **Radial equilibrium**. This implies that, for the state of complete equilibrium, the radial gradient of static pressure is exactly balanced by the centrifugal stress term in the tangential momentum equation.

In addition, the state of complete equilibrium is constrained to transport the same flux of mass ($\dot{M}$), axial momentum (X), angular momentum (Ω) and energy (E) as the initial nonuniform state. One may then extract from this initial state an equivalent state that satisfies the requirements of complete equilibrium. In what follows, flow field variables associated with the initial nonuniform state are denoted by $\widetilde{(\cdot)}$ in order to distinguish them from their counterparts at the state of complete equilibrium.

Calculation of Integral Flow Variables

The initial nonuniform state is defined by integrated quantities associated with each of the conservation requirements defined above,

$$\dot{M} = \int \tilde{\rho}(\tilde{\mathbf{V}} \cdot \tilde{\mathbf{n}}) \mathrm{d}\tilde{A} \tag{1}$$

$$X = \int \tilde{\rho}(\tilde{\mathbf{V}} \cdot \tilde{\mathbf{n}}) v_x \mathrm{d}\tilde{A} + \int \tilde{p}(\hat{\mathbf{e}}_x \cdot \tilde{\mathbf{n}}) \mathrm{d}\tilde{A} \tag{2}$$

$$\Omega = \int \tilde{\rho}(\tilde{\mathbf{V}} \cdot \tilde{\mathbf{n}}) \tilde{r} \tilde{v}_\theta \mathrm{d}\tilde{A} \tag{3}$$

$$E = \frac{\gamma \mathcal{R}}{(\gamma - 1)} \int \tilde{\rho}(\tilde{\mathbf{V}} \cdot \tilde{\mathbf{n}}) \tilde{T} \mathrm{d}\tilde{A} + \frac{1}{2} \int \tilde{\rho}(\tilde{\mathbf{V}} \cdot \tilde{\mathbf{n}})(\tilde{v}_x^2 + \tilde{v}_\theta^2 + \tilde{v}_r^2) \mathrm{d}\tilde{A}, \tag{4}$$

where $\tilde{\mathbf{V}} = \tilde{\mathbf{V}}(x, \theta, r) = [\tilde{v}_x, \tilde{v}_\theta, \tilde{v}_r]$ is the velocity vector in polar coordinates (x, θ, r) and $\tilde{p}$ and $\tilde{\rho}$ are, respectively, the static pressure and density of the initial state; furthermore, $\tilde{\mathbf{n}} = \tilde{\mathbf{n}}(x, \theta, r)$ is the local normal vector to the surface on which the initial state is specified, $\hat{\mathbf{e}}_x$ is the unit vector in the axial direction, and γ is the ratio of specific heats. In the above equations, the integration is carried out over the surface of area $\tilde{A}$ on which the initial state is provided. The static pressure and static temperature ($\tilde{T}$) at the initial state are related by the equation of state,

$$\tilde{p} = \tilde{\rho} \mathcal{R} \tilde{T}, \tag{5}$$

where $\mathcal{R}$ is the gas constant. Alternate equations of state may be used, although the final form of the following equations will differ. Nevertheless, the perfect gas equation above is a good approximation for most gas turbine flows and is commonly used in computational flow solvers.

Derivation of Radial Profiles

The state of complete equilibrium is assumed to have attained both kinematic and thermal equilibrium. The former occurs when the components of the rate-of-strain tensor (σ) vanish. Using the notation $\partial_s(\cdot) = \partial(\cdot)/\partial s$, for the case of the cylindrical coordinate system, the six independent components are,

$$\sigma_{xx} = \partial_x v_x,$$

$$\sigma_{\theta\theta} = \frac{1}{r}(\partial_\theta v_\theta + v_r),$$

$$\sigma_{rr} = \partial_r v_r,$$

$$\sigma_{\theta x} = \frac{1}{2r}(\partial_\theta v_x + r \partial_x v_\theta),$$

$$\sigma_{xr} = \frac{1}{2}(\partial_x v_r + \partial_r v_x),$$

$$\sigma_{r\theta} = \frac{1}{2r}(r^2 \partial_r (v_\theta / r) + \partial_\theta v_r)$$

as described in [4]. In the above equations, the axial, azimuthal and radial coordinate are denoted x, θ, and r respectively.

Invariance in the axial and the azimuthal coordinate requires that $\sigma_{xx} = \sigma_{\theta x} \equiv 0$. The remaining components of the rate-of-strain tensor would identically vanish when

$$\partial_r v_r = 0,$$

$$\partial_r v_x = 0,$$

$$\partial_r(v_\theta/r) = 0.$$

By inspection, it is evident that these conditions are satisfied by the following velocity distributions,

$$v_x = C_1, \tag{6}$$

$$v_\theta = C_2 r, \tag{7}$$

$$v_r \equiv 0, \tag{8}$$

where C_1 and C_2 are constants.

Similarly, the constraint of thermal equilibrium requires that

$$T = C_3,$$

yielding a static temperature distribution that is independent of the radial coordinate.

Before proceeding, it is convenient to express all quantities in dimensionless terms by normalizing them with their respective values at the outer radius, r_o, so that the radial distributions derived above now assume the form,

$$[v_x', v_\theta', T', \rho']^T = [1, r', 1, p']^T, \tag{9}$$

where use has been made of the equation of state. All primed quantities refer to normalized variables.

Equations for Complete Equilibrium State

These dimensionless forms are now inserted into the conservation equations applied at the plane where the complete equilibrium state is required. This latter plane is assumed to be normal to the axial direction and extending in the radial direction from the inner radius (r_i) to the outer radius (r_o); its azimuthal extent is assumed to be the circumferential angular pitch of the airfoil row under consideration, Θ. Using the dimensionless quantities indicated above, the continuity equation becomes

$$\dot{M} = r_o^2 \Theta \rho_o v_{x_o} \int_\mu^1 \rho' r' \mathrm{d}r' \tag{10}$$

where $\mu = r_i/r_o$ is the hub-tip ratio of the plane at which complete equilibrium occurs. The conservation of axial momentum is expressed as

$$X = r_o^2 \Theta \rho_o v_{x_o}^2 \int_\mu^1 \rho' r' \mathrm{d}r' + r_o^2 \Theta p_o \int_\mu^1 p' r' \mathrm{d}r', \tag{11}$$

and the conservation of angular momentum assumes the form

$$\Omega = r_o^3 \Theta \rho_o v_{x_o} v_{\theta_o} \int_\mu^1 \rho' v_\theta' r'^2 \mathrm{d}r'. \tag{12}$$

The conservation of energy reduces to

$$E = r_o^2 \Theta \rho_o v_{x_o} \left[\frac{\gamma \mathcal{R}}{\gamma - 1} T_o + \frac{v_{x_o}^2}{2} \right] \int_\mu^1 \rho' r' \mathrm{d}r' + \frac{1}{2} r_o^2 \Theta \rho_o v_{x_o} v_{\theta_o}^2 \int_\mu^1 \rho' v_\theta'^2 r' \mathrm{d}r'. \tag{13}$$

Finally, the condition of static pressure radial equilibrium simplifies to

$$\frac{\mathrm{d}p'}{\mathrm{d}r'} = \left(\frac{\rho_o v_{\theta_o}^2}{p_o} \right) \frac{\rho' v_\theta'^2}{r'}, \tag{14}$$

from which it is recognized that the first multiplicative term on the right hand side can be expressed in terms of the tangential Mach number at the outer radius, $M_{\theta_o} = v_{\theta_o}/a_o$ where $a_o = \sqrt{\gamma p_o/\rho_o} = \sqrt{\gamma \mathcal{R} T_o}$, is the sonic speed at that location.

Equation (14) can be integrated immediately to yield,

$$p' = \rho' = \exp\left(M_{\theta_o}^2 \frac{\gamma}{2} (r'^2 - 1) \right), \tag{15}$$

where we have used Eq. (9) and the boundary condition is the pressure on the outer wall. Since $v_\theta' = r'$, the two integrals that appear in the conservation equations above can be now evaluated,

$$\int_\mu^1 \rho' r' \mathrm{d}r' = \frac{1}{\gamma M_{\theta_o}^2} (1 - Q), \tag{16}$$

$$\int_\mu^1 \rho' r'^3 \mathrm{d}r' = \frac{1}{\gamma M_{\theta_o}^2} (1 - \mu^2 Q) - \left(\frac{2}{\gamma^2 M_{\theta_o}^4} \right) (1 - Q), \tag{17}$$

where

$$Q = \exp\left(M_{\theta_o}^2 \frac{\gamma}{2} (\mu^2 - 1) \right).$$

Using the above integrals in the conservation equations results in a set of nonlinear equations that are solved numerically as explained below.

Solution Procedure

Pianko and Wazelt [3] suggested a method for the iterative solution of these nonlinear equations by starting with an initial value for axial velocity and utilizing the other equations to arrive at its modified value. However, their method is somewhat sensitive to the initial guess and is not sufficiently robust for application to general nonuniform flow fields. The robustness is markedly improved by transforming the system of equations to a vector residual form, iterative numerical solution of which is carried out using a Newton–Raphson method.

The vector of unknowns, $\mathbf{q}$, consists of

$$\mathbf{q} = [M_{x_o}, M_{\theta_o}, \rho_o, a_o]^T \tag{18}$$

where $M_{x_o} = v_{x_o}/a_o$ is the axial Mach number at the outer radius.

The vector of residuals, of the form $\mathbf{F}(\mathbf{q}) = [F_1, F_2, F_3, F_4]^T$, is given by

$$F_1 = \frac{\dot{M}}{\gamma} - \frac{X M_{x_o}}{a_o} + \dot{M} M_{x_o}^2,$$

$$F_2 = \frac{\dot{M}}{\gamma - 1} + \frac{\dot{M}}{2} M_{x_o}^2 + \frac{\Omega}{2 r_o} \frac{M_{\theta_o}}{a_o} - \frac{E}{a_o^2},$$

$$F_3 = \rho_o M_{x_o} (1 - Q) - \frac{\gamma \dot{M}}{r_o^2 \Theta} \frac{M_{\theta_o}^2}{a_o},$$

$$F_4 = \rho_o M_{x_o} M_{\theta_o}^2 (1 - \mu^2 Q) - \frac{\gamma \Omega}{r_o^3 \Theta} \frac{M_{\theta_o}^3}{a_o^2} - \frac{2}{\gamma} \rho_o M_{x_o} (1 - Q)$$

and are solved simultaneously for $\mathbf{q}$ using the Newton–Raphson method extended to systems of equations. This extended form for the solution vector at the nth iteration, $\mathbf{q}^{(n)}$, can be expressed as

$$\mathbf{q}^{(n+1)} = \mathbf{q}^{(n)} - \mathbf{J}^{-1} \mathbf{F}(\mathbf{q}^{(n)}),$$

where $J = \partial \mathbf{F}/\partial \mathbf{q}$ is the Jacobian of the system. The Jacobian matrix here is of the form,

$$\begin{pmatrix} J_{11} & 0 & 0 & J_{14} \\ J_{21} & J_{22} & 0 & J_{24} \\ J_{31} & J_{32} & J_{33} & J_{34} \\ J_{41} & J_{42} & J_{43} & J_{44} \end{pmatrix} \tag{19}$$

where the components, defined by

$$J_{ij} = \frac{\partial F_i}{\partial q_j}, \tag{20}$$

are evaluated analytically and listed in the Appendix.

The Newton–Raphson method proceeds in the conventional manner with the vector of residuals **F** and the Jacobian J being evaluated at every iteration. A seed for this iterative procedure is calculated by circumferentially averaging the relevant quantities from the initial nonuniform state. The inversion of J is also carried out numerically, although it may alternately be computed analytically. The iteration proceeds until the residual vector decreases below a specified tolerance near zero. The solution of the vector **q** is typically obtained within 10 iterations with a residual tolerance of 10^{-9}. Intentional specification of a seed that was an order of magnitude different from one normally used, caused the iterative solver to yield a solution in less than 15 iterations, demonstrating the merit of using a Newton–Raphson method to solve the above set of equations in a robust manner.

Calculation of Averaged Variables

The result of a converged Newton–Raphson iterative procedure is the solution vector **q**, from which the radial distributions of static pressure, density and tangential velocity may be calculated; the axial velocity and static temperature are independent of the radial coordinate as indicated in Eq. (9). In addition, one may also define radial variations of absolute total temperature and pressure using,

$$T_t = T + \frac{\gamma - 1}{2\gamma\mathcal{R}}\left(\frac{v_x^2 + v_\theta^2}{T}\right), \tag{21}$$

$$p_t = p\left(\frac{T_t}{T}\right)^{(\gamma-1)/\gamma}. \tag{22}$$

In many instances, it is preferred that all quantities be represented by radially averaged values. To this end, the static pressure and density are directly area-averaged to yield,

$$\bar{p} = \frac{2}{\gamma(1-\mu^2)}\frac{p_o}{M_{\theta_o}^2}\left[1 - \exp\left(M_{\theta_o}^2\frac{\gamma}{2}(\mu^2 - 1)\right)\right], \tag{23}$$

$$\bar{\rho} = \frac{2}{\gamma(1-\mu^2)}\frac{\rho_o}{M_{\theta_o}^2}\left[1 - \exp\left(M_{\theta_o}^2\frac{\gamma}{2}(\mu^2 - 1)\right)\right]. \tag{24}$$

In a similar manner, an average total temperature may be defined,

$$\overline{T_t} = \frac{\gamma - 1}{\gamma\mathcal{R}}\frac{E}{\dot{M}}, \tag{25}$$

and an average total pressure with the conventional definition,

$$\overline{p_t} = \bar{p}\left(\frac{\overline{T_t}}{T_o}\right)^{\gamma/(\gamma-1)}. \tag{26}$$

These total quantities can then be used to compare with results from other analyses that include the loss accrued due to mixing. Values calculated from Eqs. (25) and (26) can be used to compute the efficiency of the system in the limit of complete equilibrium. Note that it is not possible to define from its linear radial profile an average tangential velocity that simultaneously satisfies Eqs. (3) and (4).

Special Case of Swirl-Free Flow

The above formulation is valid for an initial nonuniform state with arbitrary swirl which can be characterized by the swirl angle $\alpha = \tan^{-1}(M_{\theta_o}/M_{x_o})$. When the flow is swirl-free ($\alpha = 0$), the system of equations described above simplifies considerably. Since the swirl velocity, $v_{\theta_o} \equiv 0$, the condition of radial equilibrium, Eq. (14), can be trivially solved to yield, $p' = 1$, and the conservation of angular momentum is identically satisfied. The remaining equations, Eqs. (10), (11), and (13), can then be expressed as

$$\dot{M} = \rho_o v_{x_o} A, \tag{27}$$

$$X = \dot{M} v_{x_o} + p_o A, \tag{28}$$

$$E = \frac{\dot{M}\gamma}{\gamma - 1}\frac{p_o}{\rho_o} + \frac{\dot{M}}{2}v_{x_o}^2, \tag{29}$$

where A is the surface area that the initial state is defined on. Manipulation of the above equations results in a quadratic equation for v_{x_o}:

$$\left[\frac{1}{2} - \frac{\gamma}{\gamma - 1}\right]v_{x_o}^2 + \frac{\gamma}{\gamma - 1}\frac{X}{\dot{M}}v_{x_o} + \frac{-E}{\dot{M}} = 0 \tag{30}$$

which produces two solutions. The value of v_{x_o} corresponding to the subsonic solution is typically selected and the remaining quantities are calculated using Eqs. (27)–(29).

Flow in Rectangular Geometries

Having demonstrated the procedure for the calculation of the state of complete equilibrium for flows emanating from annular geometries, we now turn to those from rectangular geometries such as a linear cascade of airfoils. As mentioned previously, the natural choice for such flows is the Cartesian coordinate system. The primary difference between the methodology described below and that for the annular geometry derived above, is that the values of flow field variables at the mixed-out state are now required to be uniform over the area of the mixed-out plane. With this additional simplification in place, the mixed-out state, denoted here by over-bars, is determined from the initial nonuniform state by enforcing conservation of mass, momentum and energy between the two states. Denoting by (X, Y, Z) momentum fluxes along the Cartesian coordinates (x, y, z), we then have,

$$\dot{M} = \int \tilde{\rho}(\tilde{\mathbf{V}} \cdot \tilde{\mathbf{n}})\mathrm{d}A,$$

$$X = \int \tilde{\rho}(\tilde{\mathbf{V}} \cdot \tilde{\mathbf{n}})\widetilde{v_x}\mathrm{d}A + \int \tilde{p}(\mathbf{e}_x \cdot \tilde{\mathbf{n}})\mathrm{d}A,$$

$$Y = \int \tilde{\rho}(\tilde{\mathbf{V}} \cdot \tilde{\mathbf{n}})\widetilde{v_y}\mathrm{d}A + \int \tilde{p}(\mathbf{e}_y \cdot \tilde{\mathbf{n}})\mathrm{d}A,$$

$$Z = \int \tilde{\rho}(\tilde{\mathbf{V}} \cdot \tilde{\mathbf{n}})\widetilde{v_z}\mathrm{d}A + \int \tilde{p}(\mathbf{e}_z \cdot \tilde{\mathbf{n}})\mathrm{d}A,$$

$$E = \frac{\gamma\mathcal{R}}{(\gamma - 1)}\int \tilde{\rho}(\tilde{\mathbf{V}} \cdot \tilde{\mathbf{n}})\tilde{T}\,\mathrm{d}A + \frac{1}{2}\int \tilde{\rho}(\tilde{\mathbf{V}} \cdot \tilde{\mathbf{n}})(\widetilde{v_x^2} + \widetilde{v_y^2} + \widetilde{v_z^2})\mathrm{d}A,$$

where $\tilde{\mathbf{V}} = \tilde{\mathbf{V}}(x, y, z) = [\widetilde{v_x}, \widetilde{v_y}, \widetilde{v_z}]$ is the velocity expressed in Cartesian components with $\tilde{p}$ and $\tilde{\rho}$ being, respectively, the static pressure and density of the initial state; furthermore, $\tilde{\mathbf{n}} = \tilde{\mathbf{n}}(x, y, z)$ is the local normal vector to the surface of the initial state, and $(\mathbf{e}_x, \mathbf{e}_y, \mathbf{e}_z)$ are the unit vectors in the respective coordinate directions.

The properties at the mixed-out state are then required to satisfy the conditions,

$$\dot{M} = \bar{\rho}\overline{v_x}A,$$

$$X = \dot{M}\overline{v_x} + \bar{p}A_x,$$

$$Y = \dot{M}\overline{v_y} + \bar{p}A_y,$$

$$Z = \dot{M}\overline{v_z} + \bar{p}A_z,$$

$$E = \frac{\dot{M}}{\gamma - 1}\frac{\gamma \bar{p}}{\bar{\rho}} + \frac{\dot{M}}{2}(\overline{v_x}^2 + \overline{v_y}^2 + \overline{v_z}^2),$$

where A_s is the area projected along the relevant spatial direction. In most cases, since the initial state is usually defined on an axial plane, one has $A_y = A_z \equiv 0$.

Rearrangement of the mass conservation equation and the momentum equations, and elimination of the energy equation, yields the following quadratic equation for the average static pressure at the mixed-out state,

$$Q\bar{p}^2 + L\bar{p} + C = 0, \tag{31}$$

where the coefficients Q, L, and C are given by

$$Q = \frac{1}{\dot{M}^2}\left(A_x^2 + A_y^2 + A_z^2 - \frac{2\gamma}{\gamma - 1}AA_x\right),$$

$$L = \frac{2}{\dot{M}^2}\left(\frac{\gamma}{\gamma - 1}XA - XA_x - YA_y - ZA_z\right),$$

$$C = \frac{1}{\dot{M}^2}(X^2 + Y^2 + Z^2) - \frac{2E}{\dot{M}}.$$

Solution of Eq. (31) is given by

$$\bar{p} = \frac{-L - \sqrt{L^2 - 4QC}}{2Q}, \tag{32}$$

where the negative root, associated with the subsonic branch of the solution, has been selected.

Equation (32) can now be used to calculated all remaining quantities at the mixed-out state. The static temperature is computed from the equation of state, and the total temperature and pressure are determined using Eqs. (25) and (26).

We emphasize that a natural consequence of the procedure to estimate the mixed-out state in an annular geometry is that each quantity possesses a radial profile as well as a plane-averaged value. In contrast, for planar cascade flows, only plane-averaged values may be defined. Furthermore, this method may be directly applied to two-dimensional planar flows using the formulation developed here.

Comparison of Averaging Methods for Nonuniform Swirling Flow

As mentioned earlier, various methods exist in the literature for transforming nonuniform flow fields in annular ducts to equivalent one-dimensional or axisymmetric representations. We now compare some of these methods with results obtained using the present formulation. The flow field selected is that exiting the isolated transonic compressor rotor designated as NASA Rotor-35, which has a hub-to-tip ratio $\mu = 0.77$, an aspect ratio of 1.19 and a tip clearance of 0.96% span. The rotor operates at a tip speed of 363 m/s, which corresponds to 80% of its design speed. The configuration is depicted in Fig. 2, and the flow field is simulated using the Navier–Stokes solver developed by Ni [5] and Davis, Ni, and Carter [6]. The solver which has been thoroughly validated [7–10], uses a Lax–Wendroff scheme with a multiple-grid procedure and local time stepping to achieve solutions of the steady (time-independent) flow field. Nonreflecting boundary conditions of Giles [11] are imposed at the inlet and exit of the computational domain. The domain is discretized using an H-grid topology for the bulk of the blade passage with an O-grid in the immediate vicinity of the airfoil surface and a fully resolved tip gap. The k-ω model of Wilcox [12] is used to obtain turbulence closure.

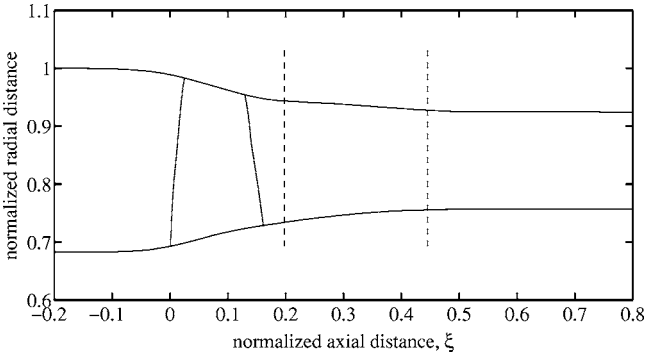

Fig. 2 Schematic of computational geometry of NASA Rotor-35. Initial states are defined on axial planes indicated by the broken lines

The procedure described above for swirling flow in an annular duct, when applied to the initial state yields radial profiles as well as radially averaged values, at the state of complete equilibrium. These are compared to values obtained by application of the averaging procedure developed by Dring and Oates [1], in which the radial profile for each flow variable is constructed from either area-, density-, or mass-weighted averages over the circumferential extent of one airfoil pitch. For example, the static pressure is area averaged, the axial velocity is density averaged and the total temperature is mass averaged to calculate each respective radial profile. Area-averaging is the simplest form of averaging, applicable to any flow variable, and is included for purposes of comparison. A commonly used method to obtain average values in CFD-based design systems employs an approximate planar mixing procedure. It consists of applying a two-dimensional version of the procedure developed above for linear cascade flow, in a spanwise manner across the circumferential direction of the initial state, thus precluding the action of spanwise mixing. Results from such an approach are also included in the comparisons. The initial state consists of flow field variables defined on a plane located at two axial stations downstream of the rotor. In what follows all coordinates are normalized by the casing radius at the inlet, and axial distances measured from the rotor leading edge are denoted ξ, as shown in Fig. 2. Comparison of radial profiles is conducted at the condition of near-stall for the rotor, corresponding to a mass flow rate of 14.8 kg/s. Overall performance comparisons between the different methods are carried out along the speedline between the near stall mass flow rate and a choking mass flow rate of 17.3 kg/s.

All spanwise profiles described below are normalized as follows: Velocities are normalized by the tip speed, U, while the pressure, and temperature are normalized by their respective far upstream values, p_∞ and T_∞. Radial profiles of axial velocity and tangential velocity, shown in Fig. 3, are found to be similar between the various circumferentially averaged methods, but markedly different from the mixed-out profile. Profiles of static pressure and temperature, shown in Figs. 4(*a*) and 4(*b*), indicate that the flow at $\xi = 0.2$ is far from being in radial or thermal equilibrium, owing to the large difference between the circumferentially averaged profile and the mixed-out one. The variation of the mixed-out total pressure profile in Fig. 4(*c*) is governed primarily by the linear velocity distribution at the state of complete equilibrium. The total temperature profile in Fig. 4(*d*) appears to be somewhat similar between the circumferential average and the mixed-out state except in the outer span where the tip clearance vortex is present. Application of the current methodology to more severely loaded airfoil rows, though not discussed here, was found to yield larger differences between the three circumferentially averaged profiles than those shown in Figs. 3 and 4.

The calculation of one-dimensional quantities such as total

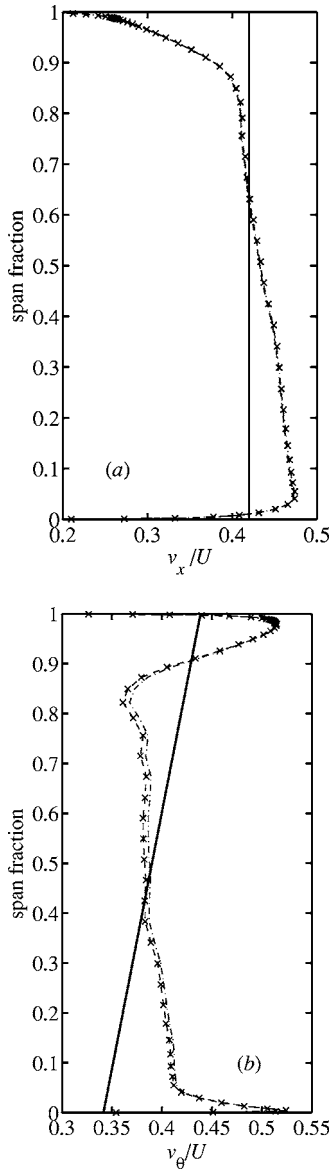

Fig. 3 Radial profile of (*a*) axial velocity, v_x, and (*b*) tangential velocity, v_θ, normalized by the tip speed U, at $\xi=0.2$. The circumferentially-averaged profiles shown are: Dring–Oates method (×), area-weighted (– · – ·) and approximated planar mixing (– – –). The mixing out procedure that yields the state of complete equilibrium is shown by the solid line (—)

pressure and total temperature are critical in evaluating the design of an airfoil row. The constraint that the energy be identical between the initial state and an averaged state necessitates mass-averaging of the total temperature. Greitzer, Tan, and Graf [2] provide a detailed discussion on the suitable choice of a method for averaging total pressure. In particular, they point out that by maintaining equality of entropy flux between the initial and the averaged state and using the mass-averaged total temperature, one can define an average total pressure. Since the total temperature (enthalpy) and entropy are conserved between the two states, they refer to it as the availability averaged total pressure; it is equivalently denoted the entropy-averaged total pressure, a nomenclature we adopt in the discussion below. As pointed out in [2], the mass-averaged total pressure approaches its entropy-averaged counterpart for flows characterized by low Mach number and uniform total temperature, and accounts for its extensive use in the estimation of airfoil row performance. Alternately, the total pressure can be uniformly weighted to yield its area-averaged value, a procedure that satisfies no conservation equation, and is included solely for comparison with the other averages. All of these averages, calculated from the initial state, are compared to that obtained by application of the procedures described above at $\xi=0.2$ and $\xi=0.45$. In what follows, it is more convenient to make comparisons between these average values through the use of a loss coefficient defined by,

$$\bar{\omega} = 1 - \Pi \times \Phi^{-\tau}$$

where Φ is the total temperature ratio, Π is the total pressure ratio and $\tau=\gamma/(\gamma-1)$. The pressure ratio Π is defined as the ratio between the average (mass-, entropy-, area-weighted, or mixed-out) and a reference value from far upstream, whereas Φ is the ratio of the mass-averaged total temperature and its far upstream reference counterpart. Note that since the total temperature is always mass-averaged, differences in $\bar{\omega}$ between averaging methods are attributable only to differences in the total pressure.

The variation of the loss coefficient is shown in Fig. 5(*a*) at $\xi=0.2$ near the rotor trailing edge, for a series of operating points along the speedline. Note that loss is presented as an excursion from its entropy-averaged value, due to the special property (invariance of availability, discussed above) that the latter possesses. The variation shown in Fig. 5(*a*) demonstrates the close agreement between the mass-averaged and entropy-averaged values. The mixed-out value is found to be generally about 0.6% higher than its corresponding entropy-average value.

Moreover, the expected additional mixing loss as one moves away from the design point (16 kg/s) is also clearly evident, especially at the extremities of the range in mass flow rate. The area-average, with uniform weighting, is found to lie between the mixed-out value and the entropy-averaged value, at the location $\xi=0.2$. Further downstream at $\xi=0.45$, the variation shown in Fig. 5(*b*) demonstrates that the difference between the mixed-out value and the entropy-averaged value decreases over the entire speedline, due to the additional mixing that occurs in the flow. The entropy- and mass-average values now appear to differ somewhat more, but the area-average value is closer to the mixed-out value. The proximity of the area-averaged value to its mixed-out counterpart is not intended to imply that the former is an acceptable approximation of the latter. Mixing that occurs between the two axial stations tends to make the flow more uniform, thus yielding the observed differences between Figs. 5(*a*) and 5(*b*).

Finally, a numerical experiment was conducted to simulate the abstract mixing process that would transform an initial nonuniform state to one of complete equilibrium. For this purpose, the computational geometry is modified so that the flow exiting the rotor enters a long annular duct of constant area as shown in Fig. 6(*a*). This constant area duct is constrained to possess inviscid walls, as indicated in the figure, allowing a finite slip velocity at the endwalls of the annulus. One should note that the mixing process to attain the state of complete equilibrium will be accomplished certainly much further downstream of the rotor, and beyond the domain exit boundary. The loss coefficient as defined above is calculated as a function of the distance along the duct, downstream of the location at which the walls are allowed to support a slip velocity. As was mentioned previously, this permits mixing of the flow due to the action of viscosity, while precluding the endwall boundary layers from evolving any further. The loss coefficient based on the entropy-averaged total pressure is again used as a basis for comparison and shown with the mass-averaged and mixed-out values in Fig. 6(*b*). As expected, the entropy-averaged loss increases rapidly close to the rotor and more gradually further downstream. The mass-averaged total pressure displays a similar variation but is slightly lower than its entropy-averaged counterpart. Numerical adjustment of the flow as it is transported from a region bounded by viscous endwalls to one with inviscid endwalls causes a localized region in the immediate vicinity of $\xi=0.6$ to display a small increase in mixed-out total

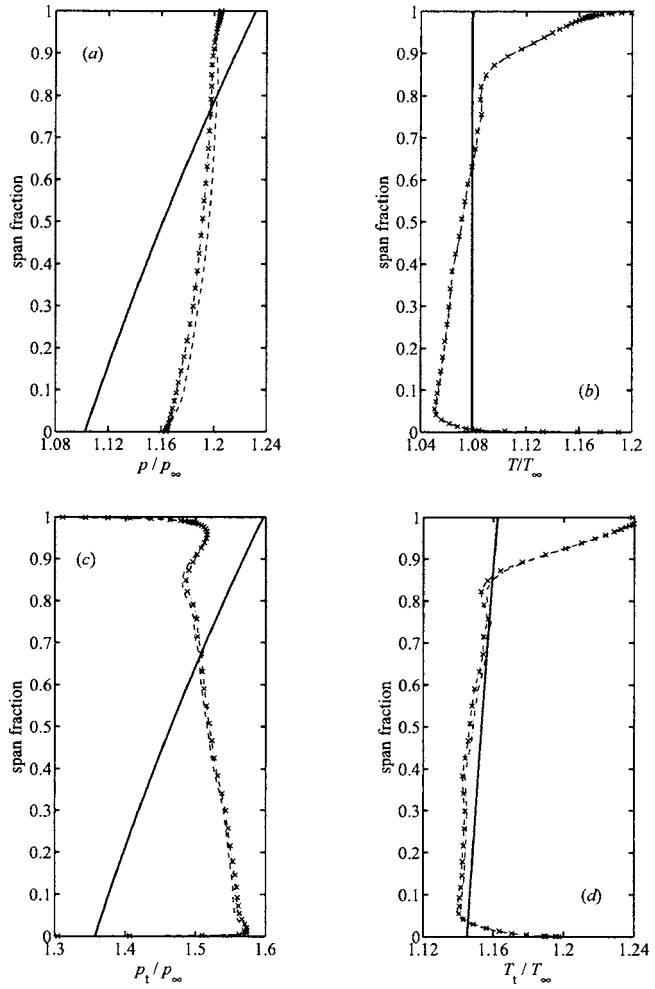

Fig. 4 Radial profile of normalized (*a*) static pressure (*b*) static temperature, (*c*) total pressure, and (*d*) total temperature at ξ=0.2. The circumferentially averaged profiles shown are: Dring–Oates method (×), area-weighted (– · – ·) and approximated planar mixing (– – –). The mixing out procedure that yields the state of complete equilibrium is shown by the solid line (—)

pressure loss; note that the curves presented in Fig. 6(*b*) commence at ξ=0.5, upstream of the location at which the walls are constrained to be inviscid. Nevertheless, for the remainder of the inviscid duct the mixed-out procedure for achieving complete equilibrium yields a loss coefficient that is virtually invariant with downstream distance, a result that confirms the validity of the implementation. Note that both the entropy- and mass-averaged loss coefficients appear to display an asymptotic axial variation relative to the mixed-out value, as would physically be expected. Finally, use of a turbulence model in the present work, necessitates a comment on the turbulent kinetic energy at the mixed-out equilibrium state. The absence of shear at this final equilibrium state guarantees that the production of turbulence would be zero, and since the mixed-out state is attained in the asymptotic limit, any turbulent fluctuations would have been dissipated by the action of viscosity at the smallest scales. Consequently, one may conclude that the turbulent kinetic energy is zero at the final equilibrium state, an aspect that is confirmed in the computation by the rapid decrease of this quantity with axial distance along the inviscid duct (not shown for brevity).

Conclusions

A rational systematic method for the calculation of the state of complete equilibrium, or mixed-out state, from an initial spatially nonuniform state is presented for swirling flows in annular geometries. The state of complete equilibrium is defined as one that can be evolved in an infinitely long duct and display no change in properties. The final equilibrium state is constrained to transport the same mass, momentum and energy as the initial state, and to be in thermal and radial equilibrium. Application of these constraints, in conjunction with the equation of state for a perfect gas, yields specific forms of radial profiles for each of the velocity components, static temperature and pressure. Solution of a set of coupled nonlinear algebraic equations, using a robust and efficient Newton–Raphson method, yields the unknown coefficients required to define the state of complete equilibrium. The resulting radial variations are used to define consistent spanwise-averaged values of total temperature and total pressure. The methodology for the calculation of the mixed-out flow in rectangular geometries is included for completeness.

The procedure developed to calculate the state of complete equilibrium is applied to the flow field predicted using a computational flow solver. The flow exiting an isolated transonic compressor rotor is examined, with particular emphasis on a comparison of the mixed-out state with other averaging methods. The latter include mass-averaging, entropy-averaging, and area-averaging. Radial profiles are compared at the near stall point of the compressor, whereas a more comprehensive comparison of the different methods is conducted over the entire speedline. In general, discrepancies between mass-averaged and entropy-averaged total pressure loss are found to be less than 0.1%, implying that for all practical purposes they can equivalently be used to quantify

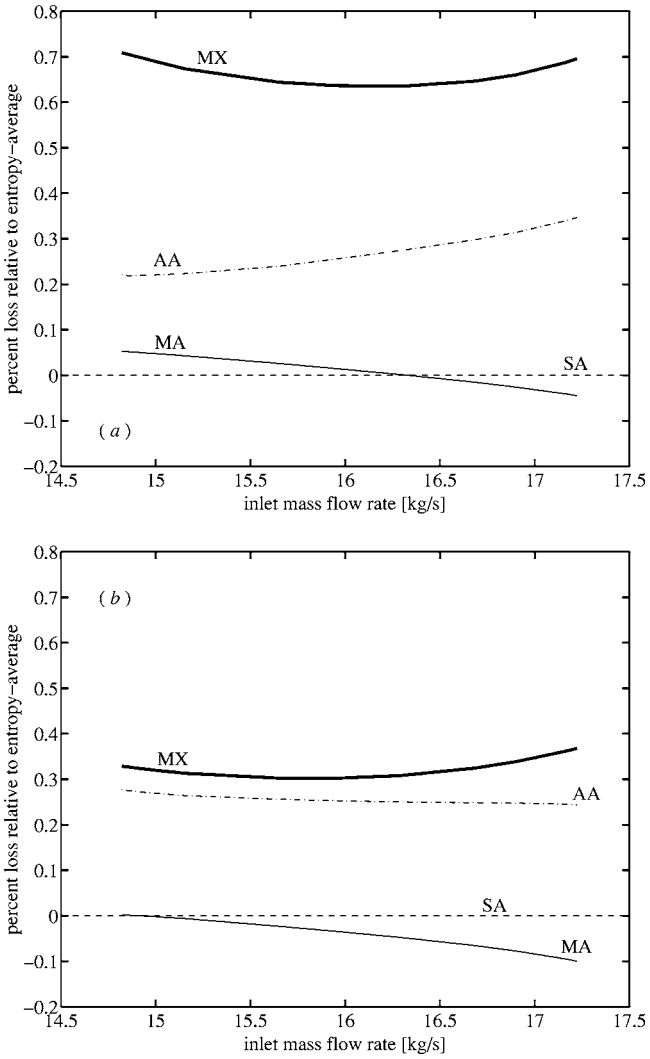

Fig. 5 Difference in loss coefficient relative to the entropy-averaged value as a function of mass flow rate at (*a*) ξ=0.2 and (*b*) ξ=0.45. Legend, SA: entropy-average, MA: mass-average, AA: area-average, and MX: mixed-out to state of complete equilibrium.

the loss generated in an airfoil row. Furthermore, differences between the entropy-averaged loss and mixed-out loss decrease as one moves downstream from the rotor, confirming the notion that the nonuniform flow gets increasingly mixed as it is transported downstream.

A numerical experiment to simulate the abstract mixing process involved in attaining the state of complete equilibrium was conducted by allowing the flow exiting the rotor to evolve in a long parallel-walled annular duct wherein the walls were constrained to be inviscid. The mixed-out loss was found to be independent of axial location along this duct, while the entropy-averaged loss was found to increase due to the mixing action of viscosity away from the walls, thereby validating the implementation of the procedure.

The present investigation demonstrates that the mixed-out procedure described here yields consistent results for the loss of an airfoil row. Unlike the entropy-averaged total pressure (or the mass-averaged value), its mixed-out counterpart accounts for all possible loss incurred downstream of the airfoil and is invariant with axial location. Thus one may state that the mixed-out procedure is preferable over other available techniques of averaging flow fields. In multistage simulations, the method is applicable to each airfoil row, as well as to the overall machine.

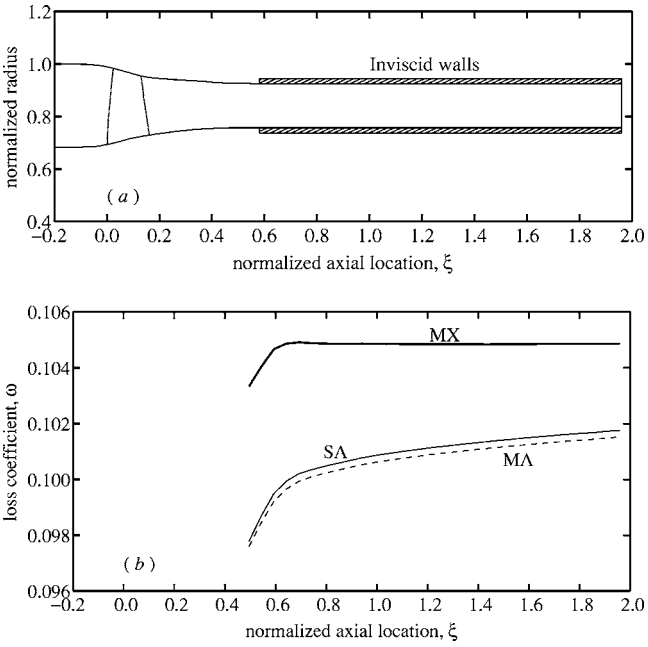

Fig. 6 Schematic of compressor geometry with long duct possessing slip walls shown as shaded regions in (*a*). Variation of loss coefficient with downstream distance is shown in (*b*), with the legend SA: entropy-averaged, MA: mass-averaged, MX: mixed-out to state of complete equilibrium

Acknowledgment

The author wishes to thank Pratt and Whitney for granting permission to publish this paper, and especially to Jayant Sabnis for his encouragement and support. The author appreciates several enlightening discussions with Gary Stetson, is indebted to Dilip Prasad for assisting with implementation of the generalized Newton–Raphson method, and would like to express his gratitude to Jinzhang Feng for his careful perusal of the manuscript.

Appendix

The nonzero elements of the Jacobian matrix Eq. (20) are

$$J_{11} = -\frac{X}{a_o} + 2\dot{M}M_{x_o}$$

$$J_{14} = X\frac{M_{x_o}}{a_o^2}$$

$$J_{21} = \dot{M}M_{x_o}$$

$$J_{22} = \frac{\Omega}{2r_o}\frac{1}{a_o}$$

$$J_{24} = -\frac{\Omega}{2r_o}\frac{M_{\theta_o}}{a_o^2} + \frac{2E}{a_o^3}$$

$$J_{31} = \rho_o(1-Q)$$

$$J_{32} = -\rho_o M_{x_o} M_{\theta_o}\gamma(\mu^2-1)Q - \frac{2\gamma\dot{M}}{r_o^2\Theta}\frac{M_{\theta_o}}{a_o}$$

$$J_{33} = M_{x_o}(1-Q)$$

$$J_{34} = \frac{\gamma \dot{M}}{r_o^2 \Theta} \frac{M_{\theta_o}^2}{a_o^2}$$

$$J_{41} = \rho_o M_{\theta_o}^2 (1 - \mu^2 Q) - \frac{2\rho_o}{\gamma}(1 - Q)$$

$$J_{42} = 2\rho_o M_{x_o} M_{\theta_o}(1 - Q) - \frac{3\Omega\gamma}{r_o^3 \Theta} \frac{M_{\theta_o}^2}{a_o^2} + - \rho_o M_{x_o} M_{\theta_o}^3 \gamma(\mu^2 - 1)\mu^2 Q$$

$$J_{43} = M_{x_o} M_{\theta_o}^2 (1 - \mu^2 Q) - \frac{2}{\gamma} M_{x_o}(1 - Q)$$

$$J_{44} = \frac{2\gamma\Omega}{r_o^3 \Theta} \frac{M_{\theta_o}^3}{a_o^3},$$

where

$$Q = \exp\left(M_{\theta_o}^2 \frac{\gamma}{2}(\mu^2 - 1) \right).$$

References

[1] Dring, R. P. and Oates, G. C., 1990, "Throughflow Theory for Non-Axisymmetric Turbomachinery Flow: Part I - Formulation," J. Turbomach., **112**, pp. 320–327.

[2] Greitzer, E. M., Tan, C. S. and Graf, M. B., 2004, *Internal Flow: Concepts and Applications*, Cambridge University Press, Cambridge, UK.

[3] Pianko, M. and Wazelt, F., 1983, "Suitable Averaging Techniques in Non-Uniform Internal Flows." *Propulsion and Energetics Panel*, Working Group 14, Chapter 3 in AGARD Advisory Report No. 182.

[4] Batchelor, G. K., 1967, *An Introduction to Fluid Dynamics*, Cambridge University Press, Cambridge, UK.

[5] Ni, R.-H., 1982, "A Multiple-Grid Scheme for Solving Euler Equations," AIAA J., **20**, pp. 1565–1571.

[6] Davis, R. L., Ni, R.-H., and Carter, J. E., 1986, "Cascade Viscous Flow Analysis Using Navier–Stokes Equations," AIAA Paper No. 86-0033.

[7] Ni, R.-H. and Bogoian, H., 1989, "Predictions of 3D Multi-Stage Turbine Flow Fields Using a Multiple-Grid Euler Solver," AIAA Paper No. 89-0233.

[8] Ni, R.-H. and Sharma, O. P., 1990, "Using a 3D Euler Flow Simulation to Assess Effects of Periodic Unsteady Flow Through Turbines," AIAA Paper No. 90-2357.

[9] Davis, R. L., Shang, T., Buteau, J. and Ni, R.-H., 1996, "Prediction of 3D Unsteady Flow in Multi-Stage Turbomachinery Using an Implicit Dual Time-Step Approach," AIAA Paper No. 96-2565.

[10] Prasad, A., 2003, "Evolution of Upstream Propagating Shock Waves from a Transonic Compressor Rotor," ASME J. Turbomach., **133**, pp. 133–140.

[11] Giles, M. B., 1990, "Non-Reflecting Boundary Conditions for Euler Equation Calculations," AIAA J., **28**, pp. 2050–2058.

[12] Wilcox, D. C., 1998, *Turbulence Modeling for CFD*, DCW Industries, Inc, La Cañada, CA.

Blade Aerodynamic Damping Variation With Rotor-Stator Gap: A Computational Study Using Single-Passage Approach

H. D Li

L. He

School of Engineering,
University of Durham,
Durham DH1 3LE, UK

One of the outstanding issues in turbomachinery aeromechanic analysis is the intrarow interaction effects. The present work is aimed at a systematic examination of rotor-stator gap effects on blade aerodynamic damping by using a three-dimensional (3D) time-domain single-passage Navier-Stokes solver. The method is based on the upwind finite volume discretization and the single-passage shape-correction approach with enhanced accuracy and efficiency for unsteady transonic flows prediction. A significant speedup (by a factor of 20) over to a conventional whole annulus solution has been achieved. A parametric study with different rotor-stator gaps (56%–216% rotor tip chord) for a 3D transonic compressor stage illustrates that the reflection from an adjacent stator row can change rotor aerodynamic damping by up to 100% depending on the intrarow gap spacing. Furthermore, this rotor aerodamping dependency on the intrarow gap seems also to be affected by the number of stator blades. The predicted nonmonotonic relationship between the rotor blade aerodynamic damping and the gap spacing suggests the existence of an optimum gap regarding rotor flutter stability and/or forced response stress levels. [DOI: 10.1115/1.1928932]

1 Introduction

Predictive capabilities for blade aeromechanical problems (i.e., flow induced blade vibrations in the form of either flutter or forced response) are becoming increasingly important as gas turbine/aeroengine development continues to be driven by requirements of higher blade loading, more compact configuration, lower component weight, lower cost, and the ability to be operated in a wider range of conditions. So far, most computational models of oscillating blades only consider an isolated blade row in a truncated domain subject to nonreflecting boundary conditions. For example, the aeroelastic response of an isolated transonic fan (NASA rotor-67) was studied by Marshall and Imregun in 1996 [1] and Doi and Alonso in 2002 [2]. Only a few previous studies have, however, examined blade row interference effects. In 1997, Silkowski and Hall [3] investigated aeroelastic characteristics of an embedded blade row using a two-dimensional (2D) coupled model. Significantly their work revealed that aeromechanical response of an embedded blade row in multistage environment could be qualitatively different from that of an isolated blade row depending on the nodal diameter (interblade phase angle) of the blade vibration mode. There are certain issues of interest to aeromechanics designers which remain to be addressed. For instance, is there any identifiable trend of intrarow gap effects on the aeroelastic stability to be used for design optimization? Are there other influential parameters related to the intrarow effects than the interblade phase angle which, though obviously important, can not be easily controlled by a designer? Thus, more systematic investigations of intrarow interaction effects on blade aeromechanics are useful.

On the other hand, from a pure aerothermal performance viewpoint, there has been considerable research effort on the intrarow gap effect, which has indicated possible performance gains for certain choices of the gap for either compressors [4,5] or turbines [6,7]. One would thus enquire the gap dependence of the aeroelastic stability (aerodynamic damping) before coming to a conclusion regarding an "optimum" gap which is both aerodynamically and aeroelastically sound. Although whole annulus assembly multirow time-domain solution methods have been developed and applied to blade flutter and forced response analysis [8,9], this kind of full-scale time-domain calculations are very computationally intensive and hence difficult to be applied to parametric studies for design and optimization. In the present work, an efficient and accurate single passage flow solver based on a Fourier-transform based methodology, "shape correction" [10], and the second-order upwind discretization (AUSMD/V [11]) has been developed for multiple (two or three) blade row configurations including blade vibration. So far, no other time-domain single-passage methods have been applied to situations with multiple periodic disturbances. In this paper, parametric studies using the developed solver for gap effects on blade aeromechanical characteristics of a 3D rotor-stator stage configuration is reported.

2 Computational Methodology

2.1 Flow Model and Numerical Scheme. For convenience of simulating flows in multiple rotor and stator blade rows with moving meshes, an integral form full Navier-Stokes equation in cylindrical coordinates system of the absolute reference frame, as described by Eq. (1), is adopted.

$$\frac{\partial}{\partial t}\int\int\int_{\delta V} Q dV + \oiint_{\delta A} [(F_x - Qu_{mg})n_x + (F_\theta - Qv_{mg})n_\theta + (F_r - Qw_{mg})n_r]dA = \int\int\int_{\delta V} S_i dV + \oiint_{\delta A} [V_x n_x + V_\theta n_\theta + V_r n_r]dA \quad (1)$$

where u_{mg}, v_{mg}, and w_{mg} are velocities of moving mesh due to blade vibration as well as rotation if the mesh is attached to a rotor. The extra terms Qu_{mg}, Qv_{mg}, and Qw_{mg} count for the contribution to the inviscid fluxes due to grid movement. Full viscous

Contributed by the International Gas Turbine Institute and presented at the International Gas Turbine and Aeroengine Congress and Exhibition, Atlanta, GA, June 16-19, 2003. Manuscript received by the IGTI December 1, 2002; final revision March 1, 2003. Paper No. GT2003-38199. Review Chair: H. R. Simmons.

stress terms are adopted and they are closed by a mixing length turbulence model.

An advanced second-order upwind scheme AUSMD/V developed by Wada and Liou [11] has been extended to cylindrical coordinates system with a moving mesh to handle flutter problems in rotating and/or stationary blade rows. The generalized advective flux can be evaluated by the following Eq. (2).

$$\{\hat{F}\} = \frac{1}{2}(\rho U)_{1/2}(\{\Phi\}_L + \{\Phi\}_R) + \frac{1}{2}|(\rho U)_{1/2}|(\{\Phi\}_R - \{\Phi\}_L) + \{F_{DV}\} + \tilde{P}\cdot\{\hat{n}\} \tag{2}$$

where, $\{\Phi\}=\{1, u, vr, w, H\}^T$

$$\{F_{DV}\} = \begin{Bmatrix} 0 \\ (0.5+\alpha)(F_V - F_D)n_x \\ (0.5+\alpha)(F_V - F_D)n_\theta \cdot r \\ (0.5+\alpha)(F_V - F_D)n_r \\ \tilde{P}\cdot U_m \end{Bmatrix}$$

$$F_V = U_L^+ \rho_L U_{AL} + U_R^- \rho_R U_{AR}$$

$$F_D = \frac{1}{2}(\rho U)_{1/2}(U_{AL} + U_{AR}) + \frac{1}{2}|(\rho U)_{1/2}|(U_{AR} - U_{AL})$$

$$U = (u - u_{mg})n_x + (v - v_{mg})n_\theta + (w - w_{mg})n_r$$

$$U_A = u\cdot n_x + v\cdot n_\theta + w\cdot n_r$$

$$U_m = u_{mg}\cdot n_x + v_{mg}\cdot n_\theta + w_{mg}\cdot n_r$$

$$(\rho U)_{1/2} = U_L^+ \rho_L + U_R^- \rho_R$$

$$\tilde{P} = P_L^+ + P_R^-$$

and α is a weighting function evaluated in the same way as [11]. Temporal integration of the discretized equations is carried out using the second-order four-step explicit Runge-Kutta scheme. The convergence is speeded up by a time-consistent multi-grid technique [7].

The baseline solver has been developed for a normal multipassage and multirow domain with the middle-blade domain arrangement [12] and the sliding mesh rotor-stator interface. This baseline multipassage time-domain solver, although useful for detailed analysis and trouble shooting, etc., is too time consuming for parametric studies. Hence it is only used for validation purposes in the present work. A significant computational efficiency gain is achieved by making use of a single-passage domain for each blade row.

2.2 Shape-Correction Method. The general shape-correction method with multiple periodic disturbances can be described as follows. Assume the number of unsteady disturbances of interest is N_{pt}, any flow variable on the periodic boundaries can be expressed as

$$U(x,y,r,t) = U_0(x,y,r) + \sum_1^{N_{pt}} U_i(x,y,r,t) \tag{3}$$

where U_0 is the time-averaged part, U_i is the unsteady part induced by the ith unsteady disturbance, and $y=r\theta$. Each unsteady part characterized by its primary disturbance frequency ω_i can be approximated by a set of Fourier series in time

$$U_i(x,y,r,t) = \sum_{n=1}^{N_{\mathrm{Fou}}} [A_{ni}(x,y,r)\sin(n\omega_i t) + B_{ni}(x,y,r)\cos(n\omega_i t)] \tag{4}$$

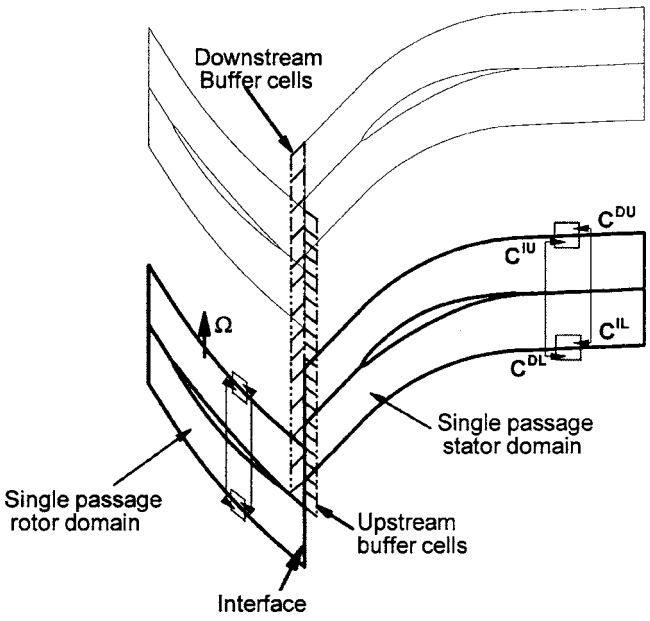

Fig. 1 Single-passage domain and implementation of the phase-shift periodicity

For the present finite volume discretization, flow variables are stored at cell centers. For any boundary cell, there is an adjacent dummy cell for which flow variables need to be identified and updated by applying corresponding boundary conditions. For a single passage domain, we have the upper and lower 'periodic' boundaries as shown on Fig. 1.

For any pair of mesh cells, $\mathbf{C^{IL}}$ (inner cell of the lower periodic boundary) and $\mathbf{C^{DU}}$ (dummy cell of the upper periodic boundary), $\mathbf{C^{IU}}$ (inner cell of the upper periodic boundary), and $\mathbf{C^{DL}}$ (dummy cell of the lower periodic boundary), we then have

$$U^{\mathrm{DL}}(x,y,r,t) = U_0^{\mathrm{IU}}(x,r) + \sum_{i=1}^{N_{pt}}\sum_{n=1}^{N_{\mathrm{Fou}}} \{A_{ni}^{\mathrm{IU}}\sin[n(\omega_i t - \sigma_i)] + B_{ni}^{\mathrm{IU}}\cos[n(\omega_i t - \sigma_i)]\}$$

$$U^{\mathrm{DU}}(x,y,r,t) = U_0^{\mathrm{IL}}(x,r) + \sum_{i=1}^{N_{pt}}\sum_{n=1}^{N_{\mathrm{Fou}}} \{A_{ni}^{\mathrm{IL}}\sin[n(\omega_i t + \sigma_i)] + B_{ni}^{\mathrm{IL}}\cos[n(\omega_i t + \sigma_i)]\} \tag{5}$$

where σ_i is the interblade phase angle of the ith disturbance, A_{ni} and B_{ni} are corresponding nth order Fourier coefficients of the disturbance i. Therefore, the dummy cell at the upper boundary will be corrected by the Fourier series evaluated from its corresponding lower side inner cell with a phase shift. The correction on the lower side dummy cells is done accordingly.

It should be pointed out that the present formulation and implementation include intrinsically the nonlinear interactions between the time-averaged flow and unsteady parts as well as those among various unsteady disturbances and harmonics (i.e., the cross-coupling effects).

A particular issue arises here regarding how to update the Fourier coefficients for multiple disturbances as each row has two disturbances for the case of rotor-stator interaction with rotor in vibration. A beating period, which is the minimal common multiple of all the disturbances' periods, could be much longer than the period of each disturbance. Therefore, if we only update the coefficients once every beating period, the solution would have a very slow convergence rate for situations with very low beating frequencies. In order to avoid this difficulty and to update the

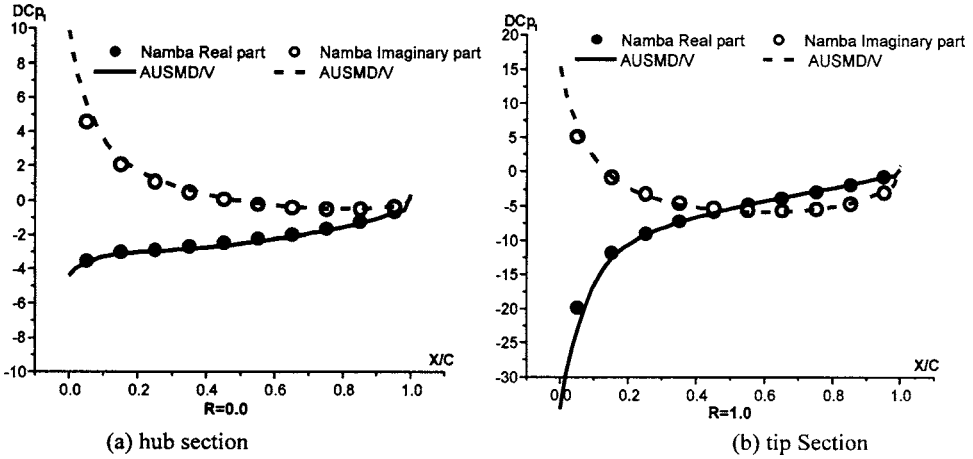

Fig. 2 First-harmonic pressure jump coefficient distribution (Namba case) (AUSMD/V: upwind scheme, Namba: semi-analytical solution)

Fourier coefficients as frequently as possible, we adopt a partial-substitution technique [10]. That is, the coefficients are evaluated through the following formula:

$$A_{ni} = \frac{\omega_i}{\pi}\sum_{1}^{N_{pt}} (U - R_i)\sin(n\omega_i t)\Delta t$$

$$B_{ni} = \frac{\omega_i}{\pi}\sum_{1}^{N_{pt}} (U - R_i)\cos(n\omega_i t)\Delta t \tag{6}$$

where $R_i = \Sigma_{j\neq i}^{N_{pt}}\Sigma_{n=1}^{N_{\mathrm{Fou}}}[A_{nj}\sin(n\omega_j t) + B_{nj}\cos(n\omega_j t)]$ is the unsteady contribution of all disturbances except that from the ith disturbance. For each unsteady disturbance, new values of the coefficients as well as the time-averaged part can be obtained after one period of the disturbance under consideration, when the partial-substitution (Eq. (6)) is used. At a rotor/stator interface, two "buffer" whole-annulus planes are introduced to make the implementation easier. Consequently, the interface treatment task is broken down into two subtasks. The first one is to reconstruct whole-annulus buffers (as shown in Fig. 1) from the single-passage information on each side of the interface according to the phase-shift periodicity. For a rotor-stator configuration with the rotor in vibration, the interface treatment needs to include all physical unsteadiness of interest. On the left side (rotor side) of the interface, the harmonics corresponding to vibration and downstream potential effects are used for reconstructing the whole annulus instantaneous buffer. On the right side (stator side) of the interface, unsteadiness corresponding to the rotor wake and that of the vibration with a frequency shift (due to the Doppler effect) have to be included. The reconstruction can be made according to Eq. (7).

$$U(y,t,np) = U_0(y,1) + \sum_{i=1}^{N_{pt}}\sum_{n=1}^{N_{\mathrm{Fou}}}\begin{bmatrix} A_{ni}\sin\{n[\omega_i t + (np-1)\sigma_i]\} \\ + B_{ni}\cos\{n[\omega_i t + (np-1)\sigma_i]\}\end{bmatrix} \tag{7}$$

The second step is to correct the flow field across the interface. Although the instantaneous relative position between the single rotor passage and the single stator passage is different due to the rotor rotation, we still can find the corresponding dummy cell of each real passage as we now have the reconstructed whole annulus buffers. Thus a direct interpolation can be applied across the interface as if we were solving a multi-passage/whole annulus domain.

3 Baseline Validation

The developed unsteady flow solver has been validated against the Namba case [13], which has semi-analytical solution. It is a linear flat plate cascade oscillating in a 3D torsion mode. The reduced frequency of vibration is one based on the inlet velocity and chord length. The same geometry and flow parameters as [13,14] are used in the current simulation with a mesh density of $81\times25\times21$ in the streamwise, pitchwise and spanwise directions respectively.

Calculated first-harmonic pressure jump coefficients (ΔCP) on the hub and tip sections for an inter-blade phase angle $\sigma=180$ deg is plotted in Fig. 2, which shows a precise agreement between the current single-passage solution and Namba's semianalytical results. It is observed that the solution accuracy has been substantially improved by using the upwind scheme AUSMD/V compared to a central difference scheme.

4 Stage Interaction With Rotor Vibration

4.1 Matching of Operation Condition. The test configuration is a transonic compressor stage known as ECL compressor tested by Ecole Centrale de LYON. The original configuration has three-rows, IGV (inlet guide vane) followed by a rotor and a stator. The compressor has 33 IGV blades, 57 rotor blades, and 58 stator blades, and it operates at a rotation speed of 11,040 RPM. Figure 3 shows the mesh distribution in the meridional plane. More detailed information about the test rig and flow conditions can be found in [15]. The reason for choosing this case is that it has a large portion of constant radius duct between the rotor and the stator which is desired for investigating gap efects.

A steady calculation was conducted first to match the operation condition. Figure 4 shows the comparison of static pressure dis-

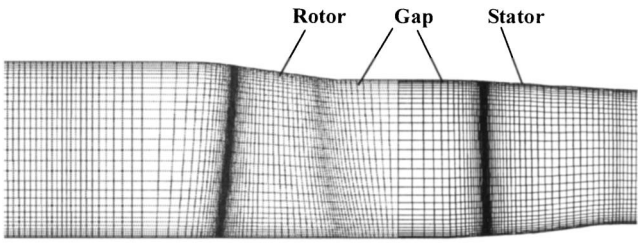

Fig. 3 Computational mesh on the meridional plane (ECLcompressor)

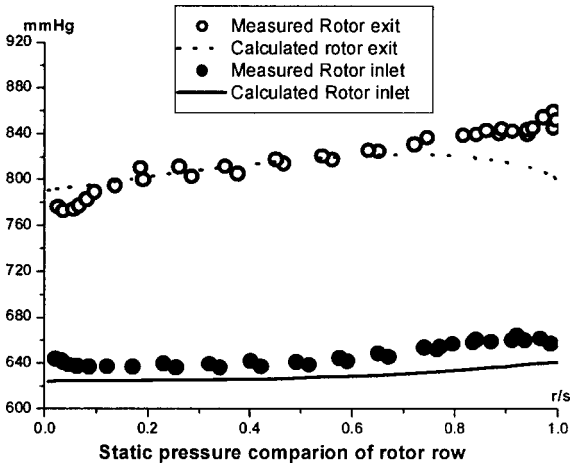

Fig. 4 Comparison of static pressure distributions at inlet and exit of the rotor row

tribution at the inlet and the exit of the rotor row. Although it is not a perfect match, it shows that the current simulated flow condition is fairly close to the experimental condition. The flow condition has also been confirmed by the solution from our previous central difference solver (as shown in Table 1), which had been extensively validated for steady and unsteady cases [7,12].

4.2 Isolated Rotor in Oscillation. In order to examine the aerodynamic damping characteristics of the realistic 3D blade, blade vibration mode shapes are obtained from finite element (FE) mode analysis using ANSYS. Figure 5 shows the FE mesh distribution, which is obtained from a CFD mesh with a simple modification in the spanwise direction. The corresponding first torsion mode shape (applied in following investigations) is shown in Fig. 6 with the largest displacement occurring at tip leading edge and

Table 1 Steady flow conditions verification (3D ECL compressor)

	Mass flow rate (kg/s)	Pressure ratio	Efficiency
TF3D (He, 2000)	16.2	1.387	0.863
AUSM (Present)	16.34	1.377	0.8601

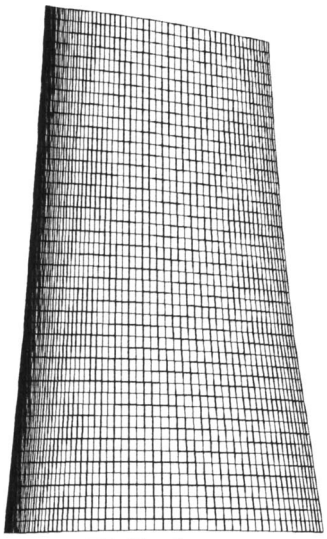

Fig. 5 FE mesh for mode analysis

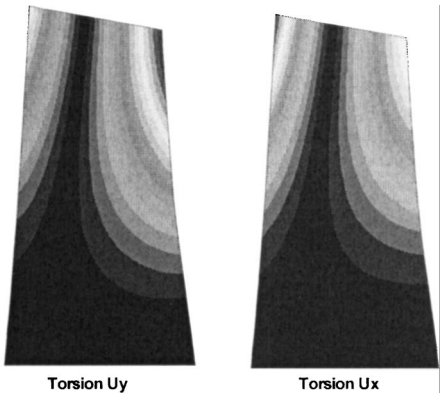

Fig. 6 Vibratory displacement (mode shape) of the first torsion mode

trailing edge area.

First of all, the aerodynamic damping characteristic of the isolated rotor in torsion vibration was examined with different nodal diameters. The results are summarized in Fig. 7, which shows the least stable mode being that of five nodes. To verify the single-passage solution, a 19 passage calculation for the three-node mode, which is very close to the most unstable mode, was performed. The comparison between two solutions is shown in Table 2 (isolated rotor case) with a discrepancy less than 1%.

4.3 Oscillating Rotor in Stage Configuration. For the stage configuration with vibrating rotor blades, a detailed comparative study between the single passage and multiple passage solutions with the reduced blade counts (19 rotor blades and 20 stator blades) was conducted first. Now both rows are subject to two primary disturbances (rotor vibration and rotor/stator blade passing). In addition, the present results show that for the stator row, one dominant subharmonic interaction should be included, and in this case the subharmonic component with a frequency being the difference between the rotor passing and the rotor vibration, was also included. For the convenience of carrying out multiple passage calculations, the vibration frequency was slightly modified so that it can beat with the stator passing frequency in every four

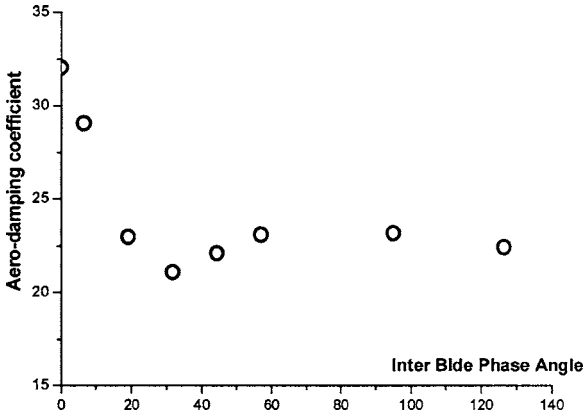

Fig. 7 Aerodamping coefficients of an isolate vibrating rotor

Table 2 Aerodynamic damping coefficient prediction (3D ECL compressor)

Gap distance	0.56 rotor tip chord	1.0 rotor tip chord	Infinity (Isolated Rotor)
MP Solution	19.9	32.94	23.07
SP Solution	20.4	34.90	23.02

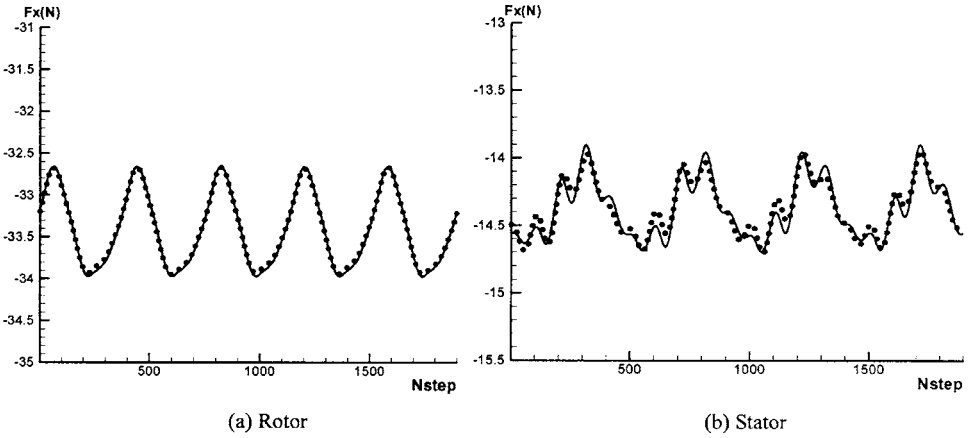

(a) Rotor (b) Stator

Fig. 8 Comparison of axial unsteady force time histories on rotor (in vibration) and stator blades (●Single passage solution, —Multipassage solution)

rotor revolutions.

Figure 8 shows the unsteady axial forces on both rotor and stator blades predicted by the single passage solution with comparison to a direct multipassage solution. An excellent agreement has been achieved on the rotor blade, but on the stator blade the single-passage solution gives some discrepancies, though still relatively small, from the multiple-passage result. The difference in some sub-peaks implies that the stator is subject to more complicated disturbances than the rotor. The rotor blades are subject to vibration effects and the potential influence from the downstream stator, while the stator blades are primarily influenced by the rotor wakes and the rotor vibration effect with a frequency shift seen in the stator frame. It has been confirmed that the frequency shift is a constant value regardless of the index of stator blades. This is different from the frequency shift of an isolated moving object seen in a stationary frame, where the frequency shift keeps changing. A further spectrum analysis of the unsteady forces from the multipassage solution was performed, and the results in Fig. 9 show that the rotor row is almost entirely dominated by the aforementioned two disturbances and their higher order harmonics. The subharmonic effects on the stator seem to have little influence on the rotor's unsteady response.

Comparative aerodynamic damping predictions at two different gap distances ($56\%C_{\text{tip}}$ and $100\%C_{\text{tip}}$) with blade vibration at a three-node mode were carried out using both single-passage and multipassage methods. The reason for choosing this mode is that it is very close to the least stable mode and this mode enables an affordable multipassage solution (i.e., 19 rotor passages and 20 stator passages) to be performed. Although the rotor aerodynamic damping is largely dependent on the vibration mode nodal diameters (or interblade phase angle) as indicated in Fig. 7, only the least stable modes are of interest to aeromechanical design. Therefore, in this paper, only the three-node mode is investigated. The corresponding aerodamping coefficients are plotted in Fig. 10 and listed in Table 2 as well. The maximum discrepancy between the two methods is less than 6.5%, which confidently demonstrates that the present shape-correction based single-passage method is capable to deal with unsteady phenomena involving two blade rows with multiple disturbances including vibration effects.

Significantly, the results shown in Fig. 10 illustrate a remarkable change of the aero-damping by up to 75% between these two gaps, highlighting the need to examine more closely the damping variation with intrarow gaps.

4.4 Rotor Aerodamping With Varying Intrarow Gap. The aerodamping prediction results of two different gaps obtained above confirmed the observation by Silkowski and Hall [3] that the aerodynamic damping of an embedded blade row could be significantly different from the isolated blade row. Furthermore the present results do not seem to suggest a simple conclusion

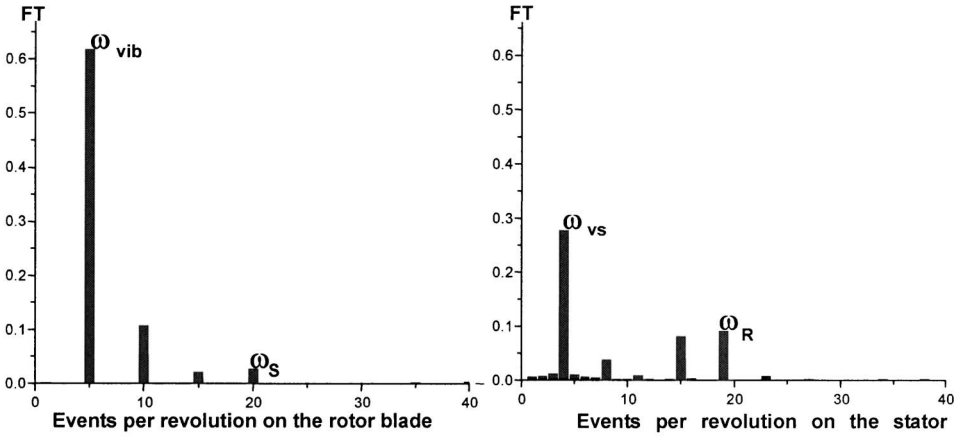

(a) Rotor (b) Stator

Fig. 9 Spectrum of unsteady axial forces on rotor and stator blades (ECL compressor stage, multi-passage solution; ω_{vib} - rotor vibration freq., ω_s - stator blade passing freq., ω_R - rotor blade passing freq, ω_{vs} - rotor vibration frequency shifted in stator frame)

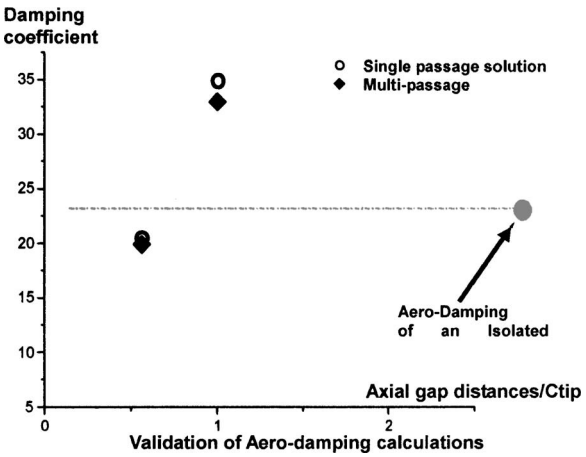

Fig. 10 Validation of aerodamping calculations using the single-passage solver for different rotor-stator gaps (3D ECL compressor, blade counts 19:20)

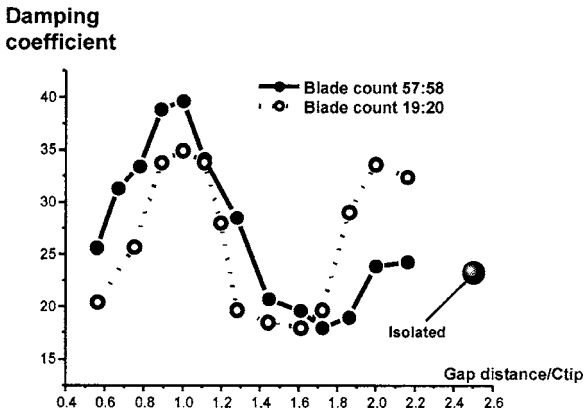

Fig. 11 Rotor aerodynamic damping variation with rotor-stator gap spacing

regarding whether or not the multirow effects would stabilize the blade row under consideration. The aerodamping in the stage configuration with the $100\%\,C_{\text{tip}}$ gap is about 50% higher than that of the isolated rotor, but the $56\%\,C_{\text{tip}}$ case is about 13% lower than that of the isolated one. Given such a wide rang of aerodamping values by varying the axial gap spacing, would it be possible to optimize aeroelastic and aeromechanical stability by adjusting the intrarow gap? To respond to this question, we need to know the relationship between the aerodamping and the gap spacing.

The validity of the current single-passage method as preliminarily demonstrated above for the rotor aerodynamic damping calculations is significant. The substantial saving in computer resources (CPU time and memory) puts it in the right position to carry out parametric studies of the intra-row interaction effect.

The gap effect on the rotor aerodynamic damping has then been investigated by varying the intrarow gap from 0.56 to 2.16 of the rotor tip chord length using the current single-passage method. The minimum gap is limited by the annulus duct section with constant outer and inner radius. For all the calculations, inlet stagnation pressure, stagnation temperature, and outlet static pressure are fixed. It is easier to keep the same back pressure rather than a fixed mass flow for a time-marching solution. Hence the calculations with different intrarow gaps do not warrant the same mean flow condition. The calculated results, however, show only a small variation in mass flow rate in a range of 0.4%. Therefore, it can be assumed that the change of the mean flow conditions and its effects at different gaps should be negligible. The marked influence of the intrarow gap on the aerodamping should thus be predominantly due to unsteady rotor-stator interactions.

From a designer's point of view, it would be very useful to identify any controllable design parameter which may affect this marked intrarow gap effect. Note that, as shown by Silkowski and Hall [3], the multirow interference is highly dependent on the interblade phase angle of the vibration mode. But in practical situations, the least stable interblade phase angle will be picked up automatically when the system goes unstable and is not an easily controllable parameter. In the present work, further calculations were carried out with exactly the same vibration mode shape, frequency, and interblade phase angle, but different rotor-stator blade counts. One case is on the configuration with 57 rotor blades and 60 stator blades. The other is on the original blade counts, i.e., 57 rotor blades and 58 stator blades. When we change the stator blade count, the blade geometry is scaled accordingly so that the overall mean loading on the stator row is more or less the same. The results are summarized in Fig. 11. Both cases show a similar trend of the damping coefficient variation with the gap spacing. The damping value has been significantly changed compared to the isolated vibrating rotor. Apparently there is no monotonic relationship between the aerodynamic damping and the gap spacing.

The difference in the damping-gap curves between two cases with different stator blade counts shows that the stator reflection is important to the seemingly strong intrarow gap effects. By changing the stator blade count from 58 to 60, the rotor-stator interference wavelength has been changed by three times, i.e., from whole annulus to one third of the annulus. But the axial propagating acoustic modes have not been changed for the given rotor configuration. Thus the observation of a strong dependence of the rotor aerodynamic damping on the stator blade count is consistent with that there is a significant influence of the circumferential wavelength on blade unsteady flow response, as revealed for an inlet distortion case [14]. Given the nonmonotonic damping variation with the gap (Fig. 11), the present results indicate that the intrarow gap spacing could be used as an effective design parameter for flutter/forced response optimization. The blade count ratio is also shown to have a marked influence on the damping-gap relationship. These interesting and potentially very significant aspects should certainly be pursued further in the future.

Regarding the CPU time, a speedup by a factor of about 20 has been achieved compared to conventional multiple-passage solutions for the whole annulus assembly (57/58 passages).

5 Concluding Remarks

A 3D Navier-Stokes flow solver based on the single-passage shape-correction method and the upwind discretization has been developed and validated for multiblade row unsteady flows with multiple disturbances. The developed flow solver has been successfully applied to blade vibration problems in a compressor rotor-stator stage configuration. A speed up by a factor up to 20 compared to multipassage solutions has been achieved. It should be mentioned that some on-going work on the single-passage approach has produced encouraging results for three-row configurations.

Parametric studies of the 3D compressor stage by varying the rotor-stator gap spacing show that the rotor aerodamping could be changed by up to 100%. The predicted nonmonotonic damping variation with the gap spacing suggests the existence of an optimum gap regarding of flutter stability and/or forced response stress level. For the cases studied, the aerodamping dependency on the intrarow gap is also shown to be affected by the stator blade count.

Acknowledgment

The authors wish to thank the Engineering and Physical Sciences Research Council (EPSRC), U.K. for sponsoring this work under Grant No. GR/M43821.

Nomenclature

Am = vibration amplitude normalized by chord
C_{dp} = aerodynamic damping coefficient (Worksum/Inlet dynamic head $\cdot \mathrm{Am}^2 \cdot \mathrm{Chord}^3$)
C_{tip} = rotor tip chord length
ΔCP = pressure jump coefficient ($\Delta P_1 / 0.5 \rho_\infty u_\infty^2 A_m$)
F_D, F_V, F_{DV} = discretized flux vector
F_x, F_θ, F_r = inviscid flux vector
Q = vector of conservative variables
$\hat{n}$ = unit cell surface normal vector
R, L = right and left status
S_i = inviscid source term
u_{mg}, v_{mg}, w_{mg} = mesh moving velocity
U = cell surface relative normal velocity
U_A = cell surface absolute normal velocity
U_m = cell surface mesh moving velocity
V_x, V_θ, V_r = viscous flux
σ = interblade phase angle

References

[1] Marshall, J. G., and Imregun, M., 1996, "An Analysis of the Aeroelastic Behavior of a Typical Fan-Blade With Emphasis on the Flutter Mechanism," ASME Paper No. 96-GT-78.

[2] Doi, M., and Alonso, J. J., 2002, "Fluid/Structure Coupled Aeroelastic Computations for Transonic Flows in Turbomachinery," ASME Paper No. GT-2002-30313.

[3] Silkowski, P. D., and Hall, K. C., 1998, "A Coupled Mode Analysis of Unsteady Multistage Flows in Turbomachinery," ASME J. Turbomach. **120**, pp. 410–421.

[4] Smith, L. H., 1969, "Casing Boundary Layers in Multistage Compressors," *Proc. Symposium on Flow Research on Blading*, Brown Boveri & Co Ltd, Baden, Switzerland.

[5] Adamczyk, J. J., 1998, "Wake Mixing in Axial Flow Compressors," ASME Paper No. 98-GT-29.

[6] Venable B. L., Delaney R. A., Busby, J. A., Davis, R. L. Dorney, D. J., Dunn, M. G., Haldeman, C. W., and Abhari, R. S., 1999, "Influence of Vane-Blade Spacing on Trasonic Turbine Stage Aerodynamics, Part 1: Time-Averaged Data and Analysis," ASME J. Turbomach. **121**(4), pp. 663–672

[7] He, L., 2000, "Three-Dimensional Unsteady Navier-Stokes Analysis of Stator-Rotor Interaction in Axial-Flow Turbines," *Proc. Inst. Mech. Eng., Part A, J. of Power and Energy*, 214, pp. 13–22.

[8] Sayma, A. I., Vahdati, M., and Imregun, M, 2000, "An Integrated Nonlinear Approach for Turbomachinery Forced Response Prediction. Part I: Formulation," J. Fluids Struct. **14**(1), pp. 87–101

[9] Silkowski, P. D., Rhie, C. M, Copeland, G. S., Eley, J. A., and Bleeg J. M., 2001, "CFD Investigation of Aeromechanics," ASME Paper No. 2001-GT-0267.

[10] He, L., 1992, "Method of Simulating Unsteady Turbomachinery Flows With Multiple Perturbations," AIAA J. **30**(11), pp. 2730–2735

[11] Wada, Y., and Liou, M-S, 1997, "An Accurate and Robust Flux Splitting Scheme for Shock and Contact Discontinuities." SIAM J. Sci. Comput. (USA), **18**(3), pp. 633–657.

[12] Li, H. D., and He, L., 2001, "Single-Passage Solution of Three-Dimensional Unsteady Flows in a Transonic Fan Rotor." Proc. Inst. Mech. Eng., Part A **215**(A6), pp. 653–662.

[13] He, L., and Denton, J. D., 1994, "Three-Dimensional Time-Marching Inviscid and Viscous Solutions for Unsteady Flows Around Vibrating Blades, ASME J. Turbomach. **116**, pp. 469–476.

[14] Li, H. D., and He, L., 2002, "Single-Passage Analysis of Unsteady Flows Around Vibrating Blades of a Transonic Fan Under Inlet Distortion," ASME J. Turbomach. **124**(2), pp. 285–292.

[15] Leboeuf, F., 1996, "Test Case 1: Transonic Compressor Stage ECL1," Seminar and Workshop on 3D Turbomachinery Flow Prediction IV, January 8–11, Courchevel, France.

Experimental Investigation of the Aerothermal Performance of a High Blockage Rib-Roughened Cooling Channel

Luca Casarsa
Dipartimento di Energetica e Macchine,
University of Udine,
via delle Scienze 208,
33100 Udine, Italy
e-mail: luca.casarsa@uniud.it

Tony Arts
Turbomachinery and Propulsion Department,
von Kármán Institute for Fluid Dynamics,
72, chaussée de Waterloo,
B1640 Rhode Saint Genèse, Belgium
e-mail: arts@vki.ac.be

The present study deals with a detailed experimental investigation of the turbulent flow inside a rib-roughened turbine blade cooling channel. The measurements are carried out in a stationary straight channel with high blockage ribs installed on one wall. The main objective is to enhance the understanding and deepen the analysis of this complex flow field with the help of highly resolved particle image velocimetry measurements. A quasi-three-dimensional view of the flow field is achieved, allowing the identification of the main time-averaged coherent structures. The combined analysis of the present aerodynamic results with available heat transfer data emphasizes the role of the mean and fluctuating flow features in the heat transfer process. In particular, the stream wise/normal to the wall component of the Reynolds stress tensor is shown to be strictly related to the heat transfer rate on the channel surfaces. A correlation to estimate the heat transfer field from the aerodynamic data is presented for the high blockage rib roughened channel flow. [DOI: 10.1115/1.1928933]

Introduction

Nowadays, the continuous demand for a higher performance of aerogas turbine engines necessitates the increase of the operating temperature to improve the thermodynamic efficiency. The turbine entry temperature has continuously been increased over the last decades, and the improvement in cooling techniques has been a major contribution to this.

Several cooling approaches are normally employed in high pressure turbines. In general, turbine blades are cooled by a combination of external film cooling, which limits the heat flux from the combustion gases, and internal convection and impingement cooling which extracts the heat from the blade material. In the latter case, the key issue is to maintain turbulent flow inside the cooling passage. This is achieved by using turbulence promoters such as rib turbulators, pin fins, dimpled surfaces, or surface roughness. These devices act to increase turbulent mixing through the enhancement of turbulence, generation of secondary flows and, in some cases, production of stream wise oriented structures. All these features provide a larger magnitude of the turbulent transport over wide flow volumes, leading to an effective augmentation of the forced convection process. Unfortunately, together with the augmentation of the heat transfer performance, the total pressure losses also increase, penalizing the engine thermal efficiency. The design of the cooling devices must therefore be optimized and, indeed, a significant portion of the design process of turbine vanes is already devoted to this task. The complexity of the channel geometries and of the three-dimensional, highly turbulent flow behavior makes this task very difficult as well by experimental as by computational (fluid dynamics) approaches.

On the experimental side, spatially resolved heat transfer and aerodynamic data, complemented by the corresponding pressure drop, are needed to better understand the aerothermal performance of the cooling passage. The detailed analysis of the flow structures, together with the heat transfer field, promotes insight into the flow features responsible for the local heat transfer augmentation and supports the development of experimental correlations and numerical models for prediction methods. It is a matter of fact that the combination of aerodynamic and heat transfer measurements on the same channel configuration and with the same boundary conditions seldom appears in the literature, and very often the data are too scarce to provide a complete quantitative description of the flow field.

The present contribution aims at remedying partially this lack of information by providing high resolution flow field measurements which, together with the corresponding wall heat transfer results already available, Çakan [1], constitute a wide and reliable experimental data base on the aerothermal performance of a high blockage rib-roughened cooling channel.

Past experiments on turbine blade internal cooling have focused on the flows within simple channels, analyzing the effect of the turbulator geometrical characteristics (such as rib shape, angle of attack, and pitch-to-height ratio) on the heat transfer distribution, Han et al. [2,3], Taslim and Wadsworth [4]. Other investigations also considered the variation of the channel aspect ratio, Han and Park [5] and Ligrani et al. [6]. More recently, thanks to the maturation of modern optical techniques, detailed aerodynamic measurements by means of laser Doppler velocimetry (LDV) in turbine cooling channels were performed by Liou and Wu [7], Servouze et al. [8], Roclawski et al. [9], Schabacker et al. [10], or Chanteloup and Boelcs [11]. Numerical simulations of the velocity and heat transfer fields were reported by Liou et al. [12], Rigby [13], and Sagaut [14]. Many other contributions are available in the open literature. Rather complete reviews of this experimental and numerical research work were provided by Han et al. [15], Ligrani et al. [6], and Iacovides and Raisee [16].

The present experimental study was carried out by using a large scale facility representative of a stationary straight cooling channel of a high pressure turbine nozzle blade. Its size allowed detailed spatially resolved aerodynamic measurements by means of the particle image velocimetry (PIV) technique. The channel has ribs installed on one wall. Earlier experiments on a similar geometry, but with a smaller blockage ratio (10%), were carried out by Rau et al. [17], using a LDV technique, with a limited spatial resolution. The present configuration, somewhat simplified with respect to the usual coolant passages with two opposite rib-

Contributed by the Turbomachinery Division of THE AMERICAN SOCIETY OF MECHANICAL ENGINEERS for publication in the JOURNAL OF TURBOMACHINERY. Manuscript received by the ASME Turbomachinery Division January 19, 2004; final revision received January 10, 2005. Associate Editor: R. S. Bunker.

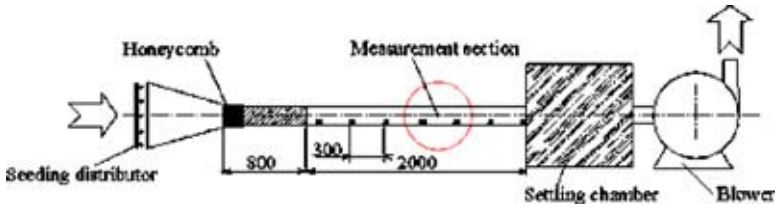

Fig. 1 Test section

roughened walls, is justified by the definite advantage of providing full optical access for PIV and heat transfer measurements with a much higher spatial resolution.

A global three-dimensional view of the velocity field is provided by applying a two-dimensional (2D) PIV technique in between two consecutive ribs along different and mutually perpendicular planes. The analysis of the detailed PIV data allows a very exhaustive description of the three-dimensional flow structures and of a number of specific flow features. The combination of the aerodynamic and the already available heat transfer data emphasizes the role of the mean flow features in the heat transfer process. The stream wise/normal to the wall component of the Reynolds stress tensor is shown to be strongly related to the heat transfer distribution.

Experimental Apparatus

A sketch of the wind tunnel used for this investigation is presented in Fig. 1. It models a straight cooling channel of a stationary turbine blade. A good optical access to apply the PIV technique and a high spatial resolution were two major requirements for this investigation. The channel was therefore characterized by a square cross section (100×100 mm) and a length of 2800 mm. The measurement section was made of 6 mm thick glass walls while the entrance section was made of wood. Seven ribs were installed on one wall of the channel. The rib cross section was 30×30 mm, providing a blockage ratio of 30%; the ribs were inclined at 90 deg to the channel axis direction. The rib pitch-to-height ratio (p/h) was equal to 10 and all the measurements were performed between the fourth and the fifth ribs, where, as reported in the literature and experimentally checked by comparing results on successive rib spacings, a mean periodicity was reached in flow and heat transfer characteristics. The ribs were made of Plexiglas, except for the fourth and fifth ribs made of polished brass in order to reflect the incident laser light and avoid light scattering spoiling the measurement quality in the near wall vicinity. Finally, the fifth rib could be replaced by a transparent one for the near wall secondary flow measurements. The optical access was ensured by a mirror inclined at 45 deg within the rib. The channel was operated at room temperature, without heating the walls as was done in previous experiments to simulate the heat transfer process on the same configuration (Çakan [1], Casarsa et al. [18]). Since the selected Reynolds number is typical of a fully turbulent flow, the natural convection process does not play any significant role on the development of the flow field. Therefore, the present results can truly be considered as the necessary complement to the wall heat transfer distributions from Çakan [1].

Air at atmospheric pressure and temperature was ducted through the test section by means of a centrifugal blower. The flow rate was quantified and controlled by measuring the inlet velocity profile and the wall static pressure. The channel was operated at a Reynolds number (based on hydraulic diameter and bulk velocity) equal to $4\cdot10^4$, in order to correctly simulate the flow existing in a real cooling channel.

A two-dimensional PIV technique was used to quantify the flow field characteristics. The measurement chain was made of a two-cavity laser by BMI, a produced by PCO, digital camera with a resolution of 1024 pixels $\times$ 1280 pixels and the related acquisition system. Different lenses were mounted on the camera, depending on the required spatial resolution. A resolution of 18,000 pixels/m was achieved by means of a 105 mm focal length lens, while a higher value of 35,000 pixels/m (to resolve the smallest flow structures) was obtained with a 35 mm focal length lens. The camera and the laser were synchronized by means of a Stanford signal generator. The camera was working at its maximum frequency, 4.1 Hz, the laser was operated at twice this value. Two lenses were used to provide the required laser sheet, namely, a cylindrical lens with a focal length equal to -19 mm and a spherical lens with a 130 mm focal length to adjust the laser sheet thickness (about 1.5 mm). To avoid the out of plane motion of the seeding particles due to the strongly three-dimensional flow, and to guarantee a sufficiently large displacement of the tracer pairs (large enough to be correctly detected by the PIV software) the best combination was found between the laser sheet thickness and the separation time between the two laser pulses. The final values used were 35 μs for the normal magnification regions and 15 μs for the high resolution region on top of the rib. This led to an average particle displacement of about seven pixels, which was correctly resolved by the processing software (whose accuracy was proved to be up to 0.01 pixels, Scarano and Riethmuller [19]) and also met the $\frac{1}{4}$ rule for the definition of the correct interrogation window size. More details about the processing parameters are provided in the PIV data analysis section.

The seeding was provided by oil evaporation using a Laskin nozzle type seeding generator developed at von Kármán Institute (Rhode Saint Genèse, Belgium) (VKI). The particle sizes ranged between 0.5 and 2 μm. This size of particles is well suited for low Mach number flows as demonstrated by Mayers [20]. The comparison of the present PIV data with earlier LDV and hot-wire (HW) data taken at VKI (not reported in the present paper) is also very good, demonstrating the reliability of the present approach.

Inlet Conditions

The inlet velocity and turbulence intensity profiles (Fig. 2) were measured at 8 D_h (800 mm) downstream of the test section entry by means of a hot-wire anemometer. They were typical of a tur-

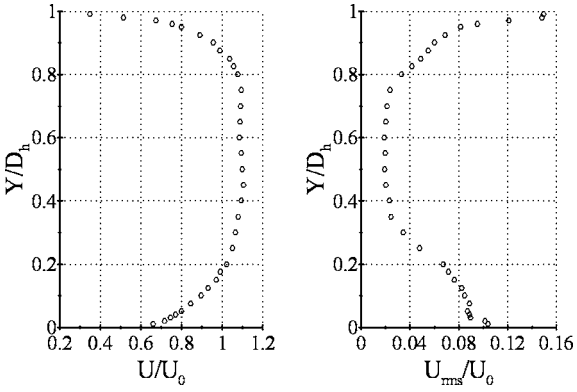

Fig. 2 Mean inlet velocity and stream wise turbulence intensity profiles

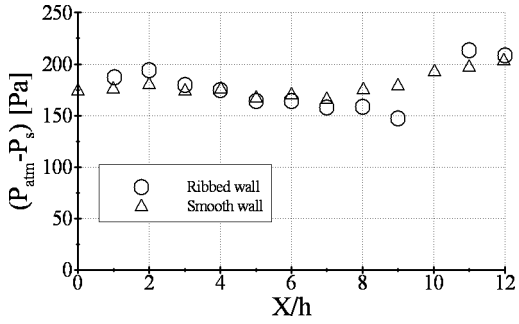

Fig. 3 Wall static pressure distribution

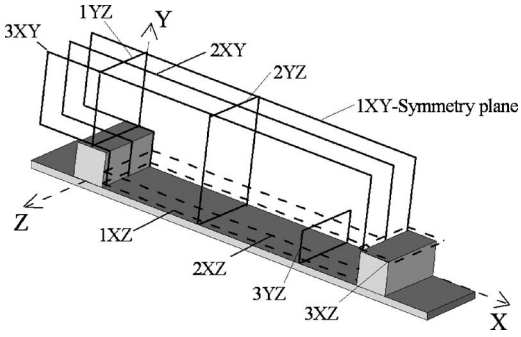

Fig. 5 Measurement planes for PIV

bulent flow, but not completely developed. This resulted from the imposed length ratio between the smooth entry section and the rib-roughened section. Furthermore, the profiles were not fully symmetric. Close to the ribbed wall, lower values of mean velocity and fluctuations were observed than on the opposite smooth wall. This asymmetry was due to the flow separation in front of the first rib which affects the upstream flow region. The measurement plane location was indeed only five rib heights upstream of the first turbulator.

Static Pressure Measurements

An important parameter to be checked in this type of flow field is the pressure drop. It provides the necessary information to define the overall cooling channel performance (heat transfer/friction) in an optimization process. The friction factor f is defined as follows:

$$f = \frac{D_h \Delta p}{2 \Delta l \rho U_0^2}$$

It was computed from the slope of the wall static pressure distributions measured over three rib spacings and made dimensionless by means of the value f_0, which would be measured, for turbulent flow conditions, at the same Reynolds number, in a circular smooth tube (Blasius correlation, based on hydraulic diameter and bulk velocity)

$$f_0 = 0.046\ \mathrm{Re}^{-0.2}$$

The measurements were performed along both the ribbed and opposite smooth walls. The uncertainties on the pressure measurements and friction factor were, respectively, equal to 0.7% and 2.5%. Of course, identical results were obtained in terms of f/f_0. The main difference between the smooth and ribbed wall static pressure distributions was observed at the rib location $X/h=10$, Fig. 3. The obstacle was locally responsible for a large pressure drop across the rib. The opposite wall distribution was also affected because of the high blockage ratio, but in a smoother way. The evolution of the normalized skin friction factor as a function of Reynolds number is presented in Fig. 4 and shows rather little

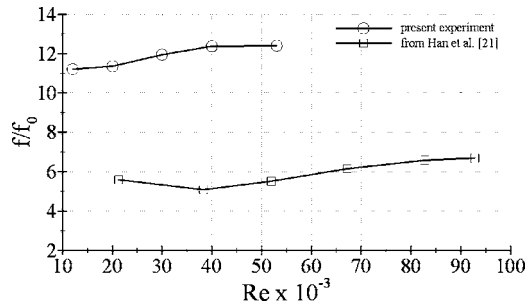

Fig. 4 Friction factor evolution with Reynolds number

variations. The present results extend, in a consistent way, the data base presented by Çakan and Arts [21].

In the same figure, the data are compared with the results obtained by Han et al. [22] on a similar geometry characterized by a smaller blockage ratio (6.25%) than the present one (30%). Despite this large difference in the two experiments, which justifies the larger friction in the present case, the same general trend is observed.

PIV Measurement Stations and Data Analysis

The PIV measurements were performed in nine different planes (Fig. 5). The first one is the symmetry plane ($1xy$), located at $Z/D_h=0$. Two additional planes ($2xy$) and ($3xy$), parallel to ($1xy$), were located toward the lateral wall at $Z/D_h=0.3$ and $Z/D_h=0.45$. Three measurement planes were parallel to the rib-roughened wall, at $Y/h=0.05$ ($1xz$), at midrib height $Y/h=0.5$ ($2xz$), and just above the rib $Y/h=1.1$ ($3xz$). Finally, three (yz) planes, selected in an attempt to measure the secondary flows, were located in the middle of the rib upper surface $X/h=0$ ($1yz$) at $X/h=4.3$ ($2yz$) and at $X/h=8$ ($3yz$). The selection of these measurement planes was partially based on the LDV results presented by Rau et al. [17] and allowed a very detailed, quasi-3D view of the whole inter-rib flow field.

To maximize the spatial resolution, each of these planes was divided into four or five measurement windows. Particular attention was paid to the selection of the experimental parameters for the measurements within the (yz) planes. Indeed, since the mean velocity was a pure cross flow with respect to the measurement planes, the application of a 2D PIV technique can lead to significant measurement errors due to parallax effects and out-of-plane motion of the seeding particles. The geometry of the optical system was checked in order to estimate the particle displacement error due to the parallax effect. Using a long focal distance lens (105 mm), this error was limited to 5% of the instantaneous displacement.

To ensure a correct convergence of the statistical quantities, such as mean and rms velocities, a sufficiently large number of samples is needed. Its evaluation was carried out by adopting the approach proposed by Riethmuller and Lourenco [23], based on an estimation of the maximum level of expected velocity fluctuations. In the present flow field, this maximum level, previously measured by means of hot-wire anemometry, was found in the stream wise velocity component, with values up to 80% of the bulk velocity. Considering such large values and assuming a 95% confidence level, the number of samples to be used quickly rose up to several thousands. Fortunately, only a small portion of the flow field was characterized by such high values (the top-upstream corner of the rib). From the preliminary study, more than 88% of the measurement points presented a level of fluctuations below 40%. Therefore, 300 samples appeared to be a reasonable choice, sufficient to yield a time-averaged flow field with a limited error on the mean velocity ($<5\%$) and its rms value ($<10\%$)

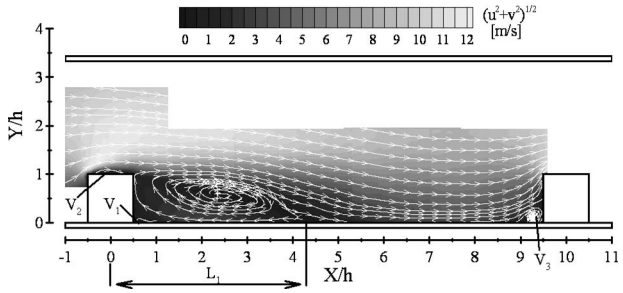

Fig. 6 Time averaged velocity field in plane 1*xy*

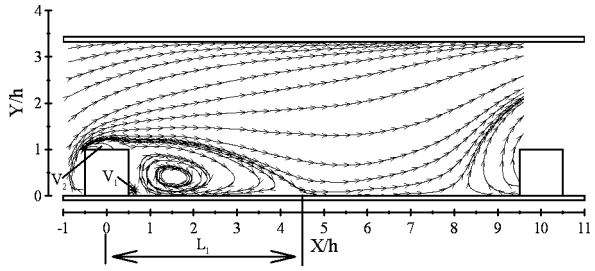

Fig. 7 Stream tracers visualization of the time averaged velocity field in plane 3*xy*

over the complete measurement domain, except for a small portion on top of the rib and in the core of the shear layer. To confirm this assumption, an ensemble average of the acquired velocity fields was performed in the region on top of the rib in plane ($1xy$), for different numbers of samples (from 100 up to 1000). The resulting mean flow patterns and turbulent correlations were found to be practically identical when more than 200 samples were used.

All PIV images were processed using W.I.D.I.M., a software developed at VKI by Scarano and Riethmuller [19,24]. All the data were processed using a 48×48 pixels first interrogation window, one single step of window size refinement, and 50% of window overlapping. Two steps of window distortion were used for each step of the refinement procedure. Finally, a Gaussian peak fitting was adopted to perform the sub-pixel interpolation. With these settings, a minimum of 8820 displacement vectors were defined in each measurement area with a resolution up to 0.03 pixels.

The velocity fluctuations and normal stresses were normalized by the mean bulk velocity U_0(=6.2 m/s). Using the Kline and Mc Clintock [25] analysis, the uncertainty on the instantaneous velocity was estimated to be below 2%.

Discussion

Time Averaged Flow Field. The time averaged velocity field in the symmetry plane ($1xy$) is presented in Fig. 6.

This result, supported by the wall static pressure distributions, shows how the obstacle, by reducing the available cross section, induces a strong acceleration of the flow. The sudden expansion downstream of the rib and the consequent flow separation lead to the appearance of a strong shear layer and a wide recirculation region which, from a time average point of view, appears as an organized swirling flow structure. After reattachment, a new boundary layer develops. It is accelerated by the free stream shear forces until it impinges on the next obstacle generating a second recirculation area (V_3). Two additional separated flow regions are finally identified. The first one is located on top of the rib (V_2) while the second one is a small counter-rotating corner vortex in the downstream bottom edge of the obstacle (V_1). High spatial resolution measurements were performed to define the size and the location of structures V_1 and V_3. These results were reported in a previous paper by Casarsa et al. [18]. A similar description of the mean flow field is found in plane ($2xy$). The data are not reported here because of a lack of space but are nevertheless available.

It is important to keep in mind that these results represent a time-averaged flow field, obtained from 300 instantaneous measurements. A further analysis about the eduction of coherent structures by means of a wavelet analysis on each instantaneous flow field, demonstrated the real existence of the structures V_2 and V_3, Casarsa and Arts [26]. This may justify the particular heat transfer field features which develop in these areas and which will be described later.

Figure 7 shows the stream tracers in plane ($3xy$) (Z/D_h=0.45). Very close to the lateral wall, the time-averaged reattachment point appears more downstream than in plane ($1xy$): X/h=4.5 instead of 4.3.

This behavior is confirmed by the results obtained in plane ($1xz$) (Y/h=0.05) (Fig. 8). The reattachment line L_1 is clearly visible. Near the lateral wall, it exhibits a particular shape, resulting from the side wall boundary layer deviation imposed by the rib. The explanation and a model describing the development of this flow feature was provided in a previous paper, Casarsa et al. [18]. In the plane ($1xz$), the entrained mean flow generally moves toward the centerline in the reattachment line vicinity and toward the lateral wall in the rib vicinity. This is in agreement with the static pressure measurements by Rau et al. [17]. In front of the rib, the separation line L_2, associated to the structure V_3, is also well defined and all the stream tracers clearly spiral around a sink (structure S_2). The same behavior is observed downstream of the rib, structure S_1. Both S_1 and S_2 are also identified in plane ($2xz$), Fig. 9. The location and size of these two mean flow features were documented by Casarsa et al. [18].

Above the rib (plane $3xz$) (Fig. 10), the flow is characterized by the separation structure V_2, as previously observed within the symmetry plane data. The structure V_2 grows while moving toward the lateral walls, in accordance with the data in the vertical (xy) planes. Around the corners between the rib edges and the lateral wall, the stream tracer patterns indicate how the mean flow is entrained by S_1 and S_2 which evidently are still present at that channel height. The combination of all the small structures around the rib (V_1, V_2, V_3, S_1, and S_2) sustains the three-dimensional separation surface around the obstacle and confirms the flow model

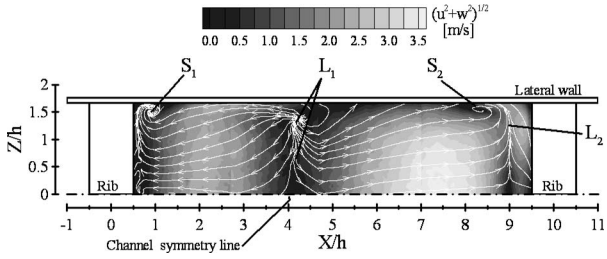

Fig. 8 Time averaged velocity field in plane 1*xz*

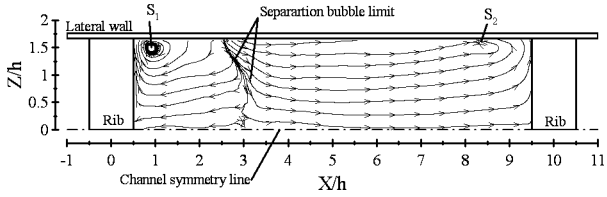

Fig. 9 Stream tracers visualization of the time averaged velocity field in plane 2*xz*

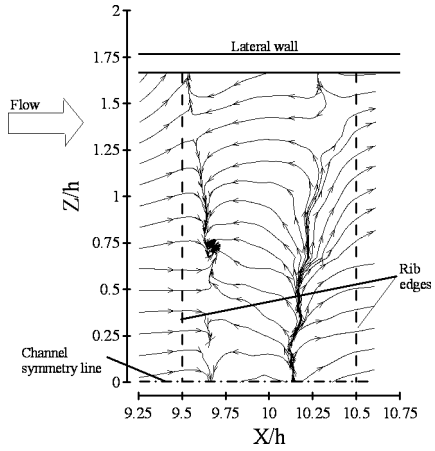

Fig. 10 Stream tracers visualization of the time averaged velocity field in plane 3*xz*

proposed by Rau et al. [17].

In plane (3*xy*), the time averaged recirculation area V_3 is not detected anymore in front of the rib. It is replaced by a strong upward flow motion (Fig. 7). This is explained by the flow accumulation in the corner between the rib and lateral wall (structure S_2), convected upward by the interaction with secondary flows. In the present configuration, the Reynolds stress induced secondary flows are made of two counter-rotating vortex cells in each half cross section of the channel, Hirota [27], with a downward motion along the channel symmetry plane. The visualization of these structures within planes (1*yz*) and (2*yz*) is shown in Fig. 11.

In plane (1*yz*), above the rib, the stream tracers path shows the recirculation bubble V_2. In the central bottom part of the same plane, the flow moves upward because of the strong deviation imposed by the rib, consistently with the results in the (*xy*) planes and in opposition with the flow motion induced by the secondary flows. At the reattachment of the main bubble (plane 2*yz*, Fig. 11), the centers of the mean secondary vortices appear at the same channel height but closer to the lateral walls when compared with the results on top of the rib. This behavior is justified by the expansion-diffusion process in the flow. On the bottom wall, the stream tracers path confirms the transverse flow motion observed in plane (1*xz*).

Stream wise and vertical velocity profiles were extracted on top ($X/h=0$) and upstream ($X/h=8$) of the rib (Fig. 12). They clearly show the effect of the secondary flow vortex cells. The magnitude of the stream wise velocity component (U) reduces while moving from (1*xy*) to (3*xy*). This is due to the effect of the boundary layer development along the smooth lateral wall. The vertical velocity component (V) profiles indicate the effect of the secondary flows: a positive value of V (upward motion from the ribbed surface of the channel) appears while moving from the channel symmetry plane toward the lateral wall.

At this point of the discussion it should be clear that the present rib-roughened channel flow is characterized by a number of structures mostly visible in the mean flow field. All these features contribute to the establishment and sustainment of a complicated 3D flow structure covering the whole inter-rib space. However, inside the 3D flow, the main contribution to the flow renewal on the channel walls, and hence to the augmented heat transfer performance, comes from the secondary flows and the transverse flow motion on the ribbed surface. Their combined effect is indeed to bring the hot flow entrained in the lower layers between the ribs toward the lateral walls and then into the free stream, replacing it with cold flow from the main stream.

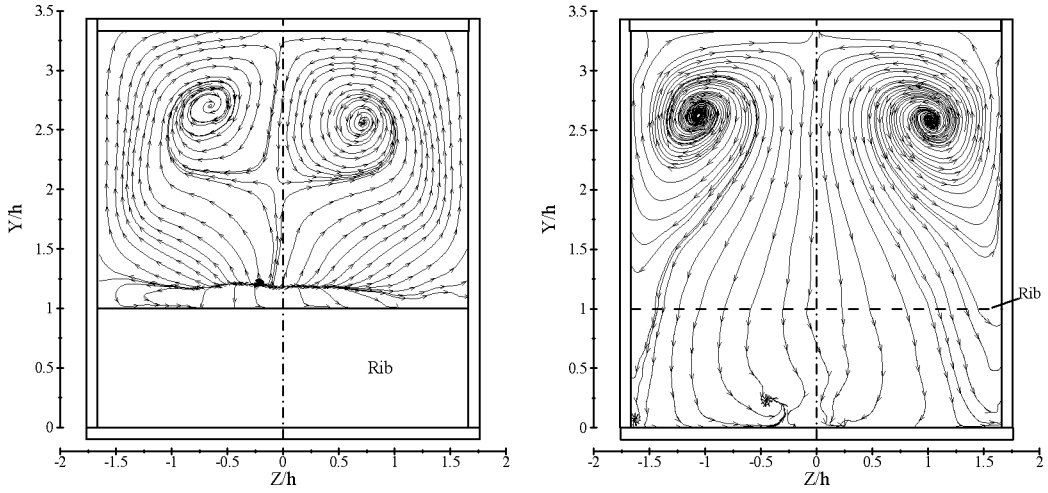

Fig. 11 Time averaged flow field in plane 1*yz* (left) and 2*yz* (right)

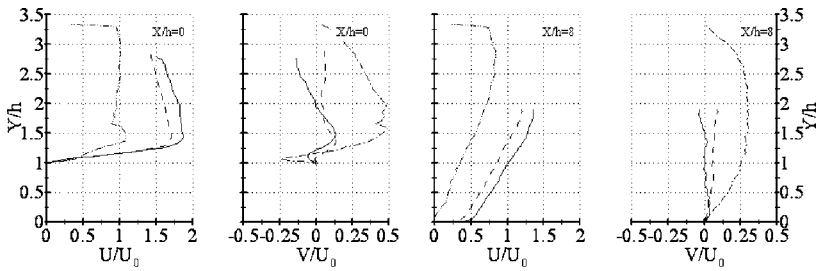

Fig. 12 Stream wise and vertical velocity distributions form planes ——1*xy*, – – – – 2*xy*, and – · – · – 3*xy*

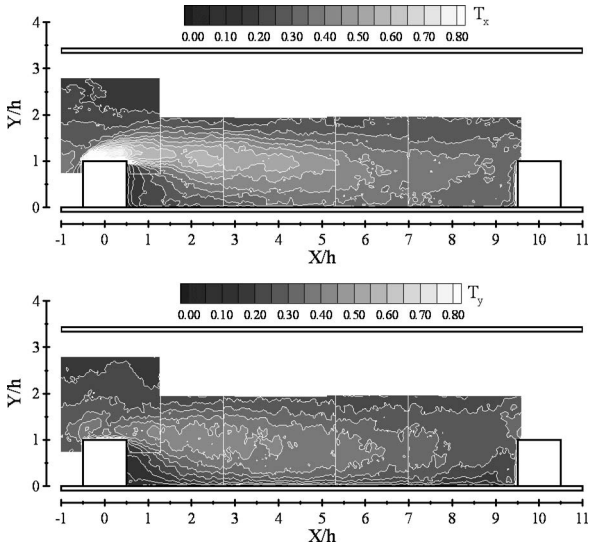

Fig. 13 Stream wise ($T_x=\sqrt{\overline{u'^2}}/U_0$, top) and vertical ($T_y=\sqrt{\overline{v'^2}}/U_0$, bottom) velocity fluctuations in plane 1*xy*

The generation of turbulence is due to the periodic flow acceleration-deceleration and separation processes. The highest turbulence values are found on top of the obstacle. This can be observed in the contour plots of the stream wise (T_x) and vertical (T_y) turbulence intensity in plane ($1xy$), Fig. 13.

The flow, behind the obstacle, separates from the rib upper surface and generates a strong shear layer, Fig. 14. Locally, the highest values for both T_x and T_y are observed within the shear layer, Fig. 13. The stream wise velocity fluctuations are generally much higher than the vertical ones, especially in the region of maximum strength of the shear layer ($0<X/h<4.5$). Significant negative values of ($u'v'$) Reynolds stresses (T_{xy} in Fig. 14) are reported in a small flow region above the upstream top corner of the rib. This behavior is due to the strong local acceleration of the flow along a preferential direction (about 35 deg), showing correlated fluctuations in the stream wise and vertical velocity components (u' and v' are both either positive or negative or, in other words, the product $u'v'$ is always positive). If, in this region, the fluctuations u' and v' were computed in a reference system whose X axis was aligned with the mean flow direction, the resulting Reynolds stresses would be positive, as normally expected.

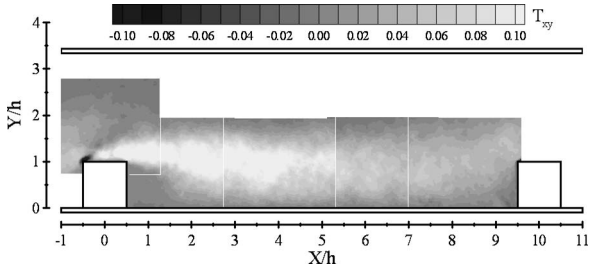

Fig. 14 Reynolds stresses ($T_{xy}=-\overline{u'v'}/U_0^2$) in plane 1*xy*

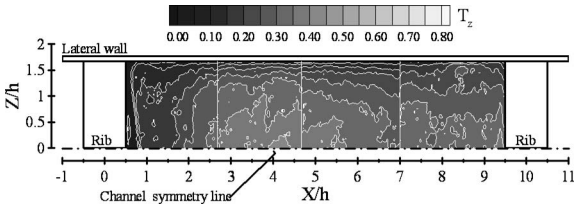

Fig. 15 Span wise velocity fluctuations ($T_z=\sqrt{\overline{w'^2}}/U_0$) in plane 1*xz*

Similar turbulence fields are observed within planes ($2xy$) and ($3xy$). However, their magnitude is generally weaker than in plane ($1xy$) because of the lateral wall boundary layer effect.

On the bottom wall (Fig. 15) high values of the span wise turbulence activity (T_z) are found around the reattachment point ($2.5<X/h<6.0$) and in a small region in front of the rib ($8.0<X/h<9.5$), where the flow turns toward the lateral wall. The stream wise fluctuations (not reported because of a lack of space) are found to be very weak when compared to the span wise component.

Within the plane ($1yz$), above the rib, the highest fluctuating values are observed near the lateral wall (Fig. 16), according to the mean flow behavior observed in the (xy) planes. Close to the upper rib surface, high activity in both vertical and span wise direction is observed inside the separated flow region V_2, remaining however much weaker than the stream wise fluctuations.

At the reattachment point and sufficiently far away from the ribbed surface, the turbulence anisotropy seems to be milder (Fig. 17). Components T_y and T_z, measured in plane ($2yz$), show a similar magnitude all over this cross section and are comparable with the values of T_x measured in plane ($2xz$) (not reported by

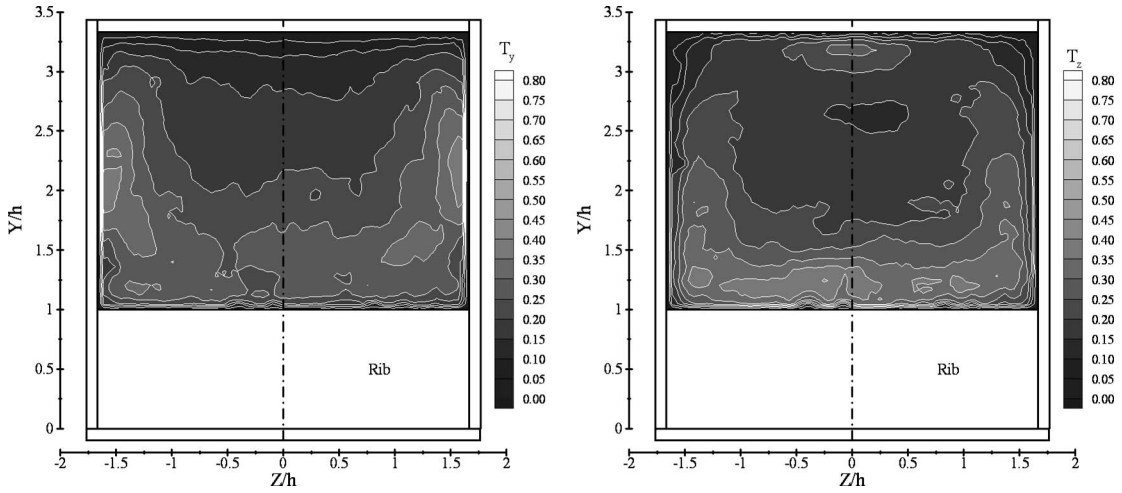

Fig. 16 Vertical (T_y) and span wise (T_z) velocity fluctuations in plane 1*yz*

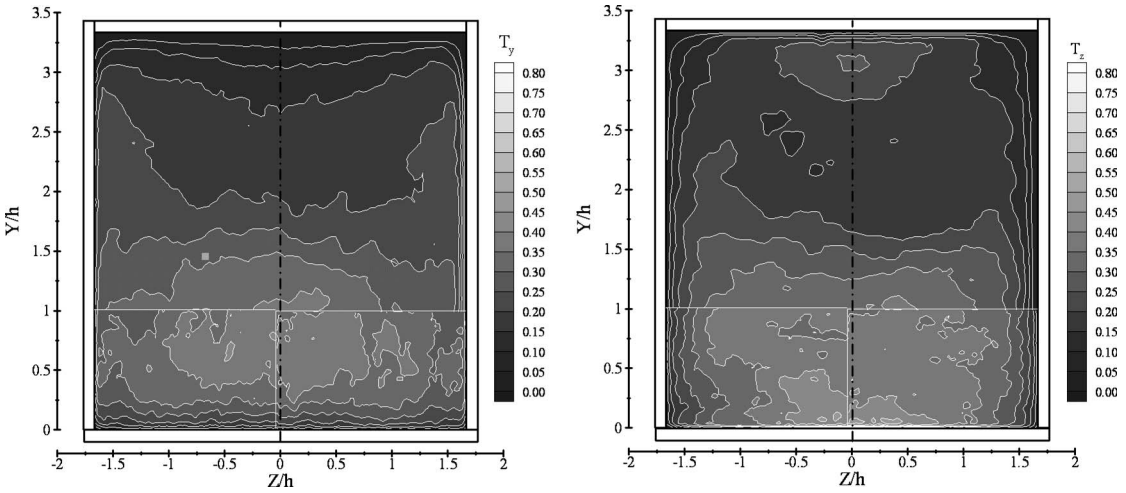

Fig. 17 Vertical (T_y) and span wise (T_z) velocity fluctuations in plane 2*yz*

lack of space) and within the (xy) planes.

From the analysis of the present data, it can be concluded that the turbulence anisotropy dominates the entire flow field. In particular, along the longitudinal planes (xy), the turbulence anisotropy weakens in the free stream and then recovers in favor of the stream wise fluctuations inside the separated shear layer. Moving further toward the ribbed wall, the span wise velocity fluctuations prevail over the other two components, especially at the reattachment location and in front of the obstacle. These results demonstrate once more the need for advanced turbulence modeling of the present type of flow which proved to be still a challenging task in modern computational fluid dynamics (CFD). Indeed, it is the experience of the present authors that the use of standard k-ε turbulence models does not lead to accurate predictions of both the flow and heat transfer fields, Casarsa [28]. The use of more advanced modeling approaches, including large eddy simulation (LES), which consider the anisotropic character of the near wall velocity fluctuations, proved to be quite effective for this kind of application, Durbin [29], Hermanson et al. [30].

Aerothermal Comparison. Çakan [1] carried out an exhaustive measurement campaign to determine the heat transfer distribution along the various walls, including the ribs, of the same channel by means of liquid crystal thermography. By combining his data and the present detailed PIV measurements, some interesting observations on the aerothermal flow behavior can be made. An early analysis of the present data, Casarsa et al. [18], showed a strong correlation between high levels of heat transfer and velocity fluctuations normal to the wall. However, this correlation did not seem to be unique in all flow regions. As a matter of fact, mainly on top of the rib, all the velocity component fluctuations appeared to be correlated with the heat transfer data. To solve this ambiguity, other choices were investigated to look for a more general correlation. The Reynolds stresses computed with normal to the wall velocity components were therefore considered, because they are closely related to the wall events which are effective on the heat transfer, such as ejection, sweep, out-, and inward events. A review paper by Jacobi and Sahah [31] on the use of longitudinal vortices to enhance the performance of heat exchangers shows how the analogy between momentum and heat transport is still valid if properly formulated. The interaction of stream wise vortical structures in the near wall regions induces flow mechanisms such as ejection, sweep, and out-, and inward events which cause high rates of flow renewal and therefore lead to heat transfer enhancement. The same mechanisms are responsible for the generation of Reynolds stresses in the stream wise/normal to the wall direction [31]. By running a direct numerical simulation code in a channel configuration similar to the present one but equipped with smaller turbulators, Sagaut [14] found out that horse-shoe type vortices are generated on the rib trailing edge. These structures then detach from the obstacle, are transported downstream by the free stream, and are stretched along the stream wise direction. In this way, stream wise vorticity is generated, especially near the ribbed and smooth walls.

On the basis of these considerations, the authors decided to investigate if, in the present flow configuration, the structures detected by Sagaut [14] were responsible for the development of the heat transfer field as suggested by Jacobi and Sahah [31]. The analysis was carried out by a careful and critical comparison of the heat transfer data with the Reynolds stress tensor components extracted from the PIV results.

The distributions of the stream wise/vertical and stream wise/span wise Reynolds stresses along the symmetry line very close to the ribbed wall (Y/h=0.05) were compared to the wall heat transfer (Fig. 18, left). Both the Nusselt number and the Reynolds stresses are normalized with the corresponding values for a smooth channel at the same Reynolds number (Nu_0,$\langle u'v'\rangle_0$). The strong correlation of the Reynolds stresses ($u'v'$) with heat transfer is clearly shown, whereas the ($u'w'$) stress fluctuates around 0. The same conclusion cannot be drawn for the data extracted in planes ($2xy$) and ($3xy$), where the strong transverse flows identified in the preceding section are responsible for the ($u'w'$) Reynolds stresses, with magnitude and distribution similar to those of ($u'v'$) [Fig. 18 (right) for ($2xy$)]. The third cross-component of the stress tensor ($v'w'$) does not correlate with the heat transfer field. This is shown in Fig. 19, where the Reynolds stress tensor component ($v'w'$) extracted form the ($2yz$) and ($3yz$) planes at (Y/h=0.05) is compared to the Nu number distribution on the ribbed wall.

In order to determine if a general scaling exists between the stream wise/wall normal Reynolds stresses and the heat transfer, valid for all the channel walls, all the Reynolds stresses and Nusselt number data were represented in Fig. 20 [bottom wall all (xy) planes, top rib surface along the ($1xy$) and ($2xy$) planes, and smooth opposite wall along plane ($3xy$)]. The Reynolds stresses data were taken along the different measurement planes indicated in the figure, at a distance from the wall equal to 0.05 nondimensional units and at a stream wise position were the isolines of the heat transfer field are found (which provide the local Nu number values in the figure) in the data provided by Çakan [1].

A consistent correlation clearly appears in this data set, obtained by a least-squares interpolation. The tendency line predicts

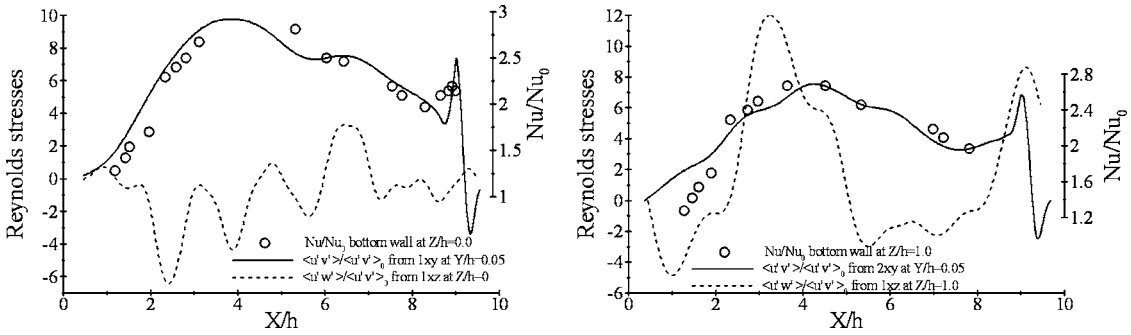

Fig. 18 Comparison between Reynolds stresses and heat transfer (1)

the value for the smooth channel case and shows an asymptotic behavior. The existence of an asymptotic value of the heat transfer rate caused by turbulent mixing sounds very physical: Increasing the turbulent agitation above a certain level has no influence on the transport mechanism.

To strengthen this interpretation, the proposed correlation was used to compute the heat transfer field from the PIV data. The results were then compared with the heat transfer measurements. To perform this kind of analysis, the complete map of the $(u'v')$ Reynolds stress data over the considered channel surface was of course needed. Although this information was not directly available from the measurements, it was possible to reconstruct it from the available data with an acceptable precision. The procedure consisted essentially in a triangulation of the data coming from the different measurement planes, after imposing the appropriate boundary conditions. The description of the entire procedure is available in Casarsa [28].

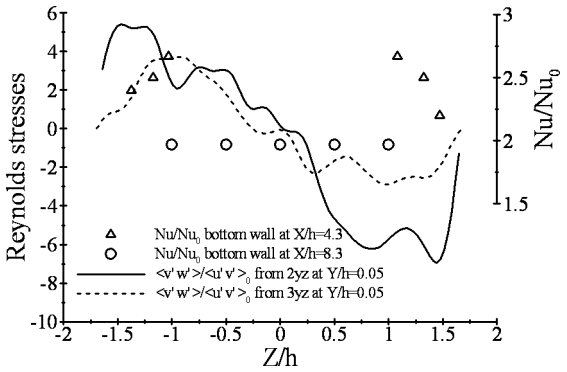

Fig. 19 Comparison between Reynolds stresses and heat transfer (2)

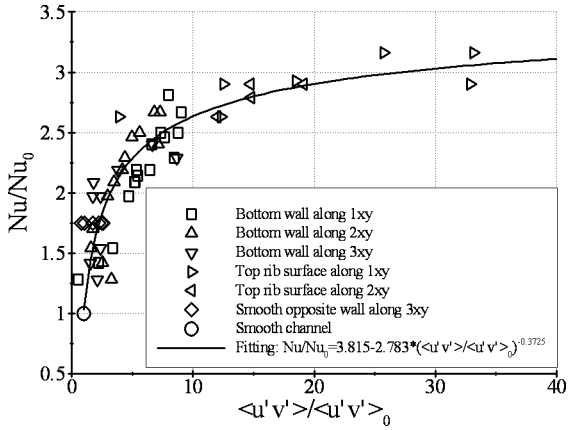

Fig. 20 Correlation between $\langle u'v' \rangle$ Reynolds stresses component and Nu number distribution at different channel location

The result of this comparison on the ribbed surface is shown in Fig. 21. The correlation is able to correctly predict the shape and magnitude of the heat transfer field. However, at the onset of strongly three-dimensional flow mechanisms, the correlation fails since the flow phenomenology on which it is based (interaction of stream wise vorticity oriented structures [31], see above) is altered. Indeed, in Fig. 21 the predicted values of the Nusselt number go to zero near the geometrical boundaries (according to the $(u'v')$ stress which vanishes on the walls), while they are different from zero due to the effect of the three-dimensional boundary layer flow developing at the corners between the bottom wall and the other channel surfaces.

Wrong levels of heat transfer rate are also predicted at the location of structure S_2 (see Fig. 8), where Çakan [1] measured two symmetric spots of low Nusselt number. Such spots are consistent with the mean flow path, where the low momentum focal structures S_2 are sweeping the channel surface while transported beyond the obstacle by the secondary flow. On the contrary, the correlation feels the very high levels of $(u'v')$ Reynolds stresses associated to the strong flow separation occurring on the vertical flow layers (Fig. 7), so predicting high values of the Nusselt number. The alteration of the flow phenomenology on which the prediction approach is based is therefore responsible for its failure also in this flow region.

Applying the correlation to the other channel surfaces (i.e., rib surfaces, lateral walls) leads to similar conclusions. In particular, the correlation predicts correctly the main features of the heat transfer field except at the onset of particular flow structures responsible for flow mechanisms which are not taken into account in the prediction method. Examples can be the upstream face of the rib where the stable instantaneous structure V_3 is located, Fig. 6, or the strong flow separation at the rib leading edge, Figs. 6 and 14.

The present interpretation of the aerothermal behavior is

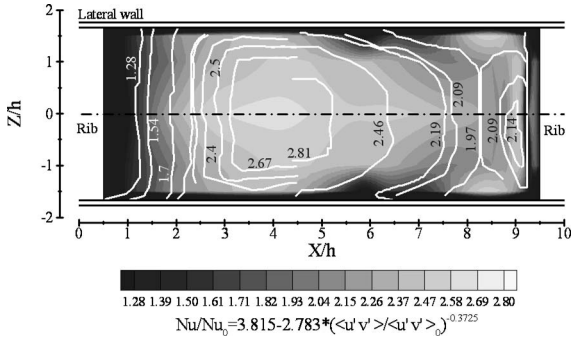

Fig. 21 Comparison between estimated (contour plot) and measured (contour lines from Çakan [1]) heat transfer rate on the ribbed surface of the channel

grounded on PIV data extracted at a fixed height from the wall ($Y/h=0.05$). This choice resulted from the need to collect data as close as possible to the walls and as free as possible from the noise that commonly affects PIV measurements near reflecting surfaces. Of course, if this height is modified, the magnitude of the considered quantities will change but, fortunately, the general trend is preserved, within a certain range of location change, as demonstrated by Casarsa [28]. Therefore, the conclusions previously drawn do not qualitatively depend on the distance from the wall at which data are extracted.

Conclusion

The velocity field inside a turbine blade coolant passage equipped with high blockage turbulence promoters was investigated in great detail by means of particle image velocimetry. The measurements were conducted on a scaled up model working at correct geometrical and kinematic similarity conditions. The time-averaged flow field provides an exhaustive description of the three-dimensional mean flow topology. The turbulent phenomena are found to be highly anisotropic, showing stream wise fluctuations two times higher than in the vertical or span wise directions. The comparison with the available wall heat transfer data leads to a quantitative correlation between the stream wise/normal to the wall Reynolds stress tensor component and the heat transfer rate. These results probably open the way to the definition of a general correlation law applicable to the design of high blockage cooling passages. It is well known that the existing correlations are valid only for small blockage ratios (in general less than 10%). The present investigation is a first attempt to remedy this deficiency. The proposed interpretation suffers from the limited amount of data used to find the tendency curve and does not consider the influence of other parameters such as the turbulent Pr number. Further efforts have to be made in trying to consolidate the proposed approach on a more statistically representative data base, considering different channel configurations and various flow regimes. The complete information, when available, might also shed some light on the selection of the appropriate turbulence model.

The results of the present work also constitute a wide and reliable data base for numerical code validation.

Nomenclature

D_h = hydraulic diameter
f = friction factor
f_0 = friction factor in a smooth tube
h = rib height
Nu = Nusselt number
Nu_0 = Nusselt number in a smooth tube
p = rib pitch
P_{atm} = atmospheric pressure
P_s = wall static pressure
Pr = Prandtl number
Δp = pressure drop
Δl = length
Re = Reynolds number
U_0 = bulk velocity
X, Y, Z = coordinates in stream wise, vertical, and lateral directions
u, v, w = stream wise, vertical, and lateral mean velocity components
u', v', w' = stream wise, vertical, and lateral fluctuating velocity components.
ρ = density

References

[1] Çakan, M., 2000, "Aero-Thermal Investigation of Fixed Rib-Roughened Cooling Passages," Ph.D. thesis, Université Catholique de Louvain, von Karman Institute for Fluid Dynamics.
[2] Han, J. C., Zhang, Y. M., and Lee, C. P., 1992, "Influence of Surface Heat Flux Ratio on Heat Transfer Augmentation in Square Channels With Parallel, Crossed and V-Shaped Angled Ribs," ASME J. Turbomach., **114**, pp. 872–880.
[3] Han, J. C., 1998, "Heat Transfer and Friction Characteristics in Rectangular Channels With Rib Turbulators," ASME J. Heat Transfer, **110**(2), pp. 321–328.
[4] Taslim, M. E., and Wadsworth, C. M., 1997, "An Experimental Investigation of the Rib Surface Averaged Heat Transfer Coefficient in a Rib Roughened Square Passage," ASME J. Turbomach., **119**, pp. 381–389.
[5] Han, J. C., and Park, J. S., 1998, "Developing Heat Transfer in Rectangular Channels With Rib Turbulators," Int. J. Heat Mass Transfer, **31**(1), pp. 183–195.
[6] Ligrani, P. M., Oliveira, M. M., and Blaskovich, T., 2003, "Comparison of Heat Transfer Augmentation Techniques," AIAA J., **41**(3), pp. 337–360.
[7] Liou, T. M., and Wu, Y. Y., 1993, "LDV Measurements of Periodic Fully Developed Main and Secondary Flows in a Channel With Rib-Disturbed Walls," J. Fluids Eng., **115**, pp. 109–114.
[8] Servouze, Y., Gicquel, E., Saccardi, E., Tanguy, B., and Sauter, V., 1999, "3D Laser Anemometry in a Rotating Cooling Ribbed U-Channel," 14th Symposium ISOABE, Florence, Italy.
[9] Roclawski, H., Jacobs, J. D., Yang, T., and McDonough, J. M., 2001, "Experimental and Computational Investigation of Flow in Gas Turbine Cooling Passages," AIAA Paper No. 2001-2925.
[10] Schabacker, J., Boelcs, A., and Johnson, B. V., 1999, "PIV Investigation of the Flow Characteristics in an Internal Coolant Passage With 45° Rib Arrangement," ASME Paper No. 99-GT-120.
[11] Chanteloup, D., and Boelcs, A., 2001, "PIV Investigation of the Flow Characteristics in 2-Leg Internal Coolant Passage of Gas Turbine Airfoils," 4th European Conference on Turbomachinery, Florence, Italy.
[12] Liou, T. M., Hwang, J. J., and Chen, S. H., 1993, "Simulation and Measurement of Enhanced Turbulent Heat Transfer in a Channel With Periodic Ribs on One Principal Wall," Int. J. Heat Mass Transfer, **36**, pp. 507–517.
[13] Rigby, D. L., 2000, "Numerical Simulation of Nonrotating and Rotating Coolant Channels Flow Fields," VKI Lecture Series 2000-03, von Karman Institute for Fluid Dynamics, Belgium.
[14] Sagaut, P., 2000, "Application of LES and DNS to Internal Cooling Channels," VKI Lecture Series 2002-03, von Karman Institute for Fluid Dynamics, Belgium.
[15] Han, J. C., Dutta, S., and Ekkad, S. V., 2000, *Gas Turbine Heat Transfer and Cooling Technology*, Taylor and Francis, New York.
[16] Iacovides, H., and Raisee, M., 1999, "Recent Progress in the Computation of Flow and Heat Transfer in Internal Cooling Passages of Turbine Blades," Int. J. Heat Fluid Flow, **20**, pp. 320–328.
[17] Rau, G., Moeller, D., Çakan, M., and Arts, T., 1998, "The Effect of Periodic Ribs on the Local Aerodynamic and Heat Transfer Performance of a Straight Cooling Channel," ASME J. Turbomach., **120**, pp. 368–375.
[18] Casarsa, L., Çakan, M., and Arts, T., 2002, "Characterization of the Velocity and Heat Transfer Fields in an Internal Cooling Channel With High Blockage Ratio," ASME Paper No. GT-2002-30207.
[19] Scarano, F., and Riethmuller, M. L., 2000, "Advance in Iterative Multigrid PIV Image Processing," Exp. Fluids, **29**, pp. 51–60.
[20] Mayers, J. F., 1991 "Generation of Particles and Seeding," VKI Lecture Series LS-1991-05, Laser Velocimetry, von Kármán Institute for Fluid Dynamics, Belgium.
[21] Çakan, M., and Arts, T., 1997, "Effect of Rib Height on Heat Transfer Enhancement in a Cooling Channel," Eurotherm Seminar No. 55, Heat Transfer in Single Phase Flows, Santorini, Greece.
[22] Han, J. C., Zhang, Y. M., and Lee, C. P., 1991, "Augmented Heat Transfer in Square Channels with Parallel, Crossed and V-Shaped Angled Ribs," ASME J. Heat Transfer, **113**, pp. 590–596.
[23] Riethmuller, M. L., and Lourenco, L., 1981, "Measurements in Particulate Two Phase Flow," VKI Lecture Series 1981-3, von Karman Institute for Fluid Dynamics, Belgium.
[24] Scarano, F., 2000, "Particle Image Velocimetry, Development and Application," Ph.D. thesis, Università di Napoli Federico Secondo, Italy.
[25] Kline, S. J., and Mc Clintock, F. A., 1953, "Describing Uncertainty in Single-Sample Experiments," Mech. Eng. (Am. Soc. Mech. Eng.), **75**, pp. 3–8.
[26] Casarsa, L., and Arts, T., 2002, "Aerodynamic Performance Investigation of a Rib-Roughened Cooling Channel Flow With High Blockage Ratio," 11th International Symposium on Applications of Laser Techniques to Fluid Mechanics, Lisbon, Portugal.
[27] Hirota, M., Yokosawa, H., and Fujita, H. M., 1992, "Turbulence Kinetic Energy in Turbulent Flows Through Ducts With Rib-Roughened Walls," Int. J. Heat Fluid Flow, **13**(1), pp. 22–29.
[28] Casarsa, L., 2003, "Aerodynamic Performance Investigation of a Fixed Rib-roughened Cooling Passage," Ph.D. thesis, Università degli Studi di Udine, Italy; von Karman Institute for Fluid Dynamics, Belgium.
[29] Durbin, P. A., 1993, "Application of a Near Wall Turbulence Model to Boundary Layers and Heat Transfer," Int. J. Heat Fluid Flow, **14**, pp. 316–323.
[30] Hermanson, K., Parneix, S., von Wolfersdorf, J., and Semmler, K., 2001, "Prediction of Pressure Loss and Heat Transfer in Internal Cooling Passages," *Heat Transfer in Gas Turbine Systems*, R. Goldstein, ed., New York Academy Sciences, Vol. 934.
[31] Jacobi, A. M., and Sahah, R. K., 1995, "Heat Transfer Surface Enhancement trough the use of Longitudinal Vortices: A Review of Recent Progress," Exp. Therm. Fluid Sci., **11**, pp. 295–309.

Toward Intra-Row Gap Optimization for One and Half Stage Transonic Compressor

H. D. Li
Research Fellow
e-mail: haidong.li@durham.ac.uk

L. He
Professor in Thermofluids
e-mail: li.he@durham.ac.uk

School of Engineering,
University of Durham,
Durham DH1 3LE, UK

Multistage effects on both aerodynamics and aeromechanics have been identified as significant. Thus, design optimizations for both aerodynamic performance and aeromechanical stability should be done in the unsteady multistage environment. The key issue preventing such a procedure to be carried out is the enormous computing time cost of multistage unsteady simulations. In this paper, a methodology based on the single-passage shape-correction method integrated with an interface disturbance truncation technique has been developed. The capability, efficiency, and accuracy of the developed methodology have been demonstrated for a one and a half stage quasi-three-dimensional transonic compressor with realistic blade counts. Furthermore, the interface disturbance truncation technique enables us to separate multirow interaction effects from the upstream and the downstream, which makes it possible to superimpose different rotor upstream gap effects and rotor downstream gap effects on the middle row rotor aerodynamic damping. In addition, a gap influence coefficient approach has been developed for investigation of all the possible gap spacing combinations of M upstream stator-rotor gaps and N downstream rotor-stator gaps. Then the number of cases that need to be computed has been reduced from $M \times N$ to $M+N$, which saved substantial computing time. The optimization analysis shows significant damping variation ($\sim 300\%$) within the chosen intrarow gap design space. The intrarow gap spacing could have either stabilizing or destabilizing effects so that the stabilizing axial spacing could be utilized to increase flutter-free margin in aeromechanical designs. The current approach also can be used for setting aeromechanical constraints for aerodynamic performance optimizations. [DOI: 10.1115/1.1928934]

1 Introduction

Industrial gas turbines and aeroengines developments all follow the trend for higher performance and more compact structural configurations. Increased aerothermal loading of each blade row would naturally lead to intensified interactions with adjacent rows at relatively small intrarow gap spacing. The impacts of the blade row interactions would not only affect the aerothermal performance (flow loss and efficiency) but also blade mechanical instability through flow induced vibration (flutter and forced response). Therefore, it is of great importance for turbomachinery designers to be able to identify and understand all influential intrarow interaction mechanisms, and furthermore to be able to control/optimize these effects during a design process.

The significance of multistage effects on aerodynamic performance has long been recognized. The theory of wake stretching and recovery in multirow interactions can be traced back to the work of Smith [1] in the 1960s and it shows that a reduced intrarow gap would lead to a reduction of the mixing loss of a wake shed from an upstream rotor row [2]. It is experimentally confirmed by Van Zante et al. [3]. However, in a transonic compressor, wake/stator boundary layer interactions could generate significant losses in the stator as indicated by Van Zante et al. [4]. Inlet guide vane (IGV) trailing edge/rotor shock interactions could break the bow shock and make it normal to the stream direction, which could reduce the stage performance, as shown by Gorrell et al. [5]. These findings imply that the aerodynamic performance of a transonic compressor is the resultant of complex conflicting effects, e.g., wake recovery, wake/boundary layer interactions, and IGV trailing edge/rotor shock interactions. Each might dominate depending on the intrarow gap spacing. On the other hand, the intrarow gap spacing has pronounced effects on the blade aeromechanics. The analysis of unsteady multistage flows by Silkowski and Hall [6] showed that multistage effects can have a significant impact on the middle row rotor aerodynamic damping. The authors' previous work [7] on a realistic three-dimensional (3D) rotor-stator compressor configuration showed that the rotor aerodynamic damping (hence flutter stability) could be changed by up to 100% when changing the rotor-stator gap spacing.

Unsteady flow analysis for a multirow configuration tends to be computationally very intensive. Conventional unsteady turbomachinery solvers will have to take a whole annulus assembly domain. The time cost for obtaining solutions can be significantly reduced if one utilizes parallel computers (e.g., Cizmas and Dorney [8] and Barakos et al. [9]). An alternative way is to modify blade counts so that only a few passages in each row are needed. But as indicated by Arnone and Pacciani [10] also based on the present authors' experience (e.g., [11]), serious inaccuracies can be introduced by blade count modifications in the rotor-stator interaction analysis, due to a large change in blade row interference wavelengths. The present authors pursue a single-passage (one passage for each blade row) method with phase-shifted periodicities for arbitrary blade counts. Several time-domain single-passage methods have been developed over the past two or three decades. One method was proposed by Erdos et al. [12] in 1977, known as the "Direct Store" method. Another one is called the time-inclination method proposed by Giles [13] in 1990 using a space-time transformation. He [14] (1992) proposed the Fourier decomposition based shape-correction method, which has been successfully applied to unsteady turbomachinery flow calculations for blade flutter [15], rotor-stator interactions [16], and inlet distortion effects on flutter [17]. Recently, Gerolymos et al. [18] also applied a Fourier decomposition based single-passage method to a

Contributed by the Turbomachinery Division of THE AMERICAN SOCIETY OF MECHANICAL ENGINEERS for publication in the JOURNAL OF TURBOMACHINERY. Manuscript received by the Turbomachinery Division, April 30, 2004; revised manuscript received, January 10, 2005. D. Prasad.

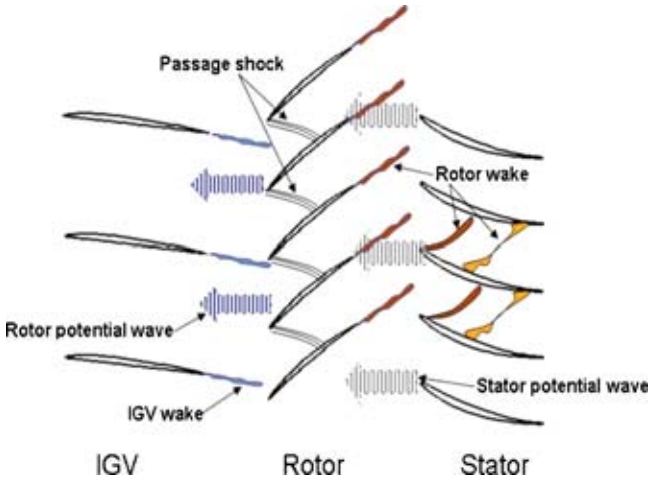

Fig. 1 Sketch diagram of IGV-rotor-stator interactions (a) single passage and (b) multipassage

one and a half stage turbine with the same number of NGV (nozzle guide vane) and stator blades. Though three blade rows were involved in that case, each blade row is only subject to single disturbance because of the equal NGV-stator blade count. It is worth emphasizing that none of these single-passage methods has been applied to a practical three-row configuration with arbitrary blade counts. The basic challenge is that the middle blade row will now be subject to at least two disturbances with distinctive frequencies. Furthermore, rotor-rotor or stator-stator interaction will generate an aperiodic flow field in the downstream row, e.g., He et al. [19], and Li and He [11], for which the phase-shifted periodicity can not be identified. All these modeling issues will be addressed and solved in the following sections.

In addition to the calculation of unsteady flow in a multirow environment with blade vibration effects, a further requirement for the present aeromechanical analysis is to be able to calculate and find the aerodynamic damping values over a wide range of upstream and downstream gap distances, which could be used as design space constraints leading to the aerodynamic performance optimization. For an embedded rotor row between two stators, we need to consider all possible gap spacing combinations of M upstream gaps and N downstream gaps. The direct approach will require $M \times N$ calculations. This direct approach could be very time consuming if M and N are large. In order to reduce the number of computations, a gap influence coefficient approach has been developed. The basic concept follows the influence coefficient method proposed by Hanamura and Tanaka [20] for oscillating only one blade, measuring/calculating its influences on all blades, and then constructing oscillating cascade data by the linear superposition. The original influence coefficient approach has been widely used for blade flutter analysis (e.g., [21–24]). The approach is extended in the present work to deal with intra-row gap effects on flutter stability.

2 Methodlogy Development

2.1 Single-Passage Method for Three-Row Configurations.

2.1.1 IGV-Rotor-Stator Interactions. IGV rotor stator is the typical configuration of front stage compressors. The unsteady interactions among these three blade rows, as illustrated on Fig. 1, are more complicated than the rotor-stator interactions. For the middle row rotor, wake disturbances (entropy/vorticity distortions) from the upstream IGV blades and potential disturbances from the downstream stator blades, are the primary unsteady sources. For the upstream IGV blades, potential waves and shock disturbances from the downstream rotor are the main unsteady sources. For the downstream stator row, there are more complex interactions among the unsteady wakes from the immediate upstream rotor row, the chopped (and hence also unsteady) wakes from the relatively stationary further upstream IGV and the stator boundary layer. In addition to these complex interactions, both IGV and stator will be subject to a frequency shifted vibration effect [6,7] when the rotor blades are in vibration.

The complex interactions plus vibration effects physically present difficulties for the application of single-passage methods. First of all, the middle row rotor is subject to two/three disturbances with distinctive different frequencies, i.e., the IGV wake disturbance, the stator potential disturbance, and/or blade vibration. Though the capability of the single-passage shape-correction method for dealing with multiple disturbances has been demonstrated, e.g., [7,14,17], it has not yet been applied to three-row configurations with arbitrary blade counts. In addition to this, the IGV-stator interactions, though relatively weak, could generate aperiodicities in the downstream stator row which further complicates the situation. Nevertheless, the previous work [11] showed that the phase-shifted periodicity is valid on the rotor row though it is subject to multiple disturbances as each disturbance can be identified by its own frequency and wavelength (i.e., interblade phase angle). The IGV-stator interaction is the secondary effect compared to the adjacent IGV-rotor and rotor-stator interaction. Therefore, the phase-shifted periodicity would also be valid in both IGV and stator if the IGV-stator interactions could be neglected. Then a single-passage method could be applied for three-row configurations with the main interaction effects being captured.

2.1.2 Shape-Correction Method. The generalized shape-correction method [14] proposed by He is a Fourier decomposition based single-passage method, which has the capability to deal with multiple disturbances and it has been extended to a realistic 3D transonic compressor stage configuration with rotor in vibration [7]. It is assumed that each unsteady disturbance can be identified by its own phase-shifted periodicity, characterized by a spatial wavelength and a constant circumferential travelling speed. Therefore the unsteady flow variables of each disturbance can be approximated by Fourier series as described by the following equation:

$$U_i(x,y,r,t) = \sum_{n=1}^{N_{\text{fou}}} [A_{ni}(x,y,r)\sin(n\omega_i t) + B_{ni}(x,y,r)\cos(n\omega_i t)] \tag{1}$$

Thus any unsteady flow variables on the periodic boundary can be decomposed into a time-averaged part plus the summation of all disturbances.

$$U(x,y,r,t) = U_0(x,y,r) + \sum_{1}^{N_{\text{dst}}} U_i(x,y,r,t) \tag{2}$$

Only the Fourier coefficients at the periodic boundaries and interfaces need to be stored and updated during the computation. On each time-marching step, flow variables on those boundary points are corrected by reconstructed values from the updated Fourier coefficients

$$U^{\text{DL}}(x,y,r,t) = U_0^{\text{IU}}(x,r) + \sum_{i=1}^{N_{\text{dst}}} \sum_{n=1}^{N_{\text{fou}}} \{A_{ni}^{\text{IU}}\sin[n(\omega_i t - \sigma_i)] + B_{ni}^{\text{IU}}\cos[n(\omega_i t - \sigma_i)]\}$$

$$U^{\text{DU}}(x,y,r,t) = U_0^{\text{IL}}(x,r) + \sum_{i=1}^{N_{\text{dst}}} \sum_{n=1}^{N_{\text{fou}}} \{A_{ni}^{\text{IL}}\sin[n(\omega_i t + \sigma_i)] + B_{ni}^{\text{IL}}\cos[n(\omega_i t + \sigma_i)]\} \tag{3}$$

where σ_i is the interblade phase angle of the ith disturbance, and A_{ni} and B_{ni} are corresponding nth-order Fourier coefficients of the

disturbance i. Therefore, the dummy cell at the upper boundary (DU) will be corrected by the Fourier series evaluated from its corresponding lower side inner cell (IL) with a phase shift. The correction on the lower side dummy cells (DL) is done accordingly. For multidisturbance cases, partial-substitution technique [14] has been adopted for speed-up updating of Fourier coefficients.

2.1.3 Interface Disturbance Truncation. For multirow interaction problems, the treatment of interfaces between adjacent rows is the key for the successful prediction of the interaction effects. For the traditional multiple-passage/whole annulus solution method, flow variables on both sides of the intrarow interface are known as part of the solution. Therefore any interpolation methods can be adopted for instantaneous information exchange across the interface. But in a single-passage solution, e.g., shape-correction method, two whole annulus buffer planes of each interface need to be reconstructed first, based on the Fourier coefficients stored for each side of the interface. Then the same interpolation process applied for multiple-passage solutions can be applied to the solution passage interfaces.

In order to truncate any unwanted disturbances (not limited to the IGV-stator interactions) in the single-passage solution method, first only those disturbances (modes) of interest are included when reconstructing the whole annulus buffer planes. For example, on the left side of the rotor-stator interface, only the rotor-stator interactions and rotor vibration disturbances are of our interest. Therefore, the disturbance from upstream IGV is not included in the reconstruction process. However, it is still included in the Fourier coefficient evaluation process for the sake of partial substitution. Consequently in the downstream stator domain, there is no disturbance from the IGV. Similarly, the potential effect from the downstream stator has to be excluded when reconstructing the right side buffer plane of the IGV-rotor interface. The phase-shifted periodicities are ensured now in each blade row.

The next step is to correct the flow field across the interface. As now we have the reconstructed whole annulus buffer planes, a direct interpolation can be applied for information exchange across the interface as if we were solving a multipassage/whole annulus domain. However, a mismatch between two sides of the interface exists due to the fact that only part of the disturbances has been included in the buffer planes reconstruction. Thus a local nonreflective 1D characteristic treatment is applied to erase this artificial jump, which enables each side of the interface only to see those disturbances it wants to see, regardless of what happened on the other side. The characteristic treatment ensures that there is no artificial reflection generated by the interface, but acoustic reflections from either the IGV or the stator still can pass through intrarow interfaces as expected.

The importance of the interface disturbance truncation technique for three-row configurations lies on the following facts. First of all, by truncating IGV-stator interactions, it does not affect the unsteadiness on the rotor row and also the adjacent blade rows interactions, i.e., IGV-rotor interactions and rotor-stator interactions, still remain. Furthermore, the truncation technique enables us to analyze individual gap spacing effects on the rotor aerodynamic damping, i.e., allows the acoustic waves reflected from either the upstream or the downstream, which cannot be easily carried out by the usual multipassage methods. Therefore, the reflection effects can be clearly separated and calculated individually, which would be helpful for the understanding of interaction mechanisms.

2.1.4 Flow Model and Boundary Conditions. The developed single-passage methodology has been implemented in a flow solver named as TF3D developed by the authors' research group. The solver is based on an integral form three-dimensional Navier-Stokes equation in the absolute cylindrical coordinate system using the second-order cell centered finite volume scheme. The computational domain consists of a single passage for each row with a blade being at the center of the passage [as shown on Fig. 2(*a*)]. The phase-shifted periodic conditions are applied on periodic boundaries and interfaces. On blade and end-wall surfaces, a log law is applied to determine the surface shear stress and the tangential velocity is left to slip. Nonreflective boundary conditions [25] based on 1D local characteristics are applied to both the inlet and the outlet. This flow model has been validated and applied to various steady and unsteady turbomachinery flow simulations, e. g., [11,15,16,25–27].

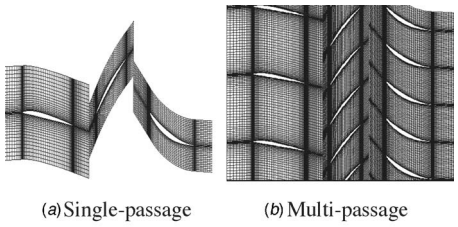

Fig. 2 Computational domains (IGV-rotor gap=rotor -stator gap=50% rotor chord). (*a*) Single-passage reconstructed solution and (*b*) multipassage solution.

2.2 Gap Influence Coefficient Approach.

2.2.1 Basic Model and Assumptions. The rotor blade flutter stability under influences from an upstream stator row and a downstream stator row is of our primary interest in the current study. Another objective function for evaluation is the rotor aerodynamic damping, which is influenced by the upstream gap between the first stator and the rotor, and the downstream gap between the rotor and the second stator. The basic three-row aerodynamic model includes all the wake and potential interactions between the upstream stator and the rotor, and between the rotor and the downstream stator. Also as discussed before, the stator-stator interactions are neglected.

In connection with the rotor aerodynamic damping, it has been shown (e.g., [7]) that intrarow influences are dominated by the acoustic reflections from immediately adjacent blade rows. Hence the three-row aeromechanical model only includes the primary reflection effects of stators on the rotor. The secondary acoustic reflections (i.e., those primary reflections from one stator going through the rotor and being further reflected back by the other stator) are assumed to be negligible. A further assumption is that the influences from the upstream and the downstream gaps can be linearly superimposed, as variation of flow variables due to different gaps are relatively small (though meaningful) quantities relative to a baseline state. As will be shown later, the linear assumption is acceptable for the present analysis of gap effects.

2.2.2 Decomposition and Superposition. The basis for the influence coefficient approach is that variation of flow variables due to a bladerow's own vibration and reflections from its adjacent rows can be decomposed and calculated individually. For the embedded rotor row between two stators with the rotor in vibration, the unsteady signals (e.g., unsteady pressure $\hat{\mathbf{p}}$) on the rotor blades associated with the vibration can be subdivided into three parts, i.e., contributions from the rotor vibration as in an isolated row ($\hat{\mathbf{p}}_{\mathbf{iso}}$), acoustic reflections from the upstream stator blades ($\hat{\mathbf{p}}_{\mathbf{up}}$) and acoustic reflections from the downstream stator blades ($\hat{\mathbf{p}}_{\mathbf{down}}$), i.e.,

$$\hat{\mathbf{p}} = \hat{\mathbf{p}}_{\mathbf{iso}} + \hat{\mathbf{p}}_{\mathbf{up}} + \hat{\mathbf{p}}_{\mathbf{down}} \tag{4}$$

Each part is a complex number with its real and imaginary parts, which are used to work out amplitude and phase angle. The first term, the contribution from the rotor itself, can be calculated using an isolated rotor row configuration with the same flow condition as it is in the three rows environment. This may not be easy for realistic 3D configurations. Alternatively, the first term could

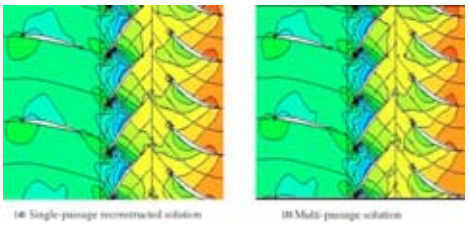

Fig. 3 Instantaneous pressure contours of IGV-rotor-stator interactions (IGV-rotor gap=rotor-stator gap=50% rotor chord)

be obtained by using the interface disturbance truncation technique on both ends of the rotor domain, so that there will be no acoustic waves to pass into and reflect back from the upstream and the downstream stator. Therefore the recorded unsteady signals on the rotor blade only contain its own vibration effects. The second and third parts represent reflection effects from the upstream and the downstream stator, respectively. Furthermore, they can be calculated separately again by using the interface disturbance truncation. For example, the $\hat{\mathbf{p}}_{\mathbf{up}}+\hat{\mathbf{p}}_{\mathbf{iso}}$ can be obtained by truncating the vibration disturbance at the outlet of the rotor domain. Once $\hat{\mathbf{p}}_{\mathbf{iso}}$ and $\hat{\mathbf{p}}_{\mathbf{up}}+\hat{\mathbf{p}}_{\mathbf{iso}}$ are known, $\hat{\mathbf{p}}_{\mathbf{up}}$ can be worked out by the vector difference. $\hat{\mathbf{p}}_{\mathbf{down}}$ can be obtained in a similar way.

For the present study of any combination of IGV-rotor gap and rotor-stator gap, if we know the variation of flow variables due to the rotor vibration, acoustic reflections from the upstream and the downstream, then the total change in flow variables (e.g., unsteady pressure) on the rotor blade can be summed up using Eq. (4). It sounds like an inverse procedure of the decomposition, but it enables us to reconstruct all combinations of different upstream and downstream gap effects. For example, if M IGV-rotor gaps and N rotor-stator gaps have been investigated with $\hat{\mathbf{p}}_{\mathbf{iso}}, \hat{\mathbf{p}}_{\mathbf{up}}$, and $\hat{\mathbf{p}}_{\mathbf{down}}$ being decomposed, then the results of $M \times N$ combinations can be evaluated using the superposition, which costs almost no time compared to direct calculations. Therefore significant time saving could be expected when M and N are large. Since Eq. (4) is a vector summation, the resultant damping value will be different from the summation of damping values calculated from each individual part.

3 Validation

3.1 Test Configuration. This is a transonic compressor stage known as ECL compressor tested by Ecole Centrale de Lyon. The original configuration has three rows: IGV followed by a rotor and a stator. The compressor has 33 IGV blades, 57 rotor blades, and 58 stator blades, and it was operated at a rotation speed of 11,040 RPM. The steady 3D three-row flow has been validated [7]. More detailed information about the test rig and flow conditions can be found in [28]. For the purpose of validation of the currently developed methodology, a quasi-3D section at 75% span is adopted and the number of stator blades is changed to 60 so that only one third of the whole annulus is needed for a multipassage solution. The modification of the stator blade count is only for multipassage calculations to be used as a benchmark for validating the single passage method. There is no restriction on blade counts for the current developed single-passage methodology.

3.2 IGV-Rotor-Stator Interactions. Single passage calculations for the three-row configuration without rotor vibration were conducted first and compared directly with multipassage solutions. Figure 2 shows the single-passage mesh along with the first few passages mesh of the multipassage domain. The computational domain is arranged in such a way with the blade in the middle which is convenient for implementation of the phase-shifted periodicity. Figure 3 shows the comparison of instantaneous pressure contours between the single-passage solution and the multipassage solution. Figure 3(*a*) is the multipassage pressure field reconstructed from the single-passage solution. First, the reconstructed pressure field agrees very well with the multipassage solution, which demonstrates the capability of the current developed methodology in dealing with the problems of three-row interactions. Not only the solution passage, but also the whole annulus solution can be obtained by reconstruction and in good accuracy. Second, pressure waves from rotor leading edge pass through the IGV-rotor interface and enter the IGV domain smoothly, which verifies the current interface treatment.

Figure 4 shows comparisons of the unsteady tangential force time traces on the reference rotor blade for two different intrarow gap spacing cases, the first one with 30% IGV-rotor gap and 30% rotor-stator gap, the second one with 50% IGV-rotor gap and 50% rotor-stator gap. The gap spacing is measured against the rotor chord length. As indicated on Fig. 4, both cases have the same time-mean forcing but very different unsteady forcing variations.

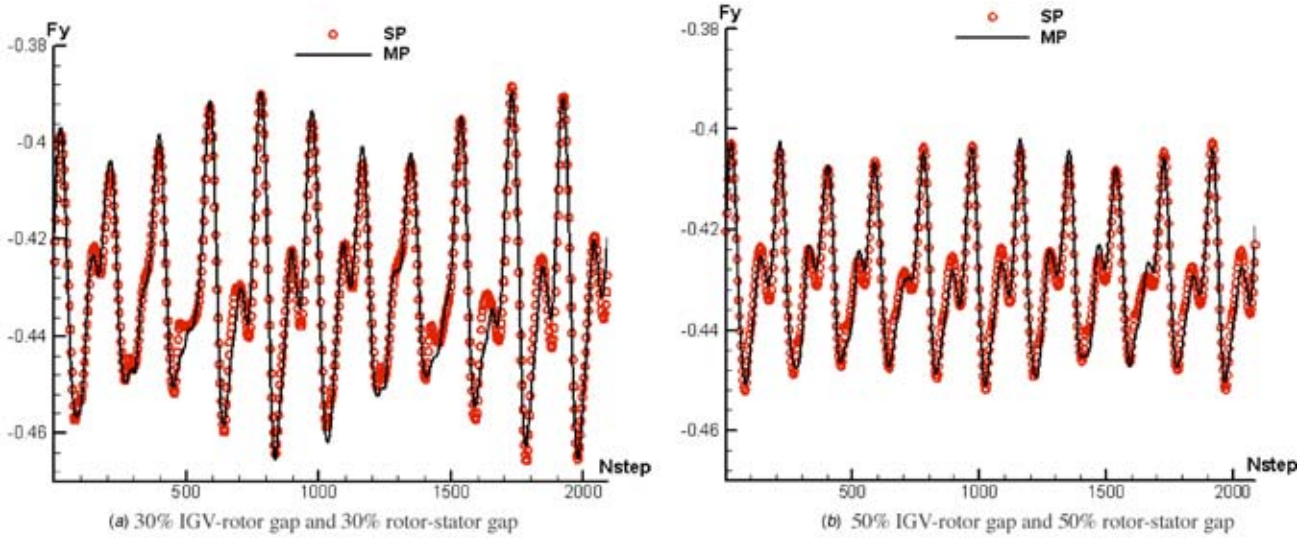

Fig. 4 Time traces of the tangential force on the rotor blade (IGV-rotor-stator configuration)

Table 1 Comparison of the stage performance and the rotor aerodynamic damping. (Single-passage (SP) solutions versus multipassage (MP) solutions.)(IGV-rotor gap spacing=rotor-stator gap spacing.)

Gaps spacing (% rotor chord)	Mass flow rate kg/s	Pressure ratio	Efficiency	Rotor aero-damping (Log_dec %)
30% (SP)	0.274	1.2987	87.95	1.679
30% (MP)	0.274	1.2989	88.16	1.759
50% (SP)	0.274	1.2992	88.32	1.233
50% (MP)	0.274	1.2991	88.26	1.262
100% (SP)	0.274	1.2992	88.14	3.067
100% (MP)	0.274	1.2991	88.19	3.115

The unsteady forcing of the 50%–50% gap case is dominated by the IGV wake and modulated by the downstream potential effects, while the one of the 30%–30% gap case shows strong interactions between the IGV wake and the stator potential featuring substantial subharmonics (nonlinear cross coupling effects). For both cases with/without nonlinear interactions, the current single-passage solution always gives the same result as those obtained from the direct multipassage solution. Table 1 lists the corresponding one and a half stage performance comparison. Again, for both cases, the single-passage results agree very well with the results from multipassage solutions, which confirms that both the unsteady forcing and the time-averaged performance parameters can be accurately predicted by the current single-passage method.

When the IGV and the stator are moved away from the rotor, i.e., increasing the gap spacing from 30% to 50%, the amplitude of the rotor unsteady forcing is decreased (shown in Fig. 4) but the efficiency is increased (indicated in Table 1) as blade rows interactions are reduced. We notice that the efficiency predicted by the single-passage (SP) solution is slightly different from the one obtained from the multipassage (MP) solution. This could be because of the neglect of the IGV-stator interactions. The relatively strong IGV-stator interaction case, i.e., 30%–30% gaps, causes more discrepancy than the weak interaction case (100%–100% gaps). The aperiodicity effects (i.e. IGV-stator interaction) on the aerodynamic performance should be further investigated in the future.

3.3 IGV-Rotor-Stator Interaction With Rotor in Vibration. Here we consider the case when the rotor blades are vibrated in a three nodes first torsion mode with amplitude of 0.5 deg. The frequency and mode shape are obtained from a 3D finite element (FE) modal analysis [7]. The reduced frequency, based on the rotor chord length and the rotor inlet relative velocity, is 2.1. The reason for choosing this mode is that it is the least stable mode based on the isolated rotor aerodynamic damping analysis (corresponding to an interblade phase angle of 19 deg. Every row is subject to at least two disturbances, i.e., the IGV is subject to the rotor potential disturbance and the frequency-shifted rotor vibration effect, the rotor is subject to IGV wake disturbance, stator potential effects, and its own blade vibration, and the stator is subject to the rotor wake disturbance and the frequency-shifted rotor vibration effect. Figure 5 shows the comparison of the unsteady tangential force time traces on the reference rotor blade with different intrarow gap spacings. Although the rotor is under the influences of three disturbances, each disturbance still can be identified by its own phase-shifted periodicity. Thus the current single-passage method still can capture all these disturbances as the multi-passage solution did for both cases.

Table 1 also lists the comparison of rotor aerodynamic damping values in logarithm decrement (log_dec), which is defined as

$$\text{Log\_Dec} = \text{Worksum}/2(\text{BladeStrainEnergy}) \tag{5}$$

The maximum discrepancy between the SP and the MP solutions is about 5%, which is deemed to be small given the wide range of the damping values. All these comparisons further confirmed that the current developed methodology can deal with three-row interactions with/without rotor in vibration in a good accuracy.

The saving of computing time of the single-passage solution against the multipassage solution is dependant on the number of blade passages involvement in the multipassage solution. For the current configuration with one third annulus involved in the multipassage solution, a speedup factor of 6 has been achieved. A 15–20 times speedup could be expected if the whole annulus is involved.

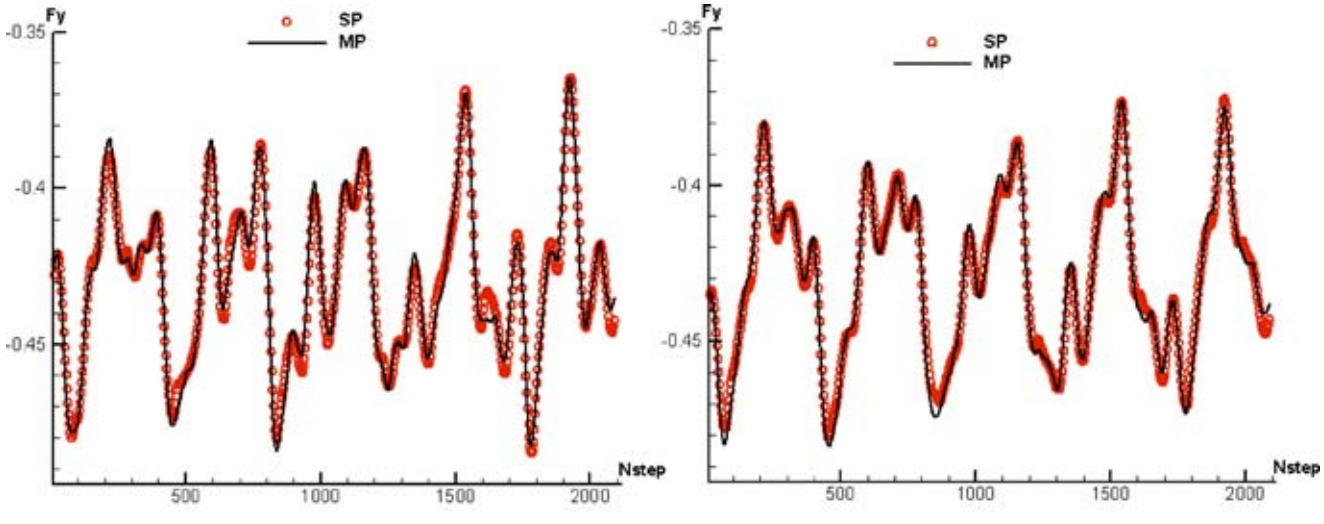

(a) 30% IGV-rotor gap and 30% rotor-stator gap

(b) 50% IGV-rotor gap and 50% rotor-stator gap

Fig. 5 Time traces of the tangential force on the rotor blade (IGV-rotor-stator configuration with rotor in vibration)

Table 2 Rotor aerodynamic damping (Log_dec %). (With truncation of the vibration effects at both ends of the rotor domain.)

Case	30%–30%	50%–50%	100%–100%
Rotor Damping (Log_dec %)	2.322	2.333	2.325

3.4 Gap Influence Coefficient Method. To validate the gap influence coefficient approach, the first step would be to demonstrate that the variation of unsteady flow variables can be subdivided and calculated independently. The first term in Eq. (4), i.e., the isolated rotor vibration effect $\hat{\mathbf{p}}_{\mathbf{iso}}$ is calculated here using the interface disturbance truncation technique. Table 2 lists the resultant damping value (in Log dec) for different gap spacing cases. All three cases give the same rotor aerodamping value confirming the effectiveness of the subdivision and the validity of the interface disturbance truncation technique. It also implies negligible interactions between the rotor vibration and the disturbances at the blade passing frequencies from the adjacent rows.

Next, the acoustic reflections from either the upstream IGV or the downstream stator can be identified by examining the first harmonic pressure distribution on the rotor blades. Figure 6 shows the first-harmonic amplitude distribution on the rotor suction surface for different gap spacing cases. Results with and without downstream stator reflections are plotted on each diagram. In both cases, the rotor works in a chocked flow condition and the passage shock is situated at 60%–70% axial chord on the suction surface and 10%–20% axial chord on the pressure surface. The unsteady surface pressure results show that the downstream reflections only change the pressure fluctuations after the passage shock wave. For the case with 30%–30% gaps, the downstream reflections suppressed the rotor unsteady pressure fluctuation, which implies that the acoustic reflective waves are out of phase with the pressures due to the rotor's own vibration. This can be seen by the first-harmonic phase angle distribution on both suction surface (Fig. 7(*a*)) and pressure surface (Fig. 8(*a*)). For the case with the downstream reflections, its phase angle after the shock wave is different from the one without reflections. On the another case with 100%–100% gaps, the downstream reflections further enhanced the rotor unsteady pressure fluctuation (shown in Fig. 6(*b*)), where the phase angle distribution with/without down stream reflections is almost the same as shown on Figs 7(*b*) and 8(*b*), i.e., the stator reflected waves are in phase with those rotor primary ones.

Finally, the accuracy of the linear superposition in the current aerodynamic damping analysis is verified. Two cases with very different gap spacings, i.e., 30%–30% gap and 100%–100% gap, are chosen for the purpose to cover a large variation of the rotor aerodynamic damping. Three calculations for each case have been carried out, i.e., calculation with truncation of vibration at the inlet of the rotor domain, calculation with truncation of vibration at the outlet of the rotor domain, and a direct multipassage calculation. For the first two calculations, the pressure time traces on the rotor blade surfaces have been recorded. Then the combined gap effects can be obtained using Eq. (4) and the damping values are evaluated accordingly. The results are summarized in Table 3. Damping values predicted by the gap influence coefficient approach are in good agreement with the direct multipassage solutions. The maximum discrepancy is less than 5%, which is very small given that variation in the damping value could be over 100% (as shown in Fig. 9).

4 Intrarow Gap Optimization Analysis

4.1 Individual Intrarow Gap Effects. In order to analyze the combined IGV-rotor gap and the rotor-stator gap effects on the rotor aerodynamic damping, individual gap effects have to be calculated in advance by applying the gap influence coefficient approach. The one and a half stage transonic compressor case studied here has the same configuration as the one used for the validation purpose. The axial spacing between the IGV and the rotor is in a range between 20% and 100% of the rotor chord length, and the rotor-stator axial spacing is between 25% and 100% of the rotor chord length. Nine axial spacings of each gap have been calculated using the current single-passage method and the results are summarized on Figs. 9 and 10. It is interesting to note that for both stage performance and rotor aerodynamic damping, the two gaps have the similar trend of effects except for the performance. The smallest IGV-rotor gap causes a slight increase of the aerodynamic efficiency while the smallest rotor-stator gap reduces the efficiency.

For the rotor aerodynamic damping variation, none of these gaps causes a monotonic variation when changing the gap spacing. Instead, two largely sinusoidal curves with similar wavelengths but different amplitudes are observed. The peak-to-peak variation of the damping value is about 30% on the effects of

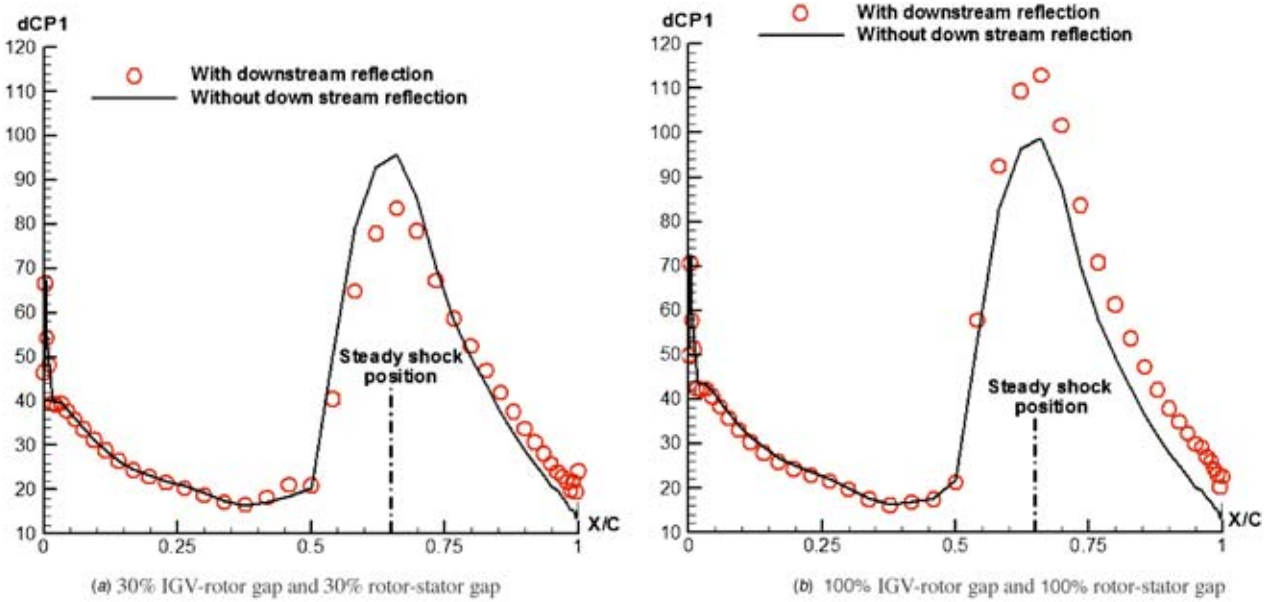

(*a*) 30% IGV-rotor gap and 30% rotor-stator gap

(*b*) 100% IGV-rotor gap and 100% rotor-stator gap

Fig. 6 Amplitude of the first-harmonic pressure on the rotor suction surface

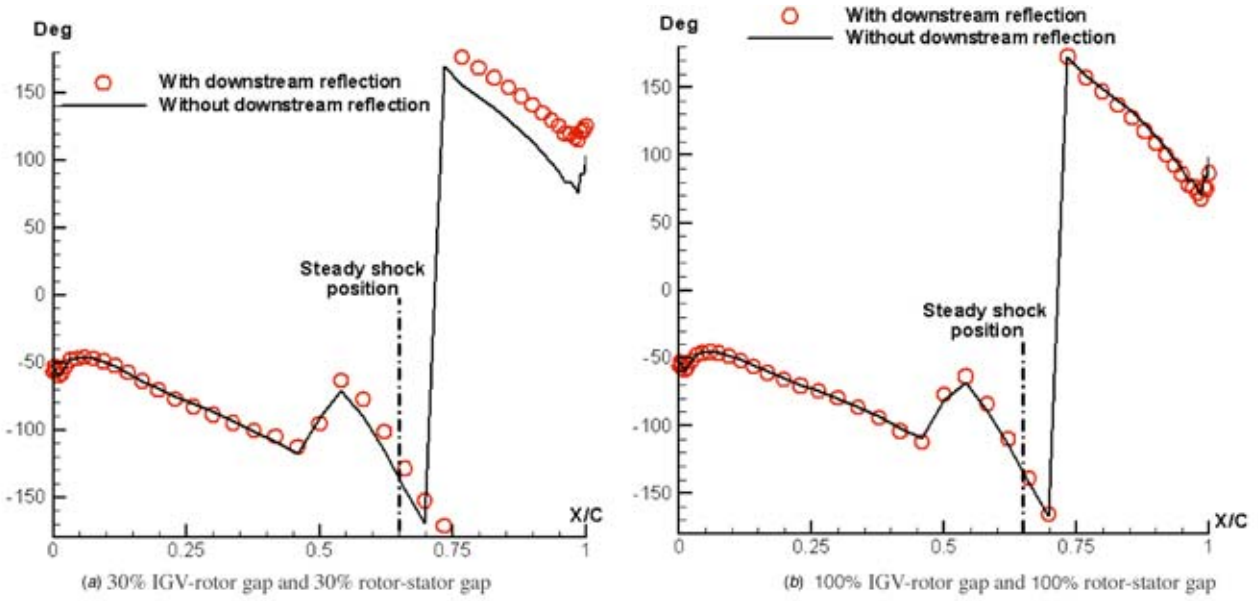

Fig. 7 Phase angles of the first-harmonic pressure on the rotor suction surface

IGV-rotor gap. But the effects of the rotor-stator gap can change the damping value over 100%. This may be well linked to the orientation of the blades as reflections of acoustic waves are usually perpendicular to the blade surfaces. The IGV blades are sitting along the axial direction so that most of the reflections will be limited between adjacent blades. On the other hand, the downstream stator blades have a larger portion of surface projection nearly perpendicular to the axial direction. Thus many more reflections from the stator blades are expected to be passed back to the rotor row.

For the gap effects on the stage performance, the overall efficiency variation due to the IGV-rotor gap spacing is very small, about 0.1%. Given the fact that truncation of IGV-stator interactions at small gaps could cause noticeable inaccuracy of performance valuation (indicated in Table 1), the effects of IGV-rotor gap on performance is not clear for the case investigated here, which should be further investigated with more detail. On the other hand, the rotor-stator gap has a clearly identifiable effect on

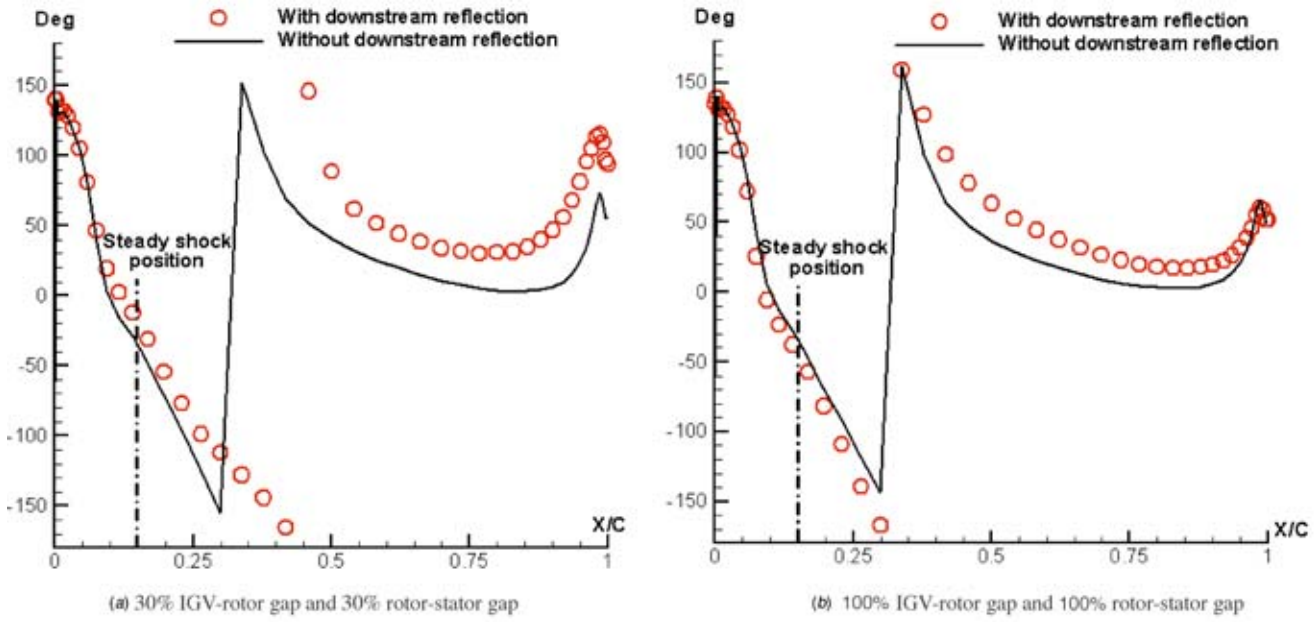

Fig. 8 Phase angles of the first-harmonic pressure on the rotor pressure surface

Table 3 Validation of the linear superposition in aerodamping (Log_dec %) prediction

Case	Truncation at rotor inlet	Truncation at rotor outlet	Superimposed damping	MP direct calculation	Error (%)
30%–30% gap	1.665	2.373	1.713	1.759	2.6
100%–100% gap	3.044	2.496	3.202	3.098	3.2

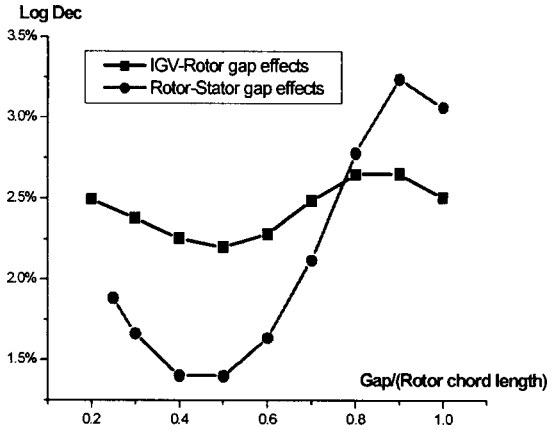

Fig. 9 Variation of the rotor aerodynamic damping

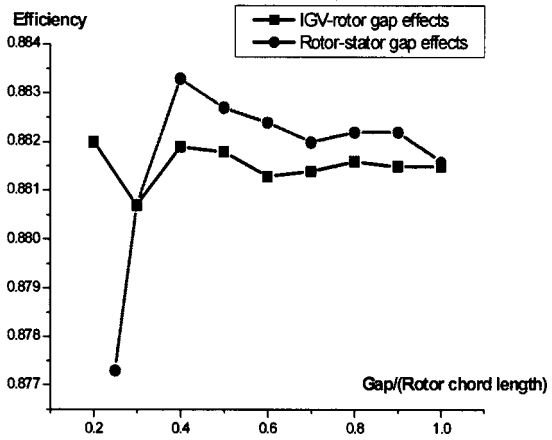

Fig. 10 Variation of the stage performance

the performance when the gap is closed from 100% to 25% of the rotor chord length. The efficiency reaches the maximum at the gap spacing of 40% and the maximum-minimum difference is about 0.6%. When closing up the rotor-stator gap, the mixing loss of the rotor wake is expected to be reduced according to the wake recovery theory, while the rotor-stator interactions are getting more intensive. When the gap spacing is reduced to less than 40%, the effects of rotor wake-stator boundary layer interactions seem to dominate, generating significant losses in the stator passage flow, as reported by Van Zante et al. [4]. Therefore the overall stage efficiency shows the trend of reducing when the gap spacing is less than 40%.

4.2 Combined Intrarow Gaps Effects. As indicated by Silkowski and Hall [6] in the coupled modes study of a one and a half stage flat-plate compressor, the rotor aerodynamic damping takes a wide range of values when the axial gaps are varied (ten combinations of different gaps were investigated). The objective of the current work is to systematically analyze the gaps effects on rotor aerodynamic damping for the realistic compressor configuration by using the gap influence coefficient method. The result of such an analysis can then be used for design optimization purposes.

In the previous section, $\hat{\mathbf{p}}_{\mathbf{up}}$ and $\hat{\mathbf{p}}_{\mathbf{down}}$ of each individual gap case have been calculated. Those results are used here as inputs of the gap influence coefficient approach. As nine gap spacings of each gap were calculated, 81 combinations can be directly superimposed. The results obtained from the gap influence approach are summarized in Fig. 11(*a*) which shows the rotor aerodynamic damping map. In line with the finding of individual gap effects discussed earlier, it also shows that the rotor-stator gap has a much stronger impact on the rotor aerodynamic damping as most of the contour lines are parallel to the axis of IGV-rotor gap.

The minimal damping is concentrated at a region near 40% IGV-rotor gap and 50% rotor-stator gap with a Log_dec value about 1.3%. The maximum damping is about 3.6% located at the point of 90% gap for both the IGV-rotor gap and the rotor-stator gap. The damping value is changed nearly threefold within the chosen design space. Both the maximum and the minimum aerodamping points have then been validated against the multipassage solutions and the comparisons are listed in Table 4. The

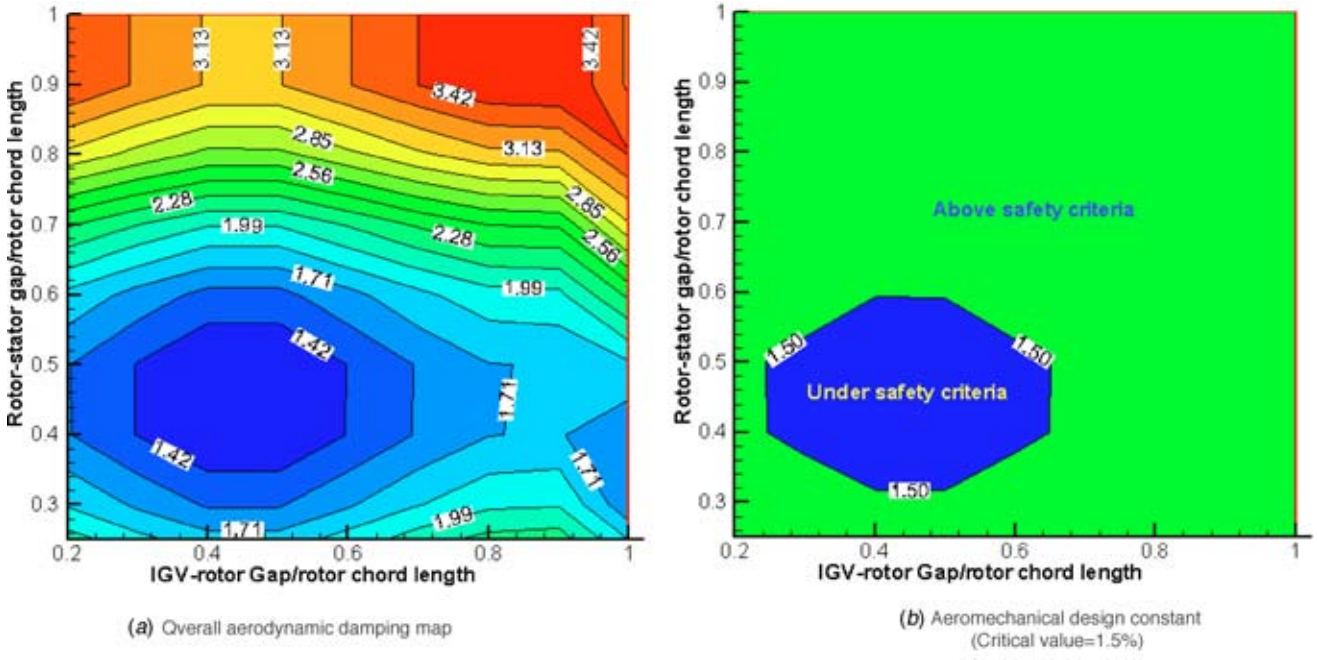

(*a*) Overall aerodynamic damping map

(*b*) Aeromechanical design constant (Critical value=1.5%)

Fig. 11 Rotor aerodynamic damping map (Log_dec %)

Table 4 Validation of the damping value extrema (Log_dec %)

Case	Maximum damping 90%–90%			Minimum damping 40%–50%		
	SP (reconstructed)	MP	Error	SP (reconstructed)	MP	Error
Rotor damping (Log_dec %)	3.551	3.447	3%	1.295	1.40	7.5%

maximum discrepancy of the damping prediction is about 7.5% at the minimum value point, where both IGV-rotor gap and rotor-stator gap are relatively small. Therefore secondary reflections (i.e., reflection from one stator going through the rotor and reflected back from the other stator), which have been neglected in the current study, could be the major source of the error. When the gaps are increased as on the maximum point, the discrepancy was reduced to 3%. Nevertheless, the 7.5% discrepancy of the damping prediction at the minimum damping point is well acceptable compared to the overall variation with the gaps by 300%. These validations sufficiently demonstrate the accuracy of the linear superposition assumption.

It should be pointed out here that the influence coefficient approach is a pure post-processing procedure which costs no time as one can superimpose as many scenarios as one wants. The CPU time-saving compared to direct simulations could be enormous when the number of scenarios is large.

As an example to illustrate how to make the current analysis available for design optimizations, a critical damping threshold is set as 1.5% in Log_dec. Then an area marked with the dark color on Fig. 11(*b*) is found, which could be considered as aeromechanical constraints for aerodynamic design optimizations. One extra comment to make is that most current design systems use the reduced frequency as design criteria to avoid flutter problems without consideration of the actual aerodynamic loading. The current study indicates that the axial gaps have either stabilizing or destabilizing effects depending on the gap spacing. Therefore stabilizing gaps spacing could be used to extend flutter-free margin without incurring blade structure and/or performance penalties.

5 Conclusions

A single-passage computational methodology for three-row interactions with the middle row in vibration has been developed, based on the shape-correction method integrated with an interface disturbance truncation technique. Results demonstrated that the developed method can handle three-row interaction problems for realistic blade counts accurately and efficiently.

A gap influence coefficient method has been developed and applied for efficiently constructing combined IGV-rotor gap effects and rotor-stator gap effects on the rotor aerodynamic damping. To investigate all the combinations of M upstream gaps and N downstream gaps, the number of cases needed to be calculated has been dramatically reduced from $M \times N$ to $M+N$ by using the influence coefficient approach; the superimposed results show good agreement with the direct multipassage solutions. The aerodynamic damping analysis indicates that the rotor damping value exhibits a variation about threefold in the chosen design space. The rotor-stator gap has much more significant impacts on the rotor aerodynamic damping than the IGV-rotor gap effects. The current study provides aeromechanical constraints (or safety criteria) for further aerodynamic blading design optimizations. It also implies that the stabilizing gap spacing could be used to enlarge the flutter-free margin which effectively provides a wider design space for mechanical design optimizations.

Acknowledgment

The authors wish to thank the sponsorships from the Engineering and Physical Sciences Research Council (EPSRC) (Grant No. GR/M43821) and Demag Delaval Industrial Turbomachinery Ltd (a wholly owned subsidiary of Siemens). Discussions with R. Wells, Y. S. Li, and W. Ning (DDIT, Siemens) are appreciated.

Nomenclature

A_{ni}, B_{ni} = Fourier coefficients
N_{fou} = number of harmonics applied
N_{dst} = number of disturbances
n = order of harmonics
$\hat{\mathbf{p}}$ = vibration induced unsteady pressure
r, x, y = coordinate
t = time
U, U_0, U_i = flow variable
ω_i = frequency of the ith disturbance
σ_i = interblade phase angle of the ith disturbance

Superscripts

DL = lower side dummy cell
DU = upper side dummy cell
IL = lower side inner cell
IU = upper side inner cell

Subscripts

down = downstream
iso = isolated blade row
up = upstream

References

[1] Smith, L. H., 1969, "Casing Boundary Layers in Multistage Compressors," *Proc. Symposium on Flow Research on Blading, Brown Boveri & Co Ltd, Baden, Switzerland.*
[2] Adamczyk, J. J., 1998, "Wake Mixing in Axial Flow Compressors," ASME paper no. 98-GT-29.
[3] Van Zante, D. E., Adamczyk, J. J., Strazisar, A. J., and Okiishi, T. H., 2002, "Wake Recovery Performance Benefit in a High-Speed Axial Compressor," ASME J. Turbomach., **124**, pp. 275–284.
[4] Van Zante, D. E., To, W. M., and Chen, J. P., 2002, "Blade Row Interaction Effects on the Performance of a Moderately Loaded NASA Transonic Compressor Stage," ASME paper no. GT-2002-30575.
[5] Gorrell, S. E., Okiishi, T. H., and Copenhaver W. W., 2003, "Stator-Rotor Interactions in a Transonic Compressor-Part 1: Effects of Blade-Row Spacing on Performance," ASME J. Turbomach., **125**, pp. 328–335.
[6] Silkowski, P. D., and Hall, K. C., 1998, "A Coupled Mode Analysis of Unsteady Multistage Flows in Turbomachinery." ASME J. Turbomach., **120**, pp. 410–421.
[7] Li, H. D., and He, L., 2003, "Blade Aerodynamic Damping Variation with Rotor-Stator Gap-A Computational Study using Single-Passage Approach," ASME paper no. GT2003-38199.
[8] Cizmas, P., and Dorney, D. J., 1999, "Parallel Computation of Turbine Blade Clocking," Int. J. Turbo Jet Engines, **16**(1), pp. 49–60.
[9] Barakos, G., Vahdati, M., Sayma, A I., Breard, C., and Imregun, M., 2001, "A Fully Distributed Unstructured Navier-Stokes Solver for Large-Scale Aeroelasticity Computations," Aeronaut. J., **105**, pp. 419–426.
[10] Arnone, A., and Pacciani, R., 1996, "Rotor-Stator Interaction Analysis Using the Navier-Stokes Equations and a Multigrid Method," ASME J. Turbomach., **118**, pp. 679–689.
[11] Li, H. D., and He, L., 2003, "Blade Count and Clocking Effects on Three-Bladerow Interaction in a Transonic Turbine," ASME J. Turbomach., **125**, pp. 632–640.
[12] Erdos, J. I., Alzner, E., and McNally W., 1977, "Numerical solution of periodic transonic flow through a fan stage," AIAA J., **15**(11), pp. 1559–1568.
[13] Giles, M. B., 1990, "Stator/rotor Interaction in a Transonic Turbine," AIAA J. Propul. Power, **6**(5), pp. 621–627.
[14] He, L., 1992, "Method of Simulating Unsteady Turbomachinery Flows with Multiple Perturbations," AIAA J., **30**(11), pp. 2730–2735.
[15] He, L., and Denton, J. D., 1994, "Three-Dimensional Time-Marching Inviscid and Viscous Solutions for Unsteady Flows around Vibrating Blades," ASME J. Turbomach., **116**, pp. 469–476.
[16] Dewhurst, S., and He, L., 2000, "Unsteady Flow Calculations Through Turbo-

machinery Stages Using Single-Passage Domain With Shape-Correction Method," 9th International Symposium on Unsteady Aerodynamics and Aeroelasticity in Turbomachines, Lyon, France, Sept.
[17] Li, H. D., and He, L., 2002, "Single-Passage Analysis of Unsteady Flows Around Vibrating Blades of a Transonic Fan Under Inlet Distortion," ASME J. Turbomach., **124**, pp. 285–292.
[18] Gerolymos, G. A., Michon, G. J., and Neubauer, J., 2002, "Analysis and Application of Chorochronic Periodicity in Turbomachinery Rotor/Stator Interaction Computations," AIAA J. Propul. Power, **18**, pp. 1139–1152.
[19] He, L., Chen, T., Wells, R. G., Li, Y. S., and Ning, W., 2002, "Analysis of Rotor-Rotor and Stator-Stator Interferences in Multi-Stage Turbomachines," ASME J. Turbomach., **124**, pp. 564–571.
[20] Hanamura, Y., and Tanaka, H., 1980, "A Simplified Method to Measure Unsteady Forces Acting on the Vibrating Blades in Cascade," Bull. JSME, **23**(180), pp. 880–887.
[21] Buffum D. H., Capece V. R., King A. J., and El-Aini Y. M., 1998, "Oscillating Cascade Aerodynamics at Large Mean Incidence," ASME J. Turbomach., **120**, pp. 122–130.
[22] Watanabe, T., and Kaji S., 1989, "Theoretical-Study on The Unsteady Aerodynamic Characteristics of an Oscillating Cascade with Tip Clearance-In The Case of a Nonloaded Cascade," JSME Int. J., Ser. II, **32**(3), pp. 368–374
[23] He, L., 1998, "Unsteady flow in Oscillating Turbine Cascade: Part 1-Linear Cascade Experiment," ASME J. Turbomach., **120**(2), pp. 262–268.
[24] Yang, H., and He, L., 2003, "Experiment on Linear Compressor Cascade with 3-D Blade Oscillation," ASME paper no. GT-2003-38434.
[25] Giles, M. B., 1990. Nonreflecting Boundary Conditions for Euler Equation Calculations," AIAA J., **28**(12), pp. 2050–2058.
[26] He, L., 2000, "Three-Dimensional Unsteady Navier-Stokes Analysis of Stator-Rotor Interaction in Axial-Flow Turbines," Proc. Inst. Mech. Eng., Part A, **214**, pp. 13-22.
[27] Li, H. D., and He, L., 2001, "Single-Passage Solution of Three-Dimensional Unsteady Flows in a Transonic Fan Rotor," Proc. Inst. Mech. Eng., Part A, **215**, pp. 653–662.
[28] Leboeuf, F., 1996, "Test Case 1: Transonic Compressor Stage ECL1," Seminar and Workshop on 3D Turbomachinery Flow Prediction IV, January 8-11, Courchevel, France.

Development and Experimental Validation of a Compressor Dynamic Model

M. Venturini
ENDIF - University of Ferrara,
Via Saragat, 1,
44100 Ferrara, Italy

In recent years, transient response analysis of energy systems is becoming more and more important in optimizing plant operation and control. Furthermore, dynamic analyses are also used to integrate steady-state diagnostic analyses, since they allow the detection of malfunctions characterized by time-dependent effects. The paper deals with the development of a nonlinear modular model for compressor dynamic simulation. After developing the compressor mathematical model through a physics-based approach (laws of conservation and thermal balances), the model is implemented through the MATLAB® SIMULINK® tool. Then, a sensitivity analysis is carried out to evaluate the influence of model parameters on the model response. Finally, the model is calibrated on a multistage axial-centrifugal small size compressor running in the test facility of the University of Ferrara (Italy) and validated through experimental data taken on the compressor under investigation. [DOI: 10.1115/1.1928935]

Introduction

The need for gas turbine simulation tools to carry out performance and diagnostic analyses is becoming ever greater. Thus, many studies have been carried out focusing on the development of useful tools able to support plant operation and/or to perform diagnostic analyses [1–4]. In particular, in addition to the analysis in steady-state conditions, there has been a growing interest in the dynamic behavior of energy systems, and so a great deal of research has also been aimed at developing dynamic simulation codes capable of reproducing transient system response [5–9].

In fact, the employment of simulation codes for transient behavior analysis finds useful application not only in power plants design phase and personnel training (as shown for instance in [9]) and in realizing plant control systems [10], but also proves particularly effective in investigating gas turbine component behavior under critical operating conditions [11] and in the presence of unsteady phenomena, such as stall and flutter [12–14], and of faults, especially those which can be recognized from unsteady data analysis [15,16]. In particular, in order to carry out diagnostic analyses, the availability of a dynamic simulation code allows:

- The identification of malfunctions which can be detected only during transient regimes (startup, acceleration, etc.) since they are characterized by time-dependent effects;
- The creation of a database of a great number of faults, together with the analysis of their effects on measurable variables (fault signature). Indeed, a series of experiments, intended to obtain such an amount of data, would be extremely expensive and difficult to perform;
- An automated diagnosis process to be performed through comparison between "healthy" and "faulty" component signatures in transient conditions, as a tool for supporting and integrating steady-state diagnostic analyses;
- The machine control system design in order to properly adapt the control logic to the actual health state of each component.

This paper deals with the development of a nonlinear modular model for the dynamic simulation of compressors. The model is implemented in MATLAB® environment through the SIMULINK® tool, which has proved to be a flexible and powerful tool for dynamic simulation [7,10,17].

The mathematical model is built in a general way through the laws of conservation (mass, momentum, energy, and moment of momentum) and heat balances, written in differential form, and by using the performance maps of the considered compressor, as done in [5,7,8,10,17]. The physics-based approach, since it requires knowledge of the phenomena taking place in the considered machine, allows a better understanding both of the physics of the processes and of the way each malfunction manifests itself, if compared to the use of "black box" models. On the other hand, the development of physics-based models presents some problems related to the quality of the calibration process. For this reason, a sensitivity analysis is carried out to evaluate the influence of the physical parameters, such as volume, friction factor, and heat transfer coefficient on model response.

Finally, the model is calibrated on a multistage axial-centrifugal small size compressor running in the test facility of the University of Ferrara (Italy) [18] and validated through experimental data taken on the compressor under investigation in different transient operating regimes.

Model Development

Mass, Momentum, and Energy Balance. The development of the physical-mathematical model to determine the laws of conservation (mass, momentum, and energy) is carried out starting from a general approach. For an infinitesimal control volume, let the frontal area be A and the infinitesimal thickness be dx. The balance for the *quantity* flowing per unit time through the control volume is

$$A\psi_e + Q_g dV = A\psi_l + \frac{\partial \Gamma}{\partial t} d\mathrm{V} \tag{1}$$

where ψ is the *quantity* flux, Γ the *quantity* concentration, Q_g the *quantity* generated per unit time and unit volume, and "e" and "l" the "entering" and "leaving" sections, respectively. It is worth noting that (i) the *quantity* has to be considered generated if it is generated inside the volume (as the mass generated in a nuclear reaction) and/or if its contribution is external to the system (as, for

Contributed by the International Gas Turbine Institute (IGTI) of THE AMERICAN SOCIETY OF MECHANICAL ENGINEERS for publication in the ASME JOURNAL OF TURBOMACHINERY. Paper presented at the International Gas Turbine and Aeroengine Congress and Exhibition, Vienna, Austria, June 13 – 17, 2004, Paper No. 2004-GT-53416. Manuscript received by IGTI, October 1, 2003; final revision, March 1, 2004. IGTI Review Chair: A. J. Strazisar.

example, the heat exchanged by the system with the outside), (ii) $\psi=\Gamma\nu$, where ν is the velocity of the fluid, and (iii) $dV=Adx$. By expressing function ψ through Taylor formula with Lagrange remainder, it is possible to obtain

$$\psi_l = \psi_e + \left.\frac{\partial\psi}{\partial x}\right|_{\xi} dx \quad \xi \in \,]0;\mathrm{dx}[$$

By substituting the above-derived expression for ψ_l into Eq. (1) and by dividing by dV, it is possible to obtain

$$\frac{\partial\psi}{\partial x} + \frac{\partial\Gamma}{\partial t} = Q_g \tag{2}$$

This general equation of conservation, obtained through the single hypothesis that the frontal area A is constant, allows the laws of conservation (mass, momentum, and energy) to be derived in a form similar as that reported in [8].

In the case of mass balance, the *quantity* is the mass, Γ is the density ρ, while $\psi=\rho\nu$. Since Q_g is equal to zero, the following equation can be obtained:

$$\frac{\partial\rho v}{\partial x} + \frac{\partial\rho}{\partial t} = 0 \tag{3}$$

In the case of momentum balance, the *quantity* is the momentum, Γ is the product $\rho\nu$, while $\psi=\rho\nu^2$. Q_g is equal to the sum of the external forces per unit volume acting on the system, i.e., pressure, friction, and body field forces. In this case, the momentum balance equation can be written as

$$\frac{\partial(\rho\nu^2)}{\partial x} + \frac{\partial\rho\nu}{\partial t} = \sum f = -\frac{\partial p}{\partial x} - f_{fr} - f_{bf}$$

By neglecting the body field forces (mainly due to gravitational field contribution) and by rearranging the terms, the following equation can be obtained:

$$\frac{\partial(p+\rho\nu^2)}{\partial x} + \frac{\partial\rho\nu}{\partial t} = -f_{fr} \tag{4}$$

In the case of energy balance, the *quantity* is the energy e, obtained as the sum of three contributions (internal energy u, body potential energy e_p, and kinetic energy), Γ is equal to ρe, while Q_g is equal to the sum of external heat and work per unit volume exchanged by the system with the outside. By isolating the term of pressure forces and by taking it to the left-hand side of the equation, the following general expression for energy balance can be obtained:

$$\frac{\partial}{\partial x}\left[\rho\nu\left(u+e_p+\frac{\nu^2}{2}+\frac{p}{\rho}\right)\right] + \frac{\partial}{\partial t}\left[\rho\left(u+e_p+\frac{\nu^2}{2}\right)\right] = q - l \tag{5}$$

Moment of Momentum Balance. The well-known equation for moment of momentum balance can be written as

$$J\frac{2\pi}{60}\frac{dN}{dt} = \mathrm{Tq}_s - \mathrm{Tq}_r - \mathrm{Tq}_{\mathrm{fr}} \tag{6}$$

where the three contributions on the right-hand side are due (i) to the torque Tq_s externally supplied (by a turbine or by a motor), (ii) to the resisting torque Tq_r, and (iii) to the torque $\mathrm{Tq}_{\mathrm{fr}}$ due to friction losses. The moment of inertia J is the total moment of inertia calculated with respect to the shaft for which the rotational speed N is evaluated.

Thermal Balance. In order to take into account the thermal phenomena which take place in the system under consideration, the Fourier flux law and the Fourier equation can be used.

The heat transfer from a surface to the free stream can be obtained by means of the balance of heat fluxes at the wall

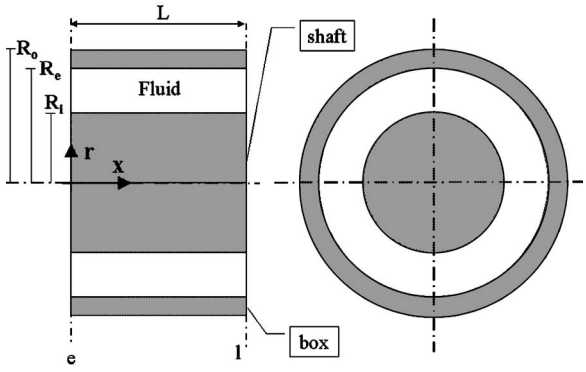

Fig. 1 Module geometrical model

$$\alpha(T_w - T) = -k\,\nabla T\big|_w \tag{7}$$

where T_w and T are the wall and free stream temperatures, respectively, and the term on the right-hand side is derived from the Fourier flux law at the wall. In Eq. (7), the surface is assumed to be at a higher temperature than the free stream.

If the term of energy generation is considered to be zero, the Fourier equation can be written as

$$\rho c\frac{\partial T}{\partial t} = k\nabla^2 T \tag{8}$$

Simplified Form of Balance Equations. Owing to the different gas turbine design characteristics (size, geometry, cooling devices, etc.) that can be encountered in practice, the first hypothesis which is introduced into the model deals with the geometry of the system. It is assumed that each component of a gas turbine can be modeled through one or more annular-shaped cylindrical modules whose length is L and whose internal and external radius are equal to R_i and R_e, respectively. As reported in Fig. 1, the fluid flows between an element called *shaft*, which plays the role of the component rotational shaft, and an element called *box*, representing the component external casing.

According to the model geometrical assumptions, a simplified expression for mass and momentum balance is derived under the following additional hypotheses, by integrating Eqs. (3) and (4) over volume Adx from the "entering" to "leaving" sections

1. Gas state equation $p/\rho=\mathrm{RT}$ and $c_p=c_p(T)$;
2. Constant gas properties in each x section;
3. Isentropic transformation (i.e., $p\rho^{-k}=$constant) and, so, by differentiating, $dp=kRTd\rho$;
4. Expression of friction forces as

$$f_{\mathrm{fr}} = \frac{\lambda}{D_h}\rho\frac{\mathrm{v}^2}{2}$$

Moreover, as shown in [5,7,8], for short-length pipes it is acceptable to integrate along x only the terms in the x derivatives, while, in the other terms (t derivatives and friction forces), T, p, and M can be considered constant with respect to x. In particular, the constant-with-x values for T and M have been assumed equal to their value in the "leaving" section, while p has been assumed equal to the value in the "entering" section in Eq. (9) and equal to the mean value between the two sections in Eq. (10), i.e., $(p_e+p_1)/2$. Thus the new expression of Eqs. (3) and (4) is

$$\frac{\partial p_e}{\partial t} = \frac{k\mathrm{RT}_1}{AL}(M_e - M_l) \tag{9}$$

$$\begin{cases} \dfrac{\partial M_l}{\partial t} = \dfrac{A}{L}(p_e - p_l) - \dfrac{\lambda}{D_h}\dfrac{R}{A}\dfrac{M_l^2 T_l}{(p_e + p_l)} - o \\ o = \dfrac{R}{\mathrm{AL}}\left(M_l^2 \dfrac{T_l}{p_l} - M_e^2 \dfrac{T_e}{p_e}\right) \end{cases} \tag{10}$$

In the general case of long-length pipes, the integration along x can be performed by representing each component as the sum of a series of short-length pipes.

A simplified expression for thermal balance equations was also derived. For the *box* element Eq. (7), written at $r=R_e$ and $r=R_o$, leads to

$$\alpha_e(T - T_{be}) = -k_b[\nabla T_b]_{r=R_e} \tag{11}$$

$$\alpha_o(T_{\mathrm{bo}} - T_{\infty b}) = -k_b[\nabla T_b]_{r=R_o} \tag{12}$$

where the negative sign on the right-hand side of the equations is in accordance with the choice of r versus and $T_{\infty b}$ is the temperature of the environment outside the compressor casing, generally equal to ambient temperature. Temperatures T_{be} and T_{bo} are *box* wall temperatures at $r=R_e$ and $r=R_o$, respectively. From Eq. (8) for the *box* element, it is then possible to obtain

$$\rho_b c_b \frac{\partial T_b}{\partial t} = k_b \nabla^2 T_b \tag{13}$$

By writing Eqs. (11), (12), and (13) in cylindrical coordinates and by assuming that (i) heat fluxes $\alpha_e(T-T_{\mathrm{be}})$ and $\alpha_o(T_{\mathrm{bo}}-T_{\infty b})$ have radial direction and (ii) T_b does not depend on x coordinate, it is possible to obtain

$$\alpha_e A_e(T - T_{\mathrm{be}}) = -k_b A_e \left[\frac{\partial T_b}{\partial r}\right]_{r=R_e} \tag{14}$$

$$\alpha_o A_o(T_{\mathrm{bo}} - T_{\infty b}) = -k_b A_o \left[\frac{\partial T_b}{\partial r}\right]_{r=R_o} \tag{15}$$

$$\rho_b c_b \frac{\partial T_b}{\partial t} = \frac{k_b}{r}\frac{\partial}{\partial r}\left(r\frac{\partial T_b}{\partial r}\right) \tag{16}$$

By integrating Eq. (16) between R_{e} and R_{o}, the following expression can be derived:

$$\int_{R_e}^{R_o} \rho_b c_b \frac{\partial T_b}{\partial t} r dr = k_b \left[r\frac{\partial T_b}{\partial r}\right]_{R_e}^{R_o} \tag{17}$$

If it is supposed that T_b does not depend on coordinate r (i.e., $T_{\mathrm{be}}=T_{\mathrm{bo}}=T_{\mathrm{b}}$) and Eqs. (14) and (15) are substituted into Eq. (17), it is possible to obtain

$$\rho_b c_b V_b \frac{\partial T_b}{\partial t} = \alpha_e A_e(T - T_b) - \alpha_o A_o(T_b - T_{\infty b}) \tag{18}$$

where $A_e=2\pi R_e L$, $A_o=2\pi R_o L$ and $V_b=\pi(R_o^2-R_e^2)L$. This equation was derived under the hypothesis that T_b does not depend on coordinates r and x, which, in turn, means that fluid conductivity is negligible if compared to *box* conductivity.

In a similar way, the thermal balance equation for the *shaft* element can be obtained

$$\rho_s c_s V_s \frac{\partial T_s}{\partial t} = \alpha_i A_i(T - T_s) - \alpha_{\mathrm{cool}} A_i(T_s - T_{\infty s}) \tag{19}$$

In particular, the term $\alpha_{\mathrm{cool}}A_i(T_s-T_{\infty s})$ accounts for the heat flow in steady-state conditions (the shaft does not have the same temperature as the gas flow in steady-state conditions, since it is not isolated from external environment), while $T_{\infty s}$ is the *shaft* cooling temperature, which can be assumed equal to the ambient or to the lube-oil temperature.

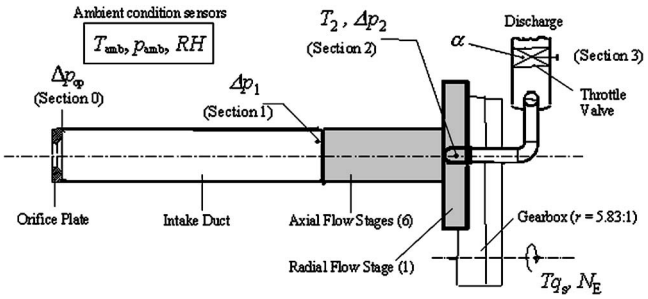

Fig. 2 Compressor test rig and measured variables

Compressor Under Investigation

Test Rig. The test facility under consideration, described in detail in [18], consists of an asynchronous reversible electric motor/brake bench, operated by an inverter. The motor can give a maximum power of 87 kW at 5000 rpm.

Compressor. The compressor, which is part of the Allison 250-C18 turbo-shaft engine, is composed of six axial stages and one centrifugal stage. The compressor operates in an open circuit. As schematically sketched in Fig. 2, the inlet section (an orifice plate) is followed by a pipe, used to perform the inlet mass flow measurement. Then, after flowing through the axial and centrifugal stages, the air is fed to a discharge volume in which a butterfly valve, whose angular position is indicated by α, is inserted for compressor mass flow rate control. A step-up gearbox with a gear ratio r equal to 5.83 (which was part of the original gas turbine) is included in the test setup to analyze a range of compressor rotational speeds up to nearly 30, 000 rpm.

Measurable Variables. Among all the available measurable variables taken on the compressor, the available measurements used for model development and validation are indicated in Fig. 2:

- Ambient temperature, pressure, and relative humidity (T_{amb}, p_{amb}, and RH), which define ambient conditions both at the inlet and at the outlet of the test facility ($T_0=T_{\mathrm{amb}}$ and $p_3=p_{\mathrm{amb}}$);
- Static differential pressure measurements Δp_{op}, Δp_1, and Δp_2. The differential pressure measurement at the orifice plate Δp_{op} is carried out in order to perform the inlet mass flow measurement, while Δp_1 and Δp_2 allow the determination of compressor pressure ratio β_{C};
- Total outlet compressor temperature T_2;
- Rotational speed of the electric motor shaft N_E and shaft torque $\mathrm{Tq_s}$. These measurements allow the determination of the power required to drive the compressor.

Performance Maps. The evaluation of compressor performance maps was carried out in steady-state conditions [18], thus allowing the polytropic efficiency η_C and the pressure ratio β_C to be expressed against the corrected mass flow μ_C for different values of the corrected rotational speed ν_C. In particular, the rotational speed of the compressor can be calculated from the shaft rotational speed by means of the relationship $N_C=rN_E$. The maps, reported in Figs. 3(a) and 3(b), were determined experimentally for different compressor rotational speeds (in the range 6000–30,000 rpm) and were then interpolated by means of a second degree polynomial curve.

Moreover, the region of compressor normal operation was identified between the surge line (occurrence of unsteady phenomena such as surge and/or rotating stall, which were detected by analyzing the dynamic trends of discharge pressure and suction mass flow rate [18]) and the line interpolating the operating points for which the throttle valve was fully open.

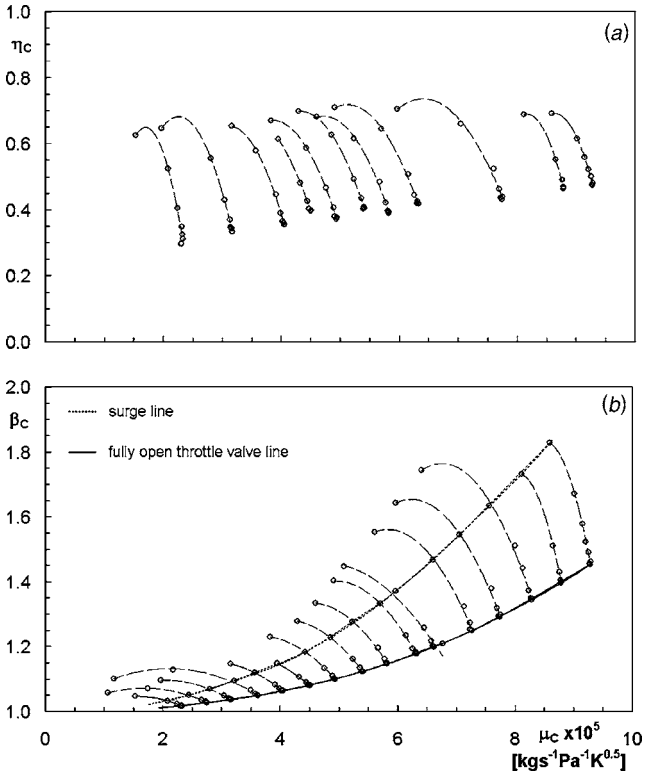

Fig. 3 Compressor performance maps: (◯) measured value; (---) second degree polynomial interpolating curve

Model Implementation

The model is implemented in MATLAB® environment through the SIMULINK® tool, which allows dynamic systems to be modeled through a user-friendly graphical interface. SIMULINK® proved particularly effective since it offered the possibility (i) to create new functions in addition to the libraries which are already available and (ii) to perform the solution of equations through different solvers. In particular, for all the developed modules, a variable-step integration algorithm was used.

A modular structure for system modeling was adopted, by identifying three subsystems (*intake duct, compressor*, and *exhaust duct*), which are sketched in Fig. 4 and are described in detail in the following sections. Each component is modeled by means of a single module, by assuming that the simplification for short-length pipes is acceptable, as previously discussed.

In particular, the *compressor* module is formed by the sum of two submodules, one for "static" and one for "dynamic" simulation [5]. In fact, rises in pressure and temperature in steady-state conditions along the compressor are taken into account by means of machine performance maps, while balance equations are used in order to consider mass storage and thermal exchange phenomena.

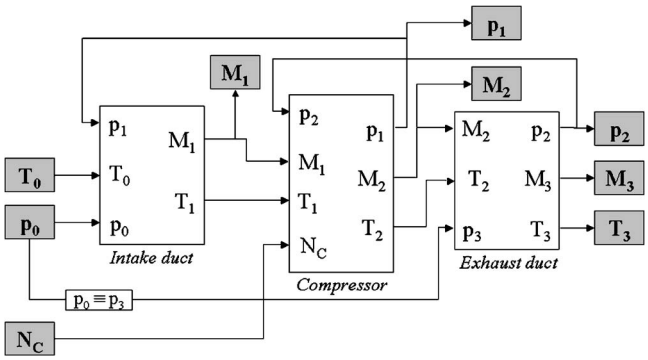

Fig. 4 Model implementation through the SIMULINK® tool

Mass storage effects in the suction and discharge piping systems are taken into account through the *intake* and *exhaust duct* modules. In particular, the application of Eq. (10) to these two modules has shown that the term o in Eq. (10) is negligible and, thus, it has been neglected. The reason for this can be attributed to the fact that the considered test facility is characterized by relatively short length piping volumes and, as a result, storage effects are not very significant. In fact, this implies that $M_e \approx M_1$ and $p_e \approx p_l$, which, in addition to the assumption that $T_e = T_l$ for both modules, finally leads to the conclusion that o is indeed negligible.

Intake Duct Module. The *intake duct* module inputs are ambient pressure p_0 and temperature T_0 and pressure p_1 (from *compressor* module). In order to calculate module outputs, the following equations are used:

- T_1 is assumed equal to T_0, by considering negligible the thermal exchange in the *intake duct*;
- M_1 is determined by means of Eq. (20), which derives from Eq. (10) calculated between sections "0" and "1", and by ignoring the term o on the right-hand side, as anticipated. Thus, the final form of the equation is the following:

$$\frac{\partial M_1}{\partial t} = \frac{A}{L}(p_0 - p_1) - \frac{\lambda}{D_h}\frac{R}{A}\frac{M_1^2 T_1}{(p_0 + p_1)} \tag{20}$$

Compressor Module. The *compressor* module requires the information derived from performance maps and takes into account the presence of heat transfer phenomena.

The *compressor* module inputs are compressor rotational speed N_C, M_1, and T_1 (from *intake duct* module) and pressure p_2 (from *exhaust duct* module). Three outputs are calculated from the module: entering pressure p_1, leaving mass flow rate M_2, and temperature T_2.

Entering pressure p_1 is determined by means of Eq. (21), which derives from Eq. (9) calculated between sections "1" and "2"

$$\frac{\partial p_1}{\partial t} = \frac{kRT_1}{AL}(M_1 - M_2) \tag{21}$$

Since p_2 is an input and p_1 is determined from Eq. (21), compressor pressure ratio is known and, thus, leaving mass flow rate M_2 can be determined from compressor performance map reported in Fig. 3(b). Once the leaving mass flow rate M_2 is known, compressor polytropic efficiency can be determined from the compressor efficiency performance map [Fig. 3(a)]. To do this, *ad hoc* libraries were developed in order to interpolate the curves and to determine the current M_2 value. In particular, a control is performed to verify whether the compressor is working in the region between the surge line and the fully open throttle valve line.

From knowledge of compressor polytropic efficiency, it is possible to calculate the "stationary" (i.e., without taking into account thermal exchange phenomena in unsteady conditions) compressor leaving temperature $T_{2\text{stat}}$ as

$$T_{2\text{stat}} = T_1 \left(\frac{p_2}{p_1}\right)^{(k-1)/(k\eta_c)}$$

Finally, the compressor leaving temperature T_2 is determined by solving the equation below

$$T_2 = T_{2\text{stat}} - \frac{1}{M_2 c_p}\left(\rho_s c_s V_s \frac{\partial T_s}{\partial t} + \rho_b c_b V_b \frac{\partial T_b}{\partial t}\right) \tag{22}$$

where temperature derivatives can be determined by means of Eqs. (18) and (19).

Table 1 Geometrical parameters (D_h and L) and friction factors (λ) used for model calibration estimated parameters indicated in boldface

	D_h[m]	L[m]	λ
Intake duct	0.1	1.00	**0.20**
Compressor	0.1	0.40	
Exhaust duct	**0.1**	**0.79**	**2.05**

Exhaust Duct Module. The *exhaust duct* module inputs are pressure p_3 (equal to ambient pressure p_0), temperature T_2, and mass flow rate M_2 (these two latter from *compressor* module). In order to calculate module outputs (T_3, p_2, and M_3), the following equations were used:

- T_3 is assumed equal to T_2, by considering negligible the thermal exchange in the *exhaust duct*;
- Entering pressure p_2 is determined by means of Eq. (23), which derives from Eq. (9) calculated between sections "2" and "3"

$$\frac{\partial p_2}{\partial t} = \frac{kRT_2}{AL}(M_2 - M_3) \tag{23}$$

- M_3 is determined by means of Eq. (24), which derives from Eq. (10) calculated between sections "2" and "3," and by ignoring the term o on the right-hand side. Thus, the final form of the equation is the following:

$$\frac{\partial M_3}{\partial t} = \frac{A}{L}(p_2 - p_3) - \frac{\lambda}{D_h}\frac{R}{A}\frac{M_3^2 T_3}{(p_2 + p_3)} \tag{24}$$

Model Calibration

Geometrical Parameters and Friction Factors. The geometrical parameters (D_h and L) and the friction factors (λ) which were used to set up the model on the compressor under investigation are reported in Table 1 for the three modules.

According to model assumptions, the compressor geometry was assumed cylindrical, with mean hydraulic diameter equal to 0.1 m and length L equal to 0.4 m.

The determination of the intake duct friction factor λ was performed by using Eq. (20) in steady-state conditions which assumes the form of Eq. (25) in which λ is the only unknown.

$$\frac{A}{L}(p_0 - p_1) = \frac{\lambda}{D_h}\frac{R}{A}\frac{M_1^2 T_1}{(p_0 + p_1)} \tag{25}$$

As regards compressor discharge, whose geometry is quite complex (two pipes which converge into a common discharge volume), the unknowns are three (D_h, L, and λ) and, so, a system of three equations was considered. The procedure for the calculation of the unknowns is as follows:

- Equation (24) is written for three different transient conditions corresponding to the same measured inlet mass flow rate. In fact, if steady-state data were used, the three equations would not be independent from each other;
- It was assumed $M_3 \approx M_0$ (M_0 is a measured quantity) and the derivative $\partial M_3/\partial t$ was evaluated numerically;
- The equation system was solved approximately, by introducing into each equation of the system the bias σ

$$\frac{\partial M_3}{\partial t} - \frac{A}{L}(p_2 - p_3) + \frac{\lambda}{D_h}\frac{R}{A}\frac{M_3^2 T_3}{(p_2 + p_3)} + \sigma = 0 \tag{26}$$

- The values of D_h, L, and λ which minimized the sum of the absolute values of the bias σ in the three equations were adopted for model calibration.

Table 2 Heat transfer parameters

Quantity	Value	Quantity	Value
A_i	0.0653 m^2	α_i	100.0 W/(m^2 K)
A_e	0.1260 m^2	α_e	100.0 W/(m^2 K)
A_o	0.1280 m^2	α_o	10.0 W/(m^2 K)
C_s	159 J/K	$\alpha_{cool}A_i$	0.3 W/K
C_b	315 J/K	T_{oil}	285 K

The numerical results of the procedure applied to the exhaust duct are reported in the third row of Table 1.

Heat Transfer. The quantities associated with the presence of heat transfer (exchange areas, heat transfer coefficients, and thermal capacities) were estimated according to the following assumptions:

- Shaft and box elements are realized in aluminum (ρ=2700 kg/m^3; c=921 J/(kg K); k=210 W/(m K));
- Heat transfer mechanism from box to outside: natural convection;
- Heat transfer mechanism from fluid to box and from fluid to shaft: forced convection.

The heat transfer parameter values adopted in the model are reported in detail in Table 2.

Model Sensitivity Analysis

The influence of geometrical parameters and of friction factors on the model output response (p_1, p_2, M_1, and T_2) was evaluated. A variation of ±10% for each parameter was considered for different values of the rotational speed and the relative variation ΔQ of each output Q was evaluated as

$$\Delta Q = \frac{Q - Q_{ref}}{Q_{ref}}$$

where Q_{ref} is the Q value in correspondence to the reference value of the considered parameter (reported in Tables 1 and 2).

The most interesting results are presented in the following sections for the friction factors of intake duct λ_{1-2} and exhaust duct λ_{2-3} and for exhaust duct hydraulic mean diameter $(D_h)_{2-3}$ and length L_{2-3} in the case of compressor rotational speed N_C equal to 29,150 rpm. The results for heat transfer coefficients are not reported in the paper since it was observed that the influence on all outputs was negligible, since they only affect model transient response, as can be seen from Eq. (22).

Intake Duct Friction Factor. It can be observed (Fig. 5) that

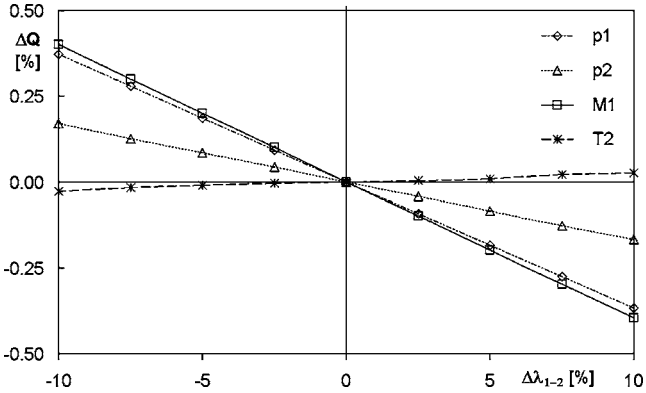

Fig. 5 Intake duct friction factor influence

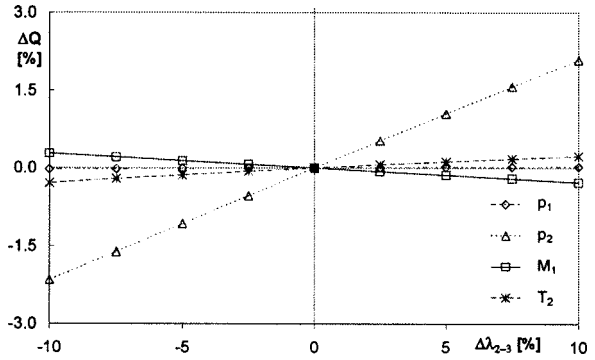

Fig. 6 Exhaust duct friction factor influence

(i) the dependence of all quantities is linear and (ii) p_1 and M_1 are the most sensitive to this parameter, while the influence on T_2 is negligible. In any case, the influence of this parameter on model output is very small: In fact, the order of magnitude of output sensitivity is of about 0.5% with respect to a 10% friction factor variation.

Exhaust Duct Friction Factor. It can be observed (Fig. 6) that (i) the dependence of all quantities is linear, (ii) p_2 is the most sensitive (up to 2%), while p_1 remains almost constant. This implies that the pressure ratio increases and, so, according to the performance maps, the mass flow rate M_1 slightly decreases, while the influence on T_2 is still negligible, according to the fact that the compressor efficiency increases. Furthermore, the evaluation of the influence of exhaust duct length on model response showed that the results are exactly the same as those obtained for exhaust duct friction factor influence, according to Eq. (24).

Exhaust Duct Hydraulic Mean Diameter. As shown in the previous section (Table 1), such a parameter could not be measured and, so, it was estimated. For this reason, the sensitivity analysis proves to be particularly helpful in order to correctly tune the model. In particular, it can be observed from Fig. 7 that an increase in the exhaust duct hydraulic mean diameter allows a greater mass flow rate (up to +1%), though the trend shows a "saturation" effect. Such behavior can be attributed to the fact that, though $(D_h)_{2-3}$ increases and, as a result, the discharge flow-through area increases, the inlet flow-through area remains the same. Moreover, p_1 remains constant, while p_2 decreases significantly (−7.5%), according to the trend of the compressor performance maps. The strong decrease of compressor pressure ratio also leads to a decrease in temperature T_2(−1.5%).

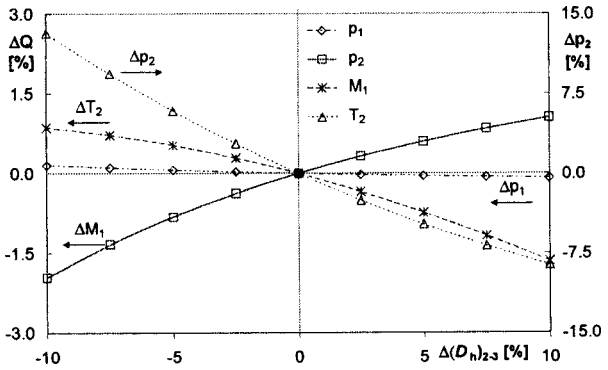

Fig. 7 Exhaust duct hydraulic mean diameter influence

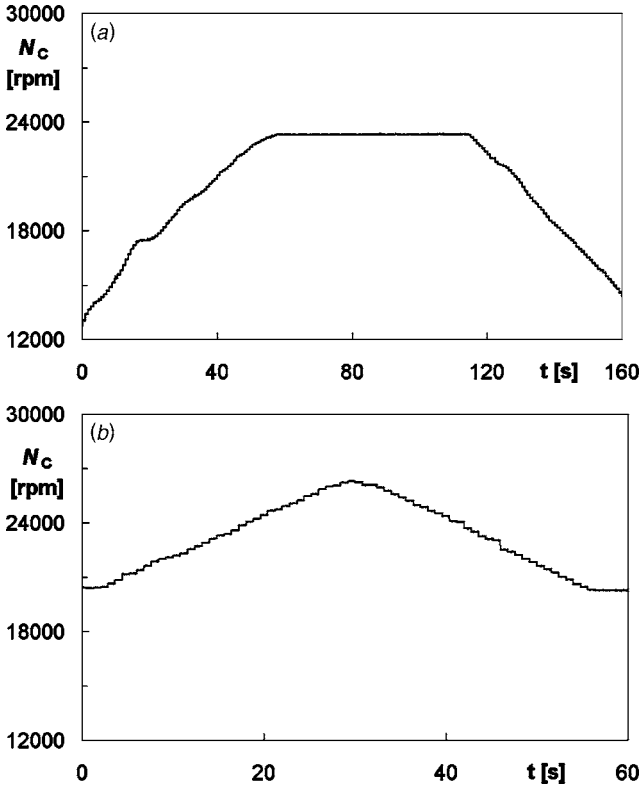

Fig. 8 Rotational speed profile versus time for the two test cases (*a*) *TC*1; (*b*) *TC*2

Model Validation

The developed model was validated by comparing the program response for all outputs (p_1, p_2, M_1, and T_2) against the corresponding measured values: This was possible for pressures p_1 and p_2 and temperature T_2 (the values of these quantities are both measured and computed by the program), while the mass flow rate M_1 was compared with the M_0 measured value since the measurement of M_1 is not available. This latter assumption is valid only in steady-state conditions, i.e., if mass storage effect is negligible between sections "0" and "1," and can be also considered acceptable in unsteady conditions due to *intake duct* small volume.

Two test cases were considered (*TC*1 and *TC*2, whose rotational speed trend is reported in Fig. 8), both taken at quasi-imaginary spin orbit (ISO) conditions ($T_{amb} \approx 17°C$; $p_{amb} \approx 102$ kPa) and representing acceleration and deceleration maneuvers for the compressor. The curves differ from each other since the *TC*1 curve covers a wide range of variation for compressor rotational speed (N_C ranges from about 13,000 up to 23,000 rpm), though rather slowly (160 s), while the *TC*2 curve is more rapid (acceleration in about 30 s), though in a more restricted region of N_C values (from about 20,000 up to 26,000 rpm).

The results of the comparison between measured and predicted values are presented in Figs. 9 and 10. For both test cases, it can be observed that predicted values are generally in good agreement with measured values, since (i) the shape of the predicted curve closely follows the experimental data and (ii) model inertia seems to be the same as physical system inertia (i.e., there is no appreciable delay between model and system response). In particular:

- p_1 is overestimated for low values of the rotational speed (Figs. 9(*a*) and 10(*a*));
- p_2 is underestimated for high values of the rotational speed, mainly in the case of the *TC*2 curve (Fig. 10(*b*));
- The error in predicting the mass flow rate is more evident in

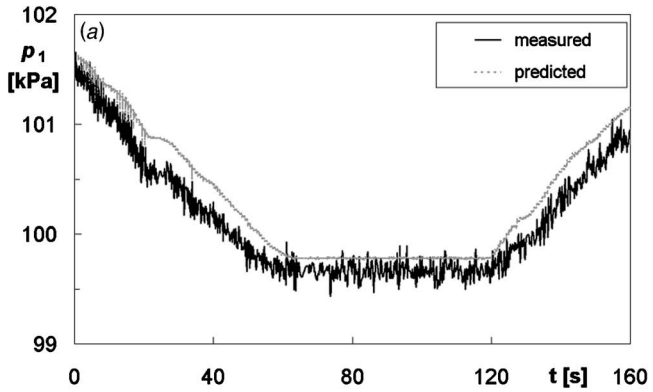

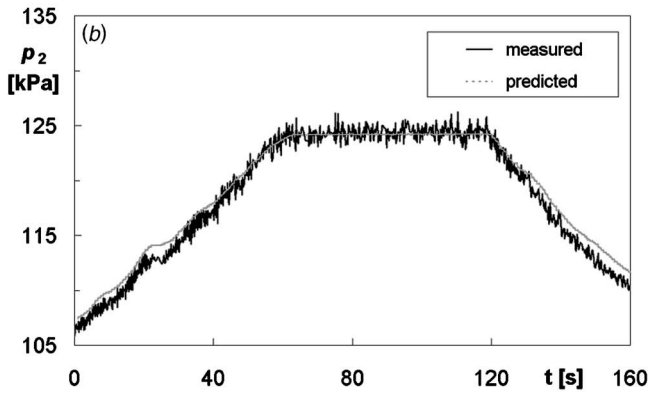

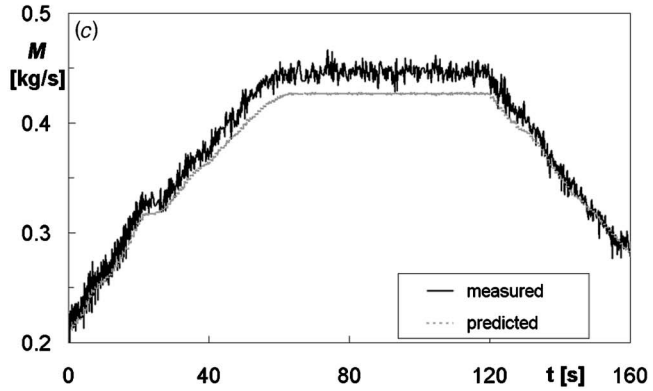

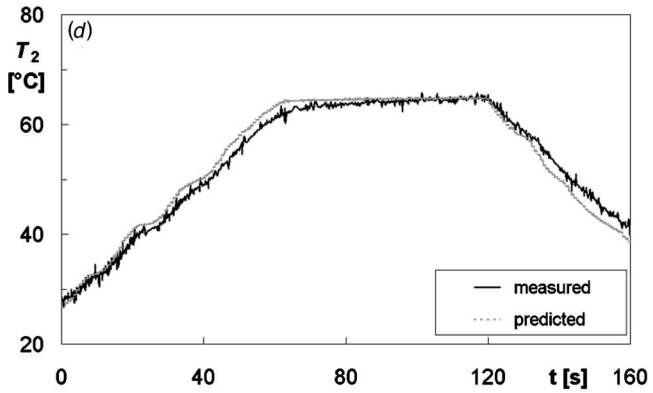

Fig. 9 Comparison of predictions and measured values for the *TC*1 curve: inlet (*a*) and outlet (*b*) compressor pressure, mass flow rate (*c*), and outlet compressor temperature (*d*)

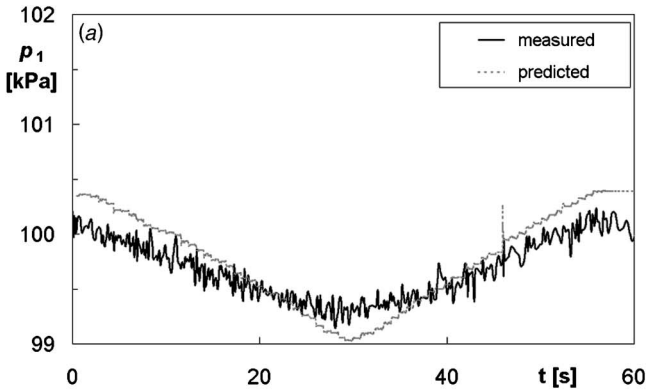

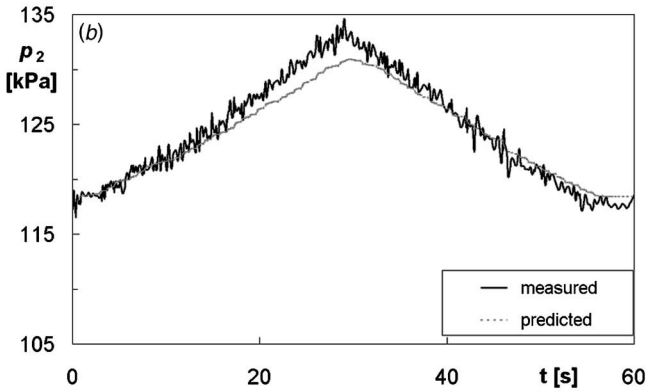

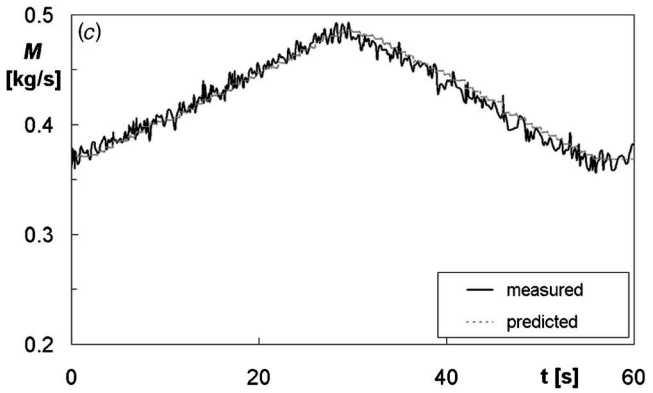

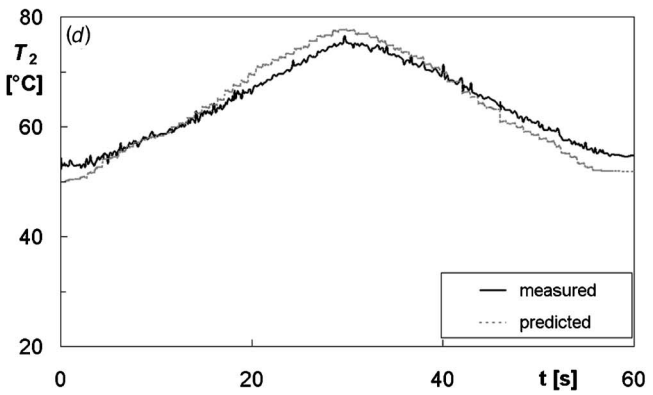

Fig. 10 Comparison of predictions and measured values for the *TC*2 curve: inlet (*a*) and outlet (*b*) compressor pressure, mass flow rate (*c*), and outlet compressor temperature (*d*)

Table 3 Maximum absolute value and standard deviation of errors and RMSE values between computed and predicted values

	TC1	*TC2*	*TC1*	*TC2*	*TC1*	*TC2*
Quantity	Max error	Max error	Stand. Dev.	Stand. Dev.	RMSE [%]	RMSE [%]
p_1[kPa]	0.531	0.481	0.234	0.207	0.233	0.207
p_2[kPa]	2.294	3.925	0.902	1.216	0.794	0.945
M_0[kg/s]	0.040	0.020	0.015	0.007	3.963	1.692
T_2[°C]	4.305	4.431	1.512	2.008	0.472	0.595
Overall					2.038	1.019

the steady-state phase of the *TC*1 curve (Fig. 9(*c*)), while in the *TC*2 curve, which is characterized only by transient regime, this effect is not detectable (Fig. 10(*c*)). This suggests the need for better tuning of the model in reproducing compressor steady-state behavior;

- T_2 is reproduced accurately in the *TC*1 curve, while in the *TC*2 curve the accordance is less evident, though the absolute error between measured and predicted values is small (about 2 °C).

In Table 3, the maximum absolute value and standard deviation of errors between computed and predicted values are reported. For the calculation of maximum absolute value and standard deviation of errors only measured and predicted values after 1 s from the beginning of the maneuvers were considered: This was done since simulated values at the beginning of the simulation are heavily influenced by model initial condition and, so, model prediction error was extremely high.

The analysis of the results presented in Table 3 shows that maximum absolute errors are very small for inlet compressor pressure p_1 (maximum value of about 0.5 kPa), while errors are more significant for outlet compressor pressure p_2 (up to 4.0 kPa) though errors are more uniformly distributed (i.e., the ratio between the standard deviation and the maximum absolute value is lower). Absolute errors between predicted and measured values also seem significant for the mass flow rate (up to 0.04 kg/s) in particular for *TC*1, if compared with measured values (highest measured mass flow rate equal to 0.45 kg/s). The greatest difference between computed and measured values of the outlet compressor temperature T_2 is of about 4.4 °C.

Moreover, Table 3 also shows the values of the root mean square error (RMSE), expressed in percentage, made by the model on the whole set of measured data for each output (p_1, p_2, M_1, and T_2) and for each curve, according to formula (27)

$$\mathrm{RMSE} = \sqrt{\frac{1}{n_{\mathrm{pred}}}\sum_{i=1}^{n_{\mathrm{pred}}}\left(\frac{Q_{\mathrm{meas},i} - Q_{\mathrm{pred},i}}{Q_{\mathrm{meas},i}}\right)^2} \tag{27}$$

where $Q_{\mathrm{meas},i}$ are the measured values, $Q_{\mathrm{pred},i}$ the values predicted through the model and n_{pred} is the number of predicted values (equal to 1383 or 392 for the *TC*1 or *TC*2 curve, respectively). The overall RMSE value was then calculated as

$$\mathrm{RMSE}_{ov} = \sqrt{\frac{1}{n_{\mathrm{o}}}\sum_{j=1}^{n_{\mathrm{o}}}(\mathrm{RMSE}_j)^2} \tag{28}$$

where n_{o} is the number of model outputs (i.e., four).

It can be observed from Table 3 that the results obtained in the simulation of the two curves are comparable for p_1, p_2, and T_2 (RMSE lower than 1% in both cases), while the RMSE for M_0 is different for the two curves and the values are considerably high (4.0% for *TC*1 and 1.7% for *TC*2 curve). For this reason, the overall RMSE value for the *TC*1 curve (about 2%) is twice the overall RMSE value for the *TC*2 curve (about 1%).

Success Rate. In order to further validate the model, a comparison between predictions and measurements for both curves was performed by calculating the success rate for each output. The success rate was determined as the ratio between the number of predicted values lying within measurement uncertainty (i.e., which do not deviate from the corresponding measured values more than the absolute measurement uncertainty) and the total number of predicted values (i.e., 1383 or 392 for *TC*1 or *TC*2 curve, respectively). The estimation of the absolute uncertainties for the measured quantities (reported in Table 4) was performed by using the results of the uncertainty analysis conducted in [18] for a single working point (N_{C} equal to about 29,000 rpm) of the compressor under investigation.

The results are reported in Table 4 for the four outputs (p_1, p_2, M_1, and T_2), by taking into consideration only measured and predicted values after 1 s from the beginning of the maneuvers, as outlined above. The results seem to be very encouraging for both curves since:

- Compressor inlet and outlet pressures are reproduced almost perfectly (success rate equal to 86% in the worst case);
- The success rate for the mass flow rate is not very high (especially for the *TC*1 curve), according to high RMSE values reported in Table 3;
- If T_2 measurement uncertainty as reported in [18] is considered (the *K*-type thermocouple used was on purpose calibrated in a thermostatic bath), the success rate is rather low (46% or 30% for the two curves). On the other hand, if the uncertainty associated to the standard type of this thermo-

Table 4 Ratio between the number of predicted values lying within measurement uncertainty and total number of predicted values (success rate)

				Success rate [%]	
Quantity	Uncertainty		Ref.	*TC*1	*TC*2
p_1	0.636	kPa	[18]	100	100
p_2	1.817	kPa	[18]	98	86
M_0	0.012	kg/s	[18]	50	90
T_2	1.0	°C	[18]	46	30
T_2	2.2	°C	[19]	84	62

couple (which is a Class 2 tolerance thermocouple [19], uncertainty equal to 2.2 °C) is considered, the success rate is more than acceptable (84% or 62%).

The results presented in this section in terms of success rate were obtained by comparing the difference between predictions and measured values to measurement uncertainty alone. Such a criterion is the most restrictive way to validate a code. In fact, as reported in [20] for computational fluid dynamics (CFD) code validation, a model can be considered validated if the difference between the measured and the computed values is lower than the combined uncertainty, which takes into account the combined uncertainty both in the measured value and in the predictions. In particular, the combined uncertainty for measured values (experimental data) takes into account experimental uncertainty. For the combined uncertainty in the predicted values, Coleman and Stern [20] propose to also consider the influence (1) of the numerical solution uncertainty and (2) of the simulation modeling uncertainty arising (a) from the use of previous experimental data and (b) from modeling assumptions. Thus, if all these effects were considered for success rate calculation, the success rate for the developed model would be undoubtedly higher. In any case, the comparison with the results of a similar analysis presented in [5] shows that the model can be considered clearly validated.

Conclusions

In the paper, a mathematical model for compressors dynamic simulation was developed and implemented through the MATLAB® SIMULINK® tool.

The physics-based approach allowed the determination of model parameter influence through a sensitivity analysis. The analysis showed that (i) intake duct friction factor mainly affects inlet compressor pressure and mass flow rate, (ii) exhaust duct friction factor influences outlet compressor pressure significantly, and (iii) an increase in the exhaust duct hydraulic mean diameter allows a greater mass flow rate, while outlet compressor pressure and outlet compressor temperature decrease.

The model was then successfully calibrated on a multi-stage axial-centrifugal small size compressor. Model validation against experimental data showed, for both considered test cases, that (i) predicted values closely follow experimental data, without appreciable delay between model and system response and (ii) for all model outputs, the number of predicted values which do not deviate from the corresponding measured values more than the absolute measurement uncertainty is clearly acceptable.

Future developments of the present study will deal with the implementation of the model which uses as an input the measured value of the torque supplied to the compressor instead of compressor rotational speed. Furthermore, neural networks will be set up in order to support already-developed physics-based models and to verify the capability of such a tool in dealing with transient data. Finally, compressor behavior in the presence of implanted faults and/or in off-design conditions will be investigated by means of both simulation tools (physics-based models and neural networks) in order to build a database in which malfunctions (ranked in type and severity) will be related to measured values and health indices variations.

Acknowledgment

The work was carried out with the support of the M.U.R.S.T. (Italian Ministry of University and Scientific & Technological Research). The author gratefully acknowledges Professor Roberto Bettocchi, Professor Pier Ruggero Spina, and Michele Pinelli PhD for the suggestions provided during the work and Dr. Mirko Morini for his precious support in the model setup.

Nomenclature

A = control volume frontal area
C = $c\rho V$ thermal capacity
c = specific heat
D_h = hydraulic mean diameter
e = specific energy
f = force per unit volume
J = moment of inertia
k = thermal conductivity, ratio of specific heats c_p/c_v
L = length
l = work per unit volume
M = mass flow rate
N = rotational speed
n_o = number of outputs
n_{pred} = number of predicted values
P = power
p = pressure
Q = quantity
q = heat per unit volume
R = radius, gas constant
r = radial coordinate, N_C/N_E gearbox velocity ratio
RH = relative humidity
RMSE = root mean square error
T = temperature
t = time
Tq = torque
u = specific internal energy
V = volume
v = flow velocity
x = axial coordinate
α = heat transfer coefficient, throttle valve position
β = pressure ratio
Γ = concentration
η = efficiency
λ = friction factor
ψ = flux
μ = $M\sqrt{T}/p$ corrected mass flow rate
ν = $N/\sqrt{T}$ corrected rotational speed
ρ = density

Subscripts and Superscripts

0,1,2,3 = model sections
amb = ambient
b = box
bf = body field
C = compressor
cool = cooling
E = electric motor
e = entering, external
fr = friction
g = generated
i = internal
l = leaving
meas = measured
o = outlet
oil = lube oil
op = orifice plate
ov = overall
p = potential, constant pressure
pred = predicted
r = resisting
ref = reference
s = shaft, supplied
stat = stationary
v = constant volume
w = wall
∞ = outside

References

[1] Madej, J., Longtin, K., and Smith, D.-P., 1996, "Monitoring and Diagnostics Service Delivery System," *Proc., 39th GE Turbine State-of-the-Art Technology Seminar*, GE Ed., GER-3956, Schnectady, Aug. 26–29, pp. 1–8.

[2] Bettocchi, R., and Spina, P. R., 1999, "Diagnosis of Gas Turbine Operating Conditions by Means of the Inverse Cycle Calculation," ASME Paper No. 99-GT-185.

[3] Tsalavoutas, A., Aretakis, N., Mathioudakis, K., and Stamatis, A., 2000, "Combining Advanced Data Analysis Methods for the Constitution of an Integrated Gas Turbine Condition Monitoring and Diagnostic System," ASME Paper No. 2000-GT-0034.

[4] Bettocchi, R., Pinelli, M., Spina, P. R., Venturini, M., and Sebastanelli, S., 2001, "A System for Health State Determination of Natural Gas Compression Gas Turbines," ASME Paper No. 2001-GT-0223.

[5] Blotemberg, W., 1993, "A Model for the Dynamic Simulation of a Two-Shaft Industrial Gas Turbine With Dry Low No_x Combustor," ASME Paper No. 93-GT-355.

[6] Schobeiri, M. T., Attia, M., and Lippe, C., 1994, "GETRAN: A Generic, Modularly Structured Computer Code for Simulation of Dynamic Behavior of Aero- and Power Generation Gas Turbine Engines," ASME J. Eng. Gas Turbines Power, **116**, pp. 483–494.

[7] Bettocchi, R., Spina, P. R., and Fabbri, F., 1996, "Dynamic Modeling of Single-Shaft Industrial Gas Turbine," ASME Paper No. 96-GT-332.

[8] Bianchi, M., Peretto, A., and Spina, P. R., 1998, "Modular Dynamic Model of Multi-Shaft Gas Turbine and Validation Test," *Proc. "The Winter Annual Meeting of ASME,"* AES - 38, ASME, New York, pp. 73–81.

[9] De Mello, F. P., and Ahner, D. J., 1994, "Dynamic Models for Combined Cycle Plants in Power System Studies," IEEE Trans. Power Appar. Syst., **9**(3), 7698–7708.

[10] Camporeale, S. M., Fortunato, B., and Mastrovito, M., 2002, "A High-Fidelity Real-Time Simulation Code of Gas Turbine Dynamics for Control Applications," ASME Paper No. GT-2002-30039.

[11] Botros, K. K., Jungowski W. M., and Richards D. J., 1996, "Compressor Station Recycle System Dynamics During Emergency Shutdown," ASME J. Eng. Gas Turbines Power, **118**, pp. 641–653.

[12] Baojie, L., Hongwei, W., Huoxing, L. Hongjun, Y., Haokang, J., and Maozhang, C., 2003, "Experimental Investigation of Unsteady Flow Field in the Tip Rregion of an Axial Compressor Rotor Passage at Near Stall Condition With SPIV," ASME Ppaper No. GT2003-38185.

[13] Sanders, A. J., Hassan, K. K., and Rabe, D. C., 2003, "Experimental and Numerical Study of Stall Flutter in a Transonic Low-Aspect Ratio Fan Blisk," ASME Paper No. GT2003-38353.

[14] Cellai, A., Ferrara, G., Ferrari, L., Mengoni, C. P., and Baldassarre, L., 2003, "Experimental Investigation and Characterization of the Rotating Stall in a High Pressure Centrifugal Compressor. Part IV: Impeller Influence on Diffuser Stability," ASME Paper No. GT2003-38394.

[15] Dedoussis, V., Mathioudakis, K., and Papailiou, K. D., 1997, "Numerical Simulation of Blade Fault Signatures From Unsteady Wall Pressure Signals," ASME J. Eng. Gas Turbines Power, **119**, pp. 362–369.

[16] Aretakis, N., Mathioudakis, K., and Stamatis, A., 1998, "Blade Fault Recognition Based on Signal Processing and Adaptive Fluid Dynamic Modeling," ASME J. Eng. Gas Turbines Power, **120**, pp. 543–549.

[17] Changduk, K., Hongsuk, R., and Kangtaek, L., 2003, "Steady-State and Transient Simulation of Turboprop Engine Using Simulink Model," ASME Paper No. GT2003-38181.

[18] Bettocchi, R., Pinelli, M., and Spina, P. R., 2003, "A Multi-Stage Compressor Test Facility: Uncertainty Analysis and Preliminary Test Results," ASME J. Eng. Gas Turbines Power, **127**(1), 170–177.

[19] *Annual Book of ASTM Standards, Temperature Measurement*, 1998, 14.03, American Society for Testing and Philadelphia, PA.

[20] Coleman, H. W., and Stern, F., 1997, "Uncertainties and CFD Code Validation," ASME J. Fluids Eng., **119**, pp. 795–803.

Adiabatic Effectiveness Measurements and Predictions of Leakage Flows Along a Blade Endwall

W. W. Ranson

K. A. Thole

Department of Mechanical Engineering,
Virginia Polytechnic Institute and State University,
Blacksburg, VA 24060

F. J. Cunha

Pratt & Whitney,
United Technologies Corporation,
East Hartford, CT 06108

Traditional cooling schemes have been developed to cool turbine blades using high-pressure compressor air that bypasses the combustor. This high-pressure forces cooling air into the hot main gas path through seal slots. While parasitic leakages can provide a cooling benefit, they also represent aerodynamic losses. The results from the combined experimental and computational studies reported in this paper address the cooling benefit from leakage flows that occur along the platform of a first stage turbine blade. A scaled-up, blade geometry with an upstream slot, a mid-passage slot, and a downstream slot was tested in a linear cascade placed in a low-speed wind tunnel. Results show that the leakage flow through the mid-passage gap provides only a small cooling benefit to the platform. There is little to no benefit to the blade platform that results by increasing the coolant flow through the mid-passage gap. Unlike the mid-passage gap, leakage flow from the upstream slot provides good cooling to the platform surface, particularly in certain regions of the platform. Relatively good agreement was observed between the computational and experimental results, although computations overpredicted the cooling. [DOI: 10.1115/1.1929809]

Introduction

First stage turbine blades are exposed to harsh operating conditions and temperatures that exceed the melting temperature of the blades. In nearly all gas turbine engines, cooler air from the compressor bypasses the combustion chamber. Traditional techniques have been used to cool turbine blades such as impingement cooling, film cooling, and convective cooling. Unfortunately, sealing interfaces inherent to rotating machinery results in gaps for high-pressure cooling flow to leak into the main hot gas path. Gaps exist between vanes and blades and between adjacent blades.

The elimination of leakage flows provides better performance. However, leakage flows also provide some cooling. Therefore, it is important to understand the effect of leakage flows on the cooling of turbine blade platforms. The work presented in this paper quantifies the benefit of coolant leakage in the platform region of a turbine blade in a linear cascade.

A detailed experimental and computational study of a turbine blade with leakage flows from a backward facing upstream slot, which represents the gap between vane and blade stages, a featherseal gap, which represents the mid-passage gap between adjacent airfoils, and a downstream slot, which represents the gap between the next turbine stage. In particular, the focus was on the effects of different leakage flow rates on the adiabatic effectiveness levels along the blade platform. Computational results were compared to experimental measurements. Additionally, thermal field measurements were taken.

Past Studies

Numerous papers have benchmarked the secondary flow fields and their effects on heat transfer along an uncooled endwall in linear cascades (Langston et al. [1], Graziani et al. [2], Sharma and Butler [3], Goldstein and Spores [4], and Kang et al. [5]). Most of the geometries that were used, however, were representative of vane designs, which typically have much different characteristics than a blade design. Though these studies have yielded a fundamental understanding of the complex flows along a vane endwall, they have not directly addressed the effects of leakage flows.

Some of the earliest work related to endwall cooling by leakage flows was performed by Blair [6], who used a two-dimensional flush slot upstream of a vane geometry. Increases in cooling effectiveness along the endwall were observed as the flow through the slot was increased. In a similar study of coolant upstream of a vane passage, Burd et al. [7] studied the effects of an upstream flush, 45° slot. By using coolant flows as high as 6% of the total passage flow, good cooling was observed over the endwall and both sides of the vanes. A study by Colban and Thole [8] measured the effects of changing the combustor liner film-cooling and junction slot flows on the effectiveness levels along the endwall of a first stage turbine vane. Their results show the coolant from the slot was not uniform across the exit, with coolant accumulating along the endwall near the suction side of the vane. Coolant injection from the upstream combustor liner causes different total pressure profiles entering the vane passage that in turn changed the secondary flow field. Studies by Zhang and Jaiswal [9], Nicklas [10], and Knost and Thole [11] have studied the combined effects of upstream slot cooling and film hole cooling in a turbine vane passage. Results showed that slots upstream of the passage provided nonuniform cooling along the vane endwall with a difficult region to cool being the pressure side.

Using a simple flat plate geometry with no turbine airfoils, Yu and Chyu [12] studied the influence of gap leakage downstream of injection cooling holes. They observed that for a moderate level of film cooling upstream of a coolant slot, the combined presence of the gap promoted better coolant film protection. However, as the film-cooling flow was increased, the coolant from the gap appeared to lift the slot flow coolant from the wall, resulting in decreased adiabatic effectiveness.

The only known study of flows from a featherseal-like slot within an airfoil passage was performed by Aunapu et al. [13].

Contributed by the Turbomachinery Division of THE AMERICAN SOCIETY OF MECHANICAL ENGINEERS for publication in the JOURNAL OF TURBOMACHINERY. Manuscript received by the ASME Turbomachinery Division September 26, 2004; final revision received January 18, 2005. Editor: D. Wisler.

Table 1 Blade geometry

Blade parameter	Value
Scaling factor	11X
Inlet angle	19.2°
Blade angle	20°
Inlet Reynolds number on true chord	3.0*E*+05
True Chord/Axial chord	1.05
Pitch/Axial chord	0.79
Span/Axial chord	1.28

They used blowing through a passage gap in an attempt to reduce the effects of a passage vortex. They hypothesized endwall blowing in the blade passage would have a similar affect seen by Chung and Simon [14], who used a fence in the middle of the passage to lift the passage vortex. Aunapu et al. [13] observed that endwall jets in the center of the blade passage effectively altered the path of the pressure side leg of the vortex. Unfortunately, the increased blowing caused higher turbulence and higher aerodynamic losses.

In summary, there have been no studies directly addressing the benefits of coolant leakage flows from small gaps within adjacent airfoil passages. Moreover, there have been no studies with combined upstream and mid-passage coolant leakage through the platform of a turbine blade. It is important to understand the effect of coolant flow from leakage points in the hub region to further the technology of turbine blade cooling.

Experimental Procedures

The blade geometry used for this work represents a modified design for the first stage of a gas turbine. The modifications from the original engine geometry were made to ensure correctly scaled pressure loading around the blades when operating in a low-speed testing environment. To ensure good measurement resolution while matching realistic engine flows, the blades were scaled up 11×. The turbine blade geometry is two dimensional, having no variation in the span direction. This uniform cross section represents the cross section at the blade–hub intersection. Additionally, the platform was modeled as a flat surface with no curvature. A summary of geometry and flow conditions is given in Table 1.

The three main leakage features studied were the upstream slot, the featherseal, and the aft slot, as shown in Fig. 1. Even though in actual gas turbines the sizes of these gaps change with temperature, the sizes of the leakage features were held constant for this study. While the aft gap was a slot with a width of 5.5% of the blade chord, the upstream slot was a backward facing slot at an angle of 17 deg. Figure 2 shows a side view of the upstream slot that was a backward facing step, and the fillet that was used at the base of the blades. The locations where the featherseal attaches to the front and aft slots are referred to as the front and aft gutter, respectively. The lengths and widths of the leakage features are summarized in Table 2.

The features were fed by three independently controlled plenums, including one for the featherseal, a second for the upstream slot and front gutter, and a third for the aft slot and aft gutter. Thus, the leakage settings for the front slot controlled the flow out of both the front slot and front gutter, and the leakage settings for the aft slot controlled flow out of both the aft slot and the aft gutter.

The test section used for this study was a four blade, three passage, linear cascade where the flow angles were matched by staggering the blades. To compare the effects of the featherseal on cooling of the endwall, the middle passage did not contain a featherseal. Figure 3 shows a top view of the test rig. By setting the flows from the upstream normal jets, the inlet turbulence intensity was 10% and the length scale was 11 cm. Inlet velocity was 11 m/s. To ensure adiabatic measurements, the platform region was constructed out of low thermal conductivity foam

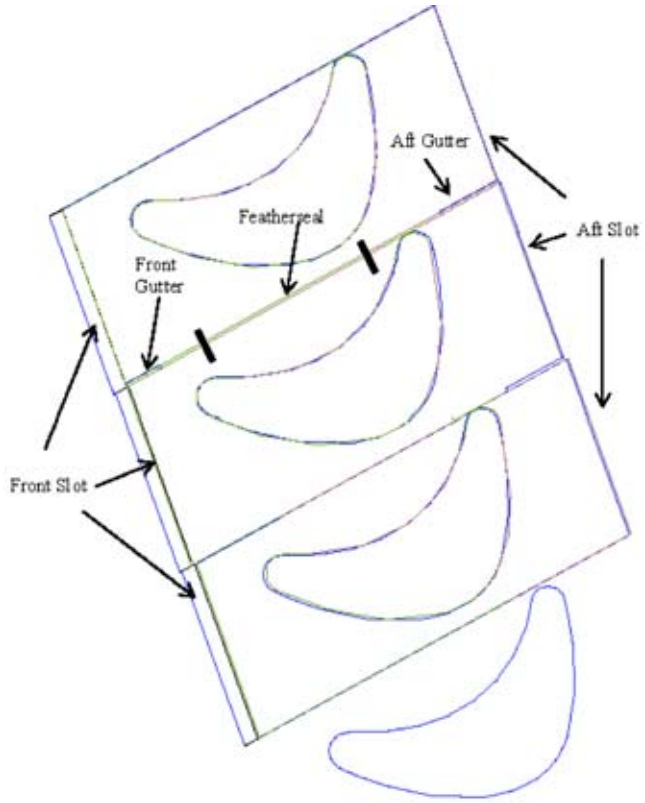

Fig. 1 Schematic of test section (thermal rake locations for Figs. 10 and 11 indicated)

(0.021 W/m K). The blades were also constructed with low thermal conductivity foam and coated with a black Teflon® film. Pressure taps were installed in the midspan of the blades to verify

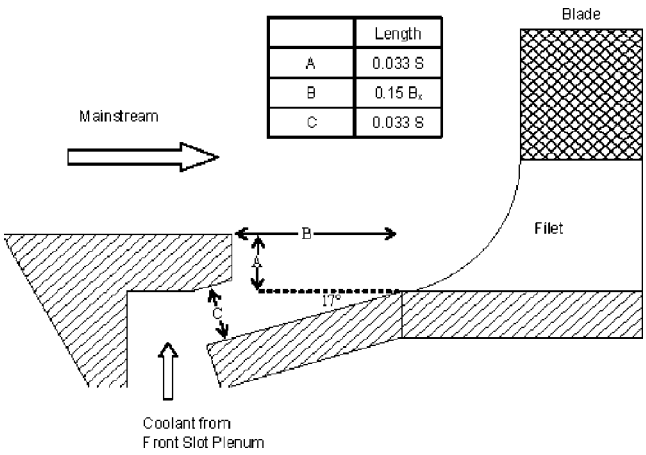

Fig. 2 Side view of backward facing step in the front slot, which contains the front gutter

Table 2 Sizes of scaled test leakage features

	Axial length	Gap width
Front slot	2.7 *P*	0.048 B_x
Aft slot	2.7 *P*	0.055 B_x
Feather seal	1.3 B_x	0.0013 *P*
Front gutter	0.14 B_x	0.008 *P*
Aft gutter	0.26 B_x	0.008 *P*

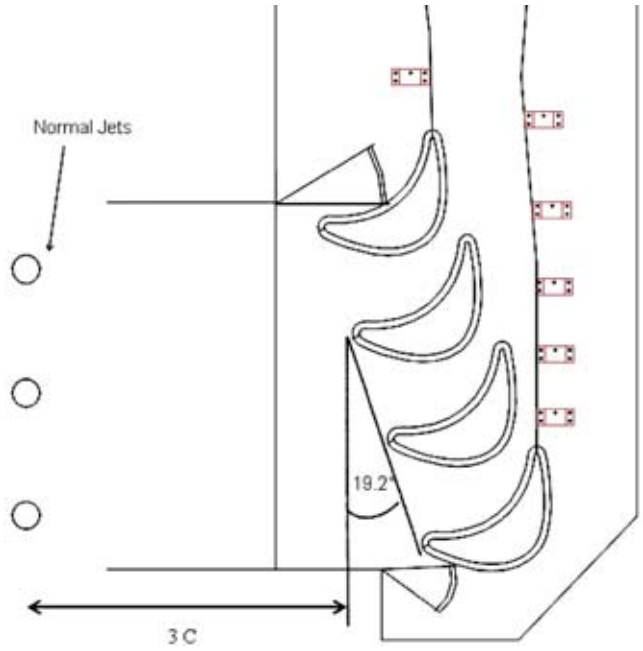

Fig. 3 Schematic of linear blade cascade, including flexible walls and upstream normal jets

the correct pressure distribution around the blades. By adjusting the flexible walls shown in Fig. 3, periodicity between the passages was ensured. Good agreement was indicated between the nondimensional pressure distribution at the midspan obtained from computational predictions and experimental measurements shown in Fig. 4.

A set of simulations focused on investigating the effects of leakage flows from the various slots, as shown in Table 3. All of the flows are listed as a percent of the total inlet core flow. The aft slot flow was set at a constant 1.5% of the inlet flow as the aft slot is sufficiently downstream of the platform region of the blades in this study. In actual turbine engines, the aft slot of this study is the front slot of the next set of stator blades.

Since the front and aft slots were supplied by flow from the bottom passage of the wind tunnel, the mass flow through the slots was calculated from the pressure difference measured between pressure taps in the plenums and the platform surface. To calculate

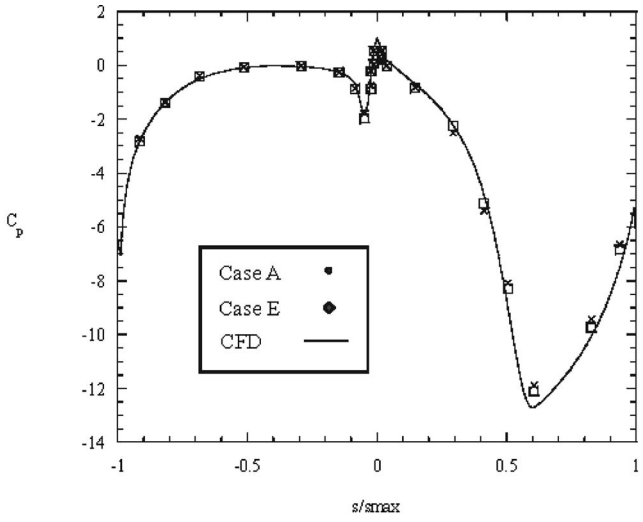

Fig. 4 Measured and predicted pressure distributions

Table 3 Text matrix. *denotes CFD modeling.

	Percent of total inlet mass flow				
	Case A*	Case B*	Case C*	Case D*	Case E
Featherseal	0.25%	0.50%	0.75%	0.75%	0.50%
Front slot	1.50%	1.50%	1.50%	2.00%	0.50%
Aft slot	1.50%	1.50%	1.50%	1.50%	1.50%
Total	3.25%	3.50%	3.75%	4.25%	2.50%

the actual mass flow from this ideal calculation, a discharge coefficient of 0.6 was assumed. The featherseal plenum was fed by compressed air, thus the mass flow was measured directly with a laminar flow element (LFE).

To accurately measure the adiabatic effectiveness levels along the endwall, we used infrared thermography. Since the viewing area of the infrared camera is dictated by the distance between the camera and the platform region (which is the blade span), 19 viewing ports were constructed in the top surface of the test rig to capture the entire platform region. To reduce the precision uncertainty in the infrared images, 5 images were taken at each of the 19 view ports for every test case. Each of the five images was averaged into one image, which was then calibrated based upon thermocouple measurements placed in the endwall. Using an in-house MATLAB [15] code, each of the 19 images was oriented in their correct position to create a complete temperature map of the entire platform region. The resulting temperature is reported in terms of adiabatic effectiveness, η. For all the testing, the typical difference between coolant and mainstream temperature was approximately 25°C. In addition to infrared thermography, thermal field measurements were taken perpendicular the featherseal at two locations, 9% and 27% of the chord length from the front slot. The thermal fields were measured using a rake consisting of 21 thermocouples that were evenly spaced 5.1 mm apart.

For the static pressure measurements, the total uncertainty in C_p was calculated to be 7.5%. The C_p uncertainty was high because this pressure quantity is calculated from three separate pressure measurements, each of which had an uncertainty that propagates through the calculation. For the temperature measurements, all of the thermocouples were calibrated in an ice bath to have a bias uncertainty of 0.2°C. The combined temperature and pressure uncertainties resulted in a mass flow uncertainty of 0.0046 kg/s, which was 11.5% of the low flow conditions and 7.6% of the high flow conditions. This uncertainty in the temperature measurement yields an uncertainty in the thermal field measurements (Θ) of 0.03. The uncertainty in the adiabatic effectiveness (η) measurements, which includes the uncertainty of the infrared camera, was 0.035, which is 17.5% of η=0.2 and 4.4% of η=0.8. The turbulence level uncertainty was 1.8%.

Computational Methodology

A commercially available computational fluid dynamics (CFD) code, FLUENT [16], was used to perform all the simulations. FLUENT is a pressure-based, incompressible flow solver that can be used with structured or unstructured grids. An unstructured grid was used for the study presented in this paper. Solutions were obtained by numerically solving the Navier–Stokes and energy equation through a control volume technique. All geometric construction and meshing were performed with GAMBIT.

Computations were performed on a single turbine blade exposed to periodic conditions along all boundaries in the pitchwise direction. Inlet conditions to the model were set as a uniform inlet velocity at one chord length upstream of the blade. Because the inlet flow from the front rim was at most 2.0% (Table 3) of the passage flow, the inlet passage flow was maintained the same for all the simulations. Flow angles were set to match those conditions of the experiments as well as the scaled values for the engine

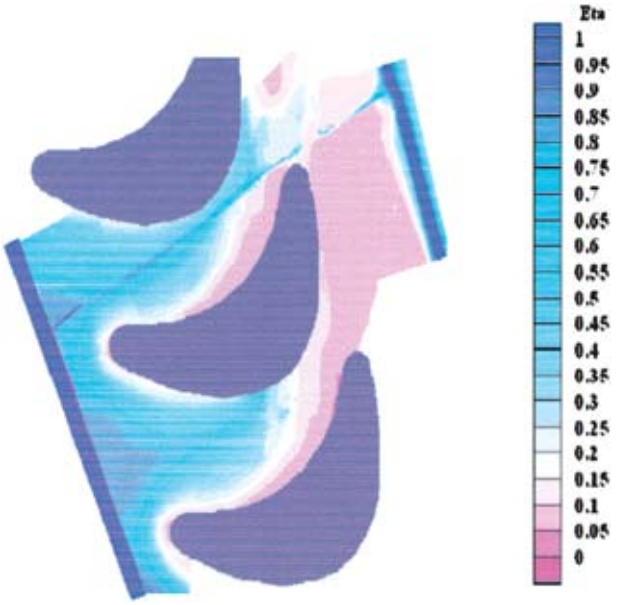

Fig. 5 Adiabatic effectiveness measurements for 1.5% front slot and aft slot, and 0.25% featherseal flow

while turbulence levels were set to 10%. Three separate inflow boundary conditions were used to supply each of the leakage features. The density ratio of the coolant to the mainstream was nearly one ($\sim$1.06) for all of the experimental and computational cases. An outflow boundary was applied 1.5 chords downstream of the blade.

Only one-half of the blade span was modeled. Comparisons made between the entire span and half the span showed no differences in the resulting pressure or thermal results. Thus, only half the span was simulated extending from the platform to the midspan. The boundary conditions at the midspan were set as a slip wall (frictionless) while a no-slip boundary condition was applied at the platform. Although the relative motion of rotor blades to stator vanes can be computationally modeled, that boundary condition was not examined in order to match the experimental studies in a linear blade cascade.

All computations were performed using the RNG κ-ε turbulence model with nonequilibrium wall functions whereby the near-wall region was resolved to y^+ values ranging between 30 and 60. Mesh insensitivity was confirmed though several grid adaptions based upon viscous wall values, velocity gradients, and temperature gradients. Typical mesh sizes were composed of 1.4 million cells. Adaptions from a mesh of 1.3 million to 2.0 million resulted in variations of the pitchwise-averaged adiabatic effectiveness values of $\Delta\eta = \pm 0.008$ at a level of $\eta = 0.4$. The convergence of residuals for continuity, x-momentum, y-momentum, z-momentum, κ and ε were resolved to levels of 10^{-4}. The energy equation was set to a convergence of residuals of 10^{-7}. Typical convergence required 1500 iterations for convergence to be met.

Experimental Results

As was indicated in the test matrix, Table 3, the data for the first three cases (Cases A–C) were simulated to determine the effect of flow through the featherseal only while flows through all of the other slots remained the same. The last three cases in Table 3 (Cases C–E) show the effects of changing the coolant flow levels through the upstream backward-facing slot.

Featherseal Coolant Effects. Figure 5 shows adiabatic effectiveness measurements for the featherseal flow of 0.25% of the total passage flow and the front and aft slot each having 1.5% of the total passage (Case A). Recall that only one of the passages actually contains the featherseal (top passage in Fig. 5). The size of the blade images in Fig. 5 is slightly larger the blade geometry since these images include the fillet at the blade–endwall juncture. As shown in Fig. 5, the front slot leakage dominates the cooling of the platform region with adiabatic effectiveness measurements between 0.8 and 0.9 just downstream of the front slot. Although the coolant from the front slot provides ample cooling of the endwall region downstream of the slot, the leading edges of the blades are not cooled. An examination of the lower passage in Fig. 5 shows the front slot coolant has almost no effect on cooling the pressure side of the blades, as the adiabatic effectiveness values near the trailing edge pressure side of the blades are close to zero. The lack of pressure side cooling from the front slot matches the results of Colban et al. [8], who also showed that even with large coolant flows from their backward-facing slot, cooling was not present near the pressure side of the vane. Additionally shown in Fig. 5, toward the trailing edge of the blades, the upstream slot flow has no affect on the aft portion of the blade along the suction side. As shown in the bottom passage, the coolant from the upstream slot affects only the first 60% of the chord length. In contrast to the lower passage, the coolant leakage from the featherseal in the upper passage provides some cooling along the aft portion of the blade along the suction side. Without the featherseal, the adiabatic effectiveness values near the trailing edge of the suction side are below 0.2, while the adiabatic effectiveness values near the trailing edge with the featherseal coolant are near 0.6. The flow from the featherseal, however, does not have a beneficial effect on the pressure side.

Coolant from the featherseal has more of an effect on the suction side of the blade because the inherent pressure distribution between the blades tends to pull flow from the pressure side to the suction side of the blades. Although flow is swept toward the suction side of the blades near the trailing edge of the blade passage, coolant from the featherseal at the passage inlet is swept toward the pressure side of the blades. In addition to the effects of pressure side to suction side flow, the featherseal coolant is also affected by the passage vortex. An analysis of this phenomenon is discussed in the Thermal Field Measurement section of this paper.

The flow is initially swept toward the pressure side of the blades because of the angle that the mainstream flow enters the test passage. The mainstream flow initially causes the featherseal coolant to flow toward the pressure side as the momentum of the flow pushes the coolant towards the pressure side of the blades. However, as the pressure distribution along the blade endwall overcomes the inlet flow momentum, the coolant from the featherseal is then swept toward the suction side of the blades. This effect will be further illustrated through the CFD results. In Fig. 5, at the inlet to the passage, the coolant is visible with an adiabatic effectiveness level of nearly one (indicating the coolant temperature). Toward the trailing edge of the featherseal, the coolant flow is less visible. The decrease in observable featherseal coolant is due to the direction of the mainstream flow.

Toward the beginning of the blade passage, the mainstream flow is nearly parallel to the featherseal. However, toward the trailing edge, the flow is nearly perpendicular to the featherseal, which sweeps flow away from the featherseal. Though there are less visible adiabatic effectiveness levels near the trailing edge, the cooling benefits of the featherseal are more observable near the trailing edge of the blades, where the effectiveness levels increase from 0.1 to 0.3. Figure 5 also shows the aft slot has less effect on the cooling near the blades than either the front slot or featherseal, as expected.

To determine the effects of the featherseal, we tested featherseal coolant levels of 0.25%, 0.5%, and 0.75% of the total passage flow while maintaining the front and aft slots each at 1.5% (Cases A–C). Figures 6(a)–6(c) show the measurements for the 0.25%, 0.5%, and 0.75% featherseal flow while the coolant levels for the front and aft slot were maintained the same at 1.5% each. All three cases show the same trends and same adiabatic effectiveness val-

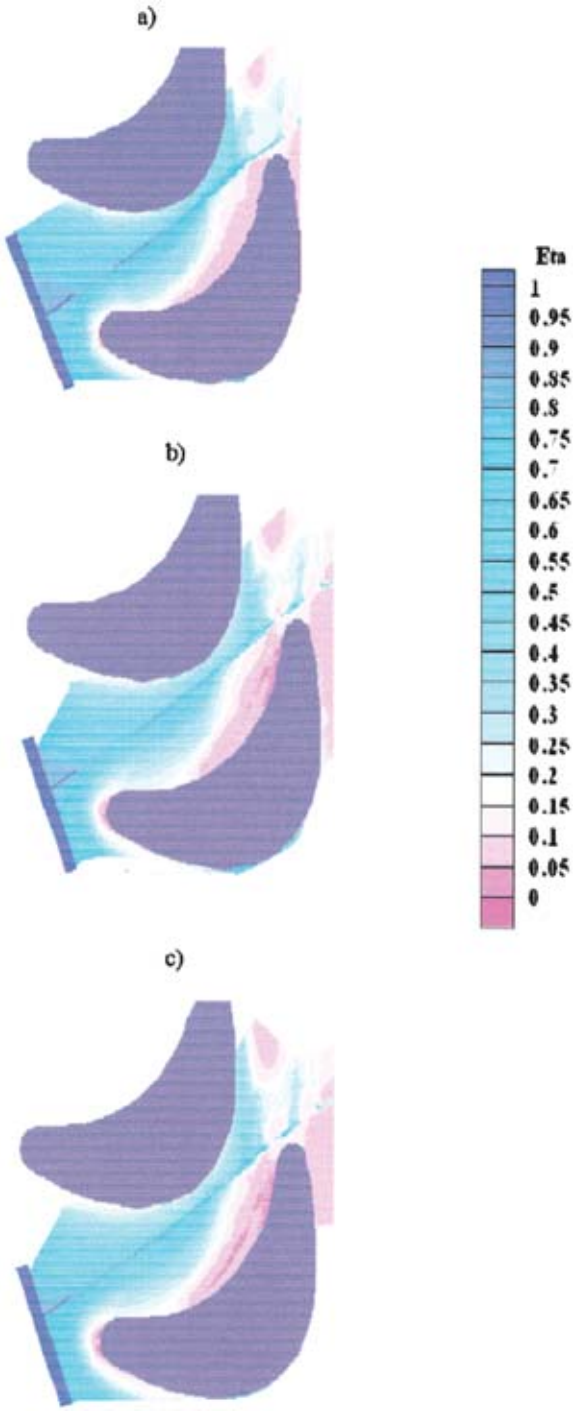

Fig. 6 Adiabatic effectiveness measurements for 1.5% front and aft slot flow with (*a*) 0.25%, (*b*) 0.5%, and (*c*) 0.75% featherseal flow

ues around the featherseal. The results in Figs. 6(*a*)–6(*c*) indicate that as the flow out of the featherseal is increased, the momentum of the coolant flow out of the featherseal causes the coolant to be blown into the mainstream, providing little cooling benefit. Since the coolant flow is swept away from the platform quickly, even at low flow conditions, it is not surprising that increasing the featherseal flow does not increase the platform cooling.

To quantify the lack of additional cooling from increasing the featherseal flow, laterally averaged adiabatic effectiveness values were calculated for the first three cases shown. Laterally averaged values were calculated based upon averages of all the adiabatic

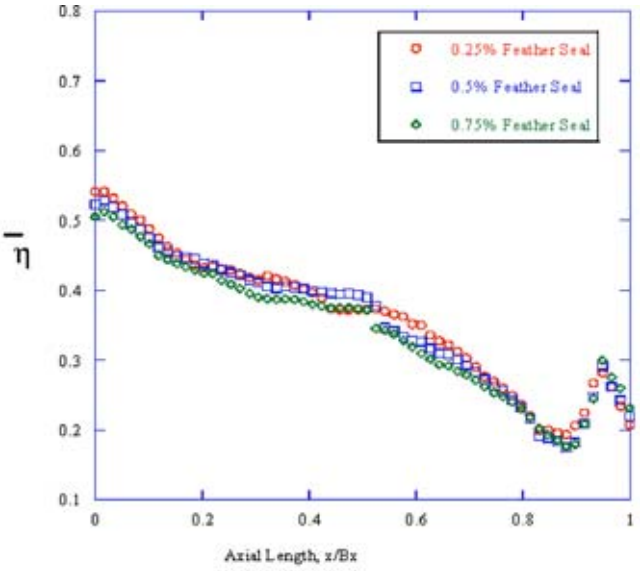

Fig. 7 Average adiabatic effectiveness measurements for the data shown in Figs. 6(*a*)–6(*c*)

effectiveness values along a line perpendicular to the featherseal. Figure 7 shows the averaged adiabatic effectiveness measurements for Figs. 6(*a*)–6(*c*). The results shown in Fig. 7 indicate that there is no cooling increase with increased featherseal flows. The increase in the laterally averaged adiabatic effectiveness values near $x/B_x=0.9$ is caused by the featherseal effects on the trailing edge suction side of the blades. Though it appears the higher featherseal flow case provides the least cooling, the uncertainty of the measurements prevents any definite conclusions from being made. There is no effect with increasing featherseal flow.

For each of the three cases shown in Figs. 6(*a*)–6(*c*), more flow exits from the trailing edge of the featherseal because the static-pressure is lower, in comparison with the leading edge. A calculation of the momentum flux (as shown in later sections) indicates that the momentum flux ratio of the slot flow to the mainstream is nearly constant across the featherseal. As will be shown through the CFD results, the coolant exiting the leading edge of the featherseal is directed by the mainstream flow toward the pressure side of the blade. The coolant exiting the trailing edge of the feather seal is directed toward the suction side of the blade. The effects from the front slot dominate the cooling of the leading edge region blade platform. Because of the dominating effect of the upstream slot and because more coolant exits the trailing edge, the largest cooling benefit from the featherseal slot is near the trailing edge. Though the featherseal does provide some platform cooling, increases in the coolant flow do not increase this cooling.

Upstream Slot Coolant Effects. Although increasing the featherseal flow does not increase the cooling on the endwall, increasing the coolant from the front slot increases the endwall cooling. Figures 8(*a*)–8(*c*) show adiabatic effectiveness measurements when the front slot flow is increased from 0.5% to 1.5% to 2.0% while the featherseal remains at 0.25% and the aft slot also remains the same at 1.5%. As the front slot cooling is increased from 1.5% to 2.0%, the temperature on the pressure side of the blades is reduced. Additionally, coolant was observed wrapping around the suction side of the blades from the passage without the featherseal. The higher front rim flow is able to cool farther into the passage. With the low front slot cooling, the temperature measurements on the trailing edges of both the pressure side and suction side of the blades is nearly the mainstream temperature, as no coolant is present.

Laterally averaged adiabatic effectiveness measurements, shown in Fig. 9, support the results of increased endwall cooling

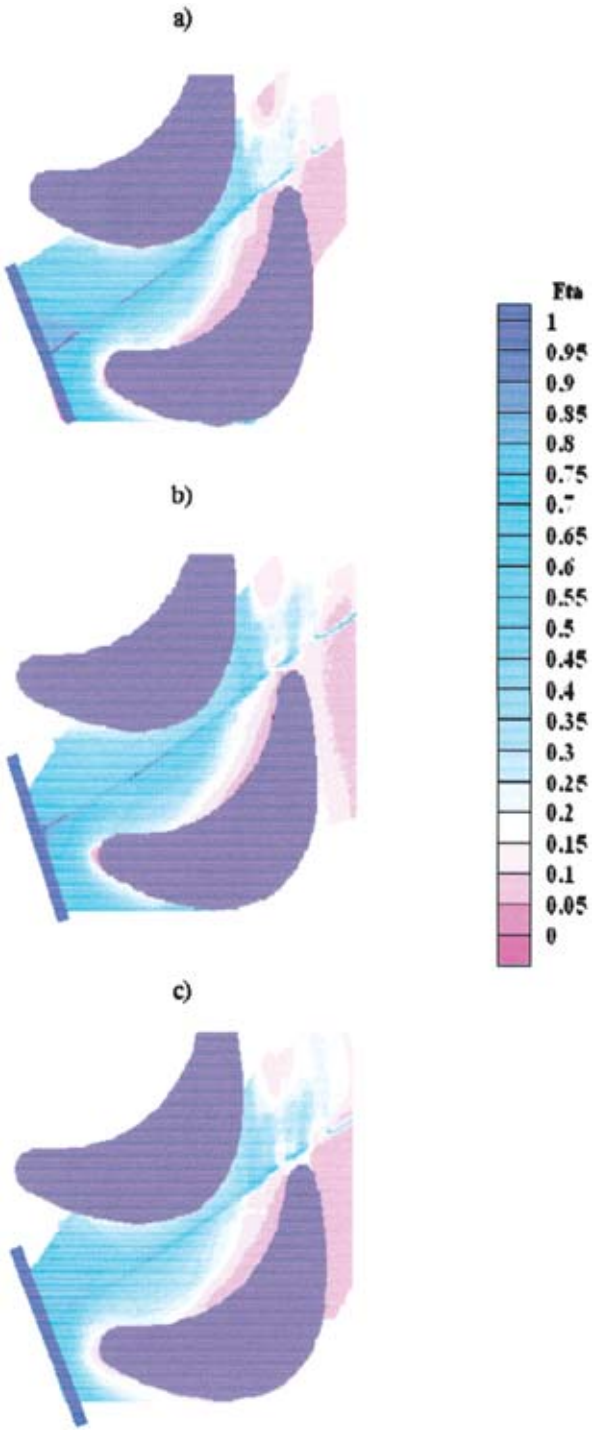

Fig. 8 Adiabatic effectiveness measurements for 0.25% featherseal flow and 1.5% aft slot flow with (*a*) 1.5% front slot, (*b*) 2.0% front slot, and (*c*) 0.5% front slot flow

with increased front slot flow. Throughout the entire blade passage, the average adiabatic effectiveness values are highest for the front slot leakage flow of 2.0%, and lowest for the front slot leakage of 0.5%. Interestingly, there was not a substantial decrease in average cooling with the 0.5% case, as the featherseal flow is able to provide cooling, especially near the trailing edge suction side of the blades. Though the local differences in Fig. 9 appear larger than those first observed in Fig. 8, it is important to note that Fig. 9 is an average across the whole passage, which includes the large temperature variations near the blade walls.

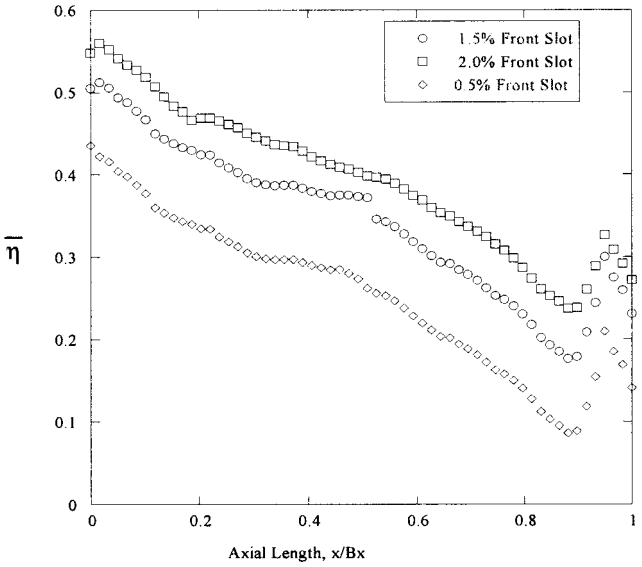

Fig. 9 Average adiabatic effectiveness measurements for the data shown in Figs. 8(*a*)–8(*c*)

Thermal Field Measurements

To better understand the leakage effects, thermal field measurements at two locations along the platform were taken that include the following: near the leading edge of the featherseal and near the trailing edge of the featherseal, as shown by the lines in Fig. 1. For these measurements the upstream slot was set at 1.5% coolant flow and the featherseal flow was varied from 0.25% to 0.75%. The thermal field measurements near the leading edge of the featherseal for the low flow condition are shown in Fig. 10(*a*), and for the high flow in Fig. 10(*b*).

These figures are shown looking downstream from the passage inlet (the pressure side of the blades is on the right-hand side of the contour plot). The location of the featherseal is indicated in each figure (at $X/P=0$), with a height of $Z/S=0$ representing the endwall.

Figure 10(*a*) shows for the low flow condition near the leading edge of the featherseal, the coolant flow is swept toward the pressure side of the blades, remaining near the platform. The additional coolant on the left side of the featherseal is coolant from the front slot leakage. As the flow out of the featherseal is increased, the thermal field measurements in Fig. 10(*b*) show a higher penetration of the coolant into the passage. These thermal field measurements near the leading edge of the blades indicate that the coolant from the upstream slot is affected when the coolant is increased from the featherseal. Figure 10(*a*) indicates more coolant toward the suction side of the featherseal than does Fig. 10(*b*).

Although the coolant from the front part of the featherseal is swept toward the pressure side of the blades, the coolant from the aft portion of the featherseal is swept toward the suction side of the blades. Figures 11(*a*) and 11(*b*) show the thermal fields measured near the trailing edge of the slot for the 0.25% and 0.75% featherseal flows. Unlike the leading edge measurements, the aft thermal rake measurements show flow that has been entrained in a vortex-like structure. Since the aft featherseal provides cooling to the platform, this cloud of coolant is from the midpassage featherseal flow that is swept off the platform. When the flow out of the featherseal is increased, as show in Fig. 11(*b*), the coolant entrained in the vortex flow is higher off the platform. Increased featherseal flow provides no additional platform cooling.

Comparisons to Computations

A number of computational simulations were conducted to better understand the leakage flow, as indicated in Table 3. Figure 12

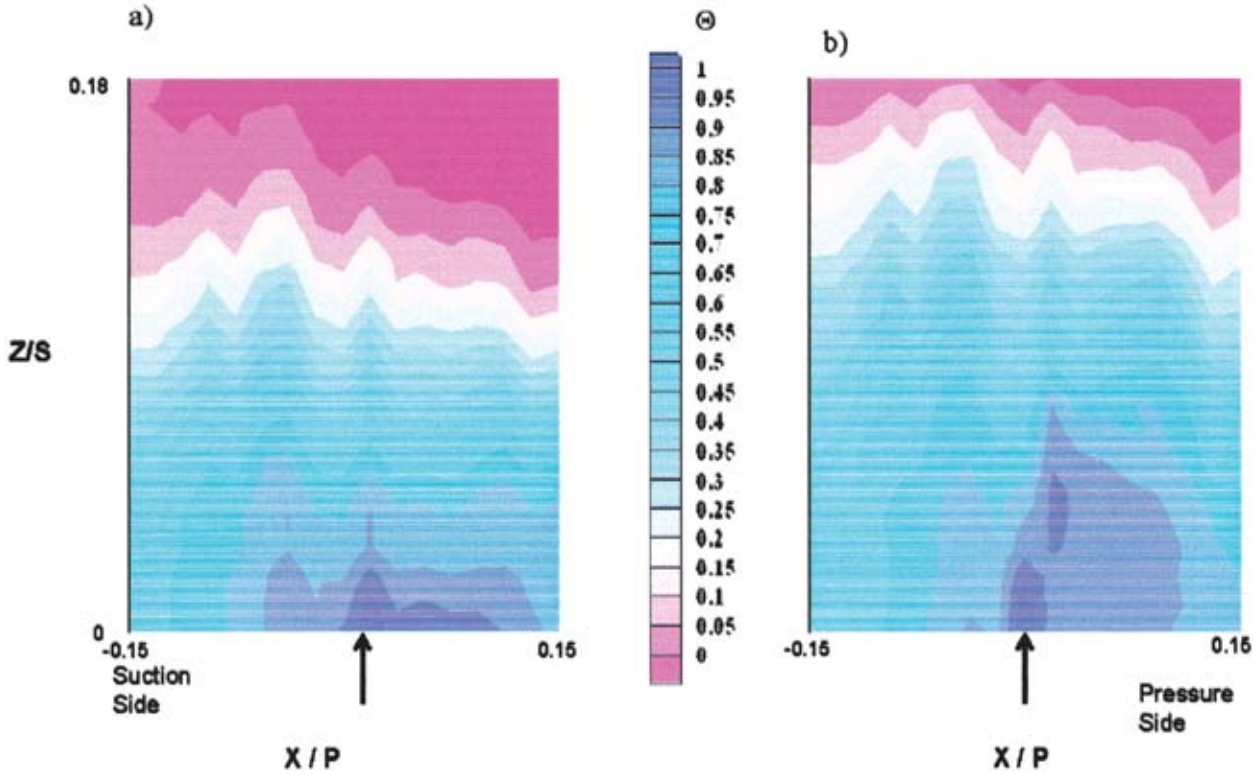

Fig. 10 Thermal rake measurements along the leading edge of the featherseal with 1.5% front slot flow for (*a*) 0.25% featherseal and (*b*) 0.75% featherseal flow

shows the adiabatic effectiveness measurements from the computational simulation with 1.5% upstream and downstream slot flows, and 0.25% featherseal flow. Although the computational predictions match the trends shown in the experimental data, the adiabatic effectiveness levels are overpredicted. We expect the cause of these overpredictions is a function of the near-wall turbulence modeling and a slight mismatch of the experimental inlet pressure conditions.

For both experimental and computational cases, there is little cooling on the pressure side of the blades, especially near the

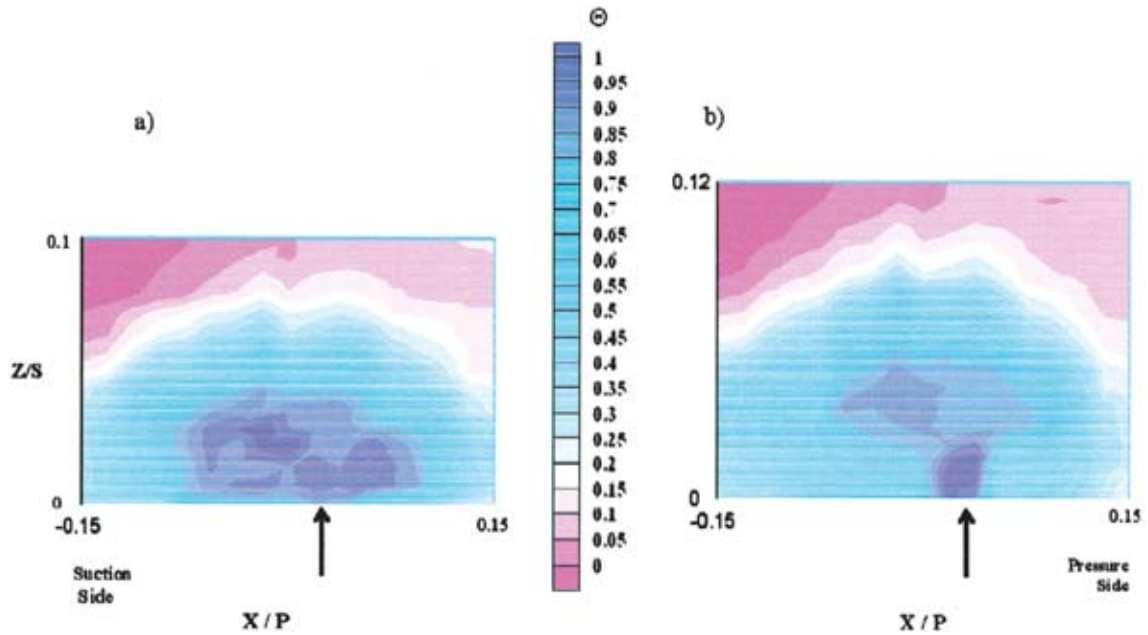

Fig. 11 Thermal rake measurements along the trailing edge of the featherseal with 1.5% front slot flow for (*a*) 0.25% featherseal and (*b*) 0.75% featherseal flow

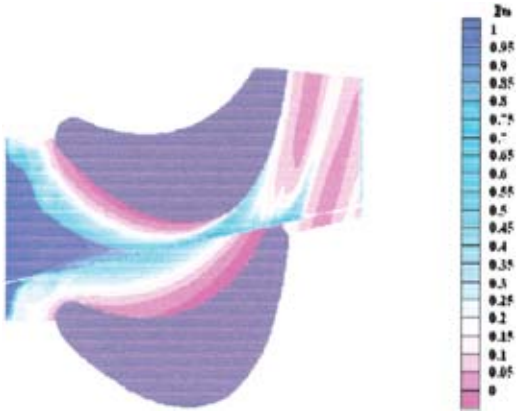

Fig. 12 Computational predictions for 1.5% front and aft slot flow and 0.25% featherseal flow

trailing edge. In both the computational and experimental data, the endwall effectiveness levels along the featherseal appear to decrease toward the trailing edge. The predicted effectiveness values near the suction side of the blades were lower than the experimentally measured values. However, these differences are attributed to the higher predicted values from the front rim.

To observe the leakage flows out of the featherseal, streamlines colored by height were released from the featherseal. Figure 13 shows streamlines released from the featherseal plenum with a flow of 0.25% and an upstream and aft slot flows each at 1.5%. The streamlines show the characteristics of the featherseal flow that were observed in the experimental testing. The streamlines are swept toward the pressure side of the blades near the leading edge followed by a sweeping toward the suction side of the blades near the trailing edge. Additionally, the secondary flows lift the featherseal off the platform in the midpassage. This lifted flow was observed in the trailing edge thermal rake measurements (Figs. 11(*a*) and 11(*b*)). Toward the trailing edge of the featherseal, the streamlines remain on the platform, providing a film cooling layer.

Computational results with higher featherseal and upstream slot flows also matched the trends measured with the experimental cases. While increases in front slot cooling from 1.5% (Fig. 14(*a*)) to 2.0% with 0.25% featherseal flow (Fig. 14(*b*)) increases the cooling of the platform region, increases in featherseal to 0.75% cooling with 2.0% front slot flow (Fig. 14(*c*)) do not provide any additional platform cooling. While front slot cooling is overpredicted, similar trends are observed.

To further compare the computational and experimental results, we calculated averaged adiabatic effectiveness values for both cases, shown in Fig. 15. As expected, near the leading edge the computational values are higher since the front slot cooling was

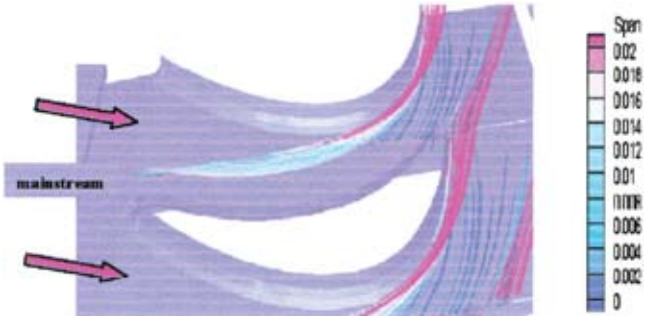

Fig. 13 Computational streamlines colored by height from the featherseal for 0.25% flow, with 1.5% front rim flow (not shown for clarity)

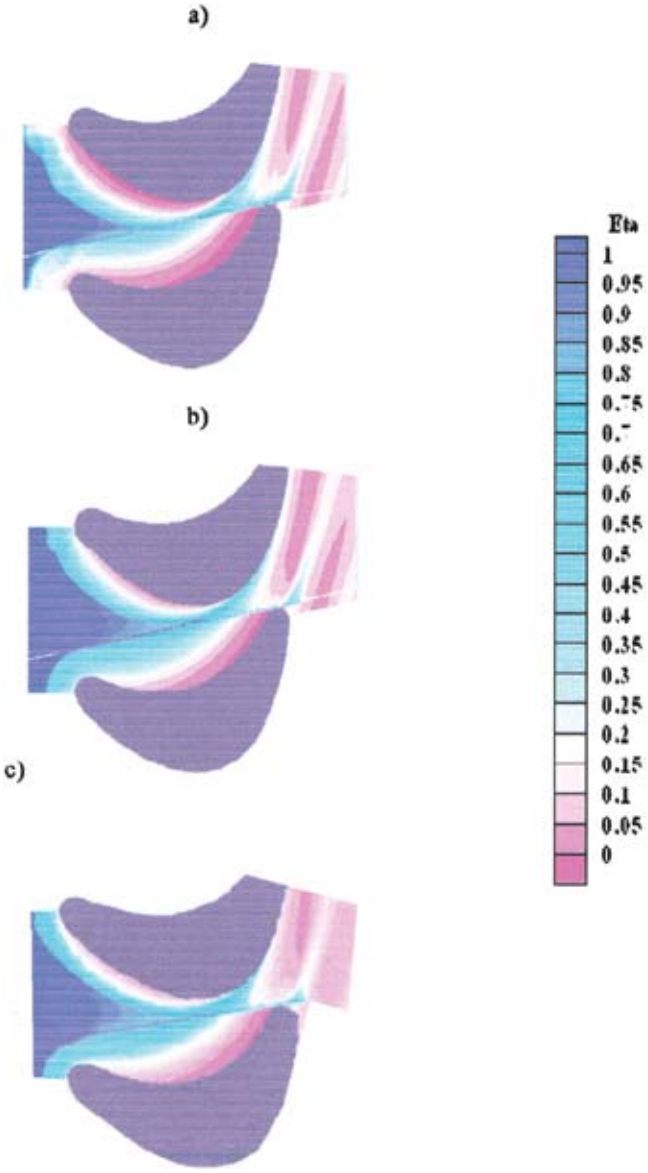

Fig. 14 Computational predictions for (*a*) 1.5% front slot and 0.25% featherseal, (*b*) 2.0% front slot and 0.25% featherseal, and (*c*) 2.0% front slot and 0.75% featherseal, all with 1.5% aft slot flow

overpredicted. However, the trends for both lines show that the computational predictions were able to match the experimental flows in the midpassage. Figure 15 shows a cooling advantage to increasing the front slot flow, while increases from the featherseal (Fig. 7) do not.

To determine if momentum flux changes in the flow from the featherseal caused the different flows out of the featherseal (as shown in Fig. 13), the computational results were used to calculate the momentum flux at the locations of the thermal rake measurements. Based upon the inviscid mainstream velocity at midspan and the static pressure measurements along the platform, a local momentum flux ratio of 1.22 (based on local velocities) was calculated for the leading edge of the featherseal, and a ratio of 1.3 was calculated for the trailing edge featherseal. Given nearly the same momentum flux, the secondary flow field affects must be causing the effects in featherseal coolant. The crossover flow from the featherseal, shown in both computational and experimental measurements, lifts the featherseal flow off the platform. These secondary cooling flows in the midpassage were observed by the

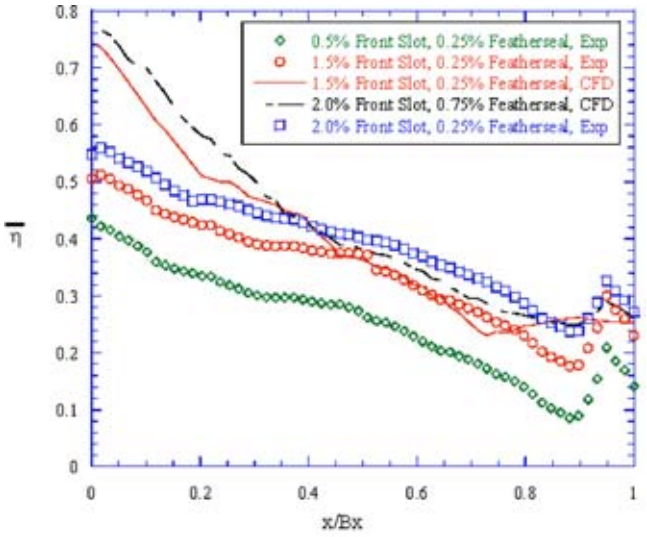

Fig. 15 Average adiabatic effectiveness measurements for the experimental data and computational predictions

thermal rake measurements along the trailing edge of the featherseal. The results in Figs. 11(*a*) and 11(*b*) are not showing the flow from that specific featherseal location being affected by the secondary flows; instead, they show the coolant vortex that is formed upstream of the thermal rake location by the secondary flows and carried down the passage.

Conclusions

Numerous simulations have been performed to address effects of leakage flows on platform cooling. The resulting adiabatic effectiveness distributions along the endwall matched many of the results observed in open literature, showing coolant from a backward-facing upstream slot provides cooling to the endwall. Although coolant was present through 50% of the blade passage, little cooling was provided to either side of the trailing edges of the blades.

Increases of flow from the midpassage featherseal slot provided little additional cooling benefits to the blade platform, with the exception being near the trailing edge of the blades. At the passage inlet, the inlet angle of the mainstream flow swept the featherseal leakage coolant towards the pressure side of the blades. Further into the blade passage, the cross-passage pressure differential between the blades swept the featherseal coolant back toward the suction side of the blades.

Laterally averaged adiabatic effectiveness measurements showed that increases in featherseal leakage did not provide an additional cooling benefit while increases in the upstream slot flow did provide additional cooling benefit to the endwall. This lack of cooling with increased featherseal flow was further quantified with thermal field measurements. The thermal fields indicated the effects of the passage vortex in the blade passage.

While the coolant flow through the trailing edge of the slot was higher than through the leading edge, the local momentum flux ratio across the featherseal remains relatively constant. Additionally, the location of featherseal crossover, which is the location where the coolant direction is changed from being directed toward the suction surface rather than pressure surface, is independent of featherseal and front slot flows.

The results from this study lead us to the conclusion that there should be tighter seals for the featherseal between the adjacent blades to minimize coolant leakage since there is relatively little benefit in terms of endwall cooling. The benefit realized from the upstream leakage, however, is more pronounced for the endwall but still limited to selected regions.

There are several recommendations for future work, based upon the results of these experiments. First, repeating these experiments with a heated, conductive platform would allow for heat transfer coefficients to be calculated for the entire hub region. Additionally, pressure loss measurements in the passage would quantify any negative effects in efficiency caused by leakage flows. By examining the effects of different front slot entrance angles, mismatched featherseal gap heights, and larger coolant leakages, improvements of hub cooling will be made.

Acknowledgments

The authors would like to acknowledge support from Pratt & Whitney for the work presented in this paper. In particular, John Wiedemer and Mike Blair are to be thanked for their contributions. Additionally, Erik Hohlfeld provided some of the initial computational results and mesh adaptions.

Nomenclature

B_x = axial chord
C = true chord
C_p = static pressure coefficient, $(P_{s,\text{local}}-P_{s,\text{inlet}})/P_{\text{dyn}}$
I = momentum flux ratio $(\rho_c V_c^2/\rho_\infty V_\infty^2)$
P = blade pitch
$P_{d,\text{in}}$ = dynamic pressure at the inlet
$P_{s,\text{in}}$ = static pressure at the inlet
$P_{s,\text{local}}$ = local static pressure
Re_C = Reynolds number based on true chord
S = span
s = surface distance along blade from stagnation point
T = temperature
X,Y,Z = wind tunnel coordinate system

Greek

η = adiabatic effectiveness $(T_\infty-T_{\text{aw}})/(T_\infty-T_c)$
θ = nondimensional temperature $(T_\infty-T)/(T_\infty-T_c)$
ρ = density
Δ = denotes a difference

Subscripts and Superscripts

$\bar{}$ = lateral average value
aw = adiabatic wall
av = averaged value
c = coolant conditions
max = maximum value
∞ = mainstream conditions

References

[1] Langston, L. S., Nice, M. L., and Hooper, R. M., 1977, "Three-Dimensional Flow Within a Turbine Cascade Passage," ASME J. Eng. Power, **99**, pp. 21–28.
[2] Graziani, R. A., Blair, M. F., Taylor, J. R., and Mayle, R. E., 1980, "An Experimental Study of Endwall and Airfoil Surface Heat Transfer in a Large Scale Turbine Blade Cascade," Trans. ASME: J. Eng. Gas Turbines Power, **102**, pp. 257–267.
[3] Sharma, O. P., and Buttler, T. C., 1987, "Reynolds Stresses and Dissipation Mechanisms Downstream of a Turbine Cascade," J. Turbomach., **109**, pp. 229–236.
[4] Goldstein, R. J., and Spores, R. A., 1988, "Turbulent Transport on the Endwall in the Region Between Adjacent Turbine Blades," J. Turbomach., **110**, pp. 862–869.
[5] Kang, M. B., Kohli, A., and Thole, K. A., 1999, "Heat Transfer and Flowfield Measurements in the Leading Edge Region of a Stator Vane Endwall," J. Turbomach., **121**, pp. 558–568.
[6] Blair, M. F., 1974, "An Experimental Study of Heat Transfer and Film Cooling on Large-Scale Turbine Endwall," ASME J. Heat Transfer, **96**, pp. 524–529.
[7] Burd, S. W., Satterness, C. J., and Simon, T. W., 2000, "Effects of Slot Bleed Injection Over a Contoured Endwall On Nozzle Guide Vane Cooling Performance: Part II—Thermal Measurements," ASME Paper No. 2000-GT-200.
[8] Colban, W. F., Thole, K. A., and Zess, G., 2003, "Combustor Turbine Interface Studies—Part 1: Endwall Effectiveness Measurements," J. Turbomach., **125**, pp. 203–209.
[9] Zhang, L. J., and Jaiswal, R. S., 2001, "Turbine Nozzle Endwall Film Cooling Study Using Pressure Sensitive Paint," J. Turbomach., **123**, pp. 730–738.

[10] Nicklas, M., 2001, "Film-Cooled Turbine Endwall in a Transonic Flow Field: Part II—Heat Transfer and Film-Cooling Effectiveness," J. Turbomach., **123**, pp. 720–729.
[11] Knost, D. G., and Thole, K. A., 2003, "Computational Predictions of Endwall Film-Cooling for a First Stage Vane," ASME Paper No. GT2003-38252.
[12] Yu, Y., and Chyu, M. K., 1998, "Influence of Gap Leakage Downstream of the Injection Holes on Film Cooling Performance," J. Turbomach., **120**, pp. 541–548.
[13] Aunapu, N. V., Volino, R. J., Flack, K. A., and Stoddard, R. M., 2000, "Secondary Flow Measurements in a Turbine Passage With Endwall Flow Modification," J. Turbomach., **122**, pp. 651–658.
[14] Chung, J. T., and Simon, T. W., 1993, "Effectiveness of the Gas Turbine Endwall Fences in Secondary Flow Control at Elevated Freestream Turbulence Levels," ASME Paper No. 93-GT-51.
[15] The Mathworks Inc., MATLAB, Version 6.5, Release 13, 2002 (Massachusetts).
[16] Fluent Inc., FLUENT User's Guide, Version 6.0, 2002 (New Hampshire).

Inverse Design of and Experimental Measurements in a Double-Passage Transonic Turbine Cascade Model

G. M. Laskowski
e-mail: gmlaska@sandia.gov

A. Vicharelli

G. Medic

C. J. Elkins

J. K. Eaton

P. A. Durbin

Flow Physics and Computation Division &
Thermosciences Division,
Department of Mechanical Engineering,
Stanford University,
Stanford, CA 94305

A new transonic turbine cascade model that accurately produces infinite cascade flow conditions with minimal compressor requirements is presented. An inverse design procedure using the Favre-averaged Navier-Stokes equations and k-ε turbulence model based on the method of steepest descent was applied to a geometry consisting of a single turbine blade in a passage. For a fixed blade geometry, the passage walls were designed such that the surface isentropic Mach number (SIMN) distribution on the blade in the passage matched the SIMN distribution on the blade in an infinite cascade, while maintaining attached flow along both passage walls. An experimental rig was built that produces realistic flow conditions, and also provides the extensive optical access needed to obtain detailed particle image velocimetry measurements around the blade. Excellent agreement was achieved between computational fluid dynamics (CFD) of the infinite cascade SIMN, CFD of the designed double passage SIMN, and the measured SIMN. [DOI: 10.1115/1.1929810]

Introduction

Computational fluid dynamics (CFD) techniques are now sufficiently robust to use in both analysis and design of aircraft engine components. This is particularly true for turbine nozzles and rotors, where the generally favorable pressure gradient through the device leads to relatively thin boundary layers, making the computational results somewhat insensitive to turbulence modeling errors. However, heat transfer rates and film cooling performance are more strongly dependent on the turbulence properties, and designers must rely heavily on empirical data [1,2]. In order to design more efficient and effective cooling strategies, a better understanding of the turbulent flow field is required. The effect of concave and convex streamline curvature [3], and the so-called stagnation point anomaly, or spurious buildup of turbulent kinetic energy in regions of strong irrotational strain [4–6], are two particular areas of concern for turbulence modeling in turbines. These effects have been investigated in simple flows, but detailed experiments are required to assess their importance in realistic turbine geometries.

Unfortunately, acquiring the detailed turbulence measurements needed to test and calibrate turbulence models in a full rotating turbine is exceedingly difficult and expensive. Giess and Kost [7] made extensive measurements of the flow field in a rotating annular turbine cascade using L2F, pneumatic probes, and pressure taps. Lang et al. [8] measured the three-dimensional velocity field between a rotor and stator in a full rotating rig using PIV. The complexity of a rotating rig makes it nearly impossible to use optical measurement techniques to study the flow between blades.

An alternative approach is to use either an annular or linear cascade. A linear cascade, with fewer blades than a full annular cascade, provides better spatial resolution for the same flow rate [9]. Baughn et al. [10] showed that linear cascades provide good midspan data as compared to their rotating equivalents. Cascades consisting of multiple blades are typically utilized by the turbomachinery community to ensure periodicity about the central blade (e.g., [11–17]). Using cascades with only one or two blade passages reduces the required flowrate and improves optical access. Ganzert and Fottner [18] conducted heat transfer measurements in a geometry consisting of three blades and two complete passages. Buck and Prakash [19] conducted film cooling effectiveness measurements in a single-passage model consisting of an entrance channel, a pressure side wall, a suction side wall, and tailboards. Suction was used to remove the boundary layers just upstream of the suction and pressure side walls and to correctly position the stagnation points. Radomsky and Thole [20] used a large-scale stator cascade to measure turbulence at low Mach numbers. Their double-passage cascade consisted of a single full blade and two half-blades comprising the outer walls of the test section. Again, suction was used to remove the upstream boundary layers. The correct design of suction bleeds is tedious [21] and can lead to serious difficulties in comparing CFD to experiments. Also, suction systems interfere with optical access for laser-based instrumentation. Tailboards also cause a number of difficulties [22], especially under transonic conditions.

The present work was motivated by the desire to build a double-passage turbine cascade that correctly represents the flow around the blade without using suction. The passage should have continuous solid walls to facilitate comparison to CFD, while still replicating all of the flow features in an infinite cascade of blades. In the transonic flow of a modern turbine, those features include regions of very strong acceleration, shock waves, and boundary layers.

We have developed a CFD-based optimization technique to design such double-passage cascades. The technique has been tested using the blade shape from a modern jet engine high-pressure turbine. Initially, the flow field for an infinite cascade was computed using the Favre-averaged Navier-Stokes equations to determine the desired surface isentropic Mach number (SIMN) distribution. Streamlines extracted from the infinite-cascade simulation were used as the initial guess for the solid outer walls of the double-passage apparatus. However, because of the presence of the boundary layers on these walls, this initial wall shape does not produce the desired SIMN distribution, and results in separated flow along the pressure side wall. The optimization scheme was

Contributed by the Turbomachinery Division of THE AMERICAN SOCIETY OF MECHANICAL ENGINEERS for publication in the JOURNAL OF TURBOMACHINERY. Manuscript received by the Turbomachinery Division September 9, 2003; revised manuscript received January 12, 2005. S. A. Sjolander.

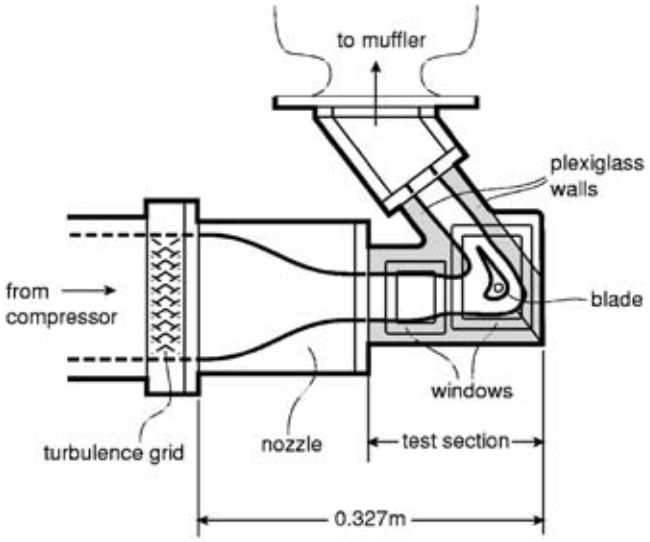

Fig. 1 Schematic of double-passage nozzle and test section

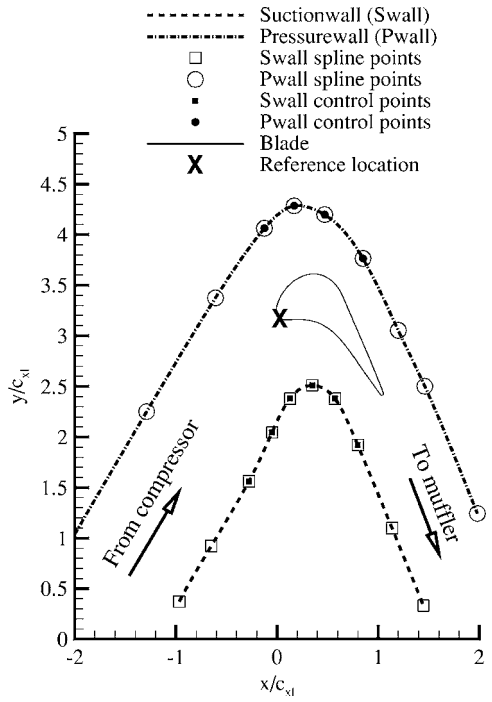

Fig. 2 Initial geometry and definitions of terminology used (not to scale)

then used to modify the wall shape until two-dimensional CFD simulations predicted the desired SIMN distribution with attached flow along both walls. The apparatus designed using the procedure was then built and tested.

In this paper, we present the design methodology with an emphasis on the construction of the cost function. The setup of the experimental rig is discussed, and results from the infinite cascade and double-passage CFD simulations are compared with measurements obtained in the rig for the initial design and the final design. After several design attempts, excellent agreement was achieved when comparing the SIMN among the CFD simulations of the infinite cascade, the double passage design, and the experimental measurements.

Inverse Problem Definition

Figure 1 shows a schematic of the desired apparatus configuration. The flow in a pressurized wind tunnel passes through a turbulence generation grid, then into a contraction that thins the boundary layers. Flow with a nearly uniform velocity profile enters the rectangular passage approaching the double passage. After passing through the cascade, the flow exits into a large plenum chamber comprising the inlet of a noise suppression system. The challenge is to shape the Plexiglass walls, shown in gray, to produce the correct flow around the blade.

In order to design the passage walls such that the flow in the double passage was representative of the flow in an infinite cascade, it was necessary to define a cost function that was also representative of the overall flow field. In doing so, we followed the practice used in airfoil design, and initially decided to match the surface pressure in the form of surface isentropic Mach number (SIMN) of the blade in the passage to that of the blade in an infinite cascade. Thus, the design optimization problem statement is

$$\min_{\phi}\{j[\phi, U(\phi)]: E[\phi, U(\phi)] = 0\} \tag{1}$$

where j is the cost function, ϕ are the control variables, U is the state variable vector, and E is the set of governing equations to be solved. The global cost function is defined as

$$j = \sum_{i=1}^{I} \alpha_i \gamma_i(U) \tag{2}$$

where α is a set of weights to be determined heuristically, I is the number of cost function components constituting the global cost function, and γ_i are the cost function components. Initially I was taken to be 1, α_1 was set to 1, and γ_1 was defined as

$$\gamma_1 = \int_{\Gamma_{\text{blade}}} \beta(s)|M - M^*|ds \tag{3}$$

Here $\beta(s)$ is a step-function scaling factor, M is the SIMN distribution (double passage), and M^* is the target SIMN distribution (infinite cascade), with the isentropic Mach number defined as

$$M = \sqrt{\frac{2}{\gamma - 1}\left(\left(\frac{P_t}{P}\right)^{\gamma - 1/\gamma} - 1\right)} \tag{4}$$

where P_t is the stagnation pressure, P is the static pressure, and γ is the ratio of specific heats, which is taken to be 1.4 for air.

The cost function was minimized by the method of steepest descent. The control variable ϕ in (1) is updated as

$$\phi_i^{k+1} = \phi_i^k - c\,\nabla j(\phi_i^k) \tag{5}$$

until the minimum of (2) is achieved. In (5), c is the step size, which was either held constant or computed using a line search based on a parabola fit. The latter is analogous to a response surface method. A simple backward difference was used for the gradient computations

$$\nabla j(\phi_i^k) = \frac{j(\phi_i^k + \Delta) - j(\phi_i^k)}{\Delta} \tag{6}$$

where Δ represents a perturbation to the control variable.

Control Variables. Since the objective was to shape the passage walls in order to achieve the correct SIMN distribution along the blade, a natural choice for the control variables was a set of spline points used to construct the wall shapes. Figure 2 presents representative spline and control point locations as well as definitions of terminology used throughout. Furthermore, three additional definitions are presented for clarification: CFD-IC is the CFD of the infinite cascade; CFD-DP is the CFD of the double passage; and EM-DP are the experimental measurements in the

double passage.

In order to keep the number of degrees of freedom to a minimum, cylindrical coordinates were used with the origin placed at the leading edge of the blade, and only the radial location of the control points was varied (refer to Fig. 2). Thus,

$$\phi = \phi(r, \theta = \text{const})$$

Once the control points were moved, either due to a perturbation or due to a gradient update, a piecewise cubic spline was fit through the points.

Governing Equations. Since the viscous boundary layers are critically important, the Favre-averaged Navier-Stokes equations were solved with the Chen two-layer k-ε model in order to determine the flow field in the passage. Referring back to Eq. (1), the state variable vector $U=\{\rho, \rho u, \rho v, \rho e, \rho k, \rho \varepsilon\}$ and $E(U)$ is

$$\frac{\partial \rho}{\partial t} + \frac{\partial (\rho u_i)}{\partial x_i} = 0$$

$$\frac{\partial \rho u_i}{\partial t} + \frac{\partial \rho u_i u_j}{\partial x_j} = \frac{\partial \tau_{ij}}{\partial x_j} \tag{7}$$

$$\frac{\partial \rho e}{\partial t} + \frac{\partial \rho e u_j}{\partial x_j} = \frac{\partial \tau_{ij} u_i}{\partial x_j} + \frac{\partial q}{\partial x_j}$$

where

$$\tau_{ij} = \mu \left(\frac{\partial u_i}{\partial x_j} + \frac{\partial u_j}{\partial x_i} \right) - \frac{2}{3} \mu \frac{\partial u_k}{\partial x_k} - p \delta_{ij}$$

$$q = -\lambda \frac{\partial \theta}{\partial x_j}, \quad e = c_v \theta$$

where $\mu = \mu_L + \mu_T$ and $\lambda = \lambda_L + \lambda_T$ represent the sum of the molecular and turbulent viscosity, and thermal conductivity, respectively. The two-equation Chen k-ε model [23] was selected based on the turbulence model assessment of [5] to compute μ_T. The model does not account for transition, and the boundary layer that develops along the passage walls and blade surface is assumed to be turbulent, which follows the work of [5]. The two-layer model was used along the blade surface, and wall functions were used along passage walls. The governing equations were solved using STAR-CD, a finite-volume commercial CFD package developed by Adapco [23]. The SIMPLE algorithm with second-order monotone advection residual scheme (MARS) for the spatial flux computations was used.

Algorithm

The infinite cascade simulation for the blade was conducted at transonic conditions. The SIMN and stagnation streamlines were extracted, the former to be used as the initial cost function definition, and the latter to be used as the initial guess for the wall shapes. Once the stagnation streamlines were offset by the pitch, a set of points was extracted to be used as both spline and control points for subsequent wall shape definitions. An algebraic grid generator was used to generate the grid for the blade-wall geometry and the CFD simulation was run until convergence was achieved. A script controlling the perturbations, spline fits, grid generation, flow field computations, and cost function evaluations was written to loop sequentially through the control points for each global iteration.

Experimental Setup

The experimental apparatus shown in Fig. 1 was attached to an existing high-pressure wind tunnel. The rig was designed so that the passage walls could be replaced with walls of a different shape, allowing for an iterative approach for the design optimization. A 4.6:1 area ratio nozzle was fabricated to reduce the wind tunnel cross section to the appropriate dimensions of the passage, with thin boundary layers at the passage inlet. A turbulence-generation section upstream of the nozzle allows for the placement of turbulence grids to create turbulence intensities ranging from 5–6 % at the nozzle inlet. The two-dimensional double-passage shape was given a depth of approximately one blade chord, allowing the apparatus to operate at full-scale Mach numbers using the 1 kg/s flow provided by the lab compressor. The flow geometry and conditions are summarized in Table 1.

Table 1 Geometric and flow conditions for experiment

Inlet total temperature	293 K	Inlet total pressure	2.6×10^5 Pa
Inlet Mach number	0.3	Exit Mach number	1.7
Flow inlet angle	0.0°	Flow exit angle	127.0 deg
Re_c[a]	660,000	Mass flow	0.63 kg/s

[a]The Reynolds number is based on inlet conditions and blade axial chord.

The passage walls were CNC machined from transparent plexiglass and polished to allow for transmission of laser light. One of the aluminum end walls is fitted with two optical-quality glass windows for PIV imaging, one to study the inlet conditions and one to examine the flow around the blade. The blade itself was manufactured from a block of stainless steel using wire EDM (electrical discharge machining), and slides into a pocket in the far end wall that holds it in place. A simple free-flow exhaust muffler is attached to the cascade exit to enable supersonic flow in the passage.

Static Pressure Measurements. The blade was equipped with 17 static pressure taps. Holes with a diameter of 0.58 mm were drilled perpendicular to the blade surface midspan and were connected to a Scanivalve (model SSS-48C-MK4) through vinyl tubes extending out the far end wall. The blade surface pressure was measured relative to the flow stagnation pressure at the cascade inlet using a Kiel probe and a Setra model 204D pressure transducer. The Kiel probe was also connected to a Bourdon tube manometer (Wallace & Tiernan FA 145), to ensure that the inlet stagnation pressure in the passage matched that of the infinite cascade, and to double-check the transducer calibration. Voltage signals were acquired using a National Instruments PC-MIO-16E-4 board, and controlled using LabVIEW software. The resulting pressure measurements were then used to calculate the SIMN distribution, using Eq. (4).

Results

Infinite Cascade Simulations. Figure 3 shows the computational grid used for the simulation of the infinite cascade. The O grid consisted of 180 points in the circumferential direction, with 51 points in the transverse direction. The inlet and the exit of the O grid were extended with an H grid. Sixteen grid points were used for the entrance section, while 24 points were used for the exit section. The maximum value of y^+ for the nearest grid point to the blade was 0.9.

Stagnation pressure and temperature corresponding to the val-

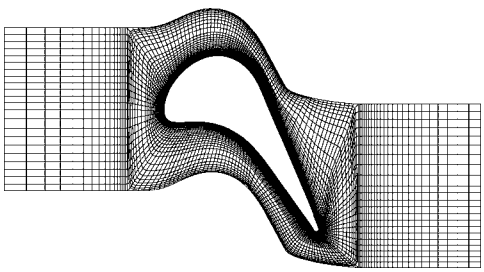

Fig. 3 Computational grid used in infinite cascade simulations (not to scale)

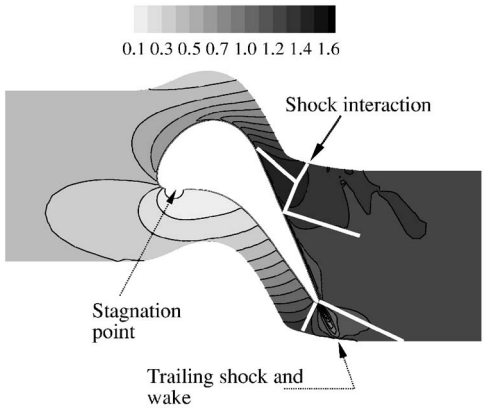

Fig. 4 Mach number contours for infinite cascade simulation (not to scale)

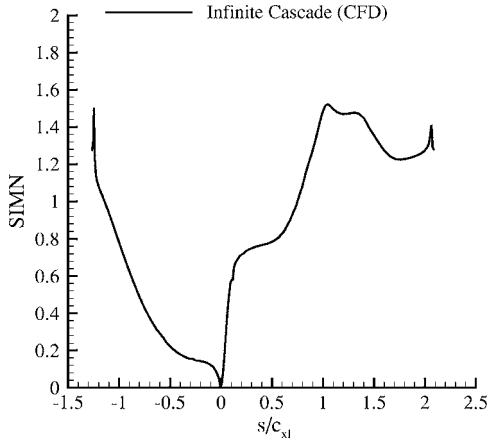

Fig. 5 SIMN corresponding to Fig. 4 plotted against the blade surface coordinate nondimensionalized by the blade axial chord where $0 \rightarrow +s/c_{xl}$ is the blade suction side from the stagnation point to the trailing edge and $0 \rightarrow -s/c_{xl}$ is the blade pressure side from the stagnation point to the trailing edge

ues in Table 1, as well as the direction cosine(0.488,0.873), turbulence intensity (5%), and turbulent length scale (0.001 m) were set at the inflow boundary to coincide with the experiment. The static pressure was set to atmospheric at the outflow boundary, with a zero gradient boundary condition for turbulence quantities and temperature. Periodic boundary conditions were set at the upper and lower boundary, along the midpitch line. Finally, adiabatic no-slip with two-layer k-ε was invoked at the blade surface. Convergence was achieved when all residuals dropped at least eight orders in magnitude.

Figure 4 presents the Mach number contours resulting from the converged solution, depicting the shock locations and stagnation streamlines. The flow stagnates at the leading edge and undergoes strong acceleration through the upper passage. An oblique shock forms near the blade midchord and interacts with the trailing-edge shock from the pressure side of the adjacent blade forming a λ-shock pattern. The flow continues to undergo weak acceleration up to the trailing edge where a terminal shock forms at the blade trailing edge. Along the suction side blade surface, the turbulent boundary layer remains attached up to the trailing edge. Through the lower passage, the flow undergoes very mild acceleration at first, and eventually goes supersonic near the blade trailing edge, thus resulting in another trailing-edge oblique shock, which, when combined with trailing edge oblique shock emanating from the suction surface, forms the well-known fish-tail shock structure for airfoils operating in transonic conditions. From this converged solution, the SIMN distribution was extracted (Fig. 5), which was used as the target distribution in the optimization (M^* in Eq. (3)). Furthermore, the stagnation streamlines were extracted and replaced with solid walls for the double-passage simulation. The stagnation streamlines were then linearly extrapolated to match the contraction exit and muffler entrance of the experimental rig, a pseudoconstraint (Fig. 2).

Double-Passage Simulations. The grid used in the infinite cascade simulation was modified for use in the double-passage simulation. Grid refinement studies showed that at least 70,000 cells were required for the simulations. The same inflow and outflow conditions as those used in the infinite cascade simulation were used, and the inflow conditions coincide with the experiment. No-slip adiabatic wall with the two-layer k-ε model was specified at the blade surface, whereas adiabatic walls with wall functions were used for the passage walls. This was done in order to keep the number of grid cells to a minimum, and it was determined that wall functions along the passage walls did not degrade the overall results. The grid was constructed, and the results were monitored, to ensure that all values of y^+ for the nearest cell to the blade surface were well within the viscous sublayer, and within the log layer along the passage walls.

Figure 6 demonstrates the SIMN resulting from the initial geometry, using stagnation streamlines shown in Fig. 2. Obviously, the initial geometry does not produce the correct pressure distribution. First, the acceleration over the leading-edge suction side of the blade is too low, leading to low values of SIMN for $x/c_{xl} = 0 \rightarrow 0.3$. Second, the shock structure is completely misrepresented as well. This geometry produces a very weak oblique shock followed by strong acceleration up to the trailing-edge fish-tail shock. The agreement along the pressure side of the blade is better, but there is an obvious shift in the SIMN predictions. Finally, the stagnation point location for CFD-DP is in error by 3.8% of the blade chord.

Initial Design. Modifying the suction wall had no discernable effect on the pressure-side pressure distribution, and vice versa. As such, the two walls were optimized simultaneously and independently for different definitions of Eq. (3). Furthermore, it was observed that the pressure wall needed to be divided into two distinct sections, a subsonic region upstream of the throat, and a downstream supersonic region. Thus, Eq. (3) takes the form

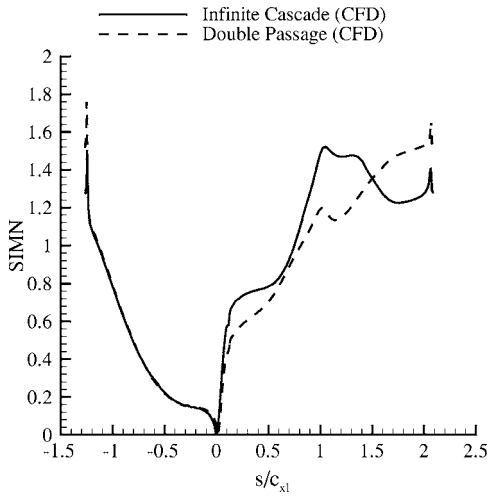

Fig. 6 SIMN for the initial geometry using stagnation streamlines (refer to Fig. 5 for explanation of the abscissa axis)

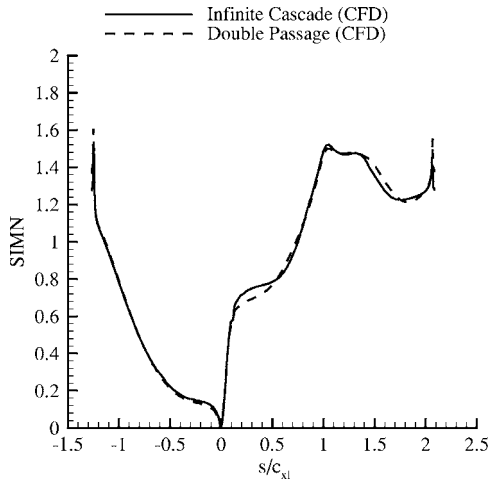

Fig. 7 SIMN for the initial geometry with separation along pressure wall (refer to Fig. 5 for explanation of the abscissa axis)

$$\gamma_{M<1} = \beta_1 \int_{\Gamma_{\text{inlet}\to\text{throat}}} |M - M^*| ds + \beta_2 \int_{\Gamma_{\text{throat}}} |M - M^*| ds$$

$$\gamma_{M>1} = \beta_2 \int_{\Gamma_{\text{throat}}} |M - M^*| ds + \beta_3 \int_{\Gamma_{\text{throat}\to\text{exit}}} |M - M^*| ds$$

where

$$\beta_2 \gg \beta_1 \text{ and } \beta_2 \gg \beta_3$$

Furthermore, the step size in Eq. (5) was held fixed.

The suction wall solution converged very quickly, and only 5–6 global iterations were required to match the SIMN along the pressure-side blade. This can be attributed to two factors. First, the flow is completely subsonic in the lower passage up to the terminal fish-tail shock. Second, the favorable pressure gradient negates the difficulty of having to deal with flow separation issues along the suction wall.

The pressure wall, on the other hand, proved to be a much stiffer problem than the suction wall. There was a region of separated flow in the region of high curvature on the pressure wall. As the optimization routine changed the passage shape, improving the SIMN, the size of the separation region increased slightly. The existence of a separation region was deemed unacceptable, since it was likely to produce unsteadiness in the experiment and possibly affect the turbulence measurements. After achieving good agreement for the SIMN distribution (Fig. 7), the wall shape was manually modified, such that the dividing streamline around the separation bubble was replaced with a solid wall (Fig. 8). After doing so, the iteration process was continued until a reasonable SIMN distribution was achieved. The first version of the experimental apparatus was built to test the concept. Figure 9 presents the initial and final wall shapes for the initial design. Figure 10 shows the corresponding SIMN compared to that of the infinite cascade and the experimental measurements.

It can be seen that the agreement between CFD-DP and EM-DP is very good up to the shock location. However, the shock structure resulting from the CFD-DP simulations is in very poor agreement with the experimental measurements. While the CFD-DP simulation predicted an oblique shock, the measurements in the passage clearly indicate a strong normal shock. This was not too surprising, as similar shock structures were observed in the optimization procedure while converging to the initial design geometry. Changes of less than 0.1 mm in the wall position in the supersonic region produced entirely different shock structures.

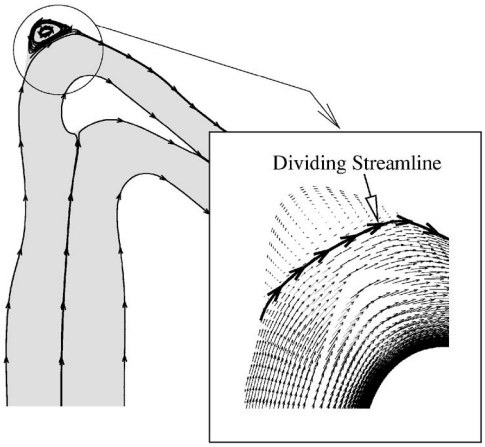

Fig. 8 Separation along pressure wall (not to scale)

These results showed that the basic methodology works, but that considerable care is needed in the supersonic region. Agreement was quite good for the pressure side of the blade between CFD-IC, CFD-DP, and EM-DP. Furthermore, there is a small error over the suction side of the blade between CFD-IC and CFD-DP. The agreement, however, between CFD-DP and EM-DP is excellent up to the shock.

Final Design. To seek an improved design, the cost function was modified in order to penalize the method for separated flow along the pressure wall, thus doing away with the need for manual fixes

$$\gamma_2 = \int_{\Gamma_{\text{pwall}}} ds \quad \forall \quad \tau_w \leqslant \tau_w^b \tag{8}$$

where τ_w^b is a lower bound on the shear stress to ensure that the boundary layer does not tend toward separation. Furthermore, the wall shear stress along the blade surface was also included as a

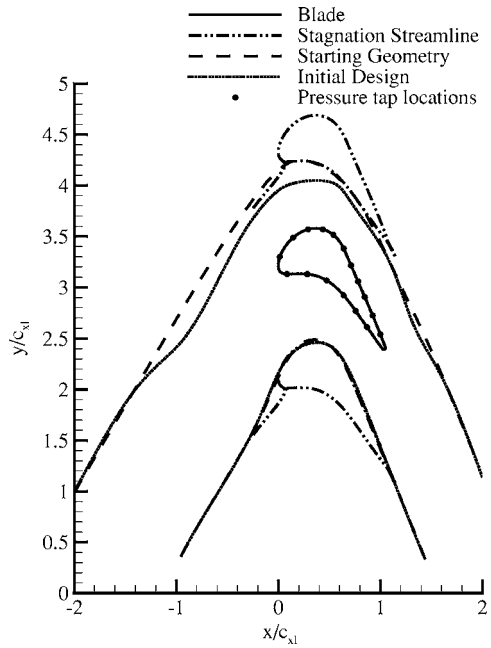

Fig. 9 Initial versus final wall geometries for the first design (not to scale)

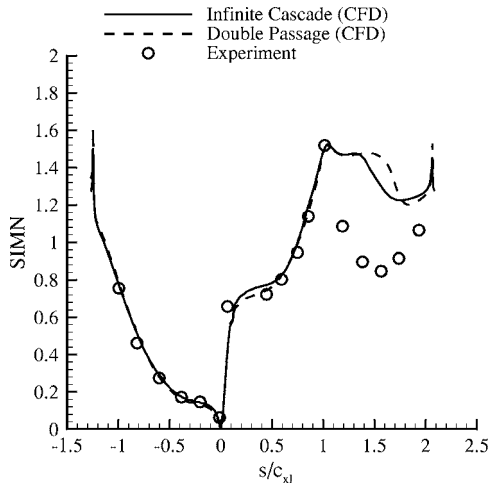

Fig. 10 SIMN corresponding to Fig. 9, without separation along pressure wall (refer to Fig. 5 for explanation of the abscissa axis)

way of ensuring that the boundary layer had similar characteristics to the infinite cascade

$$\gamma_3 = \int_{\Gamma_{\text{blade}}} |\tau_w - \tau_w^*| ds \tag{9}$$

Thus, the cost function was defined based on both an inviscid property and a viscous property. Finally, a line search was implemented for the determination of c in Eq. (5) to expedite convergence.

A total of 150 global optimization iterations were initially run in order to arrive at the final design. The resulting geometry at iteration 150 was built and tested to determine if the shock agreement could be improved. The experimental tests indicated that the correct shock structure was now achieved, and more subtle refinements were then made in order to arrive at the final design. Figure 11 presents the convergence history with the redefined cost function up to iteration 150 as well as after 150 with the modifications, which are described below.

Starting from iteration 150, several more control points were

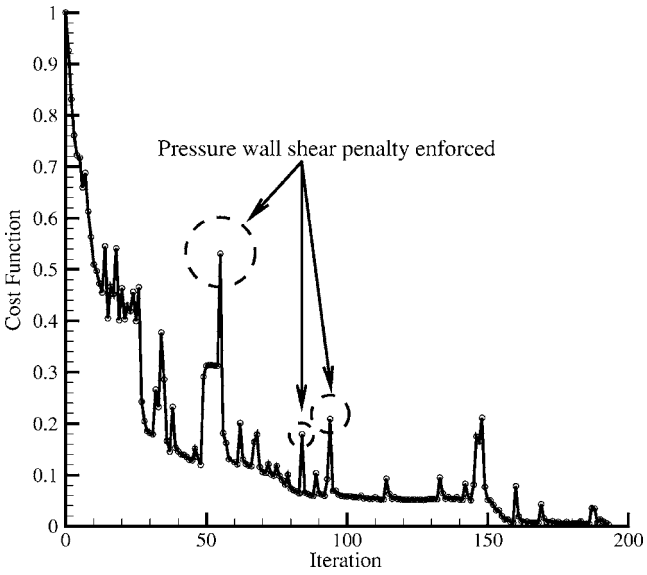

Fig. 11 Convergence history

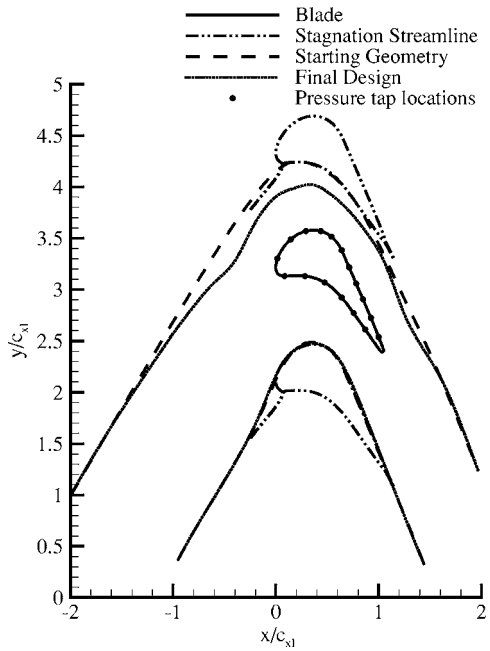

Fig. 12 Initial versus final wall geometries for the final design (not to scale)

added in the downstream region of the shock, which allowed for more subtle refinements in the wall shape to improve the agreement there. Also, the pressure wall separation penalty (τ_w^b in Eq. (8)) was relaxed, as it was observed that this would facilitate better agreement in the SIMN along the suction side. While this resulted in a thicker boundary layer, the flow was monitored to ensure that attached flow was still achieved. Referring to Fig. 11 again, it is evident that the overall cost function dropped significantly after these changes, and Fig. 12 presents the resulting geometry, which was then manufactured, installed, and tested in the rig. Figure 13 presents the resulting SIMN distributions for the final design.

Excellent agreement can be seen between the CFD-IC and CFD-DP over the entire blade section for this case. Furthermore, the experimental measurements are in very good agreement with the CFD-DP results. The only discernable discrepancy is in the peak Mach number. Whereas the CFD predicts a value of 1.52, the peak value measured was somewhat higher, with a value of 1.58

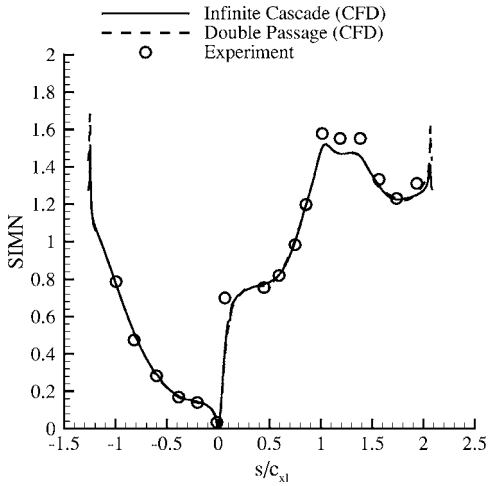

Fig. 13 SIMN corresponding to Fig. 12 (refer to Fig. 5 for explanation of the abscissa axis)

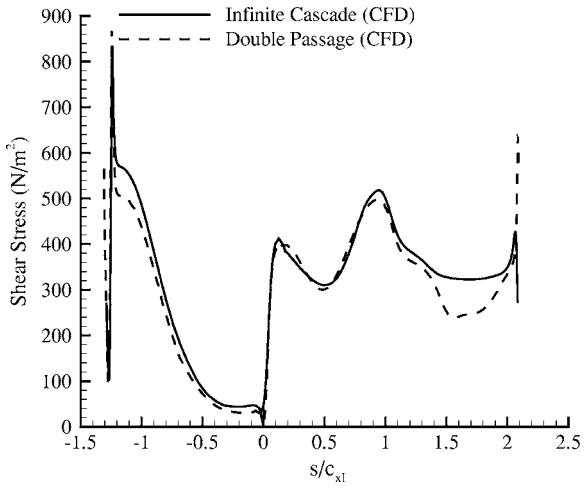

Fig. 14 Shear stress comparison for the final design (refer to Fig. 5 for explanation of the abscissa axis)

at the same axial location; a relative error of less than 4%.

Figure 14 presents the wall shear along the blade surface resulting from the CFD simulations. Again, very good agreement is observed between the CFD-IC and CFD-DP results. It is interesting to note that the shock recovery between the two cases is slightly different, indicating a different shock boundary layer interaction.

Figure 15 presents the Mach number contours for the CFD-IC and CFD-DP. Recalling the agreement in SIMN from Fig. 13, and referring to the Mach number flow field in Fig. 15, it is evident that the agreement in SIMN between CFD-DP and CFD-IC is associated with an equally similar Mach number distribution throughout the entire passage.

Upon completion of the blade surface pressure validation, an additional test of the inflow conditions was conducted. Matching the inflow conditions of the CFD with the experiment is a concern, since the domain of the CFD simulations did not include the nozzle section shown in Fig. 1, where the turbulence intensity was measured. This was done in order to keep the grid sizes to a minimum. While the total pressure and total temperature specified at the inflow agreed with the values used in the experiment, the prescribed value for the turbulence intensity was an issue. Velocity and turbulent kinetic energy profiles located just downstream of the inflow boundary for the CFD simulations were extracted and compared with preliminary PIV measurements. The agreement between the measured velocity profile and the CFD velocity profile was excellent; the error was on the order of 3%. The turbulence intensities also agreed quite well.

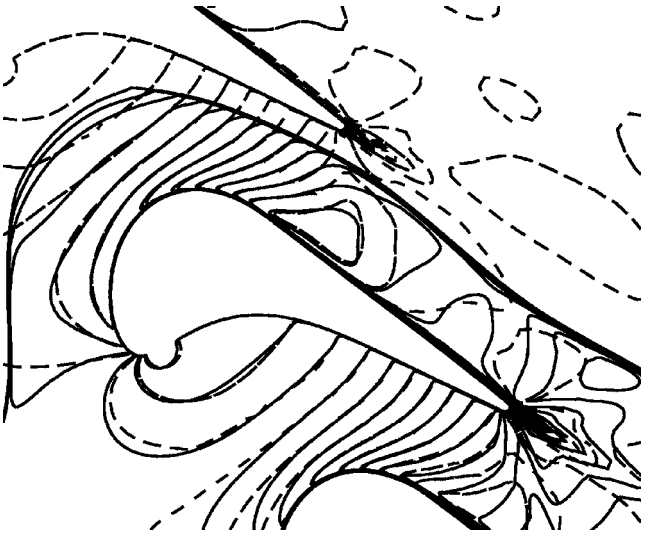

Fig. 15 Comparison between CFD-IC and CFD-DP for the final design: Mach number contour comparison (not to scale)

Finally, a 3D simulation was conducted for the final geometry to assess the effect of the passage aspect ratio. The 2D grid was extruded to the end wall, where the grid points were clustered to facilitate the use of the two-layer model. Only half of the passage width was simulated, and a symmetry boundary condition was specified at the passage midspan. The resulting flow field at the midspan location was nearly identical with the 2D simulations, confirming that the passage width was satisfactorily large.

Conclusions

A double-passage turbine cascade model was designed, built, and tested for the study of turbulent flow past a stationary turbine blade. The design was based on the Favre-averaged Navier-Stokes equations and an inverse design procedure with the objective of matching the surface isentropic Mach number (SIMN) of the blade in the passage with the SIMN of the blade in an infinite cascade, while maintaining attached flow along the passage walls. Excellent agreement was observed between the CFD results for the infinite cascade SIMN and the double-passage SIMN. Furthermore, the experimental measurements agree very well with the CFD results for the double passage in terms of the SIMN.

Acknowledgment

This work was funded by GE through the University Strategic Alliance Program and by AFOSR Contract No. F49620-02-1-0284 monitored by Thomas Beutner.

Nomenclature

c = step size, true chord length
c_v = specific heat at constant volume
c_{xl} = axial chord length
e = energy
E = set of governing equations
I = number of cost function components
j = global cost function
k = turbulent kinetic energy
l = length scale
M = isentropic Mach number
p = pressure
q = heat flux
Re = Reynolds number
s = blade surface coordinate
t = time
u = velocity component
U = state variable vector
y^+ = nondimensional wall unit

Greek

α = weight coefficient
β = scaling factor
Δ = perturbation
ε = dissipation, convergence criteria
ϕ = control variable
γ = cost function component, ratio of specific heats
Γ = bound of surface integral
λ = thermal conductivity
μ = viscosity
θ = temperature
ρ = density
τ = shear stress

Subscripts

i,j,k = indices

L = laminar
t = stagnation condition
T = turbulent
w = wall

Superscripts

b = bound
k = optimization counter number
* = target value

Abbreviations

CFD = computational fluid dynamics
CFD-DP = CFD of the double passage
CFD-IC = CFD of the infinite cascade
EM-DP = experimental measurements of the double passage
PIV = particle image velocimetry
RANS = Reynolds averaged Navier-Stokes
SIMN = surface isentropic Mach number

References

[1] Goldstein, R., 1971, "Film Cooling," Adv. Heat Transfer **7**, pp. 321–379.
[2] Dornberger, R., Stoll, P., Buche, D., and Neu, A., 2000, "Multidisciplinary Turbomachinery Blade Design Optimization," AIAA Paper No. 2000-0838.
[3] Camci, C., and Arts, T., 1985, "Short-Duration Measurements and Numerical Simulation of Heat Transfer Along the Suction Side of a Film-Cooled Gas Turbine Blade," J. Eng. Gas Turbines Power **107**, pp. 991–996.
[4] Durbin, P. A., 1996, "On the k-ε Stagnation Point Anomaly," Int. J. Heat Fluid Flow **17**, pp. 89–90.
[5] Medic, G., and Durbin, P. A., 2002, "Toward Improved Prediction of Heat Transfer on Turbine Blades," J. Turbomach. **124**, pp. 187–192.
[6] Medic, G., and Durbin, P. A., 2002, "Toward Improved Film Cooling Prediction," J. Turbomach. **124**, pp. 193–206.
[7] Giess, P. A., and Kost, F., 1997, "Detailed Experimental Survey of the Transonic Flow Field in a Rotating Turbine Cascade," *2nd European Conference on Turbomachinery–Fluid Dynamics and Thermodynamics* (Antwerpen, Belgium) March 5–7.
[8] Lang, H., Morck, T., and Woisetschlager, J., 2002, "Stereoscopic Particle Image Velocimetry in a Transonic Turbine Stage," Exp. Fluids **32**, pp. 700–709.
[9] Giel, P. W., Van Fossen, G. J., Boyle, R. J., Thurman, D. R., and Civinskas, K. C., 1999, "Blade Heat Transfer Measurements and Predictions in a Transonic Turbine Cascade," NASA/TM-1999-209296.
[10] Baughn, J. W., Butler, R. J., Byerley, A. R., and River, R. B., 1995, "An Experimental Investigation of Heat Transfer, Transition and Separation on Turbine Blades at Low Reynolds Number and High Turbulence Intensity," ASME Paper No. 95-WA/HT-25.
[11] Drost, U., and Bolcs, A., 1999, "Investigation of Detailed Film Cooling Effectiveness and Heat Transfer Distributions on a Gas Turbine Airfoil," J. Turbomach. **121**, pp. 233–242.
[12] Vogt, D. M., and Fransson, T. H., 2002, "A New Turbine Cascade for Aero-Mechanical Testing," 16th Symp. on Measuring Techniques in Transonic and Supersonic Flow in Cascades and Turbomachines.
[13] Hollon, B., and Jacob, J., 2001, "Experimental Investigations of Separation on Low Pressure Turbine Blades," AIAA Paper No. 2001-0447.
[14] Dorney, D. J., Lake, J. P., King, P. I., and Ashpis, D. E., 2000, "Experimental and Numerical Investigation of Losses in Low-Pressure Turbine Blade Rows," AIAA 38th Aerospace Sciences Meeting, Reno.
[15] Erhard, J., and Gehrer, A., 2000, "Design and Construction of a Transonic Test-Turbine Facility," ASME Paper No. 2000-GT-0480.
[16] Sanz, W., Gehrer, A., Woisetschläger, J., Forstner, M., Artner, W., and Jericha, H., 1998, "Numerical and Experimental Investigation of the Wake Flow Downstream of a Linear Turbine Cascade," ASME Paper No. 98-GT-246.
[17] Casey, M., and Innotec, S., 2001, "Classical Test Cases for the Validation of Turbomachinery CFD and the Relevance of QNET-CFD Cases," QNET-CFD Workshop, Athens.
[18] Ganzert, W., and Fottner, L., 1999, "An Experimental Study on the Aerodynamics and the Heat Transfer of a Suction Side Film Cooled Large Scale Turbine Cascade," ASME Paper No. 99-GT-39.
[19] Buck, F. A., and Prakash, C., 1995, "Design and Evaluation of a Single Passage Test Model to Obtain Turbine Airfoil Film Cooling Effectiveness Data," ASME Paper No. 95-GT-19.
[20] Radomsky, R. W., and Thole, K. A., 2000, "Flowfield Measurements for a Highly Turbulent Flow in a Stator Vane Passage," J. Turbomach. **122**, pp. 255–262.
[21] Kodzwa, P. M., Elkins, C. L., and Eaton, J. K., 2003, "Measurements of Film Cooling Performance in a Transonic Single Passage Model," 2nd Int. Conf. on Heat Transfer, Fluid Mechanics and Thermodynamics, Zambia.
[22] Ott, P., Norryd, M., and Bolcs, A., 1998, "The Influence of Tailboards on Unsteady Measurements in a Linear Cascade," ASME Gas Turbine and Aeroengine Congress.
[23] STAR-CD Version-3.10, 1999, *Methodology*, Computational Dynamics Ltd.

Computations of Flow Field and Heat Transfer in a Stator Vane Passage Using the $\overline{v^2}-f$ Turbulence Model

A. Sveningsson[1]
e-mail: andreas.sveningsson@chalmers.se

L. Davidson
Division of Thermo and Fluid Dynamics,
Department of Mechanical Engineering,
Chalmers University of Technology,
SE-412 96, Gothenburg, Sweden

In this study three-dimensional simulations of a stator vane passage flow have been performed using the $\overline{v^2}-f$ turbulence model. Both an in-house code (CALC-BFC) and the commercial software FLUENT are used. The main objective is to investigate the $\overline{v^2}-f$ model's ability to predict the secondary fluid motion in the passage and its influence on the heat transfer to the end walls between two stator vanes. Results of two versions of the $\overline{v^2}-f$ model are presented and compared to detailed mean flow field, turbulence, and heat transfer measurements. The performance of the $\overline{v^2}-f$ model is also compared with other eddy-viscosity-based turbulence models, including a version of the $\overline{v^2}-f$ model, available in FLUENT. The importance of preventing unphysical growth of turbulence kinetic energy in stator vane flows, here by use of the realizability constraint, is illustrated. It is also shown that the $\overline{v^2}-f$ model predictions of the vane passage flow agree well with experiments and that, among the eddy-viscosity closures investigated, the $\overline{v^2}-f$ model, in general, performs the best. Good agreement between the two different implementations of the $\overline{v^2}-f$ model (CALC-BFC and FLUENT) was obtained. [DOI: 10.1115/1.1929820]

Introduction and Past Studies

An important issue when designing a gas turbine engine is to reduce its influence on the environment. One trend, aiming in this direction, is to use burners designed to produce very low levels of NO_x. The working principle of these low-NO_x burners is to reduce the highest temperatures in the burner rendering a somewhat flatter turbine inlet temperature profile. This trend together with the fact that the performance of the turbine improves with increasing turbine inlet temperature leaves only one option that meets both conditions—distributing hot gas toward the hub and casing (hereafter referred to as end walls). Therefore, it becomes increasingly important to be able to accurately predict the heat transfer rate from the hot gas to the end walls. One flow feature making this rather complicated is the presence of secondary, three-dimensional flow structures, often referred to as horseshoe vortices, which enhance the rate of heat transfer to the endwall.

Previous computations of three-dimensional vane passage flows have in most cases been carried out using different versions of two-equation models for turbulence closure. The most popular ones are the $k-\varepsilon$ and $k-\omega$ models. Ho and Lakshminarayana [1] used the Chien [2] low Reynolds number form of the $k-\varepsilon$ model to compute a vane passage flow experimentally investigated by Gregory-Smith and Cleak [3]. They were able to capture most of the complex flow phenomena in the vicinity of the end wall but never computed any heat transfer data (not measured by [3]). Harvey et al. [4] used an algebraic mixing length model (zero-equation) when they computed end-wall heat transfer rates that were compared to measurements presented in the same paper. The heat transfer rates were claimed to be predicted with an accuracy of ±20% even though the turbulence model used is relatively simple. However, the overall trends in predicted end-wall Nusselt number do not compare very well with measured patterns. Another contribution to this area of research is the work performed at NASA Lewis Resarch Center. For example, Boyle and Jackson [5] computed turbine vane and end-wall heat transfer and compared them to the experiments of Harvey et al. [4]. They investigated the performance of three turbulence models and found differences among the predictions that were greater than the differences in experimental heat transfer between the two configurations computed. Their overall best results were obtained with the Cebeci-Smith turbulence model. More recently Hermanson and Thole [6,7] computed the flow measured by, e.g., Radomsky and Thole [8] using different turbulence models available in FLUENT. Here they investigated the influence of inlet conditions and Mach number on the end-wall secondary flow. Later Hermanson et al. [9] computed the same flow using the $\overline{v^2}-f$ model implemented in FLUENT. Rather good agreement with measurements, both in terms of mean flow and heat transfer, was reported. Another example of promising results using the $\overline{v^2}-f$ model in complex three-dimensional boundary layer flows was presented by Parneix et al. [10] who successfully computed the horseshoe vortex around a wall-mounted appendage.

The $\overline{v^2}-f$ turbulence model, originally suggested by Durbin (e.g., [11]) has, during the last few years, become increasingly popular because of its ability to account for near-wall damping without use of ad hoc damping functions. In this work the performance of two versions of this model will be assessed by computing the flow field in the scaled-up stator vane passage investigated by Kang and Thole [12]. Two codes, the commercial package FLUENT and the in-house code CALC-BFC will be compared by computing exactly the same flow field using similar numerical treatments and the same computational mesh.

Governing Equations

Mean Flow Equations. The steady RANS equations read

$$U_j\frac{\partial U_i}{\partial x_j}=-\frac{1}{\rho}\frac{\partial P}{\partial x_i}+\nu\frac{\partial^2 U_i}{\partial x_j^2}-\frac{\partial}{\partial x_j}\overline{u_iu_j},\quad \frac{\partial U_j}{\partial x_j}=0 \tag{1}$$

[1]To whom correspondence should be addressed.

Contributed by the Turbomachinery Division of THE AMERICAN SOCIETY OF MECHANICAL ENGINEERS for publication in the JOURNAL OF TURBOMACHINERY. Manuscript received May 17, 2004; revised manuscript received January 13, 2005. Editor: D. Wisler.

Table 1 $\overline{v^2}-f$ model constants

Model	C_μ	$C_{\varepsilon d}$	$C_{\varepsilon 2}$	C_1	C_2	σ_k	σ_ε	C_L	C_η
1	0.22	0.045	1.9	1.4	0.3	1.0	1.3	0.25	85
2	0.19	0.045	1.9	0.4	0.3	1.0	1.3	0.23	70

$$U_i\frac{\partial T}{\partial x_i}=\frac{\partial}{\partial x_i}\left(\frac{\nu}{Pr}\frac{\partial T}{\partial x_i}-\overline{u_i t}\right) \tag{2}$$

Turbulence Closure. The unknown Reynolds stresses and turbulent heat fluxes are closed using the eddy-viscosity concept, i.e.,

$$\overline{u_i u_j}=-2\nu_t S_{ij}+\frac{2}{3}k\delta_{ij};\quad \overline{u_i t}=-\frac{\nu_t}{\sigma_t}\frac{\partial T}{\partial x_i} \tag{3}$$

$$\nu_t=C_\mu\overline{v^2}\mathcal{T},\quad \text{where } \mathcal{T}=\max\left(\frac{k}{\varepsilon},6\sqrt{\frac{\nu}{\varepsilon}}\right) \tag{4}$$

The turbulent quantities k and ε are governed by

$$u_j\frac{\partial k}{\partial x_j}=\frac{\partial}{\partial x_j}\left[\left(\nu+\frac{\nu_t}{\sigma_k}\right)\frac{\partial k}{\partial x_j}\right]+P_k-\varepsilon \tag{5}$$

$$u_j\frac{\partial \varepsilon}{\partial x_j}=\frac{\partial}{\partial x_j}\left[\left(\nu+\frac{\nu_t}{\sigma_\varepsilon}\right)\frac{\partial \varepsilon}{\partial x_j}\right]+\frac{C_{\varepsilon 1}P_k-C_{\varepsilon 2}\varepsilon}{\mathcal{T}} \tag{6}$$

In this work two different $\overline{v^2}-f$ models have been used. They will hereafter be referred to as model 1 and model 2, respectively. In model 1, given in Parneix et al. [10], the wall-normal Reynolds stress component, $\overline{v^2}$, is modeled using

$$u_j\frac{\partial \overline{v^2}}{\partial x_j}=\frac{\partial}{\partial x_j}\left[\left(\nu+\frac{\nu_t}{\sigma_k}\right)\frac{\partial \overline{v^2}}{\partial x_j}\right]+kf-\frac{\overline{v^2}}{k}\varepsilon \tag{7}$$

$$L^2\frac{\partial^2 f}{\partial x_j^2}-f=\frac{C_1-1}{\mathcal{T}}\left(\frac{\overline{v^2}}{k}-\frac{2}{3}\right)-C_2\frac{P_k}{k} \tag{8}$$

The turbulent length scale L and the modified coefficient $C_{\varepsilon 1}$ are calculated using

$$L=C_L\max\left(\frac{k^{3/2}}{\varepsilon},C_\eta\frac{\nu^{3/4}}{\varepsilon^{1/4}}\right),\quad C_{\varepsilon 1}=1.4\left(1+C_{\varepsilon d}\sqrt{k/\overline{v^2}}\right) \tag{9}$$

The wall boundary conditions for the dissipation rate ε and the redistribution parameter f are

$$\varepsilon\to 2\nu\left(\frac{k}{y^2}\right);\quad f\to\frac{-20\nu^2}{\varepsilon}\left(\frac{\overline{v^2}}{y^4}\right)\ \text{as}\ y\to 0 \tag{10}$$

These boundary conditions (especially that for f) make the original formulation numerically unstable. Therefore a redefinition of f has been proposed in order to have $f=0$ on walls. This modification, used in, e.g., Kalitzin [13] and Lien and Kalitzin [14], renders the following $\overline{v^2}$ and f equations (model 2)

$$u_j\frac{\partial \overline{v^2}}{\partial x_j}=\frac{\partial}{\partial x_j}\left[\left(\nu+\frac{\nu_t}{\sigma_k}\right)\frac{\partial \overline{v^2}}{\partial x_j}\right]+kf-6\overline{v^2}\frac{\varepsilon}{k} \tag{11}$$

$$L^2\frac{\partial^2 f}{\partial x_j^2}-f=\frac{C_1}{\mathcal{T}}\left(\frac{\overline{v^2}}{k}-\frac{2}{3}\right)-C_2\frac{P_k}{k}-5\frac{\overline{v^2}}{k\mathcal{T}} \tag{12}$$

Note that the models given in Lien and Kalitzin [14] and Kalitzin [13] only differ in model constant values. For a more thorough discussion on the differences between the above models, see [15]. Finally, the turbulence model constants of models 1 and 2 are shown in Table 1.

The Realizability Constraint. Most eddy-viscosity-based turbulence models overpredict the turbulent kinetic energy k in stagnation point flows. Durbin [16] suggested a bound on the turbulent time scale $\mathcal{T}$ derived from $2k\geq\overline{u^2}\geq 0$, which significantly improves predictions of k. For $\overline{v^2}$–f models this constraint implies

$$\mathcal{T}=\min\left[\max\left(\frac{k}{\varepsilon},6\sqrt{\frac{\nu}{\varepsilon}}\right),\frac{C_{\lim}k}{3C_\mu\overline{v^2}}\frac{1}{\max\lambda_\alpha}\right] \tag{13}$$

where the constant $C_{\lim}$ has been added to allow for tuning against experiments and $\max\lambda_\alpha$ is the largest eigenvalue of the strain rate tensor S_{ij}. In this work $C_{\lim}$ is set to 0.6, which is the most commonly used value. The mechanism responsible for the improvement in k predictions is the reduction in modeled production rate of k. For further discussion on this subject, see [17].

Numerical Considerations and Test Case

The in-house code CALC-BFC is a structured code using SIMPLEC and a colocated grid arrangement with Rhie and Chow interpolation. The van Leer scheme (a bounded, second order upwind scheme) was used when discretizising both momentum and turbulence equations. The resulting set of equations were solved with either a segregated or a coupled tridiagonal matrix solver (TDMA). In the coupled solver the k–ε equations and/or the $\overline{v^2}$–f equations were solver in a coupled manner [15]. Whenever the commercial software FLUENT was used for comparison with CALC-BFC results, efforts were made to keep all numerical features similar to those described above. The $\overline{v^2}-f$ version used in FLUENT was a trial version for FLUENT 5 implemented using user-defined functions.

The three-dimensional experimental test case used for validation is the low-turbulence intensity case ($Tu_{inl}=0.6\%$) documented in Kang and Thole [12]. The heat fluxes were measured by attaching a constant heat flux film to the end wall, the film-covering locations downstream $x/C=-0.475$. This film is cooled by the passage flow and by measuring the heat flux film temperature the heat transfer coefficient can be determined. For a detailed description of the experiments, see [12]. In Fig. 1 a slice of the computational domain is shown. The inlet is located $1C$ upstream

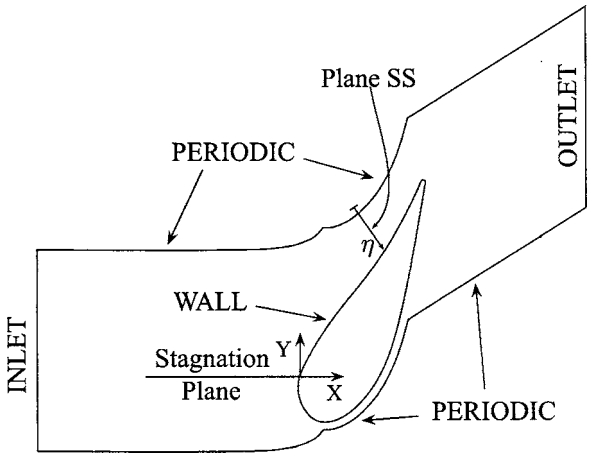

Fig. 1 Computational domain and the location of the stagnation plane and the plane SS that will be used for plotting. When the coordinate η is used $\eta=0$ is located on the suction side, $\eta=1$ on the pressure side.

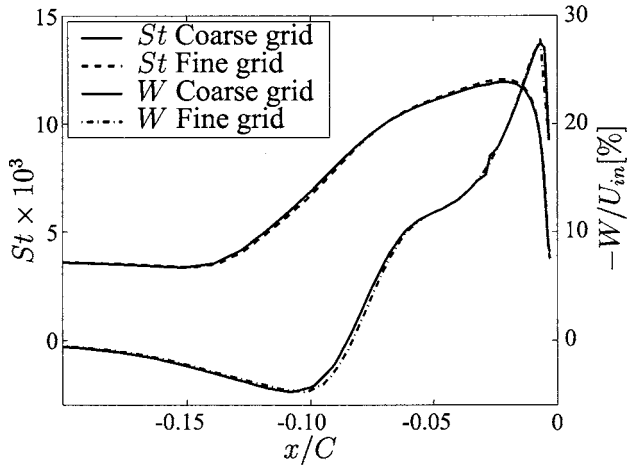

Fig. 2 End-wall Stanton number along the stagnation line ($Y=0$) and spanwise velocity along a line crossing the center of the horseshoe vortex roll-up ($Y=0$, $Z=0.014S$)

the leading edge (chord $C=0.594$ m, pitch $P=0.77C$, span $S=0.93C$). The end wall is treated as a constant heat flux wall for $x/C \geq -0.475$, otherwise adiabatic. The vane wall is also modeled as being adiabatic. At midspan a symmetry boundary condition is used. At the inlet a measured velocity profile was specified. The inlet turbulence quantities were not available (except at midspan) but were obtained from a separate computation based on the given velocity profile and the assumption that the turbulence field was fully developed. The sensitivity to these boundary conditions are investigated. All fluid properties are assumed to be independent of temperature variations. The mesh consists of an O grid around the vane and three additional blocks, one located upstream the vane, one downstream and one in the vane passage. The total number of cells for the standard mesh was 650,000. In the end-wall stagnation region y^+ values were <0.5 and all around the vane $y^+<2$. In order to investigate grid sensitivity, a finer mesh, 1.8 M nodes, was created. Some results of the grid dependency study are shown in Fig. 2. Here $\overline{v^2}-f$ model 2 predictions of the end-wall Stanton number along the stagnation line are shown for the two meshes together with the secondary (spanwise) velocity component along a line crossing the center of the horseshoe vortex roll-up. Both profiles suggest that the results are grid independent and the coarser mesh was used for most computations. The momentum equations were assumed to be fully converged when the residuals scaled with $\dot{m}U|_{\text{in}}$ were $<10^{-3}$.

2D Flow Field Results

In order to illustrate the importance of the realizability constraint contours of k/U_{in}^2 for the stator vane flow are shown in Fig. 3. In both cases $\overline{v^2}-f$ model 1 was used with the only difference that in the left figure the realizability constraint, Eq. (13), is deactivated. It can be seen that the constraint has a strong influence. For example, when the limiter is active, it is only in a region around the wake that k/U_{in}^2 exceeds levels of 10^{-3}, whereas the same quantity is well above this value in almost the entire domain if the constraint is not used.

In Fig. 4 predictions of stator vane Stanton number are compared to measurements for some $\overline{v^2}-f$ model 1 computations. Two cases with different inlet turbulence levels are computed. In the region around the stagnation point and along the pressure side of the vane the results agree well with experimental data both for the high (Tu=10%) and low (Tu=0.6%) turbulence intensity case. On the suction side, transition is predicted far too early, which has a strong impact on the heat transfer. Also included in this figure are the results of $\overline{v^2}-f$ model 1 for the low-turbulence

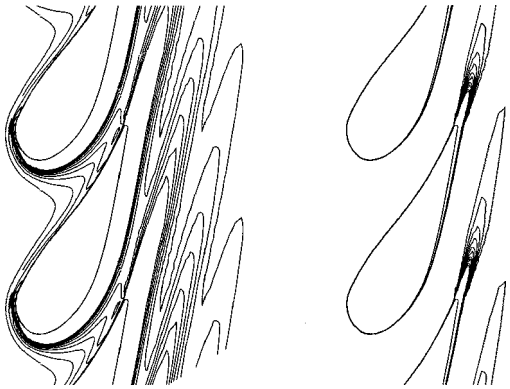

Fig. 3 Contours of k/U_{in}^2. Inlet FBW from left. Left: $\overline{v^2}-f$ Model 1 without realizability constraint; Right: As left but with relizability constraint. Contour intervals of 0.001.

intensity case where the realizability constraint has not been used. When the constraint is deactivated the predicted heat transfer on the pressure side is almost as high as for the Tu=10% case. The results are even worse on the suction side. Worth mentioning is that the $\overline{v^2}-f$ model does well in capturing the increase in heat transfer close to the pressure side trailing edge where most eddy-viscosity-based turbulence models usually fail. As an example results of the realizable $k-\varepsilon$ model are included showing too a high increase in Stanton number along the pressure side. The $\overline{v^2}-f$ model 1 and the Realizable $k-\varepsilon$ model results agree well (especially the former) with results presented by Hermanson et al. [9], who used the FLUENT version of $\overline{v^2}-f$ model 2.

Three-Dimensional Flow Field Results

In this section results of three-dimensional computations of the stator vane flow field will be presented. Most of the results are presented as either contour or vector plots in two different planes—the stagnation plane and a plane labeled SS located some distance into the vane passage. The location of the planes are shown in Fig. 1 together with a coordinate η ranging from 0 to 1, $\eta=0$ being the suction side and $\eta=1$ the pressure side.

Stagnation Region Flow Field. One of the most interesting regions of the flow field in a stator vane passage is the flow in the stagnation region. Here the main flow is retarded by the presence of the vane, and the vorticity in the in-coming boundary layer is

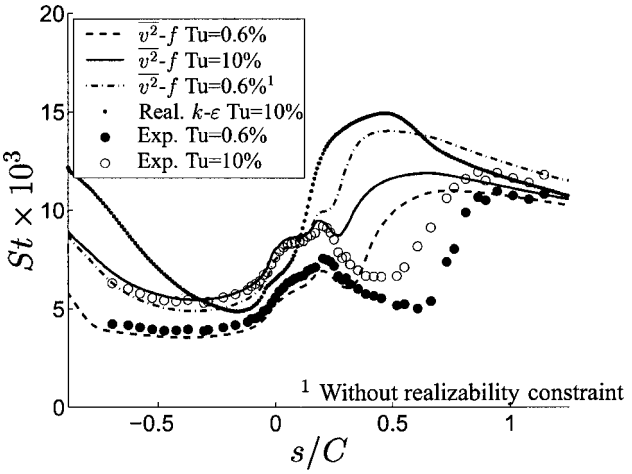

Fig. 4 Measured and predicted ($\overline{v^2}-f$ model 1 and realizable $k-\varepsilon$ model) Stanton number along the midspan of the vane. $s/C \geq 0$: suction side. $s/C \leq 0$: pressure side.

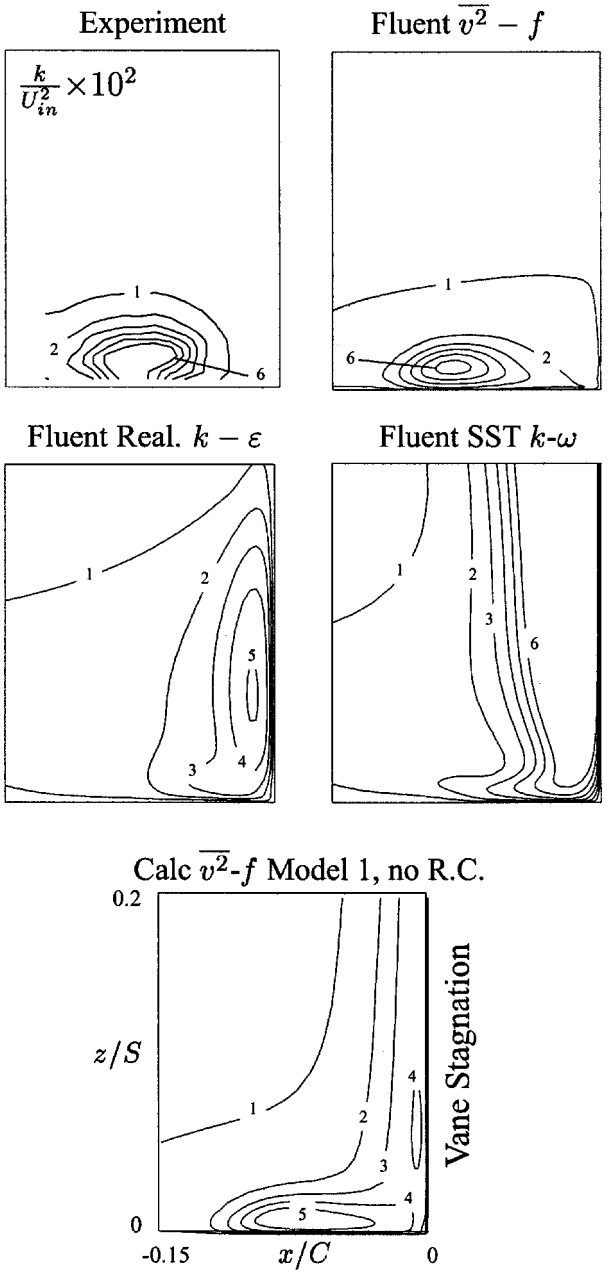

Fig. 5 Contours of $k/U_{in}^2\times 10^2$ in the stagnation plane (contour interval of $0.01k/U_{in}^2$)

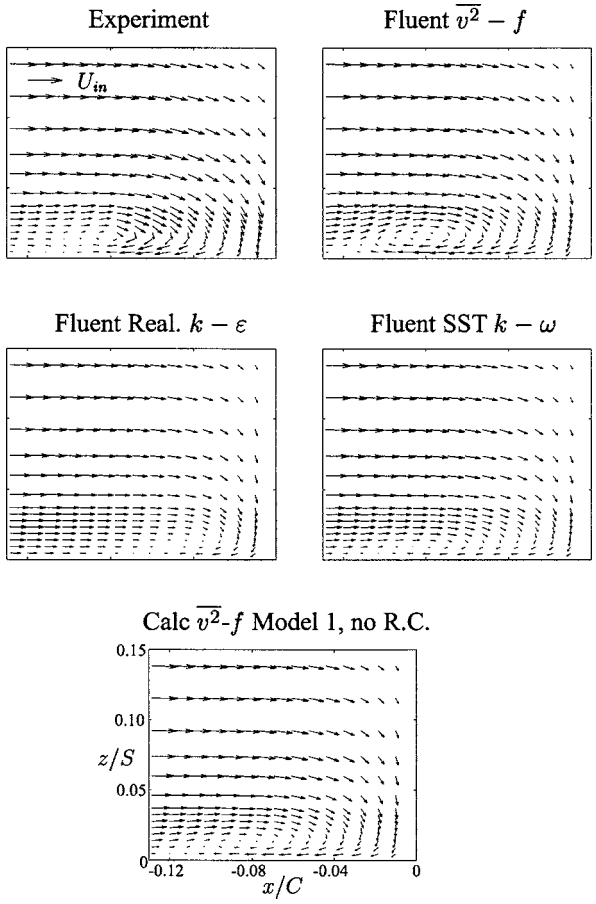

Fig. 6 Velocity vectors in the stagnation plane showing the horseshoe vortex roll-up

transformed into a so-called horseshoe vortex system. As will be illustrated later, capturing this secondary motion is important when determining the heat transfer to the end walls.

In this work the performance of the different turbulence models is investigated. The only difference between the models that affects the mean flow field will be found in the estimates of the eddy viscosity ν_t. One important flow variable in the expression for ν_t is the turbulence kinetic energy k. In Fig. 5 contours of k in the stagnation plane are shown for four different computations. The differences among the predictions are striking. For example, the peak in k coinciding with the horseshoe vortex center is correctly captured by the $\overline{v^2}-f$ model (both with and without use of the realizability constraint). With the realizable $k-\varepsilon$ model a peak in k is erroneously located along the vane stagnation line, whereas with the shear stress transport (SST) $k-\omega$ model the problem of overpredicting the growth of turbulence energy in stagnation point flows has not been solved. Note that Menter [18] suggested a limiter on the production term in the k equation of the SST model that addresses this problem. However, this limiter is obviously not implemented in the FLUENT version of the SST model. Also note that the growth problem is present also in the $\overline{v^2}-f$ computation where the realizability constraint is not used. Also note that it can be seen that the FLUENT $\overline{v^2}-f$ model prediction of k agrees well with measured data, both qualitatively and quantitatively (almost identical profiles were obtained with both $\overline{v^2}-f$ models implemented in CALC-BFC when the realizability constraint was used).

In Fig. 6 the computed velocity vectors in the stagnation plane are compared to measured velocities. It can be seen that both the location of the horseshoe vortex and its intensity is accurately predicted by the $\overline{v^2}-f$ model (predicted vortex center: $-0.0825x/C$, $0.0165z/S$, measured vortex center: $-0.083x/C$, $0.016z/S$). The intensity of the horseshoe vortex roll-up predicted by the realizable $k-\varepsilon$ and SST $k-\omega$ models are substantially weaker, the former not being able to reproduce a vortexlike signature. This is because of too a large growth of predicted eddy viscosity (which is closely related to k) having the effect that the recirculating motion in this region is restrained by turbulence momentum transport. By comparision with the k profiles in Fig. 5 these results are somewhat surprising. For example, the SST $k-\omega$ model, which suffers from the stagnation point anomaly, predicts a stronger secondary motion than the realizable $k-\varepsilon$ model does. Furthermore, the realizable $k-\varepsilon$ and the $\overline{v^2}-f$ model k profiles are equal in magnitude, but the former fails almost completely in predicting the vortex roll-up. Also note that the differences in k of the two $\overline{v^2}-f$ models has only little effect on the stagnation region mean flow field. Although not shown here, the realizability constraint has an even stronger effect on ν_t

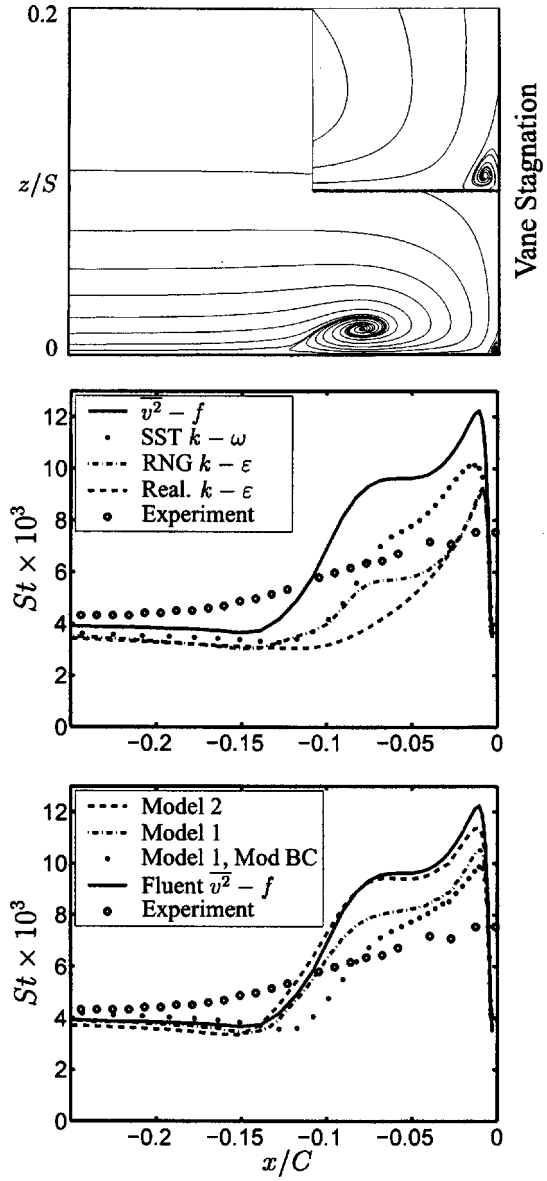

Fig. 7 Top: Streamlines of FLUENT $\overline{v^2}-f$ computation illustrating the horseshoe and leading-edge corner vortices in the stagnation plane. Middle: Measured and predicted (FLUENT) Stanton number along the end-wall stagnation line. Bottom: CALC-BFC predictions.

than on k. In this flow the constraint is activated (cf. Eq. (13)) just downstream of the inlet and as the flow reaches the vane stagnation the inlet eddy viscosity has been reduced by more than 90%. Because of the large difference in ν_t it is a surprise that mean flow fields (top right and bottom in Fig. 6) are nearly the same. However, as was seen in Fig. 4, the predicted heat fluxes were strongly influenced when the constraint was switched off. The reason why the mean flow field is less sensitive to ν_t in the stagnation region is the presence of a strong pressure gradient. This pressure gradient outweights to some extent the effect of the poorly predicted Reynolds stresses in the mean flow equations but it does not enter the energy equation. Thus, the effects of an inaccurate prediction of ν_t is often greater on heat transfer than on momentum transfer.

Another interesting feature of the stagnation region flow is illustrated in Fig. 7 (top figure). Here particle traces (restricted to a plane) in the stagnation plane are shown. The large horseshoe vortex structure is easily identified. In a close-up of the stator vane/endwall junction another much smaller (about 0.01 chord wide) counterrotating vortex is also shown. This vortex was postulated by Goldstein and Spores [19] who observed a small region of very high local heat transfer at the abovementioned junction. Later Wang et al. [20] verified its existence with detailed flow field measurements. Note that the measured velocity vectors in Fig. 6 also indicate the presence of this vortex. A possible attachment point can be seen (last row of vectors) but the resolution is not fine enough to visualize the vortex.

Stagnation Region Heat Transfer. In the preceeding section some characteristics of the mean flow field were investigated. Another important issue is how the heat transfer to the end wall is affected by the presence of the horseshoe vortex. If this vortex is strong, then it will tear up the incoming, insulating boundary layer and replace the relatively cold fluid close to the end wall with hot gas from the free-stream region. An example of this phenomenon is seen in Fig. 7 (top) where the flow is directed downward in between the center of the horseshoe vortex and the stator vane. In order to illustrate the influence this has on heat transfer, the predicted Stanton number along the end-wall stagnation line is plotted in Fig. 7 (middle) for the FLUENT computations.

Two important conclusions can immediately be drawn. The end-wall heat transfer in the region well upstream of the stator vane is fairly accurately predicted with Stanton numbers some 10–15% too low, independent of choice of turbulence model. The slight undershoot is probably due to the inlet boundary layer profiles of the turbulent quantities not being fully consistent with the experimental setup. Unfortunately, the experimental inlet profiles of k and $\overline{v^2}$ needed to verify this are not available. Second, the heat transfer in the region of the horseshoe vortex roll-up seems to be fairly independent of the inlet conditions. Instead it is determined by the intensity of the vortex itself, which is in line with the above discussion on hot and cold gas exchange. Therefore the $\overline{v^2}-f$ model, which predicts the strongest secondary motion, also gives the highest rates of heat transfer. In this case the FLUENT $\overline{v^2}-f$ model overpredicts the Stanton number by ~50% in the stagnation region. Here the SST $k-\omega$ and the renormalization group (RNG) $k-\varepsilon$ models agree the best with measurements. This is unexpected as both models underpredict the roll-up of the horseshoe vortex, which is the flow feature responsible for the stagnation region increase in heat transfer. Also note the peaks in heat transfer close to the end-wall and/or stator vane junction. At this location, between the horseshoe and the leading-edge corner vortices, the free-stream flow attaches to the end wall and a new, initially very thin, boundary layer begins to develop. This feature is absent in the experiments, which is due to either insufficient resolution or the mean flow not being stationary.

In Fig. 7 (bottom figure) the corresponding results from three different CALC-BFC $\overline{v^2}-f$ computations are shown (also included for reference is the FLUENT $\overline{v^2}-f$ computation). It can be seen that the highest heat transfer rates are predicted by the FLUENT model and $\overline{v^2}-f$ model 2. These results being almost identical suggests that the two models and their implementations in the two different codes are very similar. The $\overline{v^2}-f$ model 1 results agree rather well with measurements in the vortex dominated region and as this model in large also captures the intensity of the secondary motion it is regarded to produce the best overall agreement with measurements. In order to investigate the possible influence of the prescribed inlet boundary conditions for the turbulent quantities one additional Model-1 computation was added. Here the inlet k profile was kept the same whereas the ε and $\overline{v^2}$ were specified according to

$$\varepsilon = C_\mu \frac{k^{3/2}}{L}, \quad \overline{v^2} = \frac{2}{3}k \tag{14}$$

where L (here the measured $L=0.09$ m was used) is a characteristic turbulence length scale. As can be seen this change has some influence on the location of the horseshoe vortex and has also increased the heat transfer upstream the vortex by a few percent.

Worth mentioning is that several inlet boundary conditions were tried (constant profiles corresponding to different levels of turbulence intensity) of which the one reported here had the greatest impact on the results. The conclusion is that the end-wall heat transfer in the stagnation region is not very sensitive to the specified inlet boundary conditions. Thus it is neither expected to be sensitive to the inlet *level* of turbulence intensity, but rather to how well the roll-up of the horseshoe vortex is captured. This trend has also been seen in experiments by Radomsky and Thole [8].

The effect of the realizability constraint on the end-wall stagnation region heat transfer was rather small (not shown here). This finding is supported by the fact that the k profiles along the end wall obtained with and without the constraint are alike (cf. Fig. 5) and that the predicted secondary motions, which are of greater importance, are almost identical. Finally, note that the Stanton number signature of the horseshoe vortex is not as detailed in the experiments as in the computations. This can have only two explanations: (i) The vortex is not completely stationary but moves in the streamwise direction. This phenomenon cannot be captured in steady computations (model error). (ii) The measured end-wall temperature is influenced by heat conduction within the constant heat flux film (experimental uncertainty). Both these phenomena would smear out the time-averaged Stanton profile.

Secondary Velocities Between Two Vanes. In order to visualize the horseshoe vortices emanating from the vane–end-wall junction secondary velocities (the total local velocity minus the local velocity in the midspan flow direction, see [12] for further details) are plotted in Fig. 8 for plane SS (cf. Fig. 1). As the intensity of the secondary motion is concentrated towards the end wall only one quarter of full passage is included ($0<z/S<0.25$).

In both the experiments and the computations, two secondary structures are visible. The structure to the left is the suction-side leg of the horseshoe vortex, whereas the right structure is the motion resulting from effects of the pressure-side leg of this vortex and the passage vortex. The center locations of the vortices in this plane predicted with the $\overline{v^2}-f$ model agree fairly well with the experiment, both lying slightly too close to their respective stator wall. The strength of the vortices, especially the lower part of the passage vortex, however, is underpredicted. The reason why the secondary motion in this region is strong is that the low streamwise momentum fluid in the end-wall boundary layer is being sucked toward the suction side of the adjacent vane. Fluid higher up in the passage (at higher z/S) has higher streamwise velocity magnitude (momentum) and is therefore not as strongly affected by this pressure difference between the vanes. This "passage-vortex" effect is one of the flow features that is not very well captured in the computations.

In order to illustrate the coupling between the secondary motion and the end-wall heat transfer the Stanton number along the intersection of the end wall and plane SS is shown in Fig. 8. The circles represent measurements in one passage each (here indicating good periodicity of the experiment), whereas the lines are the computed Stanton number of $\overline{v^2}-f$ model 1 and the realizable $k-\varepsilon$ model. In both computations and measurements a peak in heat transfer is located close to the vane suction side. This peak is due to the presence of the suction-side leg of the horseshoe vortex, which distributes hot gas toward the end wall. At this particular location the hot fluid has just reattached to the end wall and the boundary layer is therefore very thin. Toward the pressure side ($\eta=1$) the heat transfer shows a much less distinct increase even though the secondary motion here is stronger. The reason is that the boundary layer here is much thicker than closer to the suction side, i.e., we are well downstream the reattachment location.

With the realizabe $k-\varepsilon$ failing to capture the secondary motion, which is important for the heat transfer, it is a surprise that the model gives an almost perfect prediction of the end-wall heat transfer. The authors argue that this is somewhat fortitious and

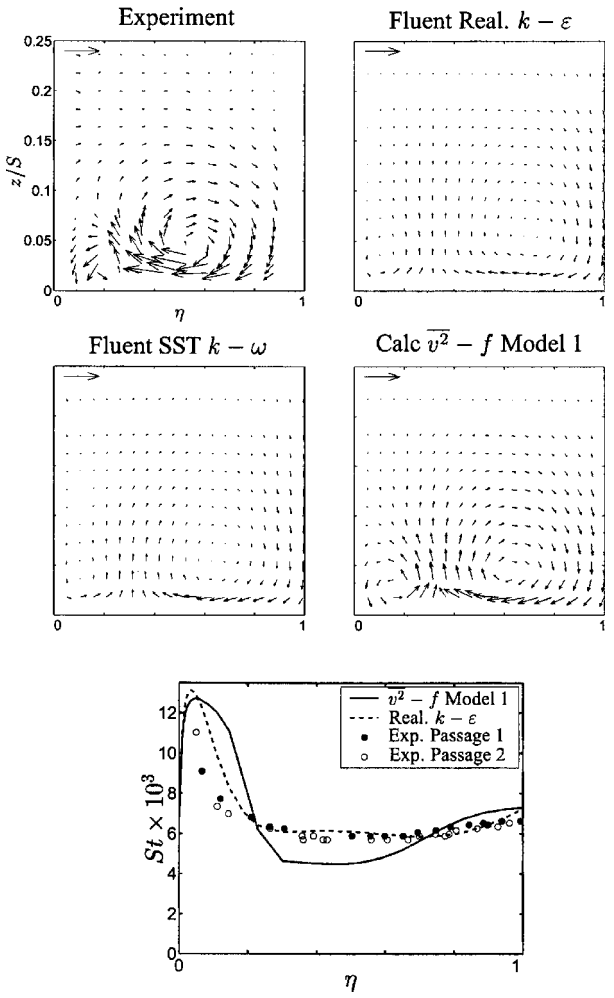

Fig. 8 Predicted secondary velocities in the lower half of plane SS (cf. Fig. 1). The reference arrows correspond to 20% of the maximum total velocity in the plane. Bottom: Endwall Stanton number along the bottom of plane SS.

results not shown here suggests that in the realizabe $k-\varepsilon$ computations the predicted thicknesses of the boundary layers are more sensitive to the strong acceleration through the passage than seen in experiment or in any other computation. The $\overline{v^2}-f$ model results agree fairly well with measurements along most of the line but in between the two vortices the heat transfer is underpredicted. As previously mentioned this might be due to the horseshoe vortex not being completely stable in the experiments but moves in the pitchwise direction. A more likely explanation is the too weak predicted motion of low-momentum fluid toward the suction side. In order to illustrate the importance of this flow feature to the end-wall heat transfer some streamlines showing the secondary motion are plotted in Fig. 9. Here streamlines A visualize the very center of the horseshoe vortex pressure leg. Of greater importance are streamlines B. They originate from well above the end wall where the fluid temperature, in general, is high. When these streamlines approach the stator vane they are bent downward by the presence of the horseshoe-passage vortex so that hot fluid is brought in contact with the end wall (this happens along a so-called attachment line) and a new, initially very thin (thermal) boundary layer begins to develop. The extent of this thin boundary layer will have a large influence on the end–wall heat transfer characteristics.

Another effect seen in this figure is that the streamlines B, after having passed plane SS tend to move upward (away from the endwall) along the suction side of the vane due to a spanwise

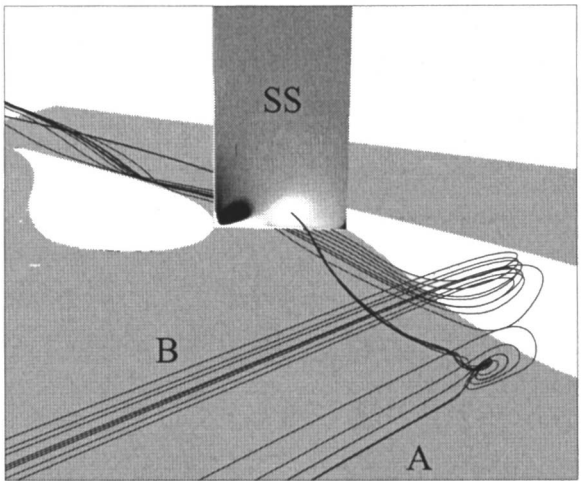

Fig. 9 Streamlines illustrating the secondary fluid motion responsible for the increase in end-wall heat transfer between two stator vanes. Streamlines A indicate the center of the pressure leg of the horseshoe vortex. Streamlines B, entering well above the end wall, are convected downward and spread along the endwall. Plane SS is colored with helicity, light region indicating clockwise rotation (passage vortex), dark region indicating anti-clockwise rotation (suction-side leg of horseshoe vortex).

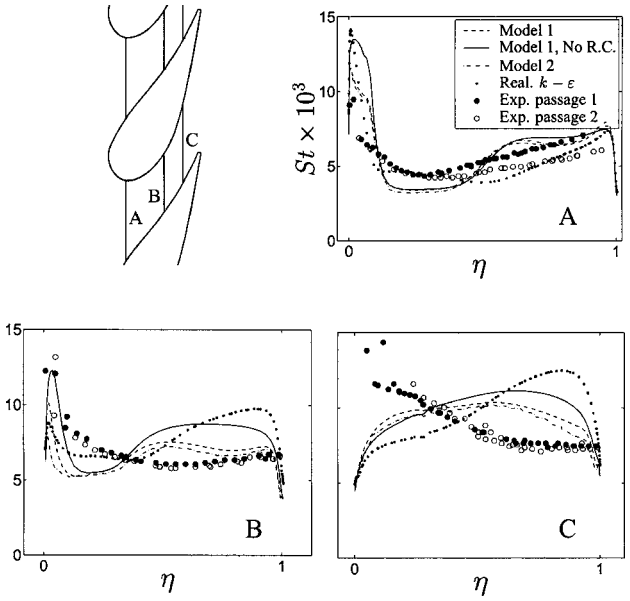

Fig. 10 Stanton number at the end wall along lines A-C

pressure gradient. Although not shown here they eventually reach a separation line located on the suction side surface. This separation line is due to yet another secondary structure, the leading-edge corner vortex also seen in Fig. 7, that also moves upward along the suction side. In Hermanson et al. [9], the presence of this flow feature was illustrated by plotting the Stanton number on the vane suction side. They found a streak of low heat transfer moving upward along the vane reaching about 15% of the full span at the trailing edge and argued that it was a passage vortex separation line. This is incorrect as the passage vortex lies close to the pressure side of the vane.

Endwall Heat Transfer Between Two Vanes. As shown in preceeding sections the computations where the $\overline{v^2}-f$ model has been used to model turbulence effects give the overall best agreement with experiments. Therefore, the *passage* end-wall heat transfer predictions of the different versions of this model will now be compared to measurements. In Fig. 10 the Stanton number along three different lines on the end wall are plotted for a set of $\overline{v^2}-f$ model computations. Included for reference are the results of the realizable $k-\varepsilon$ model.

At location A the heat transfer is accurately predicted with the exception of the region between the two main vortices mentioned earlier. Again this is due to either an underprediction of the "passage vortex effect," i.e., the pressure difference between the vanes, or the mean flow not being completely stable. In two of the computations, CALC-BFC model 1 and model 2 with use of the realizability constraint, the peak in Stanton number located near the suction side of the vane is captured to within ~10%. Not using the constraint causes an overshoot in this region due to too large turbulent heat fluxes.

At station B the Stanton number predictions indicate that the incoming boundary layer has separated from the end wall along most of the passage, which gives room for the new thinner boundary layer previously mentioned. On the pressure side of the passage ($\eta > 0.4$) CALC-BFC model 1 and model 2 still do a reasonably good job. However, at location B only the model without use of the realizability constraint captures the suction-side peak in heat transfer due to the erroneous overprediction of k. This suggests that the physically correct effect of the suction-side leg of the horseshoe vortex on end-wall heat transfer is underpredicted. Further into the passage, at station C, this deficiency of the computations is even more obvious as all models fail to capture the trend of increasingly higher heat transfer at the suction side of the passage. At this location the predictions towards the pressure side also begin to seriously deviate from the measured values.

The mismatch at the suction side can no longer be explained by the underprediction of the extent of the thin boundary layer. Instead this is probably due to the intensity of the predicted suction-side leg of the horseshoe vortex being too weak. Another possible explanation is, as the flow turning angle is large, that effect of curvature on the turbulence play an important role. A correct representation of streamline curvature require more sophisticated turbulence closures than standard eddy-viscosity models offer (e.g., Reynolds stess models). Also note that as we move into the passage it becomes increasingly more difficult to explain local differences between experiments and computations by investigating local quantities due to accumulation of upstream, "history" effects. For example, it was found that the secondary motion toward the suction side was not very well captured. The adding up of that effect will most likely influence the heat transfer characteristics some distance into the passage.

Conclusions

The performance of the $\overline{v^2}-f$ turbulence model has been assessed by computing a three-dimensional stator vane flow with complex secondary structures present. The results of two versions of this model were compared to detailed measurements of the mean flow, turbulence quantities, and heat transfer. Comparison was also made to other eddy-viscosity-based turbulence models available in FLUENT, including a version of the $\overline{v^2}-f$ model. It has been shown that the flow feature that in large determines the end-wall heat transfer in the stagnation region is the roll-up of a secondary vortex system. This has earlier been seen in experiments and in this work the mechanism behind this coupling of secondary flow and end-wall heat transfer has been illustrated. It was found that the predictions that in general agreed the best with experimental data were those computed using the $\overline{v^2}-f$ model for turbulence closure. However, also this model to some extent underpredicts the intensity of the secondary motion, which has the consequence that the endwall heat transfer characteristics is sometimes not captured. Furthermore, the importance of preventing unphysical growth of turbulence kinetic energy, here by use of a

realizability constraint, was illustrated. Very good agreement between the implementations of $\overline{v^2}-f$ model 2 in CALC-BFC (in-house code) and FLUENT (commercial code) was obtained in terms of both secondary flow fields and end-wall heat transfer. Finally, of the different versions of the $\overline{v^2}-f$ model investigated, model 1, a model very similar to that originally suggested by Durbin [21], gave the overall best agreement with experimental data.

Acknowledgment

The present work was supported by the Swedish Gas Turbine Center. The authors would also like to acknowledge Prof. K. A. Thole for supplying experimental data.

Nomenclature

C = true vane chord
C_{lim} = constant in the realizability constraint
H = helicity, $H=\omega_i U_i$
h = heat transfer coefficient, $h \equiv q_{\text{wall}}/(T_{\text{wall}}-T_{\text{in}})$
L = turbulent length scale
P = vane pitch
S = vane span; $S^2=S_{ij}S_{ij}$
S_{ij} = strain rate tensor, $S_{ij} \equiv \frac{1}{2}(\partial U_i/\partial x_j+\partial U_j/\partial x_i)$
St = Stanton number, $St \equiv h/\rho C_p U_{\text{in}}$
$\mathcal{T}$ = turbulent time scale
$\overline{u_i u_j}$ = Reynolds stress tensor
$\overline{v^2}$ = normal stress in the wall-normal direction

References

[1] Ho, Y.-H., and Lakshminarayana, B., 1996, "Computational Modelling of Three-Dimensional Endwall Fbw Through a Turbine Rotor Cascade With Strong Secondary Fbws," J. Turbomach. **118**, 250-261.
[2] Chien, K. Y., 1982, "Predictions of Channel and Boundary Layer Flows With a Low Reynolds Number Turbulence Model," AIAA J. **20**, pp. 33–38.
[3] Gregory-Smith, D., and Cleak, J., 1992, "Secondary Fbw Measurements in a Turbine Cascade With High Inlet Turbulence," J. Turbomach. **114**, 173–183.
[4] Harvey, N., Rose, M., Coupland, J., and Jones, T., 1999, "Measuremement and Calculation of Nozzle Guide Vane End Wall Heat Transfer," J. Turbomach. **121**, 184–190.
[5] Boyle, R., and Jackson, R., 1997, "Heat Transfer Predictions for Two Turbine Nozzle Geometries at High Reynolds and Mach Numbers," J. Turbomach. **119**, 270–283.
[6] Hermanson, K., and Thole, K., 2000, "Effect of Inlet Conditions on Endwall Secondary Fbws, J. Propul. Power **16**, 286–296.
[7] Hermanson, K., and Thole, K., 2000, "Effect of Mach Number on Secondary Fbw Characteristics," International Journal of Turbo and Jet Engines **17**, 179–196.
[8] Radomsky, R., and Thole, K., 2000, "High Free-Stream Turbulence Effects on Endwall Heat Transfer for a Gas Turbine Stator Vane," J. Turbomach. **122**, 699–708.
[9] Hermanson, K., Kern, S., Picker, G., and Parneix, S., 2003, "Predictions of External Heat Transfer for Turbine Vanes and Blades With Secondary Fbw-fields," J. Turbomach. **125**, 107–113.
[10] Parneix, S., Durbin, P., and Behnia, M., 1998, "Computation of 3-D Turbulent Boundary Layers Using the V2F Model," Flow, Turbul. Combust. **60**, 19–46.
[11] Durbin, P., 1991, "Near-Wall Turbulence Closure Modeling Without "damping functions"," Theor. Comput. Fluid Dyn., **3**, 1–13.
[12] Kang, M., and Thole, K., 2000, "Flowfield Measurements in the Endwall Region of a Stator Vane," J. Turbomach. **122**, 458–466.
[13] Kalitzin, G., 1999, "Application of the $\overline{v^2}-f$ Model to Aerospace Configurations," Center for Turbulence Research Annual Research Briefs.
[14] Lien, F., and Kalitzin, G., 2001, "Computations of Transonic Fbw With the $\overline{v^2}-f$ Turbulence model," Int. J. Heat Fluid Flow **22**, 53–61.
[15] Sveningsson, A., 2003, "Analysis of the Performance of Different $\overline{v^2}-f$ Turbulence Models in a Stator Vane Passage Fbw," Licentiate thesis, Dept. of Thermo and Fluid Dynamics, Chalmers University of Technology, Gothenburg, Sweden.
[16] Durbin, P., 1995, "On the $k-3$ Stagnation Point Anomaly," Int. J. Heat Fluid Flow **17**, 89–90.
[17] Sveningsson, A., and Davidson, L., 2003, "Assessment of Realizability Constraints and Boundary Conditions in $\overline{v^2}-f$ Turbulence Models," 4th Int. Symp. on Turbulence Heat and Mass Transfer, Antalya, Turkey.
[18] Menter, F., 1993, "Zonal Two-Equation $k-\omega$ Turbulence Model for Aerodynamic Fbws," in *AIAA Paper 1993-2906*.
[19] Goldstein, R., and Spores, R., 1988, "Turbulent Transport on the Endwall in the Region Between Adjacent Turbine Blades," J. Heat Transfer **110**, 862–869.
[20] Wang, H., Olsen, S., Goldstein, R., and Eckert, E., 1997, "Flow Visualisation in a Linear Turbine Cascade of High Performance Turbine Blades," J. Turbomach. **119**, 1–8.
[21] Durbin, P., 1995, "Separated Fbw Computations With the $k-\varepsilon-v^2$ Model," AIAA J. **33**, 659–664.

A Numerical and Experimental Investigation of the Slot Film-Cooling Jet With Various Angles

Rongguang Jia

Bengt Sundén[1]
e-mail: bengt.sunden@vok.lth.se

Division of Heat Transfer,
Lund Institute of Technology,
Lund 22100, Sweden

Petre Miron

Bruno Léger

LARA, Laboratoire Aquitain de
Recherche en Aérothermique,
Université de Pau,
c/o Turbomeca,
Boredes Cedex 64511, France

Numerical simulations coupled with laser Doppler velocimetry (LDV) experiments were carried out to investigate a slot jet issued into a cross flow, which is relevant in the film cooling of gas turbine combustors. The film-cooling fluid injection from slots or holes into a cross flow produces highly complicated flow fields. In this paper, the time-averaged Navier-Stokes equations were solved on a collocated body-fitted grid system with the shear stress transport $k-\omega$, V2F $k-\epsilon$, and stress-ω turbulence models. The fluid flow and turbulent Reynolds stress fields were compared to the LDV experiments for three jet angles, namely, 30, 60, and 90 deg, and the jet blowing ratio is ranging from 2 to 9. Good agreement was obtained. Therefore, the present solution procedure was also adopted to calculations of 15 and 40 deg jets. In addition, the temperature fields were computed with a simple eddy diffusivity model to obtain the film-cooling effectiveness, which, in turn, was used for evaluation of the various jet cross-flow arrangements. The results show that a recirculation bubble downstream of the jet exists for jet angles larger than 40 deg, but it vanishes when the angle is <30 deg, which is in good accordance with the experiments. The blowing ratio has a large effect on the size of the recirculation bubble and, consequently, on the film cooling effectiveness. In addition, the influence of boundary conditions for the jet and cross flow are also addressed in the paper. [DOI: 10.1115/1.1929821]

1 Introduction

Film cooling is the introduction of a secondary fluid (coolant or injected fluid) at one or more discrete locations along a surface exposed to a high-temperature environment to protect that surface not only in the immediate region of injection but also in the downstream region (cf. Goldstein [1]). It is widely used for the cooling of combustor walls and turbine blades. As reported, a continuous slot is the configuration that creates the most effective film. On the other hand, with regard to rigidity of the turbine blades against vibrations, a configuration composed of short slots or holes would be more desirable than a continuous slot.

However, the coolant requires a distance to merge together to form a uniform cooling film. Before the jet flows merge, hot spots exist between the jets; even downstream of the jet-merging location, the cooling effectiveness is not necessarily uniform. This nonuniform cooling may lead to increased NO_x formation in the combustor or result in thermal fatigue and spallation of a thermal barrier coating on the turbine blades. Therefore, reduction of spanwise nonuniformity has been an ongoing task for gas turbine heat transfer designers.

Ideally, to solve this problem, an infinite number of jet holes would serve the purpose of obtaining a uniform film over this surface. However, the same problem (i.e., the loss of rigidity) for slot film cooling will arise. One possible solution is to recess the jets into a cavity or slot before they interact with the hot gases. The slot would allow the jets to premix and achieve uniformity at the exit of the slot. Several studies have been carried out on this issue, e.g., Wang et al. [2] and Cho and Ham [3]. This kind of configuration is shown in Fig. 1(*a*). As shown in their studies, quite uniform momentum and temperature field can be obtained in the spanwise direction with proper arrangement of the jets.

This study is focused on the film cooling by continuous slots or with a spanwise uniform jet inlet, which could be developed from such a configuration as shown in Fig. 1(*a*). Even for two-dimensional (2D) slot film cooling, the flow field near the injected coolant jet is very complex, with high gradients of velocity, temperature, and turbulence intensity, and also flow separation and reattachment (cf. Fig. 1(*b*)). Various parameters (e.g., the injection angle, the blowing ratio, and the incoming boundary layer) influence the film-cooling process.

There are many film-cooling studies using a single hole or an array of holes. However, not much research has been performed using a slot jet.

Experimental work has been carried out by O'Malley, [4] Fitt et al. [5] Bergeles et al. [6] Andreopoulos, [7] Metzger et al. [8] Chen and Hwang, [9] Teekaram et al. [10] Aly, [11] Wang et al. [2], and Cho and Ham [3]. Numerical investigations are reported by Jones and Wille [12], Sarkar and Bose, and [13] Kassimatis et al. [14].

From the previous studies, the following conclusions can be drawn:

1. For large injection angles, the coolant penetrates deeper into the cross-flow, resulting in more turbulence generation, followed by enhanced mixing and a rapid turbulent diffusion, which leads to a faster decay of film-cooling effectiveness in the near field region. A flow separation also occurs just downstream of the slot exit. For small injection angles, the coolant attaches to the surface with low turbulence generation and slow mixing rate, retaining its identity for a larger length. This results in high cooling effectiveness even in the far-field region.
2. With the increase of blowing ratio, the overall downstream

[1]To whom correspondence should be addressed.

Contributed by the Turbomachinery Division of THE AMERICAN SOCIETY OF MECHANICAL ENGINEERS for publication in the JOURNAL OF TURBOMACHINERY. Manuscript received February 16, 2004; revised manuscript received January 14, 2005. Associate Editor: R. S. Bunker.

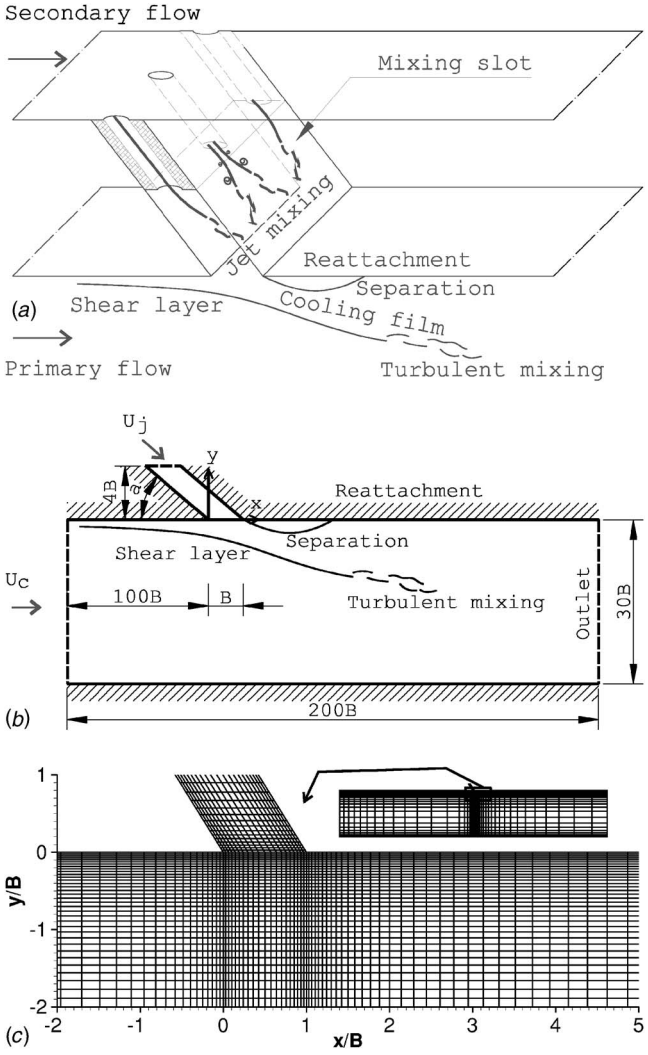

Fig. 1 The schematic view of (*a*) a mixing slot, (*b*) the computational domain and flow field, and (*c*) the grid. (There is an index skip in both *x* and *y* directions.)

film-cooling effectiveness improves because of the thickened thermal boundary layer and more available cold fluid.

3. For a jet inclined at 30 deg and discharging into the main flow, below a certain injection ratio, the injectant remains essentially attached to the surface; above this ratio, the jet lifts off the surface, allowing penetration of the mainstream fluid beneath.
4. The specification of flow conditions at the exit of the jet is a critical issue, particularly for numerical simulations.
5. The most important independent flow variable is the momentum flux ratio, but the density or temperature ratio might be of importance in real engines.

However, the following issues for slot film cooling need further investigation:

1. Does the existence of the recirculation zone downstream the slot jet depend on the blowing ratio or only on the jet inclination angle?
2. Does the inlet boundary conditions of the cross flow have a large effect on the fluid flow development and heat transfer?
3. Does the application of higher-order turbulence models, e.g., the Reynolds stress turbulence model (RSTM), explicitly improve the prediction of the mean and fluctuation field?
4. Detailed turbulent Reynolds stress and heat flux data, especially for different injection angles and blowing ratios, are desirable for validation of turbulence models in the predictions of such kind of flows.

Concerning these aspects, one purpose of this study is to provide experimental results obtained in realistic environments, which are urgently needed by engine designers to check and validate design computer codes. Another purpose is to perform a systematic evaluation of the current computational capability to compute a jet issued into a cross flow relevant to gas-turbine combustor film-cooling applications, for which experimental data for the mean and fluctuation flow field are also obtained by the means of laser Doppler velocimetry (LDV). All the studied cases are listed in Table 1. The jet nozzle width is kept at $B=4$ nm with a spanwise length 400 nm, as shown in Fig. 2(*b*).

2 Experimental Apparatus and Procedure

2.1 Wind Tunnel and Test Section. A schematic diagram of the wind tunnel and the LDV-2D system is shown in Fig. 2(*a*). The wind tunnel is an open-circuit one, powered by two electrical air fans. Each nozzle, with an exit cross section of 400 $\times$ 120 mm, continues with a rectangular duct of 2500 mm length, which leads to the test section—the Plexiglas slot model. The working conditions of the wind tunnel are the ambient temperature and atmospheric pressure, but for different velocity combinations in the two rectangular duct flows, a pressure difference is created and measured by a differential pressure indicator. The sec-

Table 1 Studied cases (Y – Experiments available, N – Not available)

	Bulk velocity (m/s)				
Case	Angle	Cross	Jet	Blowing ratio	Exp.
90-CH5	90	2.37	13	5.48	Y [9]
90-M2	90	3	6	2	Y
60-M9	60	1	9.22	9.22	Y
60-M4	60	3	12	4	Y
60-M2	60	3	6.22	2.07	Y
40-M4	40	3	12.45	4.15	N
40-M3	40	3	9.22	3.07	N
40-M2	40	3	6.22	2.07	N
30-M4	30	3	12.45	4.15	Y
30-M3	30	3	9.22	3.07	Y
30-M2	30	3	6.22	2.07	Y
30-M1	30	3	3.	1.0	N
30-M05	30	3	1.5	0.5	N
16-M4	16	3	12.45	4.15	N
16-M3	16	3	9.22	3.07	N
16-M2	16	3	6.22	2.07	N

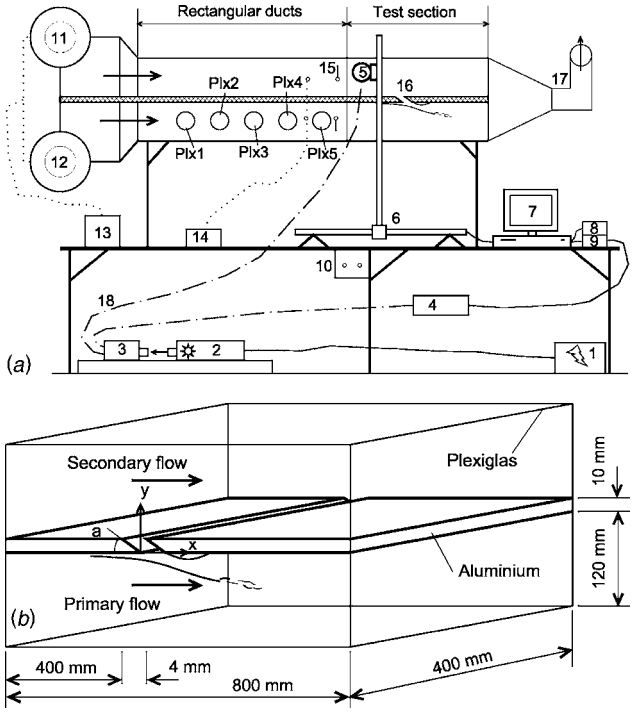

Fig. 2 Experimental setup: (*a*) 1. laser cooling system and power supply; 2. laser source generator; 3. Bragg cell; 4. photomultiplicator; 5. transmitter-receiver optics head; 6. head moving 3D system; 7. Pentium II 350 MHz PC; 8. RSA 1=real-time signal analyzer (for green channel); 9. RSA 2=real-time signal analyzer (for blue channel); 10. fan-speed potentiometers; 11. electric fan air (for superior rectangular duct); 12. electric fan air (for inferior rectangular duct); 13. smoke generator; 14. differential pressure indicator; 15. hot-wire anemometer 16. aluminium slot model test plate; 17. exhaust outlet; and 18. optic fiber drive. (*b*) 3D view of the test section.

ond rectangular duct, the inferior one, has five 80 mm hole-diameter Plexiglas windows (Plx 1, Plx 2, Plx 3, Plx 4, and Plx 5) which allow measurements of the local velocity and verifications of the development of the turbulent flow, upstream of the test-section slot model. The slot model is an aluminium plate (800 $\times 400 \times 10$ mm) placed between the *secondary flow* (coming from the superior rectangular duct) and the *primary flow* (coming from the inferior rectangular duct), see Fig. 2(*b*). One can chose among three different aluminium slot model plates with various slot angle inclinations (30, 60, and 90 deg), all the other dimensions being the same for all three plates.

2.2 Two-Component Laser Doppler Velocimeter System (LDV-2D). A 5 W argon ion laser is used. The two laser wavelengths used are 0.5145 μm (green) and 0.488 μm (blue). The tracer particle is F5 SMOGGY FLUID for use in Smoggy Smoke Machines, and the elementary particle diameter varies from 2 to 12 μm. The system parameters are shown in Table 2.

The acquisition for both channels (green and blue) is done in a coincidence mode and the running time varies from 0.5 to 30 s. The *x*- and *y*-axes origin is chosen on the inferior edge of the slot plate, and the measured domain is shown in Fig. 2(*b*). The *y* values are starting from $y=-0.2$ mm to $y=-60$ mm and the *x* values are ranging from $x=-20$ mm to $x=200$ mm. For each point of the grid, the next data variables are available: point locations *x* and *y* [mm], horizontal and vertical velocity components *U* and *V* [m/s], mean speed magnitude [m/s], root-mean square velocities u' and v' [m/s], turbulence intensity t_u and t_v [%], and the Reynolds turbulence stress tensor $\overline{uu}$, $\overline{vv}$, and $\overline{uv}$. Also a velocity

Table 2 Parameters of the LDV system

System performance estimates	
Transmitter lens focal length	250 mm
Beam waist diameter	117 and111 μm (G and B)
Probe volume length	1.5 mm
Fringe spacing	3.22 and 3.06 μm (G and B)
Processor RSA-2000-L	
Min transit time	0.3 ms
Min frequency	−35 MHz
Max frequency	110 MHz
Velocity range	−113–354 m/s
Software parameters	
High voltage	500 to maximum 980 V
Sample rate	1.25 to maximum 40 MHz
Low-pass filter	0.5* (sample rate)
Frequency shift mixer	40 MHz

mean bias correlation is calculated for each velocity component. GTWA velocity mean (gate time weighted-average velocity mean) is a correction for the average velocity, which attempts to correct for bias against slower-moving particles. Because faster particles will spend less time in the probe volume, there is a risk that more fast particles are measured, and the simple mean velocity will be higher than the true mean. This correction accounts for this bias by weighting the velocity with the gate time. This is calculated by

$$\bar{V}_{\mathrm{GTWA}} = \frac{\sum_{i=1}^{n} V_i G_i}{\sum_{i=1}^{n} G_i} \tag{1}$$

where G_i is the gate time value for particle *i*.

GTWA velocity rms (gate time weighted-average velocity standard deviation) is the standard deviation of the GTWA velocity mean, calculated by

$$V_{\mathrm{RMSGTWA}} = \sqrt{\frac{\sum_{i=1}^{n} (G_i V_i - \bar{V}_{\mathrm{GTWA}})^2}{\sum_{i=1}^{n} (G_i - \bar{G}_{\mathrm{GTWA}})}} \tag{2}$$

A large part of the uncertainty in a quantity determined by averaging a set of samples, such as the time mean velocity measured by an LDA, can be caused by the fact that only a limited number of samples are used to calculate the average. Uncertainties in the mean velocity measurements can be estimated to 1% of speed mean velocity for the mainstream flow and 3–5% for the close-to-wall flows.

The LDA probe volume is precisely positioned by a computer-controlled 3D-axis traverse system, and the positional errors are estimated to 1/60=0.016 mm. With a transmitter lens of 250 mm focal length, the probe volume length obtained is ~1.5 mm and the beam waist diameter (the smaller probe volume diameter) is 0.117 and 0.111 mm for the green and blue beams, respectively. In conclusion, the total uncertainty of the probe volume position on the *x*-*y* plane is about 3% of *B* ($B=4$ mm slot width).

Typical values of the uncertainty for the derived turbulent stresses are within 10%. All data are measured, calculated, and recorded in real time and then exported in tab-delimited text files, which are useful in further calculations or graphic representations. Some of the data are presented in this paper.

3 Methods of Computations

3.1 Governing Equations. The governing equations to be solved are the incompressible continuity, momentum, and energy equations and the transport equations for the Reynolds stresses, turbulent kinetic energy, and dissipation added through the turbulence models. The fluid properties are assumed constant, which is a reasonable assumption compared to the corresponding experiments,

$$\frac{\partial U_i}{\partial x_i} = 0 \tag{3}$$

$$\frac{\partial U_i}{\partial t} + \frac{\partial (U_j U_i)}{\partial x_j} = -\frac{1}{\rho}\frac{\partial P}{\partial x_i} + \frac{\partial}{\partial x_j}(2\nu S_{ij} - \overline{u_i' u_j'}) \tag{4}$$

$$\frac{\partial T}{\partial t} + \frac{\partial (U_j T)}{\partial x_j} = \frac{\partial}{\partial x_j}\left(\frac{\nu}{\mathrm{Pr}}\frac{\partial T}{\partial x_j} - \overline{t' u_j'}\right) \tag{5}$$

where $\tau_{ij} = -\overline{u_i' u_j'}$ is known as the specific Reynolds stress tensor and $c_p \overline{t' u_j'}$ represents the specific turbulent heat fluxes. Both of these two terms need to be modeled.

3.2 Turbulence Models. The evaluated turbulence models include the shear-stress transport $k-\omega$ model (SST) of Menter [15], the $k-\epsilon-\overline{v^2}$ model (V2F) of Durbin [16], and the stress-ω model (RSTM) of Wilcox [17]. Neither of the three models needs damping functions to account for the low-Re effect. Both the SST and V2F models have a limiter on the time scales to fulfill the realizability constraints, because the production term of kinetic energy equations is modeled, unlike the RSTM model.

The SST model is a two-equation model, named as such because the definition of the turbulent viscosity is modified to account for the transport of the principal turbulent shear stress. It is this feature that gives the SST model an advantage in terms of performance over both the standard $k-\epsilon$ model and the standard $k-\omega$ model. Other modifications include the addition of a cross-diffusion term in the ω equation and a blending function to ensure that the model equations behave appropriately in both the near-wall and far-field zones.

The V2F model is a four-equation model. In addition to k and ϵ, two more equations are solved for $\overline{v'^2}$ and f. The first, $\overline{v'^2}$, determines the velocity fluctuation normal to the streamlines. The second transport equation is solved for the global relaxation factor f. It is an elliptic relaxation equation representing nonhomogeneous effects produced by the presence of walls, which avoids the need for damping functions.

RSTM is the most "physically sound" RANS model, where Reynolds stresses are solved directly with transport equations, avoiding isotropic viscosity assumptions of the other models. Much of the research in 1990s was focused on the modeling of the nonlinear pressure-strain terms. Another focus is the modeling at the near-wall regions, where the turbulence is highly anisotropic. The RSTM model employed in the present study uses the Launder-Reece-Rodi (LRR) [18] pressure-strain model, simple eddy-diffusivity hypothesis for the diffusion terms, and the ω to compute the dissipation, which can be integrated to the near-wall region. More details about the models are beyond the scope of this paper, and readers are referred to the original literature.

3.2.1 Modeling of the Turbulent Heat Fluxes. The turbulent heat flux may be computed using a simple eddy diffusivity model (SED)

$$\overline{t' u_j'} = -\frac{\nu_t}{\mathrm{Pr}_t}\frac{\partial T}{\partial x_j} \tag{6}$$

where Pr_t is the turbulent Prandtl number. It might be modeled as a constant $\mathrm{Pr}_t = 0.89$ [19].

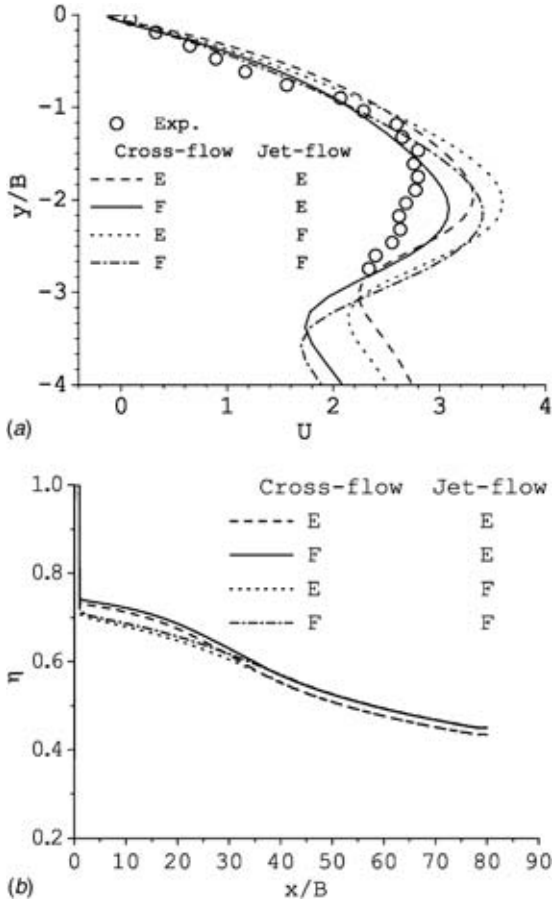

Fig. 3 The effect of the inlet boundary condition on: (*a*) velocity parallel to the wall at $x/B=1.0$, (*b*) film cooling effectivness. (E–Uniform, F–Fully developed)

3.3 Boundary Conditions. The boundaries are schematically shown in Fig. 1(*b*) for all the cases, in agreement with the experimental setup as shown in Fig. 2. However, the geometry for the 90-CH5 case is slightly different: the height of the channel is $12B$ and the bottom boundary is a symmetrical one, which are in accordance with the experimental setup of Chen and Hwang [9].

3.3.1 Solid Wall Boundaries. At solid walls, adiabatic boundary conditions are used, and the no-slip boundary condition is set as

$$U_w = 0, \quad V_w = 0, \quad W_w = 0, \quad k_w = 0, \quad \epsilon_w = 2\frac{\nu k_1}{y_1^2},$$

$$\omega_w = \frac{6\nu}{\beta_0 y_1^2} \quad \overline{u_i' u_{j_w}'} = 0, \quad \overline{v_w'^2} = 0,$$

$$f_w = -\frac{20\nu^2 \overline{v_1'^2}}{\epsilon_w y_1^4} = -\frac{10\nu}{y_1^2}\min\left(\frac{\overline{v_1'^2}}{k_1}, 2\right) \tag{7}$$

where indices w and 1 denote the wall and the first point off the wall, respectively. The limit on $\overline{v_1'^2}/k_1$ stems from the realizability constraint $2k \geq \overline{v'^2} \geq 0$.

3.3.2 Inlet Boundaries. For the mainstream and the slot jet velocity inlet, either uniform (E) or fully developed (F) profile is set. The effect of the inlet boundary conditions on the velocity profile (from the V2F model) at $x/B=1.0$ for the 90-M2 case is shown in Fig. 3(*a*), and the effect on the film cooling effectiveness is shown in Fig. 3(*b*). As shown, the mainstream flow inlet has a very large influence on the velocity, but the influence of the jet

inlet is relatively small. The effect of the inlet boundary conditions on the film-cooling effectiveness is smaller compared to that of the velocity. A careful check revealed that the fully developed mainstream inlet with flat jet inlet seems to be the closest to the experimental profile (cf. Fig. 3(*a*)). This occurs because in the experiments the slot jet nozzle is very short and the inlet is connected to a large chamber. Therefore, the uniform jet inlet is more appropriate. As for the mainstream flow, there is a long distance for it to develop, these fully developed channel flow could be reached. Therefore, in the later study, all the computations are performed with the fully developed mainstream flow inlet and uniform jet flow inlet. The temperature is set as 100 °C for the mainstream inlet, and 23 °C for the jet flow inlet.

The inlet boundary conditions for the turbulent quantities are difficult to prescribe. It is common to assume a turbulent intensity and a turbulent length scale and to apply constant turbulent properties at the inlet. The inlet boundary conditions for turbulent scalars are set as

$$k_{\text{in}} = \frac{3}{2} I^2 U_{\text{ref}}^2, \quad \epsilon_{\text{in}} = C_\mu^{0.75} \frac{k_{\text{in}}^{1.5}}{l_m}, \quad \omega_{\text{in}} = \frac{\epsilon_{\text{in}}}{\beta^* k_{\text{in}}} \quad \overline{u_i' u_{i_{\text{in}}}'} = \frac{2}{3} k_{\text{in}},$$

$$\overline{u' v'_{\text{in}}} = 0, \quad \overline{v_{\text{in}}'^2} = \frac{2}{3} k_{\text{in}}, \quad f_{\text{in}} = 0 \tag{8}$$

where I is the turbulent intensity (set as 5% in this case, which is averaged from the measured values), U_{ref} is the average absolute velocity, and l_m is the Prandtl mixing length (set as $D_h/10$, D_h the hydraulic diameter).

3.4 Numerical Solution Procedure. The computations are carried out in an in-house multiblock computer code CALC-MP [20], based on the finite volume technique. The code uses a collocated mesh arrangement and employs the improved Rhie and Chow interpolation [21] procedure to calculate the velocities at the control volume faces. The SIMPLEC algorithm [22] couples the pressure and velocity. An algorithm based on tridiagonal matrix algorithm (TDMA) is used for solving the algebraic equations. Coefficients are determined by the QUICK scheme for the momentum equations and hybrid scheme for all the other discretized equations.

Nonuniform grids were generated, and grid refinement close to the wall was applied. A typical grid is shown in Fig. 1(*c*). In the present numerical work, the first grid points are always at a dimensionless distance ($y+$) less than unity from the solid walls.

An investigation of grid dependence was carried out to find the proper mesh. The test was performed on the 90 deg jet case with three meshes. The largest difference of the local film cooling effectiveness between the coarse grid 100×50, the grid for the jet nozzle is not included here) results and the medium grid results (200×100) is $<3\%$, whereas it is $<1\%$ between the medium and fine grid (300×200). Therefore, the result from the medium grid is believed to be sufficiently accurate, and this grid is employed in the subsequent computations of all cases.

4 Results and Discussion

The computation procedure is validated with the experimental velocity and temperature data of Chen and Hwang [9] for the 90-CH5 case. Then it is further validated with the present experimental data for the whole field obtained with the LDV technique. At the same time, the experimental data are presented. Finally, the numerical procedure is employed in a study of additional different injection angles and blowing ratios, so as to calculate the film-cooling effectiveness as well as the temperature field to figure out the optimal parameters.

4.1 Comparison of the Numerical Procedure With the Data of Chen and Hwang. The experimental study of Chen and Hwang is for the mixing of one and dual-line heated jets injected normally into a cold cross flow in a rectangular channel. The mean and fluctuating velocities are measured by a LDV system with an uncertainty of $<10\%$. The mean temperature is measured by thermal couples with an uncertainty of $\sim1.2\%$.

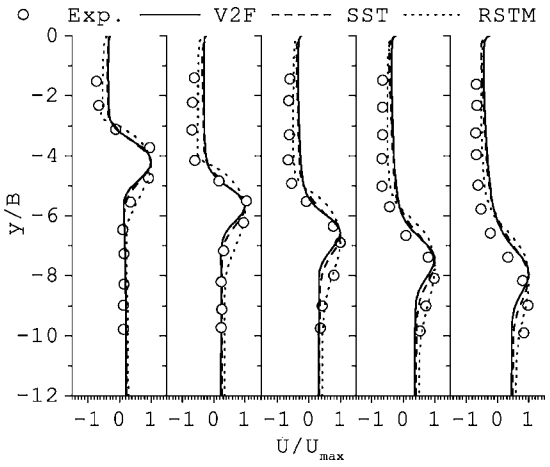

Fig. 4 Predicted distribution of the velocity parallel to the wall at *x/B*=2, 4, 6, 8, and 10, in comparison to the experimental data of Chen and Hwang [9]

Figure 4 shows the mean velocity parallel to the confined wall. The results from all the models are in decent agreement with the experiments. At the regions close to the jet injection ($x/B=2$, 4, 6), the locations of the maximum velocity are correctly predicted, i.e., correct prediction of the trajectory. Further downstream ($x/B=10$), the trajectory is underpredicted. In addition, the V2F model and the SST model provide very similar results. The results from the RSTM are in better agreement with the experiments.

Figure 5 shows the velocity fluctuation parallel to the confined wall. The maximum occurs around the inflexion points at the two sides of the velocity bulge (cf. Fig. 4). The inflexion points result in inviscid unsteadiness, consequently, higher turbulence intensity. The shape of the distribution of the numerical results are in decent agreement with the experiments. However, the magnitude is underpredicted, and the RSTM performs no better. This underprediction of fluctuation normally leads to more preservation of the jet flow, consequently, an overprediction of the trajectory. However, the trajectory is underpredicted, as shown in Fig. 4. These facts contradict each other.

Figure 6 shows the temperature distribution. Immediately downstream the jet inflow, the mixing is severely underpredicted by the numerical work. This is mainly because of the underpre-

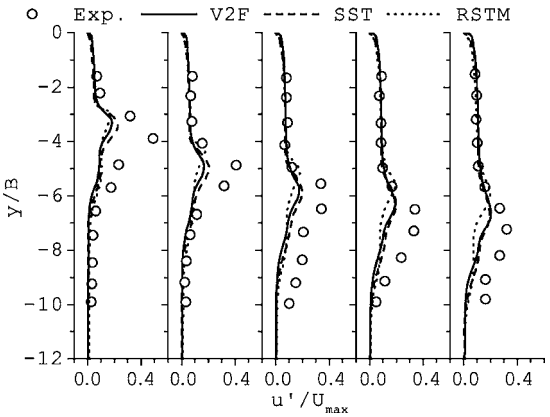

Fig. 5 The predicted distribution of the velocity fluctuation parallel to the wall at *x/B*=2, 4, 6, 8, and 10, in comparison with the experimental data of Chen and Hwang [9]

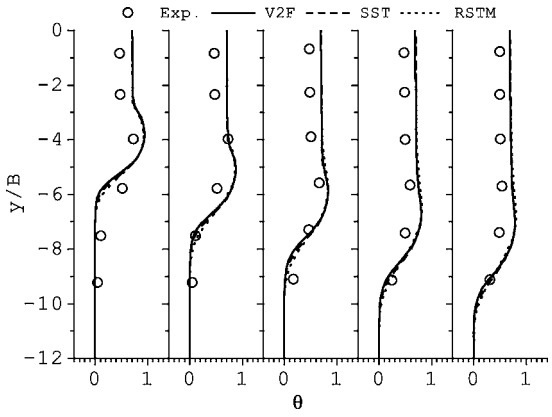

Fig. 6 Predicted distribution of the normalized temperature ($\theta=(T-T_c)/(T_j-T_c)$) parallel to the wall at $x/B=2$, 4, 6, 8, and 10, in comparison to the experimental data of Chen and Hwang [9]

diction of the turbulence stresses shown in Fig. 5. This may imply the necessity of higher-order turbulent heat flux models. This underprediction is alleviated further downstream. This is in accordance with the underprediction of the turbulence because, at $x/B=2$, the underprediction of the fluctuation is the largest (cf. Fig. 5). All the three turbulence models provide essentially the same results.

In total, the V2F and SST models provide essentially the same results. The RSTM provides slightly better prediction of the distribution of the mean velocity, but similar rms values as the other two models. All the models provide almost the same distribution of temperature. Further experimental data, especially fluctuations, are necessary for evaluation of the turbulence models.

4.2 Present Experimental Data and Validation of the Turbulence Models

4.2.1 The 90-M2 Case

4.2.1.1 Mean velocity. Figures 7(*a*)–7(*d*) show the streamline traces from the experimental and numerical results for the 90-M2 case. The agreement between the experiments and numerical simulations is reasonably good. The jet trajectory appears to be a parabolic line. There is a large recirculation downstream of the jet inflow, which is created by the negative pressure gradient due to the injection of the jet flow. This is something similar to the flow in a backward-facing step. Both the size and location of the recirculation predicted by the numerical simulation are in decent, good agreement with the experiments. However, the reattachment length predicted by all the turbulence models are longer than in the experiments. The V2F and SST models provide almost the same results. However, the RSTM predicted an unrealistic bulge around the reattachment point, as in a backward-facing-step problem, although in the experiments this bulge is also observed (cf. Fig. 7(*a*)). In any case, this does not indicate that the RSTM performs better than the other two models, because the bulge in Fig. 7(*a*) may be due to the three-dimensionality.

In addition, in the numerical results, there is a small vortex upstream the jet inflow, but this is not observed in the experimental results. The missing of the small recirculation may be due to the resolution of the experiments at the near-wall region. If this is true, the V2F model seems to be better at the jet upstream region

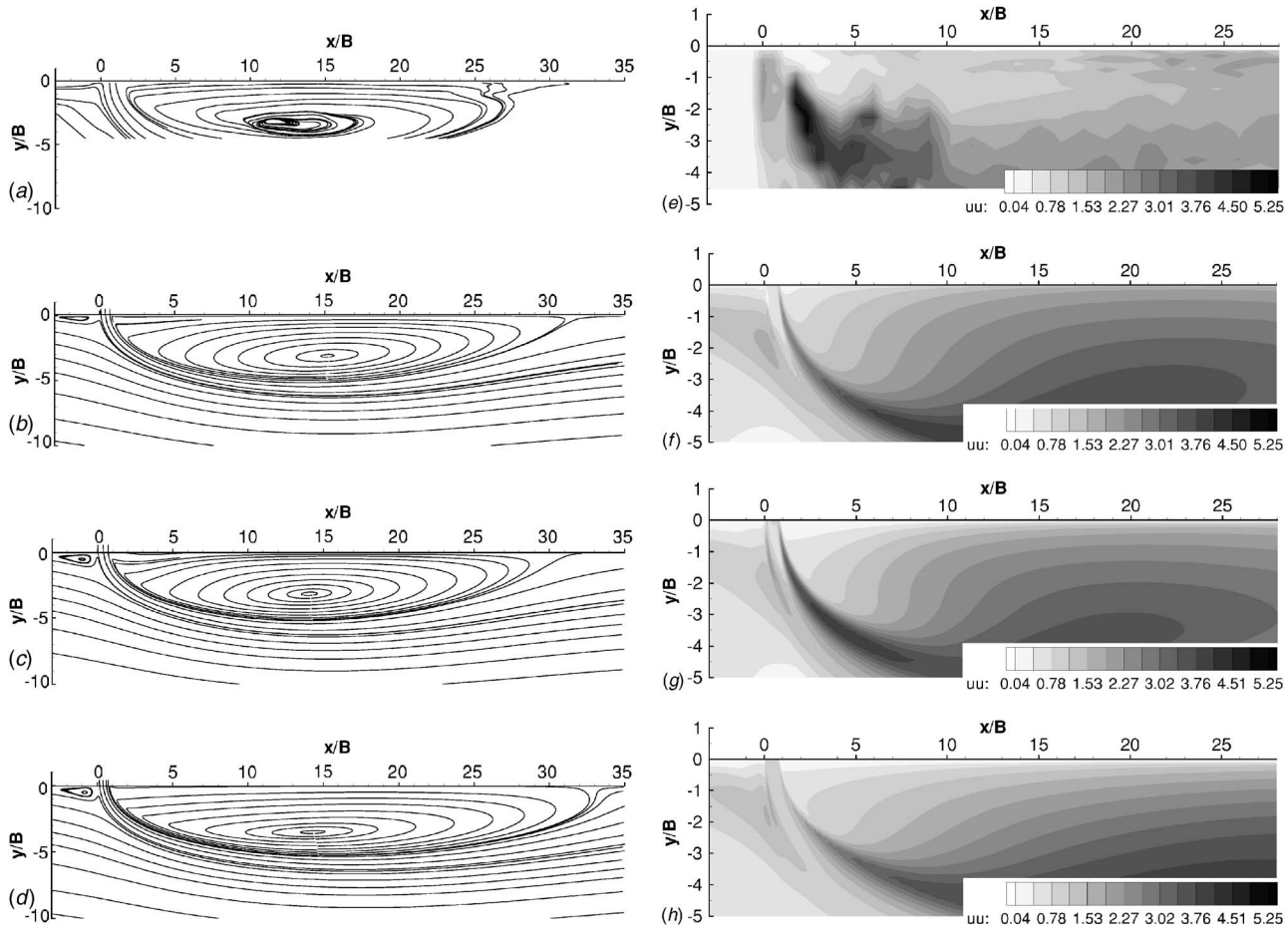

Fig. 7 Streamline trace and distribution of the normalized Reynolds stress $10(u'/U_c)$ for the 90-M2 case

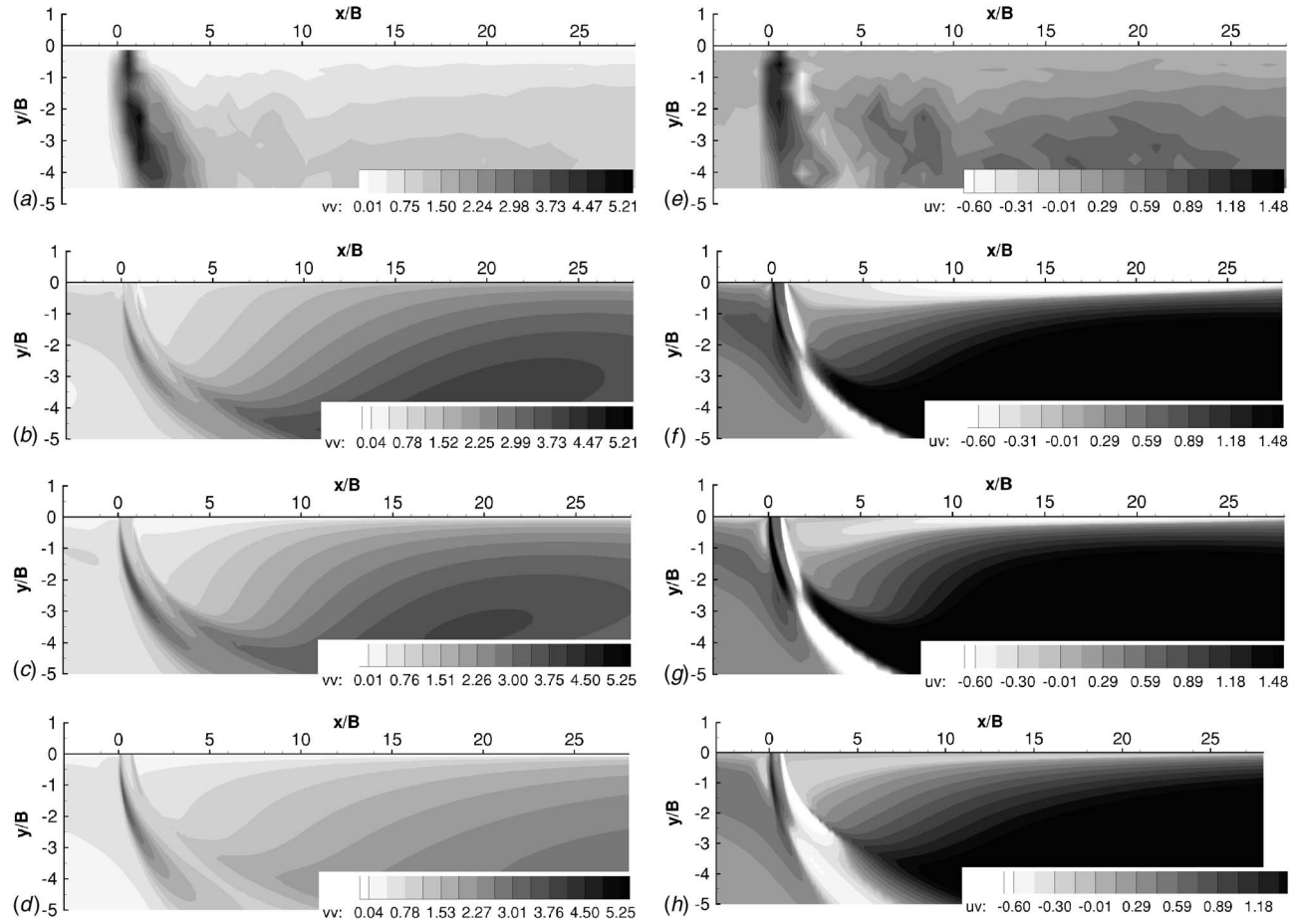

Fig. 8 Distribution of the Reynolds stresses for the 90-M2 case: $10(\overline{v'v'}/U_c)$ and $10\,\mathrm{sign}(\overline{u'v'})(|\overline{u'v'}|^{0.5}/U_c)$

than the other two models. The mainstream flow impinges on the jet flow, where a high-pressure region is formed. This higher pressure will accelerate the mainstream flow toward the wall, then toward the upstream direction, finally forming the recirculation.

4.2.1.2 The rms velocity. Figures 7(*e*)–7(*h*) show the rms velocity parallel to the confined wall. For the V2F model and SST model it is calculated as $2/3k-2\nu_t(\partial U/\partial x)$. In the experiments, the maximum $\overline{u'u'}$ occurs immediately downstream the injection (i.e., in the mixing layer), where inviscid unsteadiness exists, and this maximum is much larger than those at the remaining regions. However, this difference cannot be observed in either of the three turbulence models, although the RSTMs provide a distribution shape in slightly better agreement with the experiments. This might be because of the limitations of the steady RANS method in predicting turbulent flows with significant low-frequency turbulent kinetic energies. There exit regions up- and downstream of the jet flow, where shedding of large vortices occur. In these regions, the steady RANS method will significantly underpredict the level of turbulence. This is also true for the prediction of other fluctuation terms.

Figures 8(*a*)–8(*d*) show the rms velocity normal to the confined wall. For the V2F and SST models, it is calculated as $2/3k-2\nu_t(\partial V/\partial y)$. Unlike the $\overline{u'u'}$, the maximum occurs immediately upstream of the jet injection, which is also in the mixing layer. The RSTM performs much better than the other two models, as the jet upstream fluctuation is much larger than in the other areas.

Figures 8(*e*)–8(*h*) show the turbulent shear stress $\overline{u'v'}$. For the V2F model and SST model it is calculated as $-\nu_t(\partial U/\partial y+\partial V/\partial x)$. There is a positive region upstream of the jet flow and a negative region downstream of the jet, where the shear layers are located. This can be observed both in the experiments and in the numerical simulations. However, the level of the turbulent shear stress is overpredicted by all the models, although the overprediction by the RSTM is less than the other two models. This heavy overprediction of the shear stresses at the regions downstream of the jet is because of the modeling of the production terms, especially for the eddy-viscosity-based models: SST and V2F. From the eddy-viscosity hypothesis, the turbulence production term is calculated from the mean velocity gradients, and the gradients at the downstream recirculation zone are large. These large gradients are interpreted into high turbulence, while physically this is not always true, e.g., for flows with recirculations.

The turbulence is quite anisotropic as is evident by comparing Figs. 7(*e*)–7(*h*) and 8(*a*)–8(*d*). In the results of the V2F and SST models, the distribution of $\overline{u'u'}$ and $\overline{u'v'}$ tends to be similar, which is because of the eddy-viscosity hypothesis, whereas the RSTM reflects the anisotropy better.

In total, the V2F and SST models provide essentially similar results. The RSTM provides slightly better prediction of the distribution of the fluctuations. For the mean velocity, however, it predicts an unphysical bulge at the reattachment point. Also considering the performance of the three models in the 90-CH5 case, none of the models performs completely better than the others; therefore in the following computations, only the V2F model is considered. This choice is based on the comparison to detailed available data for this 90 deg case, but there is no guarantee that a certain model performs well in all cases.

4.2.2 Check of the Two-Dimensionality in the Experiments. For incompressible flow, the continuity equation (3) applies. By rearranging Eq. (3), one obtains

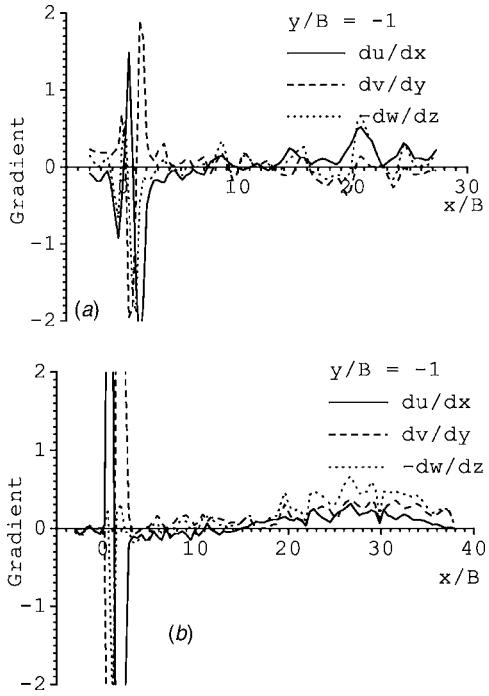

Fig. 9 Mass conservation of the experiments at $y/B=-1$: (*a*) the 90-M2 and (*b*) 60-M9 cases

$$\frac{\partial U}{\partial x}+\frac{\partial V}{\partial y}=-\frac{\partial W}{\partial z} \tag{9}$$

For 2D flow, $\partial W/\partial z$ should be zero, so it can be employed as an indicator of the two-dimensionality of the experimental flow field.

Figure 9(*a*) shows the mass conservation at the line $y/B=-1$ for the 90-M2. As shown, at the immediate upstream of the jet inflow for the 90-M2 case, the $\partial W/\partial z$ is large. At this region, a small recirculation is predicted by the numerical calculations but missing in the experiments. The 3D effect in the experiments might be the cause.

Figure 9(*b*) show the mass conservation at the line $y/B=-1$ for the 60-M9 case. At the region close to the jet inflow, $\partial W/\partial z$ is large, but it is small compared to $\partial U/\partial x$. At the region around $x/B=30$, however, $\partial W/\partial z$ is relatively large, even larger than both $\partial U/\partial x$ and $\partial V/\partial y$. This region corresponds to the mass source, as shown in Fig. 10(*a*), indicating a strong 3D effect.

4.2.3 The 60 Deg Cases. Figure 10(*a*) shows the streamline traces for the 60-M9 case, which is obtained from the experiments. At this large injection angle and blowing ratio, the separation can be observed clearly downstream of the jet inflow. This is not good for the film-cooling effectiveness. Figure 10(*b*) shows the simulation results with the V2F model. As shown, the predicted shape of the flow field is in decent agreement with the experiments. However, in the experiments, the recirculation is not formed. This is mainly due to the 3D effect, as shown in Fig. 9(*b*).

If the blowing ratio is decreased down to 4, e.g., the 60-M4 case, the recirculation downstream of the jet inflow will become much smaller, as shown in Fig. 10(*c*). This is also observed in the computations (Fig. 10(*d*)).

The detailed comparison is also made between the experiments and numerical simulation for the 60-M9 case at five regions ($x/B=1$, 2, 3, 4, and 5).

Figure 11 shows the U velocity distribution of the 60-M9 case. The numerical results are in good agreement with the experiments. However, at far down stream of the jet flow ($x/B=4$ and 5), the trajectory is overpredicted, whereas in the 90-CH5 case, the trajectory is underpredicted. This may because of the difference in the experimental conditions.

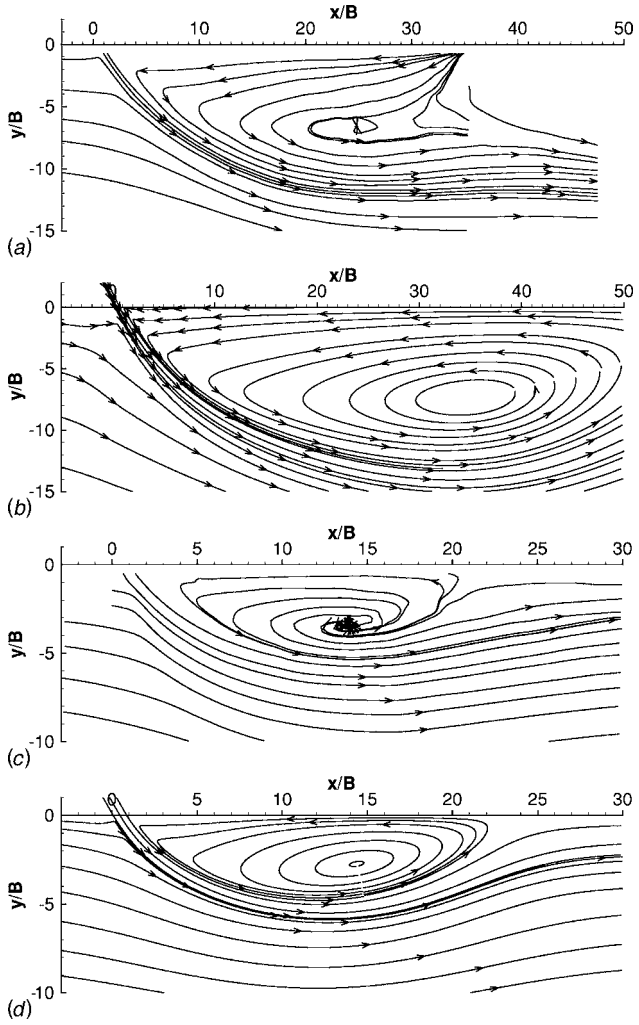

Fig. 10 Streamline trace for the 60-M9 and 60-M4 cases

Figure 12 shows the V velocity distribution of the 60-M9 case. The agreement is very similar to the U velocity. In general, the V2F model gives a satisfactory prediction of the mean velocity components.

Figure 13 shows the normalized turbulent kinetic energy distribution of the 60-M9 case. Generally speaking, the predicted magnitudes are in decent, good agreement with experimental results,

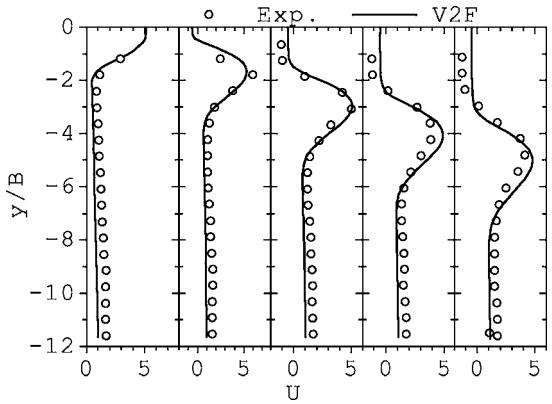

Fig. 11 Distribution of the velocity parallel to the wall at $x/B=1$, 2, 3, 4, and 5

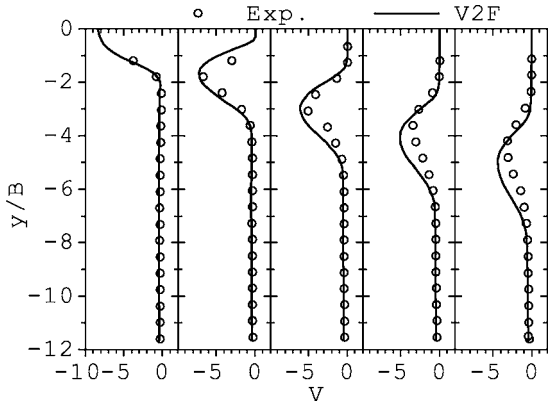

Fig. 12 Distribution of the velocity normal to the wall at x/B =–1, 2, 3, 4, and 5

better than the 90-CH5 case, although there are some underpredictions. This underprediction explains the overprediction of the trajectory because underpredicted turbulence results in the underpredicted mixing between the jet and cross flow, or, in other words, the jet flow is overpreserved. One should remember the contradiction in the 90-CH5 case, where underprediction of the turbulence resulted in an overpredicted mixing.

Figure 14 shows the normalized turbulent shear stress distribution of the 60-M9 case. The numerical results are in decent agreement with the experiments. The agreement is better than that for the turbulent kinetic energy. However, very close to the jet inflow

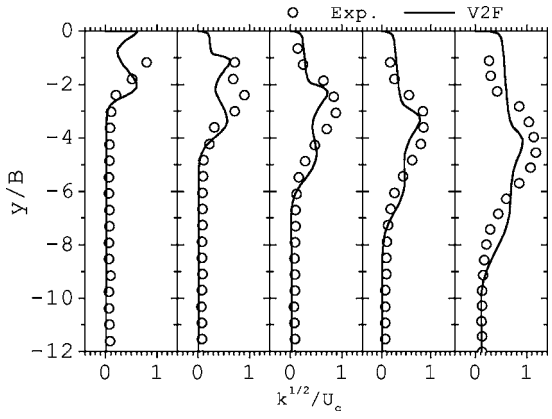

Fig. 13 Normalized distribution of the kinetic energy $[(\overline{u'u'}+\overline{v'v'})^{0.5}/U_c]$ at x/B=1, 2, 3, 4, and 5

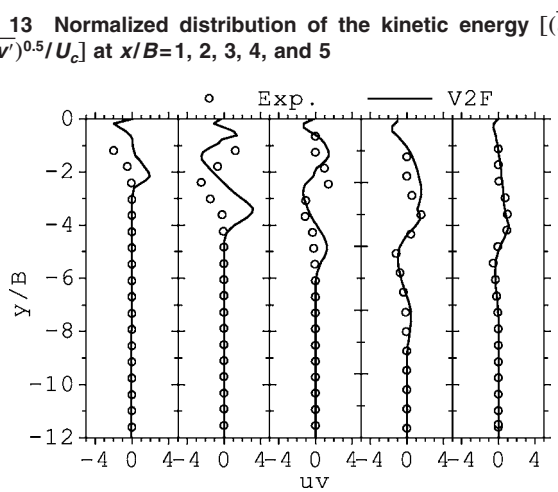

Fig. 14 Normalized distribution of the turbulent shear stress $[10\,\mathrm{sign}(\overline{u'v'})|\overline{u'v'}|^{0.5}/U_c]$ at x/B=1, 2, 3, 4, and 5

region (x/B=1, and 2), the shape of the distribution from the numerical prediction is misplaced compared to the experiments. This could be due to the very strong shear at the vicinity of the jet inflow and that the resolution of the experiments is insufficient in this region.

4.3 Other Injection Angles and Blowing Ratios. Figure 15(*a*) shows the streamline trace for the 30-M4 case. There is no separation observed downstream of the jet inflow. This is also observed in the experiments.

If the jet angle is increased up to 40 deg, the recirculation can obviously be observed, as shown in Fig. 15(*b*). The size of the recirculation region will be further increased for the 60 deg case, as shown in Fig. 10(*d*).

At a larger blowing ratio, for the 40-M4 case, the recirculation size becomes smaller, as shown in Fig. 15(*c*), compared to the lower blowing ratio case 40-M2 (Fig. 15(*b*)). This is different from the 60 deg cases (cf. Fig. 15). Therefore, at jet angles smaller than 45 deg, the larger the blowing ratio results in a smaller recirculation region downstream of the jet inflow, where the V component is smaller than the U component. These recirculations have a large influence on the mixing between the jet and mainstream fluids.

The effects of the jet angle on the mixing can be qualitatively observed from Figs. 15(*d*)–15(*f*). As shown, for the same blowing ratio, with the increase of the jet angle, the mixing increases, i.e., more hot fluids are entrained into the cooling jet flow. The better mixing results in worse film-cooling effectiveness, and the effects will be shown in the next section quantitatively.

4.4 Film-Cooling Effectiveness. In this section, CFD predictions of the film-cooling effectiveness are presented. Effects of injection angle and blowing ratio are provided.

4.4.1 Effect of Injection Angles. Figure 16 shows the effect of the jet angle on the film-cooling effectiveness for the blowing ratio M=2. Generally speaking, at large jet angles (e.g., 60 and 90 deg), the effectiveness is very low because of the strong mixing between the jet and cross flow, as discussed in the previous sections. At the close jet inflow region, the 30 deg jet performs the best. As discussed previously, there is no recirculation observed downstream of the jet inflow, so that the mixing between the jet flow and mainstream is weak or the insulation effect is good. The 40 deg jet also performs good, although it has a small recirculation. The 40 deg jet even has a better performance at the far downstream region ($x/B>40$). As for the 16 deg jet, the performance is good very close to the jet inflow region, but the adiabatic effect decays quickly downstream. Therefore, the optimal jet angle seems to be between 30 and 40 deg.

4.4.2 Effect of Blowing Ratio. Figure 17 shows the influence of the blowing ratios on the film-cooling effectiveness for the 30 deg jet, which performs best among the studied angles. For this angle, the film-cooling effectiveness decreases with the increase of the blowing ratio for $M>1$. However, the effectiveness will also decrease if the blowing ratio decreases below unity. Therefore, the ideal velocity ratio is around 1.0. This is in accordance with the study of Wang et al. [2].

5 Conclusions

A numerical and experimental study has been carried out for a slot film-cooling configuration with various blowing angles and ratios. Detailed experimental results of the mean and fluctuation velocity have been obtained in realistic environments, which could be used for validation of the computer code. In addition, the following points have been reached:

1. For the numerical simulation, fully developed mainstream flow inlet with a uniform jet flow inlet is the appropriate

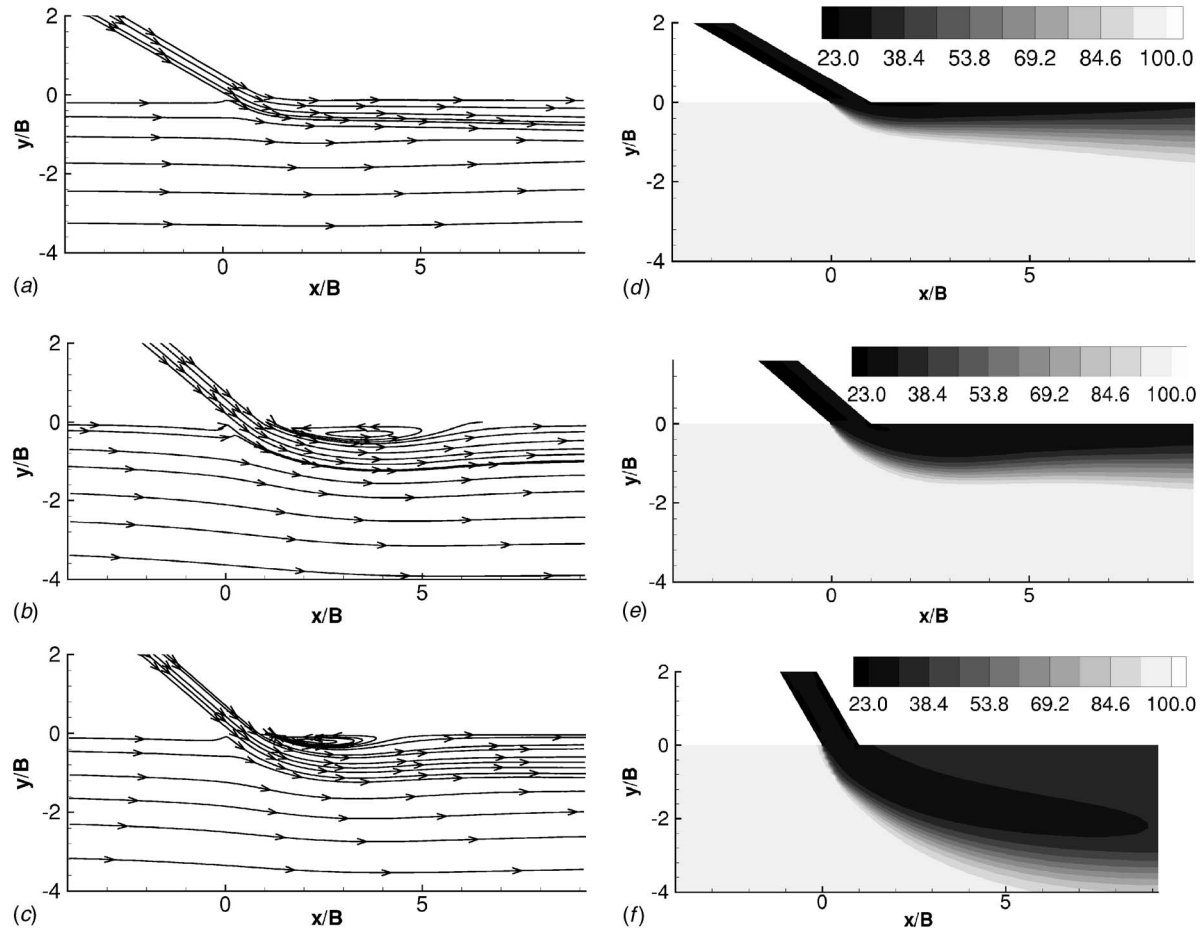

Fig. 15 Streamline traces and temperature distributions

boundary conditions, compared to the experimental data. The boundary condition has a big effect on the predicted velocity profile, but much less on the film-cooling effectiveness.

2. Generally speaking, the RSTM provides a more faithful prediction of the mean and rms velocity distributions. However, the unrealistic bulge around the reattachment point still exists. The V2F and the SST models provide essentially the same results.
3. The V2F model provides a good prediction of the mean velocity components. The agreement of the turbulent shear stresses between the experiments and numerical computations is decent. However, the profile of the turbulent kinetic energy cannot be faithfully captured.
4. The recirculation still exists for 40 deg jet, but vanishes for 30 deg and 16 deg jet. The existence of the recirculation depends only on the jet angle, but the size of the recirculation depends on the cross-to-jet flow ratio. For the 40 deg jets, stronger jet flow seems to generate a smaller recirculation zone, mainly because the mainstream component is larger than the normal mainstream component when the blowing angle is <45 deg.

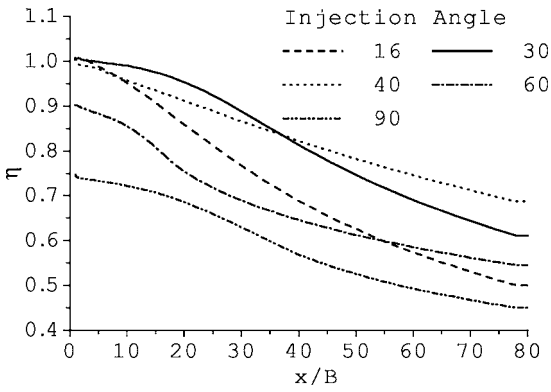

Fig. 16 Film-cooling effectiveness for various injection angles, with $M=2$

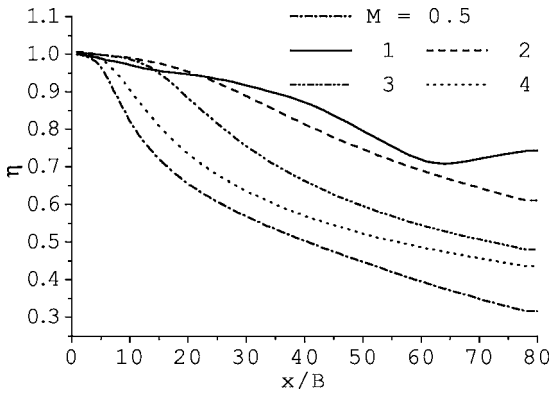

Fig. 17 Film-cooling effectiveness for various blowing ratio, with $\alpha=30$ deg

5. Among the tested blowing angles, the 30 deg jet provides the highest film-cooling effectiveness. In addition, the appropriate blowing ratio is ~1.0.

The weakness of the steady RANS method have to be pointed out here: For flow regions with significant low-frequency turbulent kinetic energies, the turbulence may be severely underpredicted, whereas at regions with large velocity gradients (e.g., at the recirculation regions), the turbulence may be largely overpredicted. For more faithful predictions of the velocity fluctuations, better turbulence models or maybe unsteady RANS or large eddy simulation are necessary. In addition, higher-order turbulent heat flux models might be needed for improvements in predicting the temperature distribution.

Acknowledgment

The Swedish Energy Agency (STEM) financially supported this research work.

Nomenclature

B = slot width, m
H = channel height, m
M = blowing ratio, $M=\rho U_j/\rho U_c$
P = pressure, Pa
P_r = Prandtl number
Re = Reynolds number $\mathrm{Re}=(U_b D_h)/\nu$
T = temperature, °C
T_c = coolant temperature, °C
T_f = film temperature, °C
T_g = mainstream fluid temperature, °C
T_w = wall surface temperature, °C
$\overline{-u_i' u_j'}$ = specific Reynolds stress tensor, m^2/s^2
$c_p\overline{t' u_j'}$ = specific turbulent heat fluxes, m^3/s^3
U_c = bulk mainstream flow velocity, m/s
U_j = bulk jet velocity, m/s
η = film cooling effectiveness $\eta=(T_g-T_f)/(T_g-T_c)$
ν = kinematic viscosity, m^2/s
ν_T = turbulent kinematic viscosity, m^2/s
σ_T = turbulent Prandtl number

References

[1] Goldstein, R. J., 1971, "Film Cooling," Adv. Heat Transfer, **7**, pp. 321–379.
[2] Wang, T., Chintalapati, S., Bunker, R. S., and Lee, C. P., 2000, "Jet Mixing in a Slot," Exp. Therm. Fluid Sci., **22**(1-2), pp. 1–17.
[3] Cho, H. H., and Ham, J. K., 2002, "Influence of Injection Type and Feed Arrangement on Flow and Heat Transfer in an Injection Slot," ASME J. Turbomach., **124**(1), pp. 132–141.
[4] O'Malley, K., 1984, "Theoretical Aspects of Film Cooling," Ph.D. thesis, University of Oxford.
[5] Fitt, A. D., Ockendon, J. R., and Jones, T. V., 1985, "Aerodynamics of Slot-Film Cooling: Theory and Experiment," J. Fluid Mech., **160**, pp. 15–30.
[6] Bergeles, G., Gosman, A. D., and Launder, B. E., 1978, "The Turbulent Jet in a Cross Stream at Low Injection Rates: A Three-dimensional Numerical Treatment," Numer. Heat Transfer, **1**, pp. 217–242.
[7] Andreopoulos, J., 1982, "Measurements on a Pipe Flow Issuing Perpendicular Into a Cross Stream," ASME J. Fluids Eng., **104**(4), pp. 493–499.
[8] Metzger, D. E., Carper, H. J., and Swank, L. R., 1968, "Heat Transfer Film Cooling Near Nontangential Injection Slots," ASME J. Eng. Power, **90**(2), pp. 157–163.
[9] Chen, K. S., and Hwang, J. Y., 1991, "Experimental Study on the Mixing of One-and Dual-Line Heated Jets With a Cold Crossflow in a Confined Channel," AIAA J., **29**(3), pp. 353–360.
[10] Teekaram, A. J. H., Forth, C. J. P., and Jones, T. V., 1991, "Film Cooling in the Presence of Mainstream Pressure Gradients," ASME J. Turbomach., **113**(3), pp. 484–492.
[11] Aly, S. E., 2000, "Injection Effect on Two Dimensional Boundary Layer," Energy Convers. Manage., **41**(6), pp. 539–550.
[12] Jones, W. P., and Wille, M., 1996, "Large-Eddy Simulation of a Plane Jet in a Cross-Flow," Int. J. Heat Fluid Flow, **17**(3), pp. 296–306.
[13] Sarkar S., and Bose, T. K., 1995, "Comparison of Different Turbulence Models for Prediction of Slot-Film Cooling: Flow and Temperature-Field," Numer. Heat Transfer, Part B, **28**(2), pp. 217–238.
[14] Kassimatis, P. G., Bergeles, G. C., Jones, T. V., and Chew, J. W., 2000, "Numerical Investigation of the Aerodynamics of the Near-Slot Film Cooling," Int. J. Numer. Methods Fluids, **32**(1), pp. 85–104.
[15] Menter, F. R., 1994, "Two-Equation Eddy-Viscosity Turbulence Models for Engineering Applications," AIAA J., **32**(8), pp. 1598–1605.
[16] Durbin, P. A., 1995, "Separated Flow Components With $k-\epsilon-\overline{v^2}$ Model," AIAA J., **33**(4), pp. 659–664.
[17] Wilcox, D. C., 1998, "*Turbulence Modelling for CFD*," DCW Industries Inc., La Cañada, CA.
[18] Launder, B. E., Reece, G., and Rodi, W. 1975, "Progress in the Development of a Reynolds-Stress Turbulence Closure," J. Fluid Mech., **68**(3), pp. 537–566.
[19] Rokni, M., 2000, "A New Low-Reynolds Version of an Explicit Algebraic Stress Model for Turbulent Convection Heat Transfer in Ducts," Numer. Heat Transfer, Part B, **37**, pp. 331–363.
[20] Jia, R., and Sundén, B., 2003, "A Multi-Block Implementation Strategy for a 3D Pressure-Based Flow and Heat Transfer Solver," Numer. Heat Transfer, Part B, **44**(5), pp. 457–472.
[21] Rhie, C. M., and Chow, W. L., 1983, "Numerical Study of the Turbulent Flow Past an Airfoil With Trailing Edge Separation," AIAA J., **21**, pp. 1525–1532.
[22] Van Doormal, J. P., and Raithby, G. D., 1984, "Enhancements of the SIMPLE Method for Predicting Incompressible Fluid Flows," Numer. Heat Transfer, **7**, pp. 147–163.

Journal of Turbomachinery

Erratum

Erratum: "Advanced High-Turning Compressor Airfoils for Low Reynolds Number Condition—Part II: Experimental and Numerical Analysis" [Journal of Turbomachinery, 2004, 126(4), pp. 482–492]

Heinz-Adolf Schreiber, Wolfgang Steinert, Toyotaka Sonoda, and Toshiyuki Arima

- Page 483, left column, 19 lines from the top, "Fig. 1 (left)" should be replaced by "Fig. 5 (left)".
- Page 483, left column, 21 lines from the top, "see Fig. 2" should be replaced by "see Fig. 12 (left)".
- Page 483, left column, 33 lines from the top, "Figures 3 and 4" should be replaced by "Figures 1 and 2".

